IMPACT OF DEEP OCEANIC PROCESSES ON CIRCULATION AND CLIMATE VARIABILITY: EXAMPLES FROM THE MEDITERRANEAN SEA AND THE GLOBAL OCEAN

EDITED BY: Vincenzo Artale, Nadia Lo Bue, Katrin Schroeder and Vassilis Zervakis

PUBLISHED IN: Frontiers in Marine Science

frontiers Research Topics

ISSN 1664-8714
ISBN 978-2-88974-240-0
DOI 10.3389/978-2-88974-240-0

About Frontiers

Frontiers is more than just an open-access publisher of scholarly articles: it is a pioneering approach to the world of academia, radically improving the way scholarly research is managed. The grand vision of Frontiers is a world where all people have an equal opportunity to seek, share and generate knowledge. Frontiers provides immediate and permanent online open access to all its publications, but this alone is not enough to realize our grand goals.

Frontiers Journal Series

The Frontiers Journal Series is a multi-tier and interdisciplinary set of open-access, online journals, promising a paradigm shift from the current review, selection and dissemination processes in academic publishing. All Frontiers journals are driven by researchers for researchers; therefore, they constitute a service to the scholarly community. At the same time, the Frontiers Journal Series operates on a revolutionary invention, the tiered publishing system, initially addressing specific communities of scholars, and gradually climbing up to broader public understanding, thus serving the interests of the lay society, too.

Dedication to Quality

Each Frontiers article is a landmark of the highest quality, thanks to genuinely collaborative interactions between authors and review editors, who include some of the world's best academicians. Research must be certified by peers before entering a stream of knowledge that may eventually reach the public - and shape society; therefore, Frontiers only applies the most rigorous and unbiased reviews.
Frontiers revolutionizes research publishing by freely delivering the most outstanding research, evaluated with no bias from both the academic and social point of view. By applying the most advanced information technologies, Frontiers is catapulting scholarly publishing into a new generation.

What are Frontiers Research Topics?

Frontiers Research Topics are very popular trademarks of the Frontiers Journals Series: they are collections of at least ten articles, all centered on a particular subject. With their unique mix of varied contributions from Original Research to Review Articles, Frontiers Research Topics unify the most influential researchers, the latest key findings and historical advances in a hot research area! Find out more on how to host your own Frontiers Research Topic or contribute to one as an author by contacting the Frontiers Editorial Office: frontiersin.org/about/contact

IMPACT OF DEEP OCEANIC PROCESSES ON CIRCULATION AND CLIMATE VARIABILITY: EXAMPLES FROM THE MEDITERRANEAN SEA AND THE GLOBAL OCEAN

Topic Editors:
Vincenzo Artale, Italian National Agency for New Technologies, Energy and Sustainable Economic Development (ENEA), Italy
Nadia Lo Bue, National Earthquake Observatory (INGV), Italy
Katrin Schroeder, Institute of Marine Science, National Research Council (CNR), Italy
Vassilis Zervakis, School of Environment, University of the Aegean, Greece

Citation: Artale, V., Lo Bue, N., Schroeder, K., Zervakis, V., eds. (2022). Impact of Deep Oceanic Processes on Circulation and Climate Variability: Examples From the Mediterranean Sea and the Global Ocean. Lausanne: Frontiers Media SA. doi: 10.3389/978-2-88974-240-0

Table of Contents

frontiers in Marine Science

EDITORIAL
published: 10 December 2021
doi: 10.3389/fmars.2021.801479

Editorial: Impact of Deep Oceanic Processes on Circulation and Climate Variability: Examples From the Mediterranean Sea and the Global Ocean

Nadia Lo Bue[1]*, *Vincenzo Artale*[2] and *Katrin Schroeder*[3]

[1] Istituto Nazionale di Geofisica e Vulcanologia (INGV), Rome, Italy, [2] National Research Council (CNR), Rome, Italy, [3] Institute of Marine Science, National Research Council (CNR), Rome, Italy

Keywords: abyssal ocean, deep dynamic process, climate variability, mixing process, Mediterranean Sea, global ocean, multidisciplinary approach

Editorial on the Research Topic

Impact of Deep Oceanic Processes on Circulation and Climate Variability: Examples From the Mediterranean Sea and the Global Ocean

INTRODUCTION AND SUMMARY

The ocean is a crucial component of the Earth's climate system. Storing heat and carbon, the ocean stabilizes global climate, nurtures biodiversity, and directly supports human well-being through food and energy resources. Today it is well-known that ocean warming is the result of an interplay of many complex processes that, in spite of the key role in the Earth's energy budget, are still far from being fully understood. More than 93% of the heating since the 1970s due to the greenhouse effect and other human activities has been absorbed by the ocean (Rhein et al., 2013). The intake of heat and CO_2 in the ocean's surface is redistributed throughout the ocean depths by the overturning circulation. Exchange across the ocean's turbulent surface boundary layer can happen rapidly, in hours or days, and significant exchange of water between the boundary layer and the stratified main thermocline occurs over timescales of years to decades. Deep water takes many decades to millennia to return to the surface, acting as long-term storage for heat and CO_2 and thereby mitigating the short-term impacts of climate change. The understanding of mechanisms and rates that control the bottom flows is essential to quantify re-transfer toward the upper layers of the energy stored at the bottom layers. These processes are significantly affecting the ocean system as a whole and could contribute to accelerating the rising climate trends (thermohaline circulation, sea-level rise, and ocean acidification).

The Research Topic about "*Impact of Deep Oceanic Processes on Circulation and Climate Variability*" happens during an exceptional time for ocean studies. In fact, the decade from 2021 to 2030, has been declared as the Decade of Ocean Science for Sustainable Development by the United Nations, aimed at providing a common framework to ensure that ocean science can fully support countries to achieve the 2030 Agenda for Sustainable Development. The Ocean Decade gives a "once in a lifetime" opportunity to create a new foundation across the science-policy interface to strengthen the management of our oceans and coasts for the benefit of humanity.

OPEN ACCESS

Edited and reviewed by:
Frédéric Cyr,
Fisheries and Oceans, Canada

***Correspondence:**
Nadia Lo Bue
nadia.lobue@ingv.it

Specialty section:
This article was submitted to Physical Oceanography, a section of the journal Frontiers in Marine Science

Received: *25 October 2021*
Accepted: *22 November 2021*
Published: *10 December 2021*

Citation:
Lo Bue N, Artale V and Schroeder K (2021) Editorial: Impact of Deep Oceanic Processes on Circulation and Climate Variability: Examples From the Mediterranean Sea and the Global Ocean. Front. Mar. Sci. 8:801479. doi: 10.3389/fmars.2021.801479

This Research Topic aims at stressing the urgent need of improving knowledge about the impacts of key deep processes, for better contributing in the assessment of climate variability and change. For a long time, classical theories about the abyssal ocean (Stommel and Arons, 1960; Munk, 1966) supported the general idea that ocean deep circulation was characterized by quasi-stationary motions, excluding the study of deep processes from the mechanisms that can affect global circulation and climate variability. The underestimation of the abyssal ocean variability has continued to persist for decades (Bagnell and De Vries, 2021), due also to the difficulty to obtain reliable observations below 2,000 m depth, as Artale et al. (2018) demonstrated for the Mediterranean Sea. The awareness of the unsteady state of the deep ocean is a fairly recent achievement. These recent assumptions (Ferrari et al., 2016; MacKinnon et al., 2017; McDougall and Ferrari, 2017; Holmes et al., 2018; Polzin and McDougall, 2021) are shedding light on the rising need to fully understand the mechanisms that can induce instability of the deep layers with a particular look at the role that seafloor roughness and shape have in triggering bottom mixing processes (de Lavergne et al., 2016; Naveira Garabato et al., 2019; Spingys et al., 2021). Observational datasets over many decades are required to document, understand, and predict the climate system as a whole. This is key to explain the role of the deep ocean as an energy reservoir, and how deep processes can redistribute such energy affecting ocean circulation and, afterwards, giving consequences on the future climate. Also, it represents an essential requirement to detect and attribute changes driven by human activities and to predict how the climate system will likely behave in the future.

The Mediterranean Sea, due to its peculiar ocean circulation characteristics, can be considered, among all marginal seas, a suitable laboratory for investigating almost all oceanic physical mechanisms of global interest, such as deep water formation/deep convection, mixing processes along the entire water column (including bottom mixing), strait dynamics, advective-convective feedbacks driving the ocean variability, and abyssal dynamic internal exchange mechanisms (Ferron et al., 2017; Vladoiu et al., 2019). All these studies are facilitated in the Mediterranean Sea, thanks to its easy accessibility, to its mild climate and weaker storms, and also to the scales of variability (in time and space) that are shorter compared to the global ocean: here the typical Rossby radius and/or the size and time of variability of mesoscale gyres are one order of magnitude less compared to those of the global ocean.

On the whole, to understand past and future climate changes, the characterization of the still unexplored deep dynamics aims to provide crucial results to support new interpretations of the paleo circulation and of those processes that have influenced ventilation and water masses overturning in the past. These new insights will also be essential for leading, in the near future, new tailored parameterizations for new generation climate numerical models taking into account adequately the dynamics below 2,000 m depth.

CONTRIBUTION TO THE FIELD, GAPS, AND PERSPECTIVES

This article collection was conceived in the framework of MedClivar (http://www.medclivar.eu/), a scientific network to promote better cooperation among different scientific disciplines, to develop a multidisciplinary vision of the evolution of the Mediterranean climate. Extending this concept also to the global ocean, the aim is to investigate the impacts associated with climate evolution, and to provide knowledge through studies that integrate all components of the climate on time scales ranging from paleo-reconstructions to future climate scenarios for contributing in the development of new adaptation strategies.

As assumed by von Schuckmann et al. (2018), the improvement of our understanding of the climate system also passes through the monitoring of heat content, including that below 2,000 m. However, the needs for and uses of deep ocean data extend well-beyond closing the heat budget in the global ocean as well as in the Mediterranean Sea. Deep ocean data is needed to initialize and constrain ocean models and improve their representation of mixing of heat downwards/upwards within the deep layers.

In this Research Topic, several studies addressing the study of deep processes through *in situ* observations and modeling spanning over different geographic areas have been collected. The collected papers get a varied overview of methodologies today used to investigate the impact that deep processes can have on climate variability, pointing out the importance of multidisciplinarity in addressing this kind of issue. They focus on the Mediterranean as a whole (Sampatakaki et al.; Amitai et al.; Li and Tanhua; Bouzaiene et al.), or just regions of the Western (Durante et al.; Ferron et al.; the two works by Vargas-Yáñez et al. (2021); García-Lafuente et al.) or Eastern (Mihanović et al.; Menna et al.; Sisma-Ventura et al.; Cardin et al.) Mediterranean Sea. But there are also examples of deep oceanic processes coming from other areas of the global ocean, i.e., the Western Pacific Ocean (Wang et al.), the Southern Ocean (Mizuta et al.), and the Japan Sea (Shin et al.). This collection also provides a variety of approaches to investigate the oceanic processes. The lagrangian approach, which is typically adopted for the surface ocean (Menna et al.; Bouzaiene et al.), with inferences for the deeper layers, or in combination with a multiplatform and integrated model experiment (such as in Mihanović et al.), has potential to be applied to deeper layers as well, with the more and more expanding (deep) Argo network. Other papers rely on eulerian data (from moorings and buoys, Wang et al.; Mizuta et al.; García-Lafuente et al.; Shin et al.) or CTD/rosette data collected by Research Vessels (Durante et al.; Ferron et al.; Li and Tanhua; the two works by Vargas-Yáñez et al. (2020); Sisma-Ventura et al.) or both (Cardin et al.). Purely modeling studies are also represented, see for instance (Amitai et al.; Sampatakaki et al.), the latter one being a paleoceanographic application.

Although the topic was addressing deep ocean processes in a broad geographical sense, it is worth noting that most of the papers focused on the Mediterranean area, confirming this area

as most accessible for studying such kinds of topics and many other fundamental oceanographic processes.

Overall, the papers in this collection have evidenced that observations in the deep ocean, both in the Mediterranean Sea and in the open ocean, are still too sparse and fragmentary and that a huge gap still exists between modeling and observational approaches both in the physical and biochemical field. Especially for this latter, the lack of data in the deep ocean is due not only to the big challenge in observation, but also to the sensor technology, which is still not fully reliable for this extreme environment (Bindoff et al., 2019).

The existing gaps highlight how much the integrated and multidisciplinary approach in the study of deep ocean processes is now an urgent question, both for the knowledge improvement and for the efficient streamlining of the existing observational infrastructures such as EMSO and Deep-Argo (Gasparin et al., 2020; Lo Bue et al., 2021). Besides, due to its intrinsic characteristics and considering its short-scale variability (Malanotte-Rizzoli et al., 2014), the Mediterranean area results in a suitable area for developing new integrated strategies able to link theory, observations, and implementation of new numerical models in the near future.

AUTHOR CONTRIBUTIONS

All the authors listed have made substantial, direct, and intellectual contributions to the work. NLB designed the structure of this editorial, contributed to its drafting, and synthesized the contributions received and made extensive editing. VA participated in the document design, he provided substantial contributions and suggestions throughout the document. KS participated in the document design, contributed to the drafting of the overall manuscript, and helped with its revision. All authors approved its publication.

ACKNOWLEDGMENTS

We thank all authors, reviewers, and editors that have contributed to this Research Topic and the MedClivar community to endorse and support it.

REFERENCES

Artale, V., Falcini, F., Marullo, S., Bensi, M., Kokoszka, F., Iudicone, D., et al. (2018). Linking mixing processes and climate variability to the heat content distribution of the Eastern Mediterranean abyss. *Sci. Rep.* 8:11317. doi: 10.1038/s41598-018-29343-4

Bagnell, A., and De Vries, T. (2021). 20th century cooling of the deep ocean contributed to delayed acceleration of Earth's energy imbalance. *Nat. Commun.* 12:4604. doi: 10.1038/s41467-021-24472-3

Bindoff, N. L., Cheung, W. W. L., Kairo, J. G., Arístegui, J., Guinder, V. A., Hallberg, R., et al. (2019). "Changing ocean, marine ecosystems, and dependent communities," in *IPCC Special Report on the Ocean and Cryosphere in a Changing Climate*, eds H.-O. Pörtner, D. C. Roberts, V. Masson-Delmotte, P. Zhai, M. Tignor, E. Poloczanska, K. Mintenbeck, A. Alegría, M. Nicolai, A. Okem, J. Petzold, B. Rama, and N. M. Weyer.

de Lavergne, C., Madec, G., Le Sommer, J., Nurser, G. A. J., and Naveira Garabato, A. C. (2016). On the consumption of Antarctic Bottom Water in the abyssal ocean. *J. Phys. Oceanogr.* 46, 635–661. doi: 10.1175/JPO-D-14-0201.1

Ferrari, R., Mashayek, A., McDougall, T. J., Nikurashin, M., and Campin, J. M. (2016). Turning ocean mixing upside down. *J. Phys. Oceanogr.* 46, 2239–2261. doi: 10.1175/JPO-D-15-0244.1

Ferron, B., Bouruet Aubertot, P., Cuypers, Y., Schroeder, K., and Borghini, M. (2017). How important are diapycnal mixing and geothermal heating for the deep circulation of the Western Mediterranean? *Geophys. Res. Lett.* 44, 7845–7854. doi: 10.1002/2017GL074169

Gasparin, F., Hamon, M., Rémy, E., and Le Traon, P.-Y. (2020). How deep argo will improve the deep ocean in an ocean reanalysis. *J. Clim.* 33, 77–94. doi: 10.1175/JCLI-D-19-0208.1

Holmes, R. M., de Lavergne, C., and McDougall, T. J. (2018). Ridges, seamounts, troughs, and bowls: topographic control of the dianeutral circulation in the abyssal ocean. *J. Phys. Oceanogr.* 48, 861–882. doi: 10.1175/JPO-D-17-0141.1

Lo Bue, N., Best, M. M. R., Embriaco, D., Abeysirigunawardena, D., Beranzoli, L., Dewey, R. K., et al. (2021). The importance of marine research infrastructures in capturing processes and impacts of extreme events. *Front. Mar. Sci.* 8:626668. doi: 10.3389/fmars.2021.626668

MacKinnon, J. A., Zhao, Z., Whalen, C. B., Waterhouse, A. F., Trossman, D. S., Sun, O. M., et al. (2017). Climate process team on internal wave–driven ocean mixing. *Bull. Am. Meteorol. Soc.* 98, 2429–2454. doi: 10.1175/BAMS-D-16-0030.1

Malanotte-Rizzoli, P., Artale, V., Borzelli-Eusebi, G. L., Brenner, S., Crise, A., Gacic, M., et al. (2014). Physical forcing and physical/biochemical variability of the Mediterranean Sea: a review of unresolved issues and directions for future research. *Ocean Sci.* 10, 281–322. doi: 10.5194/os-10-281-2014, 2014

McDougall, T. J., and Ferrari, R. (2017). Abyssal upwelling and downwelling driven by near-boundary mixing. *J. Phys. Oceanogr.* 47, 261–283. doi: 10.1175/JPO-D-16-0082.1

Munk, W. (1966). Abyssal recipes. *Deep Sea Res. Oceanogr. Abstr.* 13, 707–730. doi: 10.1016/0011-74716690602-4

Naveira Garabato, A. C., Frajka-Williams, E. E., Spingys, C. P., Legg, S., Polzin, K. L., Forryan, A., et al. (2019). Rapid mixing and exchange of deep-ocean waters in an abyssal boundary current. *Proc. Natl. Acad. Sci. U.S.A.* 116, 13233–13238. doi: 10.1073/pnas.1904087116

Polzin, K. L., and McDougall, T. J. (2021). "Chapter 7: Mixing at the ocean's bottom boundary," in *Ocean Mixing*, eds M. Meredith and A. N. Garabato (Elsevier), 145–180. doi: 10.1016/B978-0-12-821512-8.00014-1

Rhein, M., Rintoul, S. R., Aoki, S., Campos, E., Chambers, D., Feely, R. A., et al. (2013). "Observations: ocean," in *Climate Change 2013: The Physical Science Basis. Contribution of Working Group I to the Fifth Assessment Report of the Intergovernmental Panel on Climate Change*, eds T. F. Stocker, D. Qin, G.- K., Plattner, M. Tignor, S. K. Allen, J. Boschung, A. Nauels, Y. Xia, V. Bex, and P. M. Midgley (Cambridge; New York, NY: Cambridge University Press), 255–317.

Spingys, C. P., Naveira Garabato, A. C., Legg, S., Polzin, K. L., Povl Abrahamsen, E., Buckingham, C. E., et al. (2021). Mixing and transformation in a deep western boundary current: a case study. *J. Phys. Oceanogr.* 51, 1205–1222. doi: 10.1175/JPO-D-20-0132.1

Stommel, H., and Arons, A. B. (1960). On the abyssal circulation of the world ocean-II. An idealized model of the circulation pattern and amplitude in oceanic basins. *Deep Sea Res.* 6, 217–233.

Vargas-Yáñez, M., Juza, M., Balbín, R., Velez-Belchí, P., García-Martínez, M. C., Moya, F. et al. (2020). Climatological hydrographic properties and water mass transports in the balearic channels from repeated observations over 1996–2019. *Front. Mar. Sci.* 7:568602. doi: 10.3389/fmars.2020.568602

Vargas-Yáñez, M., Juza, M., García-Martínez, M. C., Moya, F., Balbín, R., Ballesteros, E., et al. (2021). Long-term changes in the water mass properties in the balearic channels over the period 1996–2019. *Front. Mar. Sci.* 8:640535. doi: 10.3389/fmars.2021.640535

Vladoiu, A., Bouruet-Aubertot, P., Cuypers, Y., Ferron, B., Schroeder, K., Borghini, M., et al. (2019). Mixing efficiency from microstructure measurements

in the Sicily Channel. *Ocean Dyn.* 69, 787–807. doi: 10.1007/s10236-019-01274-2

von Schuckmann, K., Le Traon, P.-Y., Smith, N., Pascual, A., Brasseur, P., Fennel, K., et al. (2018). Copernicus marine service ocean state report. *J. Oper. Oceanogr.* 11, S1–S142. doi: 10.1080/1755876X.2018.1489208

Conflict of Interest: The authors declare that the research was conducted in the absence of any commercial or financial relationships that could be construed as a potential conflict of interest.

Publisher's Note: All claims expressed in this article are solely those of the authors and do not necessarily represent those of their affiliated organizations, or those of the publisher, the editors and the reviewers. Any product that may be evaluated in this article, or claim that may be made by its manufacturer, is not guaranteed or endorsed by the publisher.

frontiers in Marine Science

ORIGINAL RESEARCH
published: 26 June 2020
doi: 10.3389/fmars.2020.00486

Analysis of the Surface Dispersion in the Mediterranean Sub-Basins

Maher Bouzaiene[1], Milena Menna[2], Pierre-Marie Poulain[2], Antonio Bussani[2] and Dalila Elhmaidi[1]*

[1] Thermal Radiation Laboratory, Faculty of Sciences of Tunis, University of Tunis El Manar, Tunis, Tunisia, [2] Division of Oceanography, National Institute of Oceanography and Experimental Geophysics, Sgonico, Italy

Surface dispersion properties give an immediate characterization of the spreading of passive and active tracers in the ocean, like pollutant and marine species. The Mediterranean sub-basins (Tyrrhenian, Adriatic, Ionian, Levantine and Aegean) are known as complex dynamic regions due to the presence of coherent structures on different motion scales. This paper focus on dispersion of the surface Mediterranean flow using the surface current data derived from two different drifter designs: the Coastal Ocean Dynamics Experiment (CODE) and the Surface Velocity Program (SVP) drifters. The absolute dispersion for small time scales (<2 days) shows similar anisotropic quasi-ballistic regimes in the five sub-basins. For intermediate time scales (2–15 days), the absolute dispersion shows the occurrence of an elliptic regime in all the Mediterranean sub-basins except in the Adriatic Sea, where the dominance of a hyperbolic regime is observed. The relative dispersion statistics show the presence of a non-local exponential regime in the Tyrrhenian sub-basin, with spatial scale smaller than the internal Rossby Radius of deformation D_I. For spatial scales close to D_I, two local relative dispersion regimes are found due to the influence of sub-basin scale structures: a Richardson regime in the Tyrrhenian and Aegean sub-basins and a shear/ballistic regime in other sub-basins. Furthermore, for large time scale (>15 days) and spatial scale larger than D_I, our results emphasize a similarity in all the sub-basins with the presence of a quasi Random-walk regime and a quasi diffusive regime for the absolute and relative dispersion, respectively.

Keywords: Mediterranean sub-basins, eddies, drifters, absolute dispersion, relative dispersion

OPEN ACCESS

Edited by:
Vincenzo Artale, Italian National Agency for New Technologies, Energy and Sustainable Economic Development (ENEA), Italy

Reviewed by:
Ru Chen, Tianjin University, China
Lei Zhou, Shanghai Jiao Tong University, China
Andrew Poje, The Graduate Center, The City University of New York, United States

****Correspondence:***
Maher Bouzaiene
maherbouzaiene73@gmail.com

Specialty section:
This article was submitted to Physical Oceanography, a section of the journal Frontiers in Marine Science

Received: *17 February 2020*
Accepted: *02 June 2020*
Published: *26 June 2020*

Citation:
Bouzaiene M, Menna M, Poulain P-M, Bussani A and Elhmaidi D (2020) Analysis of the Surface Dispersion in the Mediterranean Sub-Basins. Front. Mar. Sci. 7:486. doi: 10.3389/fmars.2020.00486

INTRODUCTION

The Mediterranean sub-basins (Tyrrhenian, Adriatic, Ionian, Levantine and Aegean, see **Figure 1A** for geographical references) are characterized by different dynamics and high variability of surface currents. The chaotic nature of each sub-basin lead to the generation of numerous submesoscale (∼1 km) and mesoscale (>10 km) structures (D'Ovidio et al., 2004, 2008). The Mediterranean coherent structures driven by wind and/or topography and located in a fixed geographical area are called gyres, whereas the structures driven by the instability of strong coastal currents that frequently changes their location and lifetime are named eddies (Poulain et al., 2012b).

The westernmost part of the western Mediterranean (WWM, see the **Figure 1A** for geographical limits) is characterized by strong coastal currents and mesoscale and basin-scale eddies and gyres (**Figure 1**; Zambianchi et al., 2017; Bouzaiene et al., 2018; Aulicino et al., 2019). The surface mean basin-scale circulation of the WWM is cyclonic with the dominance of zonal and meridional motions in the Algerian and the Liguro–Provençal sub-basins, respectively (Poulain et al., 2012a; Renault et al., 2012). In the northern Tyrrhenian sub-basin the Mistral wind blowing into the Strait

of Bonifacio creates the northern tyrrhenian gyre (NTG) with the presence of a strong coastal cyclonic current along the Italian coasts which is a branch of the algerian current (AC) that forming cyclonic mesoscale eddies (see for details, Poulain et al., 2013; **Figure 1A**). In the southern part of the Tyrrhenian Sea, a part of the AC enters in the Sicily Channel and formed the Atlantic Ionian Stream (AIS). The surface circulation of the Sicily Channel is characterized by numerous mesoscale permanent features (Menna et al., 2019a), well represented in **Figure 1B**. East of Malta Island, a first branch of the AC feeds into a basin wide anticyclonic circulation named Mid-Ionian Jet (MIJ), while a second branch approaches the Lybian coast in a anticyclonic circulation (Poulain et al., 2013) (see for details **Figure 1A**). This area is characterized by wind-driven currents, upwelling events off Sicily and inter annual variability of numerous mesoscale structures (Menna et al., 2019b). The mean circulation of the Ionian Sea is characterized by two anticyclonic sub-basin scale structures located in the northern and southern Ionian sub-basin. The Levantine basin-scale circulation is cyclonic with the presence of persistent surface currents; the Libyo-Egyptian Current (LEC), the Cilician Current (CC), the Asia Minor Current (AMC) and a central eastward current named Mid-Mediterranean Jet (MMJ). This region is dominated by eddies and gyres formed by the instability of along-slope and offshore currents or by the wind and can be controlled by bathymetry (Menna et al., 2012). Sub-basin and mesoscale eddies are mainly anticyclonic. The mean western Levantine eddies are referred as follow; the Pelops Gyre (PG), the Western Cretan Gyre (WCG) and the Ierapetra Gyre (IG). The mean eastern Levantine eddies are presented as follow; the Cyprus Eddy (CE), Shikmona Eddy (ShE) and the Mersa-Matruh Eddy (MME) (see Mauri et al., 2019). Between the Cyprus and east of Rhodes Islands a large cyclonic gyre named Rhodes Gyre (RG) dominates as a result of the interaction of the wind driven basin circulation with the MMJ and AMC (Menna et al., 2012; **Figure 1A**). The Adriatic and Aegean sub-basin circulations are characterized by basin wide cyclonic patterns (Poulain, 2001). In the Adriatic Sea, the instability of the currents generates three cyclonic recirculation cells with the presence of a cyclonic gyre named the Southern Adriatic Gyre (SAG) and a western coastal cyclonic current called the Western Adriatic Current (WAC) (Poulain et al., 2013; **Figure 1A**). In the Aegean sub-basin, low-salinity water enters through the Dardanelles straits from the Black Sea which is mixed with the Aegean waters and forms a semi-permanent large anticyclone in the eastern part of the sub-basin (Olson et al., 2007; Politikos et al., 2017). The southern Aegean sub-basin is characterized by anticyclonic mesoscale features which are variables in time and space (Theocharis et al., 1999). The Mediterranean submesoscale and mesoscale structures can be identified by the Finite Scale Lyapunov Exponent (FSLE). Using the spatial distribution of the FSLE, D'Ovidio et al. (2004) describe the mean currents and features of the surface Mediterranean. They showed that low dispersion rates are localized in the eddies core and a stretching of the fluid parcels are in their outer part. Nevertheless, the effect of the coherent structures and currents in turbulent dispersion regimes are still an open question in each Mediterranean sub-basin. In the last decades, it has become fundamental to understand how eddies or gyres can influence the dispersion. Furthermore, the deep coherent structures play an important role in the transport of ocean water mass and dispersion processes. In the Western Mediterranean Sea numerical simulations show a decrease of the intermediate dispersion range with depth, due to the weaker influence of the vortices (Elhmaidi et al., 2010; Nefzi et al., 2014), but there are no specific studies on the deep layers of the Mediterranean. The dispersion analysis allows us to define the complex physical phenomenon (e.g., chaotic advection, turbulence, and diffusion) for different scales of motion in specific regions (Dräger-Dietel et al., 2018). The absolute dispersion indicates the representative (squared) separation of particles with respect to their initial positions. Absolute dispersion is an appropriate measure of how far individual particles move away from their original positions, while absolute diffusion indicates how fast the tracers are dispersed (Sansón, 2015). In contrast to absolute dispersion, relative dispersion measures the separation of two particles or, equivalently, the spread of a cloud of passive tracers. We study here both absolute and relative dispersion to discuss the transport and the dispersion at small and large scales in the Mediterranean Sea. The Mediterranean coherent structures for each sub-basin can affect the local transport of passive and active tracers (pollutant, phytoplankton, fish eggs and larvae). Measuring pair separations provides an immediate characterization on the spreading of pollutant patches (e.g., oil) in the Mediterranean surface. In this study, we present a Lagrangian data analysis based on the computation of absolute and relative dispersion in the sub-basins of the Mediterranean Sea, using the available historical surface drifter data. This method offers an overview of the dispersion characteristics in the upper layer of the whole Mediterranean basin, allowing understanding how the main circulation features can affect the dispersion regimes. The method presented in this work could also be applied in the future to Lagrangian data collected in sub-surface and intermediate layers, e.g., using Argo float data. Dispersion and turbulent anomalous regimes that occur in different Mediterranean sub-basins are described and eventually connected with the local circulation characteristics.

MATERIALS AND METHODS

Data

Drifters

Mediterranean surface drifters used in this work are in total 1977 instruments deployed during the period 1986–2019. Two types of drifter design are used in the Mediterranean dataset; the Coastal Ocean Dynamics Experiment (CODE) drifter developed to measure the currents in the first meter (Poulain, 1999; Poulain and Gerin, 2019), and the Surface Velocity Program (SVP) drifter (Sybrandy and Niiler, 1991; Lumpkin and Pazos, 2007) that measures the currents in the surface layer at 15 m depth. The drifters were equipped by the Global Positioning System (GPS) and transmit their data to the Argos Data Collection and Location System (DCLS) or via the Iridium satellite system. The drifter

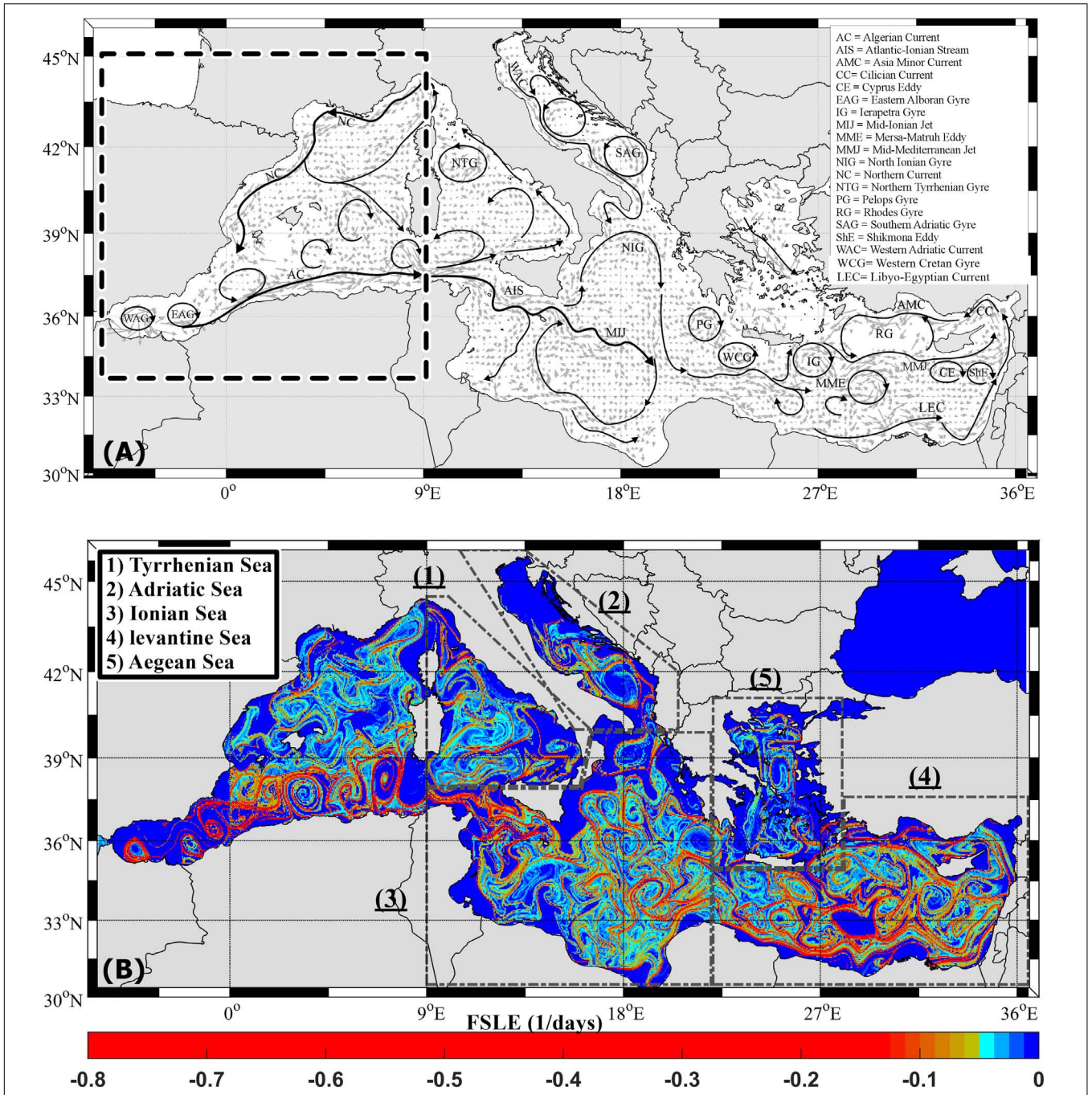

FIGURE 1 | (A) The mean surface circulation and the major circulation features in the Mediterranean Sea in bin of 0.25 × 0.25° using the available historical drifter dataset adapted from Poulain et al. (2012b) and Menna et al. (2013). The black dashed rectangle shows the geographic limits of the WWM discussed in Bouzaiene et al. (2018). The major circulation features are listed in the inset. **(B)** Snapshots of the FSLE in the Mediterranean sub-basins: in July 2012 and 2018 for the WWM; in January 2019 for the Tyrrhenian, Ionian, and Levantine sub-basins; in January 2015 for the Adriatic and in January 2018 for the Aegean sub-basin. The polygons show the geographical locations of the Mediterranean sub-basins considered in this paper.

data were first edited from spike and outliers and interpolated using the kriging method at regular 2-h intervals (Hansen and Poulain, 1996). In order to remove higher frequency current components (tidal and inertial current) the drifter positions were filtered by a Hamming filter with a cut-off period at 36-h and finally were sub-sampled at 6-h intervals. Drifter velocities were estimated from finite differences and sub-sampled at 6-h intervals (Menna et al., 2012, 2017).

The two drifter designs have been merged to compute the absolute and relative dispersion statistics, adopting the method of

Bouzaiene et al. (2018). The absolute dispersion is estimated from the pairs of individual drifter segments of 30 days length available in the Tyrrhenian, the Adriatic, the Ionian, the Levantine and the Aegean sub-basins (**Figure 2**). The range selected for the initial separation distance between the particles that forms a pair is of 0–50 km (**Figure 2**). This choice guarantees a consistent number of segments for the calculation and thus ensures a high statistical robustness. The geographical limits of each sub-basin are depicted in **Figure 1B**.

Two kinds of drifter pairs are used to estimate the dispersion: the original pairs, derived from drifters deployed together in the same area; the chance pairs, derived from drifters not deployed together but that are occasionally in the same area at the same time (LaCasce and Bower, 2000; Koszalka et al., 2009; Bouzaiene et al., 2018). Original and chance drifter pairs are selected in each sub-basin with the corresponding 30 days segments. The drifter pairs are taken every 5 days (time period larger than the Lagrangian time-scale) (Bouzaiene et al., 2018) and for initial separation distances smaller than 2 km to estimate the relative dispersion (**Figure 3**). The number of segments and drifter pairs in the Tyrrhenian and the Adriatic sub-basins is larger than in other regions and decreased dramatically with time (**Figures 2F**, **3F**). It is possible to study the relative dispersion statistics in each region, when more than 10 pairs are detected in the first thirty days (see **Figure3F**) (Poje et al., 2014).

Absolute and relative dispersion properties described in this study represent a mean estimation over the period 1986–2019, mainly ascribable to the Mediterranean coherent circulation structures described by the 30 days drifter pairs and segments selected. An overview of the mean circulation field is presented in **Figure 1A**.

Satellite Altimetry

The Finite Scale Lyapunov Exponent (FSLE) presented in this study is an altimetric product derived from the Archiving, Validation and Interpretation of Satellite Oceanographic data (AVISO). It is used to identify the coherent structures in Mediterranean sub-basins. The FSLE is backward-in-time advection and based on the largest eigenvalues of the Cauchy-Green strain tensor of the flow map; the spatial resolution is $0.04 \times 0.04°$[1]. The FSLE is defined as the exponential rate of separation, averaged over infinite time, of fluid parcels initially separated infinitesimally (D'Ovidio et al., 2004). It has been firstly introduced by Aurell et al. (1997) and Artale et al. (1997) to study the transport in closed areas. Hereafter, it was used to analyze dispersion processes, detect Lagrangian structures (e.g., eddies and gyres) and visualize eddies core regions (elliptic regions) or their surrounding (hyperbolic regions) (Lacorata et al., 2001; Koh and Legras, 2002; D'Ovidio et al., 2004, 2008).

In this paper we select more representative snapshots of the FSLE, which give an idea of the distribution of the mean sub-basin and mesoscale features in the different Mediterranean sub-basins (**Figure 1B**) and help to visualize the distributions of drifter pairs and drifter segments versus the coherent structures (**Figures 2**, **3**). The FSLE is represented in the whole Mediterranean Sea by representing snapshots for predefined months which appear similar to the surface Mediterranean circulations in the literature.

[1]www.aviso.altimetry.fr

Methods

The dispersion statistics, can be obtained both by measuring the mean squared displacement of single drifters and drifter pair separations (LaCasce, 2008; Bouzaiene et al., 2018). We consider the single drifter displacements defined by Poulain and Niiler (1989) as follow:

$$A^2 = \left\langle [X(i,t) - X(i_0,t_0) - < u > (t - t_0)]^2 \right\rangle \quad (1)$$

Where $X(i,t)$ and $X(i_0,t_0)$ are, respectively, vector positions of drifters at times t_o and t; index i is the i-direction of position vectors (in case of 2-D turbulence $i = 1, 2$), $< u >$ is the mean velocity derived from pseudo-Eulerian statistics in bin of $0.25 \times 0.25°$ performed over the whole Mediterranean drifter dataset (for more details see Menna et al., 2019a,b). The mean zonal and meridional velocities are of 3.3 and -1.4 cm.s^{-1}, respectively. We defined the absolute diffusivity as the derivative of the absolute dispersion as a function of time derived by Babiano et al. (1985) as follow:

$$\mathrm{k(t)}^{(1)} = \frac{1}{2}\frac{\mathrm{d}A^2(t)}{\mathrm{dt}} \quad (2)$$

In case of homogenous and isotropic flow, for small and large times the two classical absolute dispersion regimes are, respectively, the ballistic regime ($A^2 \sim t^2$, $k^{(1)} \sim t$) and the Random-walk regime ($A^2 \sim t$, $k^{(1)} \sim constant$) (Babiano et al., 1985; Poulain and Niiler, 1989).

At intermediate time scale, anomalous (elliptic and hyperbolic) absolute dispersion regimes are observed. The elliptic regime $A^2 \sim t^{5/3}$ is related to the region where the rotation is more relevant than the deformation, whereas the hyperbolic regime $A^2 \sim t^{5/4}$ is related to domains where the deformation is more relevant than the rotation (Elhmaidi et al., 1993). The classical asymptotic and anomalous absolute dispersion regimes are summarized in the **Table 1** (Babiano et al., 1990; Elhmaidi et al., 1993).

The relative separation of drifter pairs is defined by (Poje et al., 2014):

$$D^2(t, D_0) = \left\langle \left[r^{(1)}(t) - r^{(2)}(t) \right]^2 \right\rangle = \delta^2 \quad (3)$$

Where δ is the distance between two trajectories, the average is overall the available trajectory pairs and $r^{(1)}$ and $r^{(2)}$ are the Lagrangian positions of the two drifters forming the pair.

In the ocean, the growth of distance between pairs δ is compared to the internal Rossby Radius of deformation D_I for characterizing the effect of submesoscale and mesoscale structures on relative dispersion regimes. Different parameters deduced from relative dispersion and depending on δ which are highlighted below:

The classical relative diffusivity is defined as the derivative of relative dispersion in time by Babiano et al. (1990) as:

$$Y(t) = \frac{1}{2}\frac{dD^2}{dt} \quad (4)$$

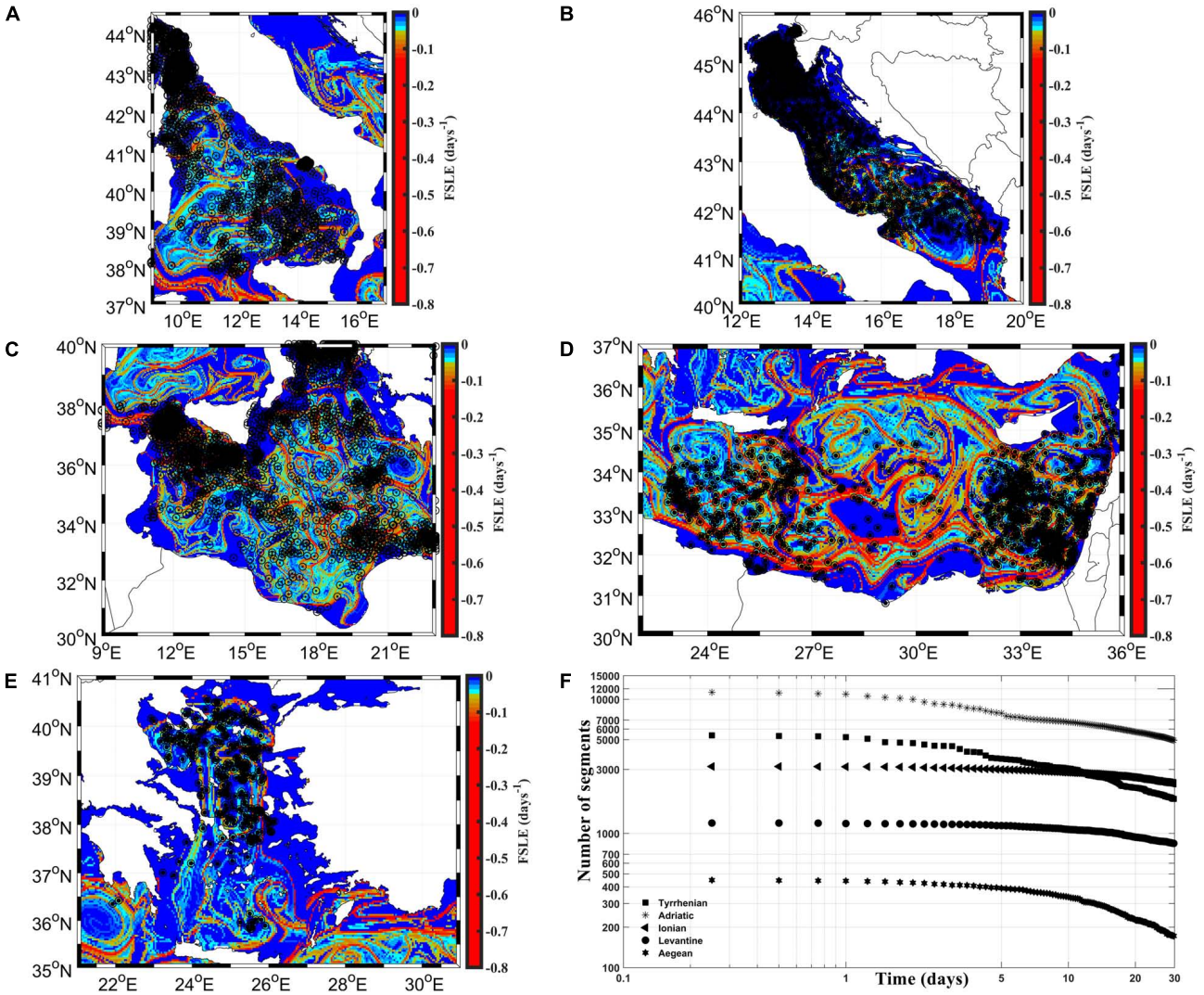

FIGURE 2 | The spatial distribution of the FSLE superposed with the initial positions of drifter segments (individual drifters, black dots inside the black circles) **(A)** in the Tyrrhenian, **(B)** the Adriatic, **(C)** the Ionian, **(D)** the Levantine, and **(E)** the Aegean sub-basins. The number of segments as a function of time is shown in **(F)**.

The second-order structure function measures the evolution of pair velocities growing in a distance δ. It is defined as follows (Berti and dos Santos, 2016):

$$S_2(\delta) = \langle [\Delta V(\delta)]^2 \rangle = \left\langle \left[V^{(1)}(t) - V^{(2)}(t) \right]^2 \right\rangle \quad (5)$$

Where $V^{(1)}$ and $V^{(2)}$ are the Lagrangian velocities of two particles separated with a predefined distance δ and the average is overall the available velocity pairs.

The relative diffusivity can be deduced from the second-order structure function and it is presented as follows (Berti and dos Santos, 2016):

$$K(\delta) = \frac{1}{2}\delta.\sqrt{S_2(\delta)} \quad (6)$$

And the Lagrangian Energy spectrum is:

$$E(k) = \frac{S_2(k)}{k} \quad (7)$$

Where $k = 2\pi/\delta$ is the wave number (Berti and dos Santos, 2016).

Classical relative dispersion regimes are summarized in the **Table 2** (Babiano et al., 1990; LaCasce and Bower, 2000; LaCasce and Ohlmann, 2003; Koszalka et al., 2009; LaCasce, 2010; Poje et al., 2014; Berti and dos Santos, 2016; Corrado et al., 2017; Bouzaiene et al., 2018; Dräger-Dietel et al., 2018; Callies et al., 2019).

The mean objective of this paper is to study the spreading of surface drifters in the Mediterranean sub-basins (Tyrrhenian, Adriatic, Ionian, Levantine and Aegean) in order to compare the different dispersion regimes and define the parameters

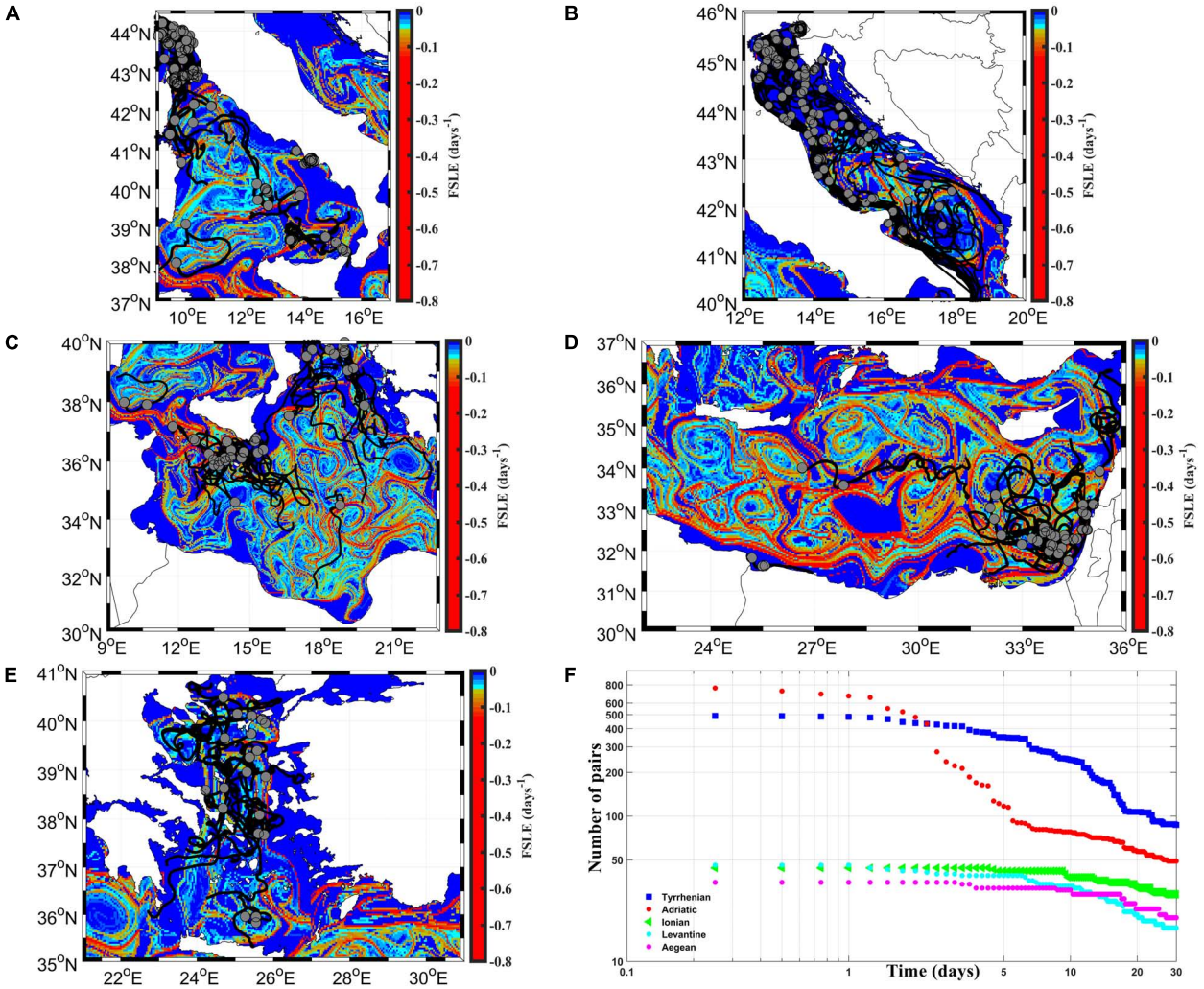

FIGURE 3 | The spatial distribution of the FSLE superposed with the initial pair positions (gray dots) and their trajectories (black lines) during 30 days **(A)** in the Tyrrhenian, **(B)** the Adriatic, **(C)** the Ionian, **(D)** the Levantine, and **(E)** the Aegean sub-basins. The number of drifter pairs as a function of time is shown in **(F)**.

common to all ocean sub-basins by calculating one and two-particle statistics from large drifter data set deployed in the Mediterranean sea between 1986–2019.

RESULTS

In this work we will not address the results of the WWM because this region of the Mediterranean Sea was already examined in Bouzaiene et al. (2018). The spatial distribution of the FSLE in the Tyrrhenian, Adriatic, Ionian, Levantine and Aegean sub-basins shows the presence of the well-known mesoscale structures in each sub-basin (**Figure 1B**). For each sub-basin we have selected monthly snapshots that better highlight the main coherent structures. The FSLE shows transport barriers, higher absolute values surrounding eddies (red, dark yellow and cyan colors) and lower absolute values in their cores (blue color). In the Ionian and the Levantine sub-basins, numerous mesoscale structures (eddies and gyres) are observed (**Figure 1B**) due to the strong currents variability in these regions (Menna et al., 2012, 2019a,b; Mauri et al., 2019). In the Aegean sub-basin the number of mesoscale structures is reduced in agreement with the results of Politikos et al. (2017). In the Adriatic sub-basin the FSLE outlines the edges of the Southern Adriatic Gyre (SAG) and of another cyclonic gyre located in the central part of the basin (Poulain et al., 2012b). In the northern part of the Tyrrhenian sub-basin, the Northern Tyrrhenian Gyre (NTG) is well detected as well as other eddies in the central part of the basin. The main basin, sub-basin and mesoscale structures detected in the five Mediterranean sub-basins are in accordance with the results presented by Menna et al. (2013) and Tintoré et al. (2019).

The 30-day drifter trajectories and their initial positions displayed in **Figures 2**, **3** show that many drifters are located in the coherent structures and move inside or around the gyres and eddies, as well as the NTG, the central Tyrrhenian

TABLE 1 | Classical absolute dispersion regimes.

Quantities	Ballistic regime	Elliptic regime	Hyperbolic regime	Random-walk regime
A^2 (t)	$\sim t^2$	$\sim t^{5/3}$	$\sim t^{5/4}$	$\sim t$
$k(t)^{(1)}$	$\sim t$	–	–	constant

TABLE 2 | Classical relative dispersion regimes. Where the parameters T and β are calculated from the data.

Quantities	Exponential regime	Shear/ballistic regime	Richardson regime	Diffusive regime
D^2 (t)	$\sim D_0^2 e^{8t/T}$	$\sim t^2$	$\sim 5.2675\beta^3 t^3$	$\sim t$
Y (δ)	$\sim \delta^2/T$	$\sim \delta^{3/2}$	$\sim \beta\delta^{4/3}$	constant
K (δ)	$\sim \delta^2$	$\sim \delta^{3/2}$	$\sim \delta^{4/3}$	–
S_2 (δ)	$\sim \delta^2$	$\sim \delta$	$\sim \delta^{2/3}$	constant
E (k)	$\sim k^{-3}$	$\sim k^{-2}$	$\sim k^{-5/3}$	–

eddies (**Figures 2A**, **3A**), the SAG, and numerous particles are advected along the boundary Adriatic currents (**Figures 2B**, **3B**). In the Ionian sub-basin (**Figures 2C**, **3C**) the drifters are mainly located in the Sicily Channel and in the northern and southern Ionian sub-basin; whereas in the Levantine sub-basin they are advected along the LEC and the CC currents, some drifters are located in WCG, IG, MME, CE, and ShE (**Figures 2D**, **3D**). In the Aegean sub-basin the drifters are homogeneously dispersed in the sub-basin and numerous drifters are dispersed in the Aegean coherent structures (**Figures 2E**, **3E**).

Absolute dispersion curves displayed in **Figure 4** show the occurrence of quasi-ballistic (t^2) and quasi-random walk (t) regimes, respectively, for small ($t < 2$ days) and large ($t > 15$ days) time scales in all sub-basins. The absolute dispersion is larger for the zonal component in all the sub-basins (**Figure 4**) and is mainly anisotropic, except in the Aegean sub-basin where it is isotropic during the last twenty days (the evolution of zonal and meridional components overlaps; **Figure 4E**). The largest value of the zonal dispersion are related to the presence of zonal gyres or eddies trapping drifters during few days or weeks and to the influence of zonal currents on the observed zonal split (mean zonal velocity larger than the meridional one). At intermediate time scales (between 2 and 15 days approximately), the absolute dispersion curves emphasize the occurrence of the hyperbolic regime ($t^{5/4}$) in the Adriatic (**Figure 4B**), suggesting that in this sub-basin prevails the effect of the coastal jets and the WAC (stretching) on the particles advection than the effect of gyre cores. In the other sub-basins (Tyrrhenian, Ionian, Levantine and Aegean), the elliptic regime ($t^{5/3}$) prevails the effect of the inner part of coherent structures on the particles transport than their outer part (**Figures 4A,C,D,E**). These results are supported by normalizing the absolute dispersion by $t^{5/4}$ for the hyperbolic and $t^{5/3}$ the elliptic regimes as shown in the **Figure 5**. Quasi short plateau is detected approximately in range of 3–5 days in the Tyrrhenian (**Figure 5A**), 3–6 days in the Ionian (**Figure 5C**), 2.5–4 days in the Levantine (**Figure 5D**) and Aegean (**Figure 5E**) sub-basins related to the elliptic regions (eddy cores) where the rotation is more relevant than the stretching. Another quasi plateau is observed between 9 and 15 days, approximately in the Adriatic sub-basin (**Figure 5B**) connected to the hyperbolic regions (surrounding eddies). The absolute diffusivity $k(t)^{(1)}$ as a function of time is approximately constant at large time scale implies the presence of the quasi-random walk regime ($t > 15$ days), while the quasi-ballistic regime at small time ($t < 2$ days, $k(t)^{(1)} \sim t$) is detected (**Figure 6**). During the occurrence of the quasi-random walk regime the $k(t)^{(1)}$ is of $\sim$100 km^2.days^{-1} in the Tyrrhenian, the Adriatic and Aegean sub-basins (**Figures 6A,B,E**). It reaches larger values of $\sim$500 km^2.days^{-1} in the Ionian (**Figure 6C**) and 250 km^2.days^{-1} in the Levantine (**Figure 6D**), connected to the large sub-basin sizes where the drifter pairs are dispersed for large separation distances. The absolute diffusivity depends explicitly on the mean velocity being the zonal diffusivity component is greater than the meridional one according to the largest mean zonal velocity (**Figure 6**).

The temporal evolution of the mean squared distance between drifter pairs (relative dispersion) as a function of time shows the occurrence of an exponential growth with $D^2(t) \sim D_0^2 e^{8t/T}$ at short time scale (less than 4 days) in the Tyrrhenian sub-basin (**Figure 7A**); no exponential growths are observed in the other sub-basins (**Figures 7B–E**). The relative dispersion evolves as $\sim 5.2675\beta^3 t^3$ in the Tyrrhenian and the Aegean sub-basins for intermediate time (Richardson-like dispersion; $2 < t < 10$ days) (**Figures 7A,E**), while it evolves as t^2 (shear-ballistic dispersion) in the other sub-basins (insets of **Figures 6B–D**). The Richardson-like dispersion is related to pairs spreading driven by eddies with scales comparable to the separation distance and to the Rossby radius (Corrado et al., 2017; Bouzaiene et al., 2018). The shear-ballistic regime is usually associated in the ocean to the dominant action of a strong and well organized current system, i.e., the Gulf Stream (Corrado et al., 2017). This regime is clearly detected in the Adriatic, Ionian and Levantine sub-basins normalizing the relative dispersion by the squared time t^2 (horizontal plateau in the insects of **Figure 7**) and is connected to the WAC, AIS/MIJ, and LEC, respectively. For large time scale (more than 15 days), the relative dispersion curves follow a quasi-linear growth as a function of time (**Figure 7**). **Figure 8** shows the difference between the four time eddy kinetic energy $4E$ and the second-order structure function S_2 as a function of time in the five sub-basins useful to estimate the uncorrelated pair velocities. When the pair velocities become decorrelated, the parameter $(4E–S_2)$ shows a value of zero (LaCasce and Bower, 2000; LaCasce and Ohlmann, 2003). The pair velocities are decorrelated very fast in the Aegean sub-basin (after the sixth day; **Figure 8E**), alter $\sim$25 days in the Tyrrhenian Sea and after 10–15 days in the Ionian and Levantine sub-basins (**Figures 8C,D**); in the Adriatic Sea the pair velocities are still correlated during the last 30 days (**Figure 8B**) due to the coastal and semi-enclosed nature of this sub-basin. In this case the dispersion is blocked to the Adriatic coasts and the pairs are not transported for separation distances as large to become uncorrelated.

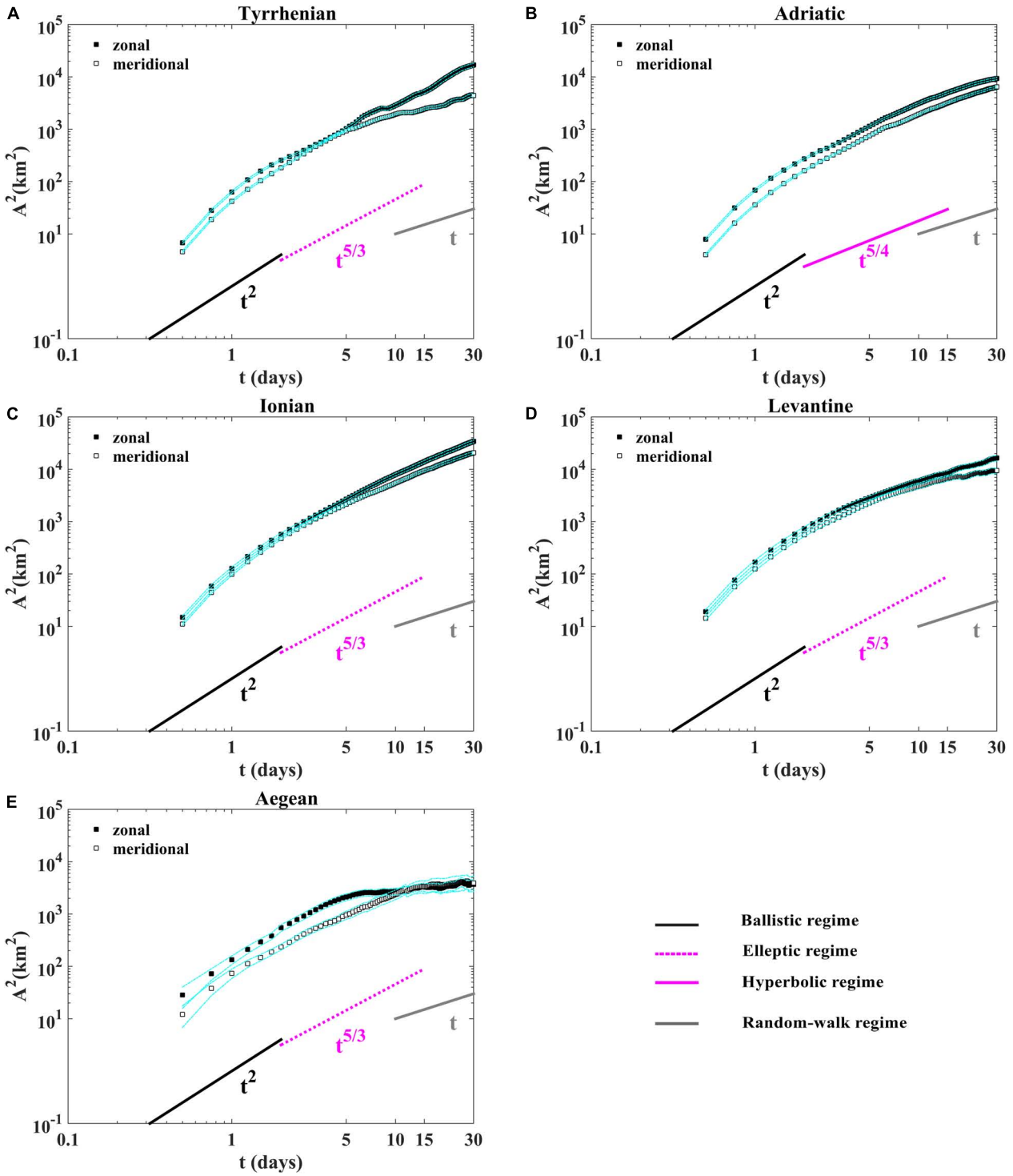

FIGURE 4 | Absolute dispersion for the zonal and meridional components as a function of time in loglog plot **(A)** in the Tyrrhenian, **(B)** the Adriatic, **(C)** the Ionian, **(D)** the Levantine, and **(E)** the Aegean sub-basins. The ballistic (black line) random-walk (gray line), the elliptic (dashed magenta line) and the hyperbolic (magenta full line) laws. The dashed cyan lines indicate the 90% confidence intervals from bootstrap resampling, give a rough idea of the uncertainties for the statistics.

The relative diffusivities are calculated as a function of separation distances in two different ways: from the derivative of the relative dispersion (classical diffusivity) (**Figure 9**) and from the second-order structure function (**Figure 10**) as reported in Eqs.4 and 6, respectively. For scales <10 km, below the internal Rossby Radius of deformation (D_I ∼10-20 km)

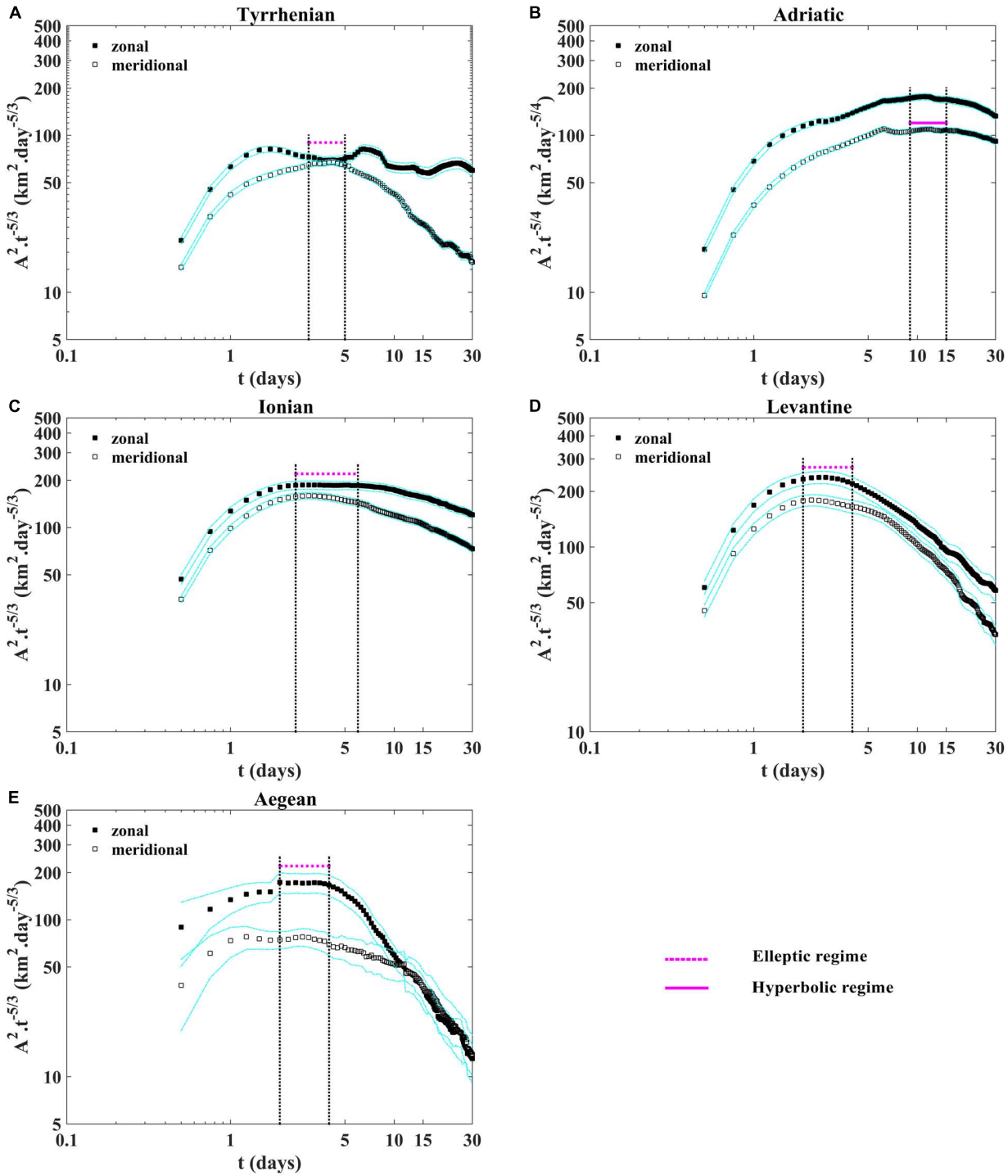

FIGURE 5 | Absolute dispersion for the zonal and meridional components normalized by $t^{5/3}$ as a function of time in loglog plot **(A)** in the Tyrrhenian, **(C)** the Ionian, **(D)** the Levantine **(E)** the Aegean and by $t^{5/4}$ **(B)** the Adriatic sub-basins. The horizontal magenta lines show the presence of plateau for the occurrence of the elliptic (dashed magenta line) and hyperbolic (magenta full line) regimes. The vertical dashed black lines show the time period of the anomalous regimes. The dashed cyan lines indicate the 90% confidence intervals from bootstrap resampling, give a rough idea of the uncertainties for the statistics.

(Schroeder et al., 2011; Beuvier et al., 2012), the diffusivities confirm the occurrence of the exponential regime in the Tyrrhenian sub-basin evolving as $\sim \delta^2/T$ (**Figure 9A**). On the other hand, the diffusivities growth as $\sim \delta^{3/2}$ in the Adriatic, the Ionian and the Levantine regions (**Figures 9B–D**) and evolve as $\sim \beta\delta^{4/3}$ in the Tyrrhenian and in the Aegean sub-basins for

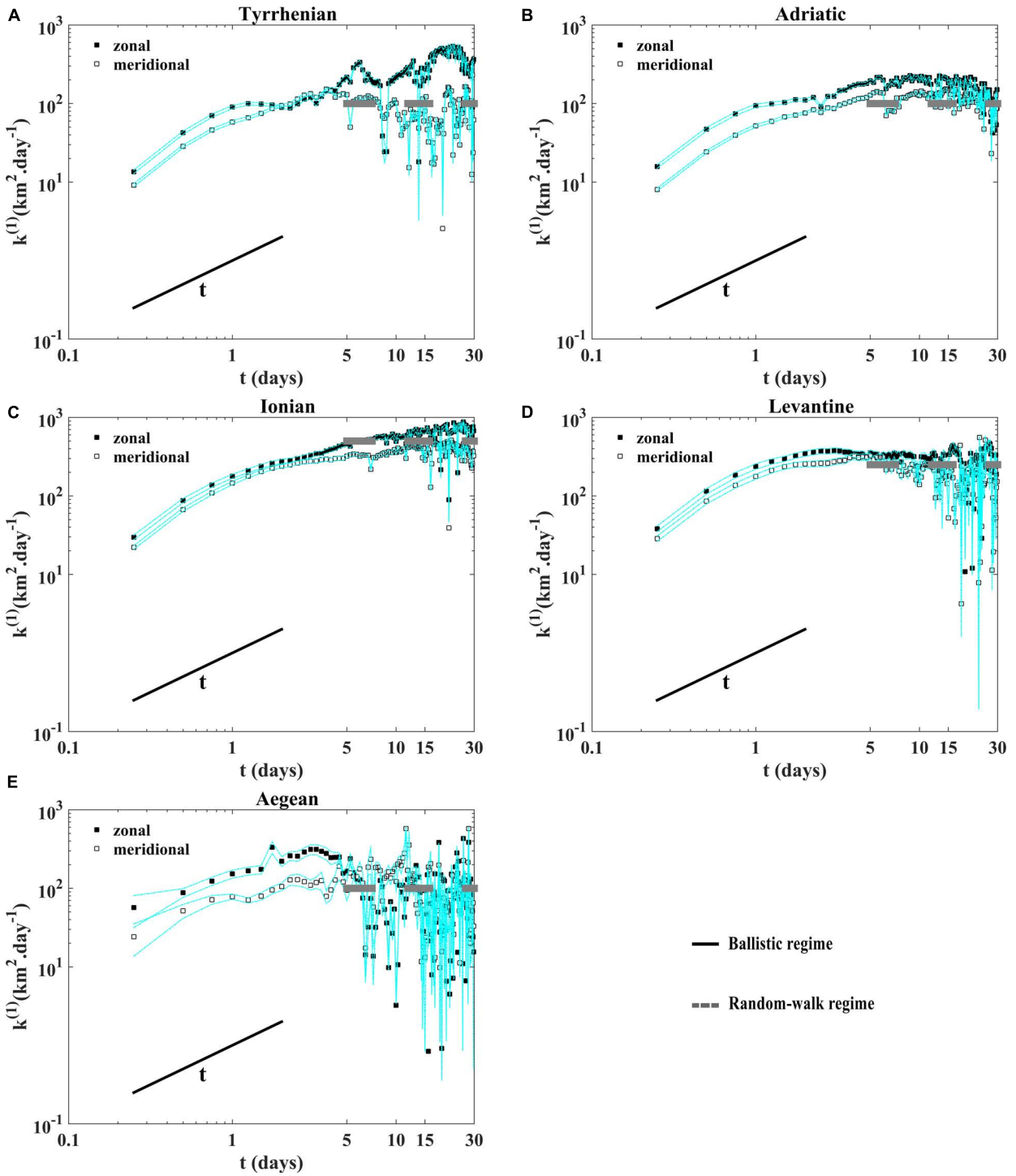

FIGURE 6 | Absolute diffusivity for the zonal and meridional components as a function of time in loglog plot **(A)** in the Tyrrhenian, **(B)** the Adriatic, **(C)** the Ionian, **(D)** the Levantine, and **(E)** the Aegean sub-basins. The diffusive random-walk is shown with the thin black line and the horizontal dashed gray lines show the constant absolute diffusivity values. The dashed cyan lines indicate the 90% confidence intervals from bootstrap resampling, give a rough idea of the uncertainties for the statistics.

scales comparables to the D_I (**Figures 9A,E**). For spatial scales larger than D_I the classical diffusivity shows approximately a constant value for all regions $Y \sim 2k(t)^{(1)}$, while it shows a lower value in the Adriatic sub-basin for a maximum distance between pairs is about 20 km because the majority pair velocities are still correlated at this maximum distance. The relative

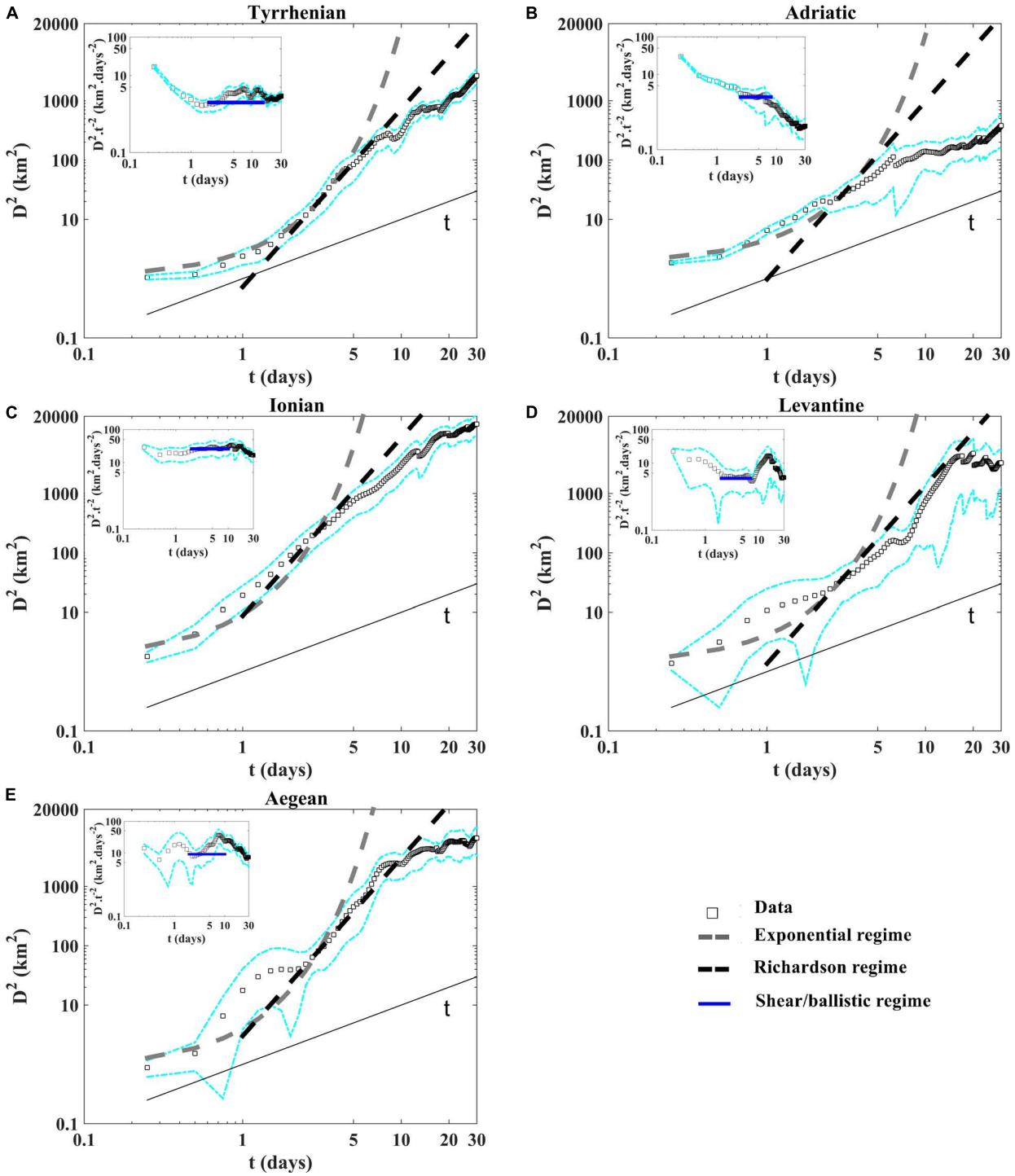

FIGURE 7 | Relative dispersion as a function of time in loglog plot **(A)** in the Tyrrhenian, **(B)** the Adriatic, **(C)** the Ionian, **(D)** the Levantine and **(E)** the Aegean sub-basins. The exponential and the Richardson regimes are shown with the dashed gray and black lines, respectively. The diffusive regime is shown with the thin black line. In the insets we show the relative dispersion normalized by the squared time t^2 would have a plateau (horizontal blue lines) for the occurrence of the shear/ballistic regime. The dashed cyan lines indicate the 90% confidence intervals from bootstrap resampling, give a rough idea of the uncertainties for the statistics.

diffusivity curves displayed in the (**Figure 10**) are in good accordance with the theoretical relative dispersion laws given by the **Table 2**. The Exponential and Richardson fits presented in the **Figures 7**, **9** are calculated with the corresponding T and β values given by the following theoretical expressions $D^2(t) = D_0^2 e^{8t/T}$ (Exponential) and $D^2(t) = 5.2675\beta^3 t^3$

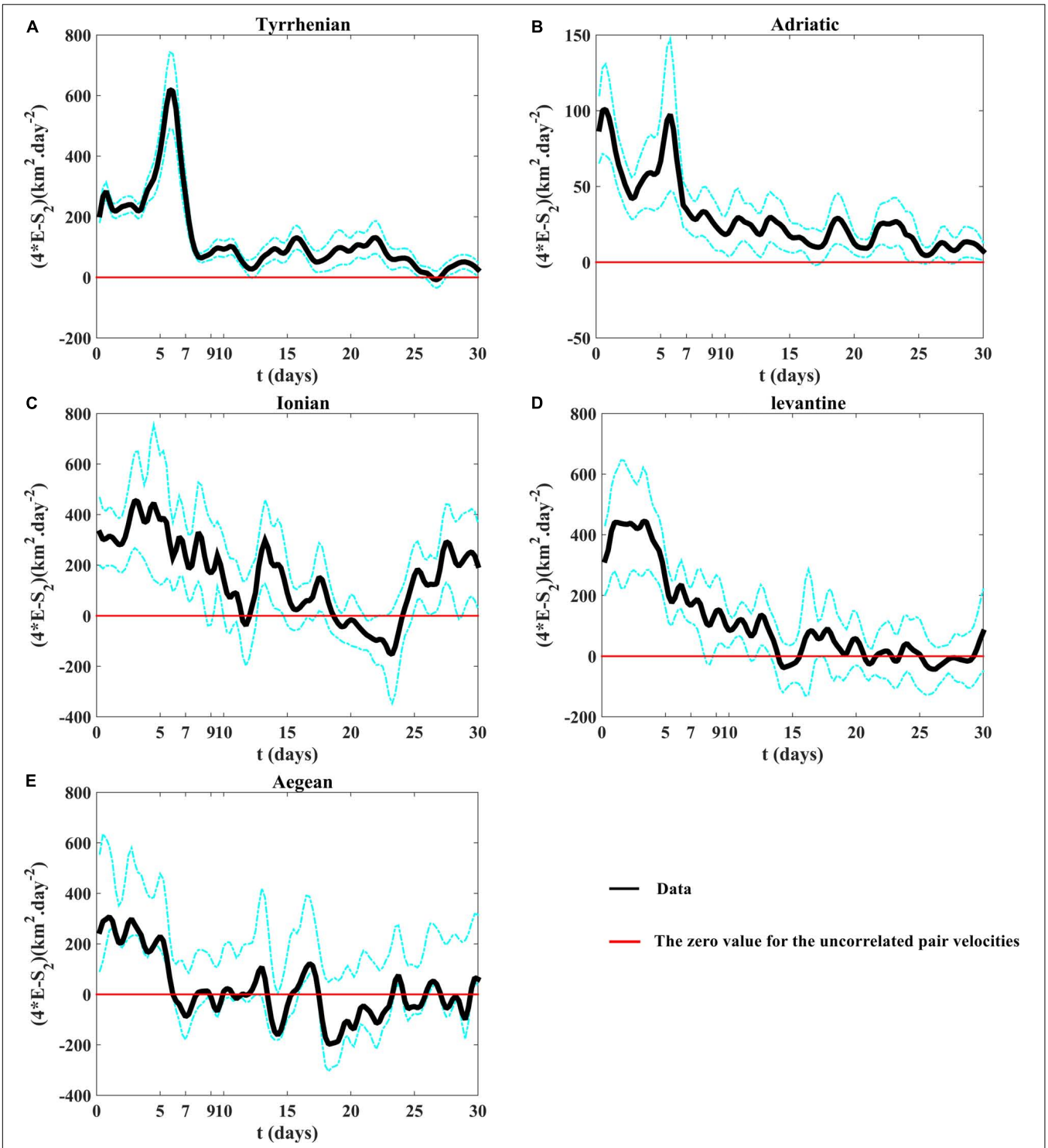

FIGURE 8 | The difference between the four time eddy kinetic energy *4E* and the second-order structure function S_2 as a function of time *(4E–S_2)(t)* **(A)** in the Tyrrhenian, **(B)** the Adriatic, **(C)** the Ionian, **(D)** the Levantine, and **(E)** the Aegean sub-basins. The uncorrelated pair velocities would have a *(4E—S_2)* of zero (horizontal red lines). The dashed cyan lines indicate the 90% confidence intervals from bootstrap resampling, give a rough idea of the uncertainties for the statistics.

(Richardson) as displayed in the **Table 2**, i.e., at fixed time $t = 3$ days,T = [8.20, 9.04, 4.92, 7.30, 5.30] days and $\beta = [0.51, 0.57, 1.18, 0.63, 0.83]$ km$^{2/3}$day^{-1} in the Tyrrhenian, Adriatic, Ionian, Levantine and Aegean sub-basins, respectively, as suggested in LaCasce (2010) and Sansón et al., 2017.

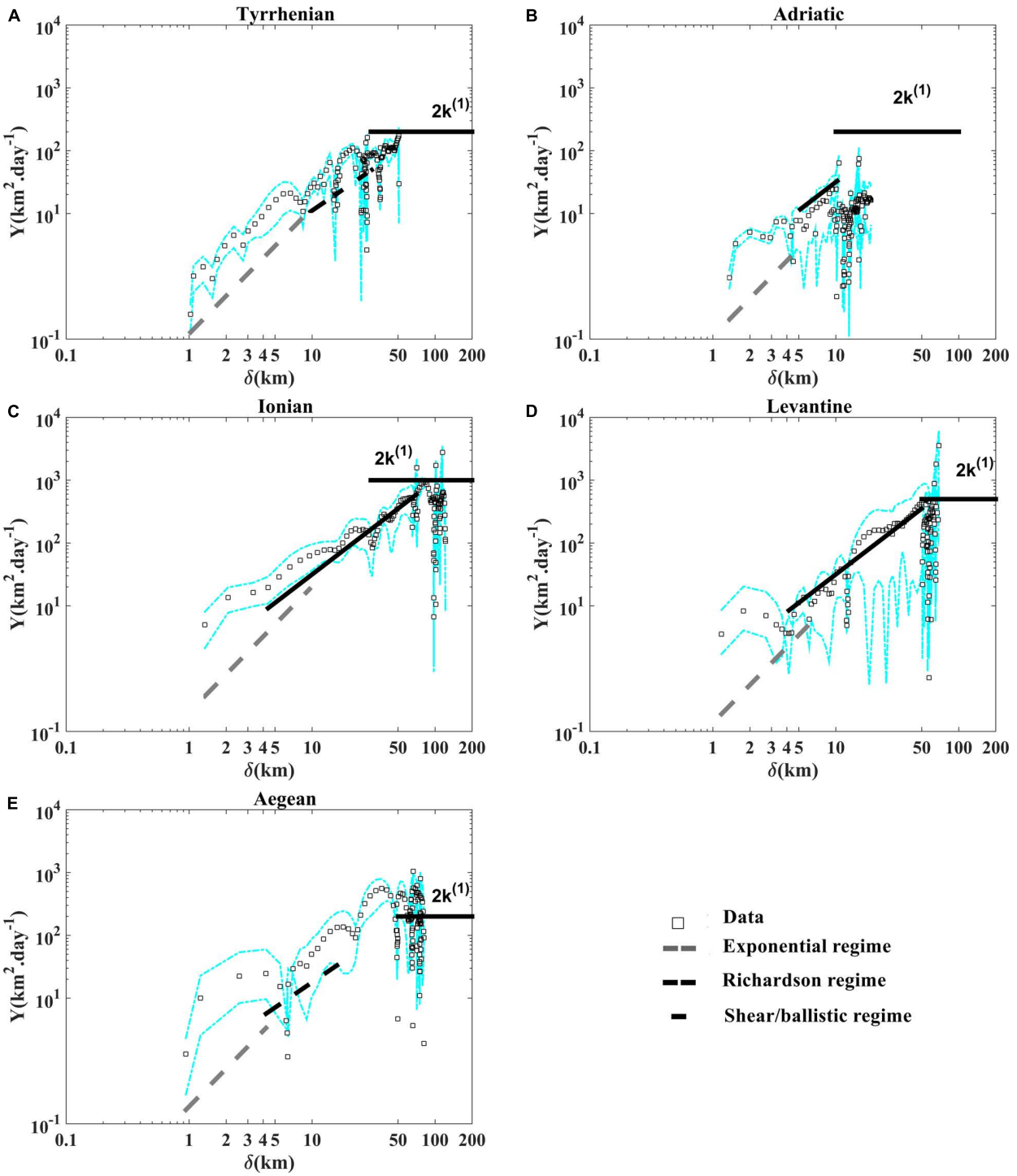

FIGURE 9 | Relative diffusivity as a function of separation distance derived from the relative dispersion in Eq. 4 **(A)** in the Tyrrhenian, **(B)** the Adriatic, **(C)** the Ionian, **(D)** the Levantine, and **(E)** the Aegean sub-basins. The exponential, the Richardson and the shear/ballistic regimes are shown with the dashed gray, dashed black and black lines, respectively. The diffusive regime is shown with the horizontal thick black line. The dashed cyan lines indicate the 90% confidence intervals from bootstrap resampling, give a rough idea of the uncertainties for the statistics.

Interestingly to represent more relative dispersion statistics in order to support the presence of the relative dispersion regimes discussed above. The second order structure function as a function of separation distance (**Figure 11**) and the energy spectra (versus wave number; **Figure 12**) are in good accordance with the classical relative dispersion regimes displayed in the

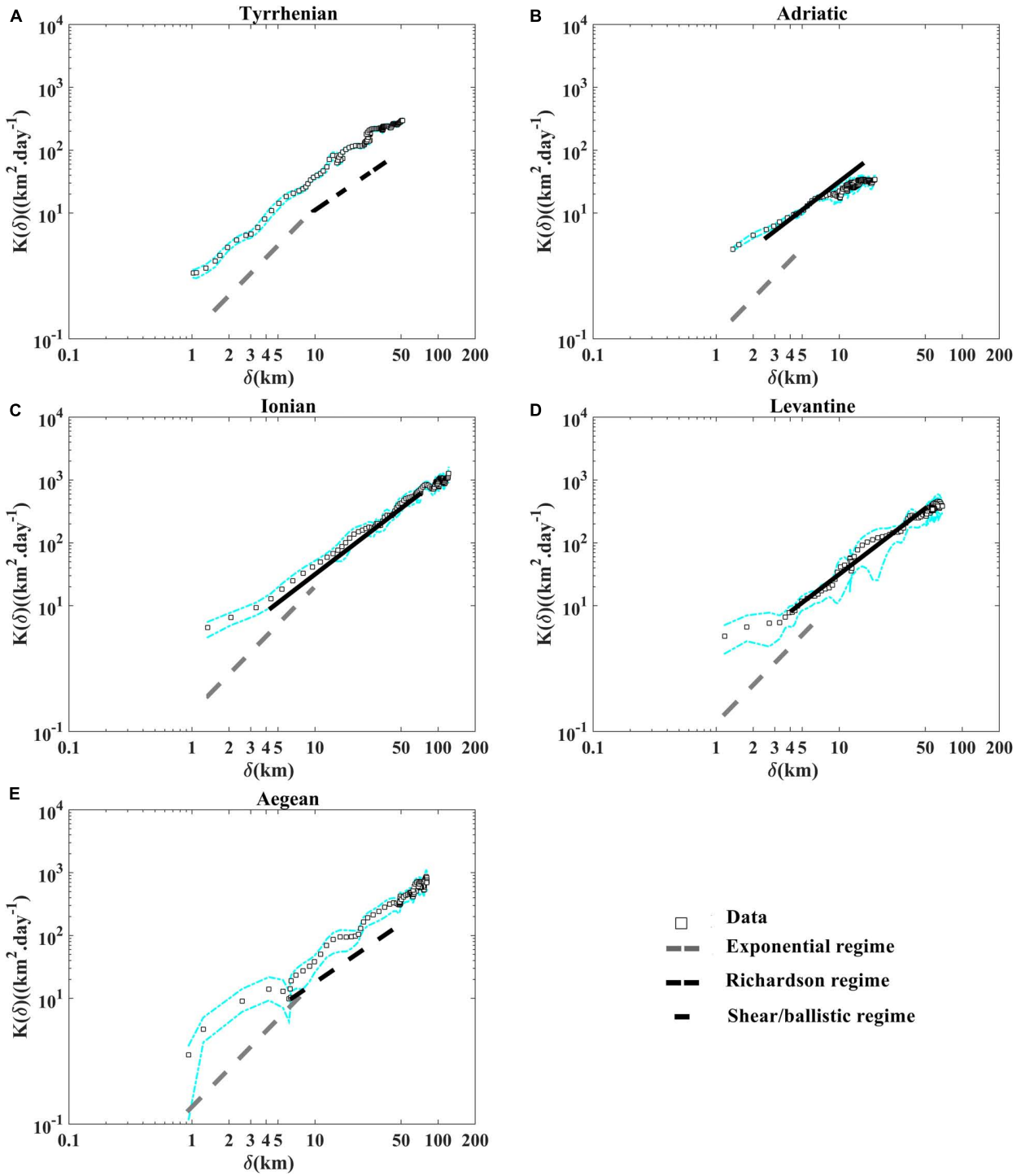

FIGURE 10 | Relative diffusivity as a function of separation distance derived from the second-order structure function in Eq. 6 **(A)** in the Tyrrhenian, **(B)** the Adriatic, **(C)** the Ionian, **(D)** the Levantine and **(E)** the Aegean sub-basins. The exponential, the Richardson and the shear/ballistic regimes are shown with the dashed gray, dashed black and black lines, respectively. The dashed cyan lines indicate the 90% confidence limits from bootstrap resampling, give a rough idea of the uncertainties for the statistics.

Table 2. Both of them emphasize the occurrence of the non-local regime for small scales in the Tyrrhenian sub-basin, the two local (Richardson) regimes in the Tyrrhenian and Aegean sub-basins and (shear/ballistic) in the Adriatic, the Ionian and Levantine sub-basins for scales comparable to D_I. Different mixing properties in the five Mediterranean

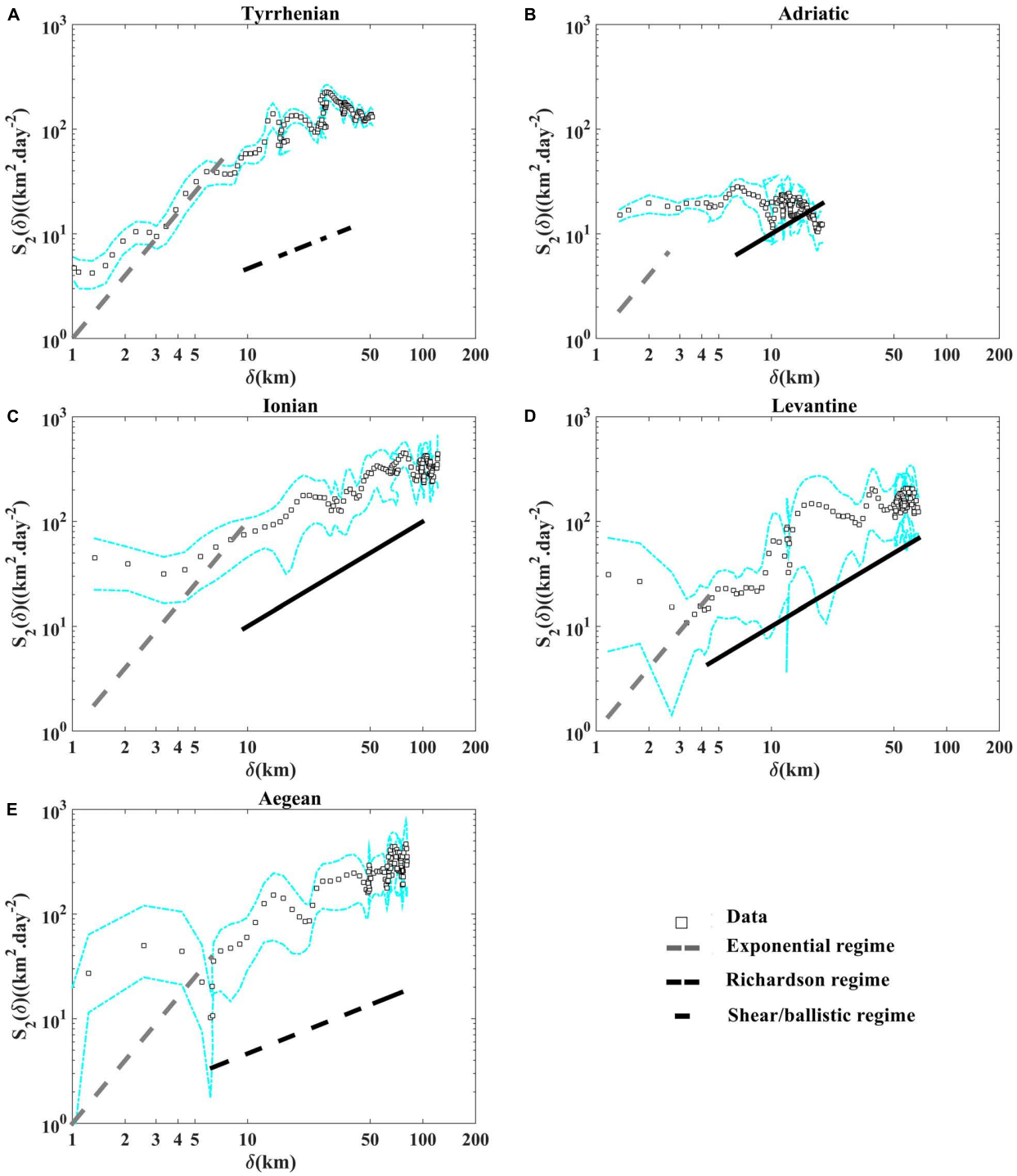

FIGURE 11 | Second-order structure function versus separation distance **(A)** in the Tyrrhenian, **(B)** the Adriatic, **(C)** the Ionian, **(D)** the Levantine, and **(E)** the Aegean sub-basins. The exponential, the Richardson and the shear/ballistic regimes are shown with the dashed gray, dashed black and black lines, respectively. The dashed cyan lines indicate the 90% confidence intervals from bootstrap resampling, give a rough idea of the uncertainties for the statistics.

sub-basins are ascribable to the total diffusivity pattern related to the eddies and to the mean flow characteristics in each regions as suggested in Ferrari and Nikurashin (2010) and Chen et al. (2014).

DISCUSSION

In this study we highlighted the occurrence of surface absolute and relative dispersion regimes related to the presence of

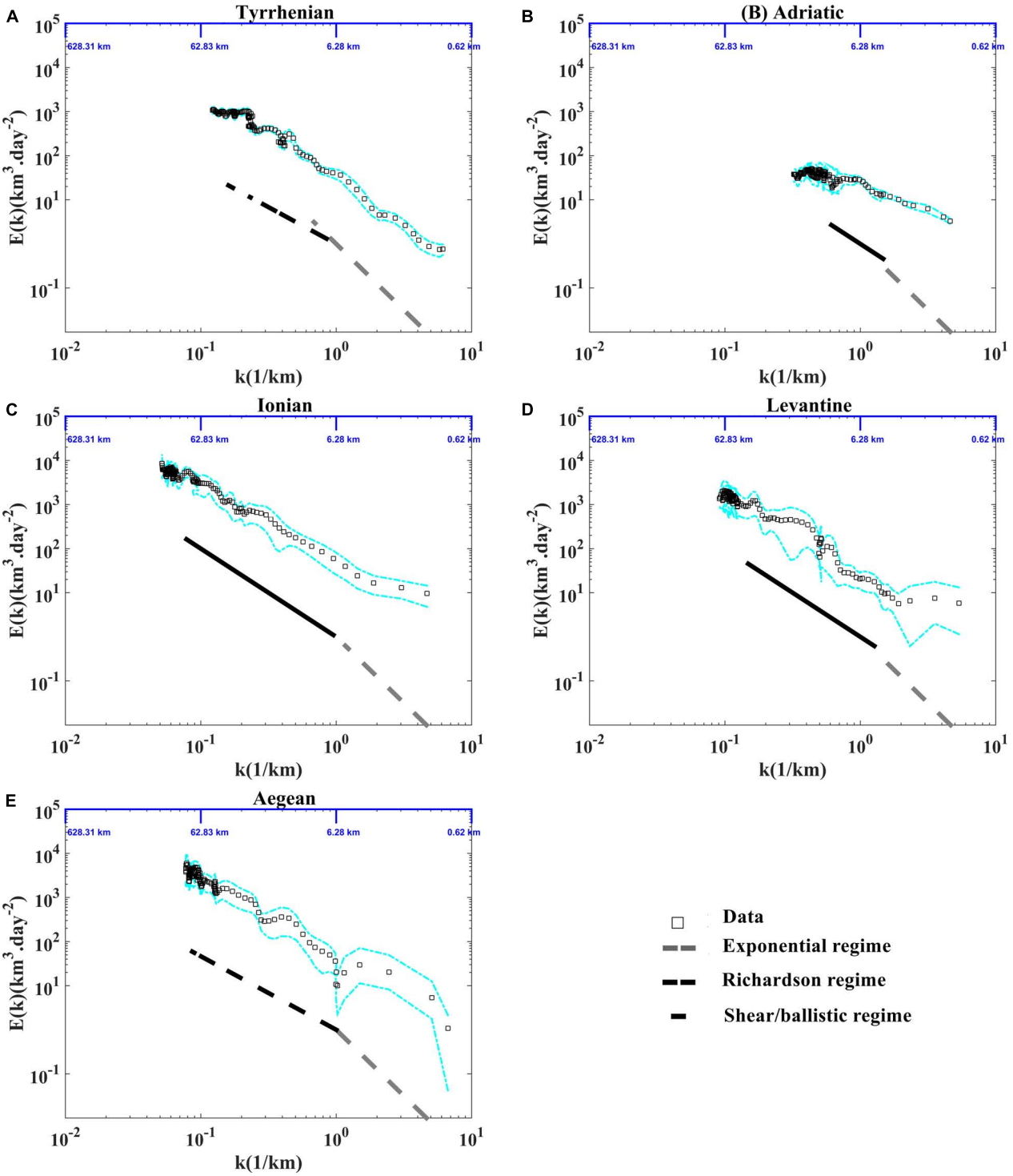

FIGURE 12 | Energy spectra in function of wave number **(A)** in the Tyrrhenian, **(B)** the Adriatic, **(C)** the Ionian, **(D)** the Levantine, and **(E)** the Aegean sub-basins. The exponential, the Richardson and the shear/ballistic regimes are shown with the dashed gray, dashed black and black lines, respectively. The dashed cyan lines indicate the 90% confidence intervals from bootstrap resampling, give a rough idea of the uncertainties for the statistics.

coherent Mediterranean structures and currents. The absolute dispersion curves show anisotropic surface flow where the zonal motion is dominant in all Mediterranean sub-basins and an isotropic Aegean surface flow over the last 20 days, indicating that the flow is more homogeneous in this region than in the other sub-basins. The occurrence of anomalous elliptic (5/3) and

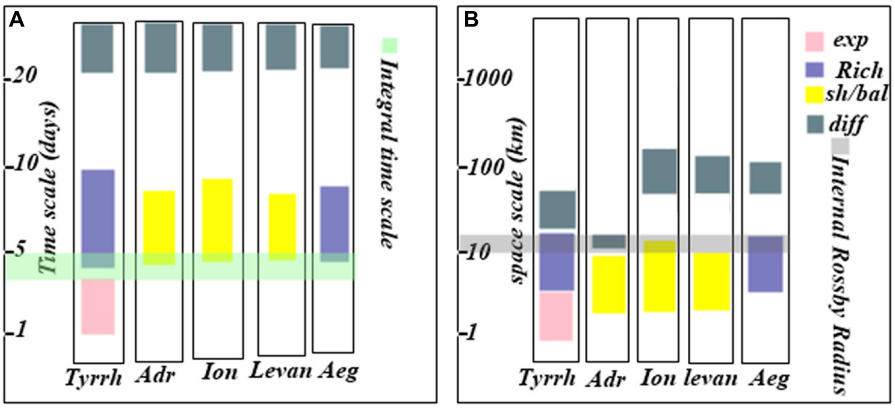

FIGURE 13 | Occurrence of different relative dispersion regimes in the Tyrrhenian, the Adriatic, the Ionian, the Levantine and the Aegean sub-basins as a function of the time scale **(A)** and space scale **(B)**. The colors are referred to relative dispersion regimes as follow: pink = exponential regime, blue-gray = Richardson regime, yellow = shear/ballistic regime and pale-blue = diffusive regime. The light green and gray colors indicate the integral time scale and the internal Rossby radius of deformation, respectively.

hyperbolic (5/4) regimes is observed due to the influence of the coherent structures. The occurrence of these anomalous regimes was studied and detected in the WWM by Bouzaiene et al. (2018). Anomalous regimes were never studied before in Mediterranean sub-basins from Lagrangian drifters. Hence, we analyze the presence of these anomalous regimes in five Mediterranean sub-basins (Tyrrhenian, Adriatic, Ionian, Levantine and Aegean). The absolute dispersion curves show the hyperbolic regime in the Adriatic sub-basin and outline the dominance of elliptic regime in the other regions. The (5/4) regime is detected only in the Adriatic sub-basins because the majority of particles were advected along the WAC and the outer part of the Adriatic gyres for a strong stretching (deformation) as presented in the (**Figure 2B**), while the (5/3) regime is observed in the other sub-basins when numerous particles are located in the domains characterized by strong rotation (eddies and gyres) as is evident in the (**Figures 2A,C,D,E**).

The main relative dispersion results are summarized in **Figure 13**. The initial pair separation ($D_0 < 2$ km) is smaller than the internal Rossby radius of deformation, giving information on the Coriolis Effect on the relative dispersion regimes. The non-local exponential regime is confirmed from all the relative dispersion statistics (relative dispersion, relative diffusivity, second-order structure function and energy spectra). This non-local regime is observed only in the Tyrrhenian sub-basin for scales comparable or less than 5 km (**Figure 13B**) because the majority of drifter pairs are located in the Tyrrhenian coherent structures (see **Figure 3A**). This result denotes the advection of particles by eddies with scales larger than their separation distances in the Tyrrhenian Sea. On the other hand, this regime is absent in the Ionian, the Adriatic and the Aegean sub-basins. The absence of the non-local regime in the other sub-basins can be related to methodological reasons, i.e., the potential inhomogeneous sampling of chance pairs as discussed in Lumpkin and Elipot (2010), and/or to a qualitatively different dispersion regimes at the submesoscale (Sansón, 2015) among the Mediterranean sub-basins. Not all these submesoscale flows are accurately resolved by the drifter dataset (Sansón, 2015). In the Adriatic Sea the presence of strong boundary currents induce the occurrence of local shear/ballistic regime, confirmed with all relative dispersion statistics, for scales $\sim D_I$ according to the results of Poulain et al. (2013). The shear/ballistic regime is observed also in the Ionian and Levantine regions, where the drifter pairs was advected from the boundary currents along the northern Ionian, Sicily Channel and the eastern Levantine coasts (**Figures 2C,D**, **13**). The Richardson regime takes place for space scale comparable to the Internal Rossby radius in the Tyrrhenian and the Aegean sub-basins (**Figure 13B**) and the pair separation distances are comparable to the scales of dominated eddies.

The relative diffusivities are calculated in two ways. In the first way, it is deduced from the derivative of relative dispersion in time (**Figure 9**) as suggested by Bouzaiene et al. (2018). It shows the presence of diffusive regime for large scales (when the pair velocities become uncorrelated) ∼50–100 km in four Mediterranean sub-basins (Tyrrhenian, Ionian, Levantine and Aegean), with the exception of the Adriatic Sea where the maximum pair separation distance after thirty days D_{max} is about 20 km. The lower diffusivity value is related to the limited size of the Adriatic basin where the pair velocities are still correlated (**Figure 8B**). The relative diffusivity in the last case fluctuates around of a constant value but it was not equivalent to twice of the absolute diffusivity $2k(t)^{(1)}$ because the majority of the pair velocities are correlated (**Figures 8B**, **9B**), the relative diffusivity would enter in the diffusive regime for scales comparable or larger than D_I (**Figure 9B**). The relative diffusivity presented in the second way is calculated from the second-order structure function and it appears less noisy than the first one (**Figure 10**). The two semi enclosed sub-basins (Adriatic and Aegean) show different behaviors related to the difference in the dynamics and eddy properties in each regions. Furthermore, the coastal Adriatic jets close to the large boundaries influence strongly the dispersion.

CONCLUSION

In this paper we present the dispersion analysis carried out in five Mediterranean sub-basins (Tyrrhenian, Adriatic, Ionian, Levantine and Aegean sub-basins). The analysis reveals the differences and similarities in term of surface dispersion regimes between the different sub-basins.

Quasi-ballistic and quasi-random walk regimes are observed at small and large time scales, respectively. A discrepancy between these two regimes and the two theoretical turbulent laws is observed, due to the non-uniform and non-stationary nature of the drifter dataset. The absolute dispersion shows that the surface Mediterranean flow is anisotropic in the five sub-basins while it seems to be isotropic in the Aegean sub-basin during the random-walk regime. The anomalous regimes (hyperbolic 5/4 and elliptic 5/3) are observed at intermediate time scales (2–15 days).

The surface relative dispersion shows the presence of an exponential relative dispersion regime for time scale smaller than the integral time scale ($3 < T_L < 5$) days and for space scales below the internal Rossby Radius of deformation D_I in the Tyrrhenian sub-basin (see, **Figures 13A,B**) with the presence of an enstrophy cascade range. For scales comparable to T_L and D_I, the relative dispersion implies the occurrence of the Richardson regime in the Tyrrhenian and Aegean sub-basins for the presence of an inverse cascade range (**Figures 13A,B**), while the shear/ballistic regime is observed in the other sub-basins (**Figures 13A,B**). For large time and space scales, the relative dispersion follows the diffusive regime (**Figures 13A,B**).

The results of this work improve our understanding of the surface dispersion mechanisms in the Mediterranean sub-basins and support the utility of Lagrangian data in the dispersion analysis of the ocean upper layer. Nowadays, there are still few dispersion studies in the intermediate and deep layers of the ocean. In the Western Mediterranean Sea numerical simulations have showed a decrease of the intermediate dispersion range with depth, due to the weaker influence of the vortices (Elhmaidi et al., 2010; Nefzi et al., 2014), but there are no specific studies on different types of regimes or comparisons between the different sub-basins. Previous analysis using *in situ* data for dispersion studies in the intermediate layer are reported in Price et al. (1987), LaCasce and Bower (2000), and Rudnickas et al. (2019). These authors use data of SOFAR and/or RAFOS floats in the Gulf Stream and North Atlantic. Roach et al. (2016, 2018) demonstrated that a two-particle analysis of Argo float trajectories produces robust estimates of horizontal mixing in the Southern Ocean and in the global ocean at float parking depth (nominally 1000 m). The method proposed here can also be applied to the Argo float trajectories available in the Mediterranean Sea (parking depth of 750 m). It would be hoped in the future to study dispersion phenomena at different depths in the Mediterranean Sea, with the help of models but also with *in situ* data acquired in specific experiments (e.g., using RAFOS floats and Argo floats or SVP drifters with drogue depths below the mixing layer). Such studies could help to understand the influence of deep processes on dispersion phenomena along the water column and their interaction with the surface layer. In this context, the method proposed in the present paper could be adapted to dispersion analysis even in deeper layers and/or to the comparison between different layers.

DATA AVAILABILITY STATEMENT

All datasets generated for this study are included in the article/supplementary material.

AUTHOR CONTRIBUTIONS

MB performed the analysis and wrote most of the manuscript. MM handled the drifter data sets, proposed the topic, supervised the work and took part in writing the manuscript. P-MP was in charge of funding acquisition, supervised and guided the work. AB handled the drifter datasets. DE supervised the manuscript preparation. All authors contributed to the article and approved the submitted version.

ACKNOWLEDGMENTS

The authors would like to thank all the people who have been involved and have kindly shared their drifter data in the Mediterranean Sea to build this work. Special thanks to Mr. Tarek Nemsi for producing some figures.

REFERENCES

Artale, V., Boffetta, G., Celani, A., Cencini, M., and Vulpiani, A. (1997). Dispersion of passive tracers in closed basins: beyond the diffusion coefficient. *Phys. Fluids* 9, 3162–3171. doi: 10.1063/1.869433

Aulicino, G., Cotroneo, Y., Olmedo, E., Cesarano, C., Fusco, G., and Budillon, G. (2019). *In situ* and satellite sea surface salinity in the algerian basin observed through ABACUS glider measurements and BEC SMOS regional products. *Remote Sens.* 11:1361. doi: 10.3390/rs11111361

Aurell, E., Boffetta, G., Crisanti, A., Paladin, G., and Vulpiani, A. (1997). Predictability in the large: an extension of the concept of Lyapunov exponent. *J. Phys. A Math. Gen.* 30, 1–26. doi: 10.1088/0305-4470/30/1/003

Babiano, A., Basdevant, C., and Larchevêque, M. (1985). Fonction de structure et spectre lagrangiens d'un écoulement turbulent bidimensionnel. *C. R. Acad. Sci. Paris* 300, 195–198.

Babiano, A., Basdevant, C., LeRoy, P., and Sadourny, R. (1990). Relative dispersion in two-dimensional turbulence. *J. Fluid Mech.* 214, 535–557. doi: 10.1017/S0022112090000258

Berti, S., and dos Santos, F. A. (2016). Relative dispersion and turbulence in theSouthwestern Atlantic Ocean from drifters data. *Chao. Mod. Sim.* 1, 9–20.

Beuvier, J., Beranger, K., Lebeaupin Brossier, C., Somot, S., Sevault, F., Drillet, Y., et al. (2012). Spreading of the western Mediterranean deep water after winter 2005: time scales and deep cyclone transport. *J. Geophys.Res. Oceans* 117:C07022. doi: 10.1029/2011JC007679

Bouzaiene, M., Menna, M., Poulain, P.-M., and Elhmaidi, D. (2018). Lagrangian dispersion characteristics in the Western Mediterranean. *J. Mar. Res.* 76, 139–161. doi: 10.1357/002224018826473290

Callies, U., Carrasco, R., Floeter, J., Horstmann, J., and Quante, M. (2019). Submesoscale dispersion of surface drifters in a coastal near offshore wind farms. *Ocean Sci.* 15, 865–889. doi: 10.5194/os-15-865-2019

Chen, R., McClean, J. L., Gille, S. T., and Griesel, A. (2014). Isopycnal eddy diffusivities and critical layers in the Kuroshio Extension from an eddying ocean model. *J. Phys. Oceanogr.* 44, 2191–2211. doi: 10.1175/JPO-D-13-0258.1

Corrado, R., Lacorata, G., Palatella, L., Santoleri, R., and Zambianchi, E. (2017). General characteristics of relative dispersion in the ocean. *J. Scient. Rep.* 7:46291. doi: 10.1038/srep46291

D'Ovidio, F., Fernandez, V., Hernandez-Garcia, E., and Lopez, C. (2004). Mixing structures in the mediterranean sea from finite-size lyapunov exponents. *Geophys. Res. Lett.* 31:L17203. doi: 10.1029/2004GL020328

D'Ovidio, F., Isern-Fontanet, J., Lopez, J., Hernandez-Garcia, E., and Garcia-Ladona, E. (2008). Comparison between Eulerian diagnostics and finite-size Lyapunov exponents computed from altimetry in the Algerian basin. *Deep Sea Res. Part I Oceanogr. Res. Pap.* 56, 15–31. doi: 10.1016/j.dsr.2008.07.014

Dräger-Dietel, G., Jochumsen, K., Griesel, A., and Badin, G. (2018). Relative dispersion of surface drifters in the benguela upwelling region. *J. Phys .Oceanogr.* 48, 2325–2341. doi: 10.1175/JPO-D-18-0027.1

Elhmaidi, D., Nefzi, H., Carton, X., and Lili, T. (2010). Particle dispersion in the Western Mediterranean basin. *Open Oceanogr. J.* 4, 137–143. doi: 10.2174/1874252101004010137

Elhmaidi, D., Provenzale, A., and Babiano, A. (1993). Elementary topology of the two-dimensional turbulence from a Lagrangian viewpoint and single particle dispersion. *J. Fluid Mech.* 257, 533–558. doi: 10.1017/S0022112093003192

Ferrari, R., and Nikurashin, M. (2010). Suppression of eddy diffusivity across jets in the Southern Ocean. *J. Phys. Oceanogr.* 40, 1501–1519. doi: 10.1175/2010JPO4278.1

Hansen, D. V., and Poulain, P.-M. (1996). Quality control and interpolations of WOCE-TOGA drifter data. *J. Atmos. Ocea. Techn.* 13, 900–909. doi: 10.1175/1520-0426(1996)013<0900:qcaiow>2.0.co;2

Koh, T., and Legras, B. (2002). Hyperbolic lines and the stratospheric polar vortex. *Chaos* 12, 382–394. doi: 10.1063/1.1480442

Koszalka, I., LaCasce, J. H., and Orvik, K. A. (2009). Relative dispersion in the Nordic Seas. *J. Mar.Res.* 67, 411–433. doi: 10.1357/002224009790741102

LaCasce, J. H. (2008). Statistics from Lagrangian observations. *Progr. Oceanogr.* 77, 1–29. doi: 10.1016/j.pocean.2008.02.002

LaCasce, J. H. (2010). Relative displacement probability distribution functions from balloons and drifters. 451 J. *Mar. Res.* 68, 433–457. doi: 10.1357/002224010794657155

LaCasce, J. H., and Bower, A. (2000). Relative dispersion in the subsurface North Atlantic. *J. Mar. Res.* 58, 863–894. doi: 10.1357/002224000763485737

LaCasce, J. H., and Ohlmann, C. (2003). Relative dispersion at the surface of the Gulf of Mexico. *J. Mar. Res.* 61, 285–312. doi: 10.1175/JPO-D-16-0105.1

Lacorata, G., Aurell, E., and Vulpiani, A. (2001). Drifter dispersion in the adriatic sea: lagrangian data and chaotic model. *Ann. Geophys.* 19, 121–129. doi: 10.5194/angeo-19-121-2001

Lumpkin, R., and Elipot, S. (2010). Surface drifter pair spreading in the North Atlantic. *J. Geophys. Res. Oceans* 115:C12017.

Lumpkin, R., and Pazos, M. (2007). "Measuring surface currents with SVP drifters: the instrument, its data and some results," in *Lagrangian Analysis and Prediction of Coastal and Ocean Dynamics*, eds A. Mariano, T. Rossby, and D. Kirwan (Cambridge, MA: Cambridge Univ. Press), 39–67. doi: 10.1017/cbo9780511535901.003

Mauri, E., Sitz, L., Gerin, R., Poulain, P.-M., Hayes, D., and Gildor, H. (2019). On the variability of the circulation and water mass properties in the Eastern Levantine Sea between September 2016–August 2017. *Water* 11:1741. doi: 10.3390/w11091741

Menna, M., Gerin, R., Bussani, A., and Poulain, P.-M. (2017). *The OGS Mediterranean drifter database: 1986-2016*. Trieste: OGS. technical report 2017/92 Sez.

Menna, M., Poulain, P.-M., Ciani, D., Doglioli, A., Notarstefano, G., and Gerin, R. (2019a). New insights of the Sicily Channel and Southern Tyrrhenian Sea variability. *Water* 11:1355. doi: 10.3390/w11071355

Menna, M., Poulain, P.-M., Mauri, E., Sampietro, D., Panzetta, F., Reguzzoni, M., et al. (2013). Mean surface geostrophic circulation of the Mediterranean Sea estimated from GOCE geoid models and Altimetric mean surface: initial validation and accuracy assessment. *Bell. Geofisica Teorica Applic.* 54, 347–365. doi: 10.4430/bgta0104

Menna, M., Poulain, P.-M., Zodiatis, G., and Gertman, I. (2012). On the surface circulation of the Levantine sub-basin derived from Lagrangian drifters and satellite altimetry data. *Deep Sea Res. I Oceanogr. Res. Pap.* 65, 46–58. doi: 10.1016/j.dsr.2012.02.008

Menna, M., Suarez, C. R., Civitarese, G., Gacic, M., Poulain, P.-M., and Rubino, A. (2019b). Decadal variations of circulation in the Central Mediterranean and its interactions with mesoscale gyres. *Deep Sea Res. II Top. Stud. Oceanogr.* 164, 14–24. doi: 10.1016/j.dsr2.2019.02.004

Nefzi, H., Elhmaidi, D., and Carton, X. (2014). Turbulent dispersion properties from a model simulation of the western Mediterranean Sea. *J. Ocean Sci.* 10, 167–175. doi: 10.5194/os-10-167-2014

Olson, D. B., Kourafalou, V. H., Johns, W. E., Samuels, G., and Veneziani, M. (2007). Aegean surface circulation from a satellite-tracked drifter array. *J. Phys. Ocean.* 37, 1898–1917. doi: 10.1175/JPO3028.1

Poje, A. C., Özgökmen, T. M., Lipphardt, B. L. Jr., Haus, B. K., Ryan, E. H., Haza, A. C., et al. (2014). Submesoscale dispersion in the vicinity of the Deepwater Horizon spill. *Proc. Nat. Acad. Sci. U.S.A.* 111, 12693–12698. doi: 10.1073/pnas.1402452111

Politikos, D. V., Ioakeimidis, C., Papatheodorou, G., and Tsiaras, K. (2017). Modeling the fate and distribution of floating litter particles in the Aegean Sea (E. Mediterranean). *Front. Mar. Sci.* 4:191. doi: 10.3389/fmars.2017.00191

Poulain, P.-M. (1999). Drifter observations of surface circulation in the Adriatic Sea between December 1994 and March 1996. *J. Mar. Sys.* 20, 231–253. doi: 10.1016/S0924-7963(98)00084-0

Poulain, P.-M. (2001). Adriatic Sea surface circulation as derived from drifter data between 1990 and 1999. *J. Mar. Sys.* 29, 3–32. doi: 10.1016/S0924-7963(01)00007-0

Poulain, P.-M., Bussani, A., Gerin, R., Jungwirth, R., Mauri, E., Menna, M., et al. (2013). Mediterranean surface currents measured with drifters: from basin to sub inertial scales. *J. Oceanogr. Soc.* 26, 38–47. doi: 10.5670/oceanog.2013.03

Poulain, P.-M., and Gerin, R. (2019). Assessment of the water-following capabilities of CODE drifters based on direct relative flow measurements. *J. Atm. Ocean* 36, 621–633. doi: 10.1175/JTECH-D-18-0097.1

Poulain, P.-M., Gerin, R., Rixen, M., Zanasca, P., Teixeira, J., Griffa, A., et al. (2012a). Aspects of the surface circulation in the Liguro-Provençal basin and Gulf of Lion as observed by satellite-tracked drifters (2007-2009). *B. Geofis. Teor. Appl.* 53, 261–279. doi: 10.5194/osd-9-3521-2012

Poulain, P.-M., Menna, M., and Mauri, E. (2012b). Surface geostrophic circulation of the Mediterranean Sea derived from drifter and satellite altimeter data. *J. Phys. Oceanogr.* 42, 973–990. doi: 10.1175/JPO-D-11-0159.1

Poulain, P. M., and Niiler, P. P. (1989). Statistical analysis of the surface circulation in the California 496 current system using satellite-tracked drifters. *J. Phy. Oceanogr.* 19, 1588–1603. doi: 10.1175/1520-0485(1989)019<1588:saotsc>2.0.co;2

Price, J. F., McKee, T. M., Owens, W. B., and Valdes, J. R. (1987). *Site L SOFAR floats experiment, 1982–1985*. Woods Hole Oceanographic Institution Technical Report, WHOI-, WHOI-97-52. Woods Hole, MA: WHOI.

Renault, L., Oguz, T., Pascual, A., Vizoso, G., and Tintore, J. (2012). Surface circulation in the Alboran Sea (western Mediterranean) inferred from remotely sensed data. *J. Geophys. Res* 117:C08009. doi: 10.1029/2011JC007659

Roach, C. J., Balwada, D., and Speer, K. (2016). Horizontal mixing in the Southern Ocean from Argo float trajectories. *J. Geophys. Res. Oceans* 121, 5570–5586. doi: 10.1002/2015JC011440

Roach, C. J., Balwada, D., and Speer, K. (2018). Global observations of horizontal mixing from Argo float and surface drifter trajectories. *J. Geophys. Res. Oceans* 123, 4560–4575. doi: 10.1029/2018JC013750

Rudnickas, D. Jr., Palter, J., Hebert, D., and Rossby, H. T. (2019). Isopycnal mixing in the North atlantic oxygen minimum zone revealed by RAFOS floats. *J. Geophys. Res. Oceans* 124, 6478–6497. doi: 10.1029/2019JC015148

Sansón, L. Z. (2015). Surface dispersion in the Gulf of California. *J. Prog. Oceanogr.* 137, 24–37. doi: 10.1016/j.pocean.2015.04.008

Sansón, L. Z., Perez-Brunius, P., and Sheinbaum, J. (2017). Surface relative dispersion in the southwestern Gulf of Mexico. *J. Phys. Oceanogr.* 47, 387–403.

Schroeder, K., Haza, A. C., Griffa, A., Ozgoekmen, T. M., Poulain, P.-M., Gerrin, R., et al. (2011). Relative dispersion in the Ligure-Provençal basin: from sub-mescoscale to mesoscale. *J. Deep Sea Res. I Oceanogr. Res. Pap.* 58, 209–228. doi: 10.1016/j.dsr.2010.11.004

Sybrandy, A. L., and Niiler, P. P. (1991). *WOCE/ TOGA Lagrangian Drifter Construction Manual*. SIO Ref. 91/6, WOCE Rep. No. 63. San Diego, CA: Scripps Institution of Oceanography.

Theocharis, A., Balopoulos, E., Kioroglou, S., Kontoyiannis, H., and Iona, A. (1999). A synthesis of the circulation and hydrography of the south Aegean Sea and the Straits of the Cretan Arc (March 1994-January 1995). *Progr. Ocean.* 44, 469–509. doi: 10.1016/S0079-6611(99)00041-5

Tintoré, J., Pinardi, N., Álvarez-Fanjul, E., Eguiar, E., Álvarez-Berastegui, E., Aguinar, E., et al. (2019). Challenges for sustained observing and forecasting systems in the Mediterranean sea. *Front. Env. Sci.* 6:568. doi: 10.3389/fmars.2019.00568

Zambianchi, E., Trani, M., and Falco, P. (2017). Lagrangian transport of marine litter in the Mediterranean Sea. *Front. Environ. Sci.* doi: 10.3389/fenvs.2017.00005

Conflict of Interest: The authors declare that the research was conducted in the absence of any commercial or financial relationships that could be construed as a potential conflict of interest.

frontiers in Marine Science

ORIGINAL RESEARCH
published: 22 July 2020
doi: 10.3389/fmars.2020.00594

Recent Changes in Deep Ventilation of the Mediterranean Sea; Evidence From Long-Term Transient Tracer Observations

*Pingyang Li and Toste Tanhua**

Marine Biogeochemistry, GEOMAR Helmholtz Centre for Ocean Research Kiel, Kiel, Germany

The Mediterranean Sea is a small region of the global ocean but with a very active overturning circulation that allows surface perturbations to be transported to the interior ocean. Understanding of ventilation is important for understanding and predicting climate change and its impact on ocean ecosystems. To quantify changes of deep ventilation, we investigated the spatiotemporal variability of transient tracers (i.e., CFC-12 and SF_6) observations combined with temporal evolution of hydrographic and oxygen observations in the Mediterranean Sea from 13 cruises conducted during 1987–2018, with emphasize on the update from 2011 to 2018. Spatially, both the Eastern and Western Mediterranean Deep Water (EMDW and WMDW) show a general west-to-east gradient of increasing salinity and potential temperature but decreasing oxygen and transient tracer concentrations. Temporally, stagnant and weak ventilation is found in most areas of the EMDW during the last decade despite the prevailing ventilation in the Adriatic Deep Water between 2011 and 2016, which could be a result of the weakened Adriatic source intensity. The EMDW has been a mixture of the older Southern Aegean Sea dense waters formed during the Eastern Mediterranean Transient (EMT) event, and the more recent ventilated deep-water of the Adriatic origin. In the western Mediterranean basin, we found uplifting of old WMDW being replaced by the new deep-water from the Western Mediterranean Transition (WMT) event and uplifting of the new WMDW toward the Alboran Sea. The temporal variability revealed enhanced ventilation after the WMT event but slightly weakened ventilation after 2016, which could be a result of combined influences from the eastern (for the weakened Adriatic source intensity) and western (for the weakened influence from the WMT event) Mediterranean Sea. Additionally, the Mediterranean Sea is characterized by a Tracer Minimum Zone (TMZ) at mid-depth of the water column attributed to the rapid deep ventilation so that the TMZ is the slowest ventilated layer. This zone of weak ventilation stretches across the whole Mediterranean Sea from the Levantine basin into the western basin.

Keywords: Mediterranean Sea, ventilation, transient tracer, CFC-12, SF_6

OPEN ACCESS

Edited by:
Nadia Lo Bue,
National Earthquake Observatory (INGV), Italy

Reviewed by:
Darryn Waugh,
Johns Hopkins University, United States
Anthony Bosse,
Aix-Marseille Université, France

***Correspondence:**
Toste Tanhua
ttanhua@geomar.de

Specialty section:
This article was submitted to Physical Oceanography, a section of the journal Frontiers in Marine Science

Received: *30 March 2020*
Accepted: *29 June 2020*
Published: *22 July 2020*

Citation:
Li P and Tanhua T (2020) Recent Changes in Deep Ventilation of the Mediterranean Sea; Evidence From Long-Term Transient Tracer Observations. Front. Mar. Sci. 7:594. doi: 10.3389/fmars.2020.00594

INTRODUCTION

Ocean ventilation is an important process in the Earth system that transports ocean surface properties, such as salinity, heat, CO_2 and dissolved gases to the interior ocean (Luyten et al., 1983; Khatiwala et al., 2012). Knowledge of the temporal and spatial variability of ocean ventilation is essential for understanding and predicting the response of the Earth system to global climate change. As a microcosm of the global ocean where climate change can be observed on a shorter time-scale (Schroeder et al., 2016), the Mediterranean Sea (**Figure 1a**) is well ventilated but with highly variable ventilation patterns in both time and space. Such ventilation patterns can directly be illustrated by, for instance, long-term observations of transient tracers. Transient tracers are taken up by the ocean at the air-sea interface and transferred into the deep ocean by the Deep/Dense Water Formation (DWF) through convection or subduction processes. There are four main DWF areas in the Mediterranean Sea: the Adriatic Sea, Southern Aegean Sea (Cretan Sea) and the Rhodes Gyre in the eastern Mediterranean basin (EMed), and the Gulf of Lions in the western Mediterranean basin (WMed). The deep water exchanges between the two basins are limited by the Strait of Sicily, which leads to a relative independent deep water circulation in each basin.

In the EMed, the Adriatic Sea used to be the main DWF region prior to the late 1980s (Roether et al., 1996). Interactions between Levantine Intermediate Water (LIW) and water masses from the Northern Adriatic Sea preconditioned the ocean to vertical mixing under the action of winter heat loss and wind stress (Artegiani et al., 1996a,b), creating high salinity dense waters by winter cooling, and leading to the formation of the Adriatic Deep Water (AdDW). After deep convection, the AdDW flowed over the Strait of Otranto sill into the Ionian Sea and then spreads southward and eastward to form the Eastern Mediterranean Deep Water (EMDW). However, the formation of the AdDW was in the "stagnation phase" from 1987 to 1999 (Manca et al., 2002; Roether et al., 2007). In the early 1990s, the Eastern Mediterranean Transient (EMT) event took place. The event marked a shift in dominant deep water source from the Adriatic Sea to the Aegean Sea characterized by massive DWF (Roether et al., 1996; Klein et al., 1999) triggered by the heat loss from the extremely cold winter in 1992–1993 (Roether et al., 2007) and high salinity (Velaoras et al., 2017). The estimated DWF rate in the Aegean Sea for the period 1989–1995 was three times higher than that of the Adriatic Sea (Lascaratos et al., 1999). Very dense water from the Aegean Sea filled the EMed and blocked the intrusion of the Adriatic-originated water into the Levantine basin (Akpinar et al., 2016). The Aegean-originated water dominated in the Levantine Sea in the 1990s also by shading the DWF in the Rhodes Cyclonic Gyre area (Malanotte-Rizzoli and Hecht, 1988). However, in 1999, the water from the Aegean source was not dense enough to reach the bottom of the adjacent Ionian and Levantine basins but was ventilating the 1500–2500 m layer (Theocharis et al., 2002). In the 2000s, the Aegean source was still characterized by dense water outflow but weakening (Velaoras et al., 2014). A reversal of the dominant source for the DWF in the EMed took place between 1999 and 2002 when the Adriatic deep water formation restarted, and the Adriatic Sea returned to be again the major source region in the EMed (Klein et al., 2000; Hainbucher et al., 2006; Rubino and Hainbucher, 2007; Cardin et al., 2015). In 2012, the extremely cold winter triggered another strong deep water formation in the Adriatic Sea (Gačić et al., 2014).

In the WMed, the Western Mediterranean Deep Water (WMDW) forms in the northwestern Mediterranean, mainly in the Gulf of Lions. Open-ocean deep convection, combined with occasional dense shelf water cascading, is the major contributor to the thermohaline circulation and ventilation in the source regions (Durrieu de Madron et al., 2013; Houpert et al., 2016; Testor et al., 2018). In addition, the EMT event has influenced the DWF processes in the Gulf of Lions in winter (Schroeder et al., 2006). Extensive DWF started from 2004 to 2006 and is known as the Western Mediterranean Transition (WMT) event (Schroeder et al., 2008, 2010). The event is thought to be triggered mainly by the atmospheric forcing in the WMed and the lateral advection of anomalously salty and warm LIW because of increased heating and evaporation in the EMed (Marshall and Schott, 1999; Schroeder et al., 2010, 2016). The WMT event caused the structure of intermediate and deep layers to abruptly change in the WMed and a near-complete renewal of WMDW (Schneider et al., 2014). Since then, the deep convection intensity in the source region decreased based on long-term surveys in the Gulf of Lions (Houpert et al., 2016).

In the Tyrrhenian Sea, the situation is a little bit different. Beneath the LIW, the transitional EMDW (tEMDW, a mixture of LIW and EMDW from the EMed) mixes with the water in the Tyrrhenian Sea and settles between 600 and 1500 m (Sparnocchia et al., 1999). Below the tEMDW, WMDW enters the Tyrrhenian Sea (Schroeder et al., 2016). The mixture of tEMDW and WMDW forms the Tyrrhenian Deep Water (TDW) with a core depth deeper than 1500 m (Astraldi et al., 2002; Buffett et al., 2017).

As the area separating the EMed and WMed, the Strait of Sicily is composed of the surface Modified Atlantic Water (MAW) flowing eastward, the lower LIW and bottom tEMDW flowing westward (Astraldi et al., 1996, 2002; Sparnocchia et al., 1999).

Transient tracers have been used to understand ventilation and circulation processes, and determine water mass characteristics in the Mediterranean Sea in multiple studies. For example, the vertical and spatial distributions of transient tracers have been described in the EMed by Roether et al. (1996) and in the WMed by Rhein et al. (1999) to quantify ventilation timescales. They have also been used to identify the water mass structure and distribution by combined analysis of hydrographic properties such as salinity and temperature (Theocharis et al., 2002; Cardin et al., 2015), as well as some biogeochemical properties such as dissolved oxygen, silicate and nitrate (Klein et al., 1999, 2000). In addition, transient tracers have been used to estimate the anthropogenic carbon content of the water (Schneider et al., 2010) by applying the Transit Time Distribution (TTD) concept (Waugh et al., 2003; Stöven and Tanhua, 2014). Therefore, a combination of

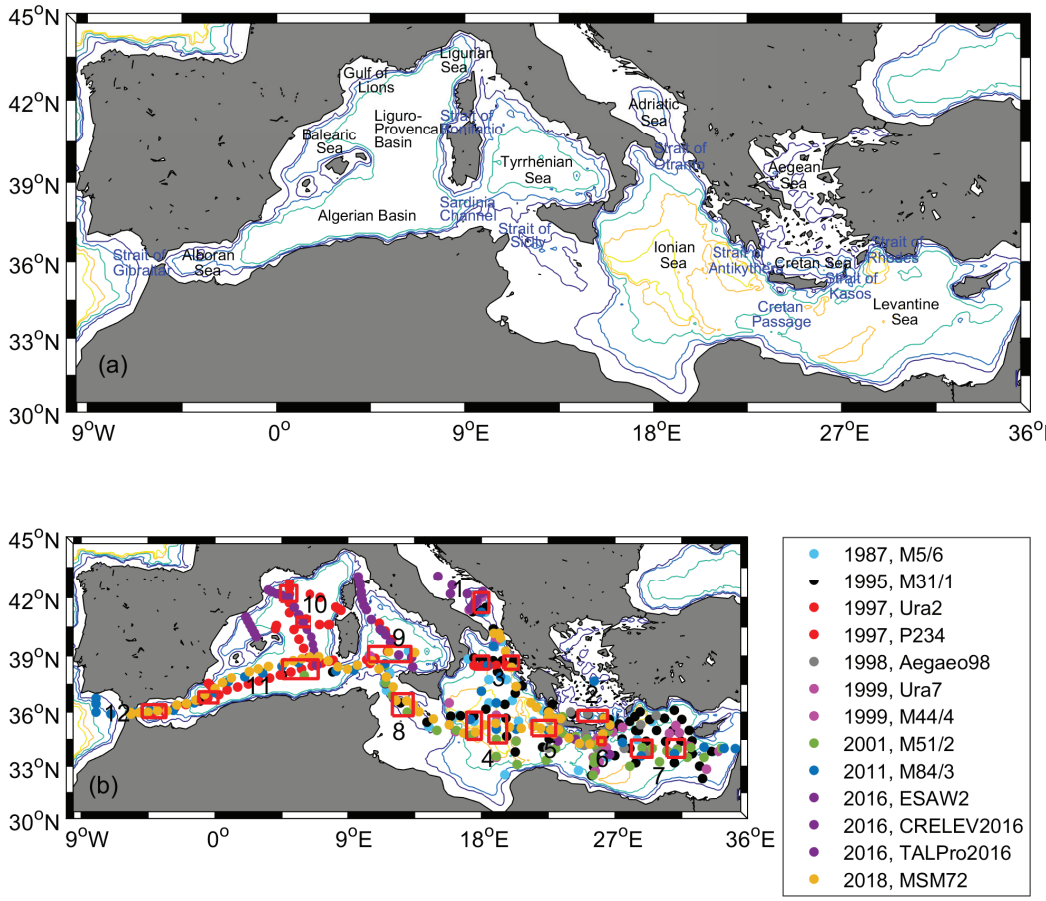

FIGURE 1 | (a) Map of the Mediterranean Sea. **(b)** Sampling sites of CFC-12 and SF_6 measurements from historical cruises listed in **Table 1** in the Mediterranean Sea; samples from a certain year (rather than cruise) have the same color, which is also used in the figures below. The small red boxes are the areas selected for assessing the temporal variability of ventilation. The areas are located in the (1) Southern Adriatic Sea, (2) Cretan Sea, (3) Northern Ionian Sea, (4) Western and Central Ionian Sea, (5) Eastern Ionian Sea, (6) Northern Cretan Passage, (7) Western and Central Levantine basins, (8) Strait of Sicily, (9) Tyrrhenian Sea, (10) Gulf of Lions and Liguro-Provençal basin, (11) Central and Western Algerian basin and (12) Alboran Sea. The depth contours are 500, 1000, 2000, 3000, and 3500 m.

transient tracers (CFC-12, SF_6, etc.), hydrographic properties (salinity, temperature, density, etc.) and oxygen can characterize ventilation processes on the basis of the water mass distributions. Previously, Schneider et al. (2014) discussed the temporal variability of ventilation in the Mediterranean Sea for the timeframe 1987–2011. The authors studied well-defined boxes in each basin and discussed the averaged vertical profiles of salinity, temperature, oxygen, CFC-12 concentration, CFC-12 tracer age, CFC-12 mean age, tritium/helium age and tritium mean age. In the study by Schneider et al. (2014), they carried out a comparison of averaged profiles from different years within relatively large boxes, whereas, in this study, we compare profiles in specific sampling stations in overlaid or close vicinity to each other (in small boxes). For this approach, there is a risk that small-scale variability, such as eddies, will bias the comparison, whereas for large boxes real variability within the box can bias the comparison.

The primary goal of this study is to investigate the temporal and spatial variability (with an emphasis on the recent changes) in deep and intermediate ventilation of the Mediterranean Sea based on transient tracer (CFC-12 and SF_6) observations. To the end, we address the spatiotemporal distributions of transient tracer (CFC-12 and SF_6) concentrations as well as the temporal evolution of potential temperature-salinity (Θ–S) diagrams and depth-profiles of CFC-12 and SF_6 concentrations, salinity, potential temperature, potential density and apparent oxygen utilization in pressure (CFC-12/SF_6/S/Θ/σ_Θ/AOU vs. P) between 1987 and 2018.

OBSERVATIONS AND METHODS

Observations From Cruises

Table 1 lists the cruises used in this work from which we have transient tracer observations. Most of the recent cruises were conducted in the framework of the Med-SHIP program (Schroeder et al., 2015). Sampling sites for each cruise are shown in **Figure 1b**. Seawater samples for CFC-12 and SF_6

were measured either on board from syringe sampling or ashore from flame-sealed glass ampoules. For cruises in 1987–2001, CFC-12 and CFC-11 were observed, although we focus on the CFC-12 observations due to no recent CFC-11 observations, whereas for cruises in 2011–2018 both CFC-12 and SF_6 data are considered. For cruise P234 in 1997, analytical issues for CFC-12 were reported by the authors (Rhein et al., 1999), in particular for the later part of the cruise (station number larger than 766), although such CFC-12 data were flagged as good (i.e., "2" or "6") from the database. Therefore, we reported the CFC-11 data in addition to the CFC-12 observations (except for the Tyrrhenian Sea where we can only use the CFC-11 values). To make the CFC-11 data comparable, we multiplied the CFC-11 partial pressures with 2.03, which is the ratio of CFC-12 and CFC-11 atmospheric mole fraction in 1997. Since the atmospheric temporal evolutions of the two tracers are similar up to about 1990, this is a reasonable proxy for estimating trends in ventilation, as can be seen from figures for the WMed in section "Temporal Variability of Properties in the WMed," although not perfect. More details on measurement methods, precisions and accuracies for the observations can be found from the correspondence references and/or cruise reports (**Table 1**). The observations of CFC-12 and SF_6 from four cruises during the years 2016–2018 are reported here for the first time. The measurement methods can refer to the corresponding cruise reports and/or Stöven and Tanhua (2014).

Methods for Assessing Spatiotemporal Variability

The Transit Time Distribution (TTD) model describes the propagation of tracer boundary conditions from the ocean surface into the interior based on the Green's function (Hall and Plumb, 1994) and is often used to assess ventilation time-scales. However, the ventilation of the Mediterranean Sea is time-variant, making it difficult to apply the TTD concept. Therefore, in this study, we used (CFC-12 and SF_6) concentrations (in ppt, part per trillions) to assess the historical evolution of ventilation and involved hydrography data to support conclusions of variability in ventilation patterns. The equilibrium concentrations (in ppt rather than in pmol kg^{-1}) of the transient trace gases into the seawater are chosen so that their dependence on the salinity and temperature are removed.

We are also using Apparent Oxygen Utilization (AOU) as a measure of ventilation. We use AOU rather than oxygen since the dependencies of S and Θ on oxygen saturation is already factored into the concept, which is similar to the case for concentrations of CFC-12 and SF_6 in ppt rather than in pmol kg^{-1}. The AOU is different from the transient tracers in that the input function is constant so that a change in AOU can be directly related to a change in ventilation, or oxygen consumption rate.

We start by discussing the spatiotemporal distribution of ventilation in the Mediterranean Sea by analyzing CFC-12 and SF_6 concentration sections at roughly the same locations in the EMed and WMed separately. As a second step, we consider the temporal variability of ventilation by comparing the structures of potential temperature and salinity (Θ–S diagrams), as well as depth-profiles of transient tracer concentrations (CFC-12 and SF_6), salinity (S), potential temperature (Θ in°C), potential density (σ_Θ in kg m^{-3} referenced to 0 dbar pressure) and apparent oxygen utilization (AOU in μmol kg^{-1}) for stations within each box in **Figure 1b**.

Tracer Age Difference

The age of a water parcel is defined as the time elapsed since it left the mixed layer where it was in contact with the atmosphere before transported into the ocean interior. The concept of tracer age does not consider turbulent mixing in the ocean interior, which is unrealistic but it provides a framework to compare the

TABLE 1 | Key meta-data for the Mediterranean Sea cruises used in this study.

Year	Cruise	Research vessel	Cruise period	W/E. Med	CFC-12/SF_6[a]	References
1987	M5/6	Meteor	1987.08.18-09.24	W, E	CFC-12	Schlitzer et al., 1991; Nellen et al., 1996
1995	M31/1	Meteor	1994.12.30-1995.03.22	W, E	CFC-12	Hemleben, 1996; Roether et al., 1996, 1998; Klein et al., 1999
1997	Ura2	Uranis	1997.08.30-09.08	E	CFC-12	Manca et al., 2002; Roether et al., 2007
1997	P234	Poseidon	1997.10.23-11.10	W	CFC-12, CFC-11	Rhein et al., 1999
1998	Aegaeo98	Aegaeo	1998.10.14-10.19	E	CFC-12	Theocharis et al., 2002
1999	Ura7	Uranis	1999.02.11-02.17	E	CFC-12	Manca et al., 2002; Roether et al., 2007
1999	M44/4	Meteor	1999.04.10-05.16	W, E	CFC-12	Pätzold, 2000; Theocharis et al., 2002
2001	M51/2	Meteor	2001.10.18-11.11	W, E	CFC-12	Hemleben et al., 2003; Roether et al., 2007; Schneider et al., 2010
2011	M84/3	Meteor	2011.04.05-04.28	W, E	CFC-12, SF_6	Tanhua et al., 2013a; Stöven and Tanhua, 2014; Schneider et al., 2014; Cardin et al., 2015
2016	ESAW2	Bios Dva	2016.04.05-04.10	E	CFC-12, SF_6	Šantiæ et al., 2019
2016	CRELEV2016	Aegaeo	2016.06.02-06.10	E	CFC-12, SF_6	Velaoras et al., 2018
2016	TALPro2016	Angeles Alvarino	2016.08.18-08.29	W	CFC-12, SF_6	Jullion, 2016
2018	MSM72	Maria S. Merian	2018.03.02-04.03	W, E	CFC-12, SF_6	Hainbucher et al., 2019

Results of CFC-12 and SF_6 from cruises in 2016–2018 have not yet been published elsewhere. [a]*All the acronyms and corresponding full names of terms used in this study can be found in* ***Supplementary Table S1****.*

ventilation time-scale at one location over time. The atmospheric temporal evolutions of CFC-12 and SF_6 overlay when the atmospheric records of SF_6 are shifted back by 14 years (Tanhua et al., 2013b). Therefore, the tracer age estimated by SF_6 should equal to that by CFC-12 based on measurements of CFC-12 taken 14 years earlier in the same region in a steady-state situation, independent of mixing patterns. Inspired by this, Schneider et al. (2014) compared the tracer ages estimated by SF_6 in 2011 and CFC-12 in 1997/98. However, as seen from the vertical dash line in **Supplementary Figure S1**, the (shifted) atmospheric records of CFC-12 and SF_6 started to diverge after 2005, which means that the time shift of 14 years doesn't work well for the two tracers after this time. In other words, comparison of tracer age between SF_6 and CFC-12 with a time gap of 14 years still works for deep and intermediate waters outside of convective areas, but not so well for more recently ventilated waters.

For this study, we were able to find locations where CFC-12 and SF_6 were measured in 2001 and 2016, respectively, in the northern Cretan Passage and the Tyrrhenian Sea. The averaged tracer ages were calculated by first interpolating the individual profiles to standard depths and then by taking the arithmetic mean of the interpolated profiles (Tanhua et al., 2010). The bias created by the changing growth rate of SF_6 from 2015 (time shift of 14 years) and 2016 is expected to be small (the standard deviation is 0.35%) based on the linear increasing atmospheric mole fraction of SF_6 (**Supplementary Figure S1**).

RESULTS

Spatial Distributions of CFC-12 and SF_6 in the EMed

We show vertical sections of CFC-12 concentrations for 1987, 1995, 1999, 2001, 2011, and 2018, and SF_6 concentrations for 2011 and 2018 to illustrate the spatial evolution of tracer distributions during the last ∼30 years in the Eastern Mediterranean Sea (**Figure 2**). For more detailed discussions on individual datasets, we refer the reader to previous studies shown in **Table 1**. In the following, we describe the observations in relation to the temporal evolution.

1987

This data set represents the only pre-EMT transient tracer observation for the Mediterranean Sea (**Figure 2a**). The high CFC-12 concentration of EMDW in the western Ionian Sea is a signal of recently formed deep water from the Adriatic Sea, with gradually decreasing CFC-12 concentrations eastward in the EMDW. The layer with the oldest water and CFC-12 concentrations less than ∼30 ppt marks the Tracer Minimum Zone (TMZ) at the depth of 1200–2800 m. This zone stretches from the Ionian Sea to the central Levantine basin where it reached close to the bottom. The low CFC-12 concentrations indicate an absence of direct ventilation for the depth ranges of the deep and intermediate layers in the east. An area of elevated CFC-12 concentration water was centered at ∼700 m depth in the northern Cretan Passage originated from the Aegean Sea, which implies that newly ventilated Cretan Intermediate Water (CIW) spread into the water below the LIW in the western Levantine basin and the Ionian Sea (Schlitzer et al., 1991). Thus, the EMDW below 1200 m depth was mainly fed by the Adriatic-originated water and the intermediate layer between 200 and 1200 m fed by CIW and LIW in 1987.

1995

The Meteor cruise in 1995 presents the first comprehensive transient tracer observations after the EMT event (**Figure 2b**) conducted in the framework of the POEM (Physical Oceanography in the Eastern Mediterranean) project (Malanotte-Rizzoli and Robinson, 1988). The CFC-12 concentrations in 1995 are dramatically different from those in 1987. The youngest water below ∼500 m was found in the northern Cretan Passage bottom water with a CFC-12 concentration of ∼220 ppt, a signal of very strong ventilation since 1987. The EMDW related to the Adriatic-derived water was still found in the western part of the section, with a CFC-12 concentration of ∼200 ppt, higher than that in 1987. The CFC-12 concentration in the oldest water (the TMZ) became younger and the TMZ split into two main cores: the western and eastern cores with CFC-12 concentrations of ∼90 and 60 ppt, respectively. The CFC-12 concentration in the TMZ thus increased significantly from 1987 to 1995. The TMZ in 1995 had a narrower depth range and was centered at a shallower depth, which has been interpreted as uplifted bottom waters by intruding Cretan Deep Water (CDW) (Roether et al., 1996). Noting that the oldest water in 1987 was replaced with the younger water, which indicates the strong renewal of water in the EMed in the early 1990s, as reported in previous studies (Roether et al., 1996; Theocharis et al., 2002; Roether et al., 2007).

1999 and 2001

The double core TMZs still existed at the time, but with some changes. In the Ionian Sea, the CFC-12 concentration increased from ∼90 ppt in 1995 to ∼120 ppt in 1999/2001 (**Figures 2c,d**). There is also a tendency for the TMZ to displace from the western to the eastern Ionian Sea. In the Levantine basin, the CFC-12 concentrations in the TMZ increased to ∼70/80 ppt in 1999/2001 and shoaled from ∼2000 to ∼1000 m. This was accompanied by a diminished thickness of the TMZ in 1999/2001 as the recently formed EMDW from the EMT event advected eastwards along with the deeper layers of the Levantine basin. On the other hand, there is a more obvious signal of high transient tracer concentration on the western slope in 2001 than in 1999, which may suggest an Adriatic source of deep water.

2011

The spatial distribution of CFC-12 concentrations in 2011 (**Figure 2e**) was quite different from the one in 2001. The new Adriatic-derived water is observed in the bottom water of the western Ionian Sea in 2011 with a CFC-12 concentration of ∼270 ppt and an SF_6 concentration of ∼2.4 ppt (**Figure 2g**). The TMZs still existed at roughly the same depth (∼1000 m) as in 2001, but with significantly higher CFC-12 concentrations: ∼160 ppt in the eastern Ionian Sea and ∼120 ppt in the Levantine basin. However, the TMZ as defined by the SF_6 concentrations

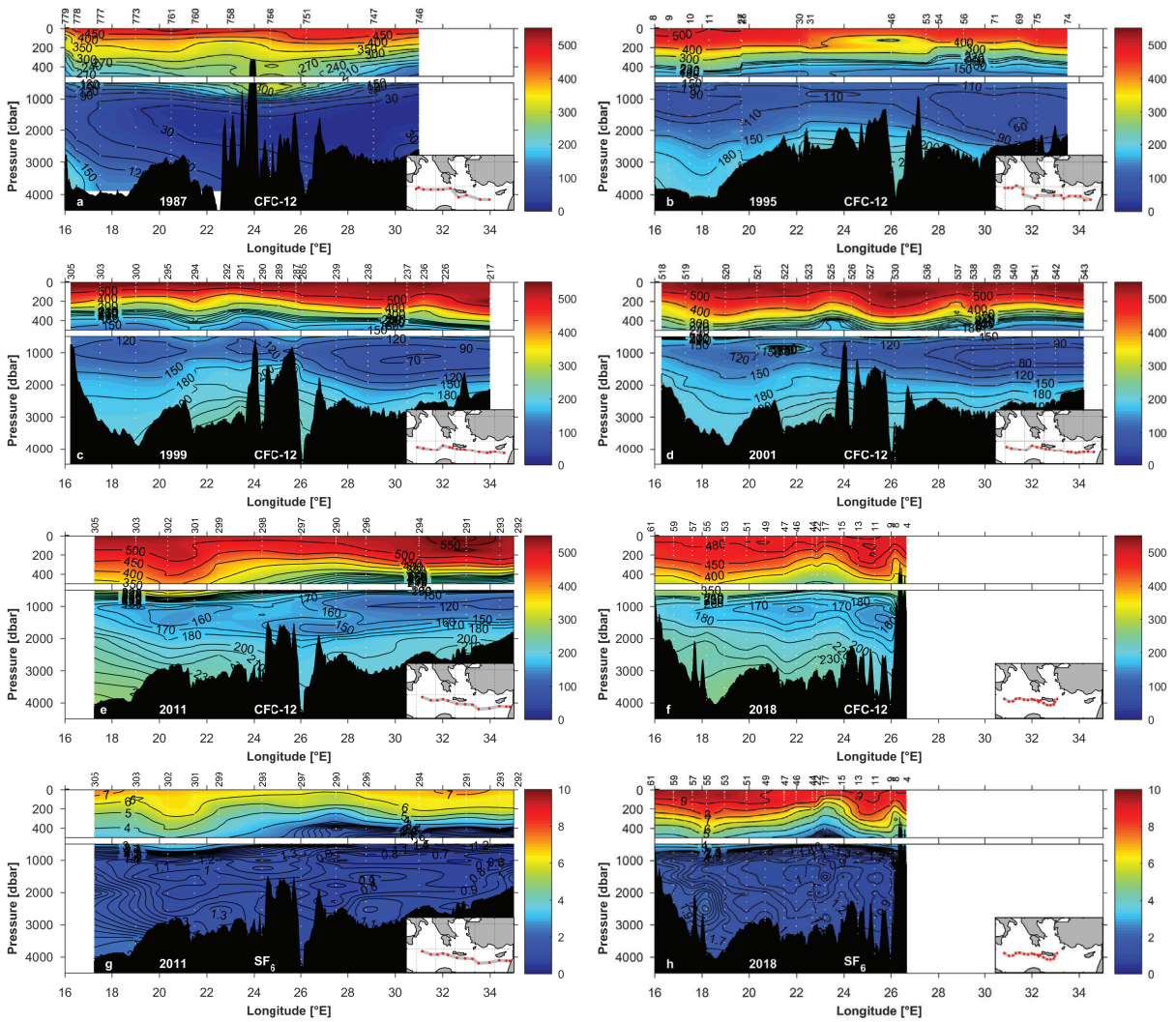

FIGURE 2 | Vertical sections of CFC-12 concentration (in ppt) in the Eastern Mediterranean Sea (see inset map for station locations) in **(a)** 1987 (Meteor M5/6), **(b)** 1995 (Meteor M31/1), **(c)** 1999 (Meteor M44/4), **(d)** 2001 (Meteor M51/2), **(e)** 2011 (Meteor M84/3), and **(f)** 2018 (Maria S. Merian MSM72) and vertical sections of SF_6 concentration (in ppt) in the EMed in **(g)** 2011 (Meteor M84/3) and **(h)** 2018 (Maria S. Merian MSM72). The same scales of longitude and pressure are used for all figures, while the same color bars are separately used for CFC-12 and SF_6 sections. The upper panels highlight the top 500 m. The markers on the top *x*-axis stand for the station number.

is better defined with ∼0.6 ppt in the Levantine basin at slightly larger depth, reflecting the different input functions of the two tracers; SF_6 being more sensitive to more recent changes in ventilation.

2018

Although the 2018 cruise was unable to sample the Levantine basin, there is evidence that the extent of the Adriatic-derived water in the EMDW in the western Ionian Sea expanded eastward and upward from 2011 to 2018 (**Figure 2f**). The spatial distribution of SF_6 concentrations in 2018 was generally similar to that of CFC-12 above 500 m, but with significant differences below this depth (**Figure 2h**). Focusing on the Ionian Sea and the northern Cretan Passage, the CFC-12 concentrations of the two cores of the TMZ in 2018 are ∼150 ppt in the northern Cretan Passage and ∼170 ppt in the eastern Ionian Sea, slightly higher than those in 2011. But for SF_6, two cores are found with ∼0.9 ppt in the north-western and north-eastern Cretan Passage, which are slightly lower than those in 2011. The double-core TMZ was more clearly observed in 2018 compared to 2011; possibly associated with well-ventilated flow through the Antikythera strait as the transient tracer profiles just west of the strait (in 2018) show enhanced concentrations at intermediate levels down to 1200 m depth. The oldest water was found at ∼1500 m and 1000–3000 m in the northern Cretan Passage defined by CFC-12 and SF_6, respectively in both 2011 and 2018. The transient tracer concentrations in the deep western Ionian Sea decreased from ∼270 to 240 ppt for CFC-12 and

from ∼2.4 to 1.9 ppt for SF_6 from 2011 to 2018, implying the weakening influence from the Adriatic Sea. The relative higher SF_6 concentrations shown in the deep layer but not in the bottom layer suggest that the water from the Adriatic source was no longer dense enough between 2011 and 2018 to reach the bottom of the Ionian Sea but ventilated the 2000–3000 m depth layer. A larger difference in the spatial distribution of CFC-12 and SF_6 concentrations took place in 2018 compared to 2011. This resulted from the weakened ability of CFC-12 in interpreting ventilation in the Mediterranean Sea considering its decreasing atmospheric history.

Temporal Variability of Properties in the EMed

Adriatic Sea

We have a time-series of properties from 1987 to 2016 in the Adriatic Sea (**Figure 3** and **Supplementary Figure S2**). The time-series show nearly identical CFC-12 concentrations in the deep-water layer (below 600 m) dominated by AdDW from 1987 to 1999, while there is a sharp increase in the CFC-12 concentration of ∼140 ppt from 1999 to 2011 and another increase of ∼100 ppt from 2011 and 2016. A similar increase during 2011–2016 is also found for the SF_6 concentration in the magnitude of ∼2 ppt. For other properties in the deep layer, the salinity (S) and potential temperature (Θ) slightly decreased from 1987 to 1995, and then increased up to 2016, with a rapid increase in salinity of ∼0.1 and Θ of ∼0.3°C between 1999 and 2011. The high near-bottom salinities in 2011 are seen through the whole deep layer in 2016. The potential density (σ_Θ) generally decreased from 1987 to 1999 and increased to 2011 followed by a decrease to 2016 in the near-bottom layer, following mainly compensating trends in S and Θ. There is a weak and variable trend for apparent oxygen utilization (AOU) to increase between 1987 and 2016. Compared to the largely increased salinity and Θ (∼0.15 and ∼0.5°C) from 1995 to 2011/16, similar AOU values are found in 1995, 2011, and 2016 in the near-bottom layer. All these changes support strong ventilation in the Adriatic Sea during the last 15–20 years (1999–2016) with the formation of new AdDW with higher S and Θ.

The Adriatic intermediate water (**Supplementary Figure S2**) showed decreased CFC-12 concentrations and increased AOU from 1987 to 1995, which highlights slow ventilation of the less saline and colder water in 1995. Opposite to this period, the increase in CFC-12 concentrations and decrease in AOU after 1995 indicate enhanced ventilation of the generally more saline and warmer water, except for the decreased salinity from 1999 to 2011.

Cretan Sea

Figure 4 and **Supplementary Figure S3** shows that CFC-12 concentrations, salinity, Θ and σ_Θ in the Cretan Sea are relatively higher than those in other areas in the Mediterranean Sea. In the deep-water layer (below ∼1300 m), largely increased salinity, σ_Θ and CFC-12 concentrations (∼60 ppt) between 1987 and 1995 are in agreement with the period of enhanced ventilation related to the EMT event, when compared with the nearly unchanged CFC-12 concentrations in the AdDW (**Figure 3**) for the same period. From 1995, the Aegean deep-water source was getting weaker as indicated by the gradually decreased salinity, σ_Θ and oxygen (increased AOU) in the Cretan Deep Water (CDW) from 1995 to 2018 (**Figure 4**). Although with weakened Aegean source intensity, the CDW was still ventilated until 2011 as indicated by the increased CFC-12 concentrations from 1998 (**Figure 4b**). The weakened ventilation after 2011 can be seen by the increased AOU and the fact that CFC-12 concentrations in 2018 are slightly lower than those in 2011, although SF_6 concentrations show the opposite change, related to decreasing CFC-12 and increasing SF_6 atmospheric mole fractions.

Above the CDW, a characteristic Θ–S inversion at 300–1300 m depth (**Figure 4**) is thought to be the core depths of the Transitional Mediterranean Water (TMW). The depth of the inversion is also the depth of "local CFC-12/salinity/Θ/oxygen minimum," indicating infrequent (weak) ventilation (renewal). In this layer (**Supplementary Figure S3**), slightly decreased CFC-12 concentrations and increased AOU from 1987 to 1995 suggest weak ventilation, but the constant AOU between 1995 and 2018 indicates constant ventilation.

Ionian Sea

Northern Ionian Sea

In this area, we examined clusters of stations from the western and eastern parts of the basin south of Otranto Strait. For the deep layer (below ∼1200 m) in the north-western Ionian Sea (**Figure 5** and **Supplementary Figure S4**), CFC-12 concentrations, as well as salinity and Θ, increased from 1987 to 2011 but with a small decrease below ∼2000 m from 1997 to 2011 for the latter two properties, while AOU decreased from 1987 to 1995 then increased to 2011. In the deep layer of the north-eastern Ionian Sea, CFC-12 concentrations increased from 1987 to 1997 but with a small decrease to 2018, while salinity and Θ increased from 1987 to 1995 but decreased to 2018 in the near-bottom layer, and AOU showed the opposite change. The dramatic increase in salinity and Θ found between 1987 and 1995 for the north-eastern Ionian Sea, but between 1995 and 1997 for the north-western Ionian Sea could be related to the spreading deep water of Aegean source. There was a large difference of CFC-12 concentrations between the north-western and north-eastern Ionian deep waters in 1987, indicating a larger Adriatic outflow that tends to follow the western slope. However, similar CFC-12 concentrations are found between the two deep waters in 1995/97, implying different sources.

For the intermediate layer (**Supplementary Figure S4**), the slightly decreased CFC-12 concentrations and increased AOU from 1987 to 1995 indicate slow ventilation in the north-western Ionian Sea. After 1995, CFC-12, salinity, Θ and AOU increased in the north-western and north-eastern Ionian intermediate waters.

Western and central Ionian Sea

In the western and central Ionian Sea (**Figure 6** and **Supplementary Figure S5**), CFC-12 concentrations increased significantly from 1987 to 1995 (90–120 ppt), gradually increased up to 2001 and another "jump" in concentrations to 2011,

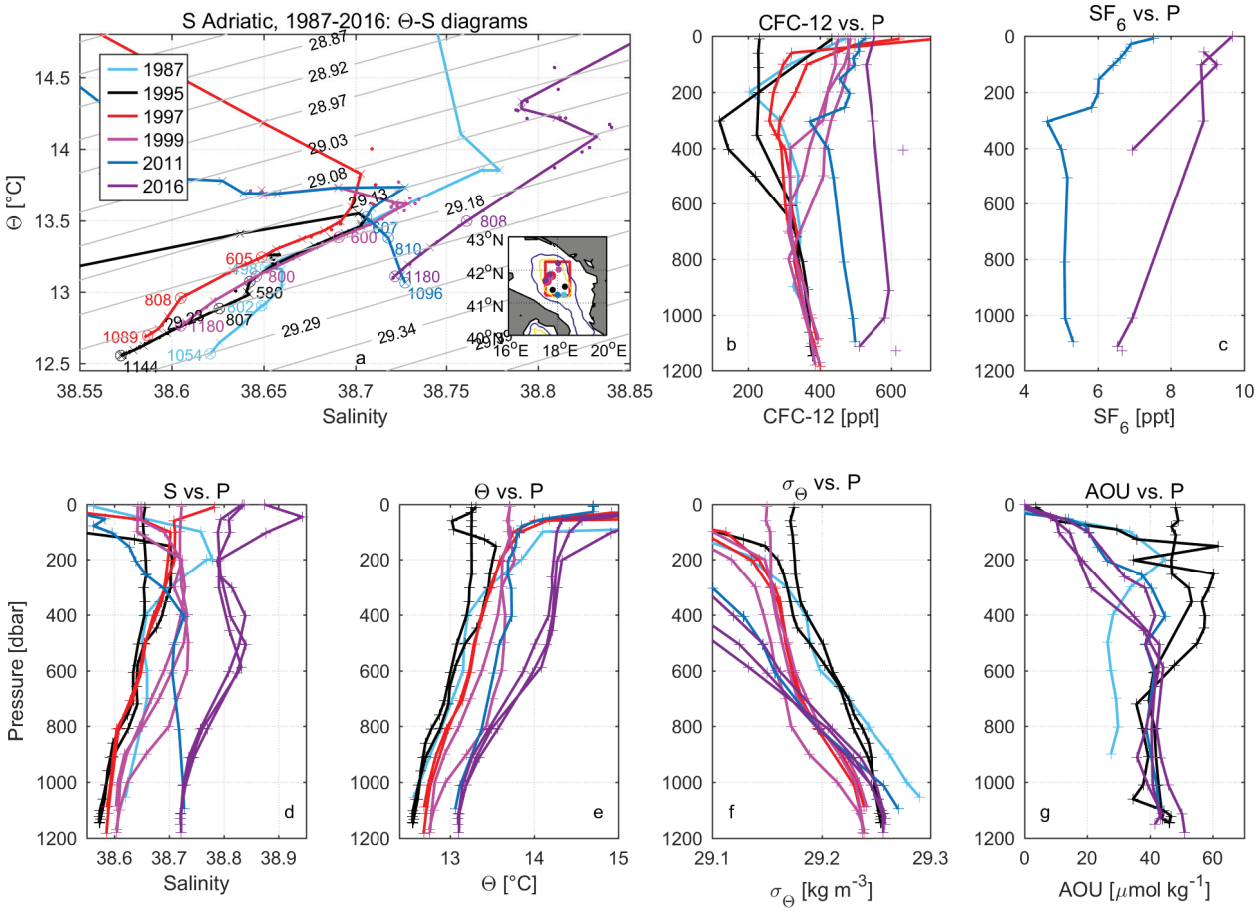

FIGURE 3 | Temporal variability of the Southern Adriatic Sea illustrated with **(a)** Θ–S diagrams with σ_Θ isolines, **(b)** CFC-12 concentration vs. pressure, **(c)** SF_6 concentration vs. pressure, **(d)** salinity vs. pressure, **(e)** potential temperature (Θ) vs. pressure, **(f)** potential density (σ_Θ) vs. pressure and **(g)** apparent oxygen utilization (AOU) vs. pressure. For sampling year see the legend and for site positions see inset map (isolines are 500, 1000, 2000, 3000, and 3500 m). The stations shown are (in the sequence of the legend) M5/6 766, M31/1 16 and 17, Ura2 18 and 11, Ura7 8, 7 and 5, M84/3 313 and ESAW2 29, 8 and 7. Bottle data is indicated by crosses (for the first station from each cruise) and dots (for the rest stations from each cruise) in Θ–S diagrams and pluses in other plots (for all stations from each cruise).

that slightly decreased or remained essentially constant to 2018, although the SF_6 concentrations slightly decreased from 2011 to 2018 in the layer below ∼3000 m. Similar to the transient tracers, the Θ/S evolution in the central Ionian is also characterized by a large increase (∼0.2°C/0.1) from 1987 to 1995, the year with the highest Θ/S of the time-series. In 1999, the Θ/S decreased significantly but did not reach the pre-EMT levels, and then gradually increased through the time-series up to 2011/18. The AOU story is again slightly different. The AOU decreased from 1987 to 1995, dramatically increased to 1999, decreased to 2001 and then slightly increased to 2018 below 1400 m. The stepwise increase and the occasional decrease in CFC-12 concentration and the dramatic change of AOU indicate variable ventilation. For instance, the increased CFC-12 concentrations and decreased AOU after 1987 and 1999 indicate enhanced ventilation during the 1987–1995 and 1999–2001 time-periods, nearly stagnated ventilation during 1995–1999 and 2011–2018 for the central Ionian and possibly slightly weakened ventilation from 2011 to 2018 for the western Ionian Sea. Such ventilation status during 2011–2018 is also supported by observations of SF_6. Note the dramatic increase in AOU from 1995 to 1999 also noticed by Klein et al. (2000) that speculate on increased oxygen consumption due to increased input of labile Dissolved Organic Carbon (DOC) with the new deep water. The dramatically Θ–S inversion and increased salinity and Θ in 1995 found in the central Ionian Sea but not in the western Ionian Sea are related to the EMT event. The difference of properties in the deep layer between the western and central Ionian Sea in 1995 are ∼30 ppt for CFC-12 concentrations, ∼0.1 for salinity, ∼0.3°C for Θ and ∼5 μmol kg^{-1} for AOU.

In the western Ionian intermediate water (**Supplementary Figure S5**), CFC-12 concentrations and salinity gradually increased from 1987 to 2018, but Θ and AOU decreased to 1999 and then increased to 2018, which depicts relatively strong ventilation between 1987 and 1999 but weak ventilation after

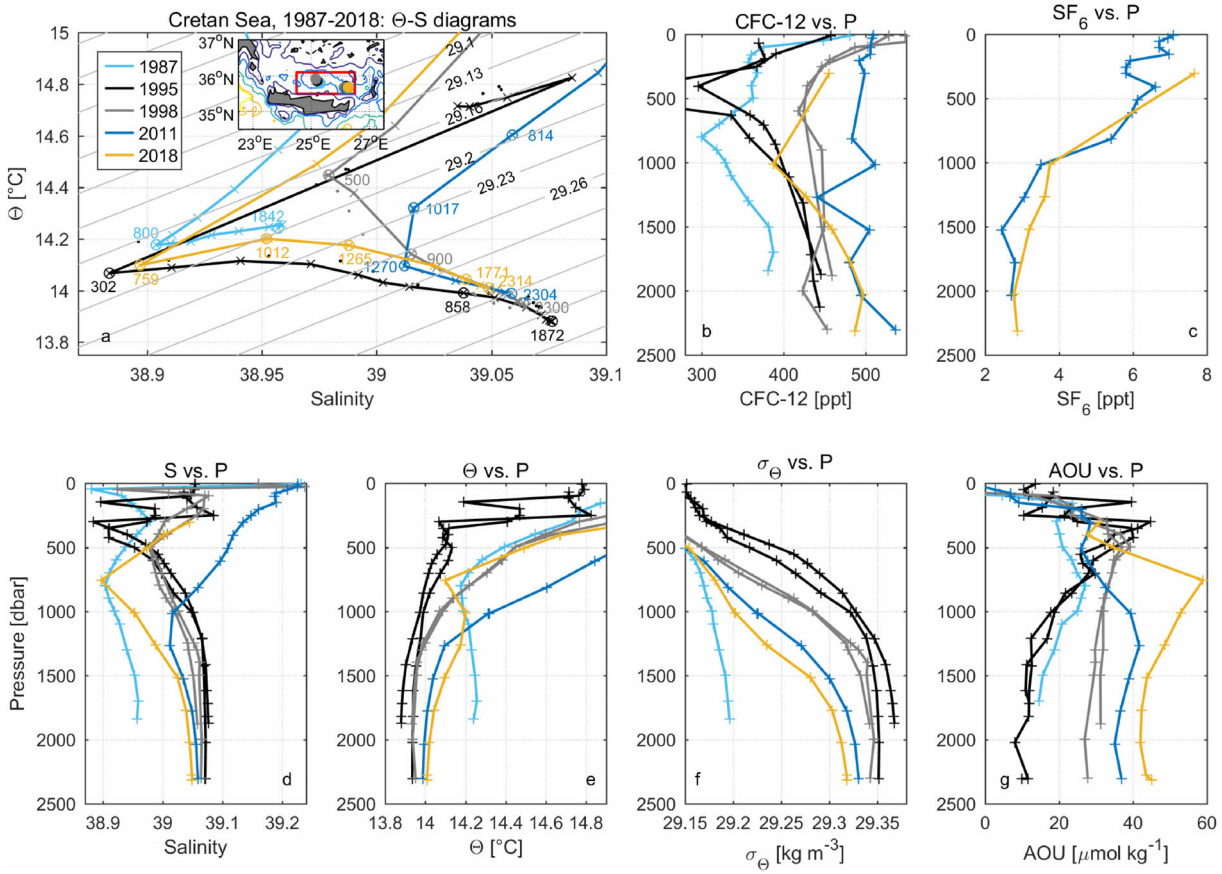

FIGURE 4 | Similar to **Figure 3** but in the Cretan Sea. The stations shown are M5/6 753, M31/1 41 and 42, Aegaeo98 10 and 13, M84/3 288, and MSM72 2.

2001. In the central Ionian intermediate water, increasing CFC-12 concentrations and decreasing AOU from 1987 to 1995 indicate intensified ventilation of the less saline, colder and higher density water, following with relatively weak ventilation to 1999 and nearly stagnant ventilation during the 2000s and 2010s.

Eastern Ionian Sea

We have a time-series of 6 occupations from 1987 to 2018 in the eastern Ionian Sea (**Figure 7** and **Supplementary Figure S6**). The time-series show CFC-12 concentrations with little differences (∼30 ppt) from 1995 to 2018 compared to its dramatic increase (∼170 ppt) from 1987 to 1995 related to the EMT event in the deep layer. A similar increase took place for other properties, such as salinity, Θ and σ_Θ from 1987 to 1995, but this was followed by a relaxation toward pre-EMT conditions, although this condition is not reached. From 2001 to 2011, salinity and Θ decreased but CFC-12 concentrations, σ_Θ, and AOU increased. As to the time range 2011–2018, properties in the two years showed similar values in general. In summary, dramatically enhanced ventilation is observed from 1987 to 1995 followed by nearly stagnated ventilation up to 2018 in the eastern Ionian Sea.

Weak ventilation was found in the eastern Ionian intermediate water from 1987 to 1995 as seen by the decreasing CFC-12 concentrations and slightly increasing AOU (**Supplementary Figure S6**). Afterward, increased CFC-12 concentrations and decreased AOU between 1999 and 2011 support strong ventilation of the more saline and warmer water. From 2011 to 2018, weak ventilation was found again with decreasing transient tracer concentrations and increasing AOU.

Northern Cretan Passage

We have a time-series of 8 occupations from 1987 to 2018 in the northern Cretan Passage (**Figure 8** and **Supplementary Figure S7**). Similar to that in the eastern Ionian Sea, the time-series show CFC-12 concentrations with little differences (∼25 ppt) from 1995 to 2018 in the layer below ∼2500 m compared to its dramatic increase (∼190 ppt) from 1987 to 1995 related to the EMT event and strong ventilation. A dramatic increase also took place for other properties, such as salinity (∼0.2), Θ (∼0.53°C) and σ_Θ (∼0.05 kg m^{-3}) but decrease for AOU (∼26 μmol kg^{-1}) from 1987 to 1995. Salinity, Θ and σ_Θ then generally decreased but AOU increased from 1995 to 2011. The small decrease in CFC-12 concentrations from the 1990s to 2011 indicates nearly stagnant ventilation after 1995. The decreased amplitude of Θ–S inversions between the EMDW of old Adriatic origin and that of Aegean origin from 1995 to 2018 illustrates the weakened Aegean source intensity after 1995 and the erosion of the EMT deep water. Although there is a

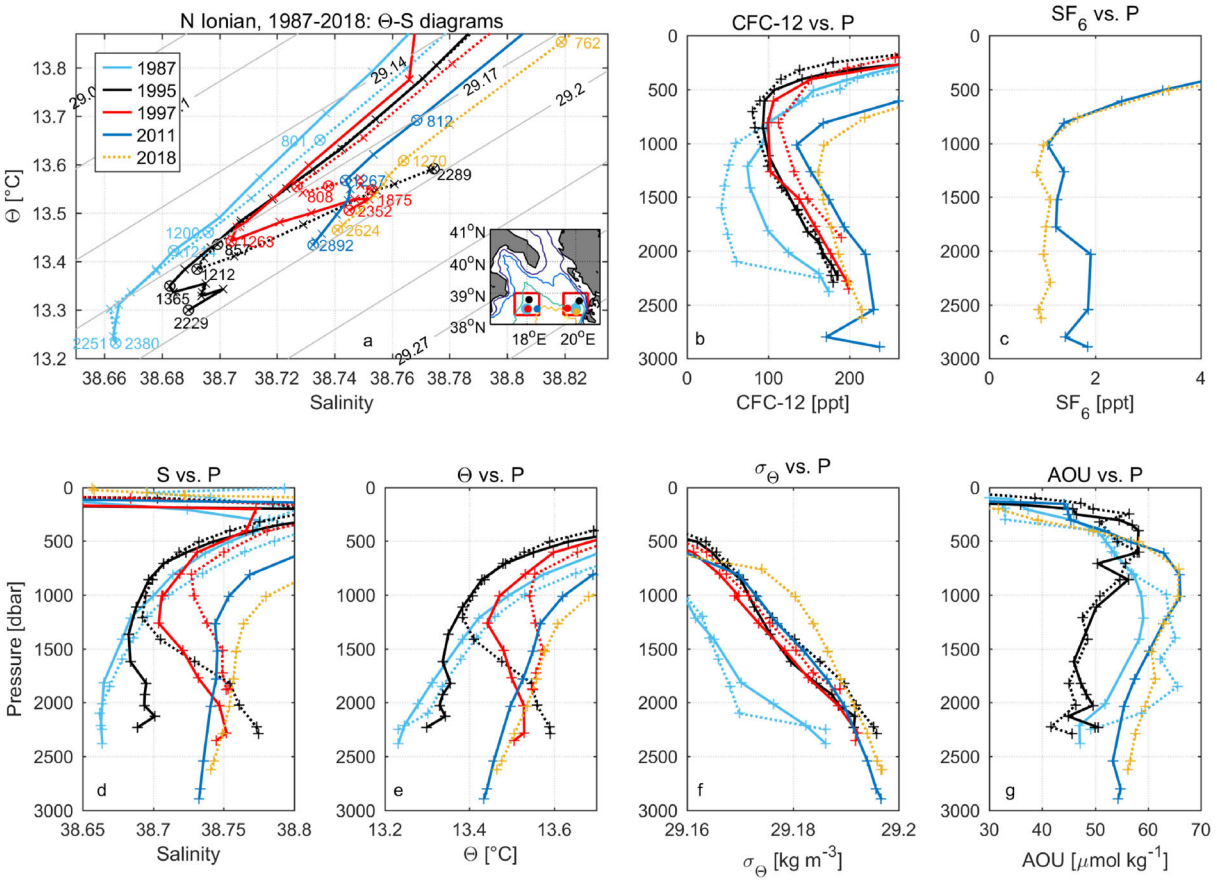

FIGURE 5 | Similar to **Figure 3** but in the northern Ionian Sea. The stations shown in the north-western Ionian Sea are M5/6 770, M31/1 13, Ura2 21, and M84/3 314 (continuous lines). The stations shown in the north-eastern Ionian Sea are M5/6 764, M31/1 23, Ura2 46, and MSM72 34 (dotted lines).

gradual change in Θ/S after 1995 toward pre-EMT conditions, there is nearly no change in CFC-12 indicating that the water that mixes with the EMT induced deep water is ventilated at a similar time scale. For the time range 2011–2018, properties showed various and small changes that can be attributed to local variability. Significantly, AOU increased from 2011 to 2018 supporting slow ventilation. Note the large increase (∼54 ppt) of CFC-12 concentrations between 2001 and 2011 at 1000–1500 m depth (**Figure 8a**), indicating that the water from the Aegean source was no longer dense enough to reach the deep layer of the northern Cretan Passage but ventilated the intermediate layer.

From the perspective of the tracer age difference (**Supplementary Figure S8a**), the 2001 profile in the northern Cretan Passage represents the post-EMT situation, while the 2016 one represents the combined influence of remnant Aegean and new Adriatic sources. Tracer ages estimated from CFC-12 in 2001 are lower than those estimated from SF_6 in 2016 in the deep layer, supporting the stagnant ventilation in this area during that ∼15 years.

Levantine Basin

Here we present two areas in the Levantine basin, east of Crete and west of Cyprus (**Figure 9**), where two Θ–S inversions have developed since 1987. The first inversion appeared in the mid-depth (1000–1800 m) in the 1995–2011 time-periods. The second inversion was found near the bottom in 2011, indicating that the influence of the new Adriatic-originated water has been spread to the Levantine basin in 2011.

Increasing CFC-12 concentrations in the EMDW in the Levantine basin below ∼1800 m from 1987 to 2011 indicates strong ventilation between 1987 and 1999 and relatively slow ventilation after that (**Figure 9** and **Supplementary Figure S9**). The dramatic change of properties took place between 1987 and 1995 for the western Levantine basin but up to 1999 for the central Levantine basin, consistent with the spreading of the Aegean source. A similar delay of influence took place in the following years. For example, larger differences of CFC-12 concentrations were observed between 1999 and 2001 in the western Levantine but between 2001 and 2011 in the central Levantine. For other properties below ∼1800 m, salinity, Θ and σ_Θ also showed increasing trends from 1987 to 1999 with the exception in 1998. After 1999, the trend continued in the deep layer, but with a slight reversal in the near-bottom layer from 2001. As a consequence of the influence of the EMT event, AOU decreased from 1987 to 1995 but increased to 1999, then decreased to 2001 and increased up to 2011 below ∼500 m.

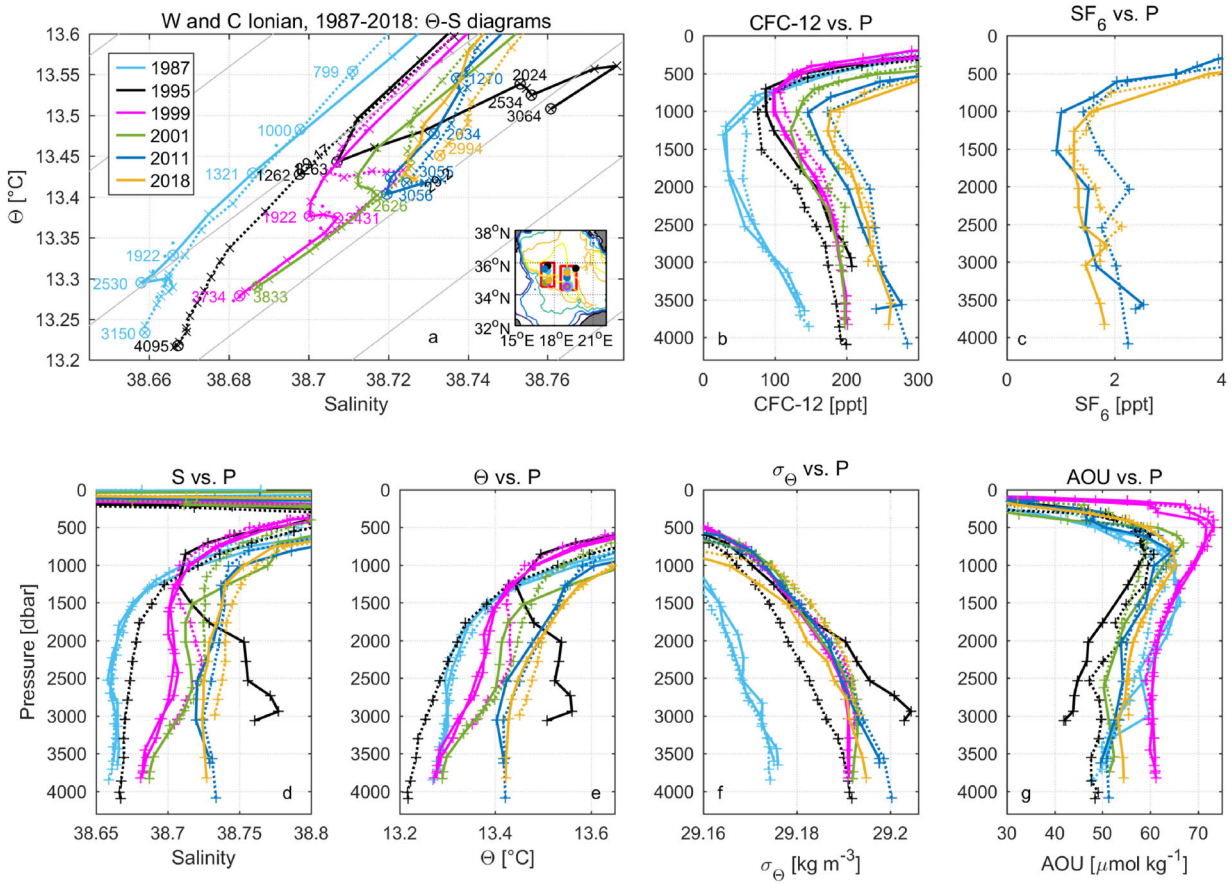

FIGURE 6 | Similar to **Figure 3** but in the western and central Ionian Sea. The stations shown in the western Ionian Sea are M5/6 777, M31/1 10, M44/4 303, M51/2 519, M84/3 305 and MSM72 57 (dotted lines). The stations in the central Ionian Sea are M5/6 773 and 774, M31/1 27, M44/4 301 and 300, M51/2 520, M84/3 303 and MSM72 53 (continuous lines).

The Levantine (especially the central Levantine) intermediate water (**Supplementary Figure S9**) was characterized by strong ventilation from 1987 to 1995 indicated by increasing CFC-12 concentrations and decreasing AOU, which was different from the intermediate layers of other basins in the EMed. After 1995, CFC-12 concentrations, salinity, Θ and AOU slightly increased to 1999 and decreased to 2001, and then increased again to 2011 for the western Levantine intermediate water.

Temporal Variability of Properties in the Strait of Sicily

The Strait of Sicily is the relatively shallow area connecting the western and eastern Mediterranean basins. In the deep-water layer (below ∼600 m), the concentration of CFC-12 shows a generally increasing trend after a small decrease between 1987 and 1995 (**Figure 10** and **Supplementary Figure S10**), as can be expected from the transient of CFC-12 in the atmosphere. The salinity and Θ also decreased slightly from 1987 to 1995 and then steadily increased to 2001. Afterward, there is a significant increase in salinity and Θ during the rather long time-period up to 2018. The simultaneous changes in both Θ and salinity tend to compensate each other in density space, but the overall effect is an increase in density from 1987 to 1995, steady density to 2001 and then decreased density in 2018, which is approaching the lower density found in 1987. The AOU shows a different pattern, with slightly increased concentrations from 1987 to 1995, significantly higher values in 1999 and then lower AOU to 2001/2018. There are large differences for all properties in the intermediate and deep layers in 1999. It is the anomalous year of 1999 with strong ventilation in the intermediate layer and slow ventilation in the deep layer. The changes of CFC-12 concentration and AOU reveal strong ventilation from 1995 to 1999 and from 2001 to 2018 for the intermediate layer (LIW), as well as strong ventilation during 1999–2001 and nearly constant ventilation during 2001–2018 for the deep water (tEMDW) in the Strait of Sicily.

Spatial Distribution of CFC-12 and SF_6 in the WMed

Sections of the vertical distribution of CFC-12 concentrations in the WMed for 1995, 1997, 2001, 2011, and 2018, and SF_6 concentrations for 2018 are presented in **Figure 11**. Similar to the EMed, the main feature of the transient tracer

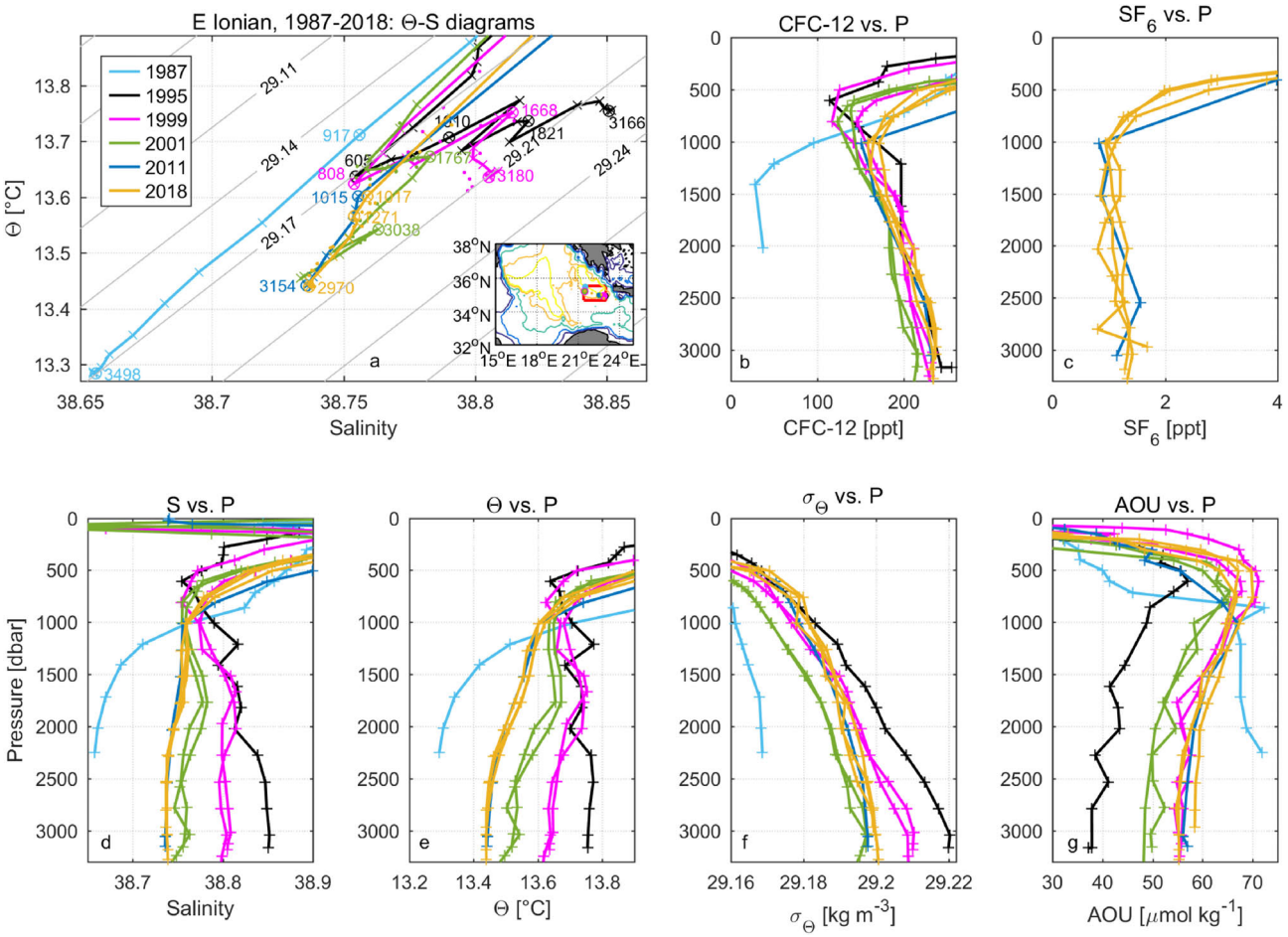

FIGURE 7 | Similar to **Figure 3** but in the eastern Ionian Sea. The stations shown are M5/6 760, M31/1 32, M44/4 292 and 294, M51/2 522 and 523, M84/3 299 and MSM72 22, 44, 46 and 47.

concentration is a TMZ centered at ∼1000 m depth. In the deeper layer, high concentrations of CFC-12 found in the bottom waters near the Sardinia Channel in 1995 is maybe not that significant considering the limited number of observations, which is supported by the CFC-11 concentrations in 1997 (Rhein et al., 1999). In 2001, the bottom tracer concentrations near the Sardinia Channel have slightly increased to ∼200 ppt, but the limited horizontal extent of that section limits the interpretation to the eastern part. Thus, the CFC-12 concentrations in the deep water changed slowly in the second half of the 1990s and the early 2000s attributed to the weak local source, as can be expected from a transient tracer in a steady-state ventilation scenario. Subsequently, due to the influence of the WMT event that started in winter 2004/05, the situations in 2011 and 2018 are different with significantly higher CFC-12 concentrations (260–290 ppt) that tend to be higher in the western part of the WMed, as opposed to the higher concentrations in the eastern part in the decade prior to 2001. The elevated CFC-12 concentrations observed in the western WMed bottom water in both 2011 and 2018 revealed the intrusion of the new WMDW toward the Alboran Sea. However, the slightly increased CFC-12 concentrations from 2011 to 2018 in the WMed, especially in the bottom water, are probably a result of the weakened influence of the WMT event during this period. The spatial distributions of CFC-12 and SF_6 concentrations in the WMed deep layer in 2018 (**Figures 11e,f**) are generally similar to three cores of higher concentrations in the WMed bottom waters.

Temporal Variability of Properties in the WMed

Tyrrhenian Sea

Although the Tyrrhenian Sea is influenced by both the EMed and WMed, no Θ–S inversions are observed in the Tyrrhenian Deep Water (TDW) during the last three decades (**Figure 12a**), which is significantly different from the cases in the two main basins (EMed and WMed). The small change in the Θ–S diagrams from 1997 to 2018 indicates the apparent synchronous change of salinity and Θ, and the influence of water masses from EMed and WMed to the Tyrrhenian Sea is not strong enough to lead to the inversions. This

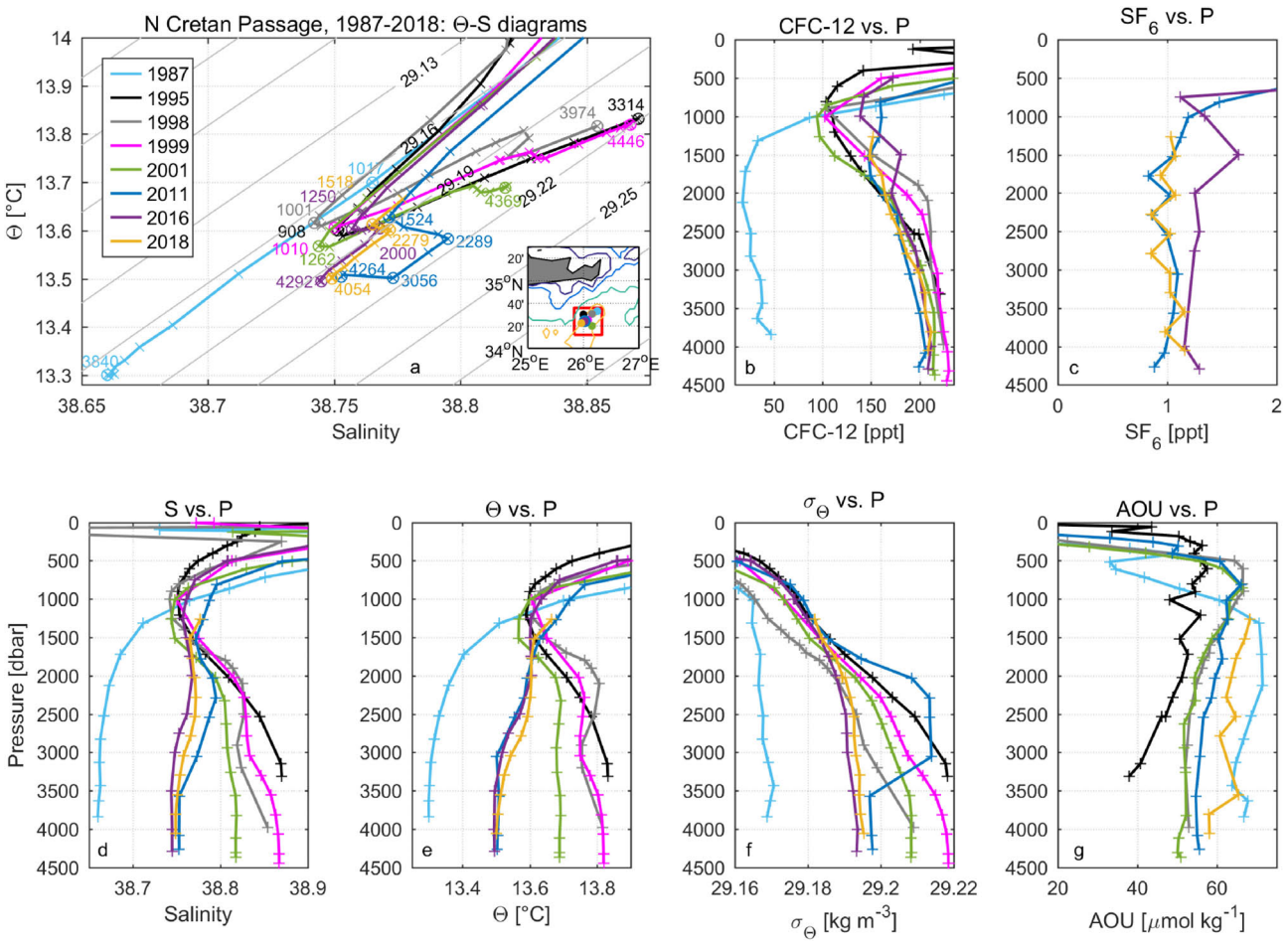

FIGURE 8 | Similar to **Figure 3** but in the northern Cretan Passage. The stations shown are M5/6 751, M31/1 46, Aegaeo98 40, M44/4 265, M51/2 530, M84/3 297, CRELEV2016 18 and MSM72 9. The structures of Θ–S diagrams in the northern Cretan Passage can be generally separated as three patterns: the one in 1987 with low salinity and Θ (38.66, 13.3) in the deepwater (EMDW of old Adriatic origin); the one in 1995–2001 with an inversion at 900–1300 m core depth (EMDW of old Adriatic origin) and the near-bottom water (EMDW of Aegean origin) with high salinity and Θ (38.87, 13.8); the one in 2011–2018 with an inversion at 1250–1500 m core depth (EMDW of old Adriatic origin) followed by another inversion at 2000–2300 m (EMDW of Aegean origin) and the near-bottom water (EMDW of new Adriatic origin) with medium salinity and Θ (38.75, 13.5).

may be because the Tyrrhenian Sea is not closely connected to the convection areas of either the eastern or western Mediterranean Sea. The transit times allow for internal mixing and topographical obstacles to prevent the inversion signals to reach this area.

The CFC-12 concentrations increased between 1987 and 1997 in the deep-water layer (below ∼1500 m) in the Tyrrhenian Sea (**Figure 12** and **Supplementary Figure S11**). This was followed by slightly increased concentrations between 1999 and 2001. It is an indication of slightly enhanced ventilation combined with the decreased AOU during the same period. In 2011, the increased transient tracer (CFC-12 and SF_6) concentrations in the TDW showed enhanced ventilation attributed to the combined influences from the LIW, EMDW, and WMDW, especially the WMT event started from 2004 to 2006. In the 2010s, the salinity and Θ in the TDW were similar in 2011, 2016, and 2018, but with increased CFC-12 concentrations and σ_Θ from 2011 to 2016/18. Although the increase in SF_6 concentrations in the TDW below 2000 m from 2011 to 2016/18 is consistent with the increased atmospheric SF_6 concentrations, the decreased AOU and the smaller increase in CFC-12 concentrations can be explained by intense ventilation of the TDW driven by the WMT event considering the decreasing CFC-12 concentrations in the atmosphere. From 2016 to 2018, the increased AOU in the TDW suggests a slowdown of the ventilation. Salinity, Θ, and σ_Θ in the TDW largely increased from 1987 to 1997. Subsequently, σ_Θ decreased slightly to 1999 and 2001, and then increased somewhat to 2011 and significantly to 2016/18. This increase in density is mainly driven by increased salinity, and somewhat compensated by increasing Θ.

In the Tyrrhenian intermediate water (**Supplementary Figure S11**), CFC-12 concentrations, salinity and Θ increased from 1987 to 2016, and SF_6 concentrations increased from 2011 to 2016, but all decreased afterward. Except for the extremely

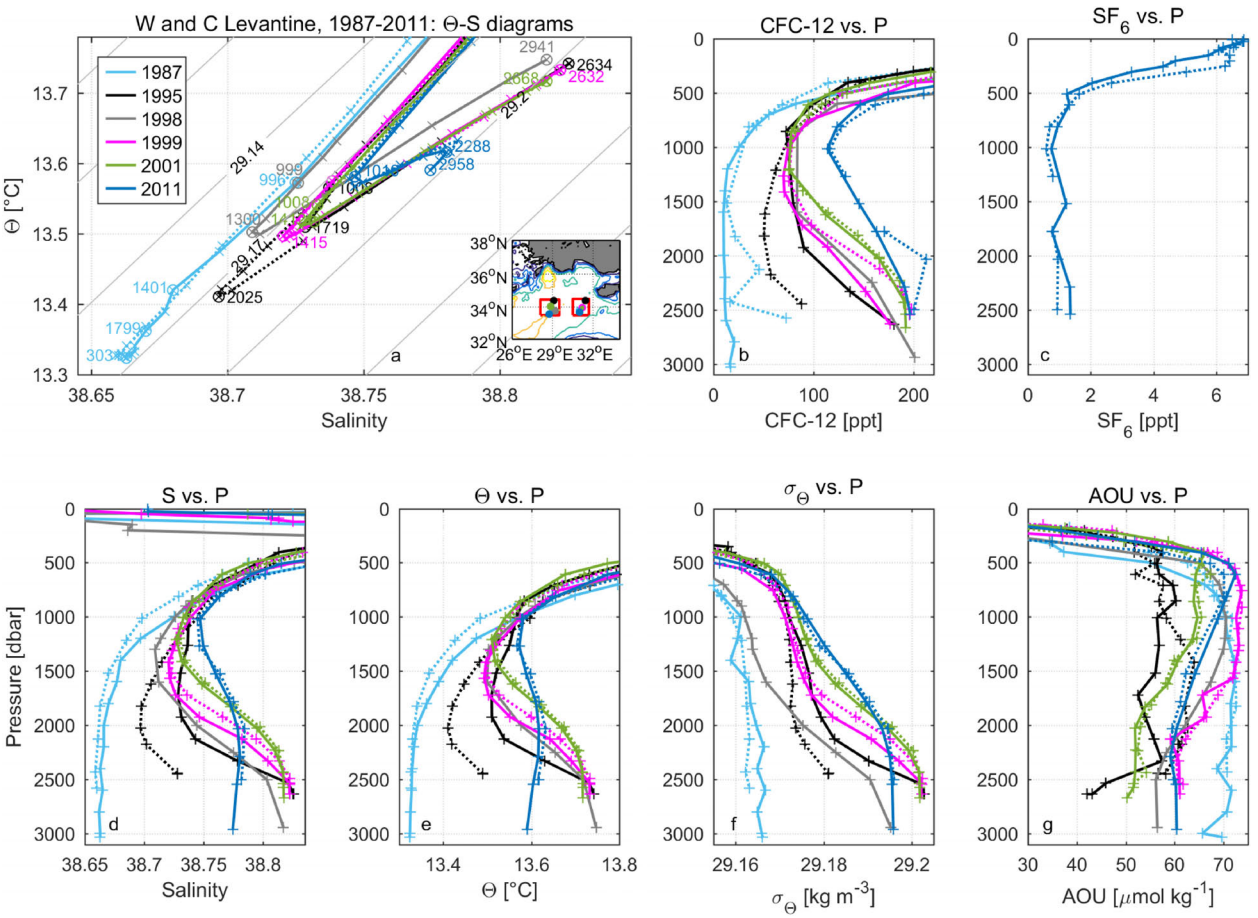

FIGURE 9 | Similar to **Figure 3** but in the western and central Levantine basin. The stations shown in the western Levantine basin are M5/6 747, M31/1 56, Aegaeo98 441, M44/4 238, M51/2 537 and M84/3 296 (continuous lines). The stations shown in the central Levantine basin are M5/6 746, M31/1 69, M44/4 236, M51/2 540 and M84/3 294 (dotted lines).

high AOU in 1999, the nearly constant AOU between 2001–2016 supports constant ventilation. But from 2016 to 2018, the slightly increasing AOU and decreasing transient tracers indicate weak ventilation.

From the perspective of the tracer age difference (**Supplementary Figure S8b**), minor changed tracer ages in the Tyrrhenian Sea between 2001 and 2016 are found at the depth below ∼1700 m, which suggests steady-state ventilation. Such a situation may be attributed to the counterbalance of the advective influence of the WMT event, the TDW and the tEMDW. The decrease in tracer ages between ∼500 and ∼1700 m during this period (i.e., increased ventilation) may be associated with the input of the LIW and the tEMDW from the EMed because of the influence of the new Adriatic source. A similar tracer age decrease above the deep layer is found in the south Liguro-Provençal basin between 1997 and 2011 (Schneider et al., 2014).

Gulf of Lions and Liguro-Provençal Basin

In the northern part of the Western Mediterranean Sea, i.e., Gulf of Lions and Liguro-Provençal basin, we have only observations in two years (1997 and 2016), so that only limited information on the temporal evolution can be made. Increased CFC-12 concentration, salinity, Θ and σ_Θ are observed in the water layer below ∼300 m (**Supplementary Figures S12, S13**) indicating the steady to increased ventilation during the period.

Algerian Basin

While similar CFC-12 concentrations in 1995, 1997, and 2001 at deep and intermediate depths of the central Algerian basin (**Figure 13** and **Supplementary Figure S14**) suggested stagnated ventilation before 2001, salinity, Θ and σ_Θ slightly increased from 1995 to 1997. The salinity showed similar values in 1997 and 2001, but σ_Θ decreased driven by increased Θ in the deep layer. Subsequently, all properties increased significantly from 2001 to 2011 due to the WMT event when intense DWF led to strong ventilation in the deep western Mediterranean basin (Schroeder et al., 2008). This trend continued up to 2018, although at a slower pace. The CFC-12 concentrations increased from 2011 to 2016 and then decreased slightly to 2018. SF_6 concentration also decreased after 2016 in the central Algerian deep water below ∼2000 m. The decreased concentration of the

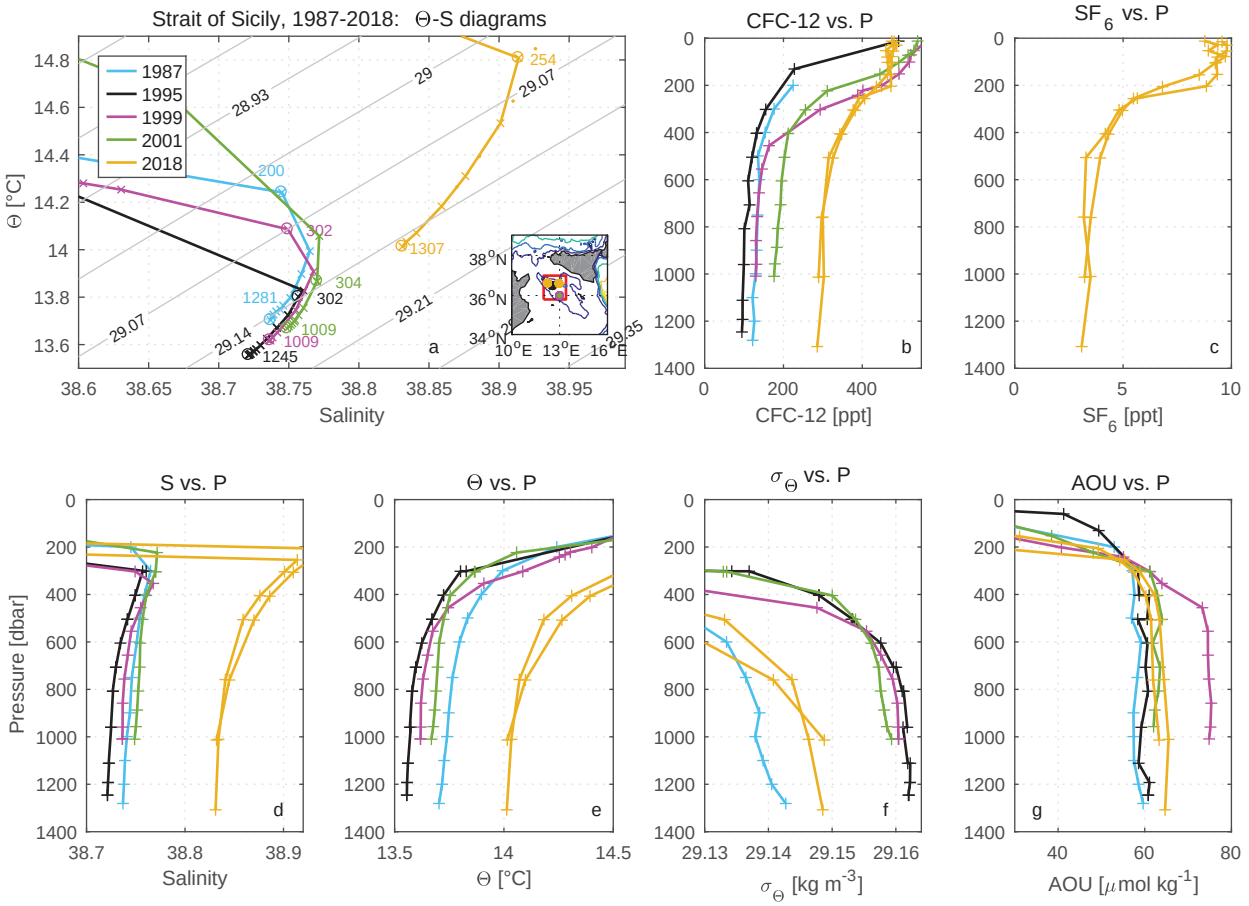

FIGURE 10 | Similar to **Figure 3** but in the Strait of Sicily. The stations shown are M5/6 781, M31/1 6, M44/4 307, M51/2 516 and MSM72 72 and 70.

transient tracers suggests weakened ventilation in the WMDW after 2016, which is also supported by the increase in AOU from 2011 to 2018. During this time, salinity, Θ and σ_Θ increased from 2011 to 2016 and showed similar values between 2016 and 2018. In the western Algerian deep layer (**Figure 13**), CFC-12 concentrations remain constant from 1995 to 1997 but increased afterward, while salinity, Θ and σ_Θ gradually increased from 1995 to 2018.

In the Algerian intermediate water (**Supplementary Figure S14**), CFC-12 concentrations, salinity, Θ and AOU increased from 1997/2001 to 2011, and again to 2018 for the western part of the basin. While for the central basin, increasing CFC-12 and decreasing AOU indicate strong ventilation from 2011 to 2016 with higher salinity and Θ. But the ventilation weakened to 2018 with lower salinity and Θ through the decreased CFC-12 concentrations and increased AOU.

Alboran Sea

In the water layer below ∼500 m in the Alboran Sea (**Supplementary Figures S15, S16**), we find trends similar to those in the western Algerian basin. That is, CFC-12 concentrations, salinity, Θ and σ_Θ increased from 1997 to 2018, and AOU increased from 2011 to 2018. The increase in CFC-12 concentrations from 1997 to 2018 depicted the generally enhanced ventilation of the Alboran Sea deep water. For the water between 200 and 450 m depth, the increasing CFC-12 from 1997 to 2018 and decreasing AOU from 2011 to 2018 indicate enhanced ventilation. Although the influence of the WMT is seen in the Alboran Sea, no Θ–S inversion is observed since the sea is not deep enough (**Figure 11**).

DISCUSSION

We have compared transient tracer observations from 1987 to 2018 (CFC-12/11 and SF_6) in the Mediterranean Sea, mainly focusing on the layers below the Levantine Intermediate Water (LIW), in order to characterize the temporal evolution of ventilation. Here we discuss trends and variability of the ventilation patterns in the Mediterranean Sea based on the combined observations of transient tracers, salinity, potential temperature, potential density and apparent oxygen utilization described in the previous section. We start with a discussion of the slowly ventilated TMZ and then discuss trends in deep water ventilation for the different basins. During recent decades, the

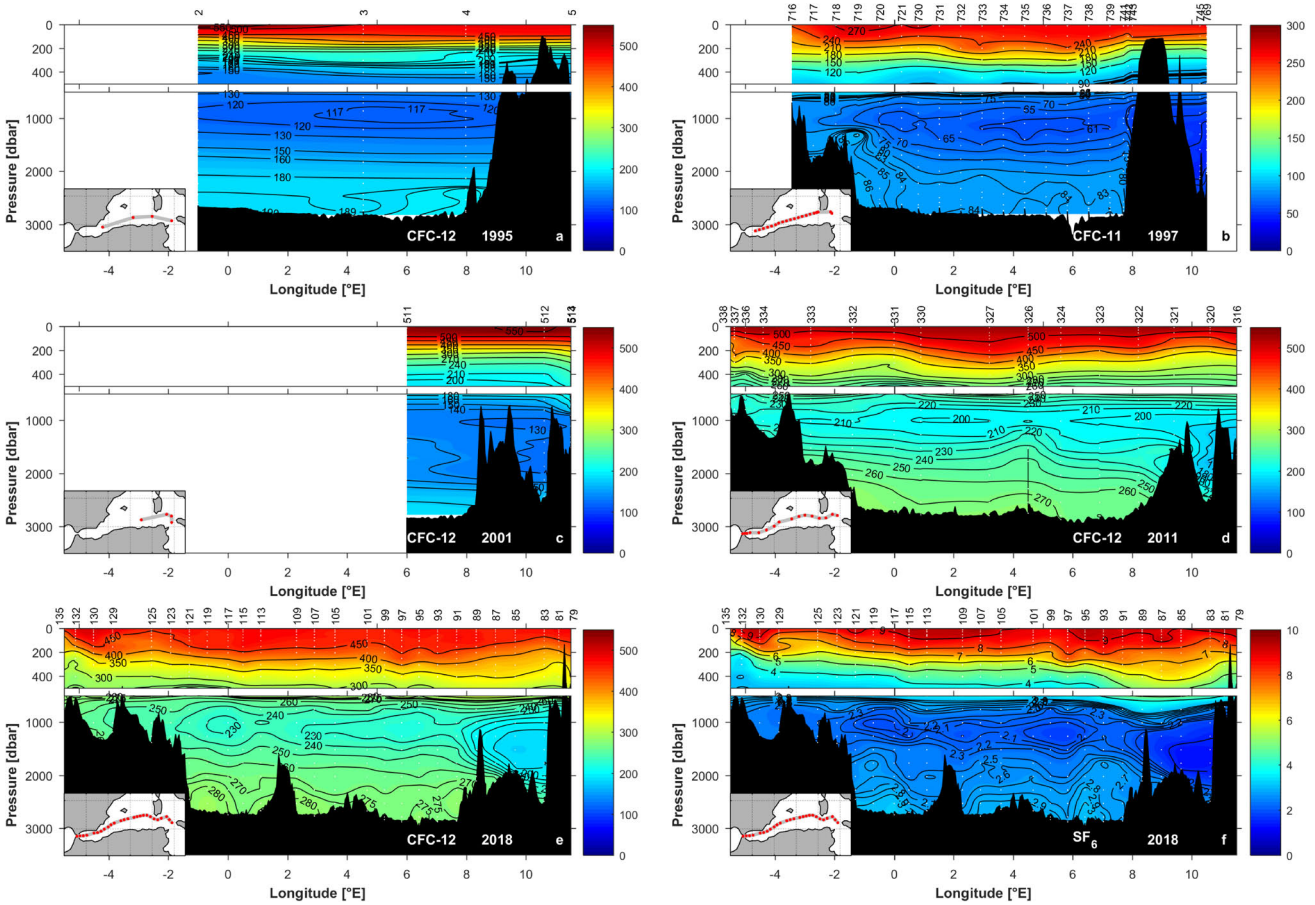

FIGURE 11 | Vertical sections of CFC-12/CFC-11 concentration (in ppt) in the Western Mediterranean Sea (see inset maps for station locations) in **(a)** 1995 (Meteor M31/1), **(b)** 1997 (Poseidon 234), **(c)** 2001 (Meteor M51/2), **(d)** 2011 (Meteor M84/3), and **(e)** 2018 (Maria S. Merian MSM72) and vertical section of SF_6 concentrations (in ppt) in the WMed in **(f)** 2018 (Maria S. Merian MSM72). The vertical section of CFC-12 concentrations in 1997 is replaced by that of CFC-11 concentration due to the higher quality of CFC-11 data (Rhein et al., 1999). The same scales of longitude and pressure are used for all figures, while the same color bars are separately used for CFC-12, CFC-11 and SF_6 sections. The upper panels highlight the top 500 m. The markers on the top *x*-axis stand for the station number.

influences of the EMT and WMT events have led to bottom and deep-water renewal that has modified the TMZ and bottom water ventilation patterns.

Tracer Minimum Zone (TMZ)

The Mediterranean Sea is one of few places in the global ocean with a pronounced TMZ at mid-depth of the water column attributed to rapid ventilation in the deep waters so that the TMZ corresponds to the slowest ventilated layer. The TMZ in the contemporary Mediterranean Sea is presented from the Levantine basin to the Alboran Sea, although with a break in the Strait of Sicily. The dominating water mass of the TMZ is the Transitional Mediterranean Water (TMW) in the EMed and the transitional EMDW (tEMDW) in the WMed. The depth of the TMZ has shallowed in both the western and eastern basins before the EMT and WMT ventilation episodes but has been deepening after these events. For the eastern basin, the TMZ shallowed from 1987 to the 1990s and then deepened up to the 2010s. In the western basin, this shift is not so obvious although the TMZ deepened from 1987 to 1995, shallowed to the mid-2000s (not shown) and then deepened slightly to the 2010s followed by slow upward motion (**Supplementary Table S2**). For instance, the TMZ shallowed from ∼1400 m (1987) to 600–800 m (the 1990s) and then deepened to 1000–1300 m (2018) in the eastern Ionian Sea, as well as deepened from ∼700 m (1987) to 900–1000 m (1995) and deepened again from 800–1000 m (2011) to 1200–1300 m (2016/18) in the central Algerian basin. The transient tracer concentrations in the TMZ have increased significantly in the EMed during the past ∼30 years, although the increase in transient tracers in the TMZ of the WMed is less pronounced. However, the transient tracer concentration in the TMZ is higher in the WMed than in the EMed for any given year.

Eastern Mediterranean Basin

We start with the Adriatic Sea as a major source region of deep waters in the Eastern Mediterranean basin. Here we observe no ventilation of the deep-water (below 600 m) from 1987

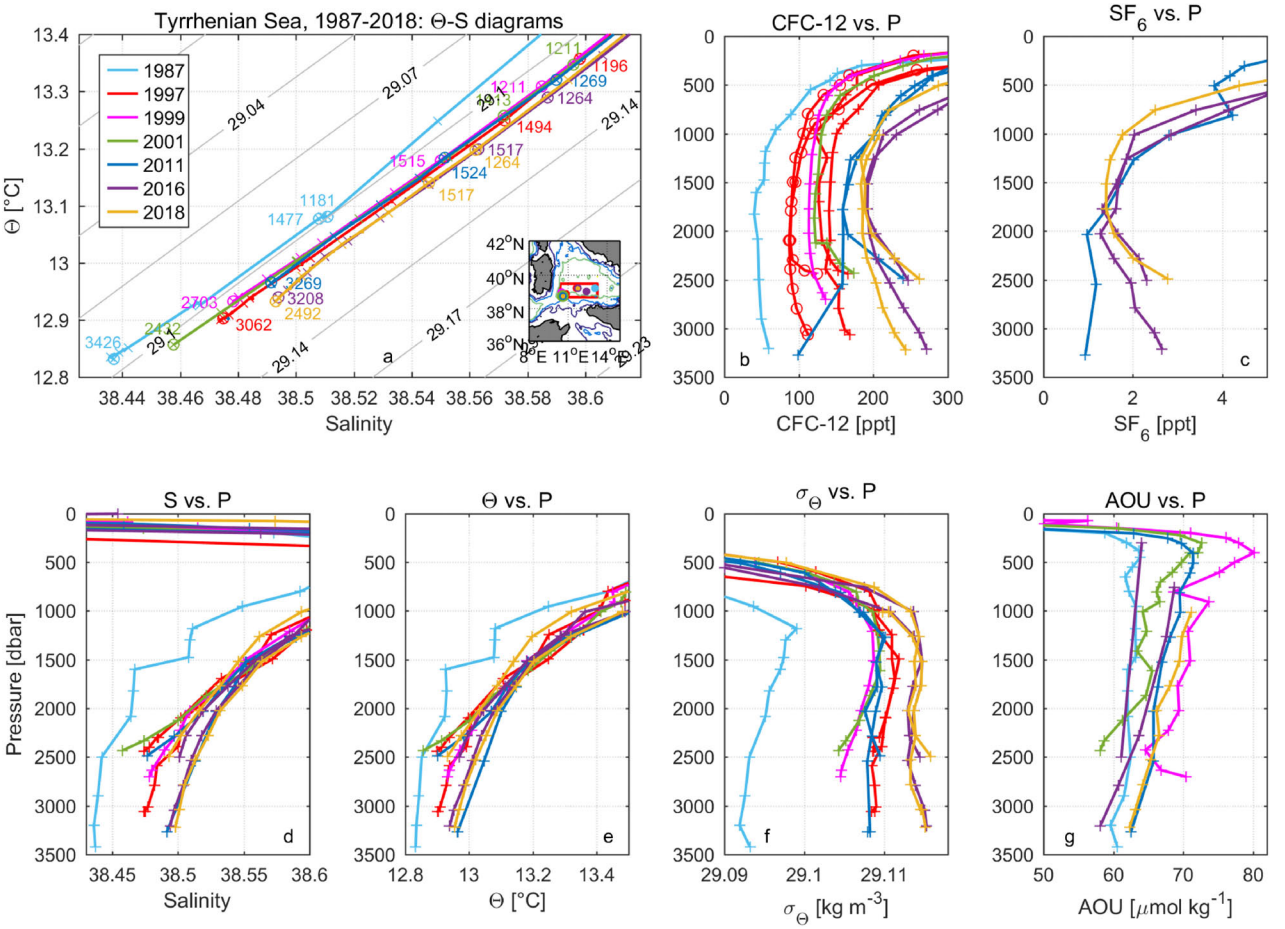

FIGURE 12 | Similar to **Figure 3** but in the Tyrrhenian Sea. The stations shown are M5/6 786, P234 767 and 768, M44/4 310, M51/2 512, M84/3 317 and 320, TALPro2016 6 and 5, and MSM72 83 and 77. In **(b)**, the 1997 data from cruise P234 with "o" symbols were calculated from CFC-11.

to 1999, but with strong ventilation between 1999 and 2011 that continued in the period 2011–2016. Even though there was no ventilation of the deep water in the Adriatic Sea up to 1999, as seen by constant CFC-12 and increased AOU, it got slightly saltier and warmer. The trend for the intermediate layer (200–600 m) is similar, but with a pronounced decrease in transient tracers between 1987 and 1995 and then increased ventilation observed in 1999, indicating how changes in this layer are different from the deep layer. The extremely cold winter in 2012 (Gačić et al., 2014) and increased transient tracer concentrations support strong ventilation in the Adriatic Deep Water between 2011 and 2016, although with decreased bottom density (Chiggiato et al., 2016). The spatial distribution of SF_6 concentrations (**Figure 2h**) reveals that the AdDW was no longer dense enough to reach the bottom of the Ionian Sea in 2018, indicating that the Adriatic source weakened during recent years. This is also supported by the decreased transient tracers and dissolved oxygen (i.e., increased AOU) from 2011 to 2018 in the western Ionian bottom water and in 2016 in the Adriatic near-bottom water column (below 1000 m). In consequence, the Adriatic Deep Water is currently the dominant deep water source in the EMed, although with weakened influence during the last decade.

The intensified ventilation in the Adriatic Sea influenced the overflow through the Strait of Otranto sill into the Ionian Sea where the EMDW is formed from the AdDW as it mixes with the remnant deep water from the Aegean source. For the other important deep water source of the EMed, the Southern Aegean Sea (i.e., the Cretan Sea), a clear trend is observed with well-ventilated waters in 1995, where after the concentrations remained essentially constant up to 1998, although with considerable variability in the data, and slightly higher concentrations in 2011 and 2018. Schneider et al. (2014) showed slow ventilation of the Cretan Sea from 1998 to 2011. This indicates that as a deep water source the Aegean source weakened after 1995 (**Figure 4**) and thus led to the current weak ventilation in the CDW.

The Adriatic and Aegean sources meet in the Ionian Sea, and the increase in CFC-12 concentrations between 1987 and 1995 in the EMDW is larger in the east, which is coincident with the east-to-west gradient of the influence of the dominant Aegean source in the Ionian Sea at that time. This is also illustrated by

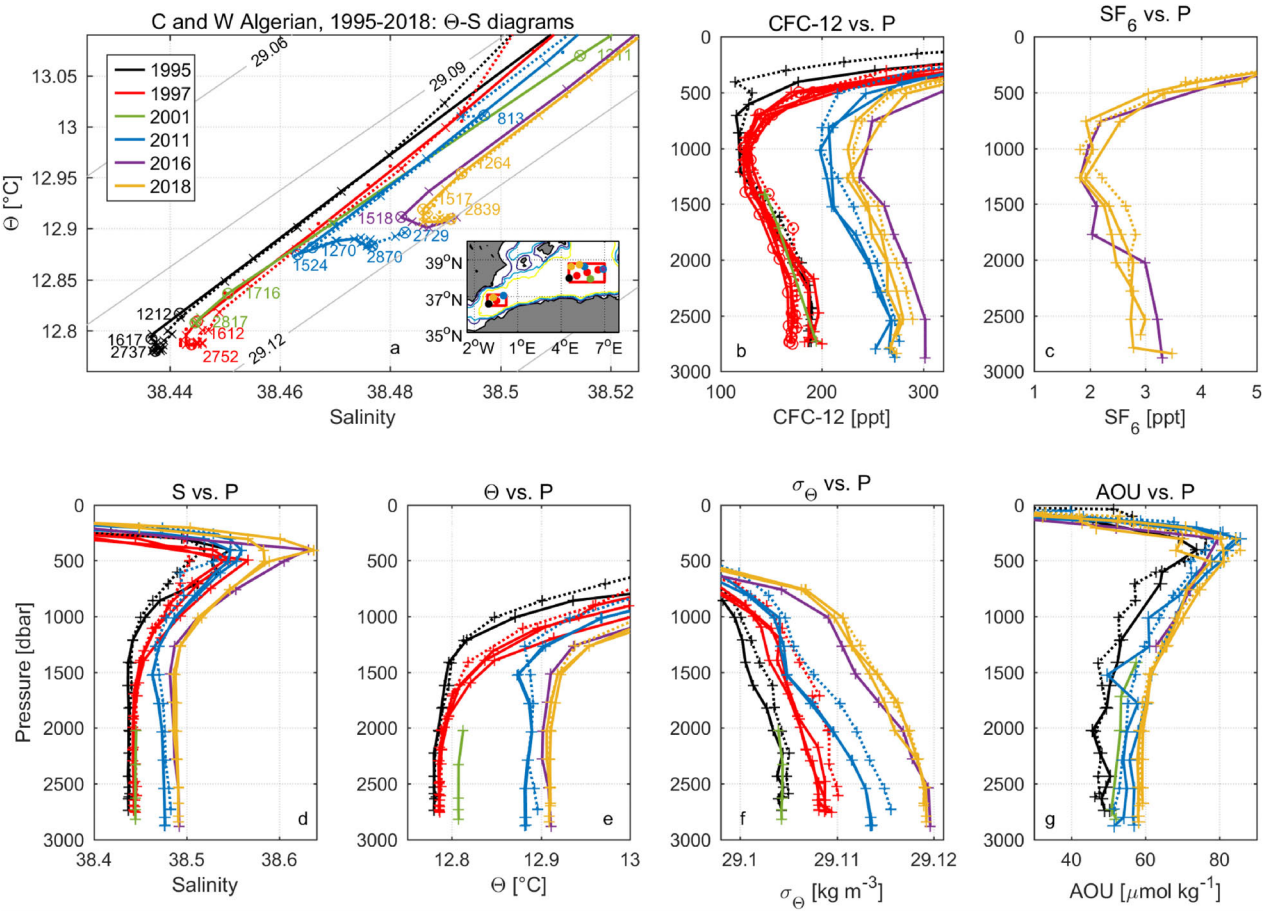

FIGURE 13 | Similar to **Figure 3** but in the central and western Algerian basin. The stations shown in the central Algerian basin are M31/1 3, P234 736, 737 and 738, M51/2 511, M84/3 324 and 323, TALPro2016 19 and MSM72 99 and 101 (continuous lines). The stations in the western Algerian basin are M31/1 2, P234 720, M84/3 331 and MSM72 119 (dotted lines). In **(b)**, we added the 1997 data with "o" symbols calculated from CFC-11.

the amplitude of Θ–S inversion related to the Aegean source, which decreases from the eastern to the western Ionian Sea, as well as from the eastern to the north-western Ionian Sea. In 1999, the influence of the Aegean source was weaker in the eastern and central Ionian deep water but stronger in the western Ionian deep water compared to those in 1995, which describes the delayed influence of the Aegean source to the western Ionian Sea. Subsequently, the amplitude of Θ–S inversions related to the Aegean source became smaller in the whole Ionian Sea and the extent of the reversal decreased from 2001 to 2018. In 2018, the Θ–S inversions created by the influence of the Aegean source became very small and even invisible. With the influence of the Aegean became weaker and found predominantly at shallower depths (Theocharis et al., 2002), the new Adriatic source started to influence the Ionian Sea from the bottom layer (Hainbucher et al., 2006; Cardin et al., 2015). This is manifested by the more pronounced increase in CFC-12 concentrations in the western and central Ionian deep water compared to the eastern Ionian deep water between 2001 and 2011, and by the increase in salinity in the water column from ∼3000 m to the bottom in the western and central Ionian Sea in 2011 (Roether et al., 2014). The new Adriatic source leads to the second Θ–S inversions with decreased salinity and Θ observed in the Ionian bottom water in 1999 and 2001. However, the weaken ventilation of the western Ionian deep water and nearly stagnated ventilation of the central and eastern Ionian deep water in 2011–2018, reveal the weakened influence of new Adriatic source to the Ionian Sea, although the AdDW has been the dominant source of deep water in the eastern Mediterranean for the last two decades. Trends in the transient tracer concentrations suggest more contribution of new Adriatic deep water to the Ionian Sea between 2001 and 2011, a signal that weakened between 2011 and 2018.

The water from the Adriatic Sea spreads eastward from the Ionian Sea toward the Cretan Passage, as indicated by the Θ–S inversions (**Figure 8a**) in 2011 (Manca et al., 2006; Velaoras et al., 2018), which led to the non-monotonous change of local salinity. The salinity decrease in the water column from ∼3000 m to the bottom in 2011 is related to the less saline new Adriatic source (Cardin et al., 2015), following the salinity decrease from 2011 to 2016 (Velaoras et al., 2018). The salinity (38.74–38.75) in the northern Cretan Passage in 2016/18 is closer to that in the Adriatic Sea in 2016 (38.72) than that in the Southern Aegean

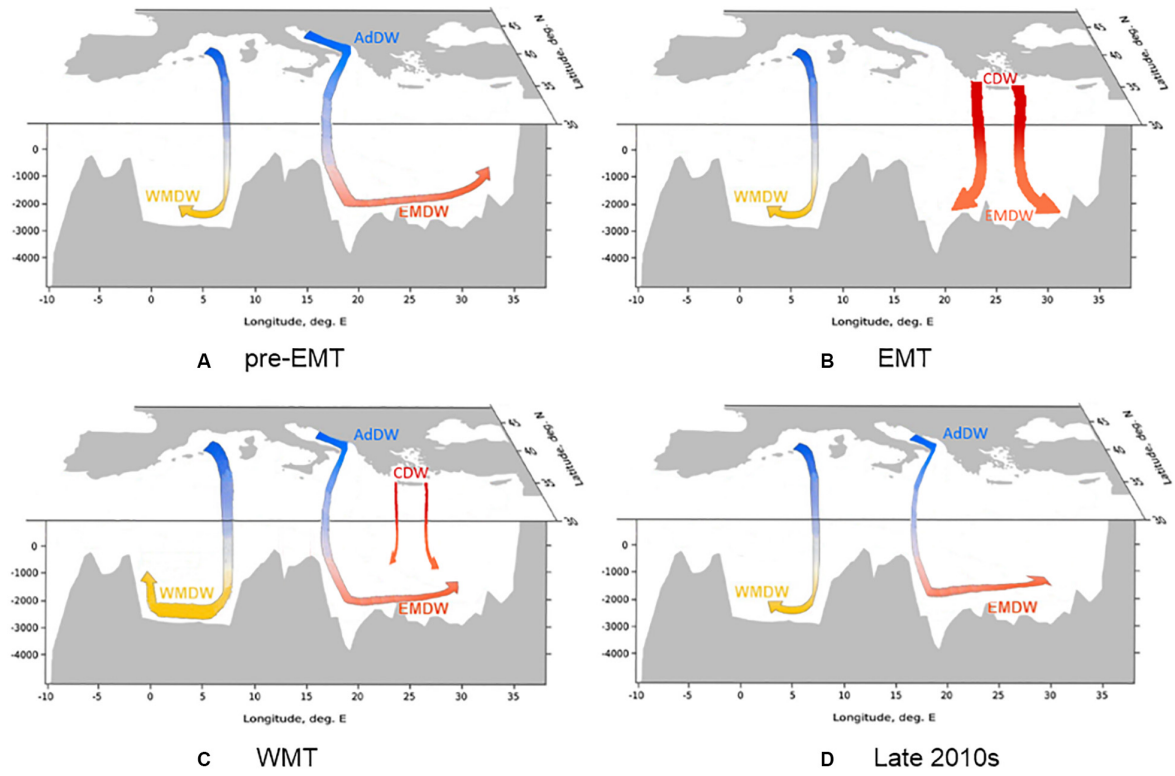

FIGURE 14 | Schematic figures of the Mediterranean deep overturning circulation **(A)** before the EMT, **(B)** during the EMT, **(C)** during the WMT, and **(D)** in the late 2010s, which were prepared based on Hainbucher et al. (2006); Tsimplis et al. (2006), Jullion et al. (2017); Somot et al. (2018) and this study. Colors highlight the approximate change in salinity (blue = low salinity and red = high salinity). Thickness of arrows represents the approximate change in source intensity (thick = high intensity and thin = low intensity). Water masses are defined as follows: AdDW, Adriatic Deep Water; CDW Cretan Deep Water; EMDW, Eastern Mediterranean Deep Water; WMDW, Western Mediterranean Deep Water.

Sea in 2018 (39.05). A similar decrease in salinity from 2015 to 2016 has been reported for the Myrtoan basin, located in the southwestern Aegean Sea (Velaoras et al., 2017). However, the salinity increased from 2016 to 2018 in the northern Cretan Passage (**Figure 8**) and from 2016 to 2017 in the Myrtoan basin (Velaoras et al., 2017), reversing the trend.

It is worth noting that the change of physical properties (such as salinity, Θ and σ_Θ) in the northern Cretan Passage deep water after 1995 is significant while the change of CFC-12 concentrations during the same time is, in practice, small. We see no evidence of new DWF in (the surrounding of) the Aegean/Cretan Sea since the EMT event so that the new Adriatic-originated water could reach into the bottom layer of the Levantine basin, where it was detected in 2011 (**Figure 10**).

Although the spatial distribution of CFC-12 concentrations in the EMed in 2018 is different from that in 1987, similar CFC-12 water column gradients (bottom-to-intermediate) were found in 1987, 2011 and 2018 in the western Ionian Sea. However, the distribution of CFC-12 in 2018 is closer to the one in 1987 than that of 2011. Similarly, the distribution pattern of SF_6 in 2018 is closer to that of CFC-12 concentrations in 1987 than that of SF_6 concentrations in 2011. This shows a trend of water mass distributions toward a pre-EMT state that is more articulated in 2018 compared to 2011. However, the hydrographic properties are still far away from the pre-EMT condition in 2018, although the transient tracers distribution support a relaxation toward pre-EMT conditions.

Strait of Sicily

The Strait of Sicily plays a significant role in the water exchanges between EMed and WMed. Due to few transient tracer data, additional Θ–S diagrams in 1985, 1986, 1992, 1997, 1998, and 2003 (Astraldi et al., 2002; Gasparini et al., 2005) are used here to refer three different phases: before the EMT event (1985–1987), during the EMT event (1991–1993) and after the EMT event (after 1995). There is a weak trend of increasing AOU in the deep waters during the whole time-series, while the CFC-12 concentration increased together with increasing Θ and salinity. The large Θ/S increase at Strait of Sicily could be related to the propagation of EMT signal being uplifted by internal mixing, finally reaching density level able to cross the sill. This reveals that the EMed continuously influences the Strait of Sicily. The time-series is punctuated by the anomalous year 1999 with clearly more ventilated intermediate waters (low AOU and high CFC-12) characterized by low salinity and high Θ (i.e., lower density), and with less ventilated deep waters (high AOU, low CFC-12). In 2018, the CFC-12 concentrations, salinity and Θ in the Strait of Sicily bottom layer (tEMDW) are higher than those in the

Ionian Sea at the same depth (**Figures 6–8**, **10**), i.e., with lower density. This is an indication that the water in the Strait of Sicily is more impacted by the ventilation of intermediate waters than deep ones from the EMed.

Western Mediterranean Basin

The Gulf of Lions is the main source region for deep water in the WMed, but we have only two repeats of transient tracers in this region. The increased transient tracer concentrations indicate intense ventilation from 1997 to 2016. When combined with more data from the CTD and mooring in 1987, 1988, 1993, 1999 (Pinardi et al., 2015), and 2007–2013 (Houpert et al., 2016; Somot et al., 2018; Testor et al., 2018), we found mild Θ–S inversions in the 1990s, but stronger ones and even double inversions starting from the winter 2004/05, which indicates the difference before and after the WMT event in the source region.

The evolution of properties in the deep waters of the Gulf of Lions is comparable to those in the adjacent Algero-Provençal basin, the main basin in the WMed. The WMed deep water is characterized by nearly constant CFC-12 concentrations, i.e., nearly stagnant ventilation, between 1995 and 2001 followed by enhanced ventilation up to 2016 and possibly slow ventilation during the last few years of the time-series up to 2018. The recent slow ventilation could be attributed to the weakened influence of the WMT event that started in winter 2004/05. The Θ–S inversions that are tell-tale of the WMT event were found in 2011, 2016 and 2018 in the central Algerian basin and 2011 and 2018 in the western Algerian basin (**Figure 13**). From the mooring data at a repeat station (2800 m, 37.98°N, 4.65°E) located in the Algerian basin (Schroeder et al., 2016), the near-bottom warm and salty water intruded in 2005, and the layer below the Θ–S inversions became ∼600 m thick in 2006, ∼1000 m in 2008, > 1200 m in 2010, 1400 m in 2013, and > 1500 m in 2015, which described the uplifting old WMDW replaced by the new one from near the bottom. From the CTD data (**Figure 13**), the depths of inversions were all ∼1500 m in the central Algerian basin, but ∼1250 m in 2011 and ∼1500 m in 2018 in the western Algerian basin. The shallower depths of Θ–S inversions in the western Algerian in 2011 revealed the uplift of the new WMDW toward the Alboran Sea (Schroeder et al., 2008, 2010).

There is no direct deep ventilation in the Tyrrhenian Sea but the signal of ventilation is imported by advected water masses. Similar to the Algerian basin, the Tyrrhenian Deep Water (TDW) is characterized by signs of intense ventilation during the 2011–2016 period followed by a possible slowdown of the ventilation after 2016. The increased transient tracer concentrations of the bottom layer around the Sardinia Channel indicate the overflow of well-ventilated WMDW from the WMT event into the deep layer of the Tyrrhenian Sea. Another sign is the weakened intensity of the EMed influence in the intermediate layer (tEMDW and LIW). The TMZ is less-developed in the Tyrrhenian Sea than those in the western basin (**Figure 13b**). This situation does change with deep-water rich in CFC-12 concentrations coming from the western basin filling the Tyrrhenian Sea in the near-bottom layer. The differences in CFC-12 concentrations between the TDW and the WMDW were ∼10 ppt in 2001, ∼60 ppt in 2011, and ∼30 ppt in 2018, a development that coincides with the influenced period of the WMT event.

As the shallow sea connected the Algerian basin with the Atlantic Ocean, the Alboran Sea is characterized by well-ventilated deep water with signs of increased ventilation between 1997 and 2018, although such ventilation signal is imported by advected water masses.

CONCLUSION

The Mediterranean Sea is one of the best-ventilated bodies of water in the global ocean and is as such characterized by high transient tracer concentrations in the deep layer below a zone of lower tracer concentrations in the intermediate layer, the Tracer Minimum Zone (TMZ). This zone of weak ventilation stretches across the whole Mediterranean Sea from the Levantine basin into the western basin. In this study, we report on spatiotemporal variability of deep and intermediate water ventilation of the Mediterranean Sea using a 30+ year time-series of transient tracer and hydrographic observations. During this period, the effects of two "events" dominate the variability of ventilation, the Eastern Mediterranean Transition (EMT) and the Western Mediterranean Transition (WMT).

We have summarized the results and conclusions of this study and depicted the Mediterranean deep and intermediate overturning circulation in the key convective areas over time (**Figure 14**). In the Eastern Mediterranean Sea, the low saline and cold Adriatic Deep Water (AdDW) was the dominant source to drive the ventilation in the Eastern Mediterranean Deep Water (EMDW) before the EMT. During the EMT, the dominant source shifted to the high saline and warm Cretan Deep Water (CDW) and led to the strong ventilation in the surrounding areas such as the eastern, north-eastern and central Ionian, northern Cretan Passage and western Levantine by 1995, far-away areas such as the western and north-western Ionian and central Levantine by 1999, and farther-away area such as the Strait of Sicily by 2001. Since then, the Aegean source intensity continuously decreased. The water from the Aegean source was not dense enough to reach the bottom of the adjacent Ionian and Levantine basins in 1999 and the bottom of the northern Cretan Passage in 2011 but ventilating in the intermediate layer 1500–2500 and 1000–1500 m, respectively. When the Aegean source was weakening, the Adriatic source restarted from 1999 and became the dominant source in the 2000s and 2010s. Recently, the Adriatic source produced slightly less dense water that didn't reach the bottom of the western Ionian but was rather ventilating the 2000–3000 m depth. In the Western Mediterranean Sea, the Western Mediterranean Deep Water (WMDW) was used to be in a steady-state ventilation scenario under the influence of deep convection in the source region, the Gulf of Lions. In the mid-2000s, the WMT event caused a near-complete renewal of WMDW. Subsequently, the deep convection intensity slowed down so that the ventilation in the WMDW weakened.

The combination of two (or more) transient tracers (e.g., CFC-12 and SF_6) can better constrain ventilation. In particular, considering the decreasing CFC-12 and increasing SF_6 atmospheric concentrations, the ability of CFC-12 alone in interpreting ventilation in the Mediterranean Sea is decreasing, while SF_6 is able to deliver information of ventilation and changes in ventilation. The complicated and variable ventilation of the Mediterranean Sea would benefit from an expanding suite of transient tracers. For instance, does a range of halogenated CFC replacement compound constitute possible additional tracers (Li et al., 2019; Li and Tanhua, 2019) or the isotope ^{39}Ar (Ebser et al., 2018) that can be used to better constrain the Transit Time Distributions as a measure of ventilation (Stöven and Tanhua, 2014). For the Mediterranean Sea, other models without the assumption of steady-state ventilation (as the Transit Time Distribution does) should be considered in the future based on its high variable ventilation patterns.

DATA AVAILABILITY STATEMENT

Cruise data in **Table 1** in 1987–2011 are from https://www.nodc.noaa.gov/ocads/oceans/Coastal/Meteor_Med_Sea.html. Observations of CFC-12 and SF_6 from cruises ESAW2 and CRELEV2016 are available on request to the corresponding author. Observations of CFC-12 and SF_6 from cruises TALPro2016 and MSM72 are available from https://cchdo.ucsd.edu/cruise/29AJ20160818 and https://cchdo.ucsd.edu/cruise/06M220180302.

AUTHOR CONTRIBUTIONS

PL performed the data processing, contributed figures and tables, and wrote the manuscript. TT conducted the sampling from cruises ESAW2, CRELEV2016, TALPro2016, and MSM72 and supported the writing process. Both authors contributed to the article and approved the submitted version.

FUNDING

The service charges for this open access publication have been covered by a Research Centre of the Helmholtz Association.

ACKNOWLEDGMENTS

We acknowledge the great support by the scientists and crew from expeditions M5/6, M31/1, Ura2, P234, Aegaeo98, Ura7, M44/4, M51/2, M84/3, ESAW2, CRELEV2016, TALPro2016, and MSM72. We thank Dr. Tim Stöven for his instructions on some MATLAB scripts. We gratefully thank support through the scholarship program from the China Scholarship Council (CSC). We also thank reviewers for their valuable suggestions.

SUPPLEMENTARY MATERIAL

The Supplementary Material for this article can be found online at: https://www.frontiersin.org/articles/10.3389/fmars.2020.00594/full#supplementary-material

REFERENCES

Akpinar, A., Yilmaz, E., Fach, B., and Salihoglu, B. (2016). "Physical oceanography of the Eastern Mediterranean Sea," in *The Turkish Part of the Mediterranean Sea*, eds K. Turan, B. Salihoglu, E. O. Ozbek, and B. Ozturk (Turkey: Turkish Marine Research Foundation), 1–14.

Artegiani, A., Paschini, E., Russo, A., Bregant, D., Raicich, F., and Pinardi, N. (1996a). The Adriatic Sea general circulation. Part I: air–sea interactions and water mass structure. *J. Phys. Oceanogr.* 27, 1492–1514. doi: 10.1175/1520-0485(1997)027<1492:tasgcp>2.0.co;2

Artegiani, A., Paschini, E., Russo, A., Bregant, D., Raicich, F., and Pinardi, N. (1996b). The Adriatic Sea general circulation. Part II: baroclinic circulation structure. *J. Phys. Oceanogr.* 27, 1515–1532. doi: 10.1175/1520-0485(1997)027<1515:tasgcp>2.0.co;2

Astraldi, M., Gasparini, G., Sparnocchia, S., Moretti, M., and Sansone, E. (1996). The characteristics of the water masses and the water transport in the Sicily Strait at long time scales. *Bull. de l'Institut Océanogr.* 95–116.

Astraldi, M., Gasparini, G., Vetrano, A., and Vignudelli, S. (2002). Hydrographic characteristics and interannual variability of water masses in the central Mediterranean: a sensitivity test for long-term changes in the Mediterranean Sea. *Deep Sea Res. I Oceanogr. Res. Pap.* 49, 661–680. doi: 10.1016/s0967-0637(01)00059-0

Buffett, G. G., Krahmann, G., Klaeschen, D., Schroeder, K., Sallares, V., Papenberg, C., et al. (2017). Seismic oceanography in the Tyrrhenian Sea: thermohaline staircases, eddies, and internal waves. *J. Geophys. Res. Oceans* 122, 8503–8523. doi: 10.1002/2017jc012726

Cardin, V., Civitarese, G., Hainbucher, D., Bensi, M., and Rubino, A. (2015). Thermohaline properties in the Eastern Mediterranean in the last three decades: is the basin returning to the pre-EMT situation? *Ocean Sci.* 11, 53–66. doi: 10.5194/os-11-53-2015

Chiggiato, J., Bergamasco, A., Borghini, M., Falcieri, F. M., Falco, P., Langone, L., et al. (2016). Dense-water bottom currents in the Southern Adriatic Sea in spring 2012. *Mar. Geol.* 375, 134–145. doi: 10.1016/j.margeo.2015.09.005

Durrieu de Madron, X., Houpert, L., Puig, P., Sanchez-Vidal, A., Testor, P., Bosse, A., et al. (2013). Interaction of dense shelf water cascading and open-sea convection in the northwestern Mediterranean during winter 2012. *Geophys. Res. Lett.* 40, 1379–1385. doi: 10.1002/grl.50331

Ebser, S., Kersting, A., Stöven, T., Feng, Z., Ringena, L., Schmidt, M., et al. (2018). 39Ar dating with small samples provides new key constraints on ocean ventilation. *Nat. Commun.* 9:5046.

Gačić, M., Civitarese, G., Kovačević, V., Ursella, L., Bensi, M., Menna, M., et al. (2014). Extreme winter 2012 in the Adriatic: an example of climatic effect on the BiOS rhythm. *Ocean Sci.* 10, 513–522. doi: 10.5194/os-10-513-2014

Gasparini, G., Ortona, A., Budillon, G., Astraldi, M., and Sansone, E. (2005). The effect of the Eastern Mediterranean Transient on the hydrographic characteristics in the Strait of Sicily and in the Tyrrhenian Sea. *Deep Sea Res. I Oceanogr. Res. Pap.* 52, 915–935. doi: 10.1016/j.dsr.2005.01.001

Hainbucher, D., Álvarez, M., Astray, B., Bachi, G., Cardin, V., Celentano, P., et al. (2019). *Variability and Trends in Physical and Biogeochemical Parameters of the Mediterranean Sea, Cruise No. MSM72, March 02, 2018 - April 03, 2018, Iraklion (Greece) - Cádiz (Spain), MED-SHIP2*. Bremen: Gutachterpanel Forschungsschiffe.

Hainbucher, D., Rubino, A., and Klein, B. (2006). Water mass characteristics in the deep layers of the western Ionian Basin observed during May 2003. *Geophys. Res. Lett.* 33:L05608.

Hall, T. M., and Plumb, R. A. (1994). Age as a diagnostic of stratospheric transport. *J. Geophys. Res. Atmos.* 99, 1059–1070.

Hemleben, C. (1996). *Oestliches Mittelmeer, Rotes Meer, Arabisches Meer: Cruise No. 31; 30 December 1994-1922 March 1995*. Hamburg: Universität Hamburg.

Hemleben, C., Hoernle, K., Jørgensen, B., and Roether, W. (2003). *Ostatlantik, Mittelmeer, Schwarzes Meer, Cruise No. 51, 12 September-28 December 2001*. Hamburg: Universität Hamburg.

Houpert, L., Durrieu De Madron, X., Testor, P., Bosse, A., D'ortenzio, F., Bouin, M.-N., et al. (2016). Observations of open-ocean deep convection in the northwestern Mediterranean Sea: seasonal and interannual variability of mixing and deep water masses for the 2007–2013 period. *J. Geophys. Res. Oceans* 121, 8139–8171. doi: 10.1002/2016jc011857

Jullion, L. (2016). *TAlPro-2016: A Tyrrhenian Sea & Alger-provencal component of the MedSHIP Programme, RV Angeles Alvariño, 18/08/16 - 29/08/16, Palermo (Italy) - Barcelona (Spain), Bremerhaven, EUROFLEETS2 Cruise Summary Report*. Available: hdl:10013/epic.5a866780-1f8a-45cf-8111-47b2b5dc29db (accessed September 20, 2019).

Jullion, L., Jacquet, S., and Tanhua, T. (2017). Untangling biogeochemical processes from the impact of ocean circulation: first insight on the Mediterranean dissolved barium dynamics. *Glob. Biogeochem. Cycles* 31, 1256–1270. doi: 10.1002/2016gb005489

Khatiwala, S., Primeau, F., and Holzer, M. (2012). Ventilation of the deep ocean constrained with tracer observations and implications for radiocarbon estimates of ideal mean age. *Earth Planet. Sci. Lett.* 325, 116–125. doi: 10.1016/j.epsl.2012.01.038

Klein, B., Roether, W., Civitarese, G., Gacic, M., Manca, B. B., and D'alcala, M. R. (2000). Is the Adriatic returning to dominate the production of Eastern Mediterranean deep water? *Geophys. Res. Lett.* 27, 3377–3380. doi: 10.1029/2000gl011620

Klein, B., Roether, W., Manca, B. B., Bregant, D., Beitzel, V., Kovacevic, V., et al. (1999). The large deep water transient in the Eastern Mediterranean. *Deep Sea Res. I Oceanogr. Res. Pap.* 46, 371–414. doi: 10.1016/s0967-0637(98)00075-2

Lascaratos, A., Roether, W., Nittis, K., and Klein, B. (1999). Recent changes in deep water formation and spreading in the eastern Mediterranean Sea: a review. *Prog. Oceanogr.* 44, 5–36. doi: 10.1016/s0079-6611(99)00019-1

Li, P., Mühle, J., Montzka, S. A., Oram, D. E., Miller, B. R., Weiss, R. F., et al. (2019). Atmospheric histories, growth rates and solubilities in seawater and other natural waters of the potential transient tracers HCFC-22, HCFC-141b, HCFC-142b, HFC-134a, HFC-125, HFC-23, PFC-14 and PFC-116. *Ocean Sci.* 15, 33–60. doi: 10.5194/os-15-33-2019

Li, P., and Tanhua, T. (2019). Medusa-Aqua system: simultaneous measurement and evaluation of novel potential halogenated transient tracers HCFCs, HFCs and PFCs in the ocean. *Ocean Sci. Discuss.* 2019, 1–34.

Luyten, J., Pedlosky, J., and Stommel, H. (1983). The ventilated thermocline. *J. Phys. Oceanogr.* 13, 292–309.

Malanotte-Rizzoli, P., and Hecht, A. (1988). Large-scale properties of the Eastern Mediterranean: a review. *Oceanol. Acta* 11, 323–335.

Malanotte-Rizzoli, P., and Robinson, A. R. (1988). POEM: physical oceanography of the eastern Miditerranean. *EOS Trans. Am. Geophys. Union* 69, 194–203.

Manca, B., Kovaĉević, V., Gaĉić, M., and Viezzoli, D. (2002). Dense water formation in the Southern Adriatic Sea and spreading into the Ionian Sea in the period 1997-1999. *J. Mar. Syst.* 3, 133–154. doi: 10.1016/s0924-7963(02)00056-8

Manca, B. B., Ibello, V., Pacciaroni, M., Scarazzato, P., and Giorgetti, A. (2006). Ventilation of deep waters in the Adriatic and Ionian Seas following changes in thermohaline circulation of the Eastern Mediterranean. *Clim. Res.* 31, 239–256. doi: 10.3354/cr031239

Marshall, J., and Schott, F. (1999). Open-ocean convection: observations, theory, and models. *Rev. Geophys.* 37, 1–64. doi: 10.1029/98rg02739

Nellen, W., Bettac, W., Roether, W., Schnack, D., Thiel, H., Weikert, H., et al. (1996). *MINDIK (Band II), Reise Nr. 5, 2 January-24 September 1987*. Hamburg: Universitat Hamburg.

Pätzold, J. (2000). *Östliches Mittelmeer-Nördliches Rotes Meer 1999: Cruise No. 44, 22 January-16 May 1999*. Hamburg: Universität Hamburg.

Pinardi, N., Zavatarelli, M., Adani, M., Coppini, G., Fratianni, C., Oddo, P., et al. (2015). Mediterranean Sea large-scale low-frequency ocean variability and water mass formation rates from 1987 to 2007: a retrospective analysis. *Prog. Oceanogr.* 132, 318–332. doi: 10.1016/j.pocean.2013.11.003

Rhein, M., Send, U., Klein, B., and Krahmann, G. (1999). Interbasin deep water exchange in the western Mediterranean. *J. Geophys. Res. Oceans* 104, 23495–23508. doi: 10.1029/1999jc900162

Roether, W., Klein, B., Beitzel, V., and Manca, B. B. (1998). Property distributions and transient-tracer ages in Levantine Intermediate Water in the Eastern Mediterranean. *J. Mar. Syst.* 18, 71–87. doi: 10.1016/s0924-7963(98)00006-2

Roether, W., Klein, B., and Hainbucher, D. (2014). The Eastern Mediterranean Transient: evidence for similar events previously. *Mediterranean Sea Temp. Variabil. Spat. Patt.* 202, 75–83. doi: 10.1002/9781118847572.ch6

Roether, W., Klein, B., Manca, B. B., Theocharis, A., and Kioroglou, S. (2007). Transient Eastern Mediterranean deep waters in response to the massive dense-water output of the Aegean Sea in the 1990s. *Prog. Oceanogr.* 74, 540–571. doi: 10.1016/j.pocean.2007.03.001

Roether, W., Manca, B. B., Klein, B., Bregant, D., Georgopoulos, D., Beitzel, V., et al. (1996). Recent changes in eastern Mediterranean deep waters. *Science* 271, 333–335. doi: 10.1126/science.271.5247.333

Rubino, A., and Hainbucher, D. (2007). A large abrupt change in the abyssal water masses of the eastern Mediterranean. *Geophys. Res. Lett.* 34:L23607.

Šantić, D., Kovačević, V., Bensi, M., Giani, M., Vrdoljak Tomaš, A., Ordulj, M., et al. (2019). Picoplankton distribution and activity in the deep waters of the Southern Adriatic Sea. *Water* 11:1655. doi: 10.3390/w11081655

Schlitzer, R., Roether, W., Oster, H., Junghans, H.-G., Hausmann, M., Johannsen, H., et al. (1991). Chlorofluoromethane and oxygen in the Eastern Mediterranean. *Deep Sea Res. A Oceanogr. Res. Pap.* 38, 1531–1551. doi: 10.1016/0198-0149(91)90088-w

Schneider, A., Tanhua, T., Körtzinger, A., and Wallace, D. W. R. (2010). High anthropogenic carbon content in the eastern Mediterranean. *J. Geophys. Res.* 115:C12050.

Schneider, A., Tanhua, T., Roether, W., and Steinfeldt, R. (2014). Changes in ventilation of the Mediterranean Sea during the past 25 year. *Ocean Sci.* 10, 1–16. doi: 10.5194/os-10-1-2014

Schroeder, K., Chiggiato, J., Bryden, H., Borghini, M., and Ismail, S. B. (2016). Abrupt climate shift in the Western Mediterranean Sea. *Sci. Rep.* 6:23009.

Schroeder, K., Gasparini, G., Tangherlini, M., and Astraldi, M. (2006). Deep and intermediate water in the western Mediterranean under the influence of the Eastern Mediterranean Transient. *Geophys. Res. Lett.* 33:L21607.

Schroeder, K., Josey, S., Herrmann, M., Grignon, L., Gasparini, G., and Bryden, H. (2010). Abrupt warming and salting of the Western Mediterranean Deep Water after 2005: atmospheric forcings and lateral advection. *J. Geophys. Res. Oceans* 115:C08029.

Schroeder, K., Ribotti, A., Borghini, M., Sorgente, R., Perilli, A., and Gasparini, G. (2008). An extensive western Mediterranean deep water renewal between 2004 and 2006. *Geophys. Res. Lett.* 35:L18605.

Schroeder, K., Tanhua, T., Bryden, H. L., Alvarez, M., Chiggiato, J., and Aracri, S. (2015). Mediterranean sea ship-based hydrographic investigations program (Med-SHIP). *Oceanography* 28, 12–15. doi: 10.5670/oceanog.2015.71

Somot, S., Houpert, L., Sevault, F., Testor, P., Bosse, A., Taupier-Letage, I., et al. (2018). Characterizing, modelling and understanding the climate variability of the deep water formation in the North-Western Mediterranean Sea. *Clim. Dyn.* 51, 1179–1210. doi: 10.1007/s00382-016-3295-0

Sparnocchia, S., Gasparini, G., Astraldi, M., Borghini, M., and Pistek, P. (1999). Dynamics and mixing of the Eastern Mediterranean outflow in the Tyrrhenian basin. *J. Mar. Syst.* 20, 301–317. doi: 10.1016/s0924-7963(98)00088-8

Stöven, T., and Tanhua, T. (2014). Ventilation of the Mediterranean Sea constrained by multiple transient tracer measurements. *Ocean Sci.* 10, 439–457. doi: 10.5194/os-10-439-2014

Tanhua, T., Hainbucher, D., Schroeder, K., Cardin, V., Álvarez, M., and Civitarese, G. (2013a). The Mediterranean Sea system: a review and an introduction to the special issue. *Ocean Sci.* 9, 789–803. doi: 10.5194/os-9-789-2013

Tanhua, T., Van Heuven, S., Key, R. M., Velo, A., Olsen, A., and Schirnick, C. (2010). Quality control procedures and methods of the CARINA database. *Earth Syst. Sci. Data* 2, 35–49. doi: 10.5194/essd-2-35-2010

Tanhua, T., Waugh, D. W., and Bullister, J. L. (2013b). Estimating changes in ocean ventilation from early 1990s CFC-12 and late 2000s SF6 measurements. *Geophys. Res. Lett.* 40, 927–932. doi: 10.1002/grl.50251

Testor, P., Bosse, A., Houpert, L., Margirier, F., Mortier, L., Legoff, H., et al. (2018). Multiscale observations of deep convection in the northwestern Mediterranean

Sea during winter 2012–2013 using multiple platforms. *J. Geophys. Res. Oceans* 123, 1745–1776. doi: 10.1002/2016jc012671

Theocharis, A., Klein, B., Nittis, K., and Roether, W. (2002). Evolution and status of the Eastern Mediterranean Transient (1997-1999). *J. Mar. Syst.* 33, 91–116. doi: 10.1016/s0924-7963(02)00054-4

Tsimplis, M. N., Zervakis, V., Josey, S. A., Peneva, E. L., Struglia, M. V., Stanev, E. V., et al. (2006). "Changes in the oceanography of the Mediterranean Sea and their link to climate variability," in *Developments in Earth and Environmental Sciences*, eds P. Lionello, P. Malanotte-Rizzoli,and R. Boscolo (Amsterdam: Elsevier), 227–282. doi: 10.1016/s1571-9197(06)80007-8

Velaoras, D., Krokos, G., Nittis, K., and Theocharis, A. (2014). Dense intermediate water outflow from the Cretan Sea: a salinity driven, recurrent phenomenon, connected to thermohaline circulation changes. *J. Geophys. Res. Oceans* 119, 4797–4820. doi: 10.1002/2014jc009937

Velaoras, D., Papadopoulos, V. P., Kontoyiannis, H., Cardin, V., and Civitarese, G. (2018). Water masses and hydrography during April and June 2016 in the Cretan Sea and Cretan Passage (Eastern Mediterranean Sea). *Deep Sea Res. II Top. Stud. Oceanogr.* 164, 25–40. doi: 10.1016/j.dsr2.2018.09.005

Velaoras, D., Papadopoulos, V. P., Kontoyiannis, H., Papageorgiou, D. K., and Pavlidou, A. (2017). The response of the Aegean Sea (eastern Mediterranean) to the extreme 2016-2017 winter. *Geophys. Res. Lett.* 44, 9416–9423. doi: 10.1002/2017gl074761

Waugh, D. W., Hall, T. M., and Haine, T. W. (2003). Relationships among tracer ages. *J. Geophys. Res. Oceans* 108:3138.

Conflict of Interest: The authors declare that the research was conducted in the absence of any commercial or financial relationships that could be construed as a potential conflict of interest.

frontiers in Marine Science

ORIGINAL RESEARCH
published: 22 September 2020
doi: 10.3389/fmars.2020.568602

Climatological Hydrographic Properties and Water Mass Transports in the Balearic Channels From Repeated Observations Over 1996–2019

Manuel Vargas-Yáñez[1], Melanie Juza[2], Rosa Balbín[3], Pedro Velez-Belchí[4], M. Carmen García-Martínez[1], Francina Moya[1] and Alonso Hernández-Guerra[5]*

[1] Instituto Español de Oceanografía, Centro Oceanográfico de Málaga, Málaga, Spain, [2] SOCIB, Balearic Islands Coastal Observing and Forecasting System, Palma de Mallorca, Spain, [3] Instituto Español de Oceanografía, Centro Oceanográfico de Baleares, Palma de Mallorca, Spain, [4] Centro Oceanográfico de Canarias, Instituto Español de Oceanografía, Santa Cruz de Tenerife, Spain, [5] Unidad Océano y Clima, Instituto de Oceanografía y Cambio Global, IOCAG, Universidad de Las Palmas de Gran Canaria, ULPGC, Unidad Asociada ULPGC-CSIC, Canary Islands, Spain

OPEN ACCESS

Edited by:
Katrin Schroeder, Italian National Research Council (CNR), Italy

Reviewed by:
Laurent Coppola, UMR 7093 Laboratoire d'Océanographie de Villefranche (LOV), France
Dimitris Velaoras, Institute of Oceanography, Greece

***Correspondence:**
Manuel Vargas-Yáñez
manolo.vargas@ieo.es

Specialty section:
This article was submitted to Physical Oceanography, a section of the journal Frontiers in Marine Science

Received: *01 June 2020*
Accepted: *26 August 2020*
Published: *22 September 2020*

Citation:
Vargas-Yáñez M, Juza M, Balbín R, Velez-Belchí P, García-Martínez MC, Moya F and Hernández-Guerra A (2020) Climatological Hydrographic Properties and Water Mass Transports in the Balearic Channels From Repeated Observations Over 1996–2019. Front. Mar. Sci. 7:568602. doi: 10.3389/fmars.2020.568602

The longest time series of CTD transects available in the Mallorca and Ibiza Channels (1996–2019) are presented. These hydrographic sections have a three-monthly periodicity and allow to resolve the seasonal cycle of water mass properties. They are organized in two closed boxes allowing the use of inverse models for the calculation of absolute geostrophic transports through the Channels. These long time series allow to establish the climatological distributions of potential temperature and salinity for each season of the year as well as other relevant statistical properties such as the variance and covariance functions. The results indicate that these distributions depart from normality making the median a better statistic than the mean value for the description of climatological fields. The salinity field shows a seasonal cycle in the upper layer indicating a higher influence of the Atlantic Water during summer, decreasing through the rest of the year. The Western Intermediate Water, which is mainly formed in the North-Western Mediterranean and the Balearic Sea, is observed preferentially in the Ibiza Channel during winter and spring. This water mass is better detected using a geometry-based method instead of the traditional criterion based on predefined temperature and salinity ranges. These water masses flow preferentially southwards through the Ibiza Channel, and northwards through the Mallorca Channel, although intrusions in the opposite directions are observed. Below, the Levantine Intermediate Water shows a similar behavior, but the mass transport analyses suggest that most of this water mass recirculates with the Balearic Current along the northern slope of the Islands. Although the depth of both Channels prevents the circulation of deep waters, a small fraction of the Western Mediterranean Deep Water could overflow the sills.

Keywords: Balearic Channels, Western Mediterranean, box inverse model, water masses, Northern and Balearic Currents

INTRODUCTION

The Mediterranean Sea circulation is ultimately forced by its net evaporation and the net heat loss through its surface. As a result of these deficits, the Mediterranean receives a surface current of fresh Atlantic Water (AW) through the Strait of Gibraltar and exports to the Atlantic, saltier waters as a deep current. This deep current is composed of different types of Mediterranean Waters (MWs) formed by intermediate and deep convection and mixing processes in different areas of the Eastern and Western Mediterranean Sea (EMED and WMED, respectively). The upper layer of the WMED is comprised of AW with a variable degree of modification depending on its resident time within this basin. The MWs circulating in the WMED are originated from the WMED or the EMED. The water masses formed in the WMED are the Western Intermediate Water (WIW), the Western Mediterranean Deep Water (WMDW), and the Tyrrhenian Dense Water (TDW). WIW is mainly formed in the continental shelf of the Gulf of Lions and the Balearic Sea by winter intermediate convection (Vargas-Yáñez et al., 2012; Juza et al., 2013, 2019). WMDW is formed by deep convection in the open sea area in front of the Gulf of Lions and in the Ligurian Sea with the contribution of AW and intermediate waters of eastern origin (MEDOC Group, 1970; Bosse et al., 2016; Testor et al., 2018). Finally, TDW is formed within the Tyrrhenian Sea by the mixing of WMDW with those waters that overflow through the Sicily/Sardinian Channels from the EMED (Sparnocchia et al., 1999). The MWs of eastern origin that flow into the WMED are the Levantine Intermediate Water (LIW) and Cretan Intermediate Water (CIW), which are formed by intermediate convection in the Levantine Basin and the Cretan Sea, respectively (Schroeder et al., 2017), and the Transitional Eastern Mediterranean Deep Water (tEMDW). This latter losses its signature within the WMED when it takes part in the formation of TDW. Concerning the CIW, it is very difficult to distinguish from the LIW once in the western basin. Therefore, LIW is the only water mass of eastern origin that will be considered in the present work.

Apart from the water volume that compensates for the net evaporation, and the fraction of AW that takes part in the formation of WIW and WMDW, the rest of this water mass flows out of the WMED through the Sicily Channel. In a similar way, all the intermediate and deep waters present in the WMED finally flow out through the Strait of Gibraltar (Millot, 2009). Nevertheless, both AW and the MWs recirculate before leaving the WMED. All these water masses follow a cyclonic circuit forced by the Coriolis force. The northern branch of this cyclonic circuit flows along the continental slope of the Ligurian Sea and the Gulf of Lions receiving the name of Northern Current (Millot and Taupier-Letage, 2005; Berta et al., 2018). Then, this permanent current is deflected southwards along the Spanish continental slope. AW and WIW flow within this current at the upper 300 m of the water column (Pinot and Ganachaud, 1999; Juza et al., 2013; Pascual et al., 2014). LIW and WMDW flow below the AW and the WIW. These water masses also describe a cyclonic circuit following the continental slope of the Liguro-provençal basin and the Catalan and Balearic Seas (Millot and Taupier-Letage, 2005). However, the Balearic Islands extend in a northeast direction from the mainland and produce an elevation of the bottom topography which intercepts the southward progression of intermediate and deep waters, modifying and restricting the circulation of the water masses, depending on their depth within the water column (**Figure 1**).

The southern part of the WMED cyclonic circuit is formed by the Algerian Current. This current is 30–50 km wide and 200–400 m deep and flows eastwards along the Algerian continental slope (Testor et al., 2005; Pascual et al., 2014). It is unstable, generating cyclonic and anticyclonic eddies. Testor et al. (2005) and Escudier et al. (2016) have shown that anticyclonic eddies have a larger size and longer lifespan than the cyclonic ones. Anticyclonic eddies can reach even the bottom of the Algerian slope and last for 3 years. These eddies follow the pathway of the main current which describes two cyclonic gyres, one of them between 1 and 3.5°E (Western Cyclonic Gyre) and a second one between 4.5 and 8°E (Eastern Cyclonic Gyre, Escudier et al., 2016). Therefore, the eddies detached from the Algerian Current flow eastwards along the Algerian slope and westwards at a latitude of 39° or 40° N. These mesoscale structures can reach the Balearic Channels and constitute a possible means for AW and LIW transport through the Channels.

The Balearic Channels, which are located between the waters flowing through the Algerian basin and those in the Liguro-Provençal area, are consequently considered as a "choke point" for the north-south water, heat and salt exchanges within the WMED (Heslop et al., 2012; Barceló-Llull et al., 2019). A proper and detailed description of the water mass properties and associated transports in the Balearic Channels is of paramount importance for the understanding of the mass, heat and salt budgets in the WMED, as well as the ocean circulation and variability in this basin.

The first attempts to establish the properties of the water masses in the Channels and their associated transports, analyzed a reduced number of oceanographic campaigns, most of them during winter or spring (García-Lafuente et al., 1995; López-Jurado et al., 1995; Pinot and Ganachaud, 1999). These works established that the Northern Current was deflected to the northeast after reaching the Balearic Islands, forming the so-called Balearic Current along the northern slope of the archipelago. Nevertheless, a fraction of the upper and intermediate water masses within this current would flow southwards. The Ibiza Channel was the preferential pathway for the modified AW and WIW flowing within the Northern Current. These authors also found that fresh AW intrusions from the south could occur at the eastern side of the Ibiza Channel and through the Mallorca one, feeding the Balearic Current. This general picture was subject to a high temporal variability and soon it became clear that the hydrographic conditions during any particular campaign could depart strongly from one to other making it necessary the study of long time series covering the complete seasonal cycle. Pinot et al. (2002) was one of the first studies addressing the seasonal variability at the Balearic Channels using a several year time series of observations. This work analyzed 13 surveys from March 1996 to June 1998 and 5 mooring lines in the Ibiza and Mallorca Channels to describe

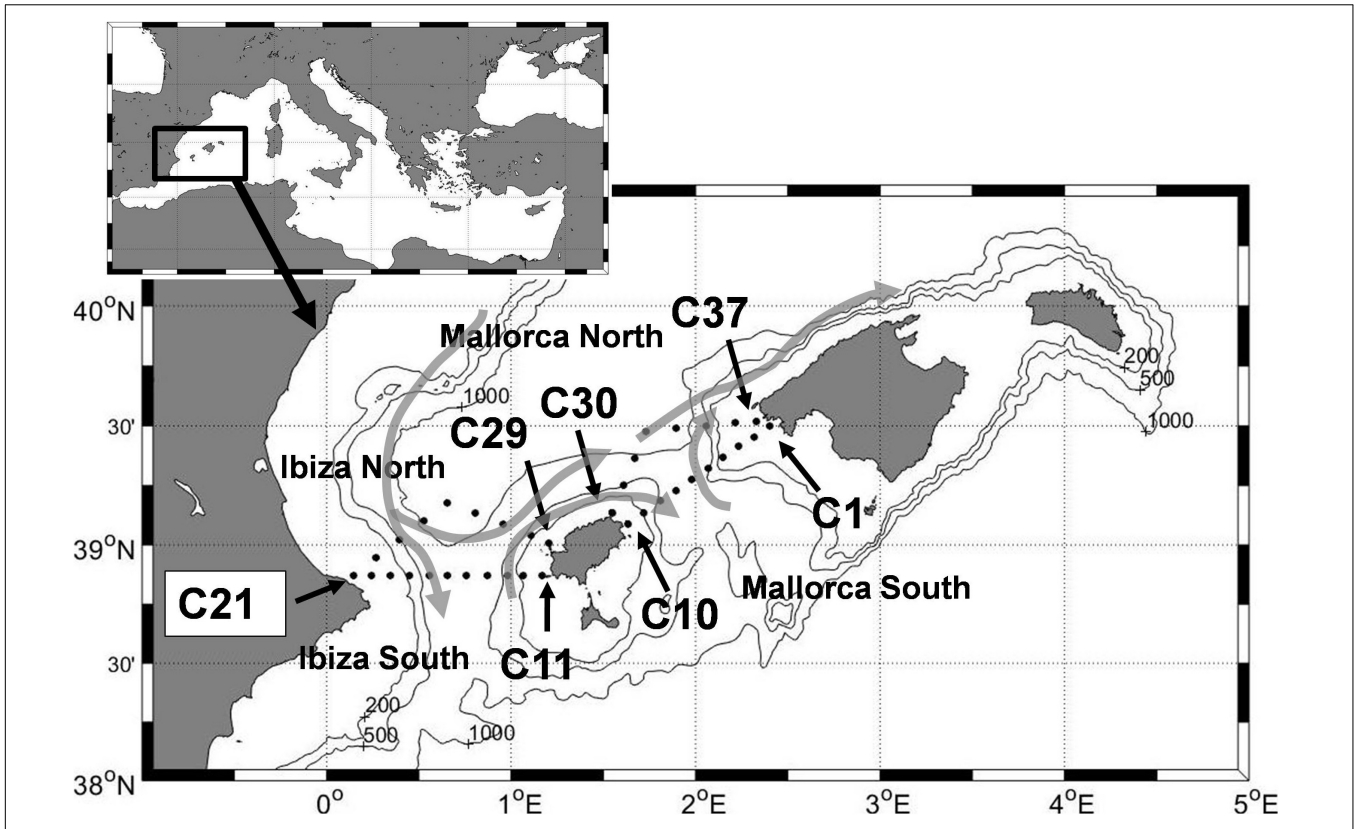

FIGURE 1 | Position of the stations monitored from 1996 to 2019 in the frame of the CANALES, CIRBAL and RADMED projects. These stations are distributed along four sections: Mallorca South (stations C1–C10), Ibiza South (C11–C21), Ibiza North (C21–C29) and Mallorca North (C30–C37). The Mallorca South and North sections form the Mallorca Channel triangle and the Ibiza South and North form the Ibiza Channel triangle. A scheme of the upper layer circulation in the Balearic Sea, inferred from the literature and this study is also included.

the water mass distributions and transports corresponding to the four seasons of the year.

Additional works have shown that the variability at short time scales could be as large as the variability at seasonal scale and consequently longer time series would be needed (Heslop et al., 2012). These authors analyzed the short time scales by means of a series of 2–3 days glider transects from January to June 2011 in the Ibiza Channel from the SOCIB observing system (Sistema de Observación y predicción Oceánica de las Islas Baleares). Juza et al. (2013) analyzed a similar high resolution data base combined with numerical simulations and Barceló-Llull et al. (2019) studied a series of glider transects in the Mallorca Channel from 2011 to 2018. All these works revealed the high variability of the circulation in the Balearic Channels, both at a seasonal scale, mainly linked to the winter intensification of the Northern Current, and at shorter time scales, associated to mesoscale activity such as eddies at both the northern and southern sides of the Channels.

This study examines the longest time series of CTD seasonal sections in the Balearic Channels from 1996 to 2019. It could be considered as an extension of that by Pinot et al. (2002), who analyzed exactly the same hydrographic stations from 1996 to 1998 in the frame of the CANALES project. The present study uses those data in Pinot et al. (2002), the first extension of CANALES project under the frame of CIRBAL project (1999–2006), and the current Mediterranean monitoring program RADMED operated by the Instituto Español de Oceanografía (IEO) from 2007 to the present. The main objective of this work is to provide a statistical description of the temperature and salinity fields within the Balearic Channels, establishing the seasonal climatologies of hydrographic properties of water masses, their ranges of variability and their mass transports through the Channels.

Data

The Instituto Español de Oceanografía (IEO, Spanish Institute for Oceanography) has monitored the oceanographic conditions in the Balearic Channels since 1996 to the present with a variable periodicity and under the umbrella of different projects. The first one was named CANALES (from the Spanish word for Channels) and lasted from 1996 to 1998. The second project, called CIRBAL (Circulation in the Balearic Channels), collected data from 1999 to 2006. Finally, in the frame of the RADMED project, the Balearic Channels have been monitored from 2007 to the present (López-Jurado et al., 2015; Tel et al., 2016). The first two projects were devoted to the study of the physical properties of the water masses and their circulation within the Balearic Channels (Pinot et al., 2002). The RADMED project is dedicated

to the multidisciplinary seasonal monitoring of the continental shelf and slope waters of the Spanish Mediterranean, including the Balearic Islands and some deep stations for the monitoring of the Mediterranean deep waters.

The sampling strategies and the collected variables have changed according to the different projects. Nevertheless, during all the oceanographic campaigns, a CTD vertical profile was collected at all the stations along the four sections within the Balearic Channels (**Figure 1**). These four sections formed two triangles, one in the Mallorca Channel (from Mallorca to Ibiza Island) and a second one in the Ibiza Channel (from Ibiza to the mainland). The distribution of the stations in triangles was fixed during the first project CANALES, which aimed at having closed boxes for the application of box inverse models (Pinot and Ganachaud, 1999; Pinot et al., 2002). The distance between stations is 5 nautical miles for the straight sections in the southern part of the Channels, and 8 nautical miles for the broken sections at the northern part of the Channels. These distances would be similar to the Rossby radius of deformation in the Balearic Channels, which is around 10 km (Pinot and Ganachaud, 1999; Send et al., 1999).

These four hydrographic sections were sampled during 71 campaigns over 1996–2009. **Supplementary Table S1** shows the monitored months and years for every campaign and the project under which each survey was carried out. These CTD data are freely available at standard depth levels in the IBAMar data base[1] and under request in Sea Data Net.

MATERIALS AND METHODS

This section and the next section ("Results") are organized following the same structure (sub-sections) to better relate and understand each specific result to the corresponding methodology and objectives. First, the normality of the temperature and salinity distributions is examined, and the mean and median values as well as the dispersion of such distributions are estimated. Secondly, the temperature and salinity covariance functions are defined and the methods used for their estimations are presented. This sub-section aims at obtaining the parameters needed for the application of Optimal Statistical Interpolation. Thirdly, the water masses (AW, WIW, LIW, and WMDW) and the criteria used to define them are described. Finally the methodology corresponding to a box inverse model is presented.

Normality and Measures of Central Tendency and Dispersion

The first objective of this work is to obtain the statistical properties of the temperature and salinity fields in the Balearic Channels, which have a strong variability at seasonal scale. For this reason, all the available campaigns were distributed into four seasonal groups: winter includes surveys from January to March, spring from April to June, summer from July to September, and autumn from October to December. The total number of surveys carried out during each season of the year were: 21 for winter, 24 for spring, 13 for summer and 13 for autumn. **Supplementary Figure S1** shows the distributions of the dates for each campaign and the earliest and the latest surveys for each season. As each survey extended along more than 1 day (4 days in general), the date corresponding to each survey is the central one.

Each campaign corresponding to a particular season and year shows different temperature and salinity values because of the natural variability of the sea and the ocean-atmosphere interaction. All the temperature and salinity data corresponding to the same season of the year and the same pressure level are distributed around a certain value. Using the usual terminology in descriptive statistics, such a value is named the central tendency of the distribution (Zar, 2010). This latter, obtained from time series as long as possible, is considered as a climatological value. The mean and the median are usual statistics used to express the central tendency of a distribution. Nevertheless, the most appropriate one depends on the distribution shape. Both values are coincident in the case of a Normal (symmetric) distribution. In case of skewed (asymmetric) distributions, the median is a more appropriate measure of the central tendency. For this reason, Shapiro-Wilk tests were carried out to check the normality of the potential temperature and salinity distributions at the pressure levels 5, 50, 100, 200, 300, 400, 500, and 1000 dbar and for each season of the year (**Figure 2**).

Besides the central tendency, the width of the distribution is a fundamental statistic since it provides the range of values that could be expected when a single measurement is obtained. Finally the mean value, the median and the standard deviation were estimated for the potential temperature and salinity for each of the four sections within the Balearic Channels and for each season of the year.

The Covariance Function. Parameters for Optimal Statistical Interpolation

The covariance function of any observed variable informs about the spatial structure of such variable. Besides this, when interpolation is required and the variable is interpolated as a linear combination of the available observations, an optimal linear interpolation can be estimated if the covariance function of the variable and the noise to signal ratio are known (Thiébaux and Pedder, 1987; Pedder, 1993; Gomis et al., 2001; **Supplementary Material** for mathematical details). In most of the cases, these functions are not known when one single realization of a hydrographic section is available, neither are known the statistical properties of the analyzed variables for the particular region of interest. In practice, the observed variables are decomposed into a background field and a signal on which we are interested plus a noise. The background field is usually modeled as a low order polynomial which should be estimated by generalized least squares, which once again require the knowledge of the covariance function. A possible approach is to estimate the background field by ordinary least squares and then the covariance function from the resulting residuals, and then proceed in an iterative way (Bretherton et al., 1976). Vargas-Yáñez et al. (2005) showed that the periodic repetition of hydrographic sections could be used for the estimation of the covariance

[1] http://www.ba.ieo.es/es/ibamar

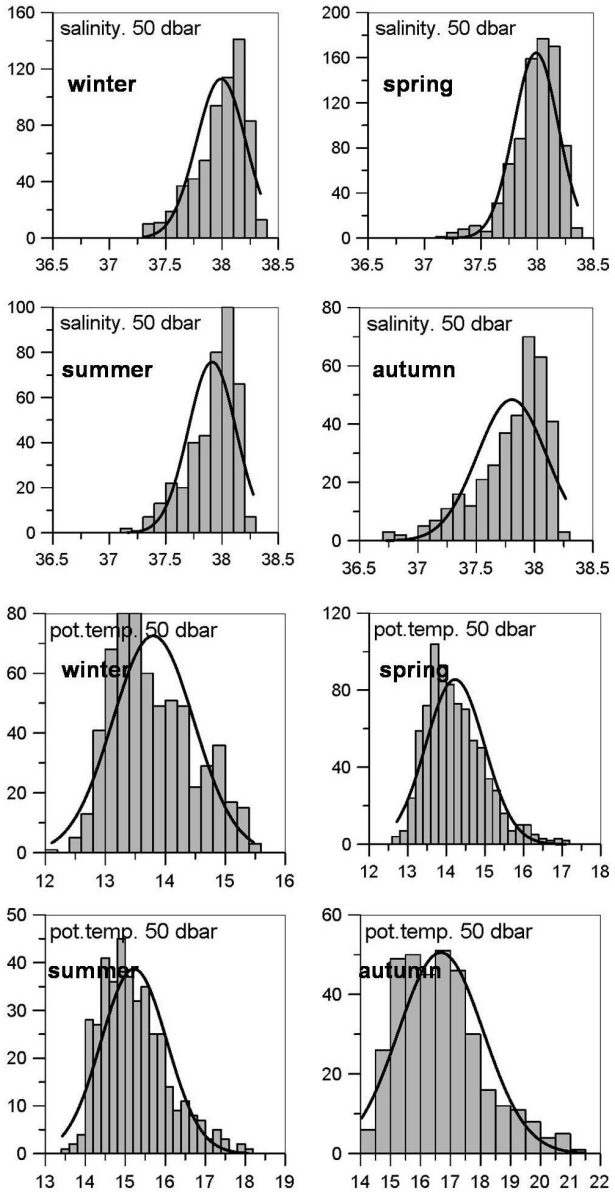

FIGURE 2 | Histograms showing the salinity and potential temperature distribution for the four seasons of the year at the 50 dbar pressure level. A normal distribution was fitted to each distribution (solid line).

function and those parameters needed for the correct use of Optimal Statistical Interpolation.

Let's consider $\phi_{i,t}$ the value of any variable (temperature, salinity, etc.) at the position $\boldsymbol{r}_i = (x_i, z_i)$ within an hydrographic section at time t. Then a background or climatological mean can be estimated for each season of the year as the sampling mean:

$$\hat{\mu}_i = \frac{\sum_{t=1}^{T} \phi_{i,t}}{T} \tag{1}$$

Being T the times such a location had been sampled for a given season of the year. The hat denotes estimation. The covariance and the correlation functions were estimated for each pair of positions $\boldsymbol{r}_i$ and $\boldsymbol{r}_j$ within the hydrographic section using Eqs (2) and (3):

$$cov\left(\bar{r}_i, \bar{r}_j\right) = \frac{\sum_{t=1}^{T} \left(\phi_{i,t} - \hat{\mu}_i\right)\left(\phi_{j,t} - \hat{\mu}_j\right)}{T} \tag{2}$$

$$corr\left(\bar{r}_i, \bar{r}_j\right) = \frac{\sum_{t=1}^{T} \left(\phi_{i,t} - \hat{\mu}_i\right)\left(\phi_{j,t} - \hat{\mu}_j\right)}{\sqrt{\sum_{t=1}^{T} \left(\phi_{i,t} - \hat{\mu}_i\right)^2 \sum_{t=1}^{T} \left(\phi_{j,t} - \hat{\mu}_i\right)^2}} \tag{3}$$

The following objective was to find the analytical dependence of the covariance and correlation functions on the coordinates (x_i, z_i) and (x_j, z_j). First, we inspected the dependence of the covariance function on the horizontal coordinates. In this case, the formulas (2) and (3) were evaluated for all pairs of points with the same vertical coordinate z and different values of x. It was assumed that for a fixed depth level, these functions only depended on the horizontal distance Δx. Then, two Gaussian functions were fitted:

$$cov\left(\Delta x\right) = \sigma^2 \exp\left[-\frac{\Delta x^2}{2L_x^2}\right] \tag{4}$$

$$corr\left(\Delta x\right) = R_0 \exp\left[-\frac{\Delta x^2}{2L_x^2}\right] \tag{5}$$

Where σ^2 and L_x are the parameters obtained from the fit of (4) to the data. σ^2 is the value of the covariance function for $\Delta x = 0$, and represents the variance of the analyzed variable, and L_x is the decaying distance for the covariance function (see also **Supplementary Material** for details). Analogously, R_0 and L_x are the parameters of the fit for the correlation function.

Notice that the fit for the correlation function assumes a R_0 value for $\Delta x = 0$ different from 1. This value accounts for the noise to signal variance ratio:

$$\gamma = \frac{1}{R_0} - 1 \tag{6}$$

The parameters σ, L_x, R_0, and γ were estimated for each depth level and consequently could depend on depth.

To find out the dependence of the covariance function on the vertical coordinate, the Eqs (2) and (3) were estimated for all pairs of points with the same x value, but different z_i and z_j values. In this case, it cannot be assumed that the covariance only depends on the vertical distance between observations but also on the specific values of z_i and z_j. The vertical covariance was modeled as:

$$cov\left(z_1, z_2\right) = \sigma_0 \exp\Big[-\alpha_1 \left(z_1 - z_0\right)^2 - \alpha_2 \left(z_2 - z_0\right)^2 - \beta \left(z_1 - z_0\right)\left(z_2 - z_0\right) \Big] \tag{7}$$

Considering the symmetry of the covariance matrix $\alpha_1 = \alpha_2$ and making the variable change:

$$z_1 = \bar{z} - \frac{\Delta z}{2} \quad z_2 = \bar{z} + \frac{\Delta z}{2}$$

the former equation for the covariance function could be expressed as:

$$cov\,(z_1, z_2) = \sigma_0 \exp\left[-\frac{(\bar{z} - z_0)^2}{2L_1^2}\right] \cdot \exp\left[-\frac{\Delta z^2}{2L_2^2}\right] \quad (8)$$

Detection of Water Masses and Determination of Their Properties

The water masses which are mainly present in the Balearic Channels, are the Atlantic Water (AW), the Western Intermediate Water (WIW), the Levantine Intermediate Water (LIW), and the Western Mediterranean Deep Water (WMDW). Once the mean and median values had been calculated for each season and hydrographic section, the potential temperature, salinity, potential density and pressure levels corresponding to each water mass were estimated, in order to re-define the climatological properties of the main water masses in the Balearic Channels.

The strongest influence of AW is observed at the sea surface. Therefore, salinity, potential temperature and density for the upper 5 dbar of the water column were averaged for each season and hydrographic section. These values can be considered as indicators of the presence of this water mass at the area of study during the different seasons of the year.

The WIW has been traditionally considered as a cold water mass with potential temperature below 13°C and salinity values ranging between 37.7 and 38.3 (Salat and Font, 1987; López-Jurado et al., 1995). Vargas-Yáñez et al. (2012) considered that the WIW potential temperature and salinity ranges could be even larger and Pinot et al. (2002). Pinot and Ganachaud (1999) used the potential density range 28.8–29.05 to define the layer within the water column occupied by this water mass. Therefore, a first method to identify the properties of the WIW was to select those θ*S* values with potential density values ranging between 28.8 and 29.05 kgm^{-3}. The minimum θ value within this density range was considered the core of the WIW and the potential temperature, salinity and depth for such minimum were considered as the WIW properties for that oceanographic station and season of the year.

Juza et al. (2019) have shown that the previous methods for the identification of WIW properties have some shortcomings. The use of pre-determined temperature and salinity ranges does not allow to detect and track spatio-temporal changes in water mass properties and may lead to erroneous characterizations and interpretations. For example, an increase of temperature which would be out of ranges would be interpreted as absence or loss of this water mass. To overcome these issues, Juza et al. (2019) have developed a geometry-based approach to detect the presence of WIW and characterize its temperature and salinity properties. This method is based on the WIW definition and the θ*S* diagram shape, taking advantage of the position of the WIW between surface layers and LIW with temperature minima. This method enables to detect properly the WIW properties and their changes at both spatial and temporal scales. Finally, both methods were used for comparison: The minimum potential temperature for the 28.8–29.05 potential density range, and the geometry-based approach.

The core of the LIW was identified as the absolute salinity maximum. Depth, potential temperature and salinity values at the position of such maximum were used to define the properties of this water mass.

Finally, WMDW is the densest water mass within the Balearic Channels. Therefore the maximum potential density was considered as the core of this water mass. In some shallow stations, the deepest levels were occupied by a mixing of LIW and WMDW and it would not be appropriate to consider these waters as WMDW. First it was considered the possibility of following Pinot and Ganachaud (1999) and identifying WMDW as the densest waters for each station with a potential density higher than 29.1 kg/m^3. Nevertheless, the analysis of the mean and median θ*S* diagrams (see "Results" section) showed that this density value was very close to the LIW core and waters with this density would be a mixing between LIW and WMDW with a higher percentage of the former water mass. Finally, the used criterion was to identify the properties of WMDW at each station as those corresponding to the maximum potential density if that value was higher than 29.11 kg/m^3. Notice that the depth of this maximum is not always the maximum depth of the station. In such cases, it simply indicates that the maximum density is reached somewhere above the bottom depth and that the potential density remained constant to the sea bottom. Also notice that for each campaign the maximum density reached at each station will be different depending on the recent history of deep convection and modification of WMDW (see for instance Schroeder et al., 2010). As a result, WMDW temperature and salinity values will also be different for each campaign. In this work, the mean and median values from the whole time series will be analyzed.

Circulation and Transports Associated to the Average θS Distributions. Application of a Box Inverse Model

Once the average distributions of potential temperature and salinity had been obtained, the circulation and the water mass transports associated to such distributions were estimated. Considering that the climatological θ*S* values are very close to the most likely values found in the Balearic Channels, the associated currents and circulation would also describe the most likely circulation patterns in this area of the WMED.

The box inverse problem method was developed by Wunsch (1978, 1996) and was used to determine the circulation in the Balearic Sea and the Balearic Channels by Pinot and Ganachaud (1999) and Pinot et al. (2002). In summary, this method assumes the conservation of certain properties through a closed box. The model used at the present work follows Pinot and Ganachaud (1999) and Pinot et al. (2002) and assumes the mass conservation for four layers defined from the sea surface to the 28.8 isopycnal, from 28.8 to 29.05, from 29.05 to 29.1, and finally from the 29.1 isopycnal to the sea bottom. In addition to the mass conservation for these four layers, a fifth equation was obtained for the mass conservation for the whole water column. An error term was included for the transport at each layer (see **Supplementary Material** for

mathematical details). Following Pinot and Ganachaud (1999) and Pinot et al. (2002), Ekman transport and diapycnal mixing was not taken into account in the conservation equations and these processes were considered as included in the error term (Wunsch, 1978, 1996; Pinot and Ganachaud, 1999; Pinot et al., 2002). This inverse box model has been extensively applied in different oceanographic regions. Thus, Hernández-Guerra and Talley (2016) and Hernández-Guerra et al. (2019) estimated the Meridonal Overturning Circulation in the Indian-Pacific and Atlantic Oceans, respectively, and Hernández-Guerra et al. (2017) and Casanova-Masjoan et al. (2018) in the western and eastern boundaries of the North Atlantic Subtropical Gyre.

RESULTS

Normality and Measures of Central Tendency and Dispersion

The potential temperature and salinity values were assorted according to their season of the year and pressure level. **Figure 2** illustrates the case for the 50 dbar level, but the same analysis was performed at 5, 50, 100, 200, 300, 400, 500, and 1000 dbar. **Figure 2** shows that the potential temperature and salinity distributions are not symmetric. Almost in all the cases, the null hypothesis (normality of the distribution) was rejected by the Shaphiro-Wilk tests. In addition, Smirnov-Kolmogorov tests produced the same results.

Hence, the median values were chosen to describe the climatological properties of water masses. **Figures 3A,B** show the median vertical salinity and potential temperature profiles for the four seasons of the year and averaged for the whole area (four sections). **Figures 3C,D** show a zoom of the upper 100 dbar of the water column. The upper 100 dbar of the water column show the presence of a seasonal thermocline which develops from spring to summer and then starts to be eroded in autumn. This is superimposed on a permanent thermocline associated to the mixing of the AW with the intermediate water masses (WIW and LIW) which flow below. During the winter, only the permanent thermocline (much smoother than the seasonal one) can be observed. A strong halocline is also observed. The surface salinity values also show some seasonality with minimum values during summer, and maximum values in winter. These fluctuations are weaker than the temperature ones and the halocline is dominated by the permanent one. The seasonal and geographic variability of the surface salinity and temperature can be checked in **Tables 1.1, 1.2, 1.3, 1.4**. These tables also indicate the hydrographic properties of the WIW, LIW and WMDW.

Figures 3E,F show the seasonal variability of the standard deviation profiles. Both salinity and potential temperature standard deviations decrease sharply with depth. In the case of salinity, the surface standard deviation has not a strong seasonality and values vary between 0.2 and 0.3 during the whole year. The surface temperature standard deviation is minimum in winter (1°C) and increases from spring with values above 2°C. Although salinity and temperature distributions depart from normality, it can be accepted that values up to 1.96 standard deviations above and below the median values are likely to be observed (Zar, 2010). Therefore, winter θS values below 13°C and above 38.1 at surface are not exceptional. Similarly, summer values above 27°C and below 37.5 cannot be considered as anomalous ones. Both salinity and temperature standard deviations decrease abruptly for the upper 100 dbar following a Gaussian function. Nevertheless, this behavior is interrupted in the case of salinity by a relative maximum centred around 200 dbar and then continues decreasing linearly to a value close to 0.04 at 400 dbar and finally keeps constant to the sea bottom. In the case of temperature, the standard deviation decreases almost linearly from 100 dbar (0.5°C) to the 400 dbar level (0.06°C) and then remains constant to the sea bottom. The standard deviation does not show a clear seasonality below the 100 dbar level.

The Covariance Function. Parameters for Optimal Statistical Interpolation

Figures 4A (winter), **C** (spring), **E** (summer), and **G** (autumn) show the salinity covariance as a function of the horizontal distance (Δx) at three selected depth levels (25, 50, and 100 m) for the four seasons of the year. This analysis was also performed for all vertical levels from the sea surface to the bottom and for the potential temperature. In order to estimate the analytical form of the salinity and potential temperature covariance, a Gaussian function was fitted for each depth level (see data and methods section and the insert at the left top of **Figure 4**). The variance, which is estimated from this fit, shows a clear dependence on depth as shown in **Figures 4B** (winter), **D** (spring), **F** (summer), and **H** (autumn). The variance seems to decrease as a normal function from the sea surface to 100 m approximately, then it decreases linearly until 400 m, and finally remains quasi-constant from 400 m to the sea bottom. On the contrary, the horizontal decaying distance does not show any clear depth dependence and it is finally considered as the mean value along the water column. The same behavior is observed for the noise/signal ratio and the mean value along the water column was chosen as a constant value not dependent on depth. To clarify these ideas, the horizontal covariance for the winter salinity at the upper 100 m, could be expressed as:

$$cov\,(\Delta x, z) = \sigma_0^2 \exp\left[-\frac{(z-z_0)^2}{2\cdot L_{z,1}^2}\right]\exp\left[-\frac{\Delta x^2}{2\cdot L_x^2}\right] = 0.054\exp\left[-\frac{(z-10)^2}{2\cdot 48^2}\right]\exp\left[-\frac{\Delta x^2}{2\cdot 50^2}\right] \quad (9)$$

The z_0 in the above formula accounts for the fact that the maximum variance is not always at the sea surface. All the parameters involved in the previous formula corresponding to the four seasons of the year and for both the salinity and potential temperature are presented in **Table 2**. The two first factors in (9) express the dependence of the variance on the depth level. It should not be confused with the decrease of the covariance with the vertical distance between pairs of points.

Figure 5 shows the salinity covariance estimated for each pair of values z_1 and z_2 using (2) for some selected stations within the Mallorca South section and for the four seasons of the year. Constant covariance isolines take the form of ellipses and the

TABLE 1 | Tables 1.1, 1.2, 1.3, and 1.4 show the climatological properties of AW, WIW, LIW, and WMDW for winter, spring, summer and autumn.

Table 1.1	**Winter**	**MS**	**MN**	**IS**	**IN**
AW	*S*	37.81	37.92	37.93	37.98
	θ	14.25	14.17	14.10	14.09
	σ_θ	28.30	28.41	28.43	28.47
	Pres.	0–5	0–5	0–5	0–5
WIW	*S*	38.37 (*)	38.32 (*)	38.28 (38.08–38.26)	38.26 (38.13–38.36)
	θ	13.23 (*)	13.22 (*)	13.16 (12.99–13.31)	13.10 (13.05–13.40)
	σ_θ	29.08	29.09	29.08	29.09
	Pres.	416	437	435	447
WMDW	*S*		38.49	38.49	38.49
	θ		12.93	12.96	12.93
	σ_θ		29.11	29.11	29.11
	Pres.		997	828	1068

Table 1.2	**Spring**	**MS**	**MN**	**IS**	**IN**
AW	*S*	37.67	37.81	37.73	37.78
	θ	19.12	20.70	20.04	20.18
	σ_θ	27.03	26.71	26.83	26.83
	Pres.	0–5	0–5	0–5	0–5
WIW	*S*	38.31 (36.14–38.38)	38.31 (38.18–38.36)	38.29 (38.11–38.39)	38.26 (38.13–38.41)
	θ	13.16 (13.09–13.42)	13.08 (13.06–13.50)	13.15 (12.88–13.41)	13.04 (12.91–13.37)
	σ_θ	28.93	28.94	28.91	28.92
	Pres.	179	160	175	185
LIW	*S*	38.51	38.52	38.51	38.53
	θ	13.17	13.17	13.21	13.21
	σ_θ	29.08	29.09	29.08	29.09
	Pres.	409	487	464	503
WMDW	*S*		38.48		38.49
	θ		12.89		12.93
	σ_θ		29.11		29.11
	Pres.		1277		986

Table 1.3	**Summer**	**MS**	**MN**	**IS**	**IN**
AW	*S*	37.54	37.62	37.77	37.77
	θ	25.26	24.87	24.90	24.75
	σ_θ	25.18	25.36	25.47	25.51
	Pres.	0–5	0–5	0–5	0–5
WIW	*S*	38.32 (36.18–38.36)	38.35 (38.20–38.39)	38.30 (38.18–38.49)	38.27 (38.16–38.39)
	θ	13.21 (13.08–13.40)	13.13 (13.09–13.45)	13.14 (13.07–13.45)	13.10 (13.04–13.50)
	σ_θ	28.92	28.97	28.92	28.91
	Pres.	182	211	172	189
LIW	*S*	38.52	38.53	38.53	38.52
	θ	13.17	13.18	13.24	13.18
	σ_θ	29.09	29.09	29.08	29.09
	Pres.	472	479	418	512
WMDW	*S*	38.48	38.49	38.49	38.49
	θ	12.93	12.92	12.94	12.92
	σ_θ	29.11	29.12	29.11	29.12
	Pres.	535	1152	797	1065

(Continued)

TABLE 1 | Continued

Table 1.4	AUTUMN	Mallorca. S	Mallorca. N	Ibiza. S	Ibiza. N
AW	*S*	37.57	37.81	37.67	37.82
	θ	21.19	20.93	21.11	21.23
	σ_θ	26.40	26.65	26.49	26.57
	Pres.	0–5	0–5	0–5	0–5
WIW	S	38.39 (36.18–38.30)	38.47 (*)	38.35 (38.18–38.29)	38.44 (38.20–38.36)
	θ	13.18 (13.00–13.44)	13.19 (*)	13.18 (13.18–13.48)	13.19 (13.21–13.42)
	σ_θ	28.99	29.05	28.95	29.02
	Pres.	225	258	225	274
LIW	S	38.51	38.53	38.53	38.53
	θ	13.17	13.20	13.20	13.20
	σ_θ	29.08	29.09	29.09	29.09
	Pres.	394	405	523	531
WMDW	*S*	38.48	38.49	–	38.49
	θ	12.88	12.93	–	12.92
	σ_θ	29.12	29.11	–	29.11
	Pres.	487	1167	–	1068

For each season of the year columns 3, 4, 5, and 6 correspond to the Mallorca South, Mallorca North, Ibiza South and Ibiza North sections, respectively. For each oceanographic station, the median values are considered for the climatological characterization due to the non-Gaussian distribution of the water mass properties as shown in ***Figure 2****. For each hydrographic section, the average values of all the oceanographic stations are presented. The properties corresponding to each water mass were determined according to the methodology presented in section 2. Values in parenthesis for the WIW correspond to the geometric method developed in Juza et al. (2019). *indicates that this water mass was not detected according to this methodology.*

covariance decreases as the semi-axis increases justifying the use of (7) and (8) to model the analytical form of this function. Nevertheless, this behavior was only observed for the upper 100 m of the water column.

Once again to clarify these results, equation (10) shows the result of the fit for the salinity winter covariance at the upper 100 m:

$$cov\,(z_1, z_2) = \sigma_0^2 \exp\left[-\frac{(\bar{z}-z_0)^2}{2L_{z,1}^2}\right]\exp\left[-\frac{\Delta z^2}{2L_{z,2}^2}\right] =$$

$$0.062\exp\left[-\frac{(\bar{z}-11)^2}{2\cdot 45^2}\right]\exp\left[-\frac{\Delta z^2}{2\cdot 53^2}\right] \qquad (10)$$

Notice that the first two factors in (10) explain the depth dependence of the variance. The only difference with (9) is that in that case there was one single depth level, while in the present case the variance decreases with the average value of both depth levels. It was checked for all the seasons of the year and for both the salinity and potential temperature that the depth dependence obtained from the analysis on the vertical direction (Eqs 7, 8, and 10) and that inferred from the analysis on the horizontal coordinate were consistent. The third factor in (10) accounts for the vertical decay of the covariance with the vertical distance between pairs of points. The combination of the results obtained from the analysis on fixed depth levels (dependence on the horizontal distance) and the analysis for fixed horizontal positions (dependence on the vertical distance) allowed us to propose the following analytical form for the covariance function:

$$cov(z_1, z_2\,\Delta x) = \sigma_0^2 \exp\left[-\frac{(\bar{z}-z_0)^2}{2L_{z,1}^2}\right]\exp\left[-\frac{\Delta z^2}{2\cdot L_{z,2}^2}\right]\exp$$

$$\left[-\frac{\Delta x^2}{2\cdot L_x^2}\right] 0 \le z \le 100m \quad (11a)$$

$$cov(z_1, z_2, \Delta x) = \left[a - b(\bar{z}-100)\right]\exp\left[-\frac{\Delta z^2}{2\cdot L_{z,2}^2}\right]\exp$$

$$\left[-\frac{\Delta x^2}{2\cdot L_x^2}\right] 100 \le z \le 400m \quad (11b)$$

$$cov(z_1, z_2, \Delta x) = c\exp\left[-\frac{\Delta z^2}{2\cdot L_{z,2}^2}\right]\exp\left[-\frac{\Delta x^2}{2\cdot L_x^2}\right]$$

$$z \ge 400m \quad (11c)$$

L_x (the horizontal decaying distance of the covariance function) and $\gamma = {}^{\sigma_\varepsilon^2}/_{\sigma^2}$ (the noise to signal ratio) were considered constant along the water column and *a, c* in (11b) and (11c) were chosen in such a way that the covariance was a continuous function.

Detection of Water Masses and Determination of Their Properties

Figures 6–9 show the θ*S* diagrams for the four hydrographic sections (Mallorca South, Mallorca North, Ibiza South and Ibiza

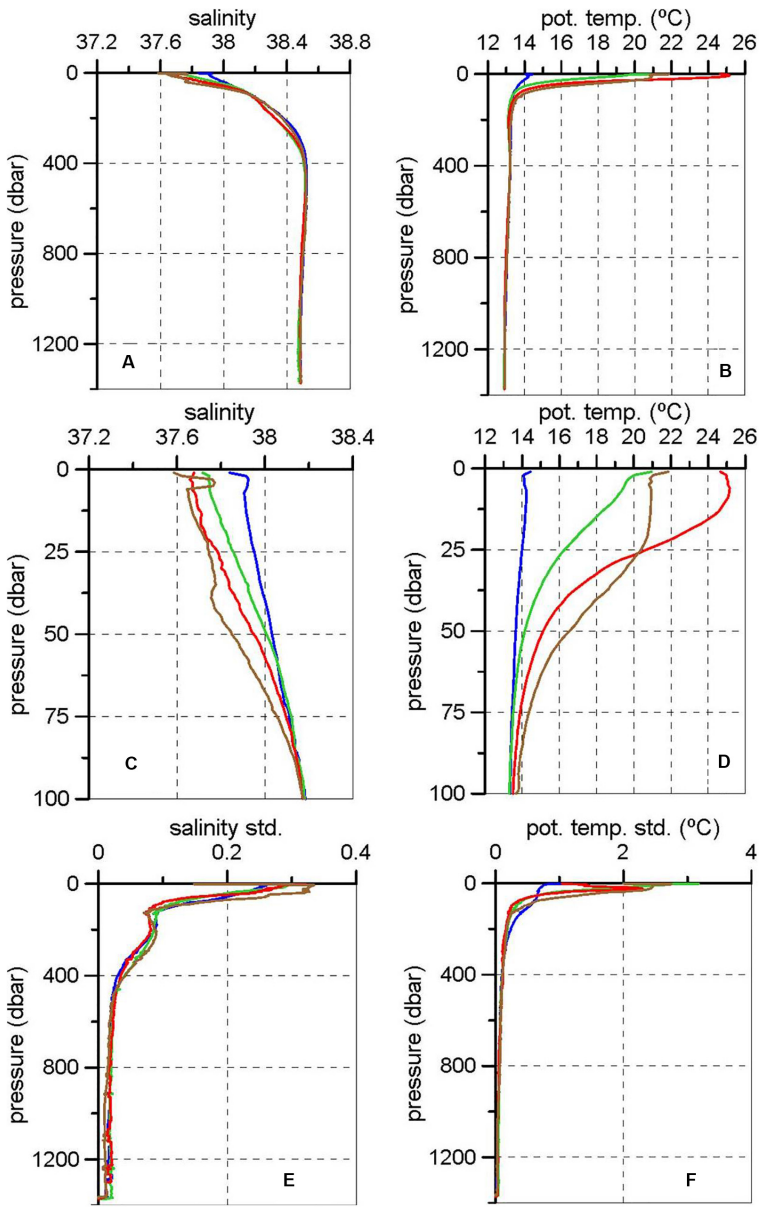

FIGURE 3 | Median vertical profiles of salinity **(A)** and potential temperature **(B)** for each season of the year for the four hydrographic sections, and respective zooms in the upper 100 dbar **(C,D)**. Vertical profiles for the salinity and potential temperature standard deviation (**E,F**, resp.). Seasons are indicated in color: winter (blue), spring (green), summer (red), and autumn (brown).

North, respectively) and for the four seasons of the year. Gray (black) dots correspond to the median (mean) values at each oceanographic station and depth level for each hydrographic section. The upper 100 dbar have not been considered in order to better highlight the properties of intermediate and deep waters.

The θ*S* diagrams based on the median climatological values in the Mallorca South and North sections (**Figures 6**, **7**) show lower potential temperature values than those based on mean values for the winter and summer seasons in the density range 28.8–29.05 which are the values considered for the WIW by Pinot and Ganachaud (1999) and Pinot et al. (2002). The same is observed for winter, summer and autumn at the Ibiza South section (**Figure 8**) and for winter and summer at Ibiza North (**Figure 9**). Some of the median values lie within the traditional temperature and salinity ranges which define the WIW at Ibiza South in winter and spring (**Figures 8A,B**) and at Ibiza North during spring (**Figure 9B**). Additionally, besides the considerable smoothing of the median and mean θ*S* diagrams, they show properties close to the usually accepted values for WIW during spring at Ibiza North and during winter only with the median values. This water mass corresponds to the potential density range

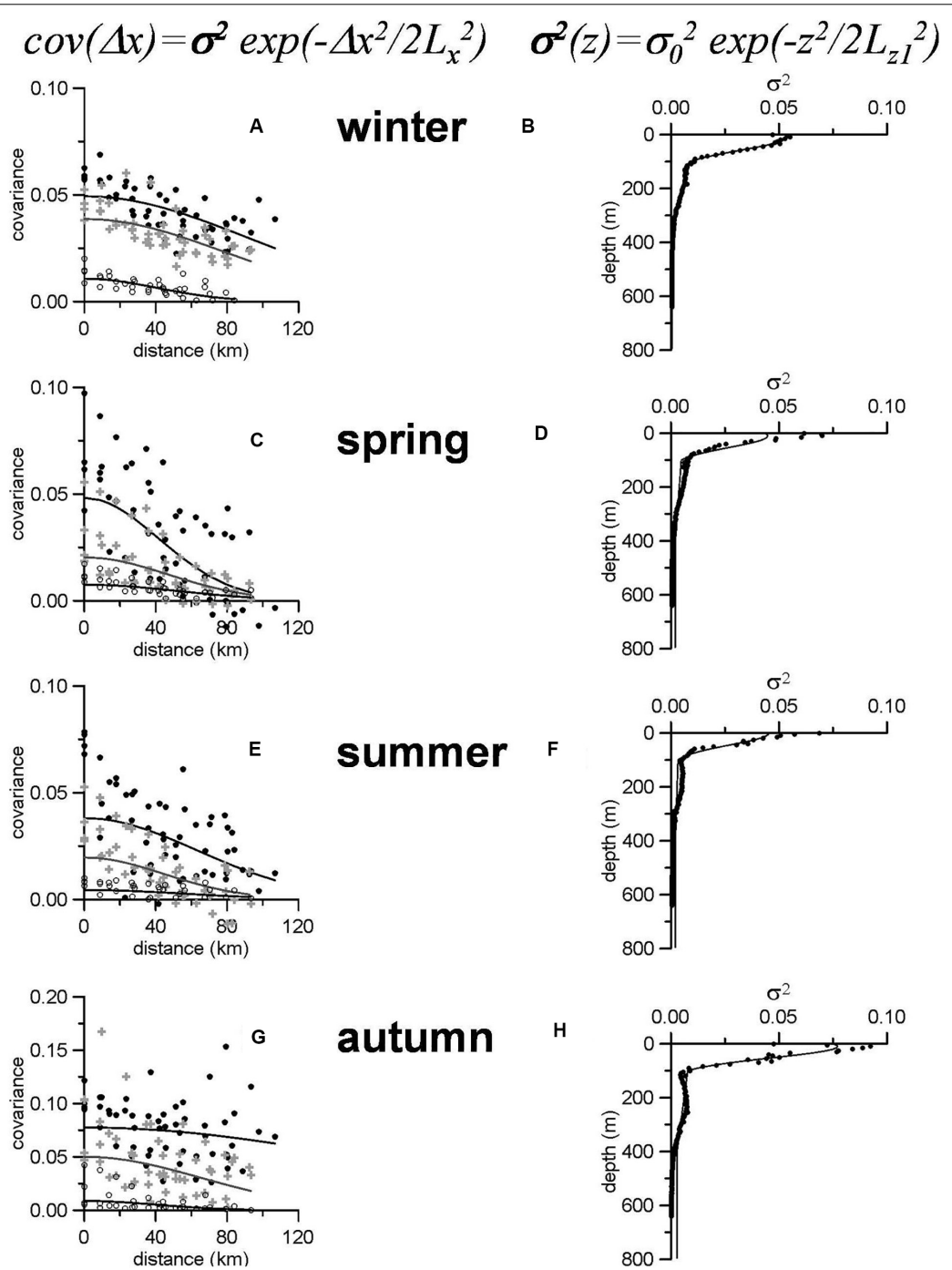

FIGURE 4 | (**A**, winter), (**C**, spring), (**E**, summer), and (**G**, autumn) are the salinity covariance as a function of the horizontal distance in km for the 25 (black dots), 50 (gray crosses) and 100 m (open circles) depths for the four seasons of the year. Solid lines are a Gaussian fit according to the formula on the left at the top of the panels. σ^2 is the variance for each depth level. (**B**, winter), (**D**, spring), (**F**, summer), and (**H**, autumn) show the depth dependence of the σ^2 value estimated for each depth level. This depth dependence for the upper 100 m is modeled by means of the formula on the right at the top of the panels. Then a linear decrease of the variance is assumed from 100 to 400 m, and a constant value below this depth level.

28.8–29.05 kg/m^3 as previously considered and its depth range oscillates between 140 and 274 m.

As previously mentioned, the θS values found for the Ibiza Channel during winter and spring are close to the WIW traditional range, with some values entering within such range. Nevertheless, the classical definition of WIW, which is based on a fixed-range criterion (with potential temperature below 13°C and salinity between 37.7 and 38.3) would fail to detect this water

TABLE 2 | Parameters for the analytical expressions for the covariance function for salinity and potential temperature in the Balearic Channels (see Eq. 11).

Salinity	σ_0^2	z_0	$L_{z,1}$	$L_{z,2}$	L_x	γ	a	b*10^{-5}	c*10^{-3}
Winter	0.054	10	48	53	50	0.12	0.0089	3.42	0.4
Spring	0.045	10	43	46	60	0.16	0.0048	1.00	1.9
Summer	0.045	1	43	38	52	0.15	0.0032	0.41	2.0
Autumn	0.077	10	42	35	49	0.14	0.0078	1.65	2.8

pot. temp.	σ_0^2	z_0	$L_{z,1}$	$L_{z,2}$	L_x	γ	a	b*10^{-5}	c*10^{-3}
Winter	0.51	1	87	53	54	0.08	0.037	15.4	6.2
Spring	2.96	1	33	21	56	0.17	0.036	9.13	8.7
Summer	1.33	20	28	21	45	0.10	0.025	4.67	11
Autumn	5.75	1	34	18	56	0.09	0.074	34.2	5.1

Notice that the Gaussian part of this function extends from the surface to 100 m and the linear one from 100 to 400 m. The only exceptions are the winter salinity when the linear part extends from 100 to 350 m and the winter potential temperature when the Gaussian function corresponds to the surface-200 m depth range.

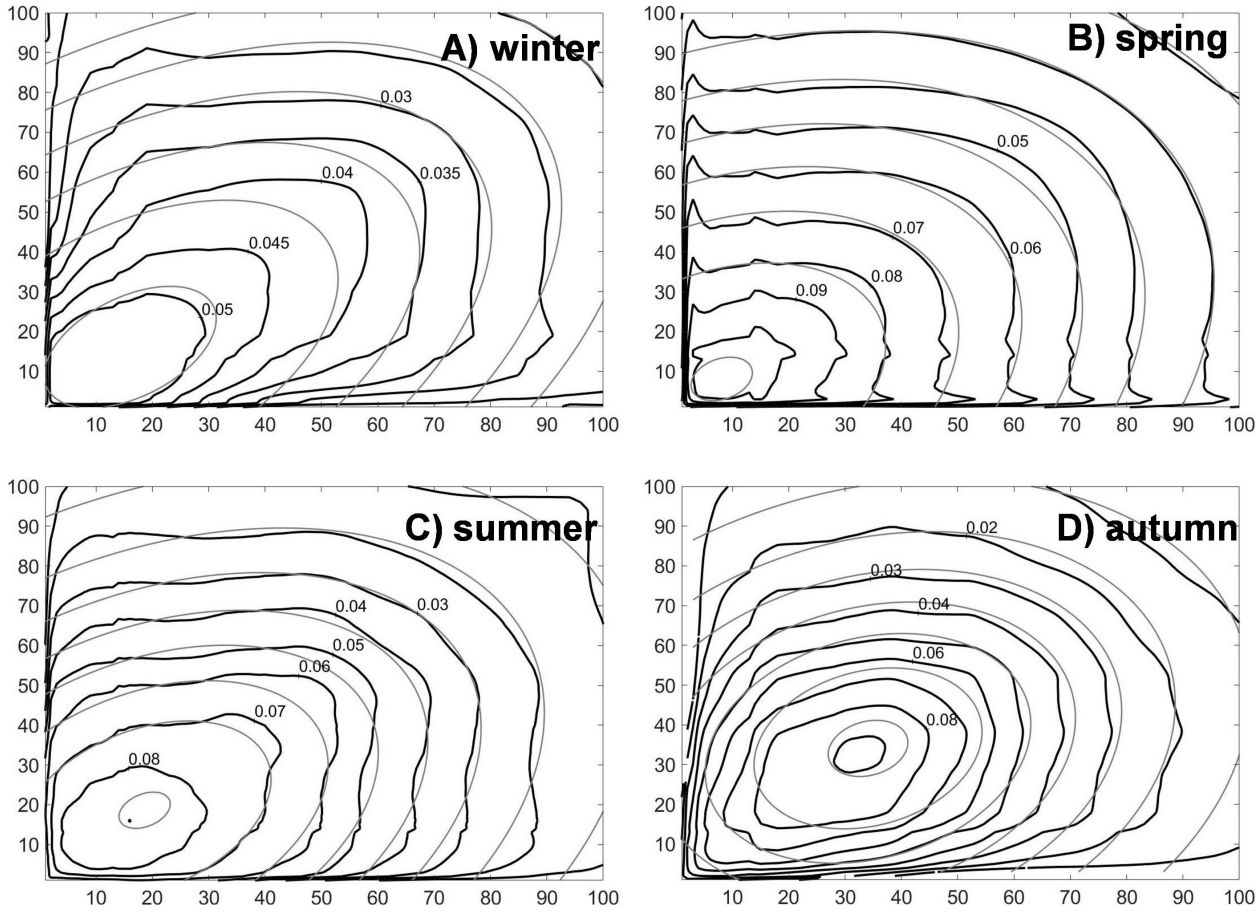

FIGURE 5 | Black lines indicate the salinity covariance estimated for pairs of points at fixed horizontal positions and depth levels z1 and z2 (horizontal axis). The gray lines are the least square fit using equations (7) and (8). **(A)** is for winter, **(B)** for spring, **(C)** for summer, and **(D)** for autumn.

mass in almost all the cases if the smoothed climatological values were used. On the contrary, the geometry-based method allows to identify as WIW θS values above the 13°C threshold. Those values have been displayed in red in **Figures 6–9**. For each season of the year and each hydrographic section, the θS range corresponding to the WIW is evaluated according to the geometric criterion. These intervals are also provided in parenthesis in **Table 1**.

The LIW also occupies the density range already considered in previous works (29.05–29.1). The salinity values at the core of this water mass are relatively constant throughout the year,

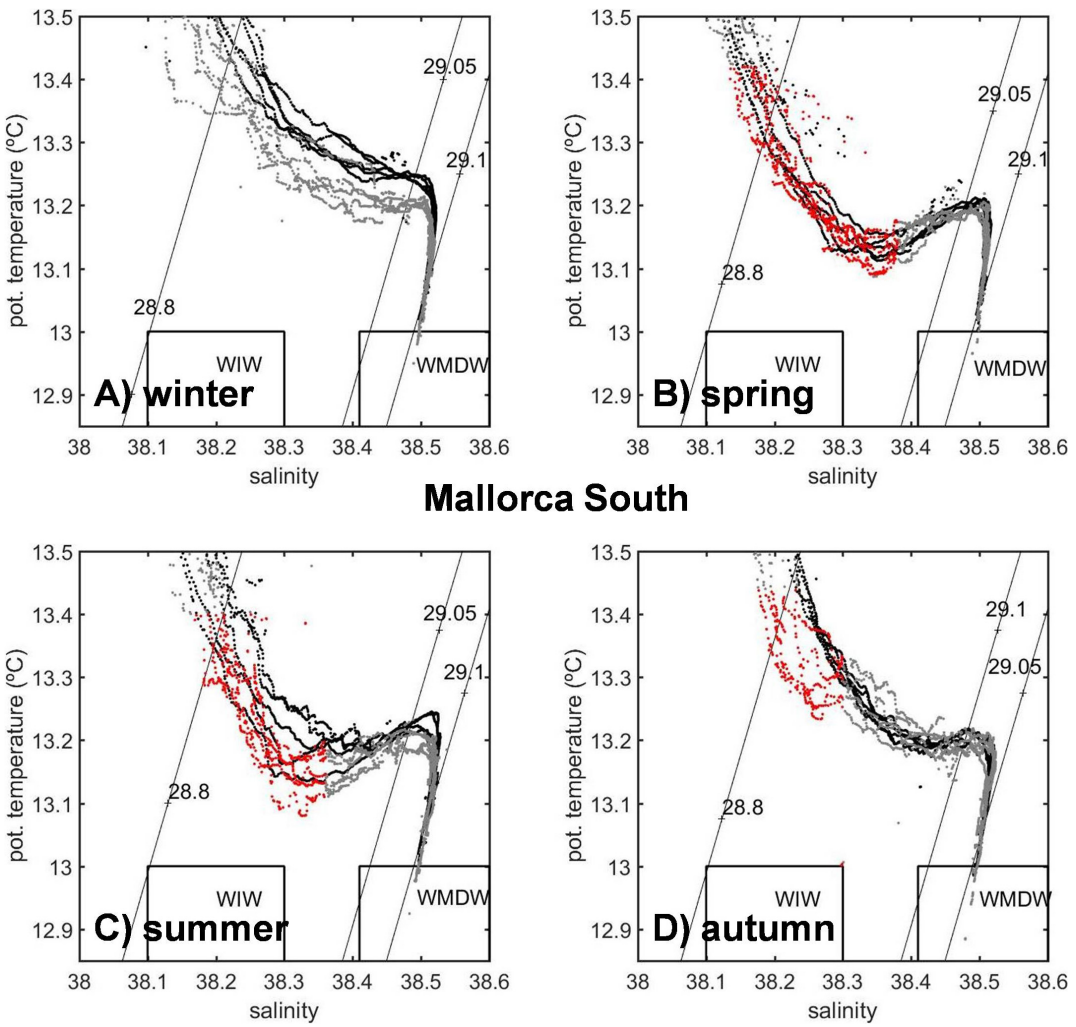

FIGURE 6 | θS diagrams for the Mallorca South section in winter **(A)**, spring **(B)**, summer **(C),** and autumn **(D)**. The upper 100 dbar have been removed to focus on the characteristics of intermediate and deep waters. σ_θ contours for sigma-theta values 28.8, 29.05, and 29.1 have been included to show the layers corresponding to the WIW (28.8–29.05), LIW (29.05–29.1), and WMDW (> 29.1) according to Pinot and Ganachaud (1999) and Pinot et al. (2002) criterion. Gray dots are median values, black dots are mean values and red dots are those values corresponding to WIW as detected by the geometry-based method in Juza et al. (2019). Median and mean values have been calculated for each oceanographic station and depth level within each hydrographic section. Two boxes indicating the θS ranges for WIW (according to López-Jurado et al., 1995) and the ranges for the WMDW (Pinot et al., 2002) have been included.

ranging from 38.51 to 38.53. Its depth range is 394–531 m. Its potential temperature varies between 13.17 and 13.23° C. Finally, the WMDW was not always detected during all the seasons of the year and all the sections according to the specified criterion (potential density larger than 29.11 kg/m^3). The maximum density values reached 29.12 kg/m^3. The WMDW salinity values oscillate between 38.48 and 38.49 and the potential temperature values between 12.88 and 12.92°C (**Table 1**).

Circulation and Transports Associated to the Average θS Distributions. Application of a Box Inverse Model

The current velocity at the reference level (sea bottom) is estimated using the mass conservation for four layers defined by the potential density values: surface/28.8/29.05/29.1/bottom. **Figure 10** shows the absolute geostrophic velocity at the Ibiza South section (the corresponding salinity section is presented in **Supplementary Figure S10**). The same results for the Mallorca South section are presented in **Figure 11** and **Supplementary Figure S11**. All the sections have been divided into an upper layer, which has been considered as the upper 300 m, and a lower layer extending from 300 dbar to the sea bottom. According to **Table 1**, the WIW depth range rarely exceeds 300 dbar, while LIW is mainly observed between 400 and 500 dbar. Therefore, it was considered that the upper 300 dbar could be useful for describing the AW and WIW properties, while LIW and WMDW would correspond to the layer below. In order to enhance the gradients observed at the upper layer, the height of both parts of the vertical sections do not keep proportionality with their depth interval.

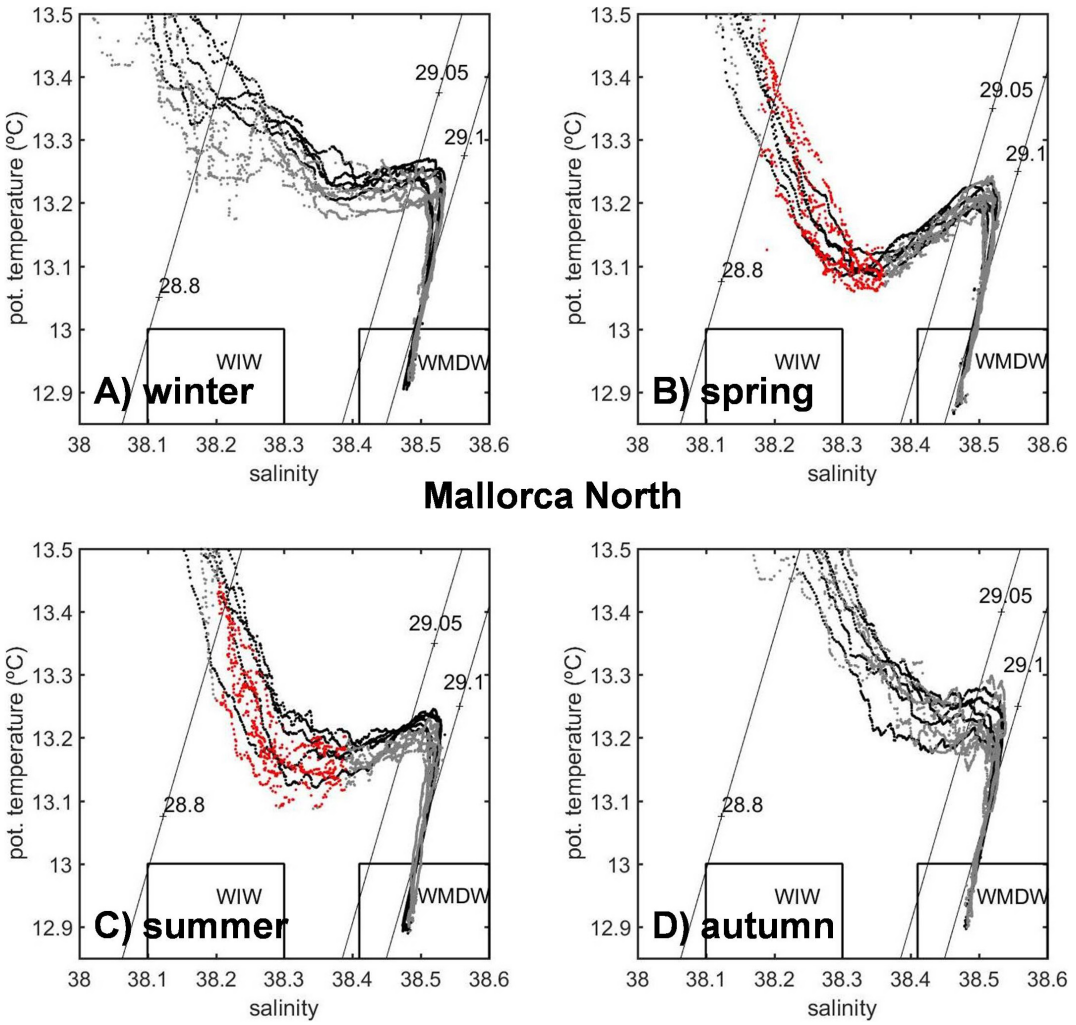

FIGURE 7 | Same as **Figure 6** for the Mallorca North section. Winter **(A)**, Spring **(B)**, Summer **(C)**, Autumn **(D)**.

Table 3 indicates the mass transports in 10^9 kg/s (approximately 1Sv) for the upper and the lower layers, for the four sections and the four seasons of the year. The upper layer is considered as the sum of the two upper layers used in the inverse model, that is, from the surface to the 28.8 kg/m^3 surface, and from the 28.8 to the 29.05 kg/m^3 surface. The lower layer is the sum of the two lower layers in the model, from 29.05 to 29.1 and from 29.1 to the bottom.

In the Ibiza Channel, the water mass transports are southwards in both layers and along the whole year, while in the Mallorca Channel, they are generally directed northwards, except at the upper layer of Mallorca South in spring, and at the deep layer of both Mallorca sections in autumn. Such transports are also higher in the Ibiza than in the Mallorca Channels. These results are in agreement with previous studies (Pinot et al., 2002; Heslop et al., 2012; Juza et al., 2013).

Figure 10 also shows that the flow has more spatial variability in the upper 300 dbar where different directions alternate, whereas it is more uniform in the lower layer. Considering the mass transports calculated between each pair of hydrographic stations (**Supplementary Tables S2A–D**), a schematic circulation for the upper layer in the Balearic Channels is proposed in **Figures 12A–D**. In the lower layer, the circulation pattern is more homogenous, hence only the net mass transports are presented in **Table 3**.

DISCUSSION

The mean values of any property, calculated from a long time series of data at different depth levels, are generally used to define the climatological values of such property. In the case of the hydrographic conditions in the Balearic Channels, we have shown that median values are more appropriate statistical estimates than mean values. As shown in **Figure 2**, the salinity and potential temperature distributions are not symmetric, and the normality of these distributions was rejected by means of Shapiro-Wilk tests. While the salinity distributions in the upper

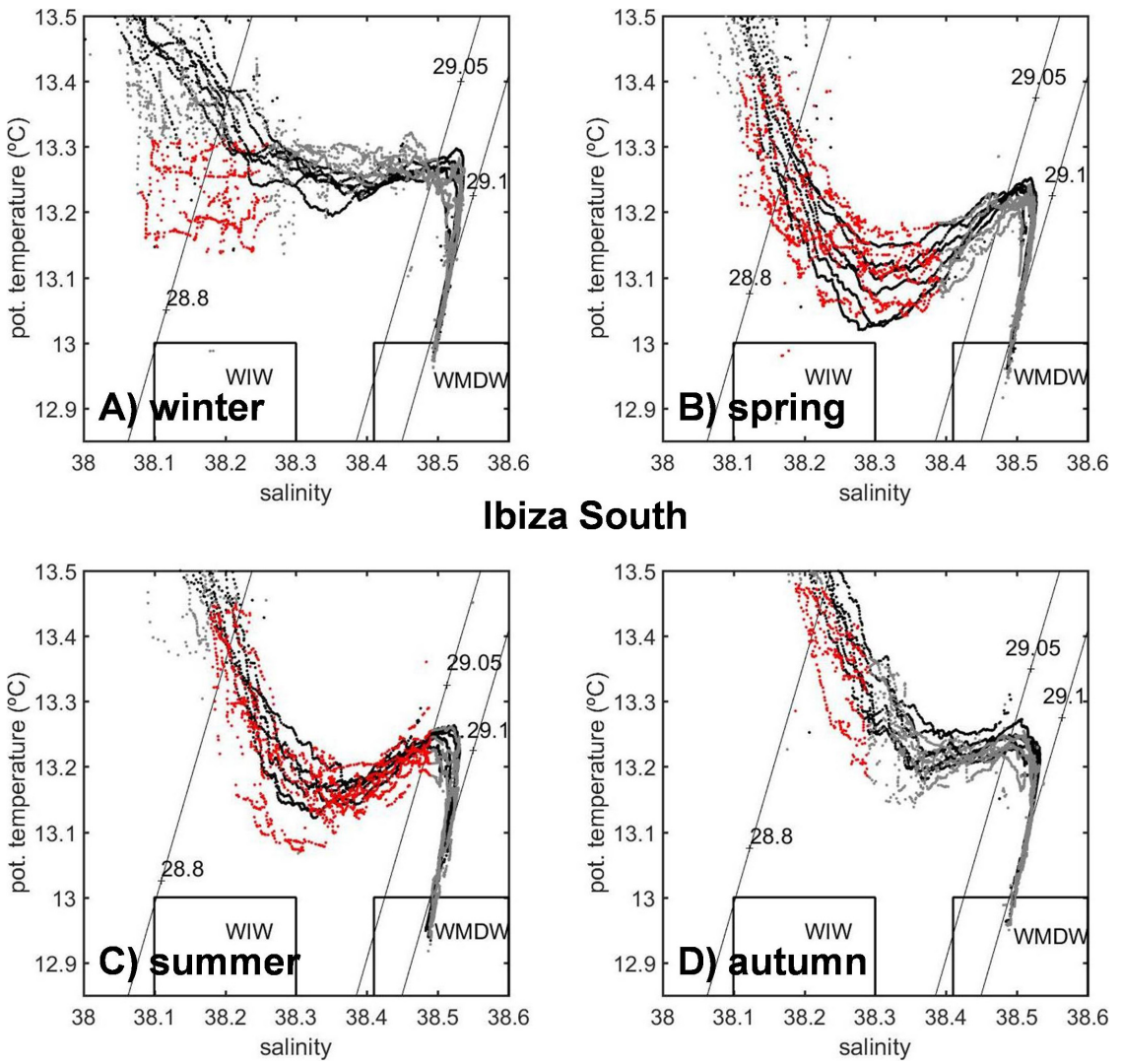

FIGURE 8 | Same as **Figure 6** for the Ibiza South section. Winter **(A)**, Spring **(B)**, Summer **(C)**, Autumn **(D)**.

layers (**Figures 2A–D**) show an asymmetric tale at low salinity values, the potential temperature distribution shows a tale for high values (**Figures 2E–H**). These features would indicate the irruptions of AW eddies or filaments detaching from the Algerian Current and moving northwards through the Balearic Channels. Another argument in favor of the use of median values arises from the analysis of θ*S* diagrams and the identification of the different water masses present in the Balearic Sea. Using both mean and median values, the vertical θ and *S* profiles or θ*S* diagrams are much smoother than those obtained for one single survey. However, the degree of smoothing associated to the mean values seems to be too high and prevent from identifying the presence of some water masses within the Balearic Channels. In particular, using mean values, the θ*S* diagram associated with the winter conditions in the Mallorca South section (**Figure 6A**) would show an almost linear mixing between AW and LIW flowing below. On the contrary, a relative temperature minimum, suggesting the presence of WIW, could be appreciated considering the median values (**Figure 6A**). During the summer and autumn, the potential temperature in the 28.8–29.05 kg/m^3 potential density range is lower with the median values than with the mean values (Ibiza South, **Figures 8C,D**). Moreover, some of the median values lie within the traditional ranges defined for WIW (**Figures 8A,B**, **9B**). On the contrary, no mean value corresponds to such ranges in any of the cases analyzed in this study. Therefore, the use of the median shows more clearly the presence and the influence of WIW in the Balearic Channels.

Another interesting feature arising from the analysis of the climatological values in the Balearic Channels is the existence of a clear seasonal cycle, not only for temperature, but also for salinity in the upper layer. The winter median temperature of the surface layer ranges between 14.09 and 14.25°C and the surface salinity ranges between 37.81 and 37.98 (**Table 1.1** and **Figure 3**). The standard deviations for winter temperature and

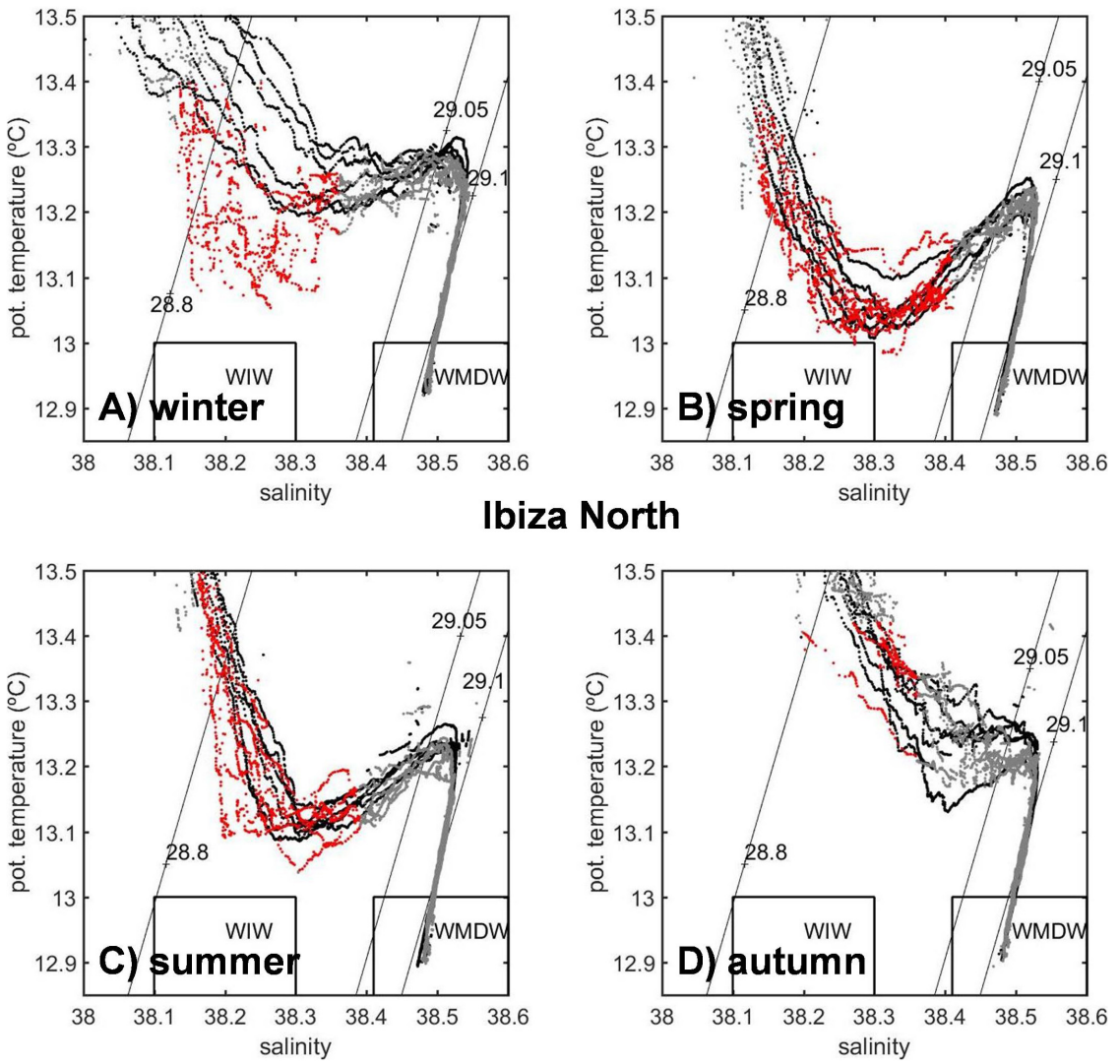

FIGURE 9 | Same as **Figure 7** for the Ibiza North section. Winter **(A)**, Spring **(B)**, Summer **(C)**, Autumn **(D)**.

salinity are around 1°C and 0.23, respectively. Hence, in the surface layer, salinity values higher than 38.1 and temperature values lower than 13°C would not be anomalous in the Balearic Channels. These latter values are similar to those observed during winter convection episodes that lead to the WIW formation (Vargas-Yáñez et al., 2012). These statistical results lead to the conclusion that the Balearic Channels are not the usual or most frequent location for WIW formation and that the WIW which is observed within the Channels is advected along the southward extension of the Northern Current from the Catalan Sea and the continental shelf of the Gulf of Lions. Juza et al. (2013) analyzed gliders and CTD data from winter/spring 2011 to the light of a numerical simulation and concluded that WIW could be observed in the Ibiza Channel during March and April. This water mass would be advected from two main formation sites. The first one would be the Gulf of Lions and WIW would arrive 40–45 days after its formation. The second one would be the Ebro Delta shelf, and in this case this water mass would take 20–25 days to arrive to the Channels. López-Jurado et al. (1995) also considered that the WIW observed in the Balearic Channels during spring had been formed in the Catalan or Gulf of Lions continental shelf during the preceding winter. Nevertheless, considering the obtained standard deviations, it can be accepted that values compatible with the local WIW formation could also be observed within the Channels for some particular years, indicating that this could be a formation site for severe winters. This result had already been evidenced during the 2010 winter (Vargas-Yáñez et al., 2012). López-Jurado et al. (1995) also observed "lenses" of WIW between 40 and 100 m depth with a lower salinity than WIW originated further to the north. Our statistical results seem to confirm this local formation process on severe winters.

The salinity at the surface layer is minimum during summer when it ranges from 37.54 to 37.77 (**Table 1.3** and **Figure 3**),

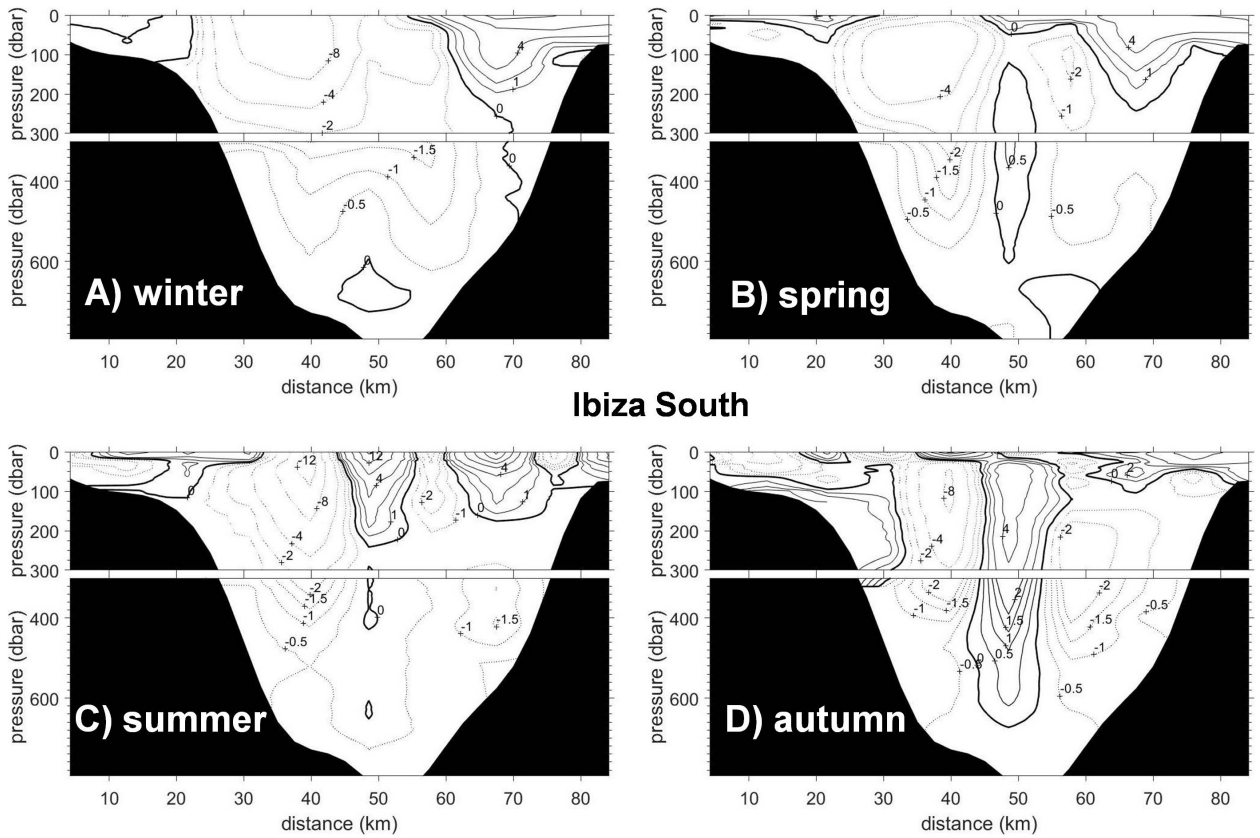

FIGURE 10 | Cross section absolute geostrophic velocity (in cm/s) at the Ibiza South section for winter **(A)**, spring **(B)**, summer **(C),** and autumn **(D)**. Solid lines correspond to positive velocities which are directed to the North (into the paper), while negative velocities are represented by dashed lines and are directed to the South (out of the paper). The velocity contour intervals for the upper 300 dbar are 0, 1, 2 4, 8, 12, 16, and 20 cm/s (both positive and negative). The contour interval for the velocity from 300 dbar to the sea bottom are 0, 0.5, 1, 1.5 and 2 cm/s (both positive and negative).

with standard deviations higher than 0.2. Hence, salinity values below 37.5, which is usually considered as the mid-point between Atlantic and Mediterranean waters in the WMED, would also be frequently found. The salinity seasonal cycle with minimum values during summer and maximum values during winter clearly indicates a higher influence of AW, recently advected into the Mediterranean Sea, during summer, and its decrease during winter. Nevertheless, Barceló-Llull et al. (2019) found that this cycle would be delayed with respect to the one evidenced by our data. These authors analyzed glider data from 2011 to 2018 in the Mallorca Channel and found that the salinity reached a minimum in autumn and a maximum in spring. On the contrary, Pinot et al. (2002) found that the main factor controlling the seasonal variability in the Balearic Channels was the intensity of the Northern Current progressing southwards. Such intensity would decrease from spring to summer favoring the northward progression of AW during summer. This northward spread of the AW was observed to be favored during summer 1996 by an increase of the turbulent activity in the Algerian Current and the detachment of eddies from this current. Vargas-Yáñez et al. (2017, 2019) showed that the existence of a salinity seasonal cycle in the Balearic Channels was not an isolated case within the Spanish Mediterranean. These authors reported a similar cycle along the whole continental shelf and slope from Malaga province, in the south-western extreme of the WMED, to Barcelona, in the Catalan Sea. The surface salinity was lower during summer and autumn and then increased during winter and spring. This cycle was consistent with the seasonality of the winds. Low wind intensities correspond to the summer months, increasing during winter and spring. In the southern part of the Spanish Mediterranean, the prevalent direction of the winds was from the west during most of the year with a shift to easterly winds during summer (Vargas-Yáñez et al., 2019). In the southern part of Mallorca Island, the winds have a low intensity and blow from the southwest during summer. Close to the Ebro Delta, to the north of the Balearic Islands, the wind blows from the southeast during summer whereas it becomes stronger and with a northwest provenance during winter (Vargas-Yáñez et al., 2019). Therefore, it cannot be discarded that the changes in wind intensity and direction along the seasonal cycle have a certain influence on the northward transport of AW through the Channels. This influence would be added to that caused by the weakening of the Northern Current and the increase of mesoscale activity in the Algerian Current.

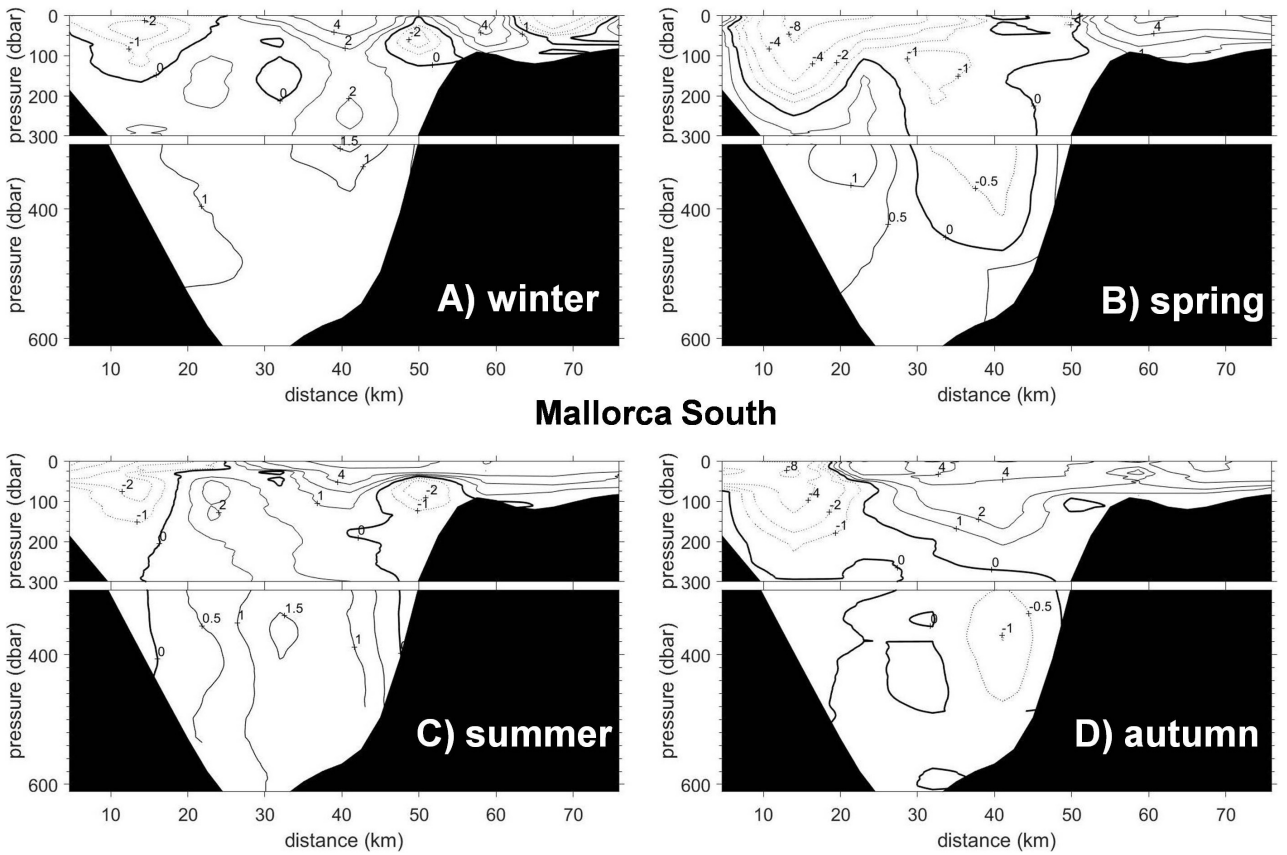

FIGURE 11 | Same as figure for the Mallorca South section. Winter **(A)**, Spring **(B)**, Summer **(C)**, Autumn **(D)**.

Another interesting result is that the presence of AW is higher in the Mallorca South section than in the Ibiza South one (**Table 1**) throughout the whole year, suggesting that the Mallorca Channel is a more favorable place for the AW intrusions which would finally feed the Balearic Current, coinciding with the circulation scheme proposed by Pinot et al. (2002). According to these authors, current meter measurements in the Ibiza Channel showed southward velocities in the central and western parts of the Channel whereas a northward velocity could be observed in the eastern part. These results were confirmed by the geostrophic transports that were directed to the south in most of the Ibiza Channel with some northward intrusions in the side of the Channel close to the Ibiza Island. On the contrary, the transport through the Mallorca Channel was weaker and mainly directed to the north with some southward transport close to the western extreme of the Channel, close to the Ibiza Island.

Below the surface layer, the salinity and temperature ranges are narrower than at surface, and make it difficult to establish the existence of any seasonal cycle. The traditional method based on fixed range values does not allow to detect such a cycle for the WIW. Applying the geometry-based method (Juza et al., 2019), two results could be observed. First, WIW is always observed in the Ibiza Channel, whereas it is only observed for some seasons of the year in the Mallorca Channel (**Table 1**). That suggests that the Ibiza Channel is the preferential pathway for this water mass in its southward progression. The lower potential temperature values of WIW which are observed in the Ibiza Channel during spring (**Table 1**) also suggest that this water mass was formed to the north of the Balearic Islands, in the Gulf of Lions and Ebro Delta continental shelf during the preceding winter (López-Jurado et al., 1995; Heslop et al., 2012; Juza et al., 2013). Notice that this result corresponds to the most frequent circulation pattern inferred from the median values obtained from the analysis of the complete time series. Nevertheless, it is compatible with the sporadic local formation hypothesized from the low temperature surface values that could be reached in winter according to the standard deviation at the surface layer.

Considering the different sections, seasons of the year and methodologies, the depth of the WIW core could fluctuate between 101 and 274 m, whereas the depth of the LIW core would range between 394 and 531 m (**Table 1**). Therefore, the vertical sections were divided in two parts. The upper 300 m were considered for the upper layer including AW and WIW, and the lower one, from 300 m to the bottom, was considered for LIW and WMDW (**Figures 10**, **11** and **Supplementary Figures S10**, **S11**). The results concerning temperature and salinity distributions of the upper layer seem to be confirmed by the absolute geostrophic transports and the circulation scheme obtained from the inverse

TABLE 3 | Transports in 10^9 kg/s for the four sections analyzed in this work.

	Layers: Surface-300 dbar. Transports in 10^9 kg/s			
	Ibiza north	**Ibiza south**	**Mallorca north**	**Mallorca south**
Winter	−0.31	−0.33	0.11	0.10
Spring	−0.22	−0.18	0.00	−0.05
Summer	−0.17	−0.14	0.12	0.13
Autumn	−0.21	−0.03	0.14	0.12
	Layers: 300 dbar-bottom. Transports in 10^9 kg/s			
	Ibiza north	**Ibiza south**	**Mallorca north**	**Mallorca south**
Winter	−0.09	−0.09	0.08	0.09
Spring	−0.06	−0.07	0.02	0.03
Summer	−0.11	−0.11	0.08	0.07
Autumn	−0.06	−0.07	−0.02	−0.02

Positive values indicate northward transport whereas negative values are for southward transports. Calculations are divided for an upper and lower layer. The upper one includes the first to layers used in the model: from the sea surface to the 28.8 and from the 28.8 to the 29.05 sigma-theta surface. These two layers approximately correspond to the AW and WIW located at the upper 300 dbar of the water column. The lower layer is the sum of the two deepest layers used in the inverse model: from 29.05 to 29.1 and from 29.1 sigma-theta to the bottom. This layer is located below the 300 dbar level and approximately corresponds to the LIW and the WMDW, or a mixing of these two water masses where WMDW values are not reached.

models (**Figures 12A–D**). The net transport through the Ibiza Channel is directed southwards throughout the whole year. In the Ibiza South section, this southward transport is maximum in winter (0.33 Sv) and then decreases to a minimum value of 0.04 Sv in autumn. In the Ibiza North section, the southward transport is also maximum in winter (0.31 Sv) and minimum in summer (0.18 Sv, **Figures 12A–D** and **Table 3**). Most of the upper 300 m in the Ibiza South section is occupied by waters flowing southwards during winter, whereas the area filled with waters moving northwards increases during summer and autumn (**Figures 10A–D**). Another evidence showing that the Ibiza Channel is the preferential pathway for the southward transport of WIW is that the net transport through Mallorca Channel is directed northwards in the upper layer for most of the year, with values of the order of 0.1 Sv. This northward flow in the upper layer of the Mallorca Channel is even more clear during summer (**Figure 11**) when almost the complete section is filled by waters moving northwards (**Figure 11C**) with a reduced area of low southward velocities in the coastal sector close to the Ibiza Island. Salinity values lower than 37.5 can also be observed in this section during summer (**Supplementary Figure S11C**). This result is in agreement with Juza et al. (2013) who found maximum southward transports of 0.33 Sv for WIW in the Ibiza Channel, while the maximum transports for this water mass in the Mallorca Channel were around 0.1 Sv. Barceló-Llull et al. (2019) also showed with glider repeated sections that the net transport through the Mallorca Channel was directed to the north along the whole year with values ranging from 0.03 to 0.08 Sv.

Below 300 m depth, the LIW occupies the layer between 394 and 531 m, with salinity and potential temperature values at its core that fluctuate between 38.51 and 38.54, and 13.16 and 13.24°C, respectively. A clear asymmetry between the

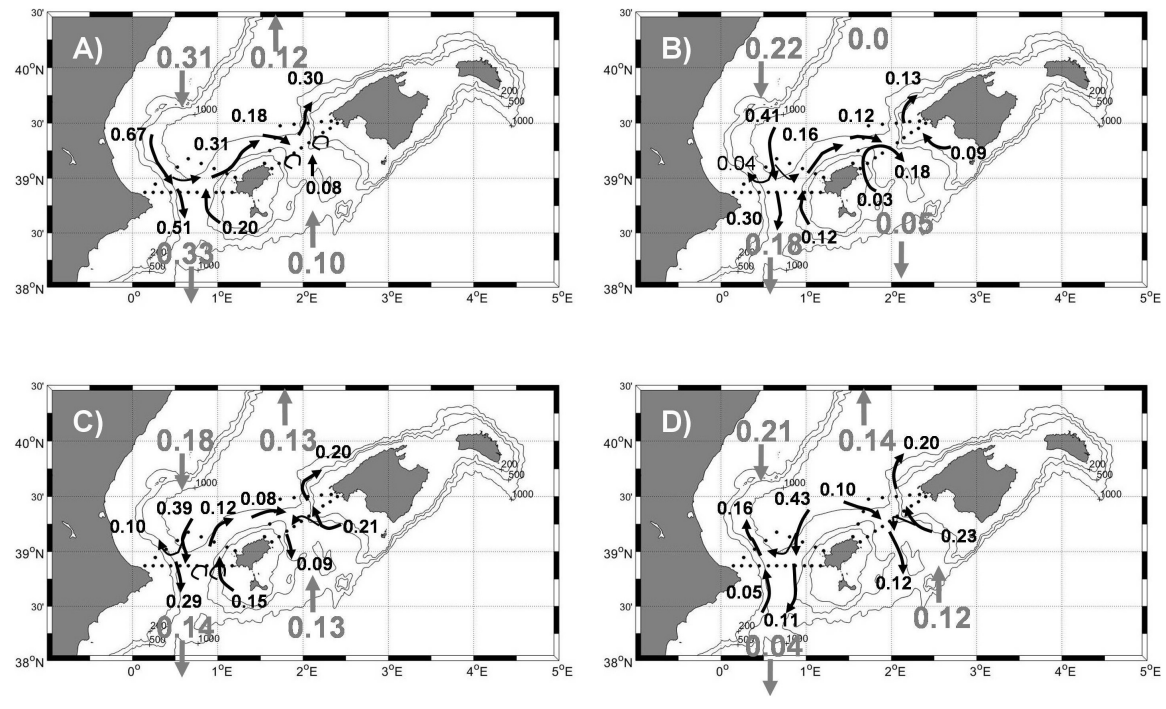

FIGURE 12 | Schematic circulation in the upper layer (AW + WIW) during winter **(A)**, spring **(B)**, summer **(C)** and autumn **(D)**. Mass transports are expressed in 10^9 kg/s, which approximately correspond to 1 Sverdrup. Net transports for the upper layer are expressed with gray numbers.

Ibiza and Mallorca Channels is also highlighted. The lower layer flow goes to the south in the Ibiza Channel during the whole year, while it is directed to the north in the Mallorca Channel. This flow is mainly comprised of LIW and mixing waters of both LIW and WMDW. Testor et al. (2005) and Escudier et al. (2016) found that the Algerian Current partly recirculates forming two cyclonic cells in the Algerian Basin. The anticyclonic eddies detached from this current would follow the path of the main current and therefore would turn westwards at the Sardinian Channel at 40°N. These eddies could reach 600 m depth and even to the sea bottom being a means for the northward transport of LIW. Dense waters with density values higher than 29.11 kg/m^3 are always present in the northern parts of the triangles of both channels, but only intermittently in the southern part of both channels. This result simply indicates that the WMDW mainly flows north-eastwards along the northern slope of the Balearic Islands since the topography of the Channels imposes a severe restriction to the flow of the densest waters which occupy deeper levels. Nevertheless it is important to remark that during some seasons of the year, waters as dense as 29.12 kg/m^3 can flow through the channels.

Besides the analysis of climatological salinity and temperature fields and the associated mass transports, the variance and covariance of such fields provide information of paramount importance. The validation of numerical models is based on the comparison with available observations. Simulations run under climatological or perpetual atmospheric forcing should not only reproduce the long-term mean or medians values, but also the variance of the variables analyzed. This variance accounts for the inter-annual and decadal natural variability of the ocean-atmosphere system. Our results show that the standard deviation (square root of the variance) of the temperature exhibits a clear seasonal cycle in the upper 100 m of the water column with minimum values of 0.71 in winter and maximum values of 2.4°C in autumn. The winter minimum is associated to the vertical homogeneity of the upper water column. In autumn, the water column remains stratified and the stormy activity starts to be intense inducing a high variability in the temperature distribution of the upper layer. It should be taken into account that all the surveys corresponding to the same season are not conducted during the same date (**Supplementary Figure S1**). Therefore, the variances estimated should be considered as an upper bound since they include both the natural variability of the sea and the date dispersion. A possible seasonal cycle for the upper layer salinity variance could not be established with the present data. The maximum standard deviation ranged from 0.21 to 0.28. The decaying horizontal length scale ranges between 49 and 56 km both for the salinity and potential temperature covariance, indicating that this could be the length scale for those eddies crossing the Balearic Channels, while the vertical decaying length scale is between 18 and 53 m, which could also be an indication of the vertical thickness of mesoscale structures.

CONCLUSION

In summary, the analysis of the longest temperature and salinity time series in the Balearic Channels has allowed to describe the median distribution of these variables and the associated absolute geostrophic transports. The ranges that define the hydrographic properties of the different water masses within the Balearic Channels could be defined in a more accurate way than using a limited number of oceanographic surveys. Results from individual campaigns could strongly depart from this climatological situation as the short time scale variability could be of the same order of magnitude than the seasonal cycle of water masses and transports (Heslop et al., 2012). The long-term climatological distributions could be more appropriate for the study of the long-term balance between the northern and southern basins of the WMED. The picture depicted by the present data shows that the Northern Current flows southwards along the Spanish continental slope, being stronger in winter when an important part of it flows through the western sector of the Ibiza Channel. AW intrusions would occur through the eastern part of the Ibiza Channel and through the Mallorca Channel. The southward transport in the upper 300 m of the water column decreases in summer and the northward transport which preferentially crosses the Mallorca Channel would increase during this season. The causes would be the weakening of the Northern Current associated to the lack of convection processes from spring, and the reversal of the prevalent wind direction and the weakening of their intensity. The southward transport of LIW occurs through the Ibiza Channel, but the low magnitude of this transport suggests that the main path of this water mass surrounds the Balearic Islands along the northern continental slope as part of the Balearic Current. The northward transport of LIW through the Mallorca Channel could only be explained by the intrusion of eddies detached from the Algerian Current. Finally, the WMDW is severely constrained by the shallow depth of the Channels and would flow in a Northeast direction along the northern slope of the Balearic Islands. Nevertheless, a small fraction of the WMDW could occasionally overflow and cross the Balearic Channels. The systematic collection of hydrographic time series such as those presented in the present work (RADMED project from IEO) or those referred in this work (glider repeated sections operated by SOCIB) could help to improve the statistics presented in this study and the knowledge about the long-term behavior of the Balearic Channels.

DATA AVAILABILITY STATEMENT

The datasets presented in this study can be found in online repositories. The names of the repository/repositories and accession number(s) can be found below: IBAMar data base (http://www.ba.ieo.es/es/ibamar).

AUTHOR CONTRIBUTIONS

MG-M and FM were involved in the monitoring design, the field work, and the data processing work. RB was involved in the data

base management and data processing work. PV-B and AH-G were involved in the inverse box modeling. MV-Y was involved in data analysis and work redaction. All authors contributed to the article and approved the submitted version.

FUNDING

This study has been supported by the research program RADMED ("Series Temporales de Datos Oceanográficos del Mediterráneo") funded by Instituto Español de Oceanografía (IEO). Partial support has been also received from the Spanish "Programa Estatal De I+D+I Orientada a Los Retos De La Sociedad (RTI2018-100844-B-C32)" through project SAGA: Flujos zonales en el Océano Atlántico sur interior.

SUPPLEMENTARY MATERIAL

The Supplementary Material for this article can be found online at: https://www.frontiersin.org/articles/10.3389/fmars.2020.568602/full#supplementary-material

REFERENCES

Barceló-Llull, B., Pascual, A., Ruiz, S., Escudier, R., Torner, M., and Tintoré, J. (2019). Temporal and spatial hydrodynamic variability in the mallorca channel (Western Mediterranean Sea) from eight years of underwater glider data. *J. Geophys. Res. Oceans* 124, 2769–2786. doi: 10.1029/2018JC014636

Berta, M., Bellomo, L., Griffa, A., Magaldi, M. G., Molcard, A., Mantovani, C., et al. (2018). Wind-induced variability in the Northern Current (northwestern Mediterranean Sea) as depicted by a multi-platform observing system. *Ocean Sci.* 14, 689–710. doi: 10.5194/os-14-689-2018

Bosse, A., Testor, P., Houpert, L., Damien, P., Prieur, L., Hayes, D., et al. (2016). Scales and dynamics of submesoscale coherent vortices formed by deep convection in the northwestern mediterranean Sea. *J. Geophys. Res. Oceans* 121:2016JC012144. doi: 10.1002/2016JC012144

Bretherton, F. P., Davis, R. E., and Fandy, C. B. (1976). A technique for objective analysis and design of oceanographic experiments applied to MODE-73. *Deep Sea Res. I* 23, 559–582. doi: 10.1016/0011-7471(76)90001-2

Casanova-Masjoan, M., Joyce, T. M., Pérez-Hernández, M. D., Vélez-Belchí, P., and Hernández-Guerra, A. (2018). Changes across 66°W, the Caribbean Sea and the Western boundaries of the North Atlantic Subtropical Gyre. *Prog. Oceanogr.* 168, 296–309. doi: 10.1016/j.pocean.2018.09.013

Escudier, R., Mourre, B., Juza, M., and Tintoré, J. (2016). Subsurface circulation and mesoscale variability in the Algerian subbasin from altimeter-derived eddy trajectories. *J. Geophys. Res Oceans* 121, 6310–6322. doi: 10.1002/2016JC011760

García-Lafuente, J., López-Jurado, J. L., Cano, N., Vargas-Yáñez, M., and Aguiar, J. (1995). Circulation of water masses through the Ibiza Channel. *Oceanol. Acta* 18, 245–252.

Gomis, D., Ruiz, S., and Pedder, M. A. (2001). Diagnostic analysis of the 3D ageostrophic circulation from a multivariate spatial interpolation of CTD and ADCP. *Deep Sea Res. I* 48, 269–295. doi: 10.1016/S0967-0637(00)00060-1

Group, M. E. D. O. C. (1970). Observation of formation of deep water in the mediterranean Sea, 1969. *Nature* 227, 1037–1040. doi: 10.1038/2271037a0

Hernández-Guerra, A., Espino-Falcón, E., Vélez-Belchí, P., Pérez-Hernández, M. D., Martínez-Marrero, A., and Cana, L. (2017). Recirculation of the canary current in fall 2014. *J. Mar. Syst.* 174, 25–39. doi: 10.1016/j.jmarsys.2017.04.002

Hernández-Guerra, A., and Talley, L. D. (2016). Meridional overturning transports at 30 S in the Indian and Pacific Oceans in 2002-2003 and 2009. *Prog. Oceanogr.* 146, 89–120. doi: 10.1016/j.pocean.2016.06.005

Hernández-Guerra, A., Talley, L. D., Pelegrí, J. L., Vélez-Belchí, P., Baringer, M. O., Macdonald, A. M., et al. (2019). The upper, deep, abyssal and overturning circulation in the Atlantic Ocean at 30°S in 2003 and 2011. *Prog. Oceanogr.* 176:102136. doi: 10.1016/j.pocean.2019.102136

Heslop, E. E., Ruiz, S., Allen, J., Lopez-Jurado, J. L., Renault, L., and Tintoré, J. (2012). Autonomous underwater gliders monitoring variability at "choke points" in our ocean system: a case study in the Western Mediterranean Sea. *Geophys. Res. Lett.* 39:L20604. doi: 10.1029/2012GL053717

Juza, M., Escudier, R., Vargas-Yáñez, M., Mourre, B., Heslop, E., Allen, J., et al. (2019). Characterization of changes in Western Intermediate water properties enabled by an innovative geometry-based detection approach. *J. Mar. Syst.* 191, 1–12. doi: 10.1016/j.jmarsys.2018.11.003

Juza, M., Renault, L., Ruiz, S., and Tintoré, J. (2013). Origin and pathways of intermediate water in the Northewestern Mediterranean Sea using observations and numerical modelling. *J. Geophys. Res. Oceans.* 118, 6621–6633. doi: 10.1002/2013JC009231

López-Jurado, J. L., Balbín, R., Amengual, B., Aparicio-González, A., Fernández, de Puelles, M. L., et al. (2015). The RADMED monitoring program: towards an ecosystem approach. *Ocean. Sci.* 11, 645–671. doi: 10.5194/osd-12-645-2015

López-Jurado, J. L., García-Lafuente, J., and Lacaya, N. (1995). Hydrographic conditions of the Ibiza Channel during November 1990, March 1991 and July 1992. *Oceanol. Acta* 18, 235–243.

Millot, C. (2009). Another description of the mediterranean Sea outflow. *Prog. Oceanogr.* 82, 101–124. doi: 10.1016/j.pocean2009.04.016

Millot, C., and Taupier-Letage, I. (2005). "Circulation in the Mediterranean Sea," in *The Mediterranean Sea. Handbook of Environmental Chemistry*, Vol. 5K, ed. A. Saliot (Berlin: Springer).

Pascual, A., Vidal-Vijande, E., Ruiz, S., Somot, S., and Papadopoulos, V. (2014). "Spatiotemporal variability of the surface circulation in the western mediterranean: a comparative study using altimetry and modeling," in *The Mediterranean Sea: Temporal Variability and Spatial Patterns*, eds G. L. E. Borzelli, M. Gačić, P. Lionello, and P. M. Rizzoli (Washington, DC: AGU), doi: 10.1002/9781118847572

Pedder, M. A. (1993). Interpolation and filtering of spatial observations using succesive corrections and Gaussian filters. *Mon. Wea. Rev.* 121, 2889–2902. doi: 10.1175/1520-0493(1993)121<2889:iafoso>2.0.co;2

Pinot, J. M., and Ganachaud, A. (1999). The role of winter intermediate waters in spring-summer circulation of the Balearic Sea: 1. hydrography and inverse modeling. *J. Geophys. Res.* 104, 29843–29864. doi: 10.1029/1999JC900071

Pinot, J.-M., López-Jurado, J. L., and Riera, M. (2002). The CANALES experiment (1996-1998). Interannual, seasonal, and mesoscale variability of the circulation in the Balearic Channels. *Prog. Oceanogr.* 55, 335–370. doi: 10.1016/S0079-6611(02)00139-8

Salat, J., and Font, J. (1987). Water mass structure near and offshore the Catalan coast during the winters of 1982 and 1983. *Ann. Geophys.* 5B, 49–54.

Schroeder, K., Chiggiato, J., Josey, S. A., Borghini, M., Aracri, S., and Sparnocchia, S. (2017). Rapid response to climate change in a marginal sea. *Sci. Rep.* 7:4065. doi: 10.1038/s41598-017-04455-5

Schroeder, K., Josey, S. A., Herrmann, M., Grignon, L., Gasparini, G. P., and Bryden, H. L. (2010). Abrupt warming and salting of the Western Mediterranean deep water after 2005: atmospheric forcings and lateral advection. *J. Geophys. Res.* 115:C08029. doi: 10.1029/2009JC005749

Send, U., Font, J., Krahmann, G., Millot, C., Rhein, M., and Tintoré, J. (1999). Recent advances in observing the physical oceanography of the western Mediterranean Sea. *Prog. Oceanogr.* 44, 37–64. doi: 10.1016/S0079-6611(99)00020-8

Sparnocchia, S., Gasparini, G. P., Astraldi, M., Borghini, M., and Pistek, P. (1999). Dynamics and mixing of the Eastern Mediterranean outflow in the Tyrrhenian basin. *J. Mar. Syst.* 20, 301–317. doi: 10.1016/S0924-7963(98)00088-8

Tel, E., Balbín, R., Cabanas, J. M., García, M. J., García-Martínez, M. C., González-Pola, C., et al. (2016). IEOOS: the spanish institute of oceanography observing system. *Ocean Sci.* 12, 345–353. doi: 10.5194/os-12-345-2016

Testor, P., Bosse, A., Houpert, L., Margirier, F., Mortier, L., Legoff, H., et al. (2018). Multiscale observations of deep convection in the Northwestern Mediterranean sea during winter 2012-2013 using multiple platforms. *J. Geophys. Res. Oceans* 123, 1745–1776. doi: 10.1002/2016JC012671

Testor, P., Send, V., Gascard, J.-C., Millot, C., Tapier-Letage, I., and Béranger, K. (2005). The mean circulation of the Southwestern Mediterranean Sea: algerian gyres. *J. Geophys. Res.* 110:C11017. doi: 10.1029/2004JC002861

Thiébaux, H. J., and Pedder, M. A. (1987). *Spatial Objective Analysis with Applications in Atmospheric Science*. London: Academic press.

Vargas-Yáñez, M., García-Martinez, M. C., Moya, F., López-Jurado, J. L., Serra, M., Santiago-Domenech, R., et al. (2019). *The Present State of Marine Ecosystems in the Spanish Mediterranean in a Climate Change Context*. Málaga: Grupo Mediterráneo de Cambio Climático.

Vargas-Yáñez, M., García-Martíneza, M. C., Moya, F., Balbín, R., López-Jurado, J. L., Serra, M., et al. (2017). Updating temperature and salinity mean values and trends in the Western Mediterranean: The RADMED project. *Prog. Oceanogr.* 157, 27–46. doi: 10.1016/j.pocean.2017.09.004

Vargas-Yáñez, M., Garivier, F., Pirra, O., and García-Martínez, M. C. (2005). Using routine hydrographic sections for estimating the parameters needed for optimal statistical interpolation. Application to the northern Alboran Sea. *Sci. Mar.* 69:435. doi: 10.3989/scimar.2005.69n4435

Vargas-Yáñez, M., Zunino, P., Schroeder, K., López-Jurado, J. L., Plaza, F., Serra, M., et al. (2012). Extreme Western Intermediate Water formation in winter 2010. *J. Mar. Syst.* 105–108, 52–59. doi: 10.1016/j.jmarsys.2012.05.010

Wunsch, C. (1978). The North Atlantic general'circulation west of 50° W determined by inverse methods. *Rev. Geophys.* 16, 583–620. doi: 10.1029/rg016i004p00583

Wunsch, C. (1996). *The Ocean Circulation Inverse Problem*. New York, NY: Cambridge University Press.

Zar, J. H. (2010). *Biostatistical Analysis*, 5th Edn, Upper Saddle River, NJ: Prentice-Hall.

Conflict of Interest: The authors declare that the research was conducted in the absence of any commercial or financial relationships that could be construed as a potential conflict of interest.

frontiers in Marine Science

ORIGINAL RESEARCH
published: 29 October 2020
doi: 10.3389/fmars.2020.579680

Intraseasonal Abyssal Current Variability of Bottom-Trapped Topographic Rossby Waves in the Southwestern East Sea (Japan Sea)

*JiYun Shin[1], Suyun Noh[2] and SungHyun Nam[1,2]**

[1] School of Earth and Environmental Sciences, Seoul National University, Seoul, South Korea, [2] Research Institute of Oceanography, Seoul National University, Seoul, South Korea

OPEN ACCESS

Edited by:
Katrin Schroeder, National Research Council (CNR), Italy

Reviewed by:
Shijian Hu, Chinese Academy of Sciences, China
Yeqiang Shu, South China Sea Institute of Oceanology (CAS), China

***Correspondence:**
SungHyun Nam
namsh@snu.ac.kr

Specialty section:
This article was submitted to Physical Oceanography, a section of the journal Frontiers in Marine Science

Received: *03 July 2020*
Accepted: *08 October 2020*
Published: *29 October 2020*

Citation:
Shin J, Noh S and Nam S (2020) Intraseasonal Abyssal Current Variability of Bottom-Trapped Topographic Rossby Waves in the Southwestern East Sea (Japan Sea). Front. Mar. Sci. 7:579680. doi: 10.3389/fmars.2020.579680

Examining the deep-water exchange through the Ulleung Interplain Gap (UIG) between the Ulleung Basin (UB) and the Japan Basin in the East Sea (Sea of Japan) is critical for understanding the vigorous circulation and material cycles of the sea. The exchange features an asymmetric flow structure across the UIG: a broad and weak inflow (into the UB) in the western UIG, and a narrow and strong outflow (out of the UB) in the eastern UIG, with the latter closely associated with the Dokdo Abyssal Current (DAC), a long-term mean, strong abyssal current near Dokdo. In this study, the linear theory of bottom-trapped topographic Rossby waves (TRWs) is applied to explain the previously unexplored longer intraseasonal band (30–50 days) DAC variability by analyzing multi-year moored current-meter observations and HYCOM reanalysis data, as they are significantly correlated in the period band (though not at the shorter intraseasonal band of 5–25 day explored previously). Bottom-intensified DAC variability is characterized by TRW parameters with a vertical trapping scale of 1100–2100 m, a horizontal wavelength of 49–111 km, a propagating speed of 1.3–3.0 km day^{-1}, and a propagating direction aligned with isobaths within a 2°–23° range (shallower water on the right). The departure angle between the energy-propagating direction of the waves and the isobath direction is estimated from the spectra of the along- and cross-slope abyssal currents and from the TRW theoretical dispersion relation for a given buoyancy frequency and bottom slope. These values are then compared to examine the significance of the bottom-trapped TRW dynamics, yielding a small (<16°) difference. The results support the significance of bottom-trapped TRWs on the longer intraseasonal variability of abyssal currents near the steeply sloped eastern side of the UIG, and an asymmetric abyssal flow structure across the UIG in the southwestern East Sea.

Keywords: abyssal currents, bottom-intensified current, East Sea (Sea of Japan), bottom-trapped topographic Rossby waves, HYCOM, intraseasonal band

INTRODUCTION

Bottom-trapped topographic Rossby waves (TRWs), generated by the stretching and squeezing of deep-water columns, propagate in the direction corresponding to the shallower water on the right-hand side in the northern hemisphere. TRWs proceed along isobaths over sloping topography and are modified by stratification (Rhines, 1970; Reid and Wang, 2004). Both observations and numerical models suggest that bottom-trapped TRWs dominate the abyssal current variability on a timescale ranging from several to hundreds of days. These TRWs with wavelengths ranging from approximately 80 to 250 km have been proven to have significant variability in deep and abyssal circulations in several regions, such as the continental rise near Cape Hatteras in the North Atlantic (Thompson and Luyten, 1976; Pickard, 1995), the Gulf of Mexico (Hamilton, 1990, 2007; Hamilton and Lugo-Fernandez, 2001; Oey and Lee, 2002; Oey et al., 2009), the Kuil–Kamchatka trench (Uehara and Miyake, 2000), and the South China Sea (Shu et al., 2016). Deep and abyssal current variability at relatively short (<6 days) periods, highly correlated with high-frequency wind forcing, has also been found in the Santa Barbara Channel, where the bottom-trapped waves mainly responsible for the variability exhibit a wavelength of 86–92 km (Auad et al., 1998). The ranges of frequencies and wavenumbers from previous studies are shown in **Figure 1**, along with the theoretical dispersion relations for ranges of different parameters accounting for intraseasonal oscillations.

The Ulleung Interplain Gap (UIG), located in the East Sea (Japan Sea), is the only deep passage (i.e., below 1500 m) connecting the Ulleung Basin (UB) in the southwestern area of the sea with the Japan Basin (JB) in the northern area (**Figures 2A,B**). Deep and abyssal currents observed below 1800 m from five moorings across the UIG for 16.5 months from November 2002 to April 2004 demonstrate an asymmetric structure of mean exchange flow with broad and weak equatorward inflow into the UB through the western UIG, and narrow and strong poleward outflow out of UB through the eastern UIG. The poleward outflow is named the Dokdo Abyssal Current (DAC) and exhibits a maximum recorded current speed of approximately 33.9 cm s^{-1} (Chang et al., 2009). Strong variability in the upper ocean circulation revealing the meandering of the Tsushima Current, and mesoscale eddies in the UIG and UB have been reported (Mitchell et al., 2005; Teague et al., 2005; Xu et al., 2009). These currents may contribute to the generation of TRWs and result in the intraseasonal variability of the DAC. Indeed, the power spectra for deep flows in the UIG indicate high spectral energies over a period of 15–60 days, particularly near Dokdo, relevant to the steeply sloping bottom topography (Chang et al., 2009). Results consistent with spectral peaks of DAC variability at the relatively shorter periods of 10.7 and 21.3 day were reported from direct current observations of approximately five moorings from November 2002 to April 2004, supporting the notion of bottom-trapped TRWs with wavelengths of 50–80 km (Kim et al., 2013). However, the forcing mechanisms of DAC variability at a longer intraseasonal band (30–50 days) remain unknown, probably due the relatively short period of mooring observations, which makes resolving the current variability at the longer intraseasonal band difficult.

This study aims to characterize and address the bottom-trapped TRWs underlying the longer-period intraseasonal DAC variability from multi-year moored current-meter observations and HYbrid Coordinate Ocean Model (HYCOM) reanalysis, and to discuss the possible cause. The data and methods used are described in the next section. Section "Results" provides the TRW characteristic results derived from both observational and reanalysis data. The results are discussed in Section "Discussion" and concluded in section "Conclusion".

DATA AND THEORY

Data Source and Processing

We used long time-series data collected using three subsurface moorings, EC1, U5, and UB2, in the UB and UIG (Noh and Nam, 2018; Noh et al., 2020) (**Figure 2B**). At EC1, 14-year time-series moored current-meter data were collected at depths of approximately 1400 and 2200 m (with slightly varying sensor depths over deployments) from January 1999 to December 2012. Time-series acoustic Doppler current profiler data collected from the upper 300 m of the EC1 mooring from December 2002 to February 2004 were also used. Similar moored current-meter data were collected at U5 at depths of 1000 and 2000 m from November 2002 to May 2006, and at UB2 at depths of 1000 and 1600 m from May 2006 to February 2010. Aanderra rotary current-meters (RCMs) and Nortek Aquadopp current-meters were used to collect the moored current-meter data at sampling intervals of 30 or 60 min. The mooring locations, nominal depths of current meters, deployment periods of moorings, and basic statistics of the moored current-meter data are listed in **Table 1**. The speeds of the horizontal current shown in **Table 1** are based on an uncertainty of an order of 0.01 cm s^{-1}, which is inversely proportional to the square root of the number of data used in averaging (Teague et al., 2005; Watts et al., 2013). The minimum current speed of an RCM is 1.1 cm s^{-1}, which is treated as a current stall, and a data gap of no longer than 5 h was filled by applying spline fits to the zonal and meridional currents (Teague et al., 2005). The moored current-meter data were vertically interpolated to estimate the zonal and meridional currents at the nominal depths.

The measured zonal (u) and meridional (v) currents were ensemble-averaged over 1 day. The ratio of EKE $= \left(\overline{u'^2} + \overline{v'^2}\right)/2$ to MKE $= \left(\overline{u^2} + \overline{v^2}\right)/2$ was calculated, where the zonal and meridional velocities (u, v) were decomposed into long-term mean $(\bar{u}, \bar{v})$ and fluctuating components (u', v'), that is, $u = \bar{u} + u'$ and $v = \bar{v} + v'$. The daily averaged u and v were bandpass-filtered to extract fluctuations at shorter (5–25 days) and longer (30–50 days) intraseasonal bands with cutoff periods of 5 and 25 days, and 30 and 50 days, respectively, using a second-order Butterworth filter. The two intraseasonal bands were based on spectral energies observed at U5 (rather than EC1), as reported in a previous study (e.g., Chang et al., 2009; **Figure 3D**). The variance-preserving spectrum of the

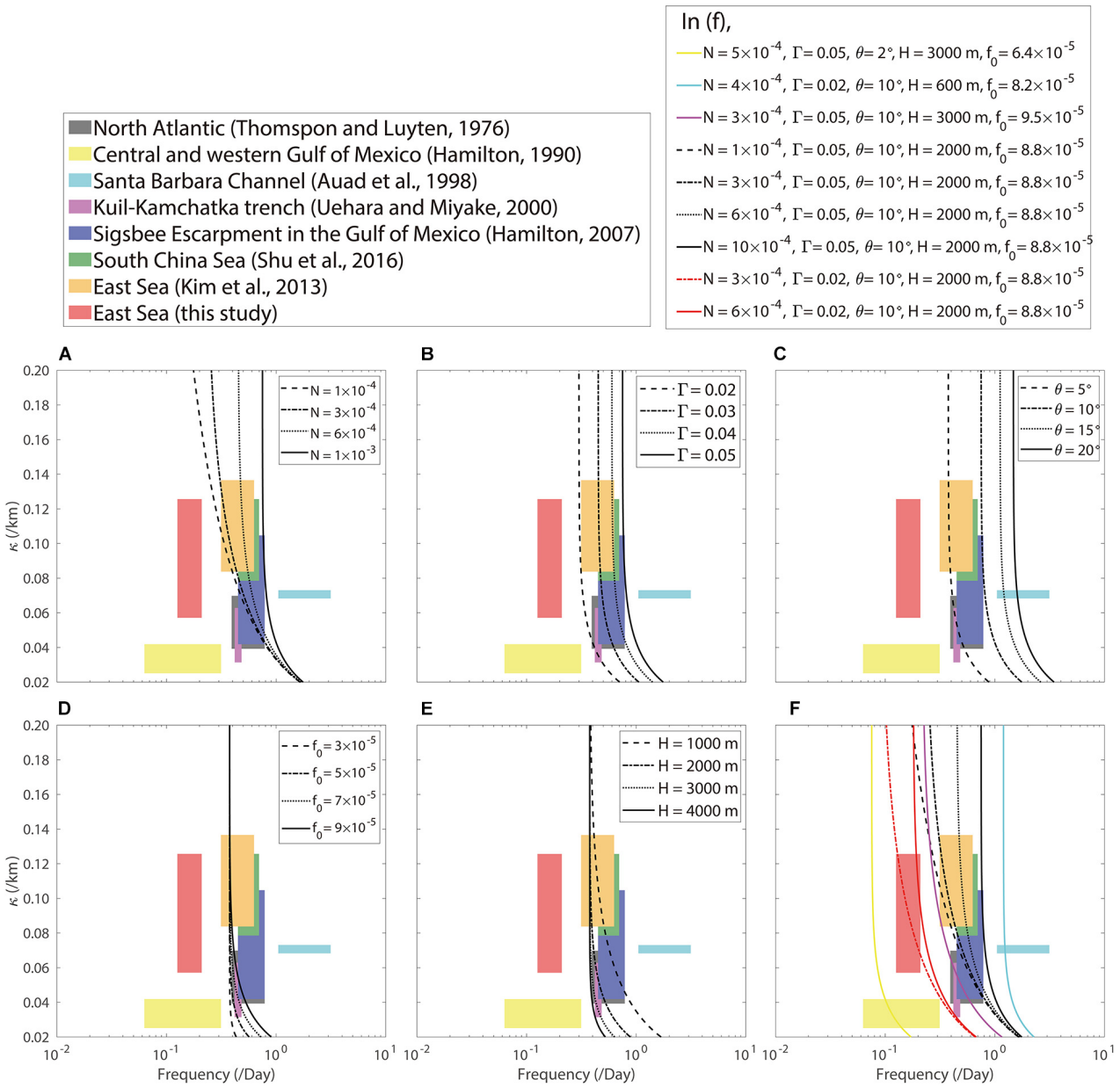

FIGURE 1 | Dispersion relation (lines) of bottom-trapped TRWs from Eq. (1) for **(A)** varying buoyancy frequency (N) with constant bottom slope ($\Gamma = 0.05$), propagating orientation angle rotated from the isobath direction ($\theta = 10°$), Coriolis parameter ($f_0 = 8.8 \times 10^{-5}$ s^{-1}), and depth level ($H = 2000$ m); **(B)** varying Γ with constant N (= 1×10^{-3} s^{-1}), θ (= 10°), f_0 (= 8.8×10^{-5} s^{-1}), and H (= 2000 m); **(C)** varying θ with constant N (= 1×10^{-3} s^{-1}), Γ (= 0.05), f_0 (= 8.8×10^{-5} s^{-1}), and H (= 2000 m); **(D)** varying f_0 with constant N (= 1×10^{-3} s^{-1}), Γ (= 0.05), θ (= 10°), and H (= 2000 m); **(E)** varying H with constant N (= 1×10^{-3} s^{-1}), Γ (= 0.05), θ (= 10°), and f_0 (= 8.8×10^{-5} s^{-1}); and **(F)** their combinations. Herein, ranges of wavenumbers (κ) and frequencies (ω) investigated in past and present studies are shaded with different colors, and references are presented.

current speed ($\sqrt{u'^2 + v'^2}$) was calculated using Welch's power spectrum methods (Welch, 1967) and Hamming windows with 50% overlap. In addition to the moored current-meter data, vertical profiles of temperature and salinity collected in the eastern UIG (near U5 and EC1) from six full-depth CTD casts in August 1995, March 1997, June 1999, September 2005, August 2008, and October 2012 were used to estimate the buoyancy frequency (**Figure 2B**).

The 20-year time-series data of daily u and v, water temperature, and salinity from October 1992 to December 2012 of HYCOM global 1/12° reanalysis data were used in this study. The horizontal resolution was 0.08°, and the vertically interpolated z-levels where the data were extracted were 100, 200, 300, 400, 500, 600, 700, 800, 900, 1000, 1250, 1500, and 2000 m. Although the data-assimilated HYCOM data may contain non-conservative momentum, vorticity, and mass

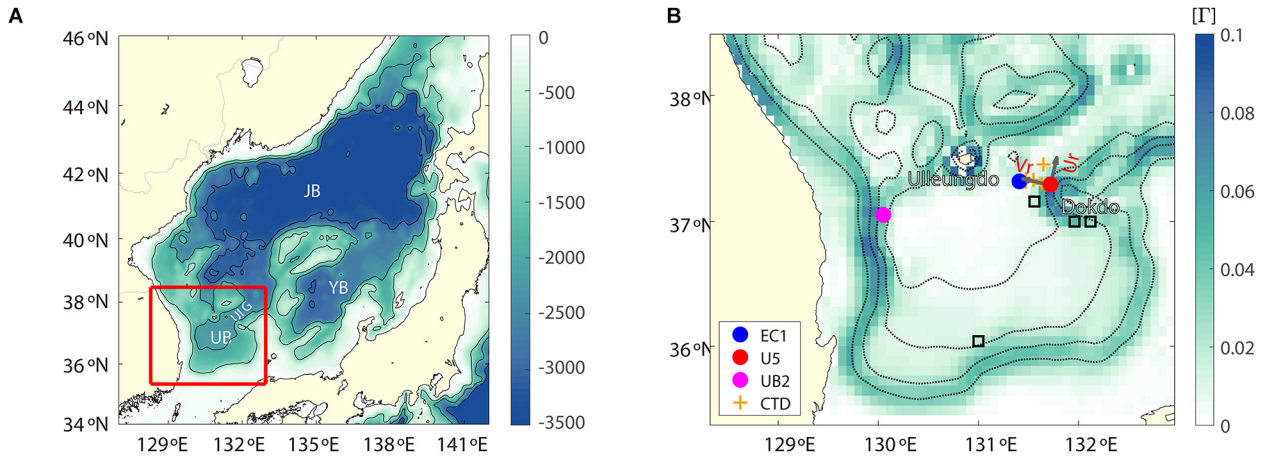

FIGURE 2 | (A) Bottom topography (depth in color) in the East Sea. JB, YB, UB, and UIG denote the Japan Basin, Yamato Basin, Ulleung Basin, and Ulleung Interplain Gap, respectively. **(B)** Bottom slope in UB and UIG (area shown in red in panel **A**) with isobaths every 500 m. Locations of current-meter moorings (EC1, U5, and UB2) and conductivity–temperature–depth (CTD) casts are shown with circles and crosses, respectively. Four locations selected for calculating the TRW characteristics are indicated by colored squares (Cases 1–4). The along-slope (U_r) and down-slope (V_r) directions are marked with arrows in panel **(B)**.

TABLE 1 | Basic statistics of daily mean currents observed at EC1 for 1999 to 2012, U5 for 2002 to 2006, and UB2 for 2006 to 2010 along with sampling time interval of the current measurements.

Station	Nominal depth (m)	Period	Sampling time interval (h)	Velocity components	Mean (cm s^{-1})	STD (cm s^{-1})	Vector mean			MKE (cm^2 s^{-2})	EKE (cm^2 s^{-2})	EKE/MKE
							Speed (cm s^{-1})	Heading (°)	Max Speed (cm s^{-1})			
EC1	1400	99/05–12/12	0.5 or 1	U	−0.80	2.66	1.43	214.0	11.39	1.02	6.52	6.39
				V	−1.18	2.44						
	2200	99/01–12/12	0.5 or 1	U	−0.92	2.96	1.49	217.8	13.87	1.12	7.72	6.89
				V	−1.18	2.58						
U5	1000	04/07–05/09	0.5	U	1.49	1.67	5.60	15.4	19.97	15.67	12.86	0.82
				V	5.40	4.80						
	2000	02/11–06/05	0.5	U	1.07	2.24	5.95	10.4	29.48	17.69	17.62	1.00
				V	5.85	5.50						
UB2	1000	06/05–10/02	0.5 or 1	U	−0.73	1.10	3.58	191.9	17.76	6.39	6.07	0.95
				V	−3.50	3.31						
	1600	06/05–10/02	0.5 or 1	U	−0.11	0.83	3.18	182.0	20.36	5.07	4.83	0.95
				V	−3.18	3.00						

All headings (horizontal direction) are measured in an angle rotated clockwise from the north. STD, MKE, and EKE denote the standard deviation, mean kinetic energy, and eddy kinetic energy, respectively.

source/sink elements, the results in the deep layer were not modified significantly with sparse or no available observational data in the region. Thus, the HYCOM data have been widely used to reveal intermediate and deep circulations in the region, which is consistent with observations reported elsewhere (Hogan and Hurlburt, 2006; Nam et al., 2016; Han et al., 2020). The HYCOM horizontal currents (u and v) were also bandpass-filtered with the same filters used to extract fluctuations at the two intraseasonal bands. Considering the bottom topography in the vicinity of U5, bandpass-filtered currents were decomposed into along-slope (U_r, 10° rotated clockwise from the north) and cross-slope (V_r) components. The bathymetry data used in the HYCOM dataset (GLBu0.08_07b) were used to estimate the along-isobath angle at scales of several tens to a few hundreds of kilometers (**Figure 2B**).

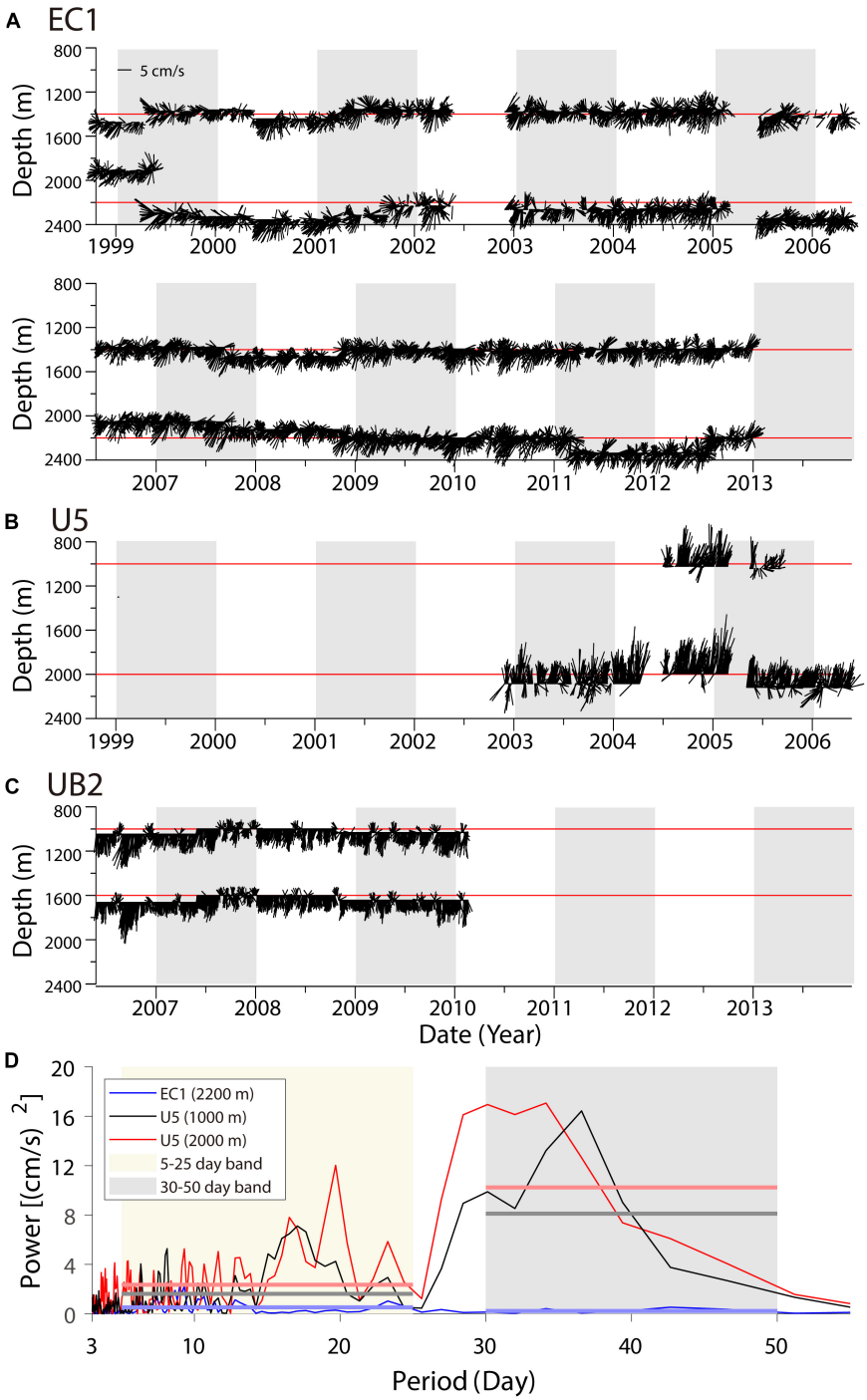

FIGURE 3 | Time series of daily mean currents observed at **(A)** EC1, **(B)**, U5, and **(C)** UB. The horizontal red bars denote the nominal depth. **(D)** Total kinetic energy spectra of EC1 (blue) and 1000 and 2000 m of U5 (black and red), in variance-preserving form of currents observed at 1000 m of U5 from July 2004 to September 2005. The horizontal bars refer to the mean spectral energy for shorter and longer intraseasonal bands (shaded).

To supplement the observational and HYCOM data, the sea surface wind from the Modern-Era Retrospective analysis for Research and Applications, Version 2 (MERRA2), and the absolute sea surface height (SSH) from the Archiving, Validation, and Interpretation of Satellite Oceanographic data (AVISO) were used. The MERRA2 wind data were produced with a time interval of 6 h, and zonal and meridional resolutions of 0.2° for the atmospheric model. The AVISO SSH data, provided by the Copernicus Marine Environment Monitoring Service (CMEMS), were provided as daily gridded data from satellite altimetry

missions, such as Jason-3 and Sentinel-3A, with a horizontal resolution of 0.25° × 0.25°.

Application of Bottom-Trapped TRW Theory

In the linear theory of bottom-trapped TRWs, the vertical structure of bottom-intensified wave motions is proportional to $V = V_0 \cosh(\kappa N z/f_0)$, where V is the horizontal velocity component, κ is the horizontal wavenumber, and z is the water depth (Rhines, 1970). Neglecting the planetary beta, the dispersion relation of TRWs in a stratified ocean can be written as

$$\omega = \Gamma N \sin\theta \coth(\kappa N H/f_0), \quad (1)$$

where ω, θ, N, H, f_0, and Γ are the wave frequency and orientation angle of the wavenumber vector from the downslope or the angle of the wave-propagating direction (direction of the group velocity vector) with respect to the isobath, buoyancy frequency, water depth, Coriolis parameter, and bottom slope, respectively. The ratio R of the kinetic energy associated with the TRWs between the two depths is expressed as:

$$R = (\cosh(\kappa N z_1/f_0)/\cosh(\kappa N z_2/f_0))^2 \text{ for } z_1 < z_2, \quad (2)$$

where z_1 and z_2 are the two depth levels. Herein, R is estimated from the ratio of U_r spectra at the upper and lower layers for the intraseasonal band, and N and f_0 are fixed (6.8×10^{-4} and 8.8×10^{-5} s^{-1}, respectively) based on the time-mean vertical profiles of the HYCOM temperature and salinity near Dokdo. The wavenumber κ and thus the wavelength ($\lambda = 2\pi/\kappa$ in km) and propagating speed ($C = \lambda/T$ in km day^{-1}, where T is the period) are estimated from the ratio R using Eq. (2). The orientation angle (θ) is calculated in two ways. The first method uses the spectra of the along-slope and cross-slope currents (U_r and V_r) observed at 2000 m following the process described in Fofonoff (1969). Herein, the angle θ_e is obtained using the co-spectrum (S_{uv}) between U_r and V_r and the autospectrum (S_{uu}, S_{vv}) of U_r and V_r as follows:

$$\theta_e = \frac{1}{2}\tan^{-1}\frac{2S_{uv}}{S_{uu} - S_{vv}}, \quad (3)$$

The second method uses the theoretical dispersion relation (θ_t) with a constant bottom slope (Γ = 0.02 for the location of U5) and the buoyancy frequency N, as derived from Eq. (1):

$$\theta_t = \sin^{-1}\left[\frac{2\pi}{T\Gamma N}\tanh\left(\frac{2\pi}{f_0}\kappa H\right)\right], \quad (4)$$

where T is the period. The difference in the orientation angle between the two methods ($\theta_d = \theta_e - \theta_t$) is used to examine the significance of the bottom-trapped TRW dynamics in the corresponding cases.

A small R, indicating the bottom intensification of intraseasonal oscillation, is a necessary condition for bottom-trapped TRWs. The eight small R cases selected in this study are listed in **Tables 2**, **3**. Note that such bottom intensification is found in limited areas where the bottom-trapped TRW theory is applicable, mostly at the eastern side of the UIG and UB (shown in the next section). For the eight selected cases with Γ values ranging from 0 to 0.1, we tested the sensitivity of the theoretical orientation angle (θ_t) to the HYCOM buoyancy frequency N ($7.0 \pm 4.0 \times 10^{-4}$ s^{-1}), which is significantly overestimated compared with that of the CTD observation (3×10^{-4} s^{-1}). The overestimation of the HYCOM stratification in the deep part of the region, accounting for most of the systematic bias in θ_d (systematically small θ_t compared with θ_e), is discussed with regard to the uncertainties of HYCOM-derived θ_t in section "Discussion".

RESULTS

Characteristics of Abyssal Circulation and Its Variability

Statistics on Abyssal Currents Observed in the UB and UIG

Weak southward and southwestward inflows from the JB into the UB via the UIG, with mean speeds of 1.43 and 1.49 cm s^{-1}, were observed at the 1400 and 2200 m levels, respectively, at EC1 in the center of the UIG. Here, an EKE 6–7-times larger than the MKE indicates significant temporal variability (**Figures 3A**, **4A** and **Table 1**). The kinetic energy spectra of abyssal currents observed at 2200 m indicate distinct, significant variances of 0.53 and 0.23 cm^2 s^{-2} at shorter and longer intraseasonal bands (5–25 and 30–50 days, respectively) at U5; however, the separation was not distinct at EC1 (**Figure 3D**). The two intraseasonal bands defined previously were based on spectral energies observed at U5 rather than EC1 (Chang et al., 2009).

Unlike EC1, relatively strong northward flows were observed at U5, with mean speeds of 5.60 cm s^{-1} at 1000 m and 5.95 cm s^{-1} at 2000 m. Southward flows were observed at UB2 with mean speeds of 3.58 cm s^{-1} at 1000 m and 3.18 cm s^{-1} at 1600 m (**Figures 3B,C**, **4A** and **Table 1**). Although U5 and EC1 are adjacent to each other, the maximum speed of abyssal currents at U5 was 29.48 cm s^{-1}, which is twice that at EC1. The difference between maximum current speeds at U5 and EC1 is due to the asymmetric flow structure across the UIG, with a wider and weaker inflow into the UB located in the western UIG, and a narrower and stronger outflow into the JB located in the eastern UIG, which is consistent with the findings of previous studies (Chang et al., 2009) and confirmed from HYCOM (**Figure 4A**). The relatively strong northward abyssal currents at U5 reaffirm the DAC in the eastern UIG.

Despite the lower ratios (∼1) at U5 and UB2 between EKE and MKE than those at EC1, temporal variability is stronger at U5 and UB2, yielding variances at 2000 m of 1.62 and 8.11 cm^2 s^{-2}, respectively, in the kinetic energy spectra of abyssal currents. These variances are several times higher than those at EC1 at shorter and longer intraseasonal bands (5–25 and 30–50 days, respectively; **Figures 3A–D**, **4A**, and **Table 1**). The spectral variances of kinetic energy at 1000 m for U5 are 2.35 and 10.24 cm^2 s^{-2} at shorter and longer intraseasonal bands, respectively. These values are lower than the spectral variances

TABLE 2 | Inputs of TRW parameters.

	Case		Longitude (°E)	Latitude (°N)	Depth (m)	N ($\times 10^{-4}$ S^{-1})	Γ	Shallow	Deep		
								S_{uu} (cm^2 s^{-2})	S_{uu} (cm^2 s^{-2})	S_{vv} (cm^2 s^{-2})	S_{uv} (cm^2 s^{-2})
HYCOM	1	A	132.16	37.04	1000 1250	5.5	0.03	9.8	13.1	1.3	3.1
	2	A	131.04	36.08	1000 1500	7.3	0.02	11.1	11.4	1.6	3.5
		B			1250 1500	7.3		9.6			
	3	A	132.00	37.04	1000 1500	7.3	0.05	12.0	15.4	1.4	4.2
		B			1250 1500	7.5		13.3			
	4	A	131.60	37.20	1000 2000	6.7	0.02	11.7	24.6	5.5	10.2
		B			1250 2000	6.6		11.0			
		C			1500 2000	6.8		10.9			
	Nearest U5		131.68	37.28	1000 2000	6.7	0.06	16.1	15.3	1.6	4.1
Observations	U5		131.72	37.29	1000 2000	3.5	0.06	14.7	16.5	0.2	1.5

N is the mean buoyancy frequency between two selected depths, Γ is the bottom slope, S_{uu}, S_{vv}, and S_{uv} is the auto- and cross-spectra of U_r and V_r for eight cases and U5 (both from HYCOM and mooring observations).

TABLE 3 | TRW parameters for eight cases and observation (U5).

Case		Longitude	Latitude	Depth (m)	R	κ (km^{-1})	λ (km)	C (km day^{-1})	μ (m)	θ_e (°)	θ_t (°)	θ_d (°)
1	A	132.16	37.04	1000 1250	0.75	0.13	49	1.31	1250	14	5	9
2	A	131.04	36.08	1000 1500	0.98	0.02	420	11.20	7800	18	2	16
	B			1250 1500	0.85	0.06	101	2.70	1900		6	12
3	A	132.00	37.04	1000 1500	0.78	0.06	111	2.96	2122	16	2	14
	B			1250 1500	0.86	0.06	106	2.82	1990		2	14
4	A	131.60	37.20	1000 2000	0.48	0.07 (0.12)	86 (51)	2.30 (1.36)	1820	23	8 (14)	15 (9)
	B			1250 2000	0.45	0.09 (0.17)	70 (37)	1.86 (1.00)	1490		9 (17)	14 (5)
	C			1500 2000	0.44	0.11 (0.25)	54 (25)	1.44 (0.67)	1110		9 (21)	14 (2)
U5		131.72	37.29	1000 2000	0.89	0.03 (0.05)	238 (124)	6.34 (3.31)	4990	5	1 (2)	4 (3)

R is the ratio of the spectra of U_r components between two different depths, κ is the horizontal wavenumber, λ is the wavelength, C is the phase velocity, and μ is vertical trapping scale. The estimated angle (θ_e) of the principle major axis at the lower depth and the angles (θ_t) predicted by the linear TRW dispersion relation are measured clockwise from the downslope for the period band of 30–50 days. The difference between the angles (θ_d) is measured. θ_t and θ_d are also measured using the mean buoyancy frequency from the observed CTD data for Case 4 in parentheses.

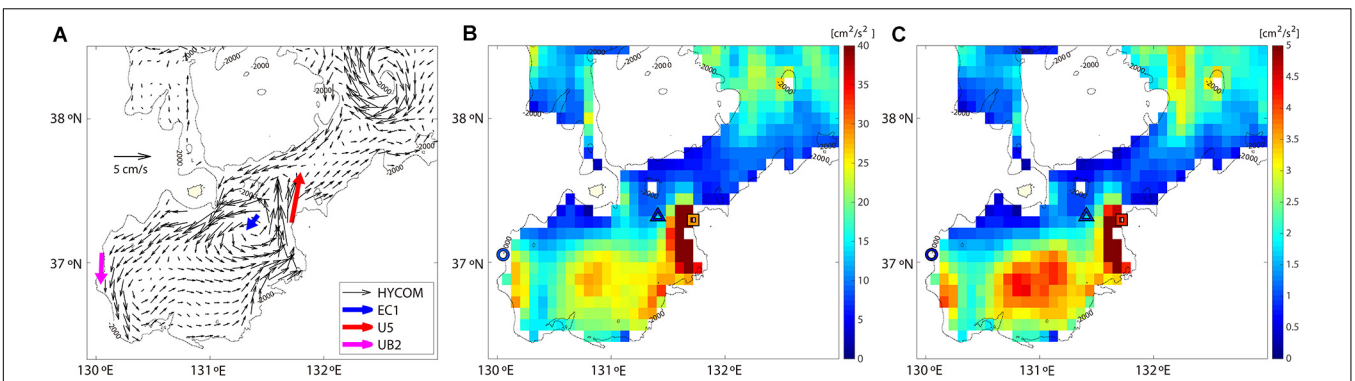

FIGURE 4 | Statistics of deep currents reproduced by HYCOM reanalysis data and moored data. **(A)** Mean velocity field using HYCOM data and moored data at EC1, U5, and UB2 (black, blue, red, and purple arrows, respectively), and variance of *v* currents for **(B)** unfiltered case and **(C)** longer intraseasonal band. In panels **(B,C)**, the colors of the symbols for EC1 (triangle), U5 (square), and UB2 (circle) denote the variance of the observed *v* currents with the same scale shown in the right color bar.

at 2000 m at U5, indicating bottom intensification. The mean and fluctuating currents (particularly at the longer intraseasonal band) are intensified at U5 on the eastern side near Dokdo, indicating eastward intensification.

Comparison of Observed and Reanalyzed Abyssal Currents

The HYCOM deep currents in the UB and UIG show cyclonic circulation along the 2000 m isobath, which consists of a weak

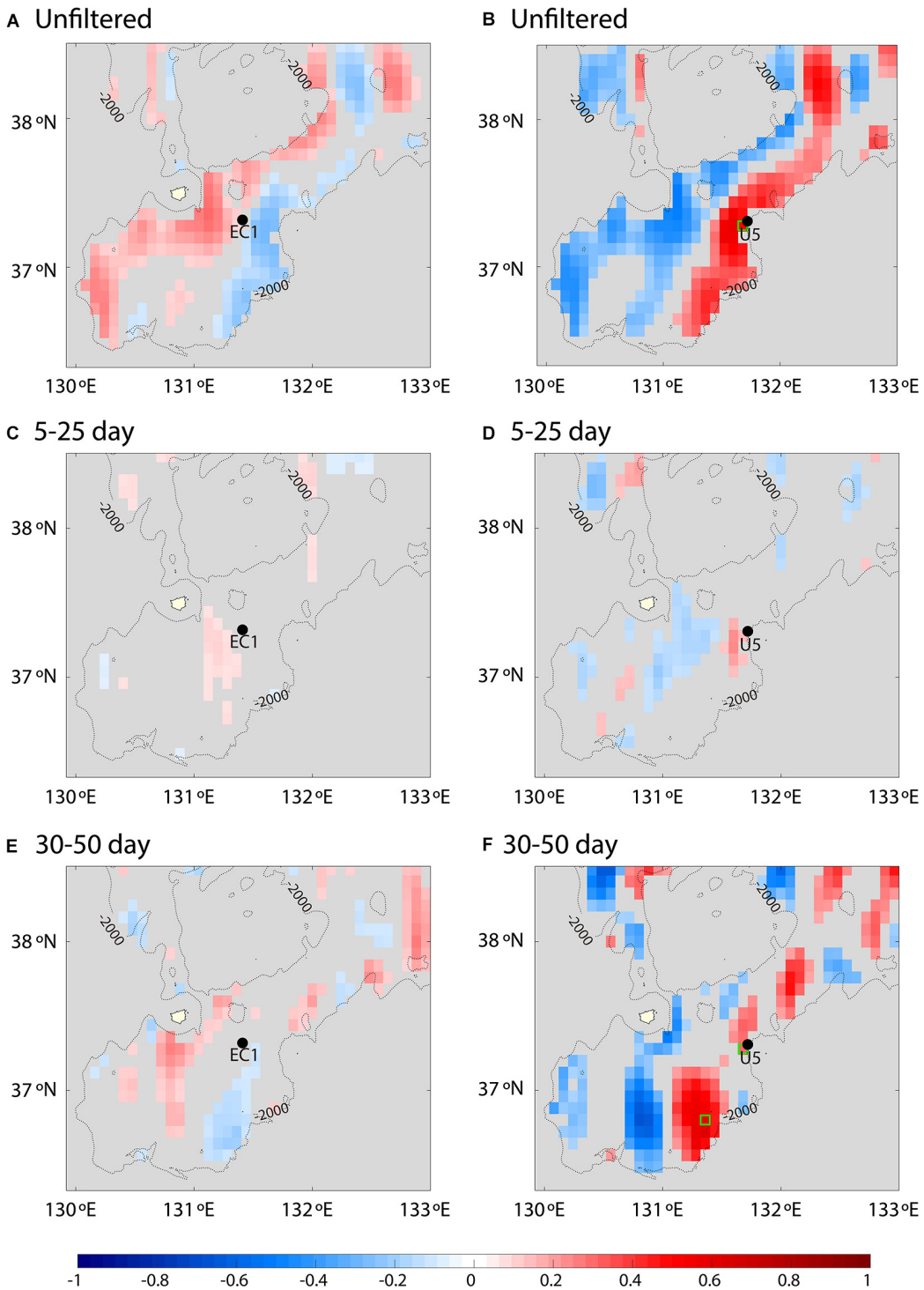

FIGURE 5 | Correlation (values below 95% confidence level are discarded) between modeled (HYCOM) and observed *v* currents for EC1 (left) and U5 (right) at 2000 m for **(A,B)** the whole period band, **(C,D)** shorter intraseasonal bands, and **(E,F)** longer intraseasonal bands. Grids selected for comparison of observed and modeled abyssal currents are marked by green squares.

southward inflow to the UB in the western UB and UIG, a weak eastward flow in the interior and southern UB, a strong northward outflow from the UB in the eastern UB and UIG, and smaller cyclonic circulation near EC1 (**Figure 4A**). The cyclonic deep and abyssal circulation are consistent with the observations at EC1, U5, and UB2. The spatial distribution of *v*

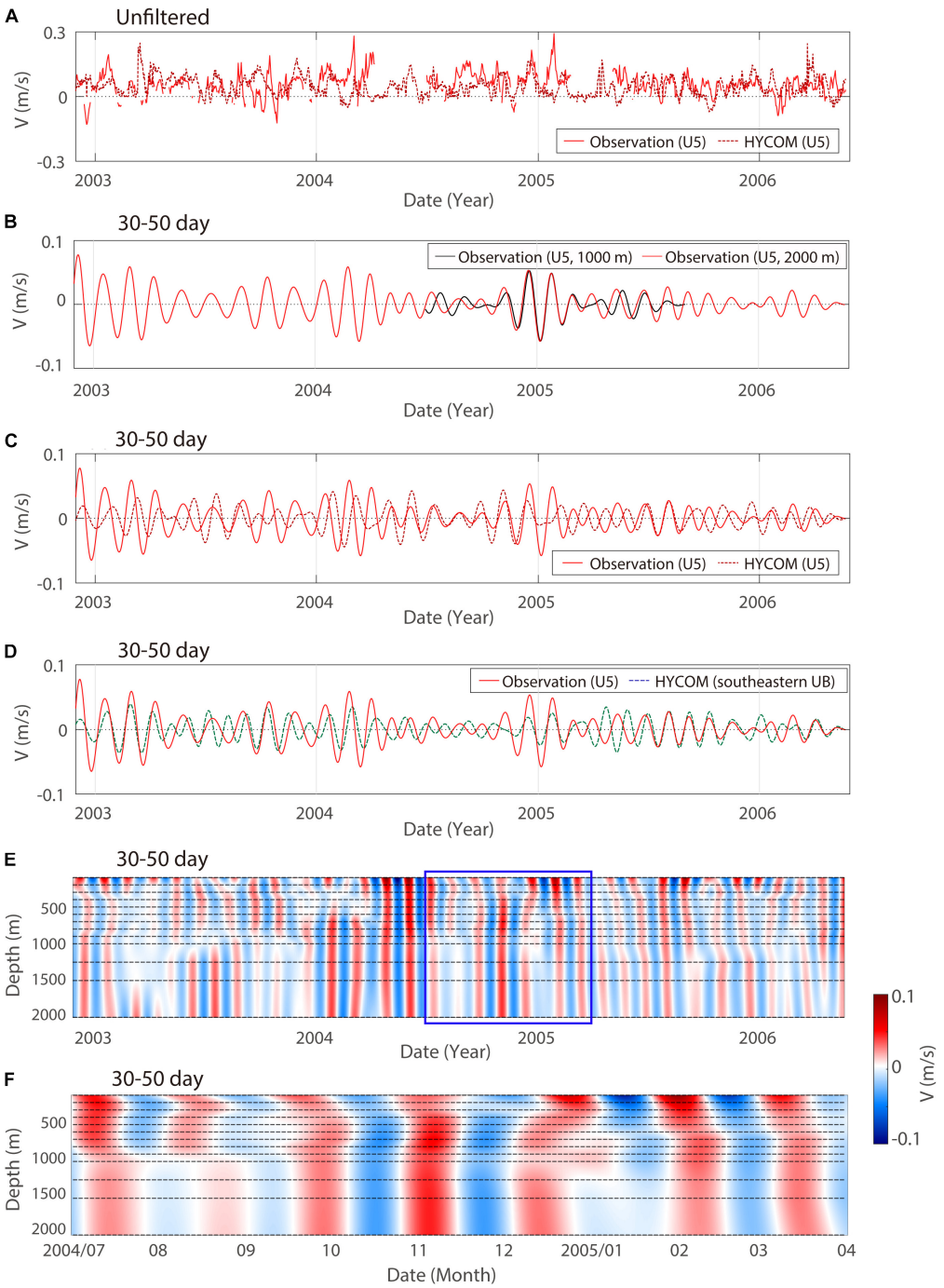

FIGURE 6 | Time series of modeled (dashed) and observed (solid) *v* currents at 2000 m of the locations of **(A,C)** U5 and **(D)** southeastern UB (green squares in **Figure 5**) for the **(A)** unfiltered and **(C,D)** longer intraseasonal band. Those of *v* currents observed at 1000 m (black) and 2000 m (red) of the location of U5 are compared in panel **(B)**. Time-depth contours of modeled *v* currents are shown for longer intraseasonal band at U5 for **(E)** total period and **(F)** period from July 2004 to April 2005. The HYCOM depth levels are denoted by black dotted horizontal lines in panels **(E,F)**.

variance at the longer intraseasonal band shows severe variability in the eastern UIG and UB, which accounts for most of the *v* variance (**Figures 4B,C**). The eastward intensification of *v* is also consistent with the observations in EC1, U5, and UB (**Figures 4B,C** and **Table 1**).

The spatial distribution of the correlation between the reanalyzed and observed *v* at EC1 and U5 in the non-filtered case, and the shorter and longer intraseasonal bands, is shown in **Figure 5**. The correlation of the non-filtered *v* current shows the tendency for asymmetric flow between the eastern and western

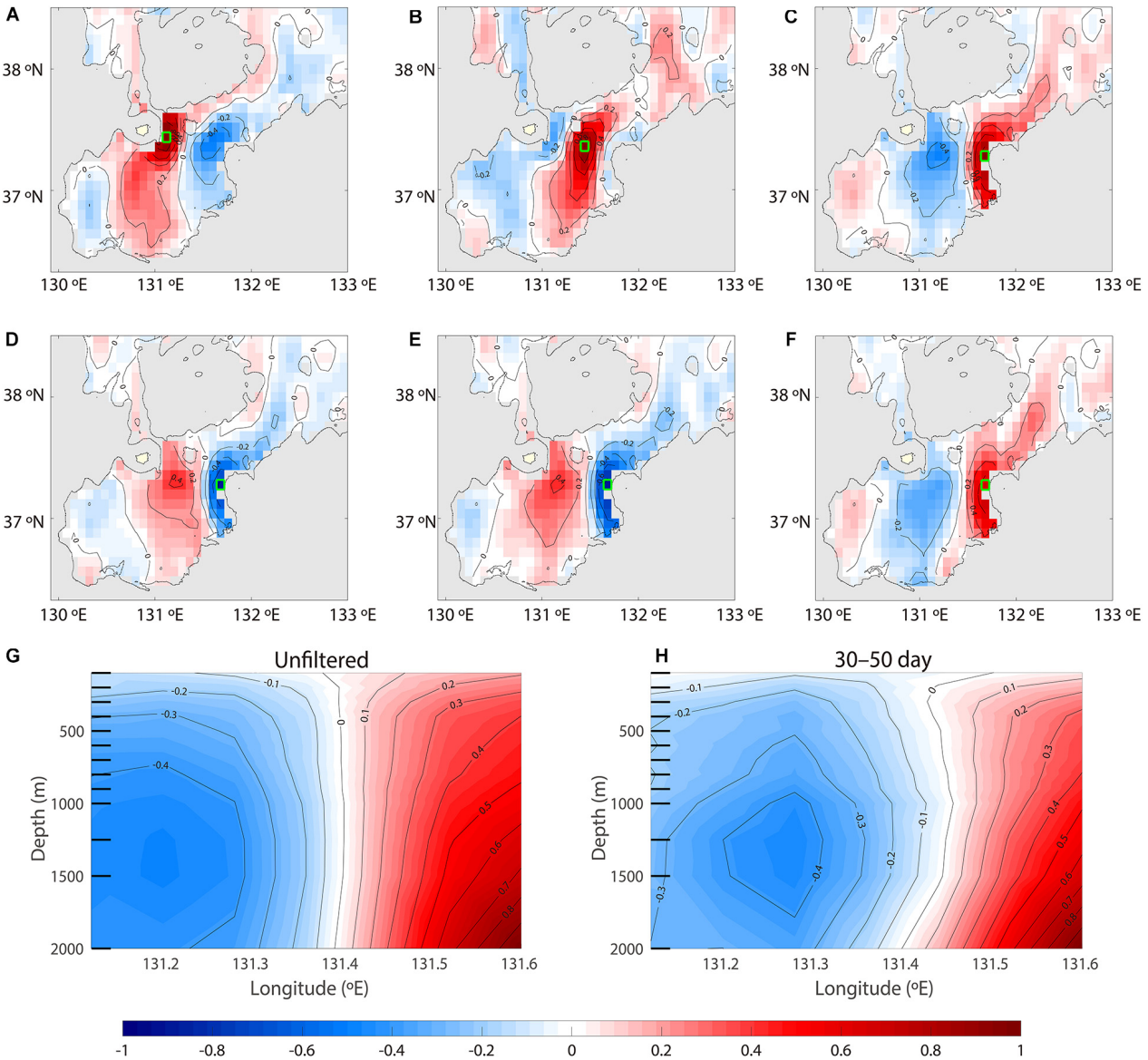

FIGURE 7 | Correlation map, with no lag, of HYCOM deep currents with those in **(A)** the western UIG, **(B)** central UIG (nearest to EC1), and **(C)** eastern UIG (nearest to U5), for the longer intraseasonal band with contours every 0.2 from −1.0 to 1.0. A lagged correlation map in the eastern UIG **(D)** before 20 days, **(E)** after 20 days, and **(F)** after 5 days. Grids of referenced HYCOM currents are marked by green squares. The correlation map, with no lag, of HYCOM meridional currents with those in deep eastern UIG (U5) are shown across the vertical UIG section **(G)** without and **(H)** with band-pass filtering (longer intraseasonal band). The HYCOM depth levels are denoted by left axis ticks in panels **(G,H)**.

UIG and UB. Although there was no significant correlation in the shorter intraseasonal band at EC1 and U5, marginally significant correlations with the longer intraseasonal band at U5 were found in large areas of the UB and UIG. However, as EC1 is located in the central UIG, which reveals a relatively clear tendency of asymmetric flow in the longer intraseasonal band, it represents the western UIG.

The marginally significant correlations in the longer intraseasonal band v observed at U5 were confirmed in the time series plots (**Figure 6**). At U5, the reanalyzed v at 2000 m is not highly correlated with the observation at U5 for the longer intraseasonal band, although it is statistically significant (correlation coefficient: ∼0.30; **Figure 6C**). A better correlation (∼0.57) with the observation is found in the southeastern UB (green square in **Figure 5F**), where the reanalyzed and observed v at 2000 m are generally consistent in both phase and amplitude (**Figure 6D**). The reanalyzed and observed v are not only marginally correlated but also consistent in terms of amplitude and vertical propagation. Vertical phase propagation was not significant for both observations and reanalyzed v except for the upper depths, particularly between 1000 and 2000 m (**Figures 6B,E,F**). At U5, the lagged cross-correlation

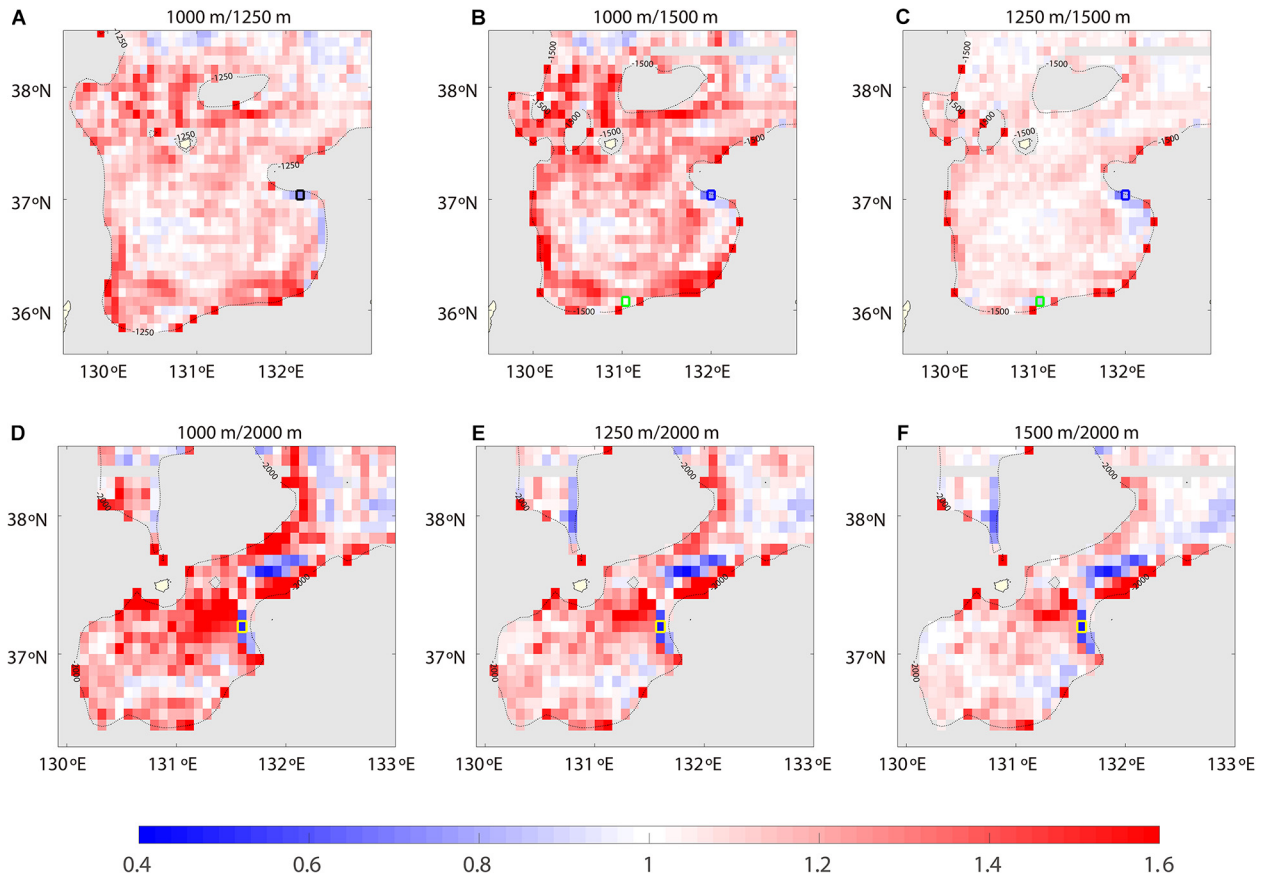

FIGURE 8 | Spatial distribution of R for the longer intraseasonal band between two different depths for **(A)** 1000 and 1250 m, **(B)** 1000 and 1500 m, **(C)** 1250 and 1500 m, **(D)** 1000 and 2000 m, **(E)** 1250 and 2000 m, and **(F)** 1500 and 2000 m. Grids where R is below 1 indicate bottom intensification and the four selected cases where the bottom intensification is distinct are marked by squares.

reached its maximum (0.79) at zero lag for reanalysis v at 1000 and 2000 m.

Characteristics of Intraseasonal Abyssal Current Variability and TRWs

Spatially Coherent Abyssal Current Variability in the Intraseasonal Band

The correlation maps of reanalyzed v show wave-like spatially coherent patterns in the western, central (corresponding to EC1), and eastern (corresponding to U5) UIG v at 2000 m (**Figures 7A–C**). The results show an opposing sign between the western and eastern sides of the UIG and UB, implying that waves were constrained by basin geometry; for example, the normal mode. The horizontal width of the coherent pattern with a positive correlation is wide at the western and narrow at the eastern UIG and UB, consistent with the asymmetrical characteristics of the observed and reanalyzed mean currents ($\bar{u}$, $\bar{v}$). The wave-like patterns with a phase change every ∼80 km indicate wavelengths comparable to the scale in this region.

Regarding the phase change, a nearly identical spatial pattern of the correlation map v was obtained with time lags before and after 20 days (half the longer intraseasonal band v). Phase changes from positive to negative and back again were observed (**Figures 7D,E**), although no significant change was observed after a 5-day lag (**Figures 7C,F**). Cross-sectional correlation maps support both the eastward and bottom intensification of the longer intraseasonal DAC oscillations, yielding e-folding decorrelation length scales of ∼11 km in the cross-slope and ∼1400 m in the vertical direction (**Figures 7G,H**). The ratio between the vertical and cross-slope scales, 0.13 (= 1400/11000), which is more than double the bottom slope at U5 (0.06, **Table 2**), is discussed in the next section. Such high ratio supports even strongly bottom-trapped or first baroclinic structures vertically (note that zero-crossing depth corresponds to the thermocline at approximately 100 m). These dominant correlation patterns, along with the eastward intensification of the intraseasonal current oscillations, raise the possibility of bottom-trapped TRW or the first mode of baroclinic Rossby waves, as presented in the next section.

Characteristics of Bottom-Trapped TRWs

Bottom intensification with a stronger HYCOM current at lower depths ($R < 1$) is found at the eastern UB and UIG along the 1250, 1500, and 2000 m isobaths, particularly near Dokdo (**Figure 8**). Although there are a few grids beyond the eastern

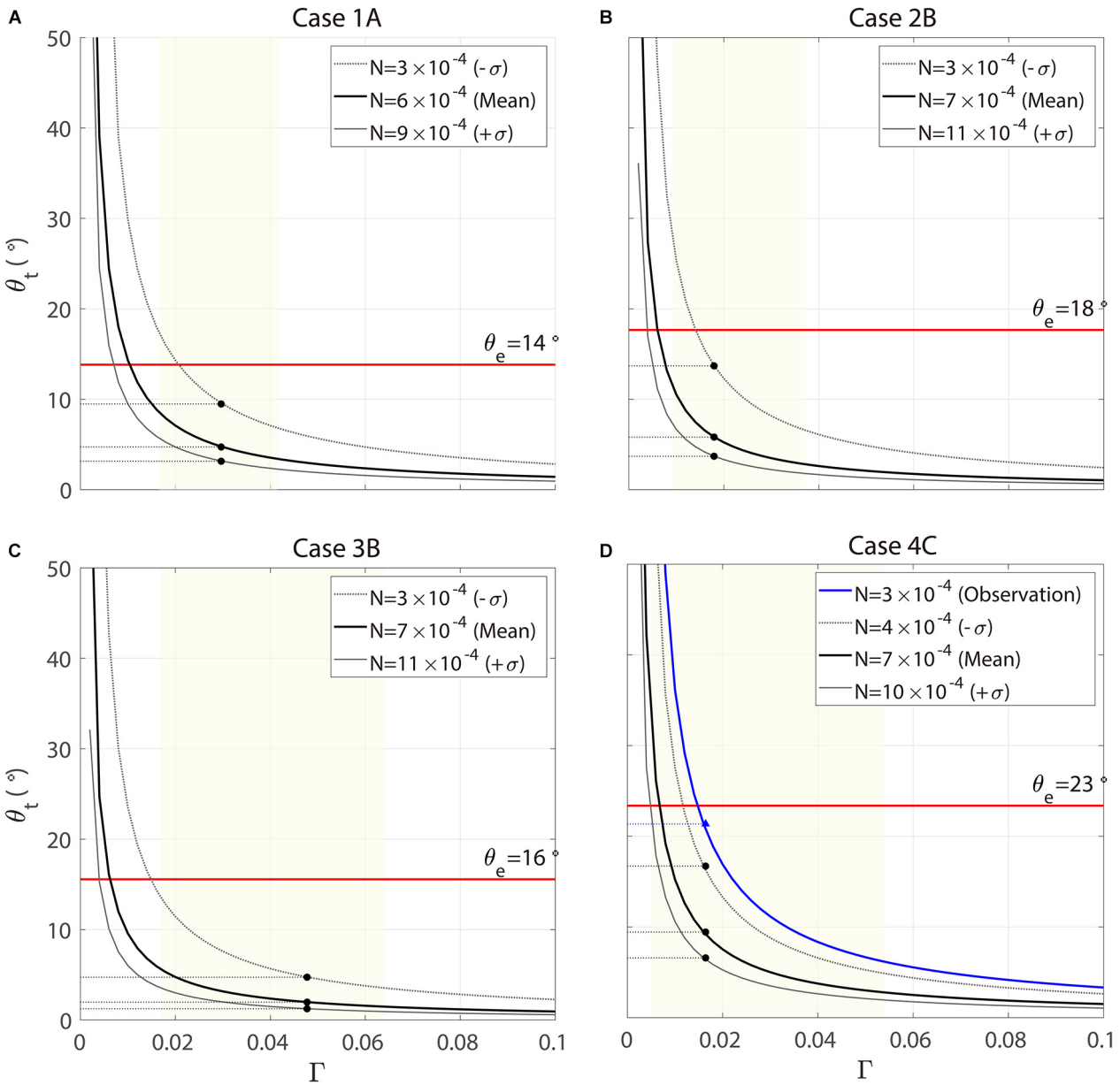

FIGURE 9 | Sensitivity analysis for TRW parameters with bottom slope and buoyancy frequency for **(A)** Case 1A, **(B)** Case 2B, **(C)** Case 3B, and **(D)** Case 4C. The horizontal red line denotes the estimated angle (θ_e), and black dots denote the corresponding slope of the predicted angles of that grid for the mean and one standard deviation above and below the mean buoyancy frequency from the HYCOM reanalysis data (gray, gray dashed, and black lines, respectively). The adjacent slope range to each grid is shown for the yellow-shaded areas. For Case 4C, the blue line denotes the mean buoyancy frequency from the observed CTD data.

side where R is less than 1.00 (e.g., in the southern UB and western interior UB), the minimum value of R is 0.91. This is significantly higher than the R values in the eastern DAC near Dokdo. Thus, the bottom-trapped TRW theory is primarily applicable for areas limited to the eastern side of the UIG and UB, where the minimum value of R is 0.45 (**Figures 8D–F**). The bottom and eastward intensification of the longer intraseasonal current variability is consistent with the observed characteristics presented in the previous section, and is characterized in association with bottom-trapped TRWs.

The horizontal wavenumber, wavelength, phase speed, orientation angle of the wavenumber vector (from the two methods), and vertical trapping scale listed in **Table 3** provide the characteristics of bottom-trapped TRWs that explain the observed abyssal current variability in the longer intraseasonal band. A small (<16°) difference in the orientation angle exists between the two methods (θ_d) for the eight cases from HYCOM reanalysis and observation at U5 (**Table 3**). The observational results, in comparison to the corresponding HYCOM case (Case 4A), show weaker bottom intensification (higher R),

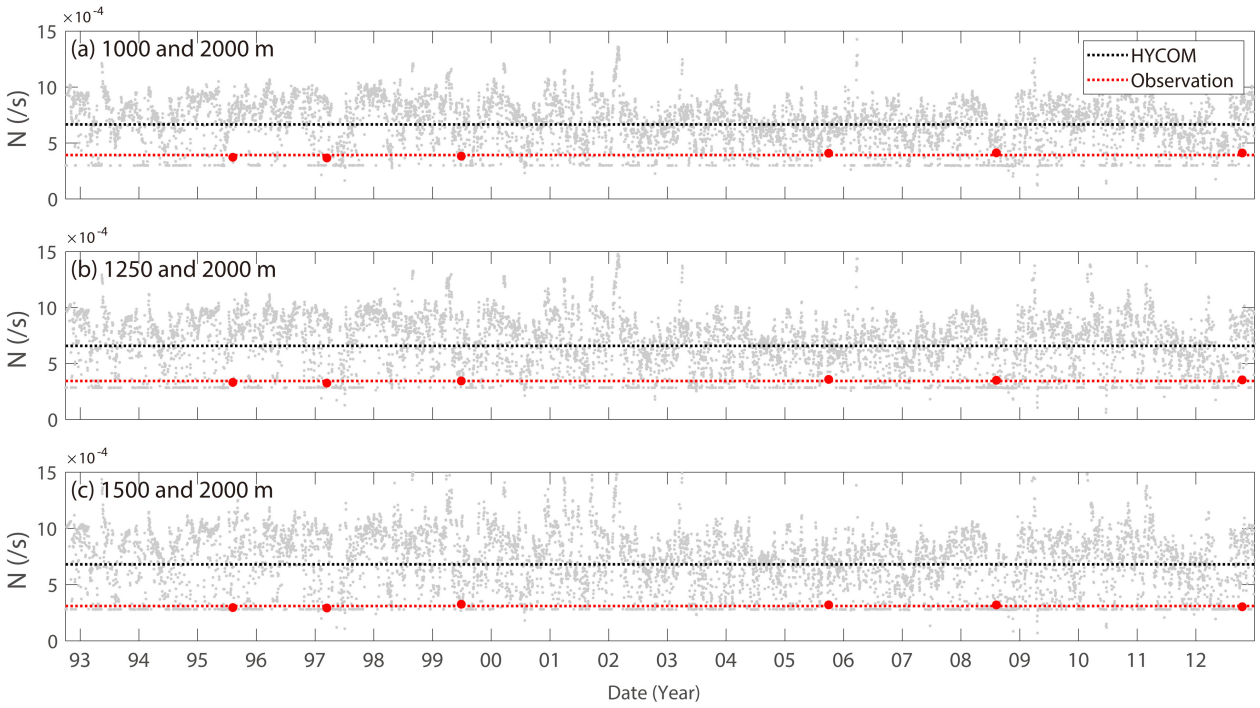

FIGURE 10 | Time series of buoyancy frequency between two depths using HYCOM data for Case 4 (gray dots). The CTD data taken near the grid in Case 4 are marked by red dots. The horizontal bars refer to the mean buoyancy frequency of the HYCOM data (black line) and CTD data (red line) at **(a)** 1000 and 2000 m, **(b)** 1250 and 2000 m, and **(c)** 1500 and 2000 m.

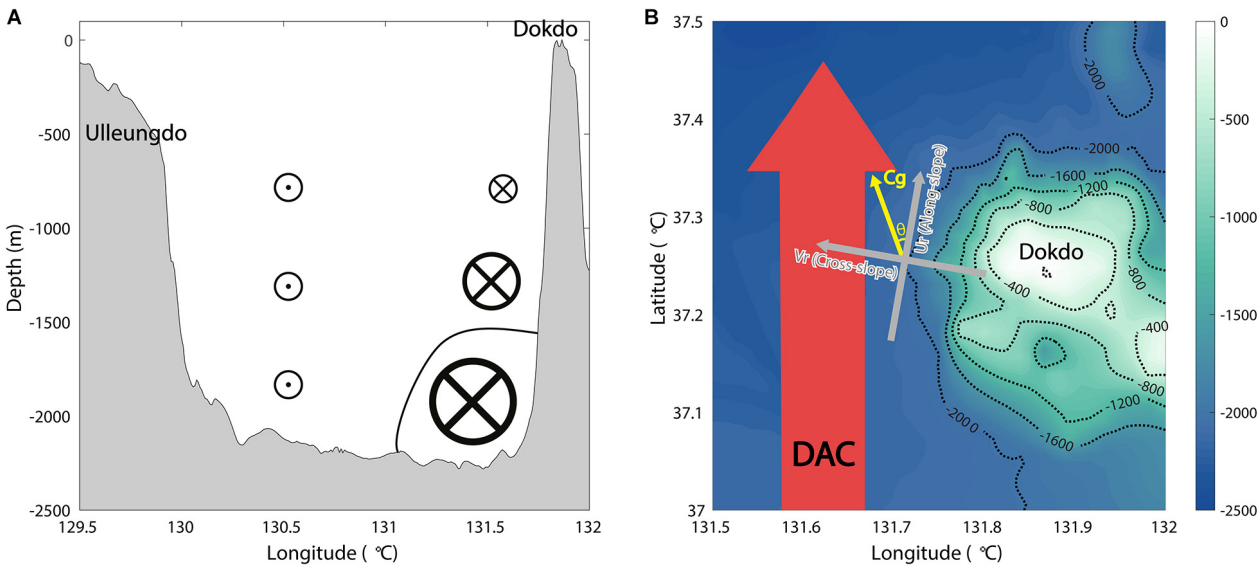

FIGURE 11 | Schematic of the TRWs. **(A)** Side view at 37.25°N between Ulleungdo and Dokdo. **(B)** Detailed bathymetry near Dokdo with isobaths every 400 m. The angle (θ) indicates the direction of the wavenumber vector.

resulting in longer wavelength, larger vertical trapping scale, lower propagating speed, and smaller θ_e. The HYCOM results yield wavelengths of 54–86 km and a propagating speed of 1.44–2.30 km day^{-1} for Case 4, in which the bottom intensification is the strongest. The vertical trapping scales of the HYCOM results are 1110–1820 m, which is consistent with the vertical structure (not shown) for Case 4. Meanwhile, θ_d ranges from 9° to 16° over all HYCOM cases, which is systematically biased to a positive value (i.e., a systematically small θ_t compared to θ_e), as discussed in the next section.

DISCUSSION

The results of the orientation angle derived from the theoretical dispersion relation (θ_t) of Eq. (4) may be sensitive to the bottom slope (Γ) and buoyancy frequency (N). The sensitivity tests result in a range of θ_t typically less than 10° for the given range of the bottom slope in the case area (shaded area in **Figure 9**), and the buoyancy frequency obtained from the HYCOM stratification (±1 standard deviation from the mean, lines in **Figure 9**). Such a robust theoretical orientation angle of bottom-trapped TRWs (θ_t) cannot explain why θ_t is systematically smaller than the orientation angle derived from the spectra of U_r and V_r (θ_e) using Eq. (3), which is consistent with the observed currents. Interestingly, when compared with the CTD data ($N = \sim 3 \times 10^{-4}$ s^{-1}), the HYCOM reanalysis overestimates the mean buoyancy frequency (N) in the deep UB and UIG by $\sim 4 \times 10^{-4}$ s^{-1} (**Figure 10**), which results in an overestimation of θ_t and θ_d for Case 4 of ∼6°–12° (**Table 3**). The parameters of TRWs using the observed N (**Table 3** in parentheses and the blue line in **Figure 9D**) show a decrease in wavelength from 54 to 25 km and in propagating speed from 1.44 to 0.67 km day^{-1} for Case 4c. The θ_t increases from 9° to 21° with the observed N, significantly decreasing θ_d from 14° to 2°. The resultant θ_d is thus within the range of uncertainty of HYCOM reanalysis data, supporting the significance of bottom-trapped TRWs in accordance with the observed stratification at the eastern side of UIG and UB.

The primary sources of TRW energy have been suggested by previous studies (Hamilton, 1990, 2007, 2009; Pickard, 1995; Auad et al., 1998; Oey et al., 2009; Oey, 2008; Shu et al., 2016). Energetic motions, such as mesoscale eddies and the meandering of the Tsushima Current, may play a role in the intraseasonal current variability in the upper layer of the southwestern East Sea, including the UB and UIG (Mitchell et al., 2005; Teague et al., 2005; Xu et al., 2009). In particular, Kim et al. (2013) reported that TRWs with periods of 10.7 and 21.3 day are generated from upper warm events (passing by the anticyclonic eddy), whereas those with periods of 40 days are less correlated with the upper warm events. The enhanced current oscillations observed (U5) and reanalyzed at the upper and lower depth levels at the longer intraseasonal band are significantly correlated with each other but less correlated with satellite altimeter-derived surface geostrophic current (not shown). Instead, these oscillations tend to intensify in winter when the longer intraseasonal band fluctuation of sea surface wind is also significant. The cause of the bottom-trapped TRWs responsible for the longer intraseasonal current variability is still obscure and needs further study.

In this study, the bottom-trapped TRW theory was applied to examine the bottom and eastward-intensified, longer intraseasonal variability in the abyssal current focusing on the eastern side of the UB and UIG. The relative importance of bottom trapping (baroclinic mode) vs. geostrophic motion (barotropic mode) can be easily evaluated with the index of $\Gamma N/f_0$ (Rhines, 1970), which is consistent with the stratification parameter (Wang and Mooers, 1976). For a given stratification and Coriolis parameter, a strong bottom trapping or baroclinic mode is dominant only when the slope is steep enough to bring the index close to or higher than the unity (high stratification parameter); otherwise, the motion is almost geostrophic or barotropic (low stratification parameter), as the index is much less than the unity with a gentle slope. For most of the UB and UIG areas, $\Gamma N/f_0 = \sim 0.1$ or < 1, and $\Gamma N/f_0 = \sim 1$ or > 1 only at limited locations on the eastern sides (**Figure 8**), indicating that the barotropic mode of TRWs significantly contributes to the abyssal current variability in these areas. However, in the limited area of the steeply sloped eastern side of the UB and UIG (e.g., U5), $\Gamma N/f_0$ becomes much higher than the unity, with a high ratio between the vertical and cross-slope decorrelation scales at U5 (**Figure 7H**) indicating the dominant bottom-trapped or first baroclinic mode. Meanwhile, as the UB can be regarded as a closed basin, the existence of a normal mode is possible (Pedlosky, 1987). The horizontal wavelength estimated herein based on bottom-trapped TRW theory (49–111 km) is consistent with that of the first normal mode baroclinic Rossby waves for an equivalent depth and eigenvalue imposed by the closed basin scale on the order of 100 km. The estimation is also reasonable based on the correlation maps shown in **Figures 7A–F**. Further studies on the modes of Rossby waves besides the bottom-trapped mode (barotropic and baroclinic modes) are needed to fully understand the intraseasonal variability in the abyssal and upper currents in the region.

In other regions where bottom-trapped TRWs dominate the intraseasonal deep or abyssal current variability (**Figure 1**), the dominant wave period is shorter than 30 days, except in the central and western parts of the Gulf of Mexico where dominant periods range from 20 to 100 days (Thompson and Luyten, 1976; Hamilton, 1990, 2007; Auad et al., 1998; Shu et al., 2016). One noticeable characteristic of UB and UIG is that their observed N (from CTD observations) is one order of magnitude smaller than that in the other regions. This increases the wavenumber from 0.05 to 0.1 km^{-1} and decreases the wavelength from 130 to 50 km, as shown by $R = 0.5$ in Eq. (2). Despite the small N, however, no significant differences in the wavenumber of bottom-trapped TRWs and propagating speed (which are one order of magnitude smaller because of the relatively longer intraseasonal band) are shown from those in the other regions because the small N is compensated by Γ and R, which shape the typical characteristics of TRWs in the UB and UIG.

CONCLUSION

To characterize and address the bottom-trapped TRWs underlying the longer-period intraseasonal variability of abyssal currents in the southwest East Sea (time scale of 30–50 days), multi-year moored current observations and HYCOM reanalysis were examined. The reanalysis data in the UB and UIG showed significant correlations (maximum 0.57 in the northeast UB) of the observed abyssal current variability in the intraseasonal band in the eastern UIG (U5), but with opposite signs: positive in the eastern region and negative in the western regions.

The bottom-trapped TRWs in the eastern UB and UIG were responsible for the bottom-intensified current variability, based on the wavelength ranging from 49 to 111 km, propagating speed ranging from 1.3 to 3.0 km day^{-1}, a vertical trapping scale ranging from 1100 to 2100 m, and the orientation angle of the group velocity from the isobath direction ranging from 2° to 23°, except for one case (Case 2A). The orientation angle was estimated using two methods: one from the along-slope and cross-slope currents (U_r and V_r) of the observed and modeled deep intraseasonal current fluctuations (θ_e), and the other from the theoretical dispersion relation of the bottom-trapped TRWs for a given buoyancy frequency and bottom slope (θ_t). The two orientation angles ranged from 14° to 23° and from 2° to 9°, respectively, yielding a relatively small (16° at the most) but positively biased difference (θ_d), in which the latter was mostly explained by the overestimation of stratification in the reanalyzed data. The results were robust (insensitive) to a reasonable range of buoyancy frequency and bottom slope in the region, suggesting that the bottom-trapped TRWs were responsible for the energetic abyssal circulation at the limited location of the eastern UB and UIG, where the bottom slope is sufficiently steep.

This study supports the important role of bottom-trapped TRWs in shaping the abyssal current variability in the eastern UIG and UB, strongly implying the exchange of water and materials between two deep basins in the East Sea: the UB in the southwest and the JB in the north. Abyssal currents are energetic as bottom-trapped TRWs propagate at a shallow depth, Dokdo, to the right (**Figure 11**). With the abyssal current variability at shorter intraseasonal periods (10–20 days) found previously, the TRWs are responsible for energetic longer intraseasonal band variabilities in the abyssal circulations in the areas of steep slope in the eastern UIG and UB. More observations are needed to further verify the HYCOM results and improve our understanding of deep, abyssal, and overturning circulation in these areas, including the barotropic and other baroclinic modes of TRWs with complex topography, as in the southwestern East Sea.

DATA AVAILABILITY STATEMENT

Publicly available datasets were analyzed in this study. This data can be found here: http://doi.org/10.17882/72344; http://doi.org/10.17882/58134; http://hycom.org; http://www.marine.copernicus.

AUTHOR CONTRIBUTIONS

All authors contributed to the article in multiple ways. SHN and JS designed the study. JS and SN performed the data processing and analysis. SHN, JS, and SN performed the synthesis and overall coordination. SHN, JS, and SN contributed to writing through discussion. SHN and SN contributed to revising through review.

FUNDING

This research was a part of the project titled 'Deep Water Circulation and Material Cycling in the East Sea,' funded by the Ministry of Oceans and Fisheries, South Korea. This work was partly supported by the Institute Civil Military Technology Cooperation, South Korea (18-SN-RB-01).

ACKNOWLEDGMENTS

We would like to thank Editage for English language editing and reviewers for their constructive comments, and Yun-Bae Kim and Kyung-Il Chang for providing current and hydrographic data.

REFERENCES

Auad, G., Hendershott, M. C., and Winant, C. D. (1998). Wind-induced currents and bottom-trapped waves in the Santa Barbara Channel. *J. Phys. Oceanogr.* 28, 85–102. doi: 10.1175/1520-04851998028<0085:WICABT<2.0.CO;2

Chang, K. I., Kim, K., Kim, Y. B., Teague, W. J., Lee, J. C., and Lee, J. H. (2009). Deep flow and transport through the Ulleung Interplain Gap in the southwestern East/Japan Sea. *Deep Sea Res. Part I Oceanogr. Res. Pap.* 56, 61–72. doi: 10.1016/j.dsr.2008.07.015

Fofonoff, N. P. (1969). Spectral characteristics of internal waves in the ocean. *Deep Sea Res.* 16, 59–71.

Hamilton, P. (1990). Deep currents in the Gulf of Mexico. *J. Phys. Oceanogr.* 20, 1087–1104. doi: 10.1175/1520-04851990020<1087:DCITGO<2.0.CO;2

Hamilton, P. (2007). Deep-current variability near the Sigsbee Escarpment in the Gulf of Mexico. *J. Phys. Oceanogr.* 37, 708–726. doi: 10.1175/JPO 2998.1

Hamilton, P. (2009). Topographic rossby waves in the Gulf of Mexico. *Prog. Oceanogr.* 82, 1–31. doi: 10.1016/j.pocean.2009.04.019

Hamilton, P., and Lugo-Fernandez, A. (2001). Observations of high speed deep currents in the northern Gulf of Mexico. *Geophys. Res. Lett.* 28, 2867–2870.

Han, M. H., Cho, Y.-K., Kang, H.-W., and Nam, S. (2020). Decadal changes in meridional overturning circulation in the East Sea (Sea of Japan). *J. Phys. Oceanogr.* 50, 1773–1791. doi: 10.1175/JPO-D-19-0248.1

Hogan, P. J., and Hurlburt, H. E. (2006). Why do intrathermocline eddies form in the Japan/East Sea? *Model. Perspect. Oceanogr.* 19, 134–143.

Kim, Y. B., Chang, K. I., Park, J. H., and Park, J. J. (2013). Variability of the dokdo abyssal current observed in the Ulleung Interplain Gap of the East/Japan Sea. *Acta Oceanol. Sin.* 32, 12–23.

Mitchell, D. A., Teague, W. J., Wimbush, M., Watts, D. R., and Sutyrin, G. G. (2005). The DOK cold eddy. *J. Phys. Oceanogr.* 35, 273–288. doi: 10.1175/JPO-2684.1

Nam, S. H., Yoon, S.-T., Park, J.-H., Kim, Y. H., and Chang, K.-I. (2016). Distinct characteristics of the intermediate water observed off the east coast of Korea during two contrasting years. *J. Geophys. Res. Oceans* 121, 5050–5068.

Noh, S., and Nam, S. (2018). *EC1, Mooring Time Series Since 1996*. SEANOE, doi: 10.17882/58134

Noh, S., Nam, S., Kim, Y. B., and Chang, K. I. (2020). *Deep Moored Current and Hydrographic Measurements in Southwestern East Sea (Japan Sea)*. SEANOE, doi: 10.17882/72344

Oey, L. Y. (2008). Loop current and deep eddies. *J. Phys. Oceanogr.* 38, 1426–1449. doi: 10.1175/2007JPO3818.1

Oey, L. Y., Chang, Y. L., Sun, Z. B., and Lin, X. H. (2009). Topocaustics. *Ocean Model.* 29, 277–286.

Oey, L. Y., and Lee, H. C. (2002). Deep eddy energy and topographic Rossby waves in the Gulf of Mexico. *J. Phys. Oceanogr.* 32, 3499–3527.

Pedlosky, J. (ed.). (1987). "Quasigeostrophic motion of a stratified fluid on a sphere," in *Geophysical Fluid Dynamics*. New York, NY: Springer, doi: 10.1007/978-1-4612-4650-3_6

Pickard, R. S. (1995). Gulf Stream–generated topographic Rossby waves. *J. Phys. Oceanogr.* 25, 574–586. doi: 10.1175/1520-04851995025<0574:GSTRW<2.0.CO;2

Reid, R. O., and Wang, O. (2004). Bottom-trapped Rossby waves in an exponentially stratified ocean. *J. Phys. Oceanogr.* 34, 961–967. doi: 10.1175/1520-04852004034<0961:BRWIAE<2.0.CO;2

Rhines, P. (1970). Edge-, bottom-, and Rossby waves in a rotating stratified fluid. *Geophys. Astrophys. Fluid Dyn.* 1, 273–302. doi:10.1080/03091927009365776

Shu, Y., Xue, H., Wang, D., Chai, F., Xie, Q., Cai, S., et al. (2016). Persistent and energetic bottom-trapped topographic Rossby waves observed in the southern South China Sea. *Sci. Rep.* 6:24338. doi: 10.1038/srep24338

Teague, W. J., Tracey, K. L., Watts, D. R., Book, J. W., Chang, K. I., Hogan, P. J., et al. (2005). Observed deep circulation in the Ulleung Basin. *Deep Sea Res. Part II Top. Stud. Oceanogr.* 52, 1802–1826. doi: 10.1016/j.dsr2.2003.10.013

Thompson, R. O., and Luyten, J. R. (1976). Evidence for bottom-trapped topographic Rossby waves from single moorings. *Deep Sea Res. Oceanogr. Abstracts* 23, 629–635. doi: 10.1016/0011-7471(76)90005-X

Uehara, K., and Miyake, H. (2000). Biweekly periodic deep flow variability on the slope inshore of the Kuril–Kamchatka Trench. *J. Phys. Oceanogr.* 30, 3249–3260. doi: 10.1175/1520-04852000030<3249:BPDFVO<2.0.CO;2

Wang, D., and Mooers, C. N. (1976). Coastal-trapped waves in a continuously stratified ocean. *J. Phys. Oceanogr.* 6, 853–863. doi: 10.1175/1520-04851976006<0853:CTWIAC<2.0.CO;2

Watts, D. R., Kennelly, M. A., Donohue, K. A., Tracey, K. L., Chereskin, T. K., Weller, R. A., et al. (2013). Four current meter models compared in strong currents in Drake Passage. *J. Atmos. Oceanic Technol.* 30, 2465–2477. doi: 10.1175/JTECH-D-13-00032.1

Welch, P. (1967). The use of fast Fourier transform for the estimation of power spectra: a method based on time averaging over short, modified periodograms. *IEEE Trans. Audio Electr.* 15, 70–73. doi: 10.1109/TAU.1967.1161901

Xu, Y., Watts, D. R., and Wimbush, M. (2009). Coupled patterns between fields of dynamic height and bottom pressure in the Japan/East Sea. *Ocean Sci. J.* 44, 35–42. doi: 10.1007/s12601-009-0005-4

Conflict of Interest: The authors declare that the research was conducted in the absence of any commercial or financial relationships that could be construed as a potential conflict of interest.

frontiers in Marine Science

ORIGINAL RESEARCH
published: 30 November 2020
doi: 10.3389/fmars.2020.565982

South Adriatic Recipes: Estimating the Vertical Mixing in the Deep Pit

Vanessa Cardin[1]*, *Achim Wirth*[2], *Maziar Khosravi*[1,3] and *Miroslav Gačić*[1]

[1] Istituto Nazionale di Oceanografia e di Geofisica Sperimentale - OGS, Trieste, Italy, [2] Université Grenoble Alpes, CNRS, Grenoble INP, LEGI, Grenoble, France, [3] Programme for Training and Research in Italian Laboratories (TRIL) Programme, Abdus Salam International Center for Theoretical Physics - ICTP, Trieste, Italy

The available historical oxygen data show that the deepest part of the South Adriatic Pit remains well-ventilated despite the winter convection reaching only the upper 700 m depth. Here, we show that the evolution of the vertical temperature structure in the deep South Adriatic Pit (dSAP) below the Otranto Strait sill depth (780 m) is described well by continuous diffusion, a continuous forcing by heat fluxes at the upper boundary (Otranto Strait sill depth) and an intermittent forcing by rare (several per decade) deep convective and gravity-current events. The analysis is based on two types of data: (i) 13-year observational data time series (2006–2019) at 750, 900, 1,000, and 1,200 m depths of the temperature from the E2M3A Observatory and (ii) 55 vertical profiles (1985–2019) in the dSAP. The analytical solution of the gravest mode of the heat equation compares well to the temperature profiles, and the numerical integration of the resulting forced heat equation compares favorably to the temporal evolution of the time-series data. The vertical mixing coefficient is obtained with three independent methods. The first is based on a best fit of the long-term evolution by the numerical diffusion-injection model to the 13-year temperature time series in the dSAP. The second is obtained by short-time (daily) turbulent fluctuations and a Prandtl mixing length approximation. The third is based on the zero and first modes of an Empirical Orthogonal Function (EOF) analysis of the time series between 2014 and 2019. All three methods are compared, and a diffusivity of approximately $\kappa = 5 \cdot 10^{-4} \mathrm{m}^2\mathrm{s}^{-1}$ is obtained. The eigenmodes of the homogeneous heat equation subject to the present boundary conditions are sine functions. It is shown that the gravest mode typically explains 99.5% of the vertical temperature variability (the first three modes typically explain 99.85%) of the vertical temperature profiles at 1 m resolution. The longest time scale of the dissipative dynamics in the dSAP, associated with the gravest mode, is found to be approximately 5 years. The first mode of the EOF analysis (85%) represents constant heating over the entire depth, and the zero mode is close to the parabolic profile predicted by the heat equation for such forcing. It is shown that the temperature structure is governed by continuous warming at the sill depth and deep convection and gravity current events play less important roles. The simple model presented here allows evaluation of the response of the temperature in the dSAP to different forcings derived from climate change scenarios, as well as feedback on the dynamics in the Adriatic and the Mediterranean Sea.

Keywords: ocean observations, vertical mixing, deep ocean, South Adriatic, time-series analysis, parameterization, climate variability

OPEN ACCESS

Edited by:
Nadia Lo Bue, National Earthquake Observatory (INGV), Italy

Reviewed by:
Benjamin Rabe, Alfred Wegener Institute Helmholtz Centre for Polar and Marine Research (AWI), Germany
Federico Falcini, National Research Council (CNR), Italy

***Correspondence:**
Vanessa Cardin
vcardin@inogs.it

Specialty section:
This article was submitted to Physical Oceanography, a section of the journal Frontiers in Marine Science

Received: *26 May 2020*
Accepted: *02 November 2020*
Published: *30 November 2020*

Citation:
Cardin V, Wirth A, Khosravi M and Gačić M (2020) South Adriatic Recipes: Estimating the Vertical Mixing in the Deep Pit. Front. Mar. Sci. 7:565982. doi: 10.3389/fmars.2020.565982

1. INTRODUCTION

The paradigm of the vertical temperature structure of the deep ocean is given by the "Abyssal recipes" of Munk (1966). It is based on a balance between an upward advective cooling and a downward diffusion of heat, which leads to an exponential profile of the temperature in the vertical direction. It explains large parts of the world's ocean temperature and salinity stratification below the thermocline. The vertical turbulent diffusion of heat needed to maintain the structure is at least two orders of magnitude larger than the molecular diffusion values of sea water, and today, it is not entirely clear where the energy that supports the vertical mixing originates from Munk and Wunsch (1998). Tides are supposed to play an important role in the mixing process due to the breaking of internal tidal waves, generated by the interaction of the barotropic tide with the topography (see i.e., de Lavergne et al., 2019; Vic et al., 2019). Mixing in the boundary layers and generation by wind-driven horizontal turbulence are other possible sources of mixing (see Vallis, 2017 for a pedagogical discussion). These considerations can be applied to the Adriatic Sea (see **Figure 1**), whose dynamics have been widely studied in a large number of publications (see, e.g., the review by Cushman-Roisin et al., 2001). As far as the deep South Adriatic Pit (dSAP) is concerned, historical studies have shown that even though the winter convection very rarely goes deeper than approximately 700 m, the bottom layer is well-oxygenated (see e.g., Zore-Armanda et al., 1991; Bensi, 2012). Ventilation events are associated with the outbreaks of the cold North Adriatic deep water but do not occur every year. Thus, the ventilation should also be associated with some other processes, such as vertical diffusion.

More specifically, we consider the temperature structure in the area of the dSAP based on a considerable number of observations, starting from 1985 and increasing in number over the last two decades. The dSAP has a maximal depth of approximately 1,230 m and is delimited at the south by the Otranto Sill (780 m deep)(see **Figure 1**). We focus on the temperature structure below the sill depth. It is significantly different from an exponential structure, as is shown below, and the theory put forward by Munk (1966) has to be supplemented. The Adriatic is also interesting because the tidal motion is negligible (see, e.g., Cushman-Roisin et al., 2001 and references therein), which simplifies the internal dynamics. An advantage of considering the dSAP is that it is easily accessible (only approximately 60 nautical miles from the coast) and has been extensively observed with considerable data coverage in space and time over the last 40 years. The present work relies on two types of data: first, *in-situ* ship-borne data measurements, 55 vertical temperature and salinity profiles at a 1 m resolution, collected in the dSAP from 1985 to 2019 (Cardin et al., 2011) and second, time series of high-frequency point measurements from 2006 to 2019 at 750, 900, 1,000, and 1,200 m nominal depths from the mooring at the E2M3A Observatory, (http://nettuno.ogs.trieste.it/e2-m3a/). The latter are positioned in the dSAP and are particularly dedicated to the study of the long-term thermohaline and biogeochemical properties. In the present work, the diffusivity processes in the deep layer are analyzed, and thus, only measurements at 750 m (considered as the reference level for the Otranto sill depth) and deeper are taken into consideration.

It was shown by Querin et al. (2016) that the dynamics in the dSAP are forced by intermittent gravity current and deep convection events that reach below the sill depth every few years and that only last from a week to a few months. The most recent events of this type occurred in March and April of 2012 and in March 2017. The former event is due to cold and very dense water from the northern Adriatic (Bensi et al., 2013), whereas the latter event is due to salty and warm water and has, so far, not been discussed in a scientific publication. The subject of the present work is to determine what happens between such events, when the vertical temperature structure is governed mainly by continuous vertical turbulent diffusion as shown by Querin et al. (2016). The different time scales associated with short-lasting convection/gravity current events and continuous diffusion allow separately consideration of the two regimes. In the present work, we investigate continuous mixing based on observational data using the dynamics of the heat equation. The aim is to show that in between deep convection/gravity current events, the dynamics are governed by turbulent diffusion and that a bulk mixing coefficient can be determined to allow efficient parameterization.

The theory is presented in the next section, followed by the description of the experimental data and methodology in section 3. The results for the profiles are given in section 4.3, and those for the time series are given in section 4.4. The results are discussed in section 5, and conclusions are given in section 6.

2. THEORY

We consider the vertical temperature structure of the dSAP and ignore the horizontal variations. This is justified by the dominance of horizontal (isopycnal) mixing over vertical (diapycnal) mixing (Ledwell et al., 1998). Conceptually, the Munk solution is not valid in the dSAP, as there is no continuous injection in the deep waters, which justifies a continuous upward velocity. Furthermore, **Figure 1** shows that the vertical gradient of the temperature vanishes toward the bottom, which indicates intense mixing without restratification effects. The data from a depth of 750 m down to the bottom have a clearly non-exponential functional form, indicating that the Munk theory of a balance between the upward advection and downward diffusion of heat does not apply. Without upward advection, only vertical turbulent diffusion remains, with no process to balance it and the only stationary solution is a constant temperature in space and time. This is not observed. Instead, the density structure is evolving in space and time with dynamics described by the heat equation, as is demonstrated below.

2.1. Heat Equation

We are interested in the evolution of the temperature $T(z,t)$ in the dSAP deeper than the sill depth ($\approx$ 780 m). The underlying assumption of the present work is, that the dynamics in the dSAP are governed by the forced heat equation:

$$\partial_t T(z,t) = \kappa\, \partial_{zz} T(z,t) + I(z,t), \tag{1}$$

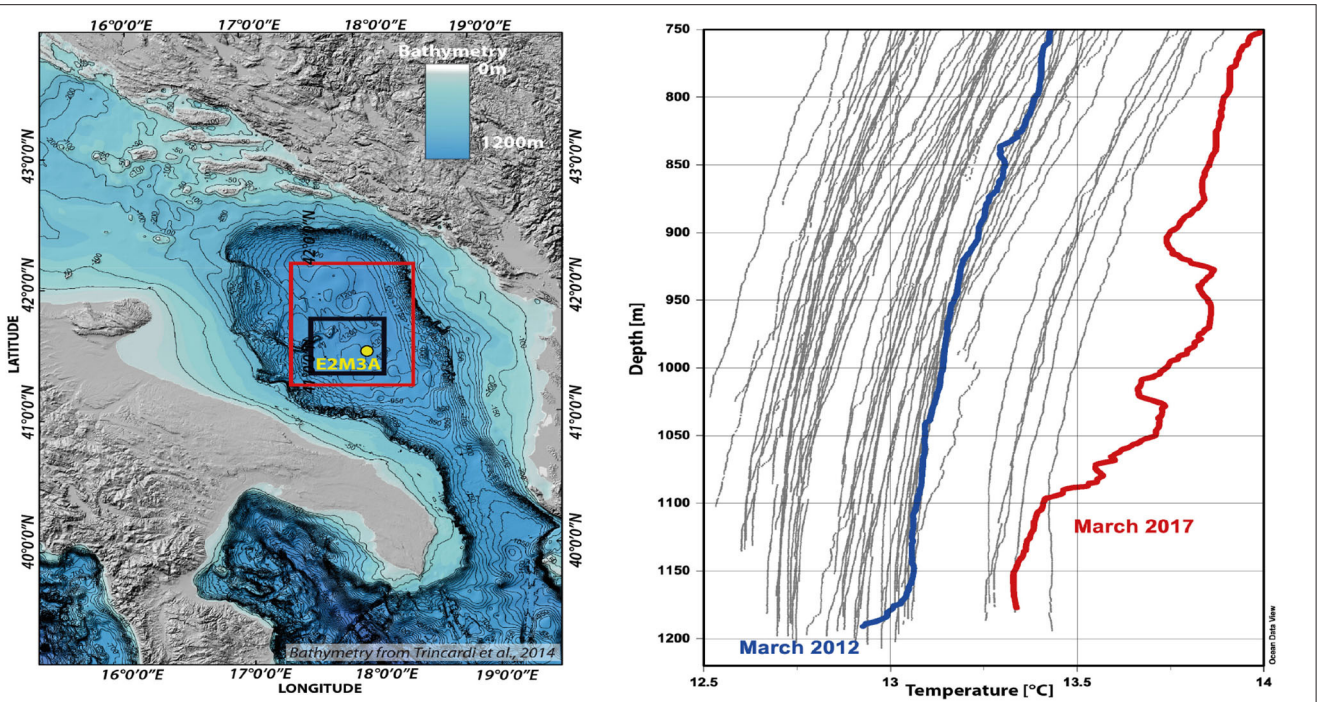

FIGURE 1 | (Left) Region of the South Adriatic Pit (SAP). The red rectangle shows the area where all the profiles originated. After 2010, data were collected within the black rectangle. The yellow dot indicates the position of the E2M3A observatory of the thermohaline time series. **(Right)** All 55 profiles of the temperature dependence with the depth. The two profiles during the deep convection/gravity current events are emphasized in blue and red.

where the only free parameter in the system is the vertical eddy diffusivity κ. The last term represents the intermittent intrusions in the form of deep convection or gravity-current events and is supposed to vanish over extended periods in time. The dynamics evolve between $z_s = -750$ m, the measurement point closest to the sill depth, and the bottom, $z_b = -1,220$ m. The boundary conditions are $T(z,t) = T_{\text{obs}}(z_s,t)$ at the sill depth and $\partial_z T(z_b,t) = 0$ at the bottom. This shows that the model is forced continuously by a time-dependent heat flux at its upper boundary that deeply diffuses, whereas there is no heat flux at the bottom. This model is called the diffusion-intrusion model in the sequel. It is linear and therefore allows us to separately obtain analytical solutions for different types of forcing and then add them to obtain the overall solution.

The unforced heat equation, Equation (1), is given by $I(z,t) = 0$ and $T_{\text{obs}}(z_s,t) = \text{const}$. In the long term, the temperature relaxes to the imposed temperature at the sill depth down to the bottom, the only time independent solution. The time-dependent evolution is given by $T^h(z,t) = T_{\text{obs}}(z_s) + r(t)m(z)$, where $r(t)$ and $m(z)$ are related by:

$$\frac{\partial_t r}{r} = \kappa \frac{\partial_{zz} m}{m} = \lambda \tag{2}$$

and λ does not depend on z or t, as m is not dependent on t and r is not dependent on z (Please see Zachmanoglou and Thoe, 1986 chapter 9.2 for more details on the calculations and the solution using the "separation of variables"). We further define the following: $\Delta T^h(z,t) = T^h(z,t) - T_{\text{obs}}(z_s,t)$. The boundary conditions of $\Delta T^h(z,t) = 0$ at the upper boundary and a vanishing temperature gradient at the lower boundary lead to the solution of the unforced heat equation of the form (z is given in meters):

$$\Delta T^h(z,t) = \sum_k A_k \sin\left(\frac{\pi(2k-1)(z-z_s)}{2(z_s-z_b)}\right) \exp(-\mu(2k-1)^2 t). \tag{3}$$

Note that only the wave numbers, with odd integers $2k-1$, satisfy the bottom boundary-condition and Equation (2) imposes

$$\mu = \kappa \left(\frac{\pi}{2(z_s - z_b)}\right)^2. \tag{4}$$

The characteristic e-folding decay time scale for a vertical eddy diffusivity of $\kappa = 5 \cdot 10^{-4} \text{m}^2\text{s}^{-1}$ (see section 4) and for the first mode, $k = 1$, is $\mu^{-1} = \kappa^{-1}(\pi/2)^{-2}(470m)^2 \approx 5.7$ years. For the following modes satisfying the boundary conditions, $k = 2,\ 3$ the time scales are 9 and 25 times shorter, respectively; the modes are damped in less than a year. The higher order modes ($k > 3$) are damped within less than a month. The interannual dynamics are therefore dominated by the mode $k = 1$ (see section 4). This shows that the unforced dynamics consists of a sum of non-interacting sine modes that decay exponentially in time at a rate that is proportional to the square of their wavenumber.

When a time-dependent forcing is applied, the dynamics of each mode are still independent. The coefficients are no longer constant in time, and we define

$B_k(t) = A_k(t)\exp(-\mu(2k-1)^2 t)$. The first coefficient $B_1(t)$ is obtained by projection on the first mode:

$$B_1(t) = \frac{4}{\pi(z_s - z_b)} \int_{z_b}^{z_s} \Delta T(z,t) \sin\left(\frac{\pi(z - z_s)}{2(z_s - z_b)}\right) dz \quad (5)$$

The projection of the data for modes $k = 2$ and 3 and for data records that do not go to the total depth of 1220 m is given in **Appendix 1**. The temporal evolution of the coefficients B_k is governed by the initial conditions at $t = 0$, the heat flux at the sill depth and the intermittent forcing.

In the case of the intermittently forced heat equation, through deep convection or gravity currents, the temperature structure changes, and higher order modes may also have large amplitudes. This intermittent forcing is represented in Equation (1) through the term $I(z,t)$. After a short (several months) intermittent event, the dynamics evolve unforced, and the amplitude of the higher modes decreases rapidly, as explained above. Only a few months after the intermittent forcing, the dynamics are again dominated by the lower order modes.

When the continuously forced heat equation is driven by increasing temperature at a depth of 750 m at a constant rate $\gamma = \partial_t T_{\text{obs}}(-750\text{m}, t)$, the solution is:

$$T^{cf}(z,t) = \gamma t + \frac{\gamma}{2\kappa}(z - z_b)^2, \quad (6)$$

which can be determined by introducing the above equation in Equation (1) with a vanishing inhomogeneous term, $I(z,t) = 0$. This corresponds to the constant temperature increase of a parabolic shaped temperature profile. The temperature difference between the sill depth and the bottom of the dSAP is constant in time and is related to the temperature increase at the sill depth by:

$$T^{cf}(z_s,t) - T^{cf}(z_b,t) = \frac{\gamma}{2\kappa}(z_s - z_b)^2 \quad (7)$$

It is important to note that the quadratic shape is not very different from the first sine mode (see **Figure 2**), and when it is projected on the sine modes, the amplitudes decay quickly with the wavenumber as $(2k-1)^{-3}$. The first sine mode explains more than 92.7% of the total variance; for the first three modes, it is almost 97%. This means that from the shape of a single temperature profile at a given time t_0, we cannot significantly determine whether the dynamics are freely decaying or forced by a constant-in-time vertical temperature flux. In other words, $T^{cf}(z,t_0)$ resembles $T^{h}(z,t_0)$ at a time t_0; however, the evolution in time for the unforced and continuously forced cases is different. In the former case, the amplitude decays exponentially, while in the latter, it stays constant.

2.2. Heat Content and Heat Flux

When a linear equation of state is supposed, the heat content, its evolution, the potential energy and its evolution as well as the increase in potential energy by mixing can be obtained independently for every mode k and are determined by the coefficients B_k. If the vertical temperature profile is close to the first sine mode, the heat flux per unit area at the sill depth is

$$H = c_p \kappa \rho \partial_z T(z_s) = c_p \kappa \rho \frac{\pi(T(z_s) - T(z_b))}{2(z_s - z_b)} \quad (8)$$

and the heat content per unit area is:

$$\mathcal{H} = c_p \rho \frac{2(z_s - z_b)}{\pi}(T(z_s) - T(z_b)). \quad (9)$$

The ratio of the heat content and the heat flux is the characteristic time scale of the first mode, which is given in Equation (4).

3. EXPERIMENTAL DATA AND METHODS

In order to validate Munk's theory using experimental data we have considered the area of the South Adriatic (see **Figure 1**) where mixing and winter convection play an important role in homogenizing the physical and chemical properties of seawater and spreading heat along the water column. To analyze the importance of these processes, two different data sets are used: The first one consists of temperature profiles, taken during ship cruises, covering a long period of time and a large spatial area, and the second is times-series data, with high frequency point measurements along the water column by the E2M3A Observatory. The latter is located in the dSAP and is particularly dedicated to the study of long-term thermohaline and biogeochemical properties. In this study, we analyze the diffusivity processes in the deep layer; therefore, we consider only measurements deeper than 750 m.

3.1. Profiles

The long-term variability of the thermal characteristics of the deep layer in the South Adriatic area is determined based on temperature data collected during several oceanographic campaigns between 1985 and 2019. The cruises were undertaken as part of Italian and European projects, and other datasets were kindly provided by the NATO UNDERSEA RESEARCH CENTER, PANGEA Data Repository (https://www.pangaea.de/) and MEDATALAS Dataset (https://nodc.inogs.it/nodc/). All the profiles were processed following the methodology described by Cardin et al. (2011) and applied for the data between 1990 and 2010, i.e., the oceanographic condition during a specific campaign is represented by a profile obtained by averaging all the CTD casts deeper than 1,000 m measured in the area between 41.25° and 42.25° N and 17.25° and 18.25° E in the SAP (**Figure 1**). For the studied period, we consider data from 55 temperature profiles deeper than 750 m. The potential temperature (hereafter referred to as temperature) is calculated from the original profiles with the surface as the reference depth. Profiles after 2010 were collected in a narrower area of $0.5^o \times 0.5^\circ$ degrees Lat/Lon located in the dSAP and near the E2M3A Observatory (black square in **Figure 1**). Further information about these cruise operations, materials and methods can be found at http://www.ogs.trieste.it:8585/biblioteca/.

3.2. Time Series

The data collected at the E2M3A Observatory enables the monitoring of changes that can be linked to variations in the general circulation of the Eastern Mediterranean Sea or, on a larger time scale, to the climate variability in the area, demonstrating the importance of high-frequency measurements to resolving events and rapid processes.

The Observatory has been working almost continuously since the end of 2006, and therefore, the high- frequency time series of physical and biochemical parameters measured at the site can be considered the longest almost continuous offshore data set available in the region (http://nettuno.ogs.trieste.it/e2-m3a/). The temperature was measured using CT-CTD sensors of the SBE37 at a sampled rate of 1 h and SBE16 with a sampling interval of 3 h. For homogeneity, all the time series were averaged on a daily basis, and the temperature values were converted to the potential temperature. A low-pass filter PL33 with a cutoff period of 33 h (Flagg et al., 1976) was applied to remove inertial oscillations (inertial period of 17.593 h at 42° N in the South Adriatic Pit) so that tidal and higher frequency fluctuations do not mask the low-frequency fluctuations in the time series driven by winds and the density field. The filter removes more than 99% of the amplitude at the semidiurnal tidal periods and more than 90% of the amplitude at the diurnal tidal periods. These subinertial non-tidal time series are considered as the starting point for the analysis.

For this study, the time series considered along the mooring line come from 4 instruments positioned at 750, 900, 1,000, and 1,200 m (Cardin and Bensi, 2014; Cardin et al., 2014, 2015, 2018). To simplify the analysis, the depths of the series are nominal. The available data used are from November 2006 to October 2019, with a gap between September 2010 and May 2011. The time series at 900 m started in November 2013. An exhaustive description of the site, data availability and data analysis can be found in Bensi (2012) and Bensi et al. (2014) and at the Observatory webpage (http://nettuno.ogs.trieste.it/e2-m3a/).

All instruments were calibrated and controlled for quality before and after each recovery and deployment, following the procedures indicated in Coppola et al. (2016) and Pearlman et al. (2019). In addition, during recovery or deployment operations, a CTD cast was performed to assess the accuracy of the measured data and to identify possible instrument drift.

3.3. Empirical Orthogonal Function Analysis

To assess the temporal variability and the vertical structure of the water column in the dSAP, we applied empirical orthogonal function analysis (EOF) (Preisendorfer and Mobley, 1988) to the temperature time series. For this purpose, time series at 750, 900, 1,000, and 1,200 m were analyzed.

Unfortunately, the time series shows gaps (not simultaneous) at different levels due to instrument failures, especially in the deepest part of the mooring line in the period from 2006 to 2010 and from 2011 to 2014. Since the EOF analysis requires data at all levels for its application, the data collected before 2014 can not be used for this analysis. Thus, we considered only the time series from September 2014 to August 2019, as it was the longest period without important gaps (only short ones -no longer than 5 days -due to the Observatory service). To eliminate these gaps, the daily time series were subsequently averaged on a weekly time scale. The filtered time series allowed us to study the time scales of interest (e.g., seasonal and interannual).

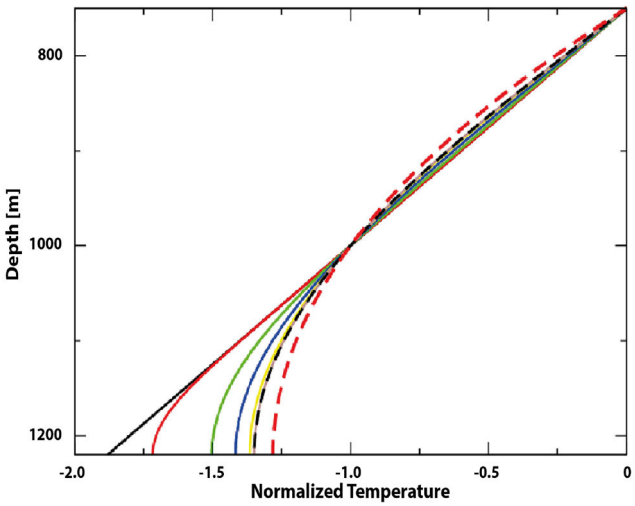

FIGURE 2 | Temperature profiles from the numerical model given by the unforced heat equation (1) (all values are divided by the temperature difference between 750 and 1,000 m depths) for the initial condition (black line), after 1 month (red), 6 months (green), 1 year (blue), 2 years (yellow), and 10 years (brown) of the integration time ($\kappa = 5 \cdot 10^{-4} \mathrm{m^2 s^{-1}}$). The black dashed line is the analytic solution of the first mode, to which the dynamics converge. The red dashed line is the parabolic profile of the continuous forcing.

4. RESULTS

4.1. Numerical Integration

We performed a numerical integration of the heat equation with an imposed temperature at approximately the sill depth $T_{\mathrm{obs}}(-750\,\mathrm{m}, t)$ (Dirichlet boundary condition) and a vanishing gradient at the bottom (1,220 m) (Neumann boundary condition). For illustration, an unforced integration that starts from a linear stratification is represented in **Figure 2**. All values are divided by the temperature difference between 750 and 1,000 m depths to emphasize the evolution of the shape and the convergence to the first mode. Snapshots are shown at 1 and 6 months and at 1, 2, and 3 years ($\kappa = 5 \cdot 10^{-4} \mathrm{m^2 s^{-1}}$). The convergence to the first sine-mode, shown in **Figure 2**, with a characteristic time scale of several months, is clearly visible. In the same figure the shape of the parabolic profile for the constant forcing case is also given for comparison.

In the numerical integration, the two types of forcing, with time-dependent temperature variation at the sill depth γ and time and space dependent intermittent forcing $I(z, t)$, can be easily combined. To reproduce the space-time dynamics of the observed data, both types of forcing are applied, and Equation (1) is integrated numerically.

4.2. Eddy Diffusivity

The only free parameter in the heat equation is the diffusivity. The vertical exchange of heat is at least two orders of magnitude larger than that predicted by molecular motion only, and most is performed by turbulent fluid motion. Its parameterization is often achieved by assuming a vertical eddy diffusivity. It cannot be calculated from first principles but has to be determined

from observations. It can be obtained based on different data analysis methods. The first method is a best fit of the time evolution of a numerical integration described in section 4.1 to the time-series data discussed in section 3.2. More precisely, we numerically solve Equation (1), which is forced at the upper boundary by imposing the temperature observed at 750 m depth and supplemented by two intermittent injections in 2012 and 2017, modeling the deep convection/gravity current events that penetrate the dSAP. The value of the diffusion constant κ is then estimated so that the evolution of the model best fits the time-series data. The second method is based on Prandtl's mixing-length concept (see Taylor, 1922, 1959; Prandtl, 1925; Bradshaw, 1974). We first calculate a typical r.m.s. vertical scale $\Delta z_{rms} = \sqrt{(T')^2}/\partial_z \overline{T}$ based on the temperature fluctuations T' at 900 m depth and an average temperature gradient $\partial_z \overline{T}$ at the same depth. We also determine the correlation time of the vertical motion by looking at the autocorrelation function of the temperature fluctuations $C(\tau) = \langle T'(t+\tau)T'(t)\rangle_t / \langle (T'(t))^2\rangle_t$, which is independent of time t for statistically stationary dynamics. We then obtain the correlation time: $\tau_{corr} = \int_0^{\tau_0} C(\tau)d\tau$, where τ_0 is the first zero crossing of $C(\tau)$. The vertical eddy diffusivity can then be estimated by:

$$\kappa_{\text{turb}} = C_s \frac{(\Delta z_{\text{rms}})^2}{\tau_{corr}}, \tag{10}$$

where C_s is a non-dimensional constant. The third method is based on the continuously forced dynamics, which leads to a balance between the temperature increase and the temperature difference between the sill depth and the bottom, as expressed by Equation (7). The three approaches for estimating the vertical eddy diffusivity are performed in sections 4.4 and 4.5.

4.3. Profiles

When considering the 55 temperature profiles taken during the period from 1985 to 2019, which are presented in **Figure 1**, a similarity of most of them to the first sinusoidal mode depicted in **Figure 2** is discernible. For a quantitative analysis, we calculated the coefficients B_k for k = 1, 2, and 3, which are given in **Figure 3**. Only the amplitude of the first mode has a value which is significantly different from zero, varying around 0.5^o K, while the amplitudes of the second and third mode are typically more than an order of magnitude smaller and have no definite sign. We further calculated the remaining variance not explained by the first mode or the first three modes in **Figure 3**. For over 2/3 of the profiles, more than 99.5% of the variance can be explained by the first mode and more than 99.85% by the first three modes. Note that the 2017 event is clearly depicted by the atypical profile from 22/03/2017, given in red in **Figure 1**. The event also has a clear signature in the amplitude of the second and third modes (**Figure 3**) and in a strong increase in the variability neither explained by the first mode nor by the first three modes (**Figure 3**). This means that for this profile, higher order modes have an increased amplitude. In the subsequent profile only 4 months later (27/07/2017), the amplitude of the second and third mode as well as the unexplained variability has decreased to the values prior to the event. This is coherent with the fact that the decay times of modes two and three are only a few months, as explained in section 2.1. The decay of even higher modes happens at scales shorter than a month. The 2012 event, however, has no conspicuous signature in the amplitude or variability data. The profile from 31/03/2012 (given in blue in **Figure 1**) shows that the dense gravity current water is just starting to arrive, and it is seen at the very bottom of the data but does not significantly impact the overall shape of the profile. No profile is available for the rest of the year, and the next profile is 1 year later (23/03/2013); at this time, the second, third and higher modes have faded away.

4.4. Time Series

We first numerically integrate the diffusion-intrusion model. An integration with $\kappa_{\text{fit}} = 5 \cdot 10^{-4}\text{m}^2\text{s}^{-1}$ and two convection or gravity-current events in March 2012 centered at the bottom and in March 2017 centered at $z = 1,100$ m manages to reproduce, to a reasonable degree, the observed temperature and salinity evolution, as shown in **Figure 4**.

Furthermore, the data at 750 and 1,200 m allows determining the amplitude of the first mode. Using this information and supposing that the higher-order modes are of low amplitude, allows to interpolate for the depths in-between. The obtained values were compared to the observed data at 900 and 1,000 m. Again, we remark a good correspondence between the observational data and the interpolation in **Figure 5**. A slight deviation is observed between years 2014 and 2017.

The eddy diffusion can be estimated based on the correlation time and the vertical r.m.s displacement of a fluid parcel, as explained in section 4.2. The former is given by the integral of the correlation function from zero to the first zero crossing. The first zero crossing is at 4 days, and the integral gives $\tau_{corr} = 1.6$ days (not shown). The latter is calculated based on the temperature fluctuations and the mean temperature gradient (box-averaged over 30 days); its average value lies around $\Delta z_{\text{rms}} = 20$ m. When we impose $\kappa_{\text{turb}} = \kappa_{\text{fit}}$ we find, using Equation (10), that $C_s \approx 0.18$. There is no surprise that it is smaller than one, as some of the vertical motion is due to internal waves, which do not lead to mixing if they do not break. Interestingly, the former is obtained based on turbulent fluctuations on a time scale of a few days, while the latter is obtained based on the evolution of the temperature profile over several years.

4.5. EOF Analysis

The modes of the EOF analysis of the time series and the temporal evolution of EOF mode 1 are presented in **Figure 6**. Note that the time average is given by EOF mode 0 and that its profile resembles the parabolic profile put forward in section 2.1 for the case with a constant forcing. The dominant evolution is given by EOF mode 1 (describing 87% of the variance), which is close to a constant-in-depth temperature increase. In this case, the temperature increase at the sill depth and the amplitude of mode 0 are related by Equation (7). The amplitude for mode 0 is $\Delta T = 0.5^o$ K (see **Figure 6A**). The warming trend is obtained by taking the product of the vertical average of mode 1 (which is close to constant see **Figure 6B**) and the trend of its amplitude (see **Figure 6C**), that is: $\gamma = 0.5 \cdot 0.64^o$ K/(5years) $= 6.4 \cdot 10^{-2o}$ K/year. A diffusivity of

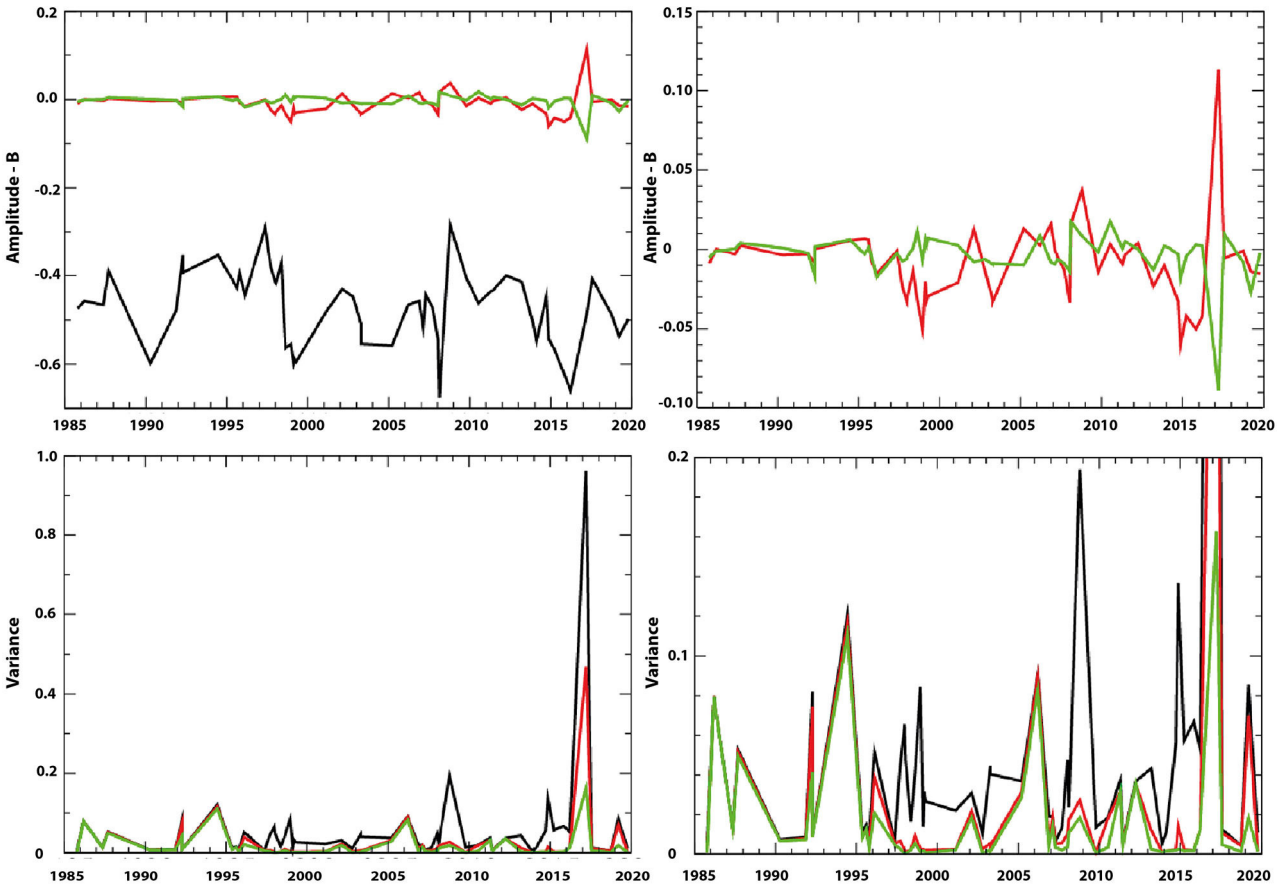

FIGURE 3 | (Upper) Evolution of the amplitudes of the sine modes B_1 (black), B_2 (red), and B_3 (green). The vertical scale gives the temperature difference between the 750 m time series and the maximum profile depth (1,219 m) of the corresponding mode. **(Lower)** Part of variability not explained by B_1 (black), $B_1 + B_2$ (red) or $B_1 + B_2 + B_3$ (green) (left) and zoom (right). Figures on the right show the same data magnified.

$\kappa_{EOF} = 4.5 \cdot 10^{-4}\,\mathrm{m^2 s^{-1}}$ is obtained from Equation (7), which is close to κ_{turb} and κ_{fit}. We remind that the Otranto Sill depth is 780 m.

The higher order EOF modes 1, 2, and 3 closely resemble discretized versions of the analytic sine modes k = 1, 2, and 3 (wavenumbers 1, 3, and 5). If we suppose that they are subject to random forcing of equal strength and diffusive damping, their relative variance should decrease as 1, 1/9, and 1/25. The observed values are 1, 1/8, and 1/48, which is within discretization and statistical error (the variance of the last EOF mode is only 0.24%).

5. DISCUSSION

All the above results based on temperature measurements show that the action of turbulent mixing in the dSAP can be modeled well by a heat equation with a constant diffusion coefficient in space and time, a prescribed heat flux at the sill depth and a forcing term that represents rare gravity current and deep convection events. The similarity between the empirical EOF analysis results (applied only to a subset of the time series between 2014 and 2019) and a solution of the forced heat equation, with a forcing that imposes a warming trend through a heat flux at 750 m depth, confirms that the heat equation satisfactorily describes the processes in the dSAP.

When the functional form of the first mode for the temperature stratification is assumed to have an amplitude of 0.5^oK, the heat flux of the dSAP is $H = 3.3\mathrm{Wm^{-2}}$ according to Equation (8), and the heat content is $\mathcal{H} = 6 \cdot 10^8\mathrm{Jm^{-2}}$ according to Equation (9). These values characterize the heat-budget of the dSAP and can help to validate numerical models and climate dynamics.

The power per square meter necessary to perform turbulent mixing of the mass (based on temperature only) is

$$P = g\alpha\rho\kappa_{\mathrm{turb}}\Delta T. \tag{11}$$

For a $\Delta T = 0.5^o$ K, this parameter is $P = 5 \cdot 10^{-4}\mathrm{W/m^2}$. A mixing efficiency of 0.2 leads to a drain of five times more kinetic energy (see, i.e., Osborn, 1980; Peltier and Caulfield, 2003). If the turbulent Prandtl number is unity, we obtain a characteristic vertical shear of $\approx 3 \cdot 10^{-3}\mathrm{s^{-1}}$.

The presented theory and observations show that from 2006 to 2019, the temperature stratification in the dSAP is determined by the continuous warming in the upper part (above the Otranto

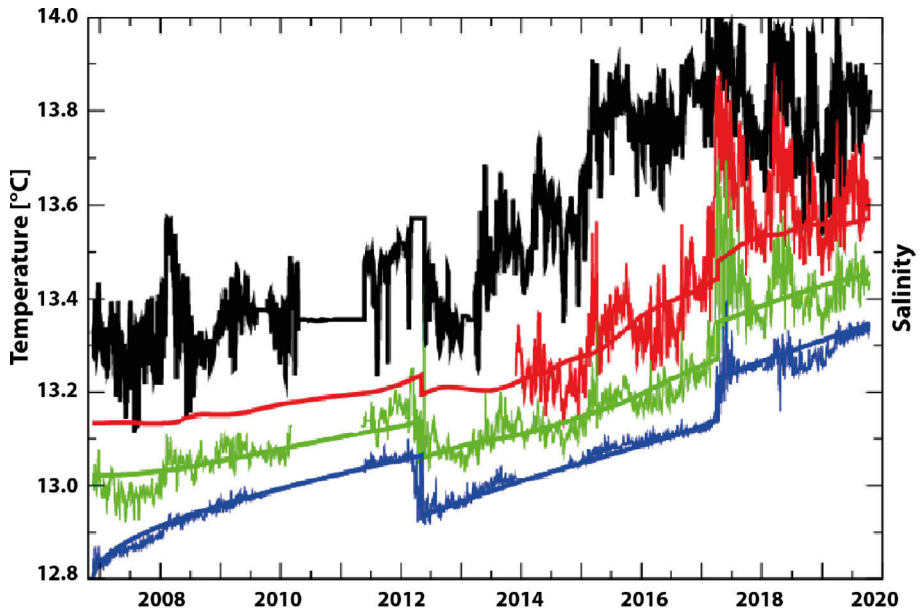

FIGURE 4 | The observational data (thin lines) and the corresponding solutions of the injection-diffusion model (thick lines) for different depths (black 750 m, red 900 m, green 1,000 m, blue 1,200 m) for temperature.

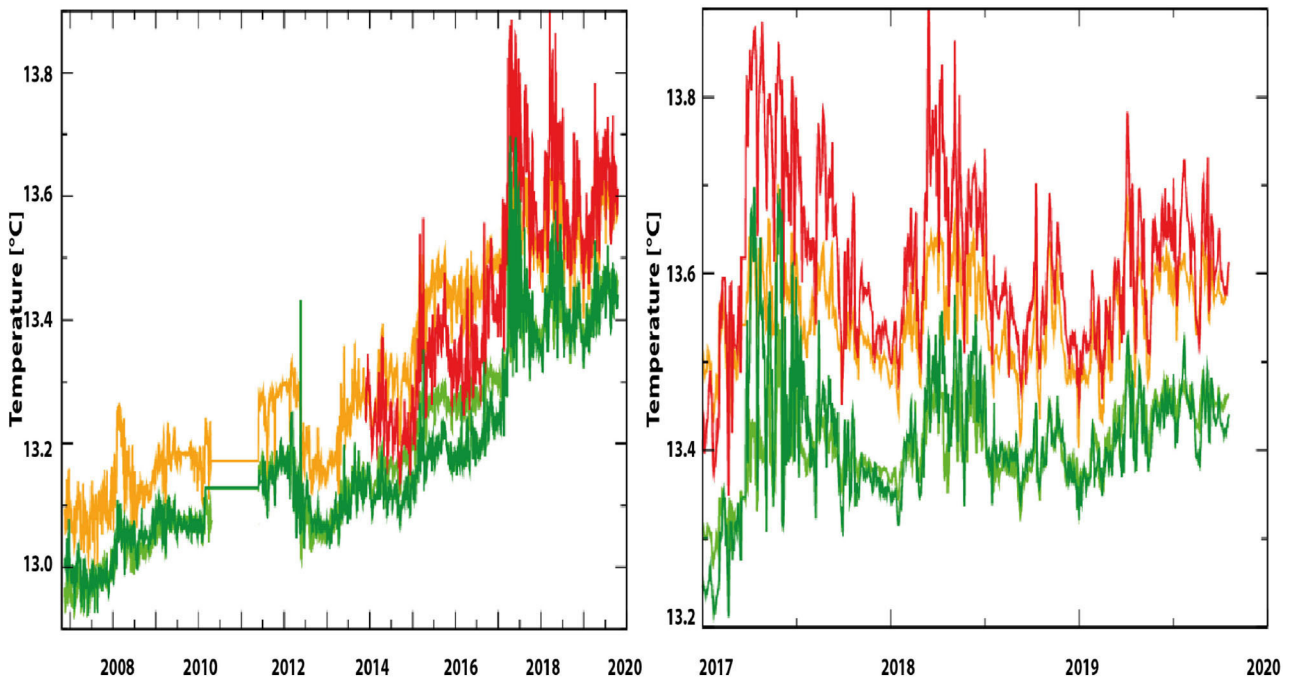

FIGURE 5 | Observed data at 900 m (red) and 1,000 m (light green) and their interpolations 900 m (orange) and 1,000 m (dark green). The right figure is a magnification of the data starting in 2017.

Sill depth) and the vertical turbulent diffusion. Other processes such as deep convection and gravity currents that penetrate the dSAP are only visible during a few months on two occasions. We obtain an upper (diffusive) limit for the characteristic time scale for the density structure of the dSAP, which is important as it tells us that the long-term changes in the circulation in the area are due to external forcing. The upper 5-year limit is also important for numerical modeling, as it gives a maximum spin-up time for numerical integrations. When the first mode is correctly estimated in the initial conditions of the numerical

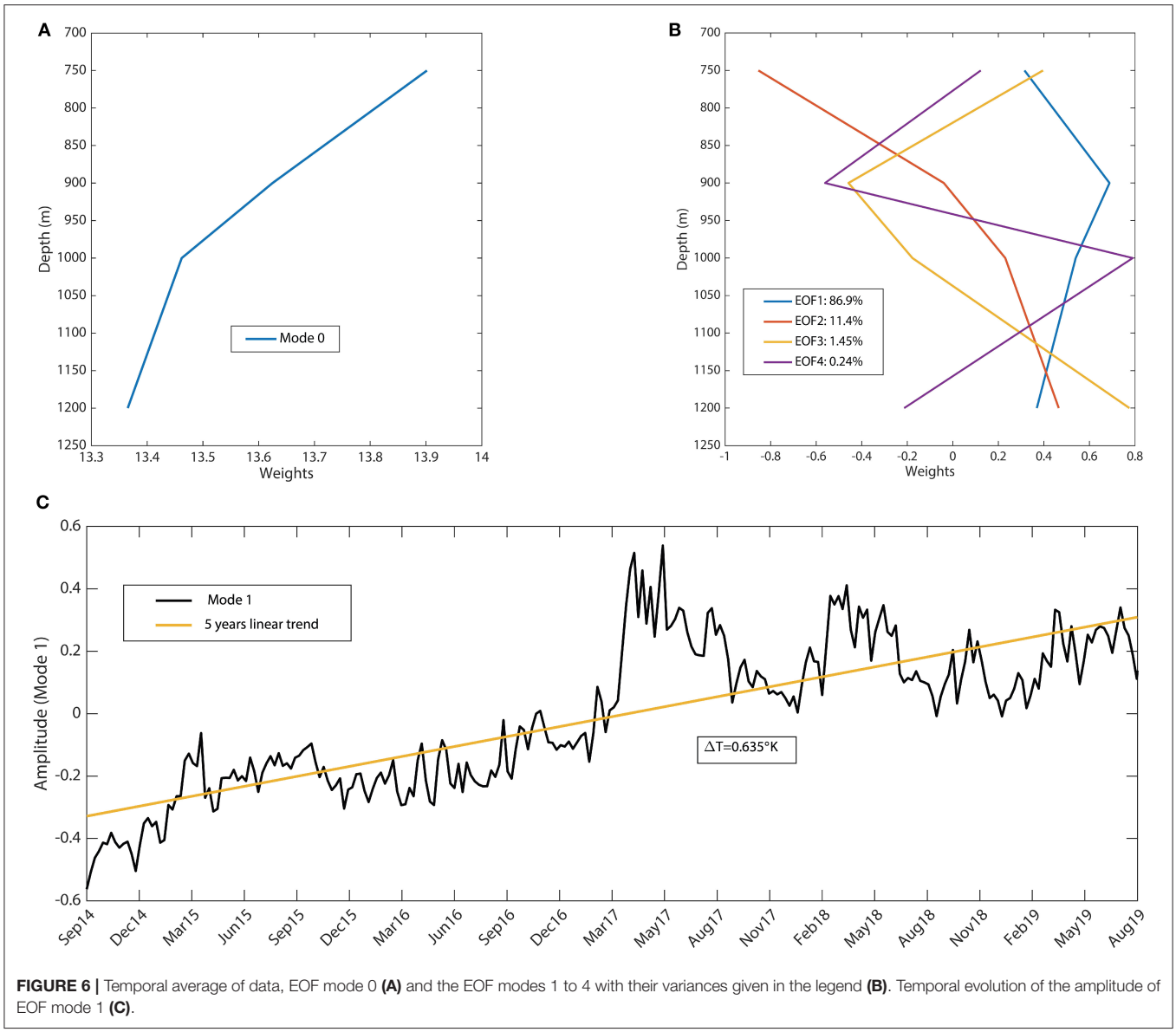

FIGURE 6 | Temporal average of data, EOF mode 0 **(A)** and the EOF modes 1 to 4 with their variances given in the legend **(B)**. Temporal evolution of the amplitude of EOF mode 1 **(C)**.

integration, a spin up of less than a year becomes sufficient, as only modes higher than $k = 1$ have to spin up.

The main result is that at a high accuracy, the spatio-temporal evolution of the temperature in the dSAP is described by a heat equation based on a constant (in space and time) vertical diffusivity of $\kappa = 5{\cdot}10^{-4}\mathrm{m}^2\mathrm{s}^{-1}$. This value is similar to published values of vertical diffusivities in other regions of the world oceans. Munk (1966), considering several stations in the interior Pacific Ocean over much larger depths, found that the dominant vertical dynamics acting on the temperature were advective diffusive, with $\kappa = 1.3 \cdot 10^{-4}\mathrm{m}^2\mathrm{s}^{-1}$. The eddy diffusivity in deep basins of the North Aegean was estimated to lie between $\kappa = 2 \cdot 10^{-4}$ to $10 \cdot 10^{-4}\mathrm{m}^2\mathrm{s}^{-1}$ below a depth of 500 m (Zervakis et al., 2003). In the deepest part of the Calypso Deep (below 4,400 m), the vertical diffusivity was found to vary around $\kappa = (4 \pm 3) \cdot 10^{-3}\mathrm{m}^2\mathrm{s}^{-1}$ by Kontoyiannis et al. (2016).

6. CONCLUSIONS AND PERSPECTIVES

We showed that the theory proposed by the "Abyssal recipes" of Munk (1966) for the world ocean is valid for the dSAP, a small oceanic basin, when forcing is added. The hypothesis of the present work is that the dynamics in the dSAP are governed by turbulent diffusion and forced by a continuous heat flux at the upper boundary and sporadic deep convection/gravity current events. A hierarchy of models, all based on the heat equation, is used. The simplest are based on the gravest or the three gravest modes of the analytically solved unforced heat equation. It is shown that the heat equation forced by a constant heat flux at the upper boundary has a functional form close to the gravest mode. The most evolved model includes a time-dependent forcing at the upper boundary as well as intermittent convection events that are solved numerically.

The models successfully describe the profiles and their spatio-temporal evolution. The functional form of the profile is described by the gravest mode of the analytical solution of the homogeneous heat equation, while the time series can be fitted well by the numerical solution of the forced heat equation. Two major deep convection/gravity current events are identified in the time series in 2012 and 2017 between 2007 and 2019 (during the winter/spring season). The longest dissipative time scale in the dSAP, associated with the gravest mode, is approximately 5 years. This does not only indicate that within this period, stratification in the dSAP disappears when forcing resides, but it represents an upper bound for the absence of deep convection events penetrating the dSAP. More precisely, when the temperature at the sill depth does not increase and no deep convection event reaches below the Otranto Sill depth within 5 years, the dSAP becomes essentially unstratified, and subsequent convection is likely to reach the bottom of the dSAP. In other words, a constant warming of the water mass above the sill depth prevents deep convection events from reaching the dSAP, and only diffusion remains; however, when there is no warming at the sill depth, a deep convection event will occur at least every 5 years.

The above developed theory about the dynamics of the dSAP allows a simple injection diffusion model of the dSAP to be built. This can be used to study the evolution of the dSAP under climate change scenarios, as well as to parameterize the feedback of the dSAP on the surrounding ocean dynamics. More precisely, the decomposition of modes with different characteristic time scales can be used to parameterize the response of the deep South Adriatic Pit to a specific process. For interannual variability, only the dynamics of the first mode have to be considered, while for a seasonal forcing, only the first two modes have to be taken into account, considerably reducing the complexity of the problem. The next step is to attempt to extrapolate the above findings to the more involved dynamics above the sill depth, where water masses are subject to horizontal advection and air-sea fluxes.

The performance of the theory and data analysis developed in this publication are not limited to the dSAP but can be equally applied to other enclosed pits in the world ocean, away from the direct influence of atmospheric forcing and strong currents. The temperature variation in the dSAP is significantly different from the exponential profile put forward by Munk (1966). As in Munk and Wunsch (1998), we have to ask the question of which process provides the power to perform the mixing in the case of the dSAP, where tides are excluded. This is one of the key open questions in physical oceanography. To answer this question, the synergy of laboratory experiments on the Coriolis platform (Grenoble) of idealized numerical simulations and of fine resolution (in time-and-space) velocity measurements in the dSAP is currently being employed.

The proposed empirical model for the vertical, one-dimensional, structure of the temperature profile, its evolution in time, as well as the determination of the vertical mixing coefficients and the forcing, relies on the synergy between mooring data with dense temporal coverage and a substantial number of profiles, providing fine resolution in the vertical direction. This dataset has been collected during the last four decades, at a single oceanic site and shows the importance of a continuous effort of collecting data over several generations of funding programs.

DATA AVAILABILITY STATEMENT

The original contributions presented in the study are included in the article/supplementary materials, further inquiries can be directed to the corresponding author/s.

AUTHOR CONTRIBUTIONS

All authors have contributed to the paper. The numerical projection and integration was performed by AW.

FUNDING

This work was funded by Labex OASUG@2020 (Investissement d'avenir - ANR10 LABX56) and OGS internal funding.

ACKNOWLEDGMENTS

Part of this work was performed when AW visited OGS and VC visited LEGI. We thank the OGS ExO and TECDEV Group so as the Captain and crew of the RV OGS Explora and RV Laura Bassi for the valuable support and work during the maintenance of the E2M3A Observatory.

REFERENCES

Bensi, M. (2012). *Thermohaline variability and mesoscale dynamics observed at the E2M3A deep-site in the South Adriatic Sea* (Ph.D. thesis). Universita degli studi di Trieste, Trieste, Italy. Available online at: https://www.openstarts.units.it/handle/10077/7387

Bensi, M., Cardin, V., and Rubino, A. (2014). "Thermohaline variability and mesoscale dynamics observed at the deep-ocean observatory e2m3a in the southern Adriatic sea," in *The Mediterranean Sea: Temporal Variability and Spatial Patterns, Geophysical Monograph Series*, eds G. L. E. Borzelli, M. Gačić, P. Lionello, and P. Malanotte-Rizzoli (Oxford, UK: John Wiley & Sons, Inc.), 139–155.

Bensi, M., Cardin, V., Rubino, A., Notarstefano, G., and Poulain, P. (2013). Effects of winter convection on the deep layer of the southern adriatic sea in 2012. *J. Geophys. Res. Oceans* 118, 6064–6075. doi: 10.1002/2013JC009432

Bradshaw, P. (1974). Possible origin of prandt's mixing-length theory. *Nature* 249, 135–136.

Cardin, V., and Bensi, M. (2014). *E2m3a-2006-2010-Time-Series-Southadriatic*. doi: 10.6092/36728450-4296-4E6A-967DD5B6DA55F306

Cardin, V., Bensi, M., and Pacciaroni, M. (2011). Variability of water mass properties in the last two decades in the south adriatic sea with emphasis on the period 2006–2009. *Continent. Shelf Res.* 31, 951–965. doi: 10.1016/j.csr.2011.03.002

Cardin, V., Bensi, M., Siena, G., and Ursella, L. (2014). *E2m3a-2011-2013-Timeseries-Southadriatic*. OGS (Istituto Nazionale di Oceanografia e di Geofisica Sperimentale), Division of Oceanography. doi: 10.6092/84CB588D-97E5-4C64-91BBBA6109DFA530

Cardin, V., Bensi, M., Ursella, L., and Siena, G. (2015). *E2m3a-2013-2015-Time-Series Southadriatic.* OGS (Istituto Nazionale di Oceanografia e di Geofisica Sperimentale), Division of Oceanography. doi: 10.6092/F8E6D18E-F877-4AA5-A983-A03B06CCB987

Cardin, V., Bensi, M., Ursella, L., and Siena, G. (2018). *E2m3a-2015-2017-Timeseries-Southadriatic.* OGS (Istituto Nazionale di Oceanografia e di Geofisica Sperimentale), Division of Oceanography. doi: 10.6092/238B5903-A173-4FC3-AC5F-5FEDF1064A39

Coppola L., Ntoumas M., Bozzano R., Bensi, M., Hartman, S. E., Charcos L. M., et al. (2016). *Handbook of Best Practices for Open Ocean Fixed Observatories 2016* (European Commission, FixO3 project, FP7 Program 2007-2013 under grant agreement no 312463). JCOMM Technical Reports Community Practices. Available online at: http://hdl.handle.net/11329/302

Cushman-Roisin, B., Gacic, M., Poulain, P.-M., and Artegiani, A. (2001). *Physical Oceanography of the Adriatic Sea: Past, Present and Future.* Dordrecht: Springer Science & Business Media.

de Lavergne, C., Falahat, S., Madec, G., Roquet, F., Nycander, J., and Vic, C. (2019). Toward global maps of internal tide energy sinks. *Ocean Modell.* 137, 52–75. doi: 10.1016/j.ocemod.2019.03.010

Flagg, C., Vermersch, J., and Beardsley, R. (1976). *Report on the 1974 MIT New England Shelf Dynamics Experiment, Part 2; the moored Array.* Department of Meteorology, Massachusetts Institute of Technology. Lab. Rep. (Unpublished.).

Kontoyiannis, H., Lykousis, V., Papadopoulos, V., Stavrakakis, S., Anassontzis, E., Belias, A., et al. (2016). Hydrography, circulation, and mixing at the calypso deep (the deepest Mediterranean trough) during 2006–09. *J. Phys. Oceanogr.* 46, 1255–1276. doi: 10.1175/JPO-D-15-0198

Landsberg, H. E., and Van Mieghem, J. (eds.). (1959). *Proceedings of Symposium on Atmospheric Diffusion and Air Pollution*, Vol. 6. New York, NY; London: Elsevier; Academic Press, 101–112.

Ledwell, J. R., Watson, A. J., and Law, C. S. (1998). Mixing of a tracer in the pycnocline. *J. Geophys. Res. Oceans* 103, 21499–21529.

Munk, W., and Wunsch, C. (1998). Abyssal recipes II: energetics of tidal and wind mixing. *Deep Sea Res. I Oceanogr. Res. Pap.* 45, 1977–2010. doi: 10.1016/S0967-0637(98)00070-3

Munk, W. H. (1966). "Abyssal recipes," in *Deep Sea Research and Oceanographic Abstracts* (Citeseer), 707–730.

Osborn, T. (1980). Estimates of the local rate of vertical diffusion from dissipation measurements. *J. Phys. Oceanogr.* 10, 83–89. doi: 10.1175/1520-0485(1980)010<0083:EOTLRO>2.0.CO;2

Pearlman, J. S., Bushnell, M., Coppola, L., Buttigieg, P. L., Pearlman, F., Simpson, P., et al. (2019). Evolving and sustaining ocean best practices and standards for the next decade. *Front. Mar. Sci.* 6:277. doi: 10.3389/fmars.2019.00277

Peltier, W., and Caulfield, C. (2003). Mixing efficiency in stratified shear flows. *Annu. Rev. Fluid Mech.* 35, 135–167. doi: 10.1146/annurev.fluid.35.101101.161144

Prandtl, L. (1925). 7. bericht über untersuchungen zur ausgebildeten turbulenz. *Zeitschrift für Angewandte Mathematik und Mechanik* 5, 136–139.

Preisendorfer, R. W., and Mobley, C. D. (1988). Principal component analysis in meteorology and oceanography. *Dev. Atmos. Sci.* 17:425.

Querin, S., Bensi, M., Cardin, V., Solidoro, C., Bacer, S., Mariotti, L., et al. (2016). Saw-tooth modulation of the deep-water thermohaline properties in the southern Adriatic sea. *J. Geophys. Res. Oceans* 121, 4585–4600. doi: 10.1002/2015JC011522

Taylor, G. I. (1922). Diffusion by continuous movements. *Proc. Lond. Math. Soc.* 2, 196–212.

Vallis, G. K. (2017). *Atmospheric and Oceanic Fluid Dynamics*. Cambridge, MA: Cambridge University Press.

Vic, C., Garabato, A. C. N., Green, J. M., Waterhouse, A. F., Zhao, Z., Melet, A., et al. (2019). Deep-ocean mixing driven by small-scale internal tides. *Nat. Commun.* 10, 1–9. doi: 10.1038/s41467-019-10149-5

Zachmanoglou, E. C., and Thoe, D. W. (1986). *Introduction to Partial Differential Equations With Applications*. Baltimore, MD: Courier Corporation.

Zervakis, V., Krasakopoulou, E., Georgopoulos, D., and Souvermezoglou, E. (2003). Vertical diffusion and oxygen consumption during stagnation periods in the deep north Aegean. *Deep Sea Res. I Oceanogr. Res. Pap.* 50, 53–71. doi: 10.1016/S0967-0637(02)00144-9

Zore-Armanda, M., Bone, M., Dadic, V., Morovic, M., Ratkovic, D., Stojanoski, L., et al. (1991). Hydrographic properties of the adriatic sea in the period from 1971 through 1983. *Acta Adriatica* 32:5544.

Conflict of Interest: The authors declare that the research was conducted in the absence of any commercial or financial relationships that could be construed as a potential conflict of interest.

A. PROJECTION

The discretized version of the projection to obtain the amplitude of the modes is given for the first three modes, it is defined iteratively by:

$$B_1(t) = \frac{\lambda_1}{2 \cdot 469} \sum_{i=750}^{1219} \Delta T(i,t) \sin(\frac{\pi(i - z_s)}{2 \cdot 469m}) \quad \text{(A1)}$$

$$B_2(t) = \frac{\lambda_2}{2 \cdot 469} \sum_{i=750}^{1219} \left(\Delta T(i,t) - B_1(t) \sin(\frac{\pi(i - z_s)}{2 \cdot 469m}) \right) \sin(3\frac{\pi(i - 750m)}{2 \cdot 469m}) \quad \text{(A2)}$$

$$B_3(t) = \frac{\lambda_3}{2 \cdot 469} \sum_{i=750}^{1219} \left(\Delta T(i,t) - B_1(t) \sin(\frac{\pi(i - z_s)}{2 \cdot 469m}) - B_2(t) \sin(3\frac{\pi(i - 750m)}{2 \cdot 469m}) \right) \sin(5\frac{\pi(i - 750)}{2 \cdot 469m}) \quad \text{(A3)}$$

If the record is over the total length $\lambda_k = 1$. If the record stops at length $z'_B < 1,219m$, so does the summation in Equations (A1)–(A3) and:

$$\lambda_k = \left(\frac{z'_B - z_s}{469m} - \frac{\sin(2(k-1)\pi \frac{z'_B - z_s}{469m})}{2(k-1)\pi \cdot 469m} \right)^{-1} \quad \text{(A4)}$$

frontiers in Marine Science

ORIGINAL RESEARCH
published: 15 January 2021
doi: 10.3389/fmars.2020.615975

The Effect of the Source of Deep Water in the Eastern Mediterranean on Western Mediterranean Intermediate and Deep Water

Yael Amitai[1]*, *Yosef Ashkenazy*[2] *and Hezi Gildor*[3]

[1] Kinneret Limnological Laboratory, Israel Oceanographic & Limnological Research Institute, Migdal, Israel, [2] Solar Energy and Environmental Physics, Ben-Gurion University of the Negev, Beersheba, Israel, [3] The Institute of Earth Sciences, The Hebrew University of Jerusalem, Jerusalem, Israel

The deep water in the western Mediterranean Sea was found to be significantly affected by a climatic event that took place in the eastern Mediterranean during the 1990s. Numerical simulations of the entire Mediterranean Sea showed that multiple equilibria states in the eastern Mediterranean can exist under present-day-like conditions. The two stable states that were found are associated with intermediate water exchange between the eastern Mediterranean's Aegean and Adriatic Basins. In the first state, the Adriatic acts as a source of deep water that flows into the deep layers of the eastern Mediterranean; in the second state, there is no source of deep water in the Adriatic and the eastern Mediterranean intermediate water is warmer and saltier. We studied the water pathways, in both stable states, into the western Mediterranean and found that the eastern Mediterranean water's properties signature can be seen as far as the Gulf of Lion, which is an important open-ocean deep water convection site. Meaning that, the eastern Mediterranean water characteristics are manifested in deep and intermediate water properties all over the Mediterranean Sea. The water propagating from the eastern to the western Mediterranean also has different flow regimes, in both states, through the Sicily Strait and in the Tyrrhenian Basin, as seen from a Lagrangian analysis.

Keywords: western Mediterranean, eastern Mediterranean, multiple equilibria states, deep water formation, Adriatic Basin, Aegean Basin, Sicily Strait

OPEN ACCESS

Edited by:
Nadia Lo Bue, National Earthquake Observatory (INGV), Italy

Reviewed by:
Anthony Bosse, Aix-Marseille Université, France
Dimitris Velaoras, Institute of Oceanography, Greece

***Correspondence:**
Yael Amitai
yael.amitai@ocean.org.il

Specialty section:
This article was submitted to Physical Oceanography, a section of the journal Frontiers in Marine Science

Received: *10 October 2020*
Accepted: *16 December 2020*
Published: *15 January 2021*

Citation:
Amitai Y, Ashkenazy Y and Gildor H (2021) The Effect of the Source of Deep Water in the Eastern Mediterranean on Western Mediterranean Intermediate and Deep Water. Front. Mar. Sci. 7:615975. doi: 10.3389/fmars.2020.615975

1. INTRODUCTION

The western Mediterranean Sea, from which warm and saline water flows to the Atlantic Ocean, has experienced substantial changes over the last decades. Its deep water has exhibited a moderate increase in temperature and salinity since the 1960s; this increase has been associated with global climate change (Bethoux et al., 1990; Krahmann and Schott, 1998). Deep water of the western Mediterranean Sea origin in open ocean convection events that take place in the Gulf of Lion area (Medoc Group et al., 1970). These were attributed to strong Mistral wind events (Cacho et al., 2000; López-Jurado et al., 2005; Font et al., 2007; Somot et al., 2018), but also to the characteristics of water masses advected from the eastern Mediterranean into the western Mediterranean (Gasparini et al., 2005; Schroeder et al., 2006). More specifically, the western Mediterranean convection events were associated with the warm, saline Levantine Intermediate Water (LIW), which crossed the Sicily

Strait (Schroeder et al., 2017) and reached the Gulf of Lion (GoL) area, enhancing (Lacombe et al., 1985), or depressing (Margirier et al., 2020) the deep convection. Numerous studies demonstrated that the properties of LIW vary over different time scales (Mauri et al., 2019; Ozer et al., 2020). Wu and Haines (1996) modeled the LIW pathways in the Mediterranean and showed that the LIW's salt content dictates the depth of convection in the GoL—namely, the saltier it is, the deeper it gets.

The observed trend of deep water temperature and salinity increase was enhanced by exceptional deep water formation events that took place in the GoL in 2004–2005 (Schroeder et al., 2006; Smith et al., 2008) and in 2012–2013 (Houpert et al., 2016; Waldman et al., 2016; Testor et al., 2018), generating a newly formed deep water mass (Schroeder et al., 2008, 2016). The deep water formed in the 2004–2005 and 2012–2013 events was denser than in other convection events and was characterized by high temperature and salinity. This is manifested in a significant jump in the time series of the western Mediterranean deep water properties (Herrmann et al., 2010). These events were identified as part of the Western Mediterranean Transient (WMT), which followed the Eastern Mediterranean Transient (EMT) that occurred at the beginning of the 1990s (Schroeder et al., 2006). The EMT refers to a change in the deep water source, from the Adriatic Basin to the Aegean Basin, causing warmer, saltier deep and intermediate water masses in the eastern Mediterranean that is also observed in Sicily Strait water properties (Schroeder et al., 2017). This climatic shift induced an increase in the LIW density flowing westward through the bottom layer of Sicily Strait. The following WMT is associated with an exceptional injection of heat and salt into the deep Tyrrhenian Basin (Astraldi et al., 2002; Gasparini et al., 2005) and with unusually deep convection in the GoL (Schroeder et al., 2006) as a consequence of the EMT signal propagating westward into the western Mediterranean. Furthermore, recent observations of warmer and saltier LIW in the GoL area were associated with weak convection between 2014 and 2018 due to strong deep stratification following 2012–2013 deep convection event (Margirier et al., 2020). Namely, the western Mediterranean deep water is under continuously impact of the eastern Mediterranean's LIW.

Many studies have investigated the causes and nature of the EMT (Lascaratos et al., 1999; Malanotte-Rizzoli et al., 1999; Theocharis et al., 1999) and whether it was atmospherically driven (Josey, 2003) or the result of an internal oceanic feedback (Gačić et al., 2010, 2011; Theocharis et al., 2014; Velaoras et al., 2014). We previously found, using a general circulation model of the entire Mediterranean, that deep water formation (DWF) in the eastern Mediterranean exhibits a hysteresis behavior and has multiple equilibria states under present-day-like atmospheric conditions (Amitai et al., 2017). The two steady states found are the following: (1) an active Adriatic DWF (dense water outflow from the Otranto Strait to the Ionian Basin) and a smaller Aegean outflow; and (2) a passive Adriatic DWF (the water entering the Adriatic is denser than that leaving it) and a stronger Aegean outflow. Henceforth, we refer to these two states as active and passive Adriatic. The passive Adriatic DWF state is the result of an initialized colder Aegean that is kept forced by a minor atmospheric temperature anomaly of $-0.2^{o}C$. The passive Adriatic state resembles circulation features of the EMT, although the seasonal atmospheric conditions were kept constant.

Here, we examine the manifestation of the two eastern Mediterranean steady states in the western Mediterranean's intermediate and deep water characteristics. The study is based on previous results (Amitai et al., 2017), focusing on the western Mediterranean with an emphasis on Sicily Strait water exchange and deep water formation in the GoL under two distinct eastern Mediterranean steady states. The GoL's deep water formation is substantially different in both spatial pattern and strength under these two steady states.

The paper is organized as follows: in section 2, we describe the main elements of our model and the particle tracking tool we used with the model output analysis. In section 3, we present our results, and we offer our conclusions in section 4.

2. MATERIALS AND METHODS

2.1. Ocean General Circulation Model

We used the Massachusetts Institute of Technology Ocean General Circulation Model (OGCM) (the MITgcm, Marshall et al., 1997a,b) to perform the simulations of the Mediterranean Sea circulation. We used the finite-volume, z-coordinate, hydrostatic, free surface, partial cell options of the MITgcm. The simulated domain consists of the entire Mediterranean Sea area, covering the west part of the strait of Gibraltar (**Figure 1**). The water column is resolved by 22 vertical levels with a resolution ranging from 10 m at the top to 500 m at the bottom. The horizontal resolution is $1/8^{\circ} \times 1/8^{\circ}$ on a spherical grid, which is about 9–14 km. The time step for both the tracers and the momentum is 20 min. For a more detailed description of the model and the parametrization of the sub-grid processes we used (see Amitai et al., 2017).

The model was initialized with climatological 3D temperature and salinity from NEMO-MED reanalysis data (obtained by Copernicus Marine Service Products, http://marine.copernicus.eu/). The wind stress was constructed from the monthly climatology of ERA-Interim reanalysis data (Dee et al., 2011). The Atlantic Ocean input was simulated by prescribing the Levitus (1982) monthly climatology of temperature and salinity in the western boundary of the model, outside the Strait of Gibraltar. Sea surface temperature (SST) and sea surface salinity (SSS) were relaxed toward the monthly averaged climatological SST and SSS of the NEMO-MED reanalysis with a relaxation time of 8 and 6 d, respectively. Then, monthly surface salt/freshwater flux was diagnosed, and the simulation continued with mixed surface boundary conditions (of prescribed freshwater flux and relaxation to NEMO-MED SST), to allow the development of natural variability in the simulations.

Our numerical simulations, which resulted in multiple equilibrium states in the Mediterranean, were inspired by studies that investigated the multiple equilibrium states of the Atlantic Ocean Meridional Overturning Circulation (MOC) as a function of freshwater forcing (Marotzke, 2000; Rahmstorf et al., 2005; Stouffer et al., 2006). As in these studies, the MOC hysteresis curves were found when we continually increasing or decreasing a boundary condition parameter between extreme values, as a

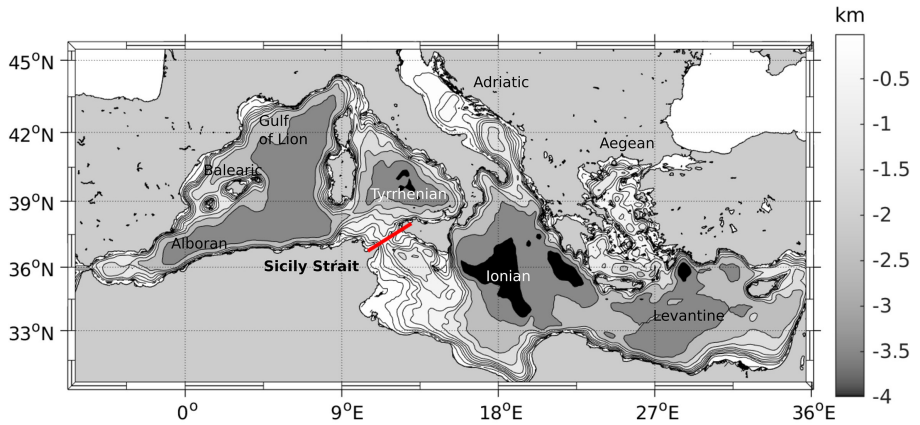

FIGURE 1 | Model's bathymetry of the Mediterranean Sea with the names of the main basins. The Sicily Strait transect used in **Figure 4** is indicated by the bold red line.

function of time. Unlike these studies, we chose the thermal forcing (restoring SST) over the Aegean and Adriatic Seas as the control parameter (see Ashkenazy et al., 2012). This was motivated by the observed severe winter cooling, of almost 3°C, over the Aegean Sea during the EMT (Josey, 2003). Hence, larger forcing boundaries between restored temperatures were chosen to detect the temperature range in which the two DWF states arise.

To obtain the two DWF states discussed in this manuscript, we modified the Aegean temperature boundary condition, i.e., the restoring temperature over the Aegean, but kept the rest of the forcing and boundary conditions as in the control run. We started from the control steady state and restored the Aegean SST to a temperature that is 5°C colder than the control run temperature, until reaching a cold steady state; we then increased the restoring temperature over the Aegean by 10°C at a rate of 0.02°C/yr. This step thus lasted 500 years and reached a restoring temperature of 5°C above the control run restoring temperature and is termed "gradual warming" (GW). Then, we kept the Aegean restoring temperature 5°C warmer than the control run restoring temperature and continued the simulation till reaching a warm steady state. Then, we started from the warm steady state and decreased the restoring temperature of the Aegean at a rate of 0.02°C/yr for 500 years, until it again reached the restoring temperature that is 5°C colder than the control run. This step is termed "gradual cooling" (GC). Finally, we kept the Aegean restoring temperature 5°C colder than the control run restoring temperature and continued the simulation till again reaching the cold steady state. All the above steps are presented in detail in Amitai et al. (2017).

These steps resulted in hysteresis curves of the Adriatic and Aegean deep water formation with respect to the restoring temperature over the Aegean. The existence of two steady states were found when we ran the model with a restoring temperature of the −0.2°C temperature anomaly over the Aegean with different initial conditions. The two runs lasted 1,500 years, starting from the model states achieved in the GW and GC experiments under the −0.2°C temperature anomaly. Thereafter, we obtained two Adriatic DWF steady states under the same Aegean forcing that is similar to present day atmospheric climatology. These two steady states were used to study the western Mediterranean deep water formation.

2.2. PaTATO Toolbox

To understand LIW pathways from the Sicily Strait to the sub-basins of the western Mediterranean, we conducted a Lagrangian transport analysis using the Particle Tracking and Analysis Toolbox (PaTATo) for Matlab (Fredj et al., 2016). From the model velocity fields, using PaTATo, we computed 3D Lagrangian trajectories of 132 water particles released in the Sicily Strait at a depth of 250 m, which is the bottom layer of the strait. We tracked the water particles, released in two successive model years, in monthly changing velocity fields for 3 years for the passive and active Adriatic DWF steady states.

3. RESULTS

Below, we describe and analyze the western Mediterranean intermediate and deep water properties under the active and the passive Adriatic DWF state found in Amitai et al. (2017). The difference between both states at the intermediate depth of 250 m (**Figure 2**) shows that there is a substantial influence of the Adriatic DWF on the Adriatic itself (as expected) and on the western Mediterranean's Tyrrhenian Basin. When the Adriatic is active, its intermediate water has similar characteristics as the surface signal; hence, it is warmer and saltier than when the Adriatic is passive. In the Tyrrhenian Basin, however, the intermediate water is colder and fresher when the Adriatic is active. This can be explained as follows: LIW leaving Sicily Strait typically flow north-eastward into the Tyrrhenian Basin, so when the Adriatic is passive the Tyrrhenian receives warmer (by $\sim 0.6^{\circ}C$) and saltier (by $\sim 0.2psu$) water than it receives when the Adriatic is active, as was observed during the EMT (Sparnocchia et al., 1999; Astraldi et al., 2001; Gasparini et al., 2005). Another difference between the two states is the appearance of a warm, saline strip in the northwestern Ionian Basin when the Adriatic

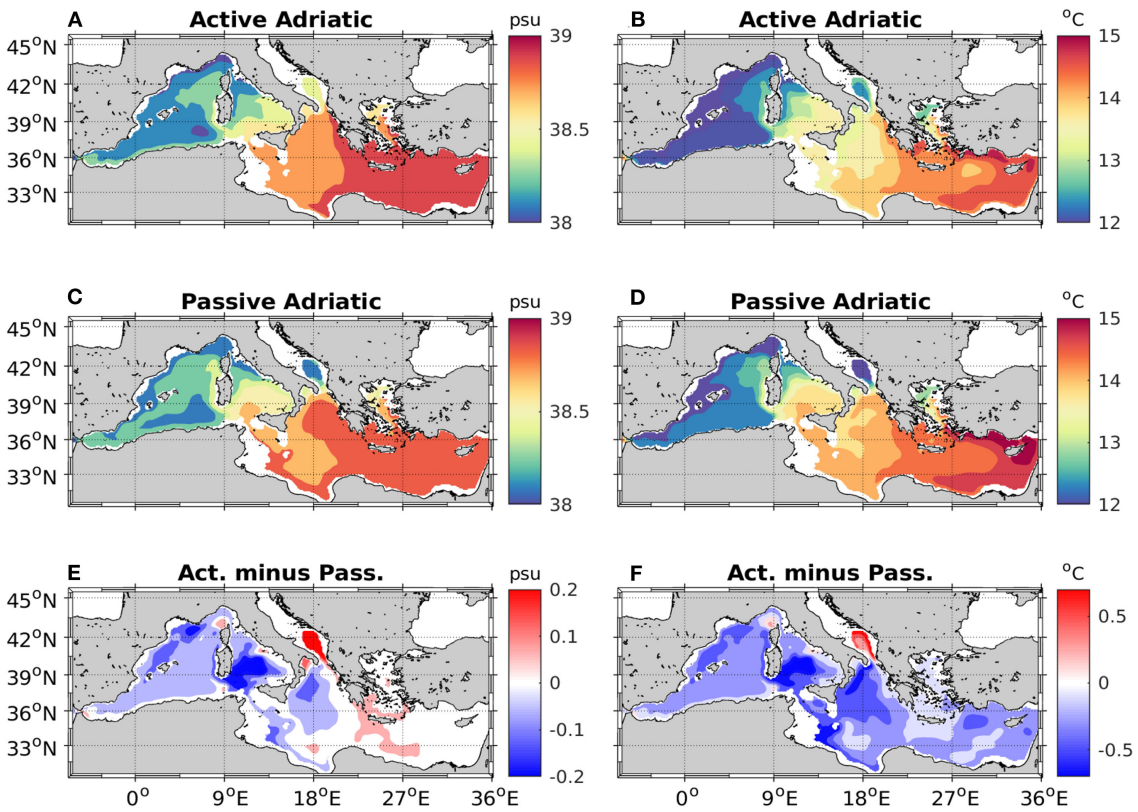

FIGURE 2 | Five-year means of salinity **(A,C)** and temperature **(B,D)** at a depth of 250 m from both steady states of active **(A,B)** and passive **(C,D)** Adriatic DWF and their difference **(E,F)**.

is passive. This water strip may be due to LIW entrainment (Astraldi et al., 2001) or transitional eastern Mediterranean deep water, which is associated with the EMT (Sparnocchia et al., 1999), following the steep topography in that region (**Figure 1**).

To better understand the intermediate anomaly in the Tyrrhenian Basin, we conducted a Lagrangian analysis using the PaTATo toolbox. We released 132 virtual particles in the bottom layer of the Sicily Strait (250 m) in two successive model years; this release was repeated for the two flow patterns created by the two steady states (**Figure 3**). The virtual water particles were released in the beginning of each year and were tracked for 3 years. The colors in **Figure 3** indicate the depth they reached at any time step and f/H contours were plotted in gray, where f is the planetary vorticity (local Coriolis parameter) and H is the bottom depth. This analysis was repeated several times, starting from various months and years, resulting in pattern similar to the one shown in **Figure 3**. When the Adriatic is passive, the water coming from the Sicily Strait widely disperses in the Tyrrhenian, following along Sardinia's eastern coast and recirculate mainly in intermediate levels before reaching the GoL region. However, when the Adriatic is active, the water flowing along the eastern Tyrrhenian, dilute with deep Tyrrhenian's water, hence less trajectories seen reaching the GoL region. In average the particles reach the convection area in the GoL $\sim$ 2 and $\sim$ 3 years after passing through the Sicily Strait under a passive and an active Adriatic states, respectively. It seems that most water particles leaving the Sicily Strait under active Adriatic state tend to follow the deeper barotropic streamlines in the eastern Tyrrhenian but this is not the case under passive Adriatic state. This may explain the presence of warm and saline intermediate water in the central and western Tyrrhenian under passive Adriatic DWF (**Figures 2E,F**). The difference in the observed circulation pattern is related to the density of the water leaving the eastern Mediterranean and may also be related to the differences in the Sicily Strait's flow regime.

Next, we examine the properties of the flow in the Sicily Strait along the transect marked in **Figure 1**. Transect of Sicily Strait water temperature (left column in **Figure 4**) and salinity (right column in **Figure 4**) are examined with contours of density (left column in **Figure 4**) and velocity (right column in **Figure 4**) superimposed above. Since the transect is diagonal, the velocity fields were rotated so that the velocity examined is the component that is perpendicular to the transect. The dashed lines in **Figures 4B,D** indicate southeastward flow, and the solid lines indicate northwestward flow. For both states, the known depiction of low salinity (density) water entering the eastern Mediterranean through the upper layer and high salinity (density) water leaving mostly through the bottom layer is seen. However, in the passive Adriatic state (**Figure 4D**), there is water outflowing from the eastern to the western

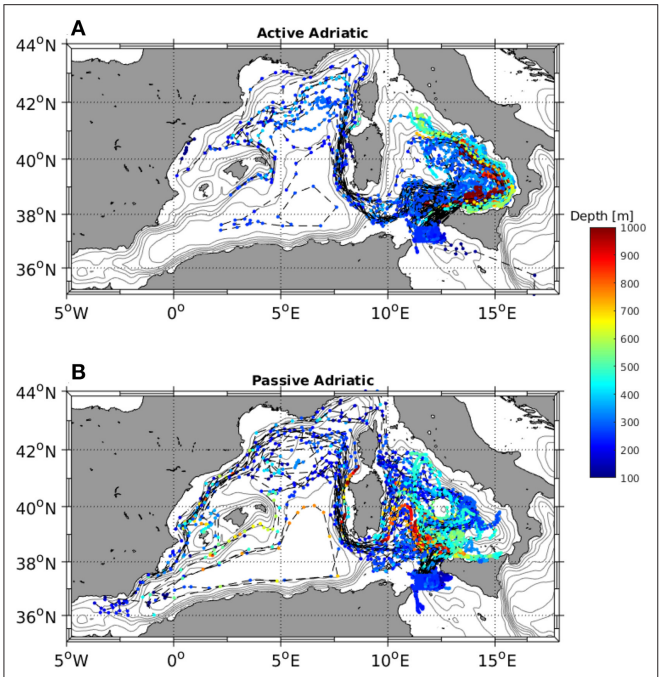

FIGURE 3 | 3D Lagrangian trajectories of 132 water particles released in the Sicily Strait at a depth of 250 m in two successive model years. The water particles were tracked for 3 years in an active Adriatic state **(A)** and a passive Adriatic state **(B)**. The colorbar indicates the depth of the particles at the given time. f/h contours are plotted in gray.

Mediterranean (northwestward velocity) in very shallow depths around longitude 11.2°*E*, which is not found in this region in the active Adriatic state (**Figure 4B**). This signal might correspond to the uplift of deep and intermediate water masses reported during the EMT (Roether et al., 1996). When looking at the differences between the active and passive states (**Figures 4E,F**), the most prominent feature is the positive salinity and density anomalies around 150 m in the middle of the strait that emerges together with velocity anomalies along the transect. It appears that when the Adriatic is passive, the flow from the eastern to the western Mediterranean in 150 m depth at the strait southwestern part is stronger but with lighter water (positive anomaly contours in **Figure 4E**). In the bottom layer of the strait, the flow strength is unchanged between states, but the density of the water leaving the eastern Mediterranean is a bit higher (negative anomaly contour beneath 250 m at **Figure 4E**), as was evidenced during the EMT. We also note that the isopycnal contours follow the salinity slopes rather than the temperature slopes along the transect, emphasizing the role of LIW salinity in dictating the Sicily Strait's flow regime.

To summarize, the shallow water in the transect is denser when the Adriatic is active, but the flow regime in the shallow layers when the Adriatic is passive is such that the water exchanges more rapidly (velocity anomalies from both sides of the transect) between eastern and western Mediterranean. The deep water flux (denser than 1029.1 kg m^{-3}) from the eastern to the western Mediterranean is 1 ± 0.08*Sv* (mean ± 1 std) in the active Adriatic case and only 0.7 ± 0.14*Sv* in the passive Adriatic case. This verifies that most water that leaves the eastern Mediterranean in a passive Adriatic state (50 vs. 40% in the active Adriatic state) is not dense enough to sink to the bottom layer of the transect and, therefore, mostly fills the shallow and intermediate levels of the Sicily Strait, as seen in the above results.

We next study the temperature and salinity differences between the active and passive Adriatic states at depths of 550 and 1,750 m (**Figure 5**) in comparison to the differences between the states at a depth of 250 m (**Figures 2E,F**). At the 550 m depth, similar to the 250 m depth, the Tyrrhenian is still warmer and saltier when the Adriatic is passive (negative anomaly in both properties). However, the Balearic and Alboran Basins of the western Mediterranean exhibit positive anomalies of temperature and salinity that are absent from the 250 m layer. These anomalies are enhanced and spread eastward to the Tyrrhenian in the 1,750 m layer. This result does not accord with the observations reported by Gasparini et al. (2005) and Schroeder et al. (2006), who showed a dramatic increase in temperature and salinity in the western Mediterranean deep water that was associated with the absence of deep water production in the Adriatic. However, this result is implied by the density transect through the Sicily Strait (**Figure 4**), which indicate a significant density difference that is confined to shallow (above 200 m) depths. This suggests that the positive salinity and temperature anomalies propagating from the eastern Mediterranean are not sufficient to reproduce the observed impact on the western Mediterranean deep water and that dry, cold atmospheric conditions are crucial to understand the deep water formation in the western Mediterranean (López-Jurado et al., 2005; Font et al., 2007; Durrieu de Madron et al., 2013). When comparing the control run (a simulation with climatological atmospheric boundary conditions) properties with both steady state properties, we evidence that the control run is almost identical to the active Adriatic state (not shown), suggesting that it is the "natural" state of the Mediterranean Sea.

Deep water formation often affects the mixed layer depth (MLD), and we now concentrate on the MLD's characteristics in the GoL region under active and passive Adriatic states. The MLD was calculated from the model results and was chosen to be the depth at which the density is $\Delta\rho = 0.02$ kg/m^3 higher than the surface density. This MLD criteria was chosen since the coupling between temperature and salinity is significant in the presence of the warm and saline LIW in the GoL deep convection process (Houpert et al., 2015; Somot et al., 2018).

When looking at a representative pattern of March MLD in an active Adriatic (**Figure 6A**) vs. a passive Adriatic (**Figure 6B**), we notice a completely different structure and amplitude of MLD in the GoL region. In an active Adriatic, the MLD amplitude is moderate (∼600 m) and spans a widespread area near the northwestern coast of the western Mediterranean. However, under a passive Adriatic state, the MLD is deeper (∼1,200 m) and its maximal values are confined to a small area farther from the coast, which can vary between years. A monthly mean, over 100 model years, of the maximal MLD in the region is shown in **Figures 6A,B** where the maximal MLD in the region ± the standard deviation is shown in **Figure 6C**. It shows that

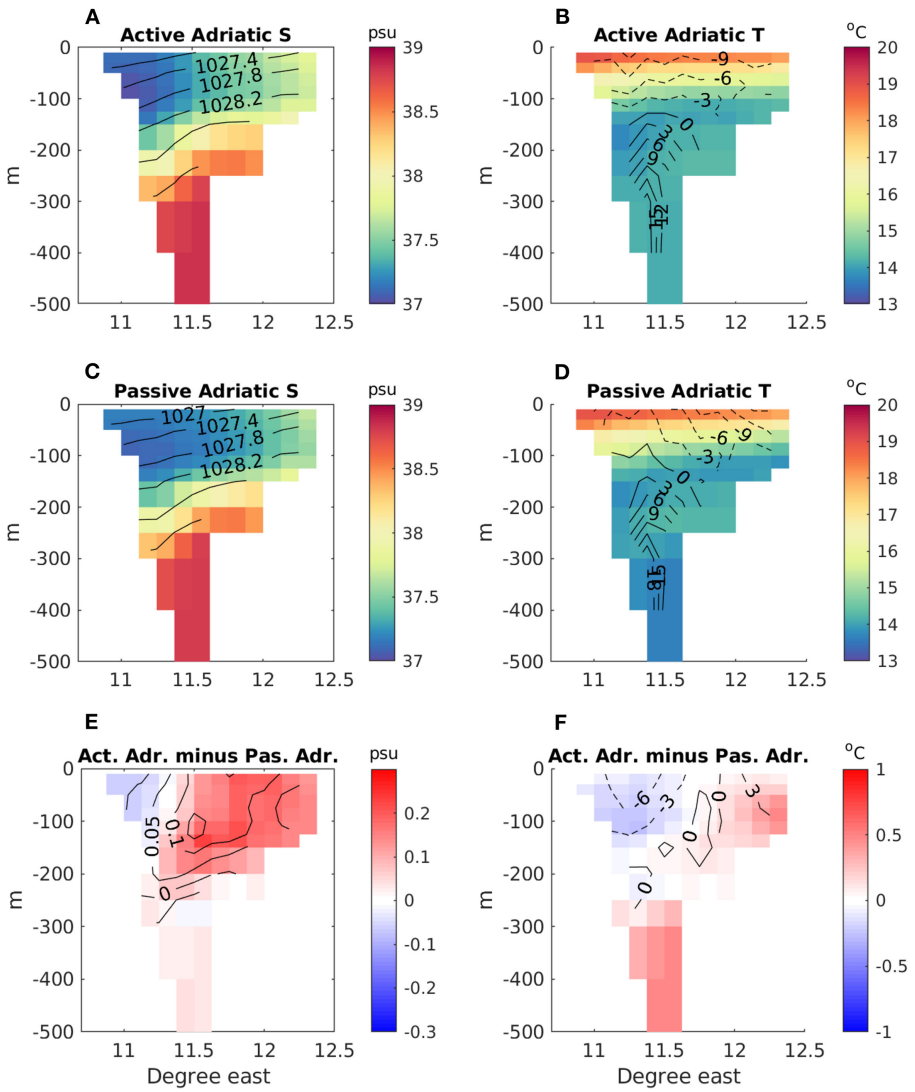

FIGURE 4 | Five-year means of salinity (left) and temperature (right) of water passing through the Sicily Strait along the transect plotted in **Figure 1**. Contours of density (left) and velocity (right) along the transect are superimposed, in an active Adriatic state **(A,B)**, passive Adriatic state **(C,D)**, and their difference **(E,F)**. The dashed (negative) lines indicate southward flow, while the solid (positive) lines indicate northward flow. The density is given in units of kg/m^3 and the velocity in units of cm/s.

the difference in maximal MLDs between the passive and active Adriatic states can vary between 200 and 700 m, suggesting deeper convection for the passive Adriatic state. All the above indicates that the passive Adriatic MOC results in circulation that enables a deeper convection. This result might be explained by the LIW's pathway in a passive Adriatic state, where the flow is through the Sicily Strait at shallow—intermediate levels (**Figure 4**) and, after recirculating in the Tyrrhenian (**Figure 3B**), reaching rapidly the region of convection in the GoL. There it enhances the production of deep water (Lacombe et al., 1985; Wu and Haines, 1996; Schroeder et al., 2006; Herrmann et al., 2010). In an active Adriatic state it seems that LIW's pathway follow the eastern Tyrrhenian coast while deepening (**Figure 3A**), hence less LIW reach the GoL and act as preconditions to deep convection.

We note that in all the simulations, the atmospheric forcing over the western Mediterranean is monthly climatology, such that the forcing has no interannual variability. Therefore, we cannot relate the role of weather conditions and their extremes to the deep water formation in the GoL (López-Jurado et al., 2005).

To further understand the difference between the two states of the Adriatic we calculated the difference in the stratification index (SI) between the active and passive Adriatic states (**Figure 6D**). The SI was previously used in studies regarding the Mediterranean Sea (Herrmann et al., 2010; Somot et al., 2018) and is defined as follows:

$$SI(H,t) = \int_0^H N^2(z,t) z dz \quad ; \quad N^2(z,t) = -\frac{g}{\rho}\frac{\partial \rho(z,t))}{\partial z} \qquad (1)$$

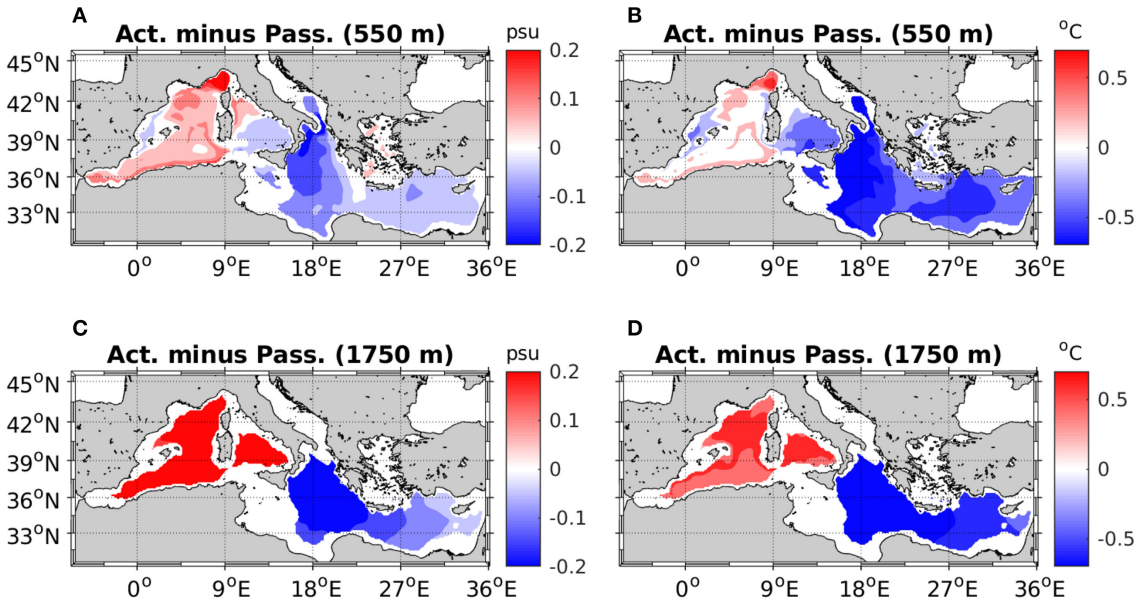

FIGURE 5 | Active and passive Adriatic states' differences in salinity and temperature, at depths of 550 m **(A,B)** and 1,750 m **(C,D)**.

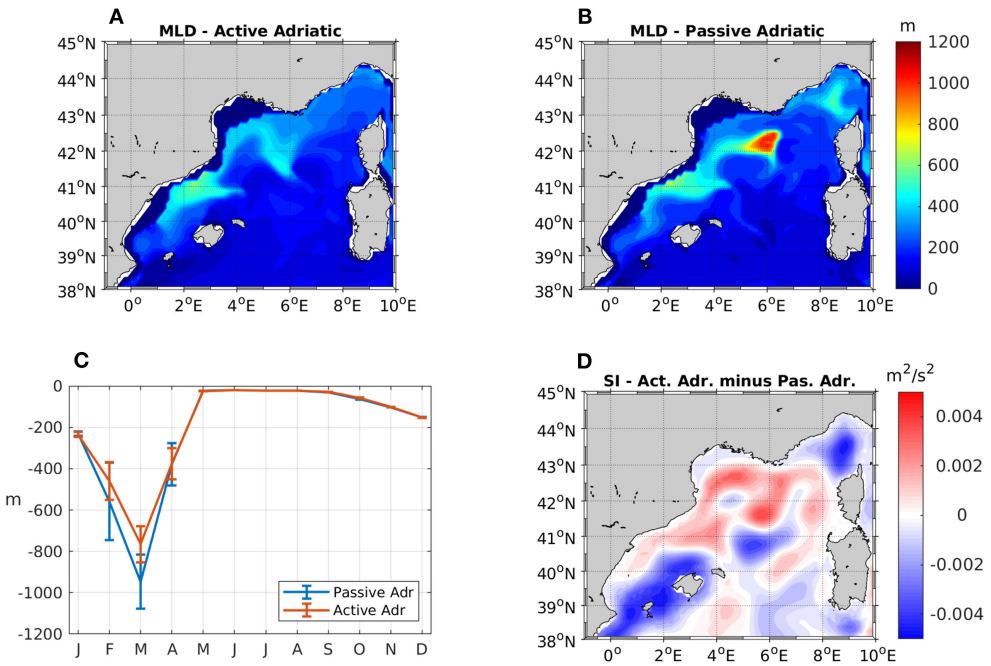

FIGURE 6 | A representative pattern of March MLD in active **(A)** and passive **(B)** Adriatic DWF states over the GoL region. Monthly mean of maximal MLD in the region depicted in the upper panels with standard deviation as error bars in both states **(C)**. Stratification Index difference between states **(D)**.

where N is the Brunt-Väisälä (buoyancy) frequency, t is the time in seconds, z the depth in meters, ρ the potential density, g the gravitational acceleration and H the depth. The larger the SI is, the stronger the vertical stratification is. Positive anomaly in the map of active Adriatic SI minus passive Adriatic SI (**Figure 6D**) emphasizes our former result that under active Adriatic there are less deep convection events in the GoL since it is more stratified than in the passive Adriatic state.

4. DISCUSSION

Our main result, based on our GCM simulations, is that the western Mediterranean is largely influenced by the DWF's location in the eastern Mediterranean. We focus on two cases (under the same forcing): active and passive sources of deep water in the Adriatic Sea. When the Adriatic DWF is active, it produces deep water in the eastern Mediterranean, and the deep layer outflow to the western Mediterranean through the Sicily Strait is larger. However, the exchange of water at depths shallower than 200 m is smaller. This flow regime creates a state where warm, saline eastern Mediterranean water significantly affects the intermediate water of the western Mediterranean under passive Adriatic state. Eventually, these eastern intermediate water reaches the GoL area and modifies the GoL's stratification, hence significantly affects the properties (shape and strength) of the western Mediterranean deep convection.

Another important result of our analysis is that although intense local convection events are simulated in a passive Adriatic DWF, as was observed after the EMT (Gasparini et al., 2005), the weather conditions over the GoL (associated with cold and dry bursts of Mistral winds) are essential for reproducing a new widespread water mass, as was observed after 2004 (Houpert et al., 2016; Schroeder et al., 2016). This result highlights the role of LIW in enabling or disabling the deep convection that appears in the GoL region (Margirier et al., 2020), even if it is spatially sporadic (**Figure 6**).

Furthermore, we found that the Tyrrhenian Basin in the western Mediterranean acts as a buffer zone between the western and the eastern Mediterranean, and dilution of LIW may take place there under an unusual flow regime, as was observed during the EMT (Sparnocchia et al., 1999).

To summarize, although our results were derived from simulations with idealized boundary conditions that only partially resemble the observed climatic transient, they contribute to the understanding of the interaction between the western and eastern Mediterranean and to characterize the propagating signals between them.

DATA AVAILABILITY STATEMENT

The original contributions presented in the study are included in the article/supplementary material, further inquiries can be directed to the corresponding author/s.

AUTHOR CONTRIBUTIONS

YAm conducted the model simulations and data analysis. All authors contributed to the experimental design, manuscript writing and revision, and read and approved the submitted version.

FUNDING

This study was supported by the Israeli Ministry of Science and the Italian Ministry of Foreign Affairs.

REFERENCES

Amitai, Y., Ashkenazy, Y., and Gildor, H. (2017). Multiple equilibria and overturning variability of the Aegean-Adriatic Seas. *Glob. Planet. Change* 151, 49–59. doi: 10.1016/j.gloplacha.2016.05.004

Ashkenazy, Y., Stone, P. H., and Malanotte-Rizzoli, P. (2012). Box modeling of the Eastern Mediterranean sea. *Phys. A* 391, 1519–1531. doi: 10.1016/j.physa.2011.08.026

Astraldi, M., Gasparini, G. P., Gervasio, L., and Salusti, E. (2001). Dense water dynamics along the Strait of Sicily (Mediterranean Sea). *J. Phys. Oceanogr.* 31, 3457–3475. doi: 10.1175/1520-0485(2001)031<3457:DWDATS>2.0.CO;2

Astraldi, M., Gasparini, G. P., Vetrano, A., and Vignudelli, S. (2002). Hydrographic characteristics and interannual variability of water masses in the central Mediterranean: a sensitivity test for long-term changes in the Mediterranean Sea. *Deep-Sea Res. Part I Oceanogr. Res. Pap.* 49, 661–680. doi: 10.1016/S0967-0637(01)00059-0

Bethoux, J. P., Gentili, B., Raunet, J., and Tailliez, D. (1990). Warming trend in the western Mediterranean deep water. *Nature* 347, 660–662. doi: 10.1038/347660a0

Cacho, I., Grimalt, J. O., Sierro, F. J., Shackleton, N., and Canals, M. (2000). Evidence for enhanced Mediterranean thermohaline circulation during rapid climatic coolings. *Earth Planet. Sci. Lett.* 183, 417–429. doi: 10.1016/S0012-821X(00)00296-X

Dee, D., Uppala, S., Simmons, A., Berrisford, P., Poli, P., Kobayashi, S., et al. (2011). The ERA-Interim reanalysis: Configuration and performance of the data assimilation system. *Q. J. R. Meteorol. Soc.* 137, 553–597. doi: 10.1002/qj.828

Durrieu de Madron, X., Houpert, L., Puig, P., Sanchez-Vidal, A., Testor, P., Bosse, A., et al. (2013). Interaction of dense shelf water cascading and open-sea convection in the northwestern Mediterranean during winter 2012. *Geophys. Res. Lett.* 40, 1379–1385. doi: 10.1002/grl.50331

Font, J., Puig, P., Salat, J., Palanques, A., and Emelianov, M. (2007). Sequence of hydrographic changes in NW mediterranean deep water due to the exceptional winter of 2005. *Sci. Mar.* 71, 339–346. doi: 10.3989/scimar.2007.71n2339

Fredj, E., Carlson, D. F., Amitai, Y., Gozolchiani, A., and Gildor, H. (2016). The particle tracking and analysis toolbox (PaTATO) for Matlab. *Limnol. Oceanogr.* 14, 586–599. doi: 10.1002/lom3.10114

Gačić, M., Borzelli, G. L. E., Civitarese, G., Cardin, V., and Yari, S. (2010). Can internal processes sustain reversals of the ocean upper circulation? The Ionian Sea example. *Geophys. Res. Lett.* 37. doi: 10.1029/2010GL043216

Gačić, M., Civitarese, G., Eusebi Borzelli, G. L., Kovačević, V., Poulain, P.-M., Theocharis, A., et al. (2011). On the relationship between the decadal oscillations of the northern Ionian Sea and the salinity distributions in the eastern Mediterranean. *J. Geophys. Res.* 116:C12002. doi: 10.1029/2011JC007280

Gasparini, G. P., Ortona, A., Budillon, G., Astraldi, M., and Sansone, E. (2005). The effect of the Eastern Mediterranean Transient on the hydrographic characteristics in the Strait of Sicily and in the Tyrrhenian Sea. *Deep-Sea Res. Part I Oceanogr. Res. Pap.* 52, 915–935. doi: 10.1016/j.dsr.2005.01.001

Herrmann, M., Sevault, F., Beuvier, J., and Somot, S. (2010). What induced the exceptional 2005 convection event in the northwestern Mediterranean basin? Answers from a modeling study. *J. Geophys. Res.* 115, 1–19. doi: 10.1029/2010JC006162

Houpert, L., Durrieu de Madron, X., Testor, P., Bosse, A., D'Ortenzio, F., Bouin, M. N., et al. (2016). Observations of open-ocean deep convection in the northwestern Mediterranean Sea: seasonal and interannual variability of mixing and deep water masses for the 2007-2013 Period. *J. Geophys. Res.* 121, 8139–8171. doi: 10.1002/2016JC011857

Houpert, L., Testor, P., de Madron, X. D., Somot, S., D?Ortenzio, F., Estournel, C., et al. (2015). Seasonal cycle of the mixed layer, the seasonal thermocline and the upper-ocean heat storage rate in the Mediterranean Sea derived from observations. *Prog. Oceanogr.* 132, 333–352. doi: 10.1016/j.pocean.2014.11.004

Josey, S. A. (2003). Changes in the heat and freshwater forcing of the eastern Mediterranean and their influence on deep water formation. *J. Geophys. Res.* 108:3237. doi: 10.1029/2003JC001778

Krahmann, G., and Schott, F. (1998). Longterm increases in Western Mediterranean salinities and temperatures: anthropogenic and climatic sources. *Geophys. Res. Lett.* 25, 4209–4212. doi: 10.1029/1998GL900143

Lacombe, H., Tchernia, P., and Gamberoni, L. (1985). Variable bottom water in the Western Mediterranean basin. *Prog. Oceanogr.* 14, 319–338. doi: 10.1016/0079-6611(85)90015-1

Lascaratos, A., Roether, W., Nittis, K., and Klein, B. (1999). Recent changes in deep water formation and spreading in the eastern Mediterranean Sea: a review. *Prog. Oceanogr.* 44, 5–36. doi: 10.1016/S0079-6611(99)00019-1

Levitus, S. (1982). *Climatological Atlas of the World Ocean*. NOAA Professional Paper, 13, U.S. Gov. Rockville, MD: U.S. Government Printing Office. p. 190.

López-Jurado, J. L., González-Pola, C., and Vélez-Belchi, P. (2005). Observation of an abrupt disruption of the long-term warming trend at the Balearic Sea, western Mediterranean Sea, in summer 2005. *Geophys. Res. Lett.* 32, 1–4. doi: 10.1029/2005GL024430

Malanotte-Rizzoli, P., Manca, B. B., d'Alcala, M. R., Theocharis, A., Brenner, S., Budillon, G., et al. (1999). The Eastern Mediterranean in the 80s and in the 90s: the big transition in the intermediate and deep circulations. *Dyn. Atmos. Oceans* 29, 365–395. doi: 10.1016/S0377-0265(99)00011-1

Margirier, F., Testor, P., Heslop, E., Mallil, K., Bosse, A., Houpert, L., et al. (2020). Abrupt warming and salinification of intermediate waters interplays with decline of deep convection in the Northwestern Mediterranean Sea. *Sci. Rep.* 10, 1–11. doi: 10.1038/s41598-020-77859-5

Marotzke, J. (2000). Abrupt climate change and thermohaline circulation: mechanisms and predictability. *Proc. Natl. Acad. Sci. U.S.A.* 97, 1347–1350. doi: 10.1073/pnas.97.4.1347

Marshall, J., Adcroft, A., Hill, C., Perelman, L., and Heisey, C. (1997a). A finite-volume, incompressible Navier Stokes model for studies of the ocean on parallel computers. *J. Geophys. Res.* 102, 5753–5766. doi: 10.1029/96JC02775

Marshall, J., Hill, C., Perelman, L., and Adcroft, A. (1997b). Hydrostatic, quasi-hydrostatic, and nonhydrostatic ocean modeling. *J. Geophys. Res.* 102, 5733–5752. doi: 10.1029/96JC02776

Mauri, E., Sitz, L., Gerin, R., Poulain, P.-M., Hayes, D., and Gildor, H. (2019). On the variability of the circulation and water mass properties in the eastern Levantine Sea between September 2016-August 2017. *Water* 11:1741. doi: 10.3390/w11091741

Medoc Group, Lacombe, H., Tchernia, P., Charcot, J., Ribet, M., Bonnot, J., et al. (1970). Observation of formation of deep water in the Mediterranean Sea, 1969. *Nature* 227, 1037–1040. doi: 10.1038/2271037a0

Ozer, T., Gertman, I., Gildor, H., Goldman, R., and Herut, B. (2020). Evidence for recent thermohaline variability and processes in the deep water of the Southeastern Levantine Basin, Mediterranean Sea. *Deep Sea Res. Part II Top. Stud. Oceanogr.* 171:104651. doi: 10.1016/j.dsr2.2019.104651

Rahmstorf, S., Crucifix, M., Ganopolski, A., Goosse, H., Kamenkovich, I., Knutti, R., et al. (2005). Thermohaline circulation hysteresis: a model intercomparison. *Geophys. Res. Lett.* 32:L23605. doi: 10.1029/2005GL023655

Roether, W., Manca, B. B., Klein, B., Bregant, D., Georgopoulos, D., Beitzel, V., et al. (1996). Recent changes in eastern Mediterranean deep waters. *Science* 271, 333–335. doi: 10.1126/science.271.5247.333

Schroeder, K., Chiggiato, J., Bryden, H. L., Borghini, M., and Ben Ismail, S. (2016). Abrupt climate shift in the Western Mediterranean Sea. *Sci. Rep.* 6, 1–7. doi: 10.1038/srep23009

Schroeder, K., Chiggiato, J., Josey, S. A., Borghini, M., Aracri, S., and Sparnocchia, S. (2017). Rapid response to climate change in a marginal sea. *Sci. Rep.* 7, 1–7. doi: 10.1038/s41598-017-04455-5

Schroeder, K., Gasparini, G., Tangherlini, M., and Astraldi, M. (2006). Deep and intermediate water in the western Mediterranean under the influence of the Eastern Mediterranean transient. *Geophys. Res. Lett.* 33:L21607. doi: 10.1029/2006GL027121

Schroeder, K., Ribotti, A., Borghini, M., Sorgente, R., Perilli, A., and Gasparini, G. P. (2008). An extensive western Mediterranean deep water renewal between 2004 and 2006. *Geophys. Res. Lett.* 35, 1–7. doi: 10.1029/2008GL035146

Smith, R. O., Bryden, H. L., and Stansfield, K. (2008). Observations of new western Mediterranean deep water formation using Argo floats. *Ocean Sci.* 4, 133–149. doi: 10.5194/os-4-133-2008

Somot, S., Houpert, L., Sevault, F., Testor, P., Bosse, A., Taupier-Letage, I., et al. (2018). Characterizing, modelling and understanding the climate variability of the deep water formation in the North-Western Mediterranean Sea. *Clim. Dyn.* 51, 1179–1210. doi: 10.1007/s00382-016-3295-0

Sparnocchia, S., Gasparini, G. P., Astraldi, M., Borghini, M., and Pistek, P. (1999). Dynamics and mixing of the Eastern Mediterranean outflow in the Tyrrhenian basin. *J. Mar. Syst.* 20, 301–317. doi: 10.1016/S0924-7963(98)00088-8

Stouffer, R. J., Yin, J., Gregory, J., Dixon, K., Spelman, M., Hurlin, W., et al. (2006). Investigating the causes of the response of the thermohaline circulation to past and future climate changes. *J. Clim.* 19, 1365–1387. doi: 10.1175/JCLI3689.1

Testor, P., Bosse, A., Houpert, L., Margirier, F., Mortier, L., Legoff, H., et al. (2018). Multiscale observations of deep convection in the northwestern Mediterranean Sea during winter 2012-2013 using multiple platforms. *J. Geophys. Res.* 123, 1745–1776. doi: 10.1002/2016JC012671

Theocharis, A., Krokos, G., Velaoras, D., and Korres, G. (2014). "An internal mechanism driving the alternation of the Eastern Mediterranean dense/deep water sources," in *The Mediterranean Sea*, eds G. L. E. Borzelli, M. Gačić, P. Lionello and P. Malanotte-Rizzoli (American Geophysical Union (AGU)). doi: 10.1002/9781118847572.ch8

Theocharis, A., Nittis, K., Kontoyiannis, H., Papageorgiou, E., and Balopoulos, E. (1999). Climatic changes in the Aegean Sea influence the Eastern Mediterranean thermohaline circulation (1986-1997). *Geophys. Res. Lett.* 26, 1617–1620. doi: 10.1029/1999GL900320

Velaoras, D., Krokos, G., Nittis, K., and Theocharis, A. (2014). Dense intermediate water outflow from the Cretan Sea: a salinity driven, recurrent phenomenon, connected to thermohaline circulation changes. *J. Geophys. Res.* 119, 4797–4820. doi: 10.1002/2014JC009937

Waldman, R., Somot, S., Herrmann, M., Testor, P., Estournel, C., Sevault, F., et al. (2016). Estimating dense water volume and its evolution for the year 2012-2013 in the Northwestern Mediterranean Sea: An observing system simulation experiment approach. *J. Geophys. Res.* 121, 6696–6716. doi: 10.1002/2016JC011694

Wu, P., and Haines, K. (1996). Modeling the dispersal of Levantine Intermediate Water and its role in Mediterranean deep water formation. *J. Geophys. Res.* 101, 6591–6607. doi: 10.1029/95JC03555

Conflict of Interest: The authors declare that the research was conducted in the absence of any commercial or financial relationships that could be construed as a potential conflict of interest.

frontiers in Marine Science

ORIGINAL RESEARCH
published: 20 January 2021
doi: 10.3389/fmars.2020.598686

Post-eastern Mediterranean Transient Oxygen Decline in the Deep Waters of the Southeast Mediterranean Sea Supports Weakening of Ventilation Rates

Guy Sisma-Ventura, Nurit Kress, Jacob Silverman, Yaron Gertner, Tal Ozer, Eli Biton, Ayah Lazar, Isaac Gertman, Eyal Rahav* and Barak Herut*

Israel Oceanographic and Limnological Research, National Institute of Oceanography, Haifa, Israel

OPEN ACCESS

Edited by:
Katrin Schroeder, National Research Council (CNR), Italy

Reviewed by:
Dimitris Velaoras, Hellenic Centre for Marine Research (HCMR), Greece
Vedrana Kovacevic, National Institute of Oceanography and Experimental Geophysics (OGS), Italy

***Correspondence:**
Guy Sisma-Ventura
guy.siv@ocean.org.il
Eyal Rahav
eyal.rahav@ocean.org.il

Specialty section:
This article was submitted to Physical Oceanography, a section of the journal Frontiers in Marine Science

Received: *25 August 2020*
Accepted: *14 December 2020*
Published: *20 January 2021*

Citation:
Sisma-Ventura G, Kress N, Silverman J, Gertner Y, Ozer T, Biton E, Lazar A, Gertman I, Rahav E and Herut B (2021) Post-eastern Mediterranean Transient Oxygen Decline in the Deep Waters of the Southeast Mediterranean Sea Supports Weakening of Ventilation Rates. Front. Mar. Sci. 7:598686. doi: 10.3389/fmars.2020.598686

Long-term trends in oxygen, salinity, and nutrients were followed in the Southeastern Mediterranean (SEMS) deep waters from 2002 to 2020. Results show a net decrease in oxygen since 2008 of −0.5 ± 0.1 μmol kg^{-1} yr^{-1} in the bathypelagic depths (1,200–2,000 m). Multiannual variability in oxygen levels superimposed this trend, and is likely associated with variations in thermohaline fluxes. The 2020 mean oxygen concentration of 179.5 ± 2.3 μmol kg^{-1} is comparable to the pre-Eastern Mediterranean Transient (EMT) mean value. The post-EMT signature is clearly demonstrated in both oxygen and salinity over the period of 2002–2013, but since 2014 it diminished, mainly due to mixing of the Aegean deep water (AegDW) mass with the overlying old Adriatic water mass. This trend reflects a switch back to the pre-EMT regime, characterized by thermohaline homogeneity of the deep water column in the SEMS. The long-term decline of deep water oxygen levels is also accompanied by a corresponding increase in dissolved inorganic nutrients, supporting aging of the deep water masses. Our results suggest that ventilation of the SEMS deep water is currently occurring at a lower, pre-EMT rate, probably as a result of moderated deep water formation in recent time.

Keywords: East Mediterranean, deep water, EMT, time series, oxygen decline, nutrients

INTRODUCTION

The ocean interior plays a major role in regulating Earth's climate, acting as a sink for anthropogenic CO_2 produced by fossil fuels burning and the heat produced by the emitted greenhouse gases (e.g., Sarmiento et al., 1998; Reid et al., 2009; Glecker et al., 2016). The evaluation of long-term changes in the ocean interior biogeochemistry is, thus, essential for better understanding of the ocean-atmosphere coupling and feedbacks that are routinely simulated in many models. Unlike the upper ocean surface layer, which is tightly related to the atmosphere, deep layers of the oceans are assumed to be constant over a much longer time frame (e.g., Sarmiento et al., 1992, 1998). However, recent studies have shown a strong coupling between atmospheric oscillations and those occurring in intermediate and deep

water masses (Watanabe et al., 2003; Ozer et al., 2017). Moreover, many observational studies have shown links between present-day climate changes and those occurring in deep-sea environments, primarily increased deep-sea temperature (Purkey and Johnson, 2010), and deoxygenation (e.g., Stramma et al., 2008; Keeling et al., 2010; Helm et al., 2011). Unfortunately, long time series with high temporal resolution of deep-sea observations are relatively sparse and thus, the effect of long and short term disturbances on the ocean interior biogeochemistry remains relatively unexplored and unconfirmed.

The Eastern Mediterranean, in particular the Levantine basin, is one of the most evaporative marginal seas in the world – a crucial area in the larger framework of the Mediterranean conveyor belt (Pinardi and Masetti, 2000; Millot and Taupier-Letage, 2005; Tanhua et al., 2013). The water body in this region is considered ultra-oligotrophic, due to the advection of low salinity, nutrient depleted Modified Atlantic Water (MAW), limited freshwater input (Hecht, 1992; Béthoux et al., 1999), and shallow vertical mixing. Moreover, the deep water residence time in the SEMS is relatively short, around 100 years (Stöven and Tanhua, 2014; Li and Tanhua, 2020). Hence, this region is an ideal location to investigate water column temporal and vertical changes, occurring over relatively short time scales, annual to decadal (Kress et al., 2014; Sisma-Ventura et al., 2016; Ozer et al., 2017, 2020). Analysis of regional deep-sea time series in the SEMS could provide strong evidence that can confirm or validate broader-based studies and modeling efforts of similar processes on oceanic scales. One such example is the Eastern Mediterranean Transient (EMT) that took place in the early 1990s, during which the source of deep water formation shifted from the Adriatic to the Aegean and resulted in significant deep water ventilation and increased oxygen levels (Roether et al., 1996; Malanotte-Rizzoli et al., 1997; Klein et al., 1999). Before the EMT, the primary source of deep water formation was the Adriatic Sea (Roether et al., 2007). Following the EMT, denser, more saline, but warmer water from the southern Aegean formed a new water mass at the bottom of the SEMS that displaced upward the old Adriatic water mass (Gertman et al., 2006; Kress et al., 2014; Ozer et al., 2020).

The massive influx of oxygen-rich surface water from the Aegean was followed by accelerated oxygen consumption (AOC) rates in the deep layers, likely due to the transport of large amounts of highly labile dissolved organic carbon, which, in turn, enhanced bacterial production/respiration, and hence oxygen consumption (Klein et al., 2003). Such perturbations of the biological carbon pump due to changes in export production or re-mineralization efficiency can explain short term trends in oxygen (Keller et al., 2002), such as the AOC episode (Klein et al., 2003). However, longer trends can be driven by a variety of other mechanisms. One important mechanism is a change in ventilation rates, which shows a considerable decadal variability (Watanabe et al., 2003; Vilibić et al., 2013) and is expected to vary in response to global warming and the increased stratification of the ocean surface layer (Keeling et al., 2010).

A recent study based on an oceanic general circulation model has shown that the meridional overturning circulation of the SEMS has multiple equilibria states under present-day-like conditions that are closely regulated by the water exchange between the Aegean and the Adriatic Seas (Amitai et al., 2017). It describes a passive mode of the Adriatic deep water (ADW) formation and ventilation, when the Aegean stops supplying saline intermediate water to the Adriatic, due to warm steady state, resulting in minor to no deep water outflow from both basins. Indeed, observational studies show that the eastern Mediterranean Sea, including the Aegean basin is undergoing a fast warming trend (Shaltout and Omstedt, 2014; Ozer et al., 2017), which could dramatically affect deep water formation and ventilation of the deep layers (Bensi et al., 2013). Simulations also show that the Adriatic-Ionian Bimodal Oscillating System (BiOS; Gačić et al., 2010, 2011) can rapidly change oceanographic properties in the middle and south Adriatic Sea (e.g., also during the EMT; Mihanović et al., 2015) where deep waters are formed. The dynamics of the Southern Adriatic and Ionian Sea are linked by the BiOS mechanism that changes the circulation of the North Ionian Gyre from cyclonic to anti-cyclonic, on a decadal time scale (Civitarese et al., 2010), effecting the circulation of the SEMS intermediate water (Ozer et al., 2017). Moreover, a thermohaline coupling between the Aegean-Levantine Seas as well as between the Adriatic-Ionian Seas was suggested by Theocharis et al. (2014) and Velaoras et al. (2014), as a driving force that regulates the observed quasi-decadal thermohaline circulation changes effecting the SEMS deep water masses.

Evidence for an abrupt, transient halt of the Mediterranean deep zonal overturning circulation under a decreased meridional temperature gradient are found in geological records of the Sapropel episodes (Rohling et al., 2015) and were simulated using models forced by paleo-atmospheric conditions (Meijer and Dijkstra, 2009). Observations report evidence of recent long-term weakening of the northwestern part of the Adriatic–Ionian thermohaline cell, possibly affecting the deep water ventilation rate (Bensi et al., 2013). This coincides with recent observations from the southeast Mediterranean indicating that the EMT signal is gradually eroding, largely due to vertical diffusional processes (Ozer et al., 2020). However, climate-driven changes in the thermohaline cell remain highly uncertain, resulting in different scenarios regarding the future of oxygen in the deep layers of the SEMS. For example, a model by Powley et al. (2016), could not predict severe dissolved oxygen (DO) depletion of the deep waters of the SEMS in the foreseeable future and other studies foresee an increase in EMT-like conditions (Adloff et al., 2015). Here, we compiled time series data of DO, salinity, and nutrients between 2002 and 2020, obtained during 35 hydrographic cruises in the southeast Levantine basin deepest water layer (>1,200–2,000 m), to elucidate long-term trends and oscillations, related to deep water formation and ventilation since the EMT.

MATERIALS AND METHODS

Data of DO, salinity, and nutrients were compiled from 35 research cruises held between 2002 and 2020 in the Levantine

basin (Eastern Mediterranean Sea) as part of the National Monitoring Program of Israel's Mediterranean waters conducted by the Israel Oceanographic and Limnological Research (IOLR). The hydrographic raw data are available in ISRAMAR data center: https://isramar.ocean.org.il/isramar2009/ and presented by Ozer et al. (2017, 2020). Here, we focus on the post-EMT DO, nutrients, and bacterial production (BP) trends at depths >1,200–1,950 m measured at the hydrographic stations G05 and H06 with bottom depths of 1,950 and 1,750 m, respectively (**Figure 1**). This study presents new data from stations H06 and G05 for the period 2011–2020, which is combined with previous years (2002–2010) published data of DO and nutrients from H06 (Kress et al., 2014). The study area represents the southeastern Levantine Basin offshore (bathyal zone) water.[1] The old ADW uplifted by the Cretan Sea Outflow water (CSOW) was identified by Kress et al. (2014) as the mid-depth minimum salinity and temperature centered at 1,000–1,200 m depth. We analyzed the time series data of DO, salinity, and nutrients for depth range below the ADW to elucidate long-term trends, related to deep water formation and ventilation. Station H06 was visited twice a year, usually during the height of summer (August–September) and winter–spring (March–April) for a total of 35 times over the entire observational period. In contrast, station G05 was visited only three times during the monitoring period (2013, 2017, and 2019) and provides snapshots of the deep layer closest to 2,000 m depth.

Seawater samples were collected using a Rosette sampler (SeaBird profiler SBE911plus). CTD oxygen electrode data were calibrated to discrete depth DO measurements using the Winkler titration method immediately upon collection (Kress et al., 2014). Dissolved inorganic nutrients [NO_x, PO_4, and $Si(OH)_4$] were determined using a Seal auto-analyzer system with colorimetric detection as described in detail in Kress et al. (2014). Quality control of the nutrient results along the years was performed with the use of internal and certified reference standards and by the participation in international laboratory performance exercises (QUASIMEME). All nutrient measurements were well beyond the limit of detection and quantification.

Bacterial production measurements were collected at discrete depths between 2013 and 2020 at station H06 using the ^{3}H-Leucine incorporation method. For detailed methodology, see Rahav et al. (2019).

RESULTS AND DISCUSSION

The DO levels in the oldest water mass of the Adriatic (800–1,100 m) remained largely unchanged (176 ± 3.0 μmol kg^{-1}) during the period 2002–2020, but significantly decreased below depths >1,200 m (**Figures 2, 3A**). During the period 2008–2020, a long-term decreasing trend in oxygen levels at a rate of −0.5 ± 0.1 μmol kg^{-1} yr^{-1} (r^2 = 0.82; p < 0.001) was observed in the water layer between 1,200 and the bottom (1,750 m) at station H06 (**Figure 2**). Prior to this, there was a short period of increasing levels since 2004, following a very steep decline within a year of 5 μmol kg^{-1} (**Figure 2**). Similar DO inter-annual variability was also observed in a time series of the entire Eastern Mediterranean Sea (1960–2011), across the depth layer of 600–2,000 m, and was associated with dynamical processes (deep-water formation variability, transients, etc.) of the thermohaline properties (Mavropoulou et al., 2020).

[1]www.doga.ogs.trieste.it/medar/climatologies/

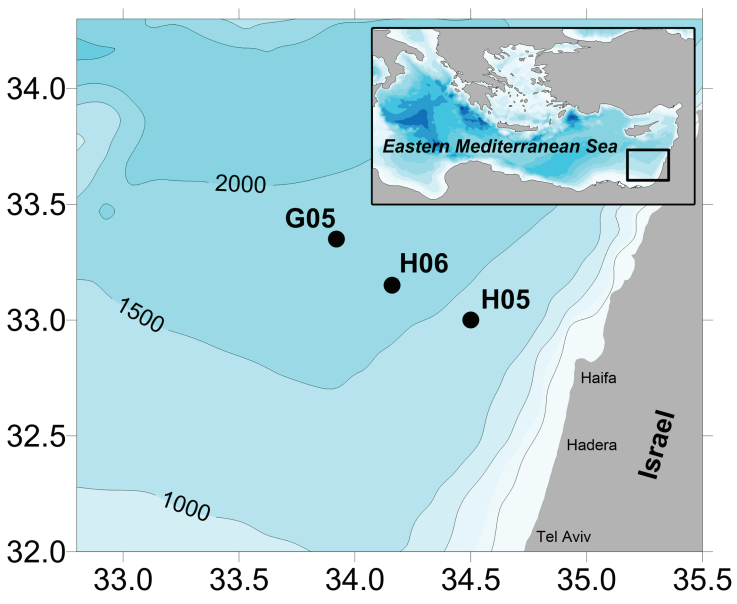

FIGURE 1 | A map showing the study site in the southeastern Mediterranean (SEMS) Sea and the long-term monitoring stations.

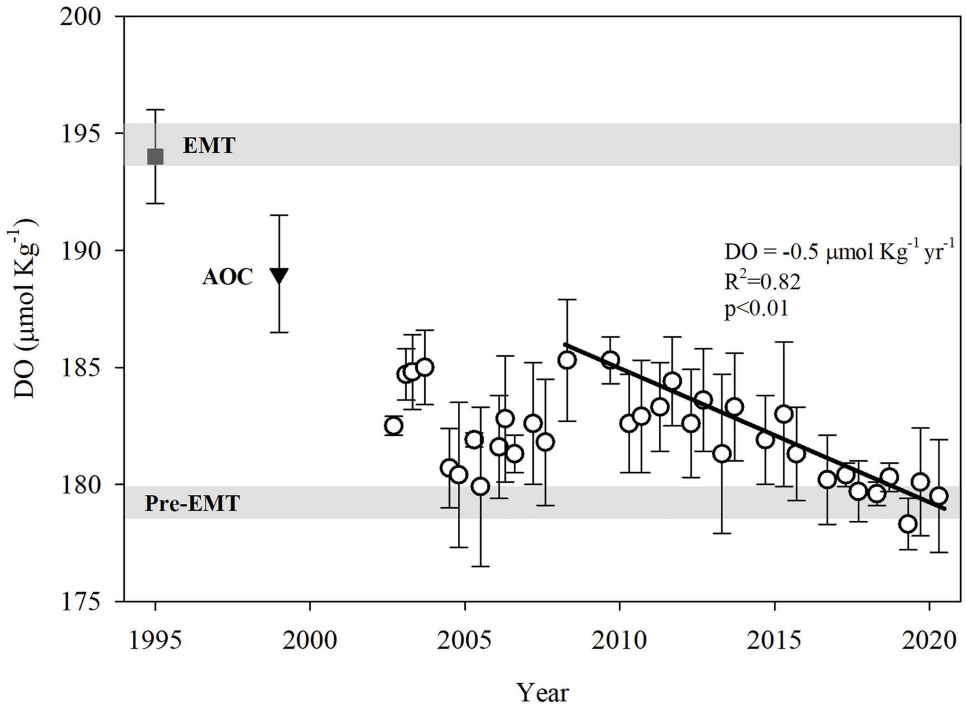

FIGURE 2 | Temporal variation of the mean oxygen concentrations measured in the deep layer (1200–1750 m) at station H06, during the period 2002–2020 (black circles). The error bars are the SDs of all the measurements made within this depth range in each cruise. The thick gray line indicates the pre-eastern mediterranean transient (EMT) oxygen concentration. The EMT and accelerated oxygen consumption (AOC) oxygen levels in the EMS, indicated by ■ and ▲, respectively, are from Klein et al. (2003). The black trend line denotes the long-term decreasing trend in oxygen levels since 2008.

The decreasing rate since 2008 agrees well with the pre-EMT oxygen utilization rate of −0.5 ± 0.2 µmol kg^{-1} yr^{-1} for depths >1,000 m that was determined on the basis of a two-dimensional kinematic model calibrated using hydrographic and tracer data (Roether and Well, 2001). Much higher utilization rates of approximately −1.3 µmol kg^{-1} yr^{-1} were observed for a few years following the EMT by Klein et al. (2003). It was proposed that this rate was driven by a large amount of dissolved organic carbon with an unusually high fraction of labile material, delivered by the Aegean deep water (AegDW) inflow. In accordance with the hypothesis made by Klein et al. (2003), integrated bacterial production measurements at H06 (1,200–1,750 m) from 2013 to 2020 show a gradual and linear increase (**Figure 4D**), suggesting high dissolved organic carbon availability.

Our data set also presents some inter-annual and multi-annual variability, with sharp changes in DO levels as large as 5.0 µmol kg^{-1} yr^{-1}. These variations are likely associated with thermohaline flux variations and delivery of organic matter, as was found in a longer time series of the Eastern Mediterranean's deep-water DO, based on positive correlation with water density (Mavropoulou et al., 2020). The peak in DO levels in 2003, ~185 µmol kg^{-1} on average, is associated by a salinity increase (**Figure 3B**). The increase in oxygen levels (ca. +3 µmole kg^{-1}) during 2007–2008 can be related to the new ADW mass, which was observed close to Crete in September 2008 and is slightly less saline and colder than the CSOW. This water mass has been observed since 2001 in the Ionian basin (Manca et al., 2006; Rubino and Hainbucher, 2007).

However, despite the evidence for short-term ventilation events of the deep water between 2001 and 2008, oxygen is gradually decreasing since 2008. Thus, the 2020 mean oxygen concentration in the depth range of 1,200–1,950 m of 179.5 ± 2.3 µmol kg^{-1} is comparable to the pre-EMT mean value (Klein et al., 2003; Kress et al., 2003). The significant change in deep water DO concentrations can be driven by two main mechanisms: (1) changes in the recycling rates driven by changes in export of labile organic carbon *via* the biological carbon pump and/or by lateral transport of POM in marginal seas (i.e., Katz et al., 2020) and (2) changes in deep water formation and ventilation rates, as well as deep advection and admixture (Keller et al., 2002). Advection of dense Aegean overflow would tend to increase both salinity and oxygen (Kress et al., 2014). This holds, for the inflow dating back to the EMT or occurring more recently, because this inflow is always comparatively high in both oxygen and salinity (Klein et al., 2003). The influx of new ADW mass, which is slightly less saline and colder compared to the CSOW, can explain inter-annual and multi-annual variations near the bottom that can amount to 5.0 µmol kg^{-1}. However, net admixture with overlying old deep Adriatic water will tend to lower both oxygen and salinity (Ozer et al., 2020). The post-EMT signature is

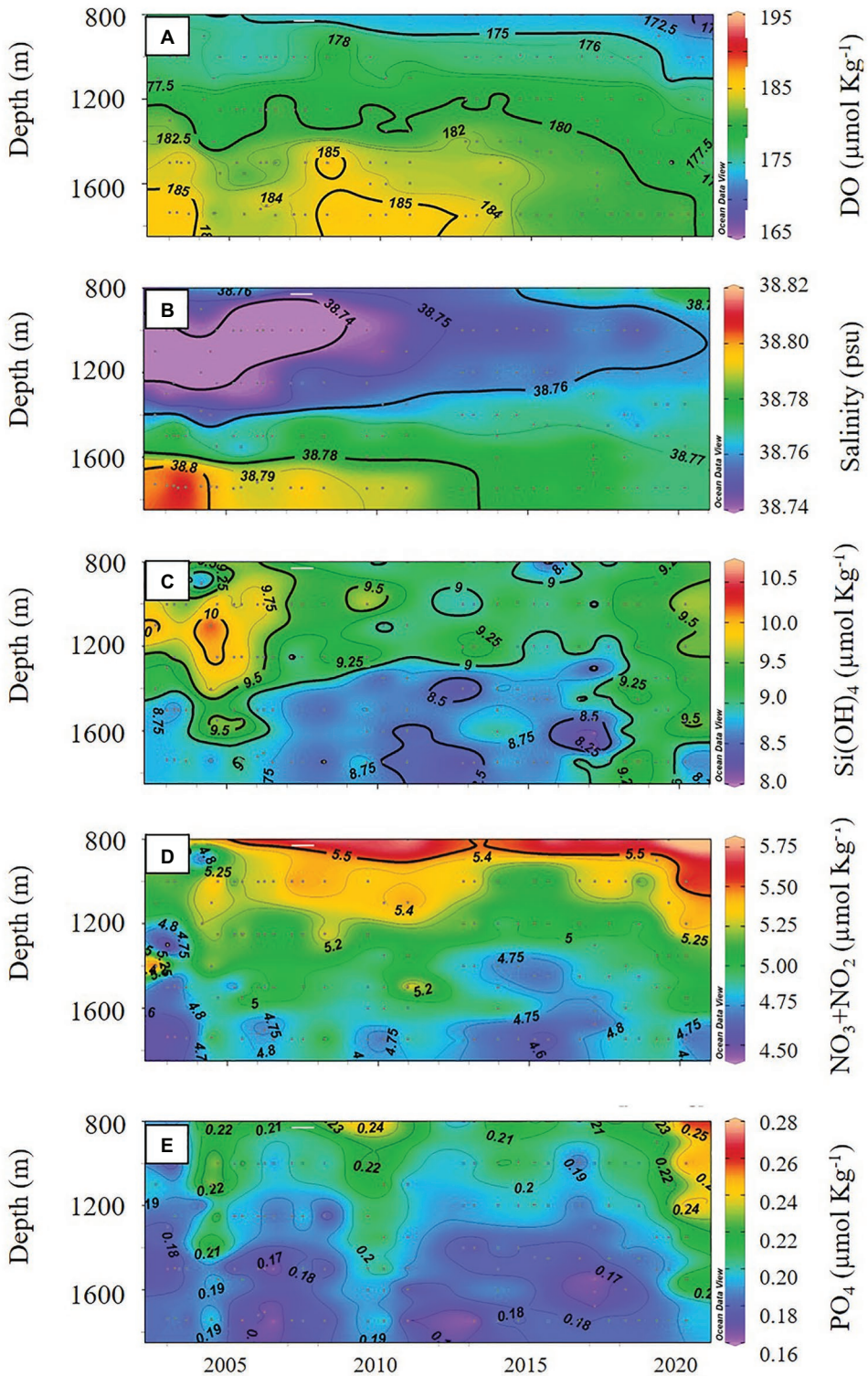

FIGURE 3 | Temporal variation in: **(A)** oxygen, **(B)** salinity, **(C)** $Si(OH)_4$, **(D)** $NO_3 + NO_2$ (NOx), and **(E)** PO_4, measured in the deep layer (1200–1750 m) at station H06.

well-observed by the vertical gradient in both oxygen and salinity (**Figures 3A,B**). These vertical gradient results from the EMT newly added AegDW higher in oxygen and salinity and the overlaying old Adriatic water with lower oxygen and salinity (Kress et al., 2003, 2014). Our observations indicate an erosion of the EMT associated vertical gradient

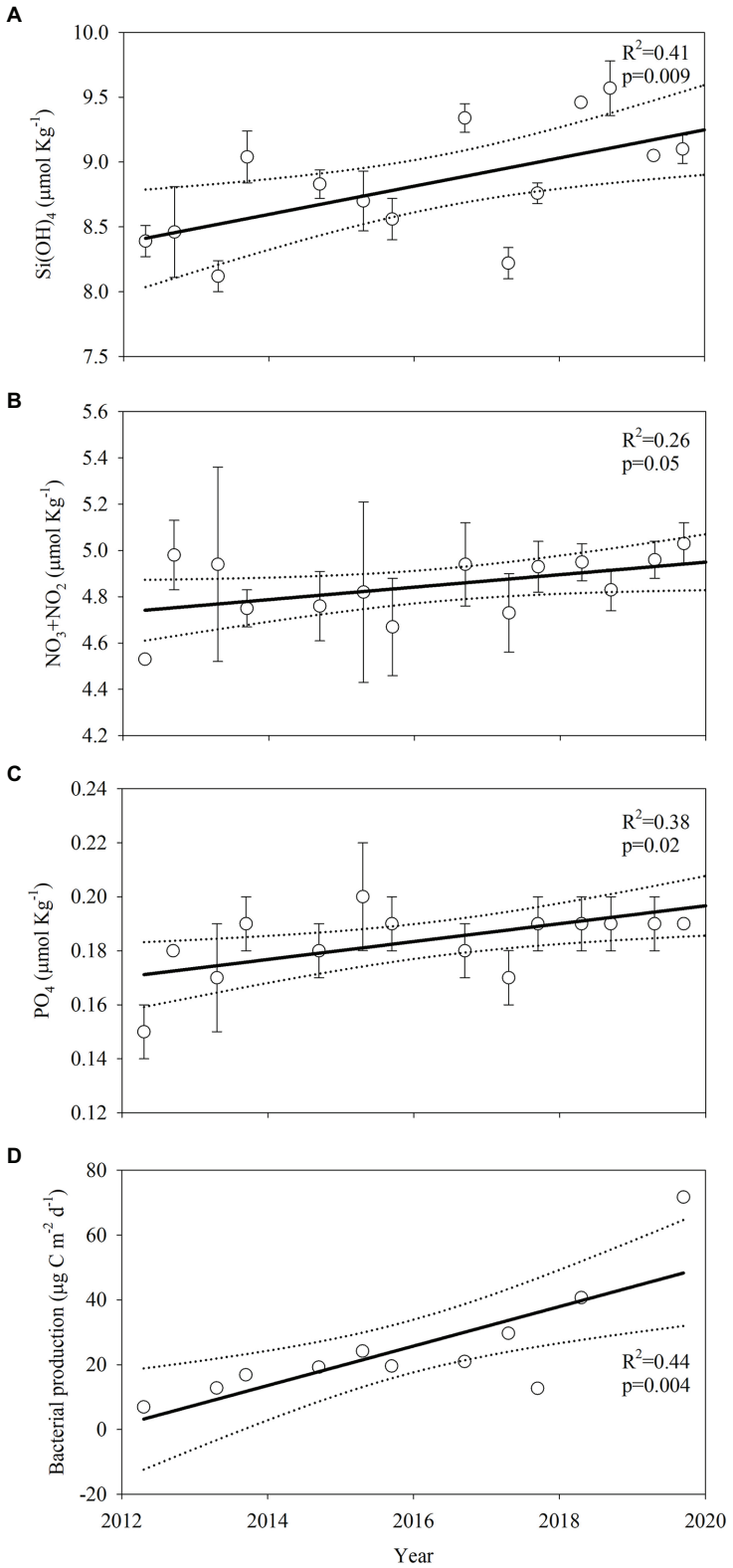

FIGURE 4 | Long term trends of mean Si(OH)$_4$ **(A)**, NO$_3$ + NO$_2$ **(B)**, and PO$_4$ **(C)** at depths of 1,200–1750 m during 2013–2020, and the integrated bacterial production **(D)**. The solid line shows the regression trend-line while the dotted lines show the 95% CI. R^2 and p denote the correlation coefficient and the corresponding significance.

and an increase in vertical homogeneity of salinity between 2002 and 2020 at a rate of 0.016–0.019 psu yr^{-1} (**Figure 3B**). This process is accompanied by a similar increase in vertical homogeneity of DO levels since 2013 (**Figure 3A**). Thus, the vertical gradients in both salinity and oxygen, associated with the EMT, are gradually eroded. Mixing with the overlying old Adriatic water mass can, thus, explain the convergence of salinity and oxygen (**Figures 3A,B**) – also indicating minor replenishment of oxygen to the deep layers of the Levantine basin since the EMT. These findings are in agreement with a monotonic salinity rise in the deep layers of the SEMS (stations H06 and H05) during the period 2012–2019, recently observed by Ozer et al. (2020) that can be largely attributed to vertical diffusional processes, gradually eroding the EMT signal.

The reduction in oxygen variability of the SEMS deep water layer (1,200–2,000 m), between 2008 and 2020, further supports a switch back into pre-EMT regime, which is defined by a homogeneous deep water column (**Figure 3B**). The recent warming of the Aegean surface water (Shaltout and Omstedt, 2014), which could lead to low production of dense water as suggested by Amitai et al. (2017), could also be responsible for the constant depth profile (from 1,250 to down 1,950 m) of DO levels. This recent weakening of ventilation rates was reported for the shallow middle Adriatic (Vilibić et al., 2013) and the southern Adriatic, where the final ADW forms (i.e., Bensi et al., 2013; Mihanović et al., 2013; Gačić et al., 2014) and is further supported by our data. We note, however, that climate-driven changes in the thermohaline circulation remains highly uncertain, and a significant DO depletion of the deep water masses of the SEMS was not predicted by near future model simulations (Adloff et al., 2015; Powley et al., 2016).

Silica concentrations at H06 increased with time since 2013 at a rate of 0.11 µmol kg^{-1} yr^{-1} (r^2 = 0.41; p = 0.010; **Figure 4A**). During the first stage of the time series, silica variability corresponded to changes in water salinity (**Figure 3C**), further supporting deep water egressing from the Adriatic Sea probably replacing the CSOW, as has been seen since 2001 in the Ionian basin (Manca et al., 2006; Rubino and Hainbucher, 2007). The increase in concentrations from 2013 can be largely explained by mixing with water masses with higher concentration, namely the old ADW, but also due to the aging of the AegDW (Kress et al., 2014).

Long-term trends in nutrient levels (**Figures 3D,E**) also reflect changes in deep water re-mineralization rates (Klein et al., 2003). Here, changes in the re-mineralization rate were assessed using the data from G05, the deepest station visited in the SEMS during 2013 and 2019 (**Figure 5**). We note that the structure of the 2013 profile at G05 is still consistent with that of post-EMT, where an extended deep-water oxygen maximum is centered in 1,200–2,000 m depth, resulting from mixing with the oxygen–enriched AegDW during the EMT (Klein et al., 1999; Roether and Well, 2001; Kress et al., 2003, 2014). We observed an average oxygen reduction of 4.2 ± 1.3 µmol/kg at G05 between 2013 and 2019 (**Figure 5A**), similar in magnitude to the oxygen reduction at H06 of ~5 µmol/kg during the period 2013–2020. During the same period, the oxygen reduction was coupled with increasing concentrations of $Si(OH)_4$, PO_4, and NO_3 (**Figures 5B–D**). A similar positive-linear increase in NOx (NO_2 + NO_3) or PO_4 was also confirmed in a time series of station H06 (**Figures 4B,C**). Assuming that the production of nutrients is the result of aerobic remineralization of organic matter, the estimated changes due to the oxygen decline applying the classical Redfield ratios, although not ideal for the SEMS (Kress and Herut, 2001), are ΔNO_3 = +0.6 µmol kg^{-1} and ΔPO_4 = +0.04 µmol kg^{-1}. However, the observed increase in NO_x and PO_4 at G05 between 2013 and 2019 accounts for about 50% of the oxygen consumption at most. Similar estimates were obtained using the time series data of H06, about 60% (PO_4) and 40% (NO_x) due to aerobic re-mineralization of organic matter. We note, however, that the measured DO:NO_3 ratio at intermediate depths (nutricline, 200–600 m) is only slightly lower (7%) than the classical Redfield ratio (**Figure 6**), and using the local ratio, the increase in NO_3 in GO5 accounts for 55% of oxygen consumption due to re-mineralization. The local DO:PO_4 of −162:1 ratio is higher than the classical Redfield ratios (by 17%), again accounting for about 60% of the PO_4 release due to re-mineralization. This agrees well with estimates by Kress and Herut (2001), indicating re-mineralization of N, and in particular, P-poor sinking organic matter in the SEMS. Our estimates support that about half of the decrease in

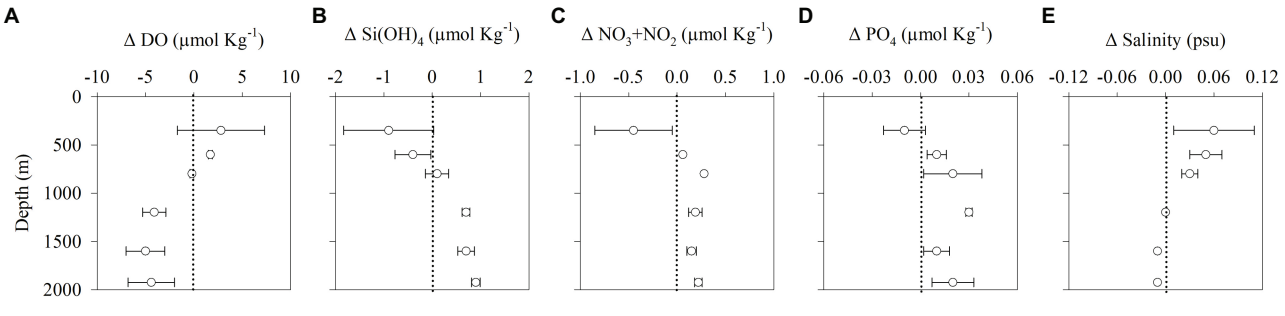

FIGURE 5 | The vertical net difference in **(A)** DO, **(B)** $Si(OH)_4$, **(C)** NOx, **(D)** PO_4, and **(E)** salinity at G05 between 2013 and 2019.

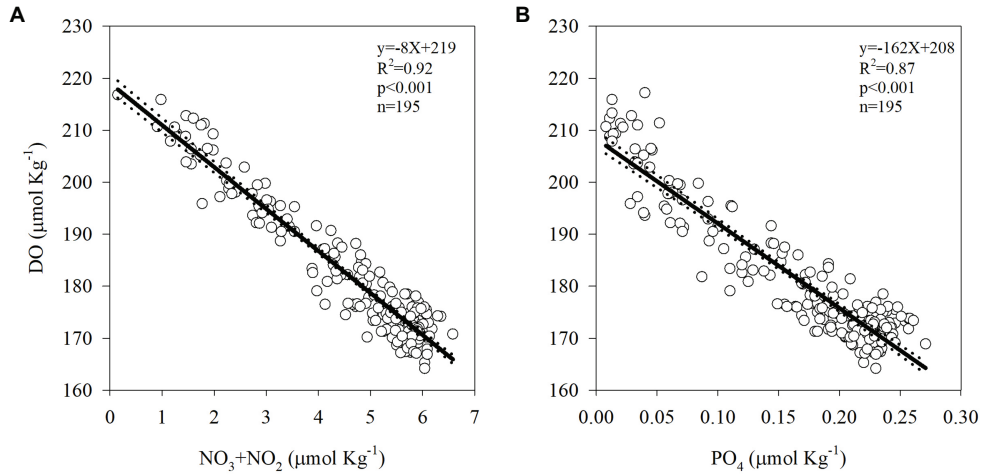

FIGURE 6 | Correlations between **(A)** DO:NO_3 + NO_2 and **(B)** DO:PO_4 within the depth range of the nutricline (200–600 m), where the majority of the organic matter sinking from the surface layer is re-mineralized in the SEMS. The solid line shows the regression trend-line while the dotted lines show the 95% CI. The data compiling this figure are from stations H05, H06, and G05.

oxygen in the deepest layer between 2013 and 2020 is due to oxygen utilization. Assuming averaged bacterial production of ~0.01 µmol C Kg^{-1} at 1,200–1,750 m (Rahav et al., 2019; **Supplementary Figure 1**) and DO:C ratio of ~1.3 (Redfield, 1934), DO uptake by microbial processes account for the period of 2009–2020 is ~1.5 µg O_2 Kg^{-1}. This suggests that microbial processes can explain ~30–40% of the average oxygen reduction at these respective depths (~1.5 µmol kg^{-1} out of 4–5 µmol kg^{-1}), similar to the estimates discussed above for nutrients. Moreover, this calculation confirms previous studies from the Mediterranean Sea indicating that the deep water is a hotspot for microbial activity (Luna et al., 2012; Rahav et al., 2019).

Our long-term record from 2002 to 2020 of oxygen levels in the deep water of the SEMS yields an overall decreasing trend −0.5 µmol kg^{-1} yr^{-1} since 2008, which agrees well with pre-EMT rates (Roether and Well, 2001). Furthermore, our results indicate that oxygen replenishment of the SEMS deep waters since the EMT has been limited. A short-term ventilation event was observed in 2008, but since then oxygen has been declining monotonically. These observations support (or at least do not oppose) the prediction that deep water ventilation rates in the Mediterranean Sea will decline due to global warming (Powley et al., 2016), as was already observed in the Adriatic Sea (Bensi et al., 2013; Mihanović et al., 2013; Vilibić et al., 2013; Gačić et al., 2014), which is a source of deep water in the SEMS. Assuming that the present trend is the result of changes in the Mediterranean thermohaline circulation associated with global warming, hypoxic conditions in the SEMS will not develop in the foreseeable future (~200 years). However, it has been suggested that even relatively small depletions in oxygen levels may impact deep water ecosystems and their services (Sweetman et al., 2017) and therefore, should be monitored and assessed regularly.

CONCLUSION

The temporal and vertical distribution of oxygen and nutrients were studied in the deepest water mass of the southeast Mediterranean Sea (Levantine basin) to evaluate long term trends during the last 20 years. The data were also evaluated in the context of the EMT ventilation event that occurred during the early 1990s, as well as bacterial activity measurements from the last ~10 years. Our time series show a significant decline in DO since the EMT and a net decrease in oxygen since 2008 of −0.5 ± 0.1 µmol kg^{-1} yr^{-1} at the bathypelagic depths (1,200–2,000 m). This was followed by an increase in dissolved inorganic nutrients and bacterial production rates, indicating an upsurge in re-mineralization rates. This trend was also accompanied by an increase in vertical homogeneity of the deep water masses, reflecting gradual erosion of the EMT core, attributed to vertical diffusional processes. Our results support the mechanism suggested by Klein et al. (2003) indicating that ventilation events transport highly labile dissolved organic carbon to the deep water masses of the SEMS, which, in turn, enhance bacterial production/respiration and hence oxygen consumption. This study highlights the physical and biological processes impacting the oxygen variability in deep water masses of the SEMS. We surmise that although oxygen levels are not likely to decline drastically in the near future (based on model simulations), the current reduction, and potential influences of climate change should be addressed in future studies.

DATA AVAILABILITY STATEMENT

The datasets presented in this study can be found in online repositories. The names of the repository/repositories and

accession number(s) can be found in ISRAMAR data center: https://isramar.ocean.org.il/isramar2009.

AUTHOR CONTRIBUTIONS

All co-authors contributed to the data acquiring and interpretation. Manuscript drafting was led by GS-V with the help of all co-authors. All authors contributed to the article and approved the submitted version.

FUNDING

This work was partly supported by the National Monitoring Program of Israel's Mediterranean waters.

ACKNOWLEDGMENTS

We would like to thank the IOLR chemistry department for their help in sampling and analyses, and the R.V. *Shikmona* and R.V. *Bat-Galim* captains and crew for help at sea.

SUPPLEMENTARY MATERIAL

The Supplementary Material for this article can be found online at: https://www.frontiersin.org/articles/10.3389/fmars.2020.598686/full#supplementary-material

Supplementary Figure 1 | Box Whisker plot showing the interquartile range (25–75th percentile) of the bacterial production measurements. The mean value is shown as a solid line.

REFERENCES

Adloff, F., Somot, S., Sevault, F., Jordà, G., Aznar, R., Déqué, M., et al. (2015). Mediterranean Sea response to climate change in an ensemble of twenty first century scenarios. *Clim. Dyn.* 45, 2775–2802. doi: 10.1007/s00382-015-2507-3

Amitai, Y., Ashkenazy, Y., and Gildor, H. (2017). Multiple equilibria and overturning variability of the Aegean-Adriatic seas. *Glob. Planet. Chang.* 151, 49–59. doi: 10.1016/j.gloplacha.2016.05.004

Bensi, M., Rubino, A., Cardin, V., Hainbucher, D., and Mancero-Mosquera, I. (2013). Structure and variability of the abyssal water masses in the Ionian Sea in the period 2003-2010. *J. Geophys. Res. Oceans* 118, 931–943. doi: 10.1029/2012jc008178

Béthoux, J. P., Gentili, B., Morin, P., Nicolas, E., Pierre, C., and Ruiz-Pino, D. (1999). The Mediterranean Sea: a miniature ocean for climatic and environmental studies and a key for the climatic functioning of the North Atlantic. *Prog. Oceanogr.* 44, 131–146. doi: 10.1016/s0079-6611(99)00023-3

Civitarese, G., Gačić, M., Lipizer, M., and Eusebi-Borzelli, G. L. (2010). On the impact of the bimodal oscillating system (BiOS) on the biogeochemistry and biology of the Adriatic and Ionian seas (eastern Mediterranean). *Biogeosciences* 7, 3987–3997. doi: 10.5194/bg-7-3987-2010

Gačić, M., Borzelli, G. L. E., Civitarese, G., Cardin, V., and Yari, S. (2010). Can internal processes sustain reversals of the ocean upper circulation? The Ionian Sea example. *Geophys. Res. Lett.* 37:L09608. doi: 10.1029/2010gl043216

Gačić, M., Civitarese, G., Eusebi Borzelli, G. L., Kovacevic, V., Poulain, P. -M., Theocharis, A., et al. (2011). On the relationship between the decadal oscillations of the northern Ionian Sea and the salinity distributions in the eastern Mediterranean. *J. Geophys. Res.* 116:C12002. doi: 10.1029/2011jc007280

Gačić, M., Civitarese, G., Kovačević, V., Ursella, L., Bensi, M., Menna, M., et al. (2014). Extreme winter 2012 in the Adriatic: an example of climatic effect on the BiOS rhythm. *Ocean Sci.* 10, 513–522. doi: 10.5194/os-10-513-2014

Gertman, I., Pinardi, N., Popov, Y., and Hecht, A. (2006). Aegean Sea water masses during the early stages of the eastern Mediterranean climatic transient (1988–90). *Phys. Oceanogr.* 36, 1841–1859. doi: 10.1175/jpo2940.1

Glecker, P. J., Durack, P. J., Stouffer, R. J., Johnson, G. C., and Forest, C. E. (2016). Industrial-era global ocean heat uptake doubles in recent decades. *Nat. Clim. Chang.* 6, 394–398. doi: 10.1038/nclimate2915

Hecht, A. (1992). Abrupt changes in the characteristics of Atlantic and Levantine intermediate waters in the south-eastern Levantine Basin. *Oceanol. Acta* 15, 25–42.

Helm, K. P., Bindoff, N. L., and Church, J. A. (2011). Observed decreases in oxygen content of the global ocean. *Geophys. Res. Lett.* 38:L23602. doi: 10.1029/2011GL049513

Katz, T., Weinstein, Y., Alkalay, R., Biton, E., Toledo, Y., Lazar, A., et al. (2020). The first deep-sea mooring station in the eastern Levantine basin (DeepLev), outline and insights into regional sedimentological processes. *Deep-Sea Res. II* 171:104663. doi: 10.1016/j.dsr2.2019.104663

Keeling, R. F., Körtzinger, A., and Gruber, N. (2010). Ocean deoxygenation in a warming world. *Annu. Rev. Mar. Sci.* 2, 199–229. doi: 10.1146/annurev.marine.010908.163855

Keller, K., Slater, R. D., Bender, M., and Key, R. M. (2002). Possible biological or physical explanations for decadal scale trends in North Pacific nutrient concentrations and oxygen utilization. *Deep-Sea Res. II* 49, 345–362. doi: 10.1016/s0967-0645(01)00106-0

Klein, B., Roether, W., Kress, N., Manca, B. B., Ribera dAlcala, M., Souvermezoglou, E., et al. (2003). Accelerated oxygen consumption in eastern Mediterranean deep waters following the recent changes in thermohaline circulation. *J. Geophys. Res.* 108:8107. doi: 10.1029/2002JC001454

Klein, B., Roether, W., Manca, B. B., Bregant, D., Beitzel, V., Kovacevic, V., et al. (1999). The large deep water transient in the eastern Mediterranean. *Deep-Sea Res. I Oceanogr. Res. Pap.* 46, 371–414. doi: 10.1016/s0967-0637(98)00075-2

Kress, N., Gertman, I., and Herut, B. (2014). Temporal evolution of physical and chemical characteristics of the water column in the easternmost Levantine basin (eastern Mediterranean Sea) from 2002 to 2010. *J. Mar. Syst.* 135, 6–13. doi: 10.1016/j.jmarsys.2013.11.016

Kress, N., and Herut, B. (2001). Spatial and seasonal evolution of dissolved oxygen and nutrients in the southern Levantine Basin (eastern Mediterranean Sea): chemical characterisation of the water masses and inferences on the N:P ratios. *Deep-Sea Res. I* 48, 2347–2372. doi: 10.1016/s0967-0637(01)00022-x

Kress, N., Manca, B. B., Klein, B., and Deponte, D. (2003). Continuing influence of the changed thermohaline circulation in the eastern Mediterranean on the distribution of dissolved oxygen and nutrients: physical and chemical characterization of the water masses. *J. Geophys. Res.* 108:8109. doi: 10.1029/2002jc001397

Li, P., and Tanhua, T. (2020). Recent changes in deep ventilation of the Mediterranean Sea, evidence from long-term transient tracer observations. *Front. Mar. Sci.* 7:594. doi: 10.3389/fmars.2020.00594

Luna, G. M., Bianchelli, S., Decembrini, F., De Domenico, E., Danovaro, R., and Dell'Anno, A. (2012). The dark portion of the Mediterranean Sea is a bioreactor of organic matter cycling. *Glob. Biogeochem. Cycles* 26, 1–14. doi: 10.1029/2011gb004168

Malanotte-Rizzoli, P., Manca, B. B., d'Alcala, M. R., Theocharis, A., Bergamasco, A., Bregant, D., et al. (1997). A synthesis of the Ionian Sea hydrography, circulation and water mass pathways during POEM-phase I. *Prog. Oceanogr.* 39, 153–204.

Manca, B. B., Ibello, V., Pacciaroni, M., Scarazzato, P., and Giorgetti, A. (2006). Ventilation of deep waters in the Adriatic and Ionian seas following changes in thermohaline circulation of the eastern Mediterranean. *Clim. Res.* 31, 239–256. doi: 10.3354/cr031239

Mavropoulou, A. M., Vervatis, V., and Sofianos, S. (2020). Dissolved oxygen variability in the Mediterranean Sea. *J. Mar. Syst.* 208:103348. doi: 10.1016/j.jmarsys.2020.103348

Meijer, P., and Dijkstra, H. A. (2009). The response of Mediterranean thermohaline circulation to climate change: a minimal model. *Clim. Past* 5, 713–720. doi: 10.5194/cp-5-713-2009

Mihanović, H., Vilibić, I., Carniel, S., Tudor, M., Russo, A., Bergamasco, A., et al. (2013). Exceptional dense water formation on the Adriatic shelf in the winter of 2012. *Ocean Sci.* 9, 561–572. doi: 10.5194/os-9-561-2013

Mihanović, H., Vilibić, I., Dunić, N. J., and Sepić, J. (2015). Mapping of decadal middle Adriatic oceanographic variability and its relation to the BiOS regime. *J. Geophys. Res. Oceans* 120, 5615–5630. doi: 10.1002/2015jc010725

Millot, C., and Taupier-Letage, I. (2005). "Circulation in the mediterranean sea" in *The handbook of environmental chemistry. Vol. 5K.* Berlin, Heidelberg: Springer, 29–66.

Ozer, T., Gertman, I., Gildor, H., Goldman, R., and Herut, B. (2020). Evidence for recent thermohaline variability and processes in the deep water of the southeastern Levantine basin, Mediterranean Sea. *Deep-Sea Res. II* 171:104651. doi: 10.1016/j.dsr2.2019.104651

Ozer, T., Gertman, I., Kress, N., Silverman, J., and Herut, B. (2017). Interannual thermohaline (1979-2014) and nutrient (2002–2014) dynamics in the Levantine surface and intermediate water masses SE Mediterranean Sea. *Glob. Planet. Chang.* 151, 60–67. doi: 10.1016/j.gloplacha.2016.04.001

Pinardi, N., and Masetti, E. (2000). Variability of the large scale general circulation of the Mediterranean Sea from observations and modelling: a review. *Palaeogeogr. Palaeoclimatol. Palaeoecol.* 158, 153–173. doi: 10.1016/s0031-0182(00)00048-1

Powley, H. R., Krom, M. D., and Van Cappellen, P. (2016). Circulation and oxygen cycling in the Mediterranean Sea: sensitivity to future climate change. *J. Geophys. Res. Oceans* 121, 8230–8247. doi: 10.1002/2016jc012224

Purkey, S. G., and Johnson, G. C. (2010). Warming of global abyssal and deep Southern Ocean waters between the 1990s and 2000s: contributions to global heat and sea level rise budgets. *J. Clim.* 23, 6336–6351. doi: 10.1175/2010jcli3682.1

Rahav, E., Silverman, J., Raveh, O., Hazan, O., Rubin-Blum, M., Zeri, C., et al. (2019). The deep water of eastern Mediterranean Sea is a hotspot for bacterial activity. *Deep-Sea Res. II* 164, 135–143. doi: 10.1016/j.dsr2.2019.03.004

Redfield, A. C. (1934). "On the proportions of organic derivatives in sea water and their relation to the composition of plankton" in *James Johnstone memorial volume*. University Press of Liverpool, 176–192.

Reid, P. C., Fischer, A. C., Lewis-Brown, E., Meredith, M. P., Sparrow, M., Andersson, A. J., et al. (2009). Impacts of the oceans on climate change. *Adv. Mar. Biol.* 56, 1–150. doi: 10.1016/S0065-2881(09)56001-4

Roether, W., Klein, B., Manca, B. B., Theocharis, A., and Kioroglou, S. (2007). Transient eastern Mediterranean deep waters in response to the massive dense-water output of the Aegean Sea in the 1990s. *Prog. Oceanogr.* 74, 540–571. doi: 10.1016/j.pocean.2007.03.001

Roether, W., Manca, B. B., Klein, B., Bregant, D., Georgopoulos, D., Beitzel, V., et al. (1996). Recent changes in eastern Mediterranean deep waters. *Science* 271, 333–335. doi: 10.1126/science.271.5247.333

Roether, W., and Well, R. (2001). Oxygen consumption in the eastern Mediterranean. *Deep-Sea Res. I* 48, 1535–1551. doi: 10.1016/s0967-0637(00)00102-3

Rohling, E. J., Marino, G., and Grant, K. (2015). Mediterranean climate and oceanography, and the periodic development of anoxic events (sapropels). *Earth-Sci. Rev.* 143, 62–97. doi: 10.1016/j.earscirev.2015.01.008

Rubino, A., and Hainbucher, D. (2007). A large abrupt change in the abyssal water masses of the eastern Mediterranean. *Geophys. Res. Lett.* 34:L23607. doi: 10.1029/2007gl031737

Sarmiento, J. L., Hughes, T. M. C., Stouffer, R. J., and Manabe, S. (1998). Simulated response of the ocean carbon cycle to anthropogenic climate warming. *Nature* 393, 245–249. doi: 10.1038/30455

Sarmiento, J. L., Orr, J. C., and Siegenthaler, U. (1992). A perturbation simulation of CO_2 uptake in an ocean general circulation model. *J. Geophys. Res.* 97, 3621–3645. doi: 10.1029/91jc02849

Shaltout, M., and Omstedt, A. (2014). Recent sea surface temperature trends and future scenarios for the Mediterranean Sea. *Oceanologia* 56, 411–443. doi: 10.5697/oc.56-3.411

Sisma-Ventura, G., Yam, R., Kress, N., and Shemesh, A. (2016). Water column distribution of stable isotopes and carbonate properties in the south-eastern Levantine basin (eastern Mediterranean): vertical and temporal change. *J. Mar. Syst.* 158, 13–25. doi: 10.1016/j.jmarsys.2016.01.012

Stöven, T., and Tanhua, T. (2014). Ventilation of the Mediterranean Sea constrained by multiple transient tracer measurements. *Ocean Sci.* 10, 439–457. doi: 10.5194/os-10-439-2014

Stramma, L., Johnson, G. C., Sprintall, J., and Mohrholz, V. (2008). Expanding oxygen-minimum zones in the tropical oceans. *Science* 320, 655–658. doi: 10.1126/science.1153847

Sweetman, A. K., Thurber, A. R., Smith, C. R., Levin, L. A., Mora, C., Wei, C. -L., et al. (2017). Major impacts of climate change on deep-sea benthic ecosystems. *Elementa Sci. Anthr.* 5:4. doi: 10.1525/elementa.203

Tanhua, T., Hainbucher, D., Schroeder, K., Cardin, V., Álvarez, M., and Civitarese, G. (2013). The Mediterranean Sea system: a review and an introduction to the special issue. *Ocean Sci.* 9, 789–803. doi: 10.5194/os-9-789-2013

Theocharis, A., Krokos, G., Velaoras, D., and Korres, G. (2014). "An internal mechanism driving the alternation of the eastern Mediterranean dense/deep water sources" in *The Mediterranean Sea: Temporal variability and spatial patterns*. eds. G. L. E. Borzelli, M. Gačić, P. Lionello and P. Malanotte-Rizzoli (Oxford, UK: John Wiley), 113–137.

Velaoras, D., Krokos, G., Nittis, K., and Theocharis, A. (2014). Dense intermediate water outflow from the Cretan Sea: a salinity driven, recurrent phenomenon, connected to thermohaline circulation changes. *J. Geophys. Res.* 119, 4797–4820. doi: 10.1002/2014JC009937

Vilibić, I., Sepić, J., and Proust, N. (2013). Weakening of thermohaline circulation in the Adriatic Sea. *Clim. Res.* 55, 217–225. doi: 10.3354/cr01128

Watanabe, Y. W., Wakita, M., Maeda, N., Ono, T., and Gamo, T. (2003). Synchronous bidecadal periodic changes of oxygen, phosphate and temperature between the Japan Sea deep water and the North Pacific intermediate water. *Geophys. Res. Lett.* 30:2273. doi: 10.1029/2003GL018338

Conflict of Interest: The authors declare that the research was conducted in the absence of any commercial or financial relationships that could be construed as a potential conflict of interest.

frontiers in Marine Science

ORIGINAL RESEARCH
published: 08 March 2021
doi: 10.3389/fmars.2021.613444

Hotter and Weaker Mediterranean Outflow as a Response to Basin-Wide Alterations

Jesús García-Lafuente[1], Simone Sammartino[2], I. Emma Huertas[3], Susana Flecha[3], Ricardo F. Sánchez-Leal[4], Cristina Naranjo[1], Irene Nadal[1] and María Jesús Bellanco[4]*

[1] Grupo de Oceanografía Física, Instituto de Biotecnología y Desarrollo Azul (IBYDA), Universidad de Málaga, Málaga, Spain, [2] Grupo de Oceanografía Física, Instituto de Ingeniería Oceánica (IIO), Universidad de Málaga, Málaga, Spain, [3] Instituto de Ciencias Marinas de Andalucía (ICMAN), Consejo Superior de Investigaciones Científicas, Ecología y Gestión Costera, Cádiz, Spain, [4] Instituto Español de Oceanografía (IEO), Centro Oceanográfico de Cádiz, Cádiz, Spain

Time series collected from 2004 to 2020 at an oceanographic station located at the westernmost sill of the Strait of Gibraltar to monitor the Mediterranean outflow into the North Atlantic have been used to give some insights on changes that have been taking place in the Mediterranean basin. Velocity data indicate that the exchange through the Strait is submaximal (that is, greater values of the exchanged flows are possible) with a mean value of -0.847 ± 0.129 Sv and a slight trend to decrease in magnitude ($+0.017 \pm 0.003$ Sv decade^{-1}). Submaximal exchange promotes footprints in the Mediterranean outflow with little or no-time delay with regards to changes occurring in the basin. An astonishing warming trend of 0.339 ± 0.008°C decade^{-1} in the deepest layer of the outflow from 2013 onwards stands out among these changes, a trend that is an order of magnitude greater than any other reported so far in the water masses of the Mediterranean Sea. Biogeochemical (*pH*) data display a negative trend indicating a gradual acidification of the outflow in the monitoring station. Data analysis suggests that these trends are compatible with a progressively larger participation of Levantine Intermediate Water (slightly warmer and characterized by a *pH* lower than that of Western Mediterranean Deep Water) in the outflow. Such interpretation is supported by climatic data analysis that indicate diminished buoyancy fluxes to the atmosphere during the seven last years of the analyzed series, which in turn would have reduced the rate of formation of Western Mediterranean Deep Water. The flow through the Strait has echoed this fact in a situation of submaximal exchange and, ultimately, reflects it in the shocking temperature trend recorded at the monitoring station.

Keywords: Strait of Gibraltar, Mediterranean Sea, Mediterranean outflow, temperature trends, buoyancy fluxes, salinity trends, pH trends

OPEN ACCESS

Edited by:
Katrin Schroeder, Institute of Marine Science (CNR), Italy

Reviewed by:
Gabriel Jorda, Spanish Institute of Oceanography, Spain
Abed El Rahman Hassoun, National Council for Scientific Research, Lebanon

****Correspondence:***
Jesús García-Lafuente
glafuente@ctima.uma.es

Specialty section:
This article was submitted to Physical Oceanography, a section of the journal Frontiers in Marine Science

Received: *02 October 2020*
Accepted: *04 February 2021*
Published: *08 March 2021*

Citation:
García-Lafuente J, Sammartino S, Huertas IE, Flecha S, Sánchez-Leal RF, Naranjo C, Nadal I and Bellanco MJ (2021) Hotter and Weaker Mediterranean Outflow as a Response to Basin-Wide Alterations. Front. Mar. Sci. 8:613444. doi: 10.3389/fmars.2021.613444

INTRODUCTION

The Mediterranean Sea (MedSea hereinafter) is the only basin away from polar regions where open-ocean deep convection reaching the ocean bottom happens, despite its location in temperate latitudes. The convection is the result of the net buoyancy flux to the atmosphere, mainly determined by the fresh water deficit (evaporation minus precipitation and river runoff, $E - P$) of the basin. It drives an open thermohaline circulation cell starting and ending in the Strait of

Gibraltar (SoG, hereinafter), the only relevant connection of the MedSea with the open ocean. The cell starts with a surface inflow of Atlantic water that travels the whole Mediterranean Sea to be transformed into the very salty Levantine Intermediate Water (LIW) in the easternmost basin of the MedSea (**Figure 1**). There, it sinks and initiates the way back to the SoG and to the open ocean as a dense underflow, thus completing the thermohaline cell (see Hopkins (1985) or Tsimplis et al. (2006), for instance, for a review on this general topic).

In addition to intermediate waters, deep waters are formed in different places of the MedSea, mainly in the Adriatic and Aegean Seas in the eastern basin (Eastern Mediterranean Deep Water, EMDW; Schlitzer et al., 1991; Roether et al., 1996), and in the Gulf of Lions in the western basin (Western Mediterranean Deep Water, WMDW; Stommel, 1972). The basic thermohaline cell becomes more complex since both basins have their own closed thermohaline circulations (Tsimplis et al., 2006) and bottom water renewal processes. The EMDW is mainly renewed by upwelling inside the eastern basin itself (Schlitzer et al., 1991; Roether and Schlitzer, 1991) and only a very small fraction seems to be drained out to the western basin through the Sicily Strait (Astraldi et al., 1999). On the contrary, a significant fraction of WMDW finds its way out to the Atlantic Ocean through the SoG (Stommel et al., 1973; Kinder and Parrilla, 1987), even though the depth of the SoG's main sill (Camarinal sill, 290m, **Figure 1**) is less than Sicily's west and east sills (360m and 430m, respectively, Astraldi et al., 1999). Bernoulli aspiration of WMDW in the Alboran Sea by the energetic lower layer flow at the SoG (Bryden and Stommel, 1982; Naranjo et al., 2012) is responsible for the differentiated pattern of both basins, as the Strait of Sicily does not hold any comparable bottom current.

Levantine Intermediate Water and WMDW make up the main bulk of the Mediterranean outflow in the SoG (Q_2 hereinafter, assumed negative as it flows westwards), to which small fractions of other intermediate and deep waters may eventually contribute (Naranjo et al., 2015). The Mediterranean outflow has to flow out beneath a slightly greater Atlantic inflow (Q_1, positive), moving over a very irregular seafloor with steep sills and marked contractions (**Figure 1**). This strongly constraining topography leads to hydraulic control of the exchanged flows, an idea first suggested by Bryden and Stommel (1984) and further addressed by Armi and Farmer (1985). A relevant result of this theory is that the exchanged flows attain a maximum value that cannot be exceeded whenever the exchange is hydraulically controlled (maximal exchange, Armi and Farmer, 1985, 1987). In other words, $|Q_2|$ has an upper limit. From this point of view, the two-layer hydraulic theory provides a useful frame to interpret the observations collected at Espartel sill (**Figure 1**), the westernmost sill of the SoG, which constitute the dataset analyzed and exploited in the present study. Next Section revises some relevant aspects of this theory applied to the SoG.

The Hydraulically-Controlled Exchange Model

The objective of this work is to infer changes in the MedSea from single-point observations at the site where it joins with the global ocean (**Figure 1**). Within the frame of two-layer theory, the usual approach is to consider the MedSea as a homogeneous basin connected to the Atlantic Ocean, also homogeneous, through a channel (the SoG). Actually, the outflow consists of different water masses of very similar density, which justifies homogeneity for dynamic purposes as a first order approach. The approach, however, cannot be applied to the water masses analysis carried out later on.

The simplest model for the SoG is a non-rotating channel of rectangular section with no mixing between layers (Armi, 1986; Farmer and Armi, 1986). Critical section is a key concept: it is a section where the composite Froude number, G, defined as

$$G^2 = F_1^2 + F_2^2 = \frac{u_1^2}{g' h_1} + \frac{u_2^2}{g' h_2} \quad (1)$$

is $G = 1$. Then, the section exerts hydraulic control on the flow. In equation [1], F_i is the internal Froude number of layer i, $g' = \left(\Delta\rho / \rho_0\right) g$ is the reduced gravity with $\Delta\rho = \rho_2 - \rho_1$ the density difference between layers (also between basins), and ρ_0 a reference density. The meaning of the remaining variables is shown in **Figure 2**.

If the flows are hydraulically controlled at two critical sections connected by a region of sub-critical flow, then the exchange is maximal (Armi and Farmer, 1987). The condition $G = 1$ is usually achieved in notable topographic sections, generally the narrowest and the shallowest. For steady exchange, the SoG fulfills these requirements at Tarifa Narrows and at the main sill of Camarinal (narrowest and shallowest sections, respectively, **Figure 1**) and, therefore, it is candidate to sustain maximal exchange (Farmer and Armi, 1988).

The constrain imposed by the maximal exchange together with the climatology over the basin, determine the global characteristics of the Mediterranean and link them to the flow properties at the SoG, a result of obvious interest to our study. The issue was first addressed by Bryden and Kinder (1991), who assumed a channel of triangular cross-section and a density difference brought about by salinity exclusively ($\Delta\rho = \beta\,(S_2 - S_1)$, β the haline contraction coefficient of seawater). The salinity of the MedSea, S_2, was left as an output of the model. For a net evaporation in the basin of 0.6 m/year (equivalent to 0.04Sv), they obtained steady-state inflow $Q_1 = 0.92$Sv and outflow $Q_2 = 0.88$Sv, and $\Delta S = S_2 - S_1 \approx 2$, close to the actual values.

At short time-scales, however, the exchange is markedly time-dependent. Tides provide a net barotropic flow strong enough to override the hydraulic control at Camarinal sill, particularly during the intensified flows of spring tides (Farmer and Armi, 1988; Sannino et al., 2004; Sánchez-Garrido et al., 2011). The loss of the control leads to the release and further radiation into the MedSea of packets of large amplitude internal waves, a well-known feature of this region (Farmer and Armi, 1988; Brandt et al., 1996; Vlasenko et al., 2009; Sánchez-Garrido et al., 2011). When this happens, the hydraulic control of Camarinal is transferred to Espartel sill, where it is in force most of the time (Sánchez-Román et al., 2009; Sannino et al., 2009). In addition, the loss of control boosts the contribution of tidally induced eddy-fluxes (positive correlations of vertical interface

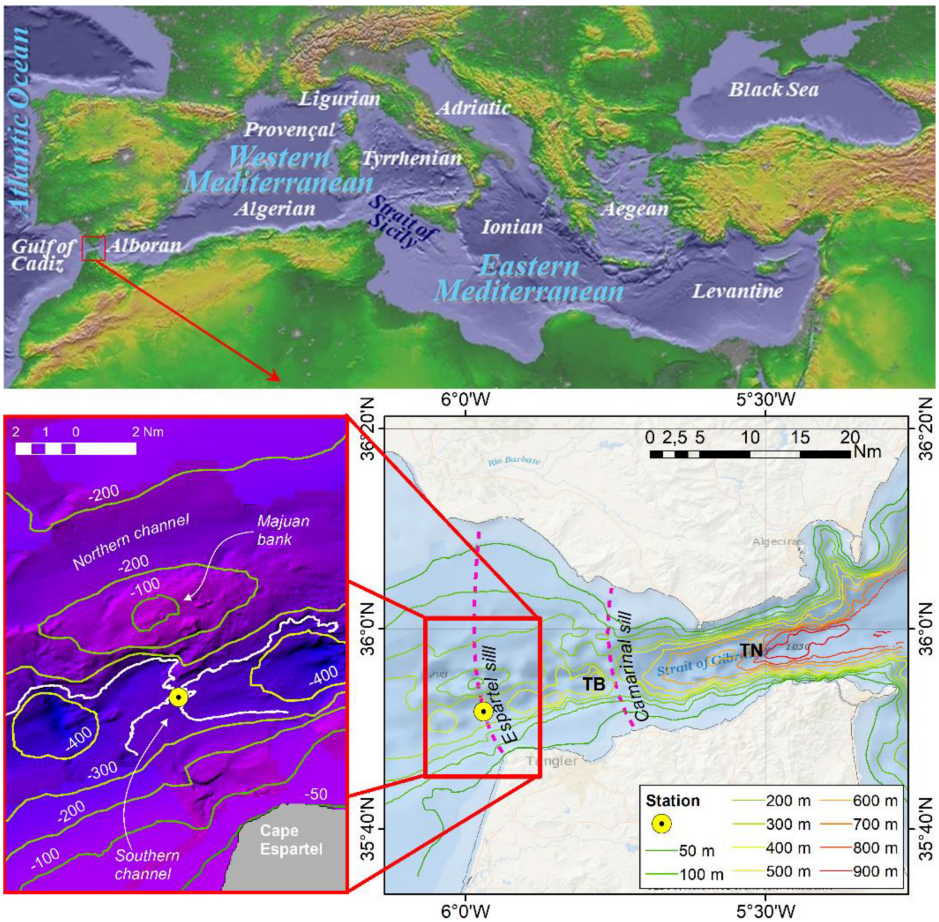

FIGURE 1 | Top panel. Map of the Mediterranean Sea with the name of the main basins and sub-basins. Red rectangle indicates the area of the Strait of Gibraltar enlarged below. Bottom-right panel: map of the Strait with indication of relevant topographic features. TN stands for Tarifa Narrows; TB, for Tangier Basin. Red rectangle indicates the zone of Espartel sill enlarged in the bottom-left panel. Yellow dot indicates the location of the monitoring station. Most of the Mediterranean outflow goes along the channel between Majuan bank and the African shore (Sánchez-Román et al., 2009; Sammartino et al., 2015).

fluctuations and tidal currents) to the exchange (Bryden et al., 1994; Sannino et al., 2004; Vargas et al., 2006) at either critical section. Therefore, large eddy-fluxes at a control section lead to hydraulic control intermittency. Alternately, very weak eddy-fluxes (or no eddy-fluxes at all) would suggest lastingness of the control. The frequent loss of hydraulic control at Camarinal sill (Farmer and Armi, 1988; García Lafuente et al., 2000, 2009; Vargas et al., 2006; Sánchez-Garrido et al., 2008, 2011) and the large associated eddy-fluxes there (up to 0.5Sv or 40% to 60% of the total exchange; Bryden et al., 1994; Sannino et al., 2004; Vargas et al., 2006) contrast with those at Espartel (∼0.04Sv or 5%; Sánchez-Román et al., 2009; Sammartino et al., 2015). This particular behavior stresses the potential of Espartel sill replacing Camarinal sill as a long-lasting hydraulic control section.

Should the critical value $G = 1$ be achieved in Espartel section, it would basically be done through F_2 (equation [1]), as the large width and thickness of the surface layer (**Figure 1**) imply very low velocity u_1. Similar reasoning applies to F_1 in Tarifa Narrows due to the large thickness of layer 2. These approximations, already suggested by Farmer and Armi (1986), may be interpreted as if Tarifa Narrows controls the inflow Q_1, which is the active layer there, while Espartel sill does the same with the outflow Q_2. It underlines the experimental benefits of monitoring the outflow in this section in order to discriminate the state of the exchange: $F_2 = 1$ for possible maximal exchange (F_1 in Tarifa Narrows must be inspected), and $F_2 < 1$ for submaximal exchange. It also emphasizes the importance of the collected data in relation to the global properties of the MedSea, particularly in case of submaximal exchange, as it is outlined next.

Buoyancy Fluxes, Water Formation and Outflow

In our simple MedSea–SoG system the other key variable is the amount of Mediterranean water (Q_M) formed due to buoyancy fluxes (B_0) to the atmosphere, which should be equal to $|Q_2|$ in an ideal steady-state on yearly basis. In maximal exchange ($G = 1$), $|Q_2|$ has attained its maximum. If, eventually, $Q_M > |Q_2|$ during

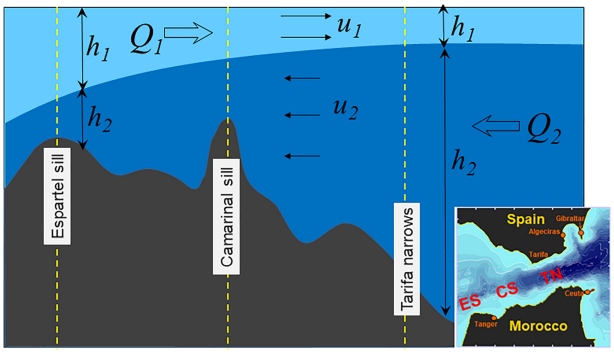

FIGURE 2 | Sketch of the two-layer exchange in the Strait of Gibraltar. Subscripts 1 and 2 stand for variables in the upper and lower layers, whose densities are ρ_1 and ρ_2, respectively. In a steady state, Q_i's are constant but u_i and h_i are not. The three notable topographic sections, Espartel and Camarinal sills and Tarifa narrows, have been indicated in both, the sketch and the inset map. Camarinal sill and Tarifa narrows are the candidate critical sections for steady exchange. In case of time-dependent flow (tides) Espartel sill and Tarifa narrows are much more likely candidates for critical sections (see text).

a given period, the excess of formed water cannot flow out unless either the interface goes up or g' increases (equation [1]), which requires larger density difference $\Delta\rho$. The interface cannot rise because it would block partially the inflow, preventing the water balance of the basin $Q_1 + Q_2 = (E - P)$ The excess of water has to remain in the basin contributing to increase its density (hence, $\Delta\rho$) in successive years until reaching a new equilibrium. This is how the hydraulics of the SoG determines the MedSea properties. If, on the contrary, $Q_M < |Q_2|$ the equilibrium is easily maintained as $|Q_2|$ has no constrain for diminishing. But the exchange would change to submaximal. If the exchange was already submaximal, there is no impediment for $|Q_2|$ to increase if $Q_M > |Q_2|$ or to decrease if $Q_M < |Q_2|$, making G (F_2 in the previous approximation) increase or decrease accordingly. As pointed out by Garrett et al. (1990), it is only if the exchange is submaximal that changes occurring in the MedSea can bring about a non-lagged footprint in the outflow at the SoG (i.e., at Espartel section). If it were maximal, such changes would be only reflected in Q_2 after several years (Garrett et al., 1990).

The formed water Q_M is proportional to the buoyancy flux B_0, given by Gill (1982)

$$B_0 = g\left[-\frac{\alpha}{c_p}Q_{net} + \rho_0\beta S\,(E-P)\right] \tag{2}$$

where g is gravity acceleration, α and β the thermal expansion and haline contraction coefficients of seawater, c_p its heat capacity, and ρ_0 and S a reference density and surface salinity, respectively (g = 9.81ms^{-2}, α = 2.6·10^{-4}K^{-1}, β = 7.44·10^{-4}, c_p = 3984JKg^{-1}K^{-1}, ρ_0 = 1028kgm^{-3} and S = 37 in this study). Q_{net} is the net heat flux into the sea (Wm^{-2}, positive downwards), and $(E - P)$ is the net evaporation which includes river run-off (ms^{-1}, positive upwards). They give the buoyancy flux B_0 in kgm^{-1}s^{-3} (Nm^{-2}s^{-1}). Negative heat flux (cooling) and positive net evaporation cause positive buoyancy flux to the atmosphere.

A crude estimation of the amount of water of density ρ_2 that could be formed from water of density ρ_1 under a constant and homogeneous buoyancy flux B_0 acting on a basin of area A_{MED} (say, the MedSea) would be

$$Q_M = \frac{B_0\,A_{MED}}{g\,(\rho_2 - \rho_1)} \tag{3}$$

(for $Q_{net}\approx -3$Wm^{-2} and $(E-P)\approx 0.7$ m/year (=2.22·10^{-8}ms^{-1}), representative values of the Mediterranean basin, $B_0\approx 8\cdot10^{-6}$Nm^{-2}s^{-1} from equation [2], which gives the realistic value of $Q_M\approx 1.03$Sv in equation [3] with $A_{MED} = 2.5\cdot10^{12}$m^2 and $\Delta\rho\approx 2$kgm^{-3}). Obviously, the actual processes of deep water formation are much more complex (pioneer paper by MEDOC Group (1970), or Houpert et al. (2016) for a recent comprehensive study). The simplicity of equation [3], however, provides a linear relationship for the expected dependence of Q_M on B_0. The simple two-layer model summarized above links Q_M and Q_2, thus extending this relationship to the outflow and the buoyancy flux, and is a well-suited first approximation for the discussion of the results presented in this study. The model, however, is a steady-state model that could be possibly extended to very slowly (long-term) varying conditions such as trends, but not to short-term scales. Therefore, the present study focuses on these long-term changes or trends.

A SHORT DESCRIPTION OF THE DATA SETS

Currentmeter and Temperature/Salinity Data

The monitoring station at Espartel sill is located at 35°51.71′N and 5°58.22′W (**Figure 1**) at ∼360 m depth. The instrumented mooring line is equipped with an up-looking Acoustic Doppler Current Profiler (ADCP RDI Workhorse Long Ranger 75 kHz), embedded in a 1.5 m wide buoy deployed at ∼17 m above the seafloor, a Conductivity-Temperature sensor (CT, Seabird SBE37-SMP) and a single point current meter (Nortek Aquadopp DW), both clamped approximately 3 m below. Sampling interval for all instruments has been set to 30 min. The station was first deployed in October 2004, and has been working since, with a large gap in 2011-12 due to a line loss, and few shorter gaps due to different technical issues. The dataset used in this study covers the period from October 2004 to February 2020.

The accurate calibration of CT probes is critical because the instrumental drift of the sensors ($O(10^{-3})$°Cyr^{-1} for temperature; $O(10^{-3})$yr^{-1} for salinity) is comparable to the trends of the Mediterranean water masses characteristics reported in the literature (see Vargas-Yañez et al., 2017, for instance). CT data in this study come from a bunch of 6 different instruments, all which have been regularly calibrated throughout the probe life every one or two years. Details about ADCP datasets are presented in **Supplementary Appendix A**, which includes a short history of the station and other relevant issues.

Biogeochemical Data

After the gap, in year 2012, autonomous sensors for continuous recording of *pH* (at total scale and reference temperature of 25°C) and CO_2 partial pressure (pCO_2, µatm) (SAMI-*pH* and SAMI-pCO_2, Sunburst Sensors, LLC.) were incorporated to the monitoring line and placed at the same depth as the CT probe. Unfortunately, the instruments were lost in year 2017 after an accident underwent by the mooring line and they have not been replaced until very recently. It reduces the *pH* data availability from August 2012 to March 2017, and to a shorter period in the case of pCO_2 data. The sampling interval was initially set to 60 min, but a battery run off happened in summer 2013 (which caused a six-month data gap) advised changing the interval to 120min to extend the battery life.

According to manufacturer, precision and accuracy of measurements were ∼0.001 and ± 0.003 units for *pH* and ∼ 1 µatm and ± 3 µatm for pCO_2, approximately. Repeated measurements conducted in the laboratory with the probes submersed in aged seawater and high CO_2 seawater to validate these specifications provided values of ∼0.003 and ± 0.005 units for *pH* and ∼3 µatm and ± 5 µatm for pCO_2. SAMI-devices were nonetheless, regularly checked upon periodic servicing of the line on board and *pH* data obtained by the spectrophotometric technique (Clayton and Byrne, 1993) in samples collected in oceanographic cruises carried out in the area were used to validate the series and identify possible drifts and drops of the autonomous sensors (see section "Other Biogeochemical Properties"). Thus, samples at the mooring site were taken within the Mediterranean outflow in August 2012 (4), May 2013 (4), November 2014 (2), June 2015 (5), and March 2017 (9) under the frame of the Gibraltar Fixed Time Series monitoring program (GIFT, Flecha et al., 2019). Samples were taken directly from Niskin bottles in 10 cm path-length optical glass cells and submitted to a Shimadzu UV-2401PC spectrophotometer containing a 25°C-thermostated cells holder after addition of m-cresol purple as indicator. Precision and accuracy of these discrete and independent pH_{T25} measurements were determined from measurements of certified reference material (CRM batches #97 and #136 provided by Prof. Andrew Dickson, Scripps Institution of Oceanography, La Jolla, CA, United States) and were equivalent to ± 0.0048 and ± 0.0047 units for pH_{T25}.

Other Data

Data of mass and heat fluxes to the atmosphere from the fifth generation of ECMWF atmospheric reanalysis of the global climate (ERA5, Hersbach et al., 2020), distributed by the Copernicus Climate Change Service (C3S), have been retrieved in order to estimate buoyancy fluxes in the Mediterranean basin.

WATER PROPERTIES OF THE OUTFLOW AT THE MONITORING STATION

Temperature, Salinity, Density

Figure 3 displays the potential temperature θ registered at ∼14 m above the seafloor in the monitoring site. This short distance implies that the instrument is sampling the densest (hence, coldest) water that leaves the MedSea. Temperature fluctuates noticeably at tidal timescale due to mixing (light-gray dots in **Figure 3**). It is not local mixing (the instrument is far enough from the interface for local mixing to reach its depth) but advection of waters mixed upstream in the Tangier basin (**Figure 1**), where intense mixing happens (Wesson and Gregg, 1994). Conventional numerical filtering is not advisable to remove these fluctuations because the low-passed series smooths out the footprint of the coldest samples, which are particularly relevant since they inform about the deepest waters that are leaving the MedSea. A possibility of removing tidal fluctuations without losing this information is to extract the coldest sample in each semi-diurnal tidal cycle and decimate the series to a sample per cycle (García Lafuente et al., 2007; Naranjo et al., 2012, 2017). Light-blue dots in **Figure 3** show the resulting series where most semidiurnal and diurnal tidal variability has been removed.

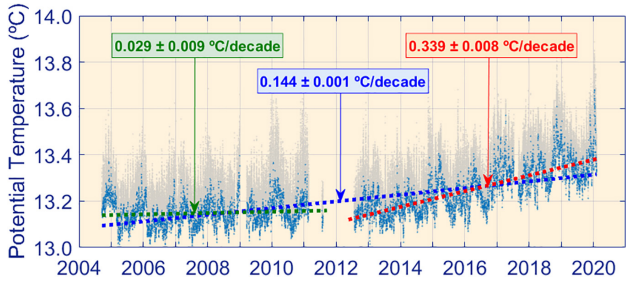

FIGURE 3 | Potential temperature at 14m above seafloor in the monitoring station sampled every 30 min (gray dots) and series of minimum θ in each tidal cycle (light-blue dots). Dashed lines show θ trends for the whole period (blue line), from the beginning of the series to the data-gap in 2011-12 (green line), and from the gap to the end of the series (red line).

Dashed-blue line in **Figure 3** shows a clear trend of 0.144°C/decade in θ (see also **Table 1**). This value, however, is misleading as the trend during the first half of the record is much less (0.029°C/decade, dashed-green line), whereas it is more than double in the second half (0.339°C/decade, dashed-red line). It seems to be around year 2013 that the trend changed. And it did in an order of magnitude with regards to the before-2012 value! Although this pattern was anticipated in Naranjo et al. (2017), they could not give definitive ratification as they used a correspondingly shorter length of this time series (up to year 2015). The extended series available nowadays does confirm the existence of that trend, which is so large and unexpected that has motivated the present study.

Similar analysis has also been carried out for salinity, *S*. Only salinities corresponding to the samples of minimum θ have been selected in order to use the same subset of data for both variables. The analysis yields a positive trend of 0.023 decade^{-1} for the whole series (**Table 1**), which increases to 0.040 decade^{-1} in the second part of the series after the year 2012 gap. Before 2012, the trend does not differ from 0 within the 95% confidence level (**Table 1**). Because of the opposite effects of temperature and salinity, the density trend depends on the relative weight of θ and

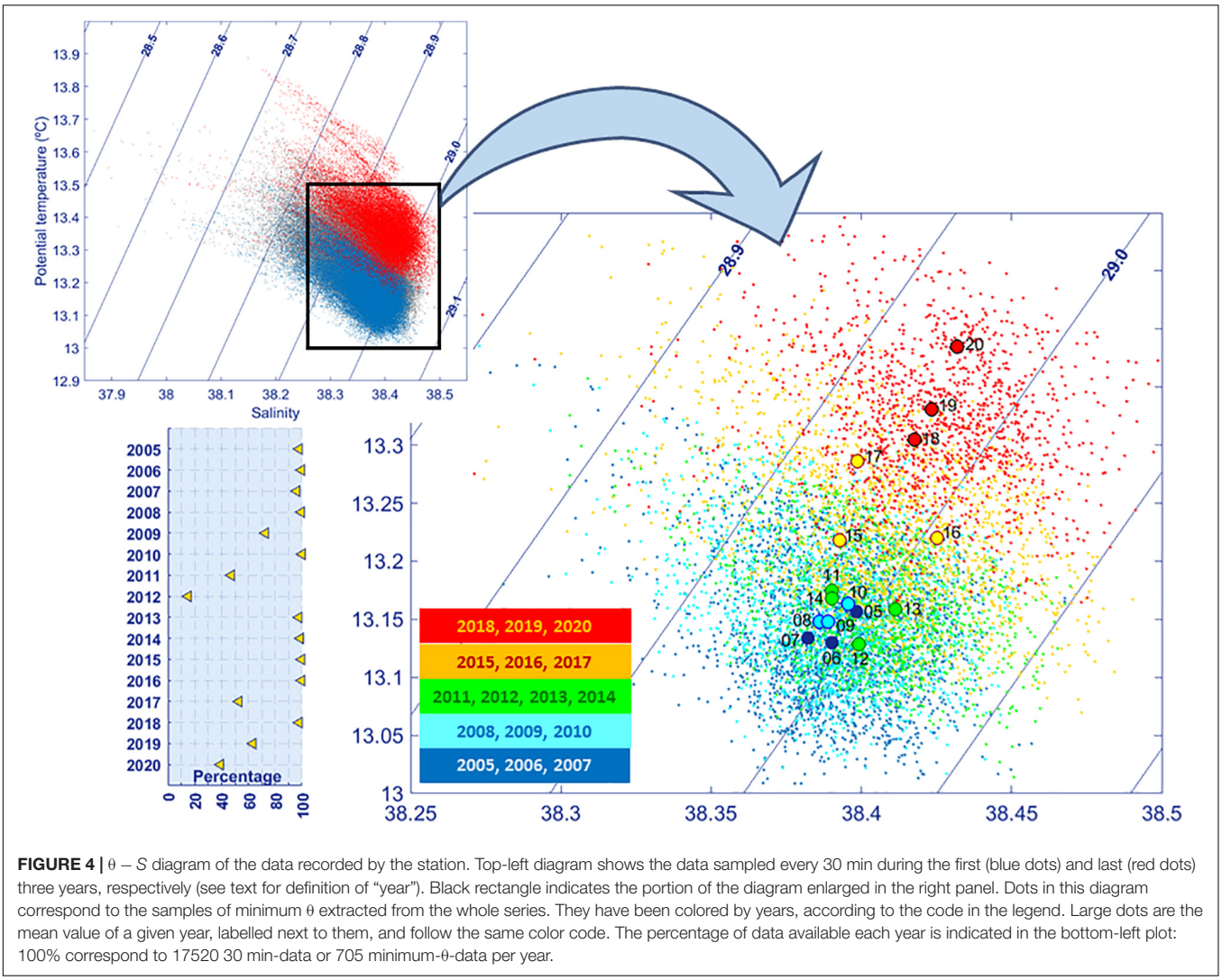

FIGURE 4 | $\theta - S$ diagram of the data recorded by the station. Top-left diagram shows the data sampled every 30 min during the first (blue dots) and last (red dots) three years, respectively (see text for definition of "year"). Black rectangle indicates the portion of the diagram enlarged in the right panel. Dots in this diagram correspond to the samples of minimum θ extracted from the whole series. They have been colored by years, according to the code in the legend. Large dots are the mean value of a given year, labelled next to them, and follow the same color code. The percentage of data available each year is indicated in the bottom-left plot: 100% correspond to 17520 30 min-data or 705 minimum-θ-data per year.

S trends. In this case, the former prevails and the trend of density anomaly σ_θ is negative: -0.009 kgm^{-3}/decade for the whole series (**Table 1**). It changes markedly to -0.034 kgm^{-3}/decade in the second part of the series as a consequence of the sharp increase of θ during the same period.

These results are illustrated in the θ-*S* diagrams of **Figure 4**. The available data have been grouped together by years. As the monitoring station was first deployed in October 2004, years have been defined from October 1 to September 30 of the following year: year 2005 goes from October 1, 2004 to September 30, 2005 and so on. Light-blue dots in the top-left panel show the data sampled at Δt = 30min during the first three years (2005, 2006, 2007, see legend), and red dots do the same for the last three years (2018, 2019, 2020). The increase of potential temperature of the water flowing past the station is palpable. The rise of salinity and the diminution of density are less obvious but still detectable.

Right panel shows the samples of minimum θ and their yearly mean (large dots). The lack of data in some years can bias the mean, as it could be the case of year 2012 with a low percentage of data (bottom-left plot), although, curiously, it remains close to the neighbor years. The distribution of large dots clearly suggests two different periods, a pattern that would still stand even if some means are biased: a first one from 2005 to 2014 when years group close together around θ = 13.15°C, *S* = 38.4, and a second period of continuous and marked rise of mean θ and also of *S* to a lesser extent, with the exception of year 2016. The partition agrees with the previous one found in the analysis of trends.

Other Biogeochemical Properties

Figure 5A shows the *pH* time series in total scale at a reference temperature of T = 25°C (pH_{T25}) measured at the monitoring station. No data during the first part of the series are available, as the biogeochemical sensors were only deployed in summer 2012. Therefore, they illustrate the temporal evolution of this variable in the Mediterranean outflow until 2017.

These series have been contrasted against the discrete spectrophotometric *pH* values deduced from the seawater samples collected in the outflow layer during the five cruises that overlapped the monitoring period. The resulting pH_{T25} values,

TABLE 1 | Summary of estimated trends (with 95% confidence level), mean and std (in italics) and number of data used in each calculation (in bold in brackets) for different variables of the study: Q_2 is the total outflow, Q_{2s-v} is the slowly part of it and Q_{2E-F} is the tidally driven contribution of the eddy-fluxes; h is the interface height, θ is the potential temperature, S the salinity, σ_θ the density anomaly, F_2 the lower layer Froude number, pH_{T25} the seawater pH and pCO_2 the CO_2 partial pressure.

Variable	Trend ± 95% confidence level *mean ± std* (Number of data)		
	2004-2020	**2004-2012**	**2013-2020**
Q_2	+0.016 ± 0.001 *−0.854 ± 0.132* **(N = 229100)**	−0.068 ± 0.004 *−0.865 ± 0.136* **(N = 107384)**	+0.017 ± 0.003 *−0.847 ± 0.129* **(N = 121716)**
Q_{2s-v}	+0.014 ± 0.001 *−0.812 ± 0.127* **(N = 229100)**	−0.067 ± 0.004 *−0.821 ± 0.128* **(N = 107384)**	+0.025 ± 0.003 *−0.804 ± 0.126* **(N = 121716)**
Q_{2E-F}	+0.002 ± 0.001 *−0.042 ± 0.026* **(N = 229100)**	$6.2 \pm 8.1\ 10^{-4}$ *−0.044 ± 0.026* **(N = 107384)**	−0.008 ± 0.001 *−0.042 ± 0.027* **(N = 121716)**
h	+1.96 ± 0.12 *172.8 ± 14.9* **(N = 229100)**	+2.44 ± 0.50 *171.8 ± 14.6* **(N = 107384)**	0.07 ± 0.23 *173.7 ± 15.2* **(N = 121716)**
θ	+0.144 ± 0.001 *13.206 ± 0.098* **(N = 9536)**	+0.029 ± 0.009 *13.148 ± 0.058* **(N = 4626)**	+0.339 ± 0.008 *13.254 ± 0.099* **(N = 4910)**
S	+0.023 ± 0.002 *38.400 ± 0.030* **(N = 9319)**	−0.004 ± 0.004 *38.390 ± 0.025* **(N = 4472)**	+0.040 ± 0.004 *38.410 ± 0.032* **(N = 4847)**
σ_θ	−0.009 ± 0.002 *28.990 ± 0.030* **(N = 9319)**	−0.008 ± 0.004 *28.992 ± 0.026* **(N = 4472)**	−0.034 ± 0.004 *28.988 ± 0.033* **(N = 4847)**
F_2	−0.030 ± 0.001 *0.741 ± 0.052* **(N = 229100)**	+0.036 ± 0.002 *0.757 ± 0.049* **(N = 107384)**	−0.018 ± 0.001 *0.725 ± 0.051* **(N = 121716)**
pH_{T25}	—	—	−0.0462 ± 0.0006 *7.8878 ± 0.0091* **(N = 21190)**
pCO_2	—	—	186.8 ± 1.3 *435.7 ± 24.1* **(N = 21283)**

All trends are for decade^{-1} (Sv for the flows, m for h, °C for θ, kgm^{-3} for σ_θ, and μatm for pCO_2; S, F_2 and pH_{T25} are dimensionless). Shaded cells indicate trends no different from 0 at the 95% confidence level. Three values are given for each variable, corresponding to the whole series, and the first and second parts, respectively (as indicated in the Table heading), except for pH_{T25} and pCO_2, whose data only covers a portion of the second part.

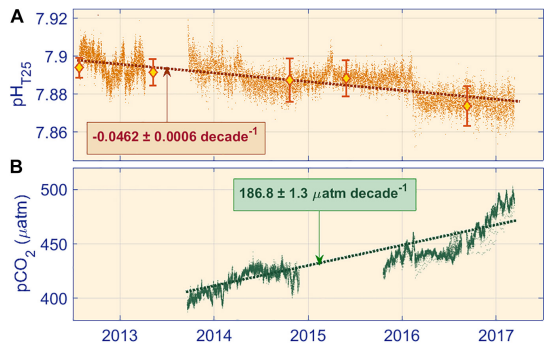

FIGURE 5 | (A) Time evolution of the SAMI-pH data and the estimated linear trend (dashed line) from August 2012 to March 2017. **(B)** Same as **(A)**, but for pCO_2 data. Red diamonds and associated bars in panel **(A)** are the mean and std of the discrete pH_{T25} values obtained directly from seawater samples through the spectrophotometric technique.

which come from independent samples, are shown in **Figure 5A** in red symbols, and agree with the overall trend of the series quite satisfactorily.

During the four-and-half-year period, pH_{T25} data ranged between a maximum of 7.9193 measured in October 2013 to a minimum of 7.8520 in January 2017 and exhibits the expected trend to diminish in the present scenario of ocean acidification, a trend also confirmed by the values obtained through spectrophotometry (red diamonds in **Figure 5A**). The decrease is not steady but step-like, the most obvious jump occurring in early 2016. Overall, the series shows a remarkable negative trend of -0.0462 ± 0.0006 decade^{-1}, significant at the 95% confidence level.

Figure 5B shows complementary *in situ* pCO_2 data from the SAMI sensor, which exhibits a trend inversely and significantly correlated to that of pH_{T25} (not shown). During the period of available data, the pCO_2 in the outflow at the depth of the monitoring station showed a remarkable rise of 186.8 ± 1.3 µatm decade^{-1}. Nevertheless, and in concordance with the pH_{T25} series, pCO_2 evolution did not exhibit a smooth increase but a more evident rise from early 2016.

The Interface Between Atlantic and Mediterranean Waters

The first step to estimate the Mediterranean outflow is the computation of the height of the interface between Atlantic and Mediterranean waters, which implicitly requires a *definition* of interface. Much has been written about this issue and different solutions have been proposed (Bryden et al., 1994; García Lafuente et al., 2000, 2011, 2019; Tsimplis and Bryden, 2000; Sánchez-Román et al., 2009, 2012; Naranjo et al., 2014; Sammartino et al., 2015). The depth of null velocity, the obvious definition in a two-way steady exchange, is not applicable due to tidally driven reversal of the flows, which makes both layers to flow in the same direction during a portion of the tidal cycle and prevents zero-velocity from being achieved. Selecting a material surface is another possibility. Salinity is the best

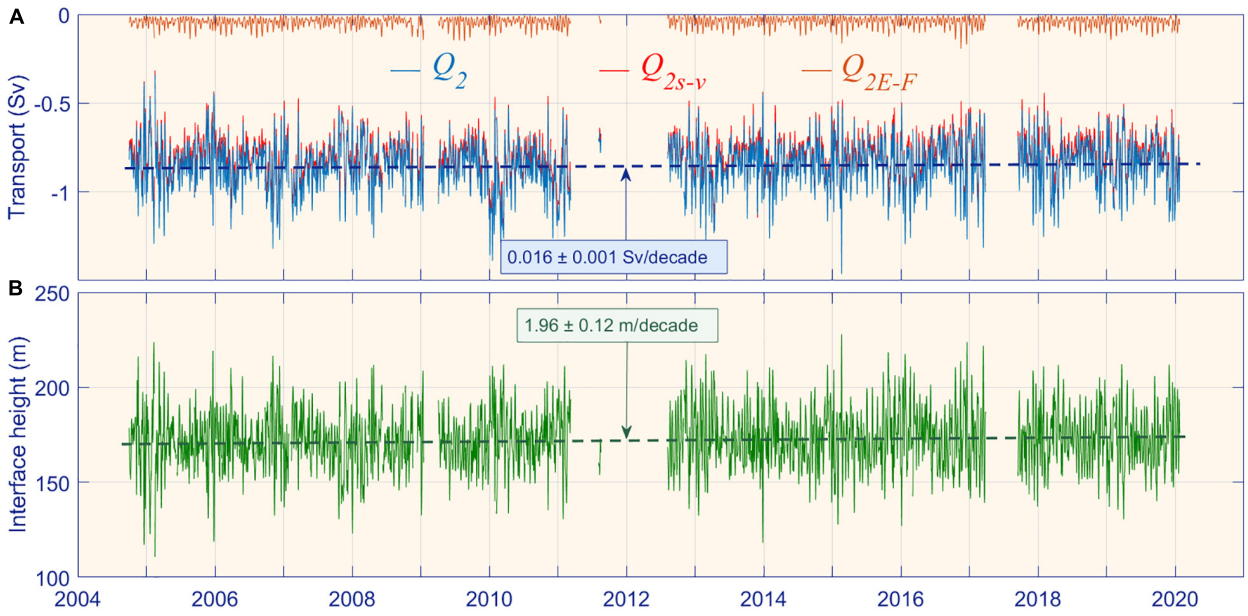

FIGURE 6 | (A) Total outflow Q_2 at Espartel section computed from the available velocity profiles (blue line), and the slowly varying Q_{2s-v} (red line) and eddy-fluxes Q_{2E-F} (sienna line) contributions (see text for details). Deep-blue dashed line is the linear trend in the whole period. **(B)** Interface height h_2 at the position of the monitoring station and its linear trend (dashed-green line). All series have been filtered to remove tidal variability so that the marked fluctuations in both panels reflect subinertial and seasonal variability.

candidate and specific isohalines have been proposed and used to this aim (Bryden et al., 1994; García Lafuente et al., 2000, 2013, 2019). It requires time series of S profiles throughout the water column. If they are not available, which is the case in this study, the procedure is not affordable. A third possibility is to link the interface position with the depth of maximum vertical shear of horizontal velocity (Tsimplis and Bryden, 2000; Sánchez-Román et al., 2009, 2012; Naranjo et al., 2014; Sammartino et al., 2015). The technique is well suited to the available series of ADCP velocity profiles and has been adopted here. The detailed description of the procedure can be seen in Sammartino et al. (2015) and has been followed to the letter in this work.

Figure 6B shows the time evolution of the interface height h_2 at the monitoring station, whose mean value is 172.8 m from the seafloor (**Table 1**). A marked subinertial variability stands out (the substantially larger tidal oscillations have been filtered out) overlapping an unclear, but still recognizable, seasonal cycle with the interface higher in spring and deeper in late summer-autumn. A comprehensive description of these issues can be seen in Sammartino et al. (2015) and are not addressed here. For the purpose of this work, the result of interest is the trend of the interface to become shallower at a rate of 1.96 m/decade. Following the splitting of the whole series in two parts suggested by θ (**Figure 3**), the same differentiation has been accomplished with this series. **Table 1** indicates that most of the interface elevation took place in the first part before the data gap of year 2012, whereas the trend is not significantly different from 0 at the 95% confidence level during the second one.

The Estimated Outflow

The outflow Q_2 has been also calculated following the procedure in Sammartino et al. (2015) after revising the lower part of the vertical profiles of horizontal velocity. The revision has been motivated by the availability of near-bottom velocity data collected by a new instrument incorporated into the monitoring station since September 2016. The data offer an ameliorated description of the bottom boundary layer and compel to modify the vertical profile of velocities within a few tens of meters above the seafloor with regards to the profile used in Sammartino et al. (2015). A detailed explanation of how it has been recalculated in light of these new data is presented in **Supplementary Appendix A**.

The low-passed (subinertial) outflow Q_2 computed with the new profiles (**Figure 6A**, blue line) differ only slightly from the one computed using Sammartino et al. (2015)'s velocity profiles. Its mean value (2004 to 2020) is -0.85 ± 0.13 Sv (standard deviation), whereas it is −0.82 ± 0.16 Sv if Sammartino et al. (2015)'s profiles were used instead. The ameliorated estimation gives a 3.7% greater and, also, less fluctuating outflow. Of interest is the positive trend identified in the whole series of Q_2 (**Figure 6A**, dashed-blue line, **Table 1**), estimated in +0.016 Sv/decade (**Table 1**). Since Q_2 is negative, this trend diminishes the outflow. Care must be taken, however, because the trend was negative before the gap of year 2012 (**Table 1**), meaning that Q_2 was increasing during the first part, to reverse the tendency in the second one.

Red line in **Figure 6A** displays the slowly varying part of the outflow (Q_{2s-v}), which results from filtering out tidal fluctuations from the horizontal velocity and interface motions,

and computing the transport with the low-passed series. The result differs from the total outflow (blue line) because of the already mentioned eddy-fluxes (Q_{2E-F}; see Vargas et al., 2006, for details about Q_{2s-v} and Q_{2E-F} computations), which hardly contribute by ∼5% to the outflow (sienna line in **Figure 6A**, see **Table 1**) in agreement with Sánchez-Román et al. (2012) and Sammartino et al. (2015). Both terms exhibit positive trends for the whole series (**Table 1**), the trend of Q_{2s-v} being comparable to the one of Q_2, whereas the trend of Q_{2E-F} is much smaller. During the second part the sign of both trends is different (**Table 1**), a fact that will be discussed later.

INTERPRETATION OF RESULTS

The Froude Number at Espartel Section

The Froude number at Espartel has been computed in order to assess the hydraulic state of the exchange. The lack of information in the upper layer only allows for the estimation of F_2 in equation [1]. Notwithstanding and according to the arguments given in Section "The Hydraulically-Controlled Exchange Model", $F_2 \approx G$ is a reasonable approximation and, therefore, F_2 is a good indicator of that state. It can be evaluated in terms of Q_2 (instead of u_2) and the interface height h_2 as (see **Supplementary Appendix B** and **Supplementary Figure B1** for details)

$$F_2 = \frac{|Q_2|\left(W_b + ch_2\right)^{1/2}}{\left(W_b h_2 + 0.5ch_2^2\right)^{3/2} g'^{1/2}} \quad (4)$$

for a realistic trapezoidal cross section of bases W_b(=2100m) at the sea bottom and W_0(=7000m) at the mean height of the interface H_0(=173m). Dimensionless constant c is defined as $c = (W_0 - W_B)/H_0 = 28.32$. **Figure 7** displays the time series of F_2 computed from the series of Q_2 and h_2 presented in **Figure 6**.

Except for an isolated event by the end of year 2009, F_2 does not reach the critical value of 1. Including F_1 in the estimation of G in equation [1] does not change the result because F_1 hardly reaches 0.1 due to the low vertically averaged velocity u_1 in this section. Despite being close, Espartel does not meet the condition of critical section and, therefore, the exchange is not maximal, but submaximal. Greater exchanged flows are possible.

Figure 7 indicates a decreasing trend of F_2, which could have been anticipated from the tendencies of Q_2 to diminish in magnitude and h_2 to increase (**Figure 6**), as both them act in the same direction to diminish F_2 (equation [4]). The simultaneity of such trends in Q_2 and h_2 are counterintuitive: the higher the interface, the larger the cross-area for the Mediterranean water to flow out. The expected result would be an increased outflow and not a diminution. The explanation of the paradox is in **Table 1**. The rise of the interface took place during the first part of the series previous to the data-gap, when Q_2 had negative trend that increased the magnitude of the outflow. It is the intuitive physical behavior, which leads to a positive trend of F_2 in this first part (**Table 1**). Thus, F_2 increased driven by the augmented outflow, which approached maximal exchange conditions that, in the end, did not attain. The interface had no significant trend during the second part whereas the one of Q_2 changed sign (**Table 1**), reducing progressively the outflow and, therefore, F_2 .

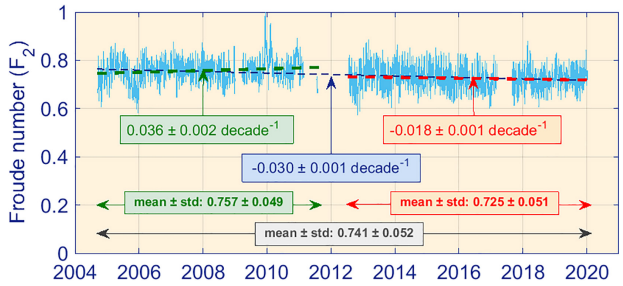

FIGURE 7 | Time evolution of the lower layer Froude number (F_2) computed according to equation [4]. Dashed blue line is the linear trend for the whole series and dashed green and red lines show the trends before and after the gap of year 2012, respectively. All numerical values, including 95% confidence levels, are indicated inside the text-boxes with the same color code. Mean and standard deviation for the whole series, and for the first and second parts are also indicated.

Buoyancy Fluxes and Water Formation

Figure 8A shows the yearly value of B_0 averaged during winter months from 2004 to 2020, using the outputs of ERA reanalysis. There is a marked interannual variability with years of strong buoyancy flux, which supposedly correspond to years of large volume of newly formed deep water. It is the case of year 2005 (Schroeder et al., 2008) or years 2009, 2010, 2012 (Houpert et al., 2016) with regards to the WMDW in the western MedSea. But there also exists years of weak buoyancy flux such

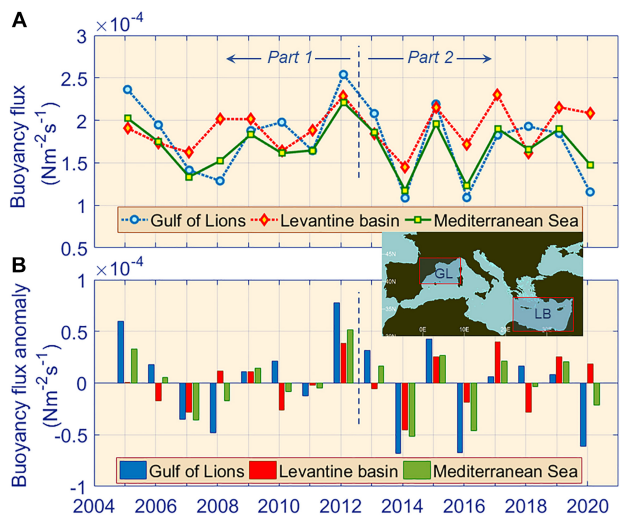

FIGURE 8 | (A) Time-averaged buoyancy flux B_0 during winter months (December, January and February) from 2004 to 2020 (sixteen data, starting in December 2004 and ending in February 2020). The fluxes have been spatially averaged for three regions, Gulf of Lions (GL in the inset map), Levantine basin (LB in the map) and the whole MedSea, as indicated in the legend. **(B)** Buoyancy flux anomaly of the data showed in panel **(A)** referred to the 2004-2020 mean. Vertical dashed line separates parts 1 and 2.

as 2008 or 2011, when no WMDW was reported to have been formed (Houpert et al., 2016).

In the Gulf of Lions, buoyancy flux of three out of the seven last years, namely 2014, 2016 and 2020, had the largest negative anomaly of the whole series (**Figure 8B**). Except for year 2020, the same applies to the whole basin (green bars). They showed minima well below the mean, which makes the second half of the period be negatively anomalous in both, the Gulf of Lions and the whole basin. These results agree with Margirier et al. (2020), who indicate the absence of intense deep convection in the Gulf of Lions between 2014 and 2017 (their study ends in year 2018). Interestingly, this period coincides with the second part of the oceanographic observations, when the strong trend of θ was detected in the monitoring station. The coincidence encourages a similar partition of the B_0 series and estimating the trends before and after year 2013 separately.

Table 2 shows the results of such analysis. In addition to the three-winter-month averages presented in **Figure 8** (DJF, Winter3 block in **Table 2**), two other averages have been considered: five-winter-month (NDJFM, Winter5 block) and all year round (Annual block). Trends are given in $Nm^{-2}s^{-1}decade^{-1}$ and the cells in **Table 2** have been tagged according to the sign of the estimated trend. They are no-significant at the 95% confidence level, which is not surprising considering the reduced number of data-points in the fits. There is, however, a remarkable pattern in the Table: all trends during the period 2013-2020 are negative except for the positive one found in the Levantine basin in block Winter3 (although it is the less positive of the three trends in Winter3 block). Moreover, most trends in the period 2005-2012 are positive (Gulf of Lions and MedSea in block Winter5 are the exceptions). All in all, the conclusion that during the first part of the series the trend of the buoyancy was positive and changed to negative during the second part is reasonably supported. Equation [3] would indicate the same signs in the trends of Q_M. Within the framework of the two-layer SoG-MedSea model with balance between water production and export, during the first part Q_2 should increase (negative trend, as it is a negative quantity) and decrease during the second part (positive trend), which is what **Table 1** reflects.

Fraction Composition of the Outflow

The time evolution of the properties of the water flowing pass the monitoring station may be the result of changes in the proportion of the Mediterranean waters in the outflow, or a concomitant evolution of the properties of each of the Mediterranean waters that form the outflow, or both. We focus on the WMDW and LIW, which are the main bulk of the outflow at the monitoring station, the rest being a very small fraction of Atlantic water, mainly North Atlantic Central Water (NACW) entrained by the Mediterranean flow a short distance upstream in the Tangier Basin (García Lafuente et al., 2007, García Lafuente et al., 2011).

An estimation of the fraction of the different water masses in the outflow has been carried out following García Lafuente et al. (2007). The triplet of points used by these authors was [12.8°C, 38.45], [13.22°C, 38.56] and [15°C, 36.2], representing WMDW, LIW and NACW, respectively. The water masses characteristics change from place to place and with time, and there are no unique values to represent them. A requirement for the fraction analysis to be feasible is that the θ-S points of the water samples to be decomposed lay inside the triangle defined by the triplet of reference to avoid fractions greater than 1 or less than 0, which have no meaning. The selection of the triplet is a trade-off between fulfilling this requirement and maintaining values as representative of the implied water masses as possible. The points used in García Lafuente et al. (2007) do not fulfill the first condition with the present series (left panel of **Figure 9**) because data of the available series at that time were grouped closer to WMDW-type (cooler, see **Figure 4**). A new triplet has been therefore chosen to enclose all data: [12.9°C, 38.45], [13.42°C, 38.57] and [16°C, 36.2] for WMDW, LIW and AW, respectively (**Figure 9**).

The first hypothesis that the time evolution of water characteristics stems from changes in the fractions of each contributor implicitly assumes that the θ-S characteristics of the triplet remain unchanged. Right panel of **Figure 9** shows a sudden increase of LIW-type fraction from year 2015 onwards, along with a corresponding diminution of the WMDW. The fraction of AW was kept essentially unaffected. LIW would become the main

TABLE 2 | Estimated trends of averaged buoyancy flux ($Nm^{-2}s^{-1}$/decade) during the period of available data in the monitoring station with the 95% confidence interval.

Average	Period	MedSea	Levantine	Gulf Lions
Annual (Oct-Sept)	2005-2020	$\mathbf{-4 \pm 9\ 10^{-6}}$	$+1 \pm 9\ 10^{-6}$	$\mathbf{-5 \pm 13\ 10^{-6}}$
	2005-2012	$+7 \pm 27\ 10^{-6}$	$+13 \pm 29\ 10^{-6}$	$+7 \pm 43\ 10^{-6}$
	2013-2020	$\mathbf{-13 \pm 35\ 10^{-6}}$	$\mathbf{-9 \pm 36\ 10^{-6}}$	$\mathbf{-13 \pm 44\ 10^{-6}}$
Winter5 (NDJFM)	2005-2020	$\mathbf{-9 \pm 19\ 10^{-6}}$	$+1 \pm 23\ 10^{-6}$	$\mathbf{-20 \pm 25\ 10^{-6}}$
	2005-2012	$\mathbf{-10 \pm 73\ 10^{-6}}$	$+20 \pm 67\ 10^{-6}$	$\mathbf{-26 \pm 91\ 10^{-6}}$
	2013-2020	$\mathbf{-13 \pm 55\ 10^{-6}}$	$\mathbf{-9 \pm 80\ 10^{-6}}$	$\mathbf{-26 \pm 70\ 10^{-6}}$
Winter3 (DJF)	2005-2020	$\mathbf{-5 \pm 35\ 10^{-6}}$	$+14 \pm 30\ 10^{-6}$	$\mathbf{-23 \pm 52\ 10^{-6}}$
	2005-2012	$+23 \pm 64\ 10^{-6}$	$+41 \pm 81\ 10^{-6}$	$+24 \pm 98\ 1^{--6}$
	2013-2020	$\mathbf{-32 \pm 98\ 10^{-6}}$	$+10 \pm 99\ 10^{-6}$	$\mathbf{-82 \pm 130\ 10^{-6}}$

Three different averaging intervals have been used: Annual (12-month average, from October year X to September year X+1), Winter5 (5-month, from November year X to March year X+1) and Winter3 (3-month, from December year X to February year X+1). Trends for the whole series (2005-2020) and the subseries corresponding to part 1 and part 2 of the oceanographic data (2005-2012, and 2013-2020, respectively) have been estimated. The computations have been carried out for the entire basin (MedSea column) and for Levantine and Gulf of Lions sub-basins. Negative and positive trends are in bold and italic, respectively.

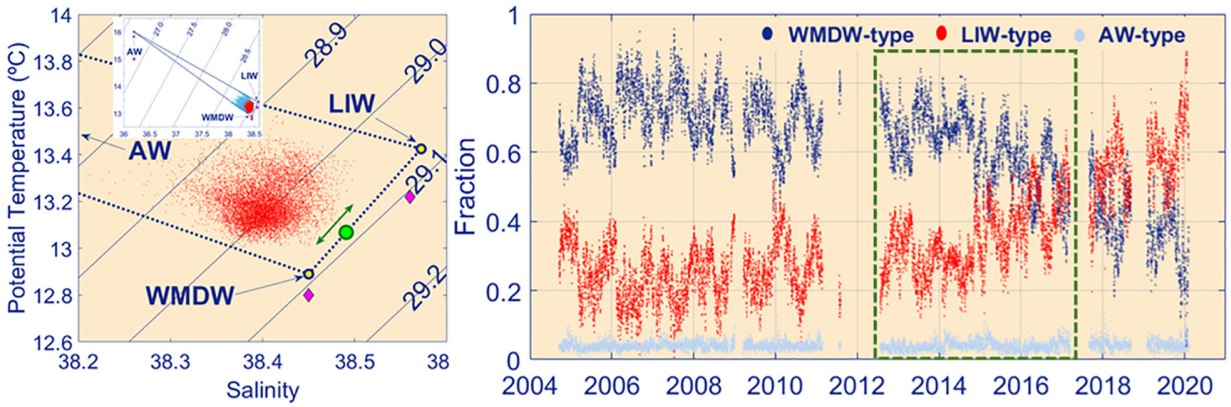

FIGURE 9 | Left panel: θ – *S* diagram of the θ-minimum samples. Circles indicate the triplet of reference used for the fraction decomposition. The inset is the θ-*S* diagram for all (light blue dots) and θ-minimum (red dots) samples, included to show that all samples lay inside the triangle defined by the triplet. Magenta diamonds are the points used in García Lafuente et al. (2007). Green circle and the arrow represent a hypothetical evolution of WMDW-type along the line joining the initial WMDW and LIW that would change the initial triplet (see text for more explanations). Right panel: time evolution of the fraction of the different waters using the triplet initially defined. Dashed green rectangle embraces the period of available biogeochemical data.

contributor in the mixing after year 2017, replacing the prevailing role of WMDW before this year.

The second hypothesis is that the time evolution of water properties in the monitoring station was the result of a concomitant change of properties of the water masses participating in the outflow instead of variations in the fractions. To keep water samples after year 2015 with, approximately, the same fractions as before 2015, the WMDW-type characteristics should evolve to saltier and warmer, as sketched by the green dot in **Figure 9**. By the end of the series (February 2020), its new θ-*S* values should be [13.1°C, 38.50] assuming a simple evolution along the dotted line joining the initial values assigned to WMDW and LIW. Right panel suggests that the starting time of the change would have been the beginning of year 2015, which would imply trends in WMDW of ∼0.4°C/decade and ∼0.1 decade^{-1} for θ and *S*, respectively, during the last five years.

There are no numerical values in the literature for such a recent period to check with, but these trends in WMDW are clearly unrealistic. For instance, Vargas-Yañez et al. (2017) report 0.03°C/decade and 0.02 decade^{-1} in the 600m-to-bottom layer in the Alboran Sea during 1943-2015; Houpert et al. (2016) indicate annual changes of 0.0032 ± 0.0005°C and 0.0033 ± 0.0002 for θ and *S* during the period 2009-2013 in the 600-2300 m layer in the Gulf of Lions (equivalent to trends of 0.032 ± 0.005°C/decade and 0.033 ± 0.002decade^{-1}). They are one order of magnitude less than the rate necessary to validate the second hypothesis, which therefore should be discarded. Certainly, the trend could be partially due to the warming and salinification of LIW instead of WMDW. To this regard, a noticeable warming of LIW in the Gulf of Lions from 2007 to 2018 has been recently reported (Margirier et al., 2020). Even so, a consistent diminution of the proportion of WMDW in the Mediterranean outflow at the depth of the monitoring station is still necessary for that warming to manifest itself in the form of the observed trend in the Mediterranean outflow. Thus, the approach followed in this work is that the recent θ-*S* changes in the monitoring station (**Figure 3**) have been mainly caused by the progressive increase of LIW fraction in the outflow and the corresponding diminution of WMDW from around year 2013 onwards.

Estimates of *PH* and PCO_2 in the Outflow Water Masses

Figure 5 illustrates a remarkable acidification of the Mediterranean outflow at the monitoring station, particularly from 2016 onwards. As in the case of θ discussed above, the observed pH_{T25} and pCO_2 trends could be the result of similar trends in the LIW and WMDW, the main components of the outflow, the change with time of the fractions of each water mass in the outflow, or both. In order to gain insights on the origin of this issue, the fraction analysis performed above (**Figure 9**, dashed-green box) was combined with the multi-linear regression model developed by *Flecha et al.* (2015) to obtain the individual pH_{T25} and pCO_2 values characterizing the LIW and the WMDW separately. This procedure has been applied successfully to discriminate between the components of the outflow and to estimate the values of oceanographic properties in each water body separately (Flecha et al., 2012, 2015, 2019). **Figure 10** displays the time evolution of the pH_{T25} and pCO_2 assigned to each water mass in the outflow from 2012 to 2017.

The analysis provides time-averages of 7.8718 ± 0.0004 and 7.9030 ± 0.0003 for pH_{T25} of the LIW and WDMW, respectively (**Figure 10**), values that are slightly lower than those reported by *Flecha et al.* (2015) who used a shorter time series spanning from 2012 to 2015. The difference can be interpreted as a gradual acidification attributed to the increase in CO_2 content in the Mediterranean waters. In fact, during the last portion of the available *pH* data (June 2015 to March 2017), the time-averages of the pH_{T25} series dropped to 7.8654 ± 0.0005 in the case of LIW and 7.8978 ± 0.0004 in WMDW, which were accompanied by a rise of pCO_2 (**Figures 10C,D**).

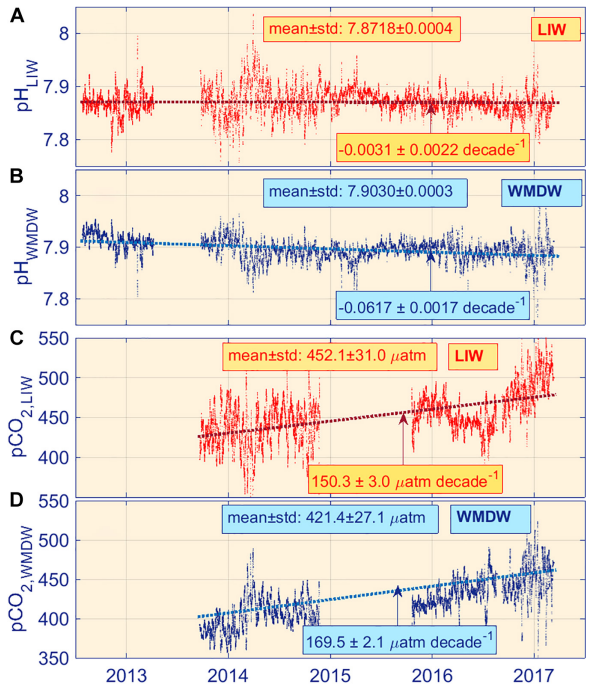

FIGURE 10 | (A) and **(B)**. Time series of pH_{T25} assigned to LIW and WMDW, respectively, applying the water masses fraction analysis specified in Section "Fraction Composition of the Outflow." **(C)** and **(D)** Idem for pCO_2.

The four-and-half-year time series in this study also revealed a striking and sudden decrease of pH_{T25} by the beginning of year 2016 in the outflow. It occurred concomitantly with a progressive rise in pCO_2 (**Figure 5**), the trends in both properties remaining relatively stable from then onwards. Signatures of the pH_{T25} decrease and pCO_2 rise can be indeed detected in the LIW and WMDW separately (**Figure 10**) and therefore, it is plausible to assume that both water masses are contributing to the overall patterns detected in the outflow. However, water fraction analysis reveals that the warmer LIW prevailed in the outflow from January 2016 with the corresponding decline of WMDW fraction (**Figure 9**, green box), a situation more evident in the spring of this year. Fractions kept increasing (LIW) and decreasing (WMDW) rather steadily from September 2016 onwards.

According to former studies that used shorter series of this SAMI pH dataset (up to 2015, Flecha et al., 2015) or discrete pH_{T25} measurements (Flecha et al., 2019), LIW was invariably characterized by pH_{T25} values lower than those in WMDW and relatively constant. These results agree with previous studies that report pH minima in the LIW in several Mediterranean sub-basins in relation to the rest of Mediterranean waters (Alvarez et al., 2014; Hassoun et al., 2015). Such minima have been attributed to the remineralization of organic matter during aging of the LIW. As this water flows at intermediate depths isolated from the atmosphere in its way back to the Atlantic ocean, anthropogenic carbon absorption is prevented, making its pH levels remain stable (Alvarez et al., 2014). On the contrary, deep convection and/or shelf water cascade that drive the winter formation of WMDW from the very surface in the Gulf of Lions accumulates anthropogenic carbon in the newly formed water, which favors a WMDW acidification trend (Hassoun et al., 2015; Flecha et al., 2019). Patterns of pH_{T25} and pCO_2 up to 2015 in **Figure 10** corroborate these findings: lower but relatively constant pH_{T25} in the LIW versus higher but decreasing-over time pH_{T25} in the WMDW. But **Figure 10** also suggests a novel acidification trend in the LIW since 2016, which, along with the suggested prevalence of LIW fraction over that of WMDW in the observed outflow (**Figure 9**), would result in the pH_{T25} and pCO_2 trends visible in **Figure 5** during the last one year and a half of data.

DISCUSSION AND CONCLUSION

Despite a few vicissitudes inherent to field work in harsh environments, the monitoring station deployed at Espartel sill in the SoG in late 2004 is providing worthy information about the outflow of the Mediterranean water and its properties. The outflow in turn reflects changes in the MedSea and provides an integrated overview of what is going on in the basin. Investigating likely links between changes in the MedSea properties and the outflow is the objective of this study.

A sequence of misfortunes in the experimental work caused an important data gap around year 2012. A detailed inspection of the series of collected and derived variables suggests two distinct periods in the series, with differentiated patterns of time evolution: a first period before the gap (2004-2012) and a second one after the gap (2013-2020). The most striking result is the trend of θ, which increased markedly starting by year 2013 and kept on up to the date of writing this work. In fact, the change was so outstanding (**Figure 3**) that not only motivated the inspection of the other variables searching for similar patterns, but also the present study.

The total outflow Q_2 showed an overall small positive trend of +0.016Sv/decade (**Table 1**), which reduces its size. During the first part, however, the trend was negative, −0.068 Sv/decade (the outflow increased), and then it changed sign after the gap in the second part (**Table 1**). The contribution of the eddy-fluxes Q_{2E-F} to the total outflow deserves a little attention. In Espartel section Q_{2E-F} hardly reaches −0.04Sv or ∼5% (**Table 1**), in agreement with previous findings (Sánchez-Román et al., 2009; Sammartino et al., 2015). The percentage is very similar to the one in the eastern section of the SoG (García Lafuente et al., 2000; Baschek et al., 2001; Sannino et al., 2004). The smallness of Q_{2E-F} in these two sections points at a two-layer exchange hydraulically controlled at Espartel sill (instead of Camarinal) and Tarifa Narrows and the possibility of maximal exchange. Notwithstanding, the latter was not achieved ($F_2 \approx 0.74 < 1$, **Figure 7**).

An interesting fact in this regards is the behavior of the two components of the total outflow, Q_{2s-v} and Q_{2E-F}. In the first part of the series, the trend of Q_2 originated in Q_{2s-v}, Q_{2E-F} having no contribution (**Table 1**). In the second part, however, the positive trend of Q_{2s-v} was noticeably higher than the trend

of Q_2 and a negative trend of Q_{2E-F} was necessary to conciliate the mismatch. As Q_{2E-F} is negative, eddy-fluxes increased in magnitude, whereas the slowly-varying contribution diminished during this part. This is the expected behavior of each component of the flow if it separates away from the critical condition. Such a separation agrees with the decreasing trend of F_2 during the second part (**Table 1** and **Figure 7**). Although F_2 showed overall tendency to decrease, that is, to accentuate the submaximal exchange (remind that $F_2 \sim G$ due to the smallness of F_1), it had positive trend that pushed the flow towards critical during the first part. In the end, it did not reach it because of the sign change of the trend in the second part. In view of the results in **Table 1**, the conclusion is that F_2 mimics the behavior of Q_2: a first part with Q_2 increasing in magnitude that drove F_2 to higher values until Q_2 changed trend in the second part, reversing F_2 trend as well.

In the simple steady-state model of the exchange that includes the MedSea, the rate of production of Mediterranean water, Q_M, must equal the outflow $|Q_2|$. Since the former depends on the buoyancy losses of the MedSea, buoyancy fluxes B_0 were computed to get some insight on the variability of Q_M production (**Figure 8A**). The estimated B_0 agrees with the available data of annual deep water formation in the Gulf of Lions (Houpert et al., 2016; Margirier et al., 2020), which supports the use of B_0 as the proxy of Q_M production postulated by equation [3]. It must be recalled that the steady-state nature of the model limits its application to long-term changes. In other words, trends of B_0 that could be inferred from data in **Figure 8** are expected to be echoed by similar trends in Q_2 according to the model, but year-to-year fluctuations do not have to fulfill this expectation. Therefore, the discussion is restricted to these long-term changes.

Even though no definitive pattern can be confirmed, there are reasonable indications that the two-part differentiation carried out in the oceanographic variables is still applicable to B_0 (**Table 2**): a first part in which buoyancy fluxes tended to increase followed by a second one with the opposite trend. This second part sustained the three years of larger B_0 negative anomaly out of the sixteen year examined in the Gulf of Lions (**Figure 8B**), with the expectable result of no (or weak) WMDW formation those years, as stated in Margirier et al. (2020).

All in all, the scenario that emerges is as follows. At the time of the beginning of the series, the outflow was submaximal (in terms of two-layer model) as a consequence of the weakness of winter buoyancy loss since 1988 in the northwestern MedSea (Herrmann et al., 2010; Margirier et al., 2020). It prevented strong convection and the formation of significant volumes of WMDW during the 1990s and early 2000s and enabled the increase of heat and salt content in the region. Within this scenario of preconditioned water, further favored by the arrival of the so-called Eastern Mediterranean Transient to the Gulf of Lions (Schroeder et al., 2006), the large buoyancy loss in 2004-2005 winter (**Figure 8A**) propitiated the formation of an extraordinary volume of WMDW (López-Jurado et al., 2005; Schroeder et al., 2008), which left a clear footprint in the θ series of the monitoring station in early spring, 2005 (García Lafuente et al., 2007). It was not the only consequence. The Q_M production exceeded the outflow Q_2 at that time, forcing it to increase (a feasible result, since it was submaximal) and likely triggered the period of negative trend of Q_2 (greater outflow) found in our analysis (**Table 1**). Successive winters of moderate or large volume of deep water formation (2012, for instance, as suggested by **Figure 8A**, see also Houpert et al., 2016) kept this trend until the production relaxed or, even, stopped. According to Houpert et al. (2016), there was no formation of deep water in year 2013, nor was there any appreciable formation between years 2014 and 2017 (Margirier et al., 2020). This situation of very few Q_M formation caused $|Q_2|$ to diminish (particularly its Q_{2s-v} contribution, **Table 1**) and reversed the trend, which changed to positive (reduced outflow) up to the end of the series. Froude number F_2 diminished accordingly, thus moving away from the critical value it had been approaching during the first part. The increased contribution of eddy-fluxes Q_{2E-F} to Q_2 (**Table 1**) would agree with the augmented departure from the critical value, in the same manner as the relatively fast response of Q_2 to buoyancy changes point at submaximal exchange through the SoG (Garrett et al., 1990). This last aspect, which is applicable to the whole period, is in full agreement with the subcritical value exhibited by F_2 in **Figure 7** throughout the series.

The time evolution of θ in **Figure 3**, whose sharp increase in the second part of the analyzed period motivated the present study, suggests a double origin for θ trends in **Table 1**. During the first part of the series, the estimated trend was $+0.029 \pm 0.009$°C/decade, which is very similar to trends reported in the literature for LIW or for WMDW (Vargas-Yañez et al., 2017; Houpert et al., 2016). But the one-order-magnitude greater trend in the second part ($+0.339 \pm 0.008$°C/decade) is well above any reported value in the Mediterranean Sea for deep waters. A more appropriate explanation for this trend is the progressive replacement of WMDW by the slightly warmer LIW in the outflow Q_2, a situation that seems to persist nowadays. Biogeochemical data also agree with this hypothesis: pH_{T25} data indicate a noticeable acidification of the outflow (-0.0462 ± 0.0006 decade^{-1}), which is particularly evident from year 2016. The decline of pH_{T25} with time and the concomitant rise in pCO_2 of LIW and WMDW detected when these variables were discriminated for both water masses (**Figure 10**), the striking CO_2 rise in the LIW from that particular year and its greater participation in the outflow, all of them contribute to shape the acidification trend observed in the monitoring station. The reasons for the continuous enrichment in carbon content of the LIW are out of the scope of this study, but some basin processes can be invoked. Although properties of deep waters suggest enhanced ventilation in the Gulf of Lions from early 2000 to 2016 (Li and Tanhua, 2020), deep water ventilation is highly variable in time and space. For instance, in the very severe winter of 2011-12 (**Figure 8**), the uplift of the LIW layer in this region caused by the massive formation of WMDW reported in Schroeder et al. (2016) would have brought this water mass closer to the surface and exposed it partially to atmospheric influence. The likely increment of anthropogenic carbon fraction associated with this rising, enhanced by the expected increase in respiration that occurs in heavily ventilated waters, would have resulted in a noticeable pH_{T25} decrease. On the other hand, Schroeder et al. (2016) suggest that WMDW formed in the Gulf

of Lions may take around 33 months to reach the vicinity of the SoG, a figure that could be applicable to that LIW exposed to atmospheric effects. This time delay, which is also supported by age calculations carried out for both water masses in the Alboran Sea (Rhein and Hinrichsen, 1993; Flecha et al., 2019), would relate the pH_{T25} decrease observed in the time series in year 2016 with that cold event of winter 2012. Unrevealing the origin of changes in the properties of the carbon system detected in the LIW from 2016 onwards requires a thorough assessment of the whole bulk of biogeochemical properties recorded in the area over the last four years, particularly dissolved oxygen and organic matter content, a study that is presently under way. The analysis is particularly relevant due to the significant acidification rates recently measured in waters of the Levantine Basin (Hassoun et al., 2019), which will eventually reach the SoG and exit the basin as part of the outflow, with implications in the biogeochemistry of the North Atlantic.

The prevailing negative anomaly of buoyancy flux B_0 in the whole basin during the second part (green bars, **Figure 8B**) suggests a reduced formation of Mediterranean water Q_M, which in turn gave rise to the concomitant reduction of the outflow Q_2 (**Table 1**), as discussed earlier. However, the B_0 anomaly was not homogeneously distributed over the basin. It was more accentuated in the Gulf of Lions (blue bars) than in the Levantine basin (red bars) where, in fact, the time-averaged anomaly in the second part was nearly null. Therefore, the eventual reduction of Q_M would have partially had its origin in the scarce production of WMDW in this period, confirmed by Margirier et al. (2020), with the collateral effect of leaving room for LIW to replace progressively the WMDW fraction in Q_2, as suggested by **Figure 9**. In this Figure, the evolution of LIW fraction resembles the evolution of θ in **Figure 3** because the variability of temperature prevails over that of salinity.

A remark must be made regarding this conclusion. Fractions in **Figure 9** refer to the water outflowing at the depth of the monitoring station, close to the bottom, and should not be extrapolated to the rest of the Mediterranean layer above the station. If LIW contributes to the outflow more than WMDW, as it is generally accepted, the fractions above the depth of the station (but yet in the Mediterranean layer) will change to give LIW the dominant role. In the deepest portion of the outflow layer, though, the proportion of the WMDW used to prevail, as suggested by its fraction during the first part of the series (**Figure 9**; see also García Lafuente et al., 2007). But the recent data collected by the station indicated that, even at great depth, LIW would be becoming the prevailing water mass in the mixing. It is an expectable result if the diminished buoyancy flux to the atmosphere during the latest years were causing a WMDW production shortage that reduced its participation in the outflow. Harsh winters to come would halt this situation by increasing the formation rate of WMDW and, likely, reverse the recent outstanding θ trend observed in the monitoring station at Espartel section. Further research is needed to assess and confirm these changes as well as the mentioned acidification trend in the LIW from 2016 (and, hence, in the outflow through the SoG), which highlights the importance of maintaining the observation program whose data have propitiated this study.

DATA AVAILABILITY STATEMENT

The raw data supporting the conclusions of this article will be made available by the authors, without undue reservation.

AUTHOR CONTRIBUTIONS

JG-L designed the study and wrote the bulk of the manuscript. SS, IEH, and SF also contributed to the writing. SS, JG-L, CN, and IN processed the physical time series. IEH and SF acquired and processed biogeochemical data. RS-L and MJB organized most of the oceanographic surveys for servicing the monitoring station. All authors participated in the data acquisition and in the field campaigns and contributed to the interpretation, result discussion and revision of the manuscript. JG-L and IN carried out the manuscript edition.

FUNDING

Time series analyzed in this paper have been collected within the frame of INGRES Projects, INGRES1 (REN2003_01608), INGRES2 (CTM2006_02326/MAR), and INGRES3 (CTM2010_21229-C02-01/MAR), Special Action CTM2009-05810-E/MAR, funded by the Spanish Government. Since year 2016, the monitoring station is part of the Spanish Oceanographic Institute (IEO) internal project STOCA in which frame the station is presently serviced with the participation of Málaga University and researchers of the Interdisciplinary Thematic Platform of the CSIC WATER:iOS, with funding provided by the Ministry of Science and Innovation (EQC2018-004285-P) and the European Commission through the project COMFORT (H2020-820989). The mooring line is included in the Mediterranean Sea monitoring network of HYDROCHANGES project sponsored by CIESM, which is part of the CMEMS Marine Copernicus *In Situ* TAC Program, registered as WMO ID 6202100 in the JCOMM *in situ* Observations Program Support.

ACKNOWLEDGMENTS

We are especially gratefully to the crew of IEO research vessels 'Odón de Buen', 'Francisco de Paula Navarro', 'Ramón Margalef' and 'Ángeles Alvariño' for their assistance and help in the maintenance and servicing of the monitoring station. CN acknowledges a postdoc fellowship from the University of Málaga.

SUPPLEMENTARY MATERIAL

The Supplementary Material for this article can be found online at: https://www.frontiersin.org/articles/10.3389/fmars.2021.613444/full#supplementary-material

REFERENCES

Alvarez, M., Sanleon-Bartolomé, H., Tanhua, T., Mintrop, L., Luchetta, A., Cantoni, C., et al. (2014). The CO2 system in the Mediterranean Sea: a basin wide perspective. *Ocean Sci.* 10, 69–92. doi: 10.5194/os-10-69-2014

Armi, L. (1986). The hydraulics of two flowing layers with different densities. *J. Fluid Mech.* 163, 27–58.

Armi, L., and Farmer, D. (1985). The internal hydraulics of the Strait of Gibraltar and associated sills and narrows. *Oceanol. Acta* 8, 37–46.

Armi, L., and Farmer, D. (1987). A generalization of the concept of maximal exchange in a strait. *J. Geophys. Res.* 92, 14679–14680.

Astraldi, M., Balopoulos, S., Candela, J., Font, J., Gacic, M., Gasparini, G. P., et al. (1999). The role of straits and channels in understanding the characteristics of the Mediterranean circulation. *Prog. Oceanogr.* 44, 65–108.

Baschek, B., Send, U., García Lafuente, J., and Candela, J. (2001). Transport estimates in the Strait of Gibraltar with a tidal inverse model. *J. Geophys. Res.* 106, 31033–31044.

Brandt, P., Alpers, W., and Backhaus, J. (1996). Study of the generation and propagation of internal waves in the strait of Gibraltar using a numerical model and synthetic aperture radar images of the European ERS1 satellite. *J. Geophys. Res.* 101:252.

Bryden, H. L., Candela, J., and Kinder, T. H. (1994). Exchange through the Strait of Gibraltar. *Prog. Oceanogr.* 33, 201–248. doi: 10.1016/0079-6611(94)90028-0

Bryden, H. L., and Kinder, T. H. (1991). Steady two-layer exchange through the Strait of Gibraltar. *Deep Sea Res.* 38, S445–S463. doi: 10.1016/S0198-0149(12)80020-3

Bryden, H. L., and Stommel, H. M. (1982). Origin of the Mediterranean outflow. *J. Mar. Res.* 40, 55–71.

Bryden, H. L., and Stommel, H. M. (1984). Limiting processes that determine basic features of the circulation in the Mediterranean Sea. *Oceanol. Acta* 7, 289–296.

Clayton, T. D., and Byrne, R. H. (1993). Spectrophotometric seawater pH measurements: total hydrogen ion concentration scale calibration of m-cresol purple and at-sea results. *Deep Sea Res. Part I* 40, 2115–2129.

Farmer, D., and Armi, L. (1986). Maximal two-layer exchange over a sill and through the combination of a sill and contraction with barotropic flow. *J. Fluid Mech.* 164, 53–76.

Farmer, D., and Armi, L. (1988). The flow of Mediterranean water through the Strait of Gibraltar. *Prog. Oceanogr.* 21, 1–106.

Flecha, S., Fiz, F. F., Navarro, G., Ruiz, J., Olivé, I., Rodríguez-Gálvez, S., et al. (2012). Anthropogenic carbon inventory in the Gulf of Cadiz. *J. Mar. Sys.* 92, 67–75. doi: 10.1016/j.jmarsys.2011.10.010

Flecha, S., Pérez, F. F., García Lafuente, J., Sammartino, S., Ríos, A. F., and Huertas, I. E. (2015). Trends of pH decrease in the Mediterranean Sea through high frequency observational data: indication of ocean acidification in the basin. *Sci. Rep.* 5:16770. . https://doi.org/10.1038/srep16770,

Flecha, S., Pérez, F. F., Murata, A., Makaui, A., and Huertas, E. I. (2019). Decadal acidification in Atlantic and Mediterranean water masses exchanging at the Strait of Gibraltar. *Sci. Rep.* 9:15533. doi: 10.1038/s41598-019-52084-x

García Lafuente, J., Bruque Pozas, E., Sánchez Garrido, J. C., Sannino, G., and Sammartino, S. (2013). The interface mixing layer and the tidal dynamics at the eastern part of the Strait of Gibraltar. *J. Mar. Sys.* 117–118, 31–42. doi: 10.1016/j.jmarsys.2013.02.014

García Lafuente, J., Delgado, J., Sánchez Román, A., Soto, J., Carracedo, L., and Díaz del Río, G. (2009). Interannual variability of the Mediterranean outflow observed in Espartel sill, western Strait of Gibraltar. *J. Geophys. Res. Oceans* 114:C10018. doi: 10.1029/2009JC005496

García Lafuente, J., Sánchez Román, A., Naranjo, C., and Sánchez Garrido, J. C. (2011). The very first transformation of the Mediterranean outflow in the Strait of Gibraltar. *J. Geophys. Res. Oceans* 116:C07010. doi: 10.1029/2011JC006967

García Lafuente, J., Sánchez Román, A., Sannino, G., and Sánchez Garrido. (2007). Recent observations of seasonal variability of the Mediterranean outflow in the Strait of Gibraltar. *J. Geophys. Res. Oceans* 112:C10005. doi: 10.1029/2006JC003992

García Lafuente, J., Vargas, J. M., Plaza, F., Sarhan, T., Candela, J., and Bascheck, B. (2000). Tide at the eastern section of the Strait of Gibraltar. *J. Geophys. Res. Oceans* 105, 14197–14213. doi: 10.1029/2000JC900007

García Lafuente, J., Naranjo, C., Sammartino, S., and Sánchez-Garrido, J. C. (2019). On the role of the Bay of Algeciras in the exchange across the Strait of Gibraltar. *Reg. Stud. Mar. Sci.* 29:100620. doi: 10.1016/j.rsma.2019.100620

Garrett, C., Bormans, M., and Thomson, K. R. (1990). "Is the Exchange through the Strait of Gibraltar Maximal or Submaximal?," in *The Physical Oceanography of Sea Straits. NATO ASI Series (Mathematical and Physical Sciences)*, Vol. 318, ed. L. J. Pratt (Dordrecht: Springer), 271–294. doi: 10.1007/978-94-009-0677-8_13

Gill, A. E. (1982). *Atmosphere-Ocean Dynamics*. London: Academic Press, 681.

Hassoun, A. E. R., Gemayel, E., Krasakopoulou, E., Goyet, C., Abboud-Abi Saab, M., Guglielmi, V., et al. (2015). Acidification of the Mediterranean Sea from anthropogenic carbon penetration. *Deep Sea Res. Part I* 102, 1–15. doi: 10.1016/j.dsr.2015.04.005

Hassoun, A. E. R., Fakhri, M., Raad, N., Abboud-Abi Saab, M., Gemayel, E., and De Carlo, E. H. (2019). The carbonate system of the Eastern-most Mediterranean Sea, Levantine Sub-basin: Variations and drivers. *Deep Sea Res. Part II* 164, 54–73. doi: 10.1016/j.dsr2.2019.03.008

Herrmann, M., Sevault, F., Beuvier, J., and Somot, S. (2010). What induced the exceptional 2005 convection event in the northwestern Mediterranean basin? Answers from a modeling study. *J. Geophys. Res.* 115:C12051. doi: 10.1029/2010JC006162

Hersbach, H., Bell, B., and Berrisford, P. (2020). The ERA5 global reanalysis. *Q. J. R. Meteorol. Soc.* 2020, 1–51. doi: 10.1002/qj.3803

Hopkins, T. S. (1985). "The physics of the Sea," in *Western Mediterranean*, ed. R. Margalef (New York: Pergamon), 100–125.

Houpert, L., Durrieu de Madron, X., Testor, P., Bosse, A., D'Ortenzio, F., and Bouin, M. N. (2016). Observations of open-ocean deep convection in the northwestern Mediterranean Sea: Seasonal and interannual variability of mixing and deep water masses for the 2007–2013 period. *J. Geophys. Res. Oceans* 121, 8139–8171. doi: 10.1002/2016JC011857

Kinder, T. H., and Parrilla, G. (1987). Yes, some of the Mediterranean outflow does come from great depth. *J. Geophys. Res.* 92, 2901–2906.

Li, P., and Tanhua, T. (2020). Recent changes in deep ventilation of the Mediterranean Sea; evidence from long-term transient tracer observations. *Front. Mar. Sci.* 7:594. doi: 10.3389/fmars.2020.00594

López-Jurado, J. L., González-Pola, C., and Vélez-Belchí, P. V. (2005). Observation of an abrupt disruption of the long-term warming trend at the Balearic Sea, western Mediterranean Sea, in summer 2005. *Geophys. Res. Lett.* 32:L24606. doi: 10.1029/2005GL024430

Margirier, F., Testor, P., Heslop, E., Mallil, K., Bosse, A., Houpert, L., et al. (2020). Abrupt warming and salinification of intermediate waters interplays with decline of deep convection in the Northwestern Mediterranean Sea. *Sci. Rep.* 10:20923. doi: 10.1038/s41598-020-77859-5

MEDOC Group. (1970). Observation of formation of deep water in the Mediterranean Sea, 1969. *Nature* 227, 1037–1040. doi: 10.1038/2271037a0

Naranjo, C., García-Lafuente, J., Sánchez-Garrido, J. C., Sánchez-Román, A., and Delgado, J. (2012). The Western Alboran Gyre helps ventilate the Western Mediterranean Deep Water through Gibraltar. *Deep Sea Res. Part I Oceanogr. Res. Papers* 63, 157–163.

Naranjo, C., Garcia-Lafuente, J., Sannino, G., and Sanchez-Garrido, J. C. (2014). How much do tides affect the circulation of the Mediterranean Sea? From local processes in the strait of gibraltar to basin-scale effects. *Progress Oceanogr.* 127, 108–116. doi: 10.1016/j.pocean.2014.06.005

Naranjo, C., García-Lafuente, J., Sammartino, S., Sánchez-Garrido, J. C., Sánchez-Leal, R., and Bellanco, M. J. (2017). Recent changes (2004–2016) of temperature and salinity in the Mediterranean outflow. *Geophys. Res. Lett.* 44:615. doi: 10.1002/2017GL072615

Naranjo, C., Sammartino, S., García-Lafuente, J., Bellanco, M. J., and Taupier-Letage, I. (2015). Mediterranean waters along and across the Strait of Gibraltar, characterization and zonal modification. *Deep Sea Res. Part I* 105, 41–52. doi: 10.1016/j.dsr.2015.08.003

Rhein, M., and Hinrichsen, H. (1993). Modification of Mediterranean Water in the Gulf of Cadiz, studied with hydrographic, nutrient and chlorofluoromethane data. *Deep Sea Res. Part I* 40, 267–291.

Roether, W., Manca, B. B., Klein, B., Bregant, D., Georgopoulos, D., Beitzel, V., et al. (1996). Recent changes in the Eastern Mediterranean deep waters. *Science* 271, 333–335. doi: 10.1126/science.271.5247.333

Roether, W., and Schlitzer, R. (1991). Eastern Mediterranean deep water renewal on the basis of chlorofluoromethane and tritium data. *Dyn. Atm. Oceans* 15, 333–354. doi: 10.1016/0377-0265(91)90025-B

Sammartino, S., Garcıa Lafuente, J., Naranjo, C., Sánchez-Garrido, J. C., Sanchez Leal, R., and Sánchez-Román, A. (2015). Ten years of marine current measurements in Espartel Sill, Strait of Gibraltar. *J. Geophys. Res. Oceans* 120, 6309–6328. doi: 10.1002/2014JC010674

Sánchez-Garrido, J. C., García Lafuente, J., Criado Aldeanueva, F., Baquerizo, A., and Sannino, G. (2008). Time-spatial variability observed in velocity of propagation of the internal bore in the Strait of Gibraltar. *J. Geophys. Res.* 113:C07034. doi: 10.1029/2007JC004624

Sánchez-Garrido, J. C., Sannino, G., Liberti, L., García Lafuente, J., and Pratt, L. (2011). Numerical modeling of three-dimensional stratified tidal flow over Camarinal Sill, Strait of Gibraltar. *J. Geophys. Res. Oceans* 116:C12026. doi: 10.1029/2011JC007093

Sánchez-Román, A., Sannino, G., García Lafuente, J., Carillo, A., and Criado Aldeanueva, F. (2009). Transport estimates at the western section of the Strait of Gibraltar: A combined experimental and numerical modeling study. *J. Geophys. Res. Oceans* 114:C06002. doi: 10.1029/2008JC005023

Sánchez-Román, A., García-Lafuente, J., Delgado, J., Sánchez-Garrido, J. C., and Naranjo, C. (2012). Spatial and temporal variability of tidal flow in the Strait of Gibraltar. *J. Mar. Syst.* 98–99, 9–17. doi: 10.1016/j.jmarsys.2012.02.011

Sannino, G., Bargagli, A., and Artale, V. (2004). Numerical modeling of the semidiurnal tidal exchange through the Strait of Gibraltar. *J. Geophys. Res. Oceans* 109:C05011. doi: 10.1029/2003JC002057

Sannino, G., Pratt, L., and Carillo, A. (2009). Hydraulic criticality of the exchange flow through the Strait of Gibraltar. *J. Phys. Oceanogr.* 39, 2779–2799. doi: 10.1175/2009JPO4075.1

Schlitzer, R., Roether, W., Oster, H., Junghans, H., Hausmann, M., Johannsen, H., et al. (1991). Chlorofluoromethane and oxygen in the Eastern Mediterranean. *Deep Sea Res. Part A* 38, 1531–1155. doi: 10.1016/0198-0149(91)90088-W

Schroeder, K., Chiggiato, J., Bryden, H., Borghini, M., and Ismail, S. B. (2016). Abrupt climate shift in the Western Mediterranean Sea. *Sci. Rep.* 6:23009. doi: 10.1038/srep23009

Schroeder, K., Gasparini, G. P., Tangherlini, M., and Astraldi, M. (2006). Deep and intermediate water in the western Mediterranean under the influence of the Eastern Mediterranean Transient. *Geophys. Res. Lett.* 33:L21607. doi: 10.1029/2006GL027121

Schroeder, K., Ribotti, A., Borghini, M., Sorgente, M., Perilli, R., and Gasparini, A. (2008). An extensive western Mediterranean deep water renewal between 2004 and 2006. *Geophys. Res. Lett.* 35:L18605. doi: 10.1029/2008GL035146

Stommel, H. (1972). "Deep winter-time convection in the Western Mediterranean Sea," in *Studies in Physical Oceanography*, Vol. 2, ed. A. L. Gordon (New York: Gordon & Breach), 207–218.

Stommel, H., Bryden, H., and Mangelsdorf, P. (1973). Does some of the Mediterranean outflow come from great depth? *Pure Appl. Geophys.* 105, 879–889.

Tsimplis, M. N., and Bryden, H. L. (2000). Estimation of the transports through the Strait of Gibraltar. *Deep Sea Res. Part I* 47, 2219–2242.

Tsimplis, M. N., Zervakis, V., Josey, S. A., Peneva, E. L., Struglia, M. V., Stanev, E. V., et al. (2006). "Changes in the oceanography of the Mediterranean Sea and their link to climate variability,"in *Mediterranean Climate Variability, Developments in Earth and Environmental Sciences.* eds P. Lionello, P. Malanotte-Rizzoli, R. Boscolo. Amsterdam: Elsevier, 227–282.

Vargas, J. M., García Lafuente, J., Candela, J., and Sánchez, A. (2006). Fortnightly and monthly variability of the exchange through the Strait of Gibraltar. *Prog. Oceanogr.* 70, 466–485.

Vargas-Yañez, M., García-Martínez, M. C., Moya, F., Balbín, R., López-Jurado, J. L., Serra, M., et al. (2017). Updating temperature and salinity mean values and trends in the Western Mediterranean: The RADMED project. *Prog. Ocean.* 157, 27–46. doi: 10.1016/j.pocean.2017.09.004

Vlasenko, V., Sánchez Garrido, J. C., Stashchuk, N., García Lafuente, J., and Losada, M. (2009). Three-dimensional evolution of large-amplitude internal waves in the Strait of Gibraltar. *J. Phys. Oceanogr.* 39, 2230–2246.

Wesson, J. C., and Gregg, M. C. (1994). Mixing at Camarinal Sill in the Strait of Gibraltar. *J. Geophys Res. Oceans* 99, 9847–9878.

Conflict of Interest: The authors declare that the research was conducted in the absence of any commercial or financial relationships that could be construed as a potential conflict of interest.

frontiers in Marine Science

ORIGINAL RESEARCH
published: 12 March 2021
doi: 10.3389/fmars.2021.640535

Long-Term Changes in the Water Mass Properties in the Balearic Channels Over the Period 1996–2019

Manuel Vargas-Yáñez[1], Mélanie Juza[2], M. Carmen García-Martínez[1], Francina Moya[1], Rosa Balbín[3], Enrique Ballesteros[1], María Muñoz[1], Elena Tel[4], Josep Pascual[5], Pedro Vélez-Belchí[6] and Jordi Salat[5]*

[1] Centro Oceanográfico de Malaga, Instituto Español de Oceanografía, Málaga, Spain, [2] Balearic Islands Coastal Observing and Forecasting System (SOCIB), Palma de Mallorca, Spain, [3] Centro Oceanográfico de Baleares, Instituto Español de Oceanografía, Palma de Mallorca, Spain, [4] Servicios Centrales, Instituto Español de Oceanografía, Madrid, Spain, [5] Instituto de Ciencias del Mar, Consejo Superior de Investigaciones Científicas, Barcelona, Spain, [6] Centro Oceanográfico de Canarias, Instituto Español de Oceanografía, Santa Cruz de Tenerife, Spain

OPEN ACCESS

Edited by:
Katrin Schroeder, Institute of Marine Science (CNR), Italy

Reviewed by:
Barak Herut, Israel Oceanographic & Limnological Research, Israel
Adam Thomas Devlin, The Chinese University of Hong Kong, China

***Correspondence:**
Manuel Vargas-Yáñez
manolo.vargas@ieo.es

Specialty section:
This article was submitted to Physical Oceanography, a section of the journal Frontiers in Marine Science

Received: *11 December 2020*
Accepted: *22 February 2021*
Published: *12 March 2021*

Citation:
Vargas-Yáñez M, Juza M, García-Martínez MC, Moya F, Balbín R, Ballesteros E, Muñoz M, Tel E, Pascual J, Vélez-Belchí P and Salat J (2021) Long-Term Changes in the Water Mass Properties in the Balearic Channels Over the Period 1996–2019. Front. Mar. Sci. 8:640535. doi: 10.3389/fmars.2021.640535

The analysis of a 24-year time series of Conductivity-Temperature-Depth (CTD) casts collected in the Balearic Channels (1996–2019) has allowed detecting and quantifying long-term changes in water mass properties in the Western Mediterranean. For the complete period, the intermediate waters have experienced warming and salting at rates of 1.4°C/100yr and 0.3–0.6/100yr for the Western Intermediate Water, and 1°C/100yr and 0.3–0.4/100yr for the Levantine Intermediate Water. The density of these two water masses has not changed. The deep waters, defined as those denser than 29.1 kg/m^3, showed positive trends in temperature, salinity, and density (0.8°C/100yr, 0.2/100yr, and 0.02 kg.m^{-3}/100yr, respectively). The high temporal variability of the upper layer makes the detection of long-term changes more difficult. Nevertheless, combining CTD data with temperature data from the oceanographic station at L'Estartit and simulated data from the NCEP/NCAR reanalysis, it can be established that the Atlantic Water increased its temperature at a rate of 2.1–2.8°C/100yr and likely its salinity at a rate of 0.6/100yr. The water column absorbed heat at a rate equivalent to 1–1.2 W/m^2. All these trends are much higher than those reported in previous works (more than double in some cases). The warming of the water column produced an increase in the thermosteric component of sea level. However, this increase was compensated by the decrease in the halosteric component. Besides these changes, other alterations related to the Western Mediterranean Transition have been observed over shorter periods. The temperature and salinity of the intermediate waters increased before the winter of 2004/2005 and then the temperature and salinity of the deep waters increased dramatically in 2005. The density of the deep water reached values unprecedented before 2005. Deep and intermediate waters were uplifted by the presence of such dense deep waters. The arrival of warmer and saltier intermediate waters from the Eastern Mediterranean is also observed, mainly after 2010.

Keywords: water mass properties, linear trends, climate change, Balearic Channels, Western Mediterranean Transition

INTRODUCTION

From the beginnings of modern oceanography in the Mediterranean Sea (Nielsen, 1912) and during most of the twentieth century, it was accepted the existence of an equilibrium between the heat and freshwater fluxes through the sea surface and the heat and water transports at the Strait of Gibraltar. At the same time, it was considered that the total salt content of the Mediterranean Sea was constant as a result of a zero net salt flux at the Gibraltar Strait (Bethoux, 1979). However, this picture has changed since, at least, the beginning of the 1990s decade, when the comparison of temperature and salinity data collected during the twentieth century showed warming and salting of the intermediate and deep waters (Bethoux et al., 1990; Rohling and Bryden, 1992; Vargas-Yáñez et al., 2010, 2017). According to these works, this process was accelerated during the second part of the twentieth century. Atlantic waters flowing at the upper layer of the Mediterranean Sea also experienced an intense warming since the beginning of the 1970s (Nykjaer, 2009; Skliris et al., 2012; Salat et al., 2019). The warming of the Mediterranean Sea simply reflects the behavior of the global ocean which has absorbed more than 90% of the heat gained by the Earth as a consequence of global warming (Rhein et al., 2013). The salting of the Mediterranean Sea is associated with the increase of the net evaporation (evaporation minus precipitation and river run-off) during the twentieth century and the beginning of the twenty-first. Therefore, it cannot be considered that the water volume and the salt content of the Mediterranean Sea are in an equilibrium state expressed by the Knudsen equations (Borghini et al., 2014). Neither it can be considered that the net heat loss through the sea surface balances the transport of heat through the Strait of Gibraltar (Jordà et al., 2017). There are some uncertainties concerning the future evolution of the salinity of those waters formed within the Mediterranean Sea (hereafter Mediterranean Waters, MWs), because of the possible influence of Arctic ice melting (Jordà et al., 2017). Nevertheless, most of the ocean climate projections show an intense increase in the salinity and temperature of the Mediterranean during the twenty-first century (Somot et al., 2006; Adloff et al., 2015) as a result of a higher net evaporation rate (Sanchez-Gomez et al., 2009; Mariotti et al., 2015), and a reduction of the net heat loss to the atmosphere (Somot et al., 2008; Dubois et al., 2012; Jordà et al., 2017).

Besides these long-term changes linked to global climate change, both the Western and Eastern Mediterranean (WMED and EMED, respectively) have experienced abrupt changes during the end of the twentieth century and the beginning of the twenty-first. Such alterations were caused by shifts in the areas of deep water formation, the main circulation pathways of water masses, or changes in the properties and production rates of intermediate and deep waters. These sharp changes are known as the Eastern Mediterranean Transient (EMT, Roether et al., 1996; Lascaratos et al., 1999; Theocharis et al., 1999), affecting the EMED, and the Western Mediterranean Transition (WMT, López-Jurado et al., 2005; Font et al., 2007; Smith et al., 2008; Schroeder et al., 2010, 2017, 2019), affecting the WMED. It is not clear yet whether these changes will be recurrent in the future and will contribute to shaping the circulation and water mass properties of the Mediterranean Sea permanently. Neither it is clear whether the EMT and WMT are related to the long-term climate change experienced by the Mediterranean region or if they are caused by exceptional episodes of extreme ocean-atmosphere fluxes.

The understanding of these changes requires the analysis of long time series of temperature and salinity. Recent monitoring programs such as Hydrochanges (Schroeder et al., 2013) or MedARGO (Poulain et al., 2007) have considerably contributed to provide the data required for climatic studies in the Mediterranean Sea. However, the data scarcity, mainly before 2010, makes the estimation of long-term changes very sensitive to the data processing methods and increases considerably the uncertainty associated with the estimation of linear trends (Vargas-Yáñez et al., 2010, 2012; Jordá and Gomis, 2013; Llasses et al., 2015). In this context, permanent *in situ* oceanographic stations are of primary importance, but such stations are very scarce in the Mediterranean Sea. Some of these stations in the WMED are those corresponding to the RADMED monitoring program (see **Figure 1**) supported by the Instituto Español de Oceanografía (IEO; López-Jurado et al., 2015). This program was initiated in 2007 but includes the oceanographic stations monitored by IEO in the frame of previous projects since 1996 in the Balearic Channels. The availability of long time series of CTD casts at fixed positions over 1996–2019, with a seasonal periodicity, provides the opportunity of detecting and analyzing the changes experienced by the Atlantic and Mediterranean

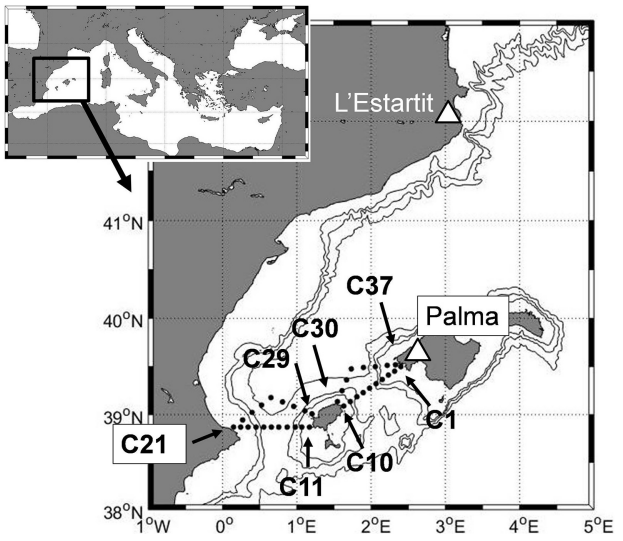

FIGURE 1 | Position of the stations monitored from 1996 to 2019 in the frame of the CANALES, CIRBAL, and RADMED projects. These stations are distributed along four sections: Mallorca South (stations C1–C10), Ibiza South (C11–C21), Ibiza North (C21–C29), and Mallorca North (C30–C37). The Mallorca South and North sections form the Mallorca Channel triangle and the Ibiza South and North form the Ibiza Channel triangle. White triangles show the position of the Palma de Mallorca tide gauge and the position of the L'Estartit coastal station.

waters in the WMED. The Balearic Channels have been described as a choke point for the exchange of water mass, heat, and salt in the WMED (Heslop et al., 2012; Barceló-Llull et al., 2019; Vargas-Yáñez et al., 2020, this volume). Fresh Atlantic Water (AW) from the Algerian Current can flow northwards through the Mallorca Channel (between Ibiza and Mallorca Islands), whereas severely modified AW flows southwards along the Ibiza Channel (between Ibiza Island and the mainland). The Western Intermediate Water (WIW) can be formed in the Catalan shelf, the Gulf of Lions, the Ligurian Sea, and even around the Balearic Islands during severe winters. This water mass is frequently detected in the Balearic channels. The Levantine Intermediate Water (LIW) flows preferentially through the Ibiza Channel and in some cases, the Western Mediterranean Deep Water (WMDW), formed in the nearby Gulf of Lions, can be found at the bottom layers of this region (Vargas-Yáñez et al., 2020). These features of the circulation and the water masses present in the Balearic Channels, and the long time series of CTD profiles obtained with a constant methodology, make this region an ideal spot for the detection and analysis of water mass changes. This is the objective of the present work: detecting and quantifying changes in the water masses of the WMED, discussing such changes in the present context of climate change and in light of the recent dynamics of the WMT. The impact of the temperature and salinity variations on the sea level of this region will also be addressed.

DATA AND METHODS

CTD Time Series

Time series of CTD casts were obtained at 37 oceanographic stations regularly distributed in the Mallorca and Ibiza Channels during 71 campaigns from 1996 to 2019 (**Figure 1**). These campaigns were carried out under the umbrella of three different projects: CANALES (1996–1998), CIRBAL (1999–2006), and RADMED (2007-present). These stations were sampled on a seasonal basis, although numerous gaps are present in the final time series because of the weather conditions or the lack of vessel availability. The dates for each of the 71 campaigns and the project under which each survey was carried out is presented in Vargas-Yáñez et al. (2020). Here, we include this information in **Supplementary Table 1** for the completeness of the work. At each station, temperature and salinity profiles were obtained using a CTD, mainly of the model SBE911 and as spare instruments, the models SBE 25 or SBE 19+, installed in a carousel water sampler. The instruments were periodically calibrated by the manufacturer (at least once every 2 years). Besides this, the conductivity sensor was calibrated using the carousel water samples. Calibrations were performed for selected depths of the water column at the beginning and at the end of the campaigns. The spare CTD was cross calibrated with the SBE911 using the carousel at least once every campaign (for more details see López-Jurado et al., 2015).

AW Properties

The oceanographic stations are located in the Balearic Channels, a choke point of the WMED where water mass exchanges occur (Heslop et al., 2012; Juza et al., 2019). The channels can intercept both fresh AW recently advected into the Mediterranean Sea through the Strait of Gibraltar and AW with a higher degree of modification after completing a cyclonic circuit within the WMED. In this region of the WMED, the strongest influence of this water mass is observed at the sea surface and then decreases with depth (The average temperature, salinity and density of the AW at the sea surface in the Balearic Channels are presented in **Supplementary Table 2**). The 37.5 isohaline is usually considered as the surface of separation between the AW and the MWs in the nearby Alboran Sea. This criterion could also be used for the identification of the AW transported northwards from the Algerian Current, but would not be appropriate for the severely modified AW flowing southwards within the Northern Current. The AW flows at the upper layer above the Western Intermediate Water (WIW) which is found below 100 m (Vargas-Yáñez et al., 2020). Therefore, a possibility is to consider the average properties of the upper 100 m of the water column as representative of the AW. This criterion is somehow subjective and other depth ranges could be chosen. To check if the definition of the upper layer has any influence on the obtained results, four different time series were constructed for each variable (potential temperature, salinity and potential density). These time series consisted on the average values at fixed depth ranges (0–25, 0–50, 0–75, and 0–100 m), for the 37 stations and for each of the 71 available campaigns.

The AW temperature, salinity and density have clear seasonal cycles (Vargas-Yáñez et al., 2017, 2019). The variance associated with such cycles should be removed prior to the analysis of long-term trends. Therefore, the seasonal climatological temperature, salinity and density cycles were estimated for each depth level. These cycles were estimated as the mean values for all the data corresponding to winter (January to March), spring (April to June), summer (July to September) and autumn (October to December). Then, the seasonal climatological cycles, estimated for each depth level, were subtracted from the original time series. The final ones were made of residuals or deviations with respect to the climatological seasonal cycles. **Supplementary Table 2** shows the values corresponding to the seasonal cycles of salinity, potential temperature and density for the surface layer. This procedure was not needed for the MWs for which the seasonal cycle was absent or very weak, not affecting the trend estimation. However, the seasonal cycles for the salinity, potential temperature, density and pressure for the WIW, LIW, and WMDW are also presented in **Supplementary Table 2** for the completeness of the work.

WIW Properties

The WIW flows below the AW at a depth ranging from 100 to 300 m (see **Supplementary Table 2** for a description of the average properties of this water mass; Salat and Font, 1987; López-Jurado et al., 1995; Juza et al., 2013, 2019; Vargas-Yáñez et al., 2020). The density range for this water mass is 28.8–29.05 (Pinot et al., 2002). A first criterion used to define the properties of this water mass during each campaign was to select all the θS values within the selected density range for each oceanographic station. The minimum θ value within

this range was considered as the core of the WIW at that particular station. The salinity, potential density and depth corresponding to this minimum were considered as the WIW properties for that particular oceanographic station. In order to obtain one single value for each campaign, two different criteria were used. In the first case, the mean value of the 37 stations was considered and the standard deviation was also estimated. These values would reflect the average properties of the WIW in the Balearic Channels during that survey (method 1 hereafter). A second criterion was to select the minimum of the 37 values. This value would be indicative of the properties of those waters with the highest influence or contribution of WIW during that survey (method 2). Juza et al. (2019) have evidenced that using pre-defined density, temperature or salinity ranges could fail to detect WIW in some cases. Instead of these traditional methods, Juza et al. (2019) proposed the use of a geometry-based detection approach. For each campaign and for the 37 stations this method provides a range of θ*S* values that could be considered as corresponding to the presence of the WIW. The 50th percentile was used to construct the time series of WIW properties in the Balearic Channels (potential temperature, salinity, potential density and depth), and the 17th and 83rd percentiles were used to define the dispersion for each survey (method 3).

LIW Properties

The core of the LIW was identified as the absolute salinity maximum within each salinity profile (see **Supplementary Table 2**). Potential temperature, salinity, potential density and depth for this LIW core were determined for each station corresponding to each campaign. The mean value and the standard deviation from the 37 stations were calculated for each campaign (method 1). As in the case of the WIW, this first method makes an estimation of the average properties of LIW during each survey. A second method consisted of selecting the maximum salinity of the 37 stations. This would represent the properties of the LIW for those waters with a maximum influence of this water mass (method 2).

Deep Water Properties

The WMDW was considered by Pinot and Ganachaud (1999) and Pinot et al. (2002) as the waters with potential density higher than 29.1 kg/m^3. Nevertheless, the θ*S* diagram for the whole data set (**Figure 2**) showed that the 29.1 kg/m^3 potential density corresponded to the mixing line between the LIW salinity maximum and the deepest waters, and in some cases it was closer to the LIW extreme of the mixing line. Hence, the first criterion used to construct time series for the deep water properties was to calculate the potential temperature, salinity, potential density and depth of those waters exceeding the value 29.11 kg/m^3, averaged for the 37 stations and for each campaign (method 1). However, the 29.11 kg/m^3 density was not reached during most of the initial campaigns, reducing considerably the final length of the time series. For this reason, the time series of deep water properties were also estimated using the threshold of 29.1 kg/m^3 (method 2).

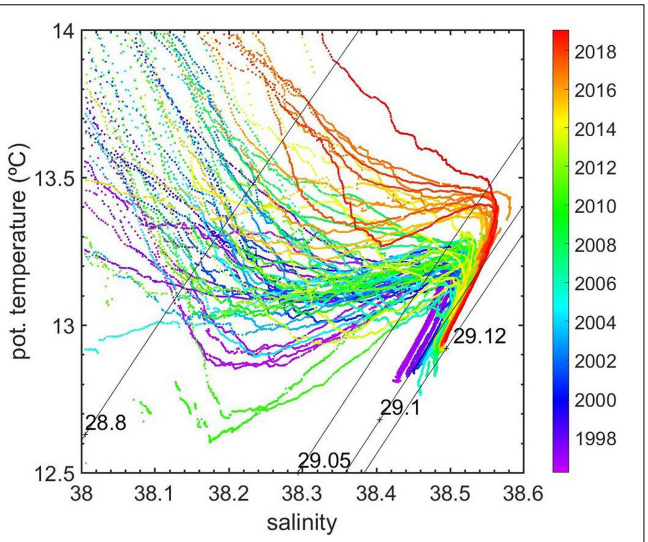

FIGURE 2 | Potential temperature-salinity (θ*S*) diagrams for the complete time series from 1996 to 2019. For each of the 71 oceanographic campaigns, one single θ-*S* diagram is presented, averaging the data from all the oceanographic stations forming the four sections that cover the Balearic Channels. The color scale shows the time corresponding to each survey. Some specific isopycnals have been included. WIW would have a potential density higher than 28.8 and lower than 29.05. The 29.05 isopycnal could be associated to the LIW core, and the 29.1 would be representative of the WMDW previously to the WMT. The 29.12 is also included as this density value is observed after the WMT.

Temperature and Sea Level Time Series at L'Estartit and Palma de Mallorca

Monthly time series of temperature at 0, 20, 50, and 80 m depth were constructed from weekly time series at L'Estartit oceanographic station (operated by ICM/CSIC, **Figure 1**, Salat et al., 2019). Monthly time series of sea level were also constructed from hourly data at the same location. A climatological seasonal cycle was obtained for each time series averaging all the data corresponding to the same month of the year over the available period. Time series of anomalies or residuals were obtained subtracting the seasonal cycle to the original time series. Temperature time series at 0, 20, 50, and 80 m extend from 1970 to 2019, whereas sea level time series extends from 1990 to 2019 (Salat et al., 2019).

Monthly sea level data were obtained from hourly data at the tide gauge located at Palma de Mallorca and operated by IEO (**Figure 1**). As in the case of L'Estartit, a climatological seasonal cycle was obtained averaging all the data corresponding to the same month of the year over the available period. A time series of anomalies was obtained subtracting the seasonal cycle from the Palma sea level time series.

Sea Surface Temperature and Atmospheric Pressure Data

The temperature of the upper 100 m of the sea has a very strong variability because of the ocean-atmosphere interaction. The seasonal variability can be removed, as previously explained,

but the resulting time series of residuals has a large variance associated with monthly and inter-annual time scales. Hence, trends and long-term changes are very difficult to detect. This variability can partially be filtered out when the time series has a high temporal resolution, as for the sea level and sea temperature time series at L'Estartit. On the contrary, short temporal scales artificially appear as part of longer time scales (aliasing) when the sampling is 3-monthly, as in the case of CTD time series. For this reason and to check the robustness of the results dealing with the properties of the upper layer, time series of monthly sea surface temperature (SST) were obtained from the reanalysis of the NCEP/NCAR (Kalnay et al., 1996). SST data were averaged for the area delimited from 41° N to 42.9° N and from 1.9° E to 3.8° E. The resulting time series was considered for comparison with L'Estartit time series and will be referred to as the Northern Sector SST. SST data were also averaged for the area from 39° N to 41° N and from 1.9° E to 3.8°E. This time series was considered for comparison with results from the Balearic Channels and will be referred to as the Balearic Channels SST.

The sea level is affected by atmospheric pressure, among many other factors. In an ideal situation, a pressure increase of 1 mbar produces a sea level decrease of 1 cm. This is known as the inverse barometer effect. Therefore, persistent changes or trends in atmospheric pressure could induce trends in the sea level, as was the case from 1960 to mid-1990s in the WMED (Tsimplis and Baker, 2000; Tsimplis and Josey, 2001). For this reason, time series of monthly atmospheric pressure were also obtained from the reanalysis of NCEP/NCAR. As for the SST, two different time series were extracted. The first one, for comparison with the Palma tide gauge, corresponded to the same area used for the construction of the Balearic Channels SST (39° N-41° N, 1.9° E-3.8° E). The second one, for comparison with the L'Estartit sea level time series, corresponded to the same area used for constructing the Northern Sector SST time series (41° N-42.9° N, 1.9° E-3.8° E).

Analysis of the Steric, Thermosteric and Halosteric Sea Level and the Absorbed Heat

The changes in the water column height between two pressure levels with respect to a reference climatological density profile (ρ_0) were estimated using the hydrostatic equation:

$$\int_{p1}^{p2}\left[\frac{1}{g\rho\left(s,\theta,p\right)}-\frac{1}{g\rho_0}\right]dp \tag{1}$$

If p_1 is taken as zero (sea surface) and p_2 is the maximum pressure reached for a certain station, then this expression is an estimation of the steric sea level. Time series of steric sea level anomalies were obtained for each campaign. The reference profile corresponded to the mean temperature and salinity profiles averaged for the 37 stations covering the Balearic Channels and for the complete period (1996–2019).

The temperature (thermosteric) contribution to the steric sea level anomaly was estimated as:

$$\int_{p1}^{p2}\left[\frac{1}{g\rho_0\left(1+\alpha\Delta\theta\right)}-\frac{1}{g\rho_0}\right]dp \tag{2}$$

Where $\Delta\theta$ is the deviation with respect to the climatological temperature profile. Similarly, the salinity (halosteric) component of the steric anomaly was estimated as:

$$\int_{p1}^{p2}\left[\frac{1}{g\rho_0\left(1+\beta\Delta S\right)}-\frac{1}{g\rho_0}\right]dp \tag{3}$$

Where α and β are the thermal expansion and the haline contraction coefficients respectively.

The anomaly of heat absorbed by a water column of one square meter between the pressure levels p_1 and p_2 was estimated as:

$$Q=\int_{p1}^{p2}\rho c_p\Delta\theta dp \tag{4}$$

Once again if p_1 is set equal to zero and p_2 is the maximum pressure reached, then the equation above represents the heat absorbed by the whole water column.

The maximum pressure level reached in the analyzed oceanographic stations was 1385 dbar. Since the CTD casts did not always reach the same depth, the reference level considered for the calculation of the steric sea level and absorbed heat was fixed at 1200 dbar. The steric, thermosteric and halosteric sea level anomalies, as well as the heat absorbed, were calculated within two vertical layers: from the sea surface to 1200 dbar and from 100 to 1200 dbar. This second pressure range was used to study the influence of variations experienced by the MWs on the sea level and absorbed heat. Furthermore, excluding the upper 100 dbar of the water column allowed eliminating the seasonal variability in these time series.

Decomposition of Changes on Pressure Levels

The potential temperature and salinity changes at fixed pressure levels can be decomposed in two contributions. The first one is caused by the variations of temperature and salinity experienced by the isopycnals occupying such pressure levels, and the second contribution is associated with the vertical displacement of the isopycnals (Bindoff and McDougall, 1994; Zunino et al., 2012). This decomposition can be written as:

$$\Delta\theta|_p=\Delta\theta|_\sigma-\Delta p\big|_\sigma\cdot\frac{\partial\theta}{\partial p} \tag{5.1}$$

$$\Delta S|_p=\Delta S|_\sigma-\Delta p\big|_\sigma\cdot\frac{\partial S}{\partial p} \tag{5.2}$$

The climatological profiles of potential temperature, salinity and potential density were estimated as functions of pressure, averaging all the profiles from the 71 campaigns, and were considered as the references. The temperature, salinity, and density profiles from each campaign were then compared with the references and the changes were decomposed according to the equations above.

RESULTS

Long-Term Trends in Water Mass Properties

Figure 3 shows the time series of residuals for potential temperature, salinity and potential density for the AW in the Balearic Channels from 1996 to 2019. For each variable, four different time series are displayed, corresponding to the average value in the upper 25, 50, 75 m, and for the upper 100 m. Both potential temperature and salinity of the AW showed positive trends for the four time series over the analyzed period. Nevertheless, temperature trends were not statistically significant. The salinity trends were statistically significant at the 90% confidence level (**Table 1**). The potential density trends were negative for the 0–25 m layer and positive in the other three layers, but these trends were not significant in any of the four depth ranges. **Table 1** shows that the (not significant) temperature trends varied between 0.9 and 1.8°C/100yr, depending on the depth range considered, whereas the salinity trends were approximately 0.6/100yr in all the cases.

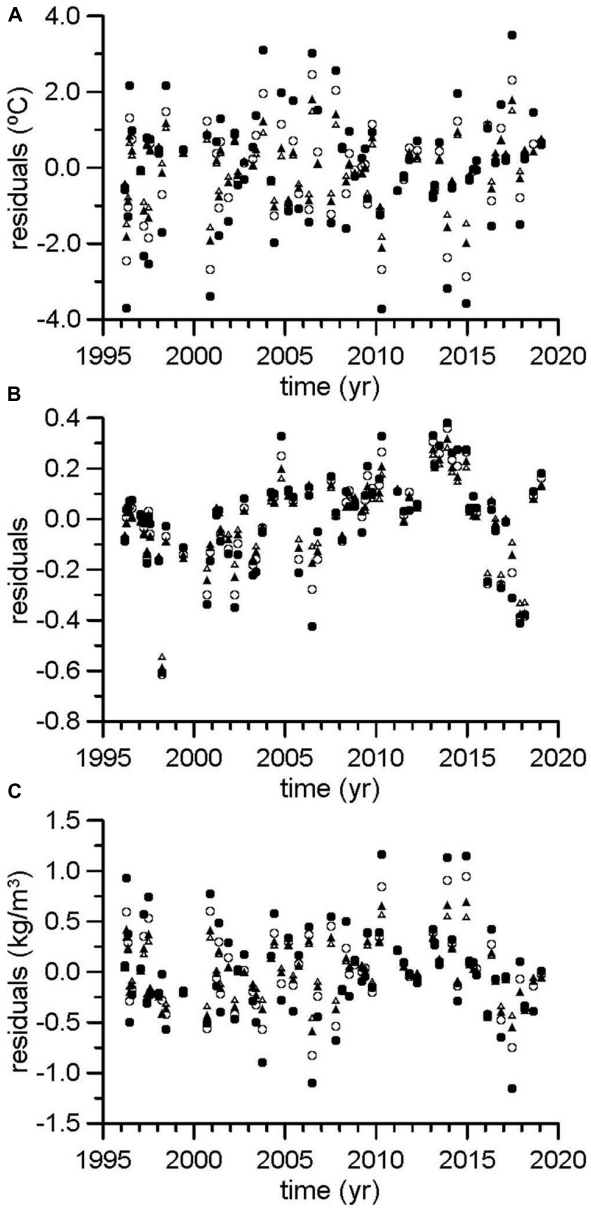

FIGURE 3 | Residuals or anomalies of potential temperature **(A)**, salinity **(B)**, and potential density **(C)** for the AW layer. Residuals are obtained subtracting a seasonal cycle to the original time series. For each variable, four different time series are presented. The first one is made of the mean value of the upper 25 dbar (black filled circles), 50 dbar (open circles), 75 dbar (black filled triangles), and 100 dbar (open triangles).

The lack of significance in the trends estimated for the AW temperature could be due to the substantial intra and inter-annual variability exhibited by these time series, the large sampling interval (3 months) and the existence of gaps within the time series (see section "Discussion"). It is interesting to note that the temperature and salinity anomalies were negatively and significantly correlated, with positive temperature anomalies corresponding to negative salinity anomalies and vice-versa.

Figures 4A,C shows the potential temperature and salinity time series for WIW using the methods 1 and 2 (as described in section "Data and Methods"). For method 1, the standard deviation corresponding to the 37 oceanographic stations is included as error bars. **Figures 4B,D** shows the 17th, 50th and 83rd percentiles for the potential temperature and salinity values obtained by the geometry-based method. The three methodologies led to the same results: the WIW potential temperature and salinity increased over the period 1996–2019. The potential temperature trends were around 1.4°C/100yr for the three methods used and were statistically significant at the 95% confidence level (**Table 1**). The WIW salinity trends were around 0.55/100yr using methods 1 and 2 and lower with the geometry-based method with a value of 0.29/100yr. While the potential density trend estimated from method 1 was positive and statistically significant at the 90% confidence level, the trend was negative but not statistically significant using method 2 and the geometry-based method (method 3). No significant trend was observed for the depth level occupied by the WIW for any of the methodologies used (**Table 1**). The WIW depth remained stable between 100 and 300 m over the analyzed period with a strong inter-annual variability (not shown).

Figure 5 shows the evolution of the potential temperature, salinity and potential density of the LIW, as obtained using the method 1 (LIW core properties averaged for the 37 stations for each survey) and the method 2 (maximum values of the LIW core properties for each survey). The LIW potential temperature and salinity experienced positive trends of 0.92–0.96°C/100yr and 0.28/100yr, respectively (**Table 1**). These trends were statistically significant at the 95% confidence level with the same order of magnitude as those estimated for the WIW. On the contrary, the LIW potential density trends were significant only at the 90% level for the method 1 and not significant for the method 2, and showed weak values for both methods (**Table 1**). The depth level occupied by this water mass was displaced upwards during the analyzed period with a negative trend between −3 and −4 dbar/yr (**Table 1**).

TABLE 1 | Atlantic Water: Linear trends for the AW potential temperature, salinity, and potential density averaged for the upper 25, 50, 75, and 100 m layers.

Atlantic Water								
	Pot. Temperature		**Salinity**		**Pot. Density**		**Depth**	
	b	**CI**	***B***	**CI**	***b***	**CI**	**B**	**CI**
0–25	1.77	5.56	0.60	0.68	–0.02	1.65		
0–50	0.87	3.97	0.59	0.61	0.23	1.24		
0–75	0.95	2.93	0.54	0.55	0.19	0.97		
0–100	1.06	2.45	**0.54**	0.48	0.17	0.83		
Western Intermediate Water								
method1	**1.40**	0.57	**0.55**	0.30	0.14	0.15	0.79	1.79
method2	**1.36**	0.88	**0.55**	0.42	0.15	0.20	1.50	2.24
method3	**1.42**	0.58	**0.29**	0.28	–0.10	0.21	–0.79	1.62
Levantine Intermediate Water								
method1	**0.92**	0.22	**0.28**	0.04	**0.02**	0.02	**–3.25**	1.51
method2	**0.96**	0.23	**0.28**	0.04	0.02	0.03	**–4.16**	1.78
Western Mediterranean Deep Water								
method1	0.10	0.35	0.01	0.09	**–0.01**	0.01	**19.82**	12.58
method2	**0.75**	0.14	**0.22**	0.04	**0.02**	0.01	**–9.56**	4.70

Western Intermediate Water: Linear trends for the potential temperature, salinity, potential density, and depth level for the WIW detected by three different methods (see section "Data and Methods"). Levantine Intermediate Water: Linear trends for the aforementioned variables for the LIW using two different methodologies (see section "Data and Methods"). Western Mediterranean Deep Water: Linear trends for the WMDW using two different methodologies (see section "Data and Methods"). In all the cases, the trends are estimated over the period 1996–2019, b stands for the linear trends expressed in °C, practical salinity units and kg/m^3 per 100 year. Trends for the depth level are expressed in dbar/yr. CI is the confidence interval at the 95% confidence level. Significant trends are presented in bold. Gray bold numbers correspond to the trends significant at the 90% confidence level. Units for CI are the same as for the corresponding b values.

Using the threshold of 29.11 to define the properties of WMDW (method 1), the length of time series is considerably reduced as this density value was reached only once before 2005. The associated potential temperature and salinity trends were not statistically significant whereas the potential density became progressively lower and the depth range increased, both in a statistically significant way (**Table 1** and **Figure 6**). The time series obtained using the threshold of 29.1 (method 2) were longer and showed statistically significant trends for the potential temperature (0.75°C/100yr), salinity (0.22/100yr), potential density (0.02 kg.m^{-3}/100yr) and depth (–9.6 dbar/yr). Except for 2001, 2005 is the first year when potential density values higher than 29.11 were found. This value corresponded to exceptionally cold and fresh waters (**Figures 6A,B**) that progressively became warmer and saltier until 2019, but keeping density values higher than those recorded before 2005.

Long-Term Trends Inferred From SST Reanalysis Data and Temperature Time Series at L'Estartit

Figure 7A shows the SST in the Northern Sector and the Balearic Channels area. The former time series starts in 1970, for comparison with the L'Estartit time series, whereas the latter one starts in1996 for comparison with the CTD time series. The SST increased with strong positive linear trends of 2.2 and 2.7°C/100yr in the Northern Sector and the Balearic Channels region, respectively (**Figure 7A** and **Table 2**). These results were very similar to those obtained from the analysis of the temperature at 0, 20, 50, and 80 m depth at the L'Estartit station. **Figure 7B** shows the time series at these four depths. The linear trends ranged between 2.1°C/100yr for the deepest time series and 2.8°C/100yr for the surface one (**Table 2**).

Analysis of Sea Level Data at Palma and L'Estartit Tide Gauges. The Influence of Atmospheric Pressure

Figure 8A shows the sea level time series at Palma de Mallorca from 1997 to 2019, and **Figure 8B** shows the regression of monthly residuals of sea level on atmospheric pressure in the Balearic Channels sector. The sea level and atmospheric pressure anomalies were significantly correlated. The slope of the linear regression indicated that an increase of 1 mbar in atmospheric pressure corresponded to a decrease in sea level of 1.1 cm (see insert in **Figure 8B**). A similar correlation was found between the sea level at L'Estartit and the atmospheric pressure at the Northern Sector, where a pressure increase of 1 mbar corresponded to a decrease of 1.4 cm in sea level (see insert in **Figure 8D**). Besides the inverse linear relationship between the sea level and atmospheric pressure at both locations (inverse barometer effect), the sea level increased with linear trends of 2.4 ± 1.2 mm/yr and 3.2 ± 0.7 mm/yr at Palma and L'Estartit, respectively (see **Table 2** and inserts in **Figures 8A,C**). It should be noted that the period covered by both time series is not exactly the same. If the linear trend at L'Estartit is estimated for the same period of time covered by the Palma sea level time series (1997–2019), then the trend estimation is 2.8 ± 1.0 mm/yr (see insert in **Figure 8C**).

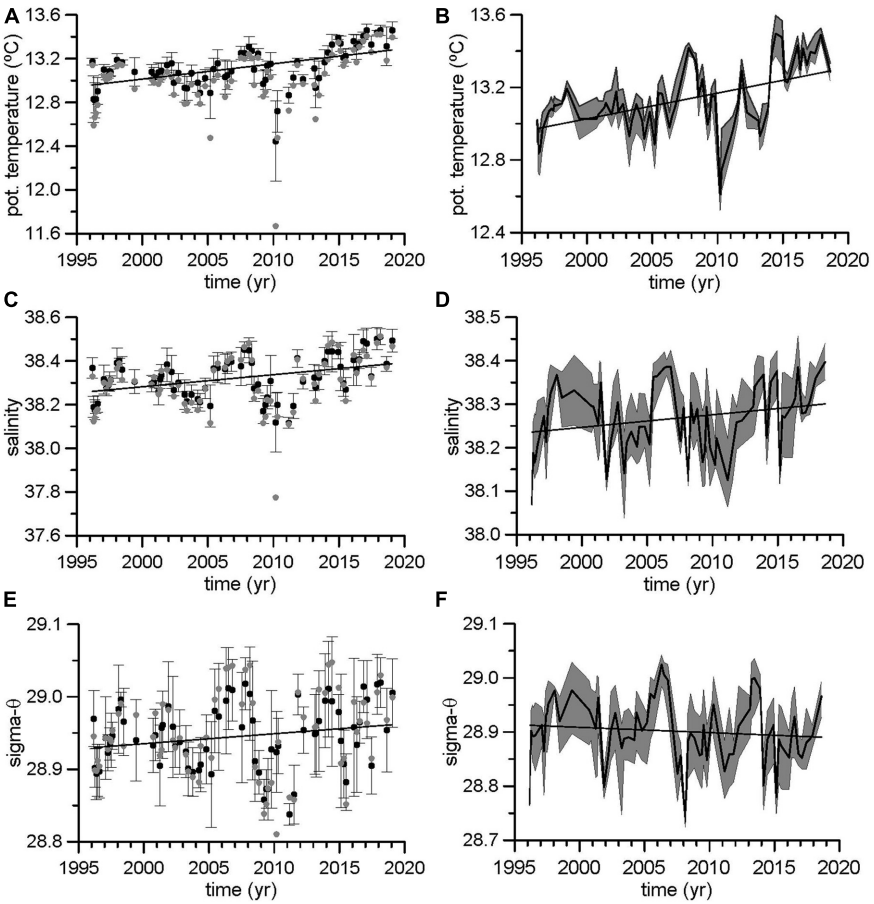

FIGURE 4 | Time series for the potential temperature **(A,B)**, salinity **(C,D)**, and potential density **(E,F)** for the WIW. Black dots in **(A,C,E)** correspond to the WIW properties obtained using method 1. Error bars for this method represent one standard deviation. Gray dots correspond to method 2. **(B,D,F)** Show the WIW properties obtained using the geometric method in Juza et al. (2019). Black lines represent the 50th percentile and the shaded areas correspond to the 17th and 83rd percentiles.

The atmospheric pressure decreased along the periods of time corresponding to the sea level time series. The negative trend in the Balearic Channels was –0.003 mbar/yr. According to the inverse barometer effect for this location, this would induce a positive trend of 0.033 mm/yr in the Palma sea level. However, this atmospheric pressure trend was very weak and not statistically significant. The atmospheric pressure decreased at a rate of –0.041 mbar/yr in the Northern Sector (significant, **Table 2**). This negative trend would induce a positive sea level increase of 0.6 mm/yr.

Long-Term Trends for Heat Absorbed and Steric Sea Level

Figure 9A shows the heat absorbed from the sea surface to 1200 dbar and the heat absorbed from 100 to 1200 dbar. In both cases, the heat absorbed showed similar behavior with strong positive trends of 1.12 and 1.0 W/m^2 over 1996–2019, respectively (**Table 3**). The variance of the absorbed heat time series was higher when the upper 100 dbar were included, which resulted in larger confidence intervals (**Table 3**). Larger values of the absorbed heat were also obtained when the whole water column was considered. The contribution of the absorbed heat to the sea level increase is reflected in the thermosteric sea level which showed positive and significant linear trends of 1.86 and 1.63 mm/yr in the 0–1200 and 100–1200 dbar layers, respectively (**Table 3** and **Figure 9B**). On the contrary, the halosteric component had an opposite effect on sea level (**Figure 9C**). The effect of salinity on density dominated over the temperature one and the steric sea level showed a decreasing linear trend (**Figure 9D**). However, this trend was not statistically significant for the 0–1200 dbar case, very likely because of the large variance of the upper layer. The steric level decreased in a significant way for the 100–1200 dbar layer, with a trend of –0.65 mm/yr over 1996–2019 (**Table 3**).

DISCUSSION

The analysis of a data set, obtained with the same methodology at the same oceanographic stations for a period of 24 years (1996–2019) has shown the temperature and salinity increase of the

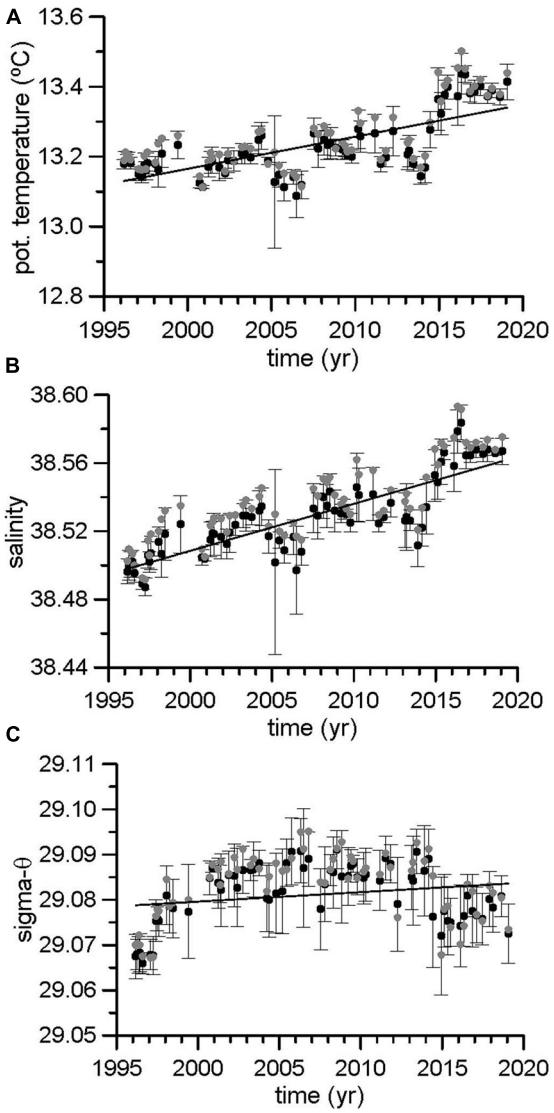

FIGURE 5 | Time series of potential temperature **(A)**, salinity **(B)**, and potential density **(C)** for the LIW. Black dots and error bars (one standard deviation) correspond to the LIW properties obtained using method 1, and gray dots correspond to the properties obtained using method 2.

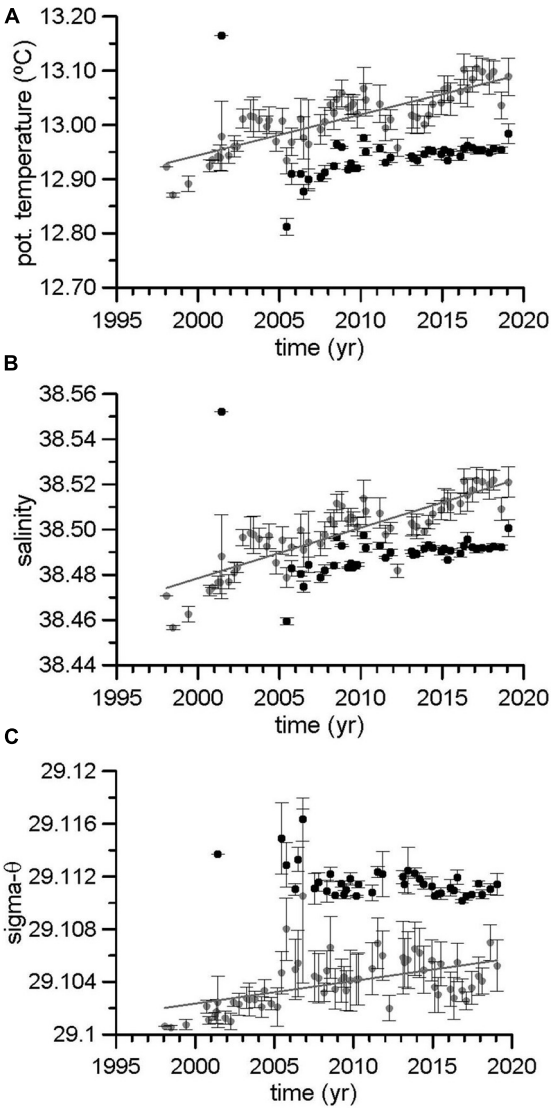

FIGURE 6 | Time series of potential temperature **(A)**, salinity **(B)**, and potential density **(C)** of the deep waters. Black dots and error bars (one standard deviation) correspond to properties obtained using method 1 (waters with a potential density higher than 29.11 kg/m^3) whereas gray dots and error bars correspond to properties obtained using method 2 (waters with potential temperature higher than 29.1 kg/m^3).

waters in the Balearic Channels. In this discussion, a distinction is made between the changes operating over long time scales (at least of the order of the length of the complete time series) and those with time scales of a few years or even one decade.

First, we focus on the rate of change in properties for the complete period analyzed 1996–2019. The WIW temperature and salinity have increased. Both changes have compensated each other and no variations in the density and depth level of this water mass have been observed (**Table 1** and **Figure 4**). This result is not dependent on the different methods used to define this water mass and to calculate its hydrographic properties. The temperature trends are around 1.4°C/100yr and the salinity trends range between 0.3 and 0.6/100yr. These significant changes are greater than those reported in previous works (refer to the summary table of results from different works in Garcia Martinez et al., 2018). Our results concerning the LIW properties are also robust and it can be stated that the temperature and salinity of this water mass have increased with rates greater than those observed during the last century with values of∼1°C/100yr and 0.3–0.4/100yr, respectively (**Table 1** and **Figure 5**). Once again, no significant change was observed for the potential density. The depth range occupied by the LIW became shallower at rates ranging between –3 and –4 dbar/yr. In the case that the LIW density had changed, its equilibrium depth would also change and this could explain the upward displacement of this water

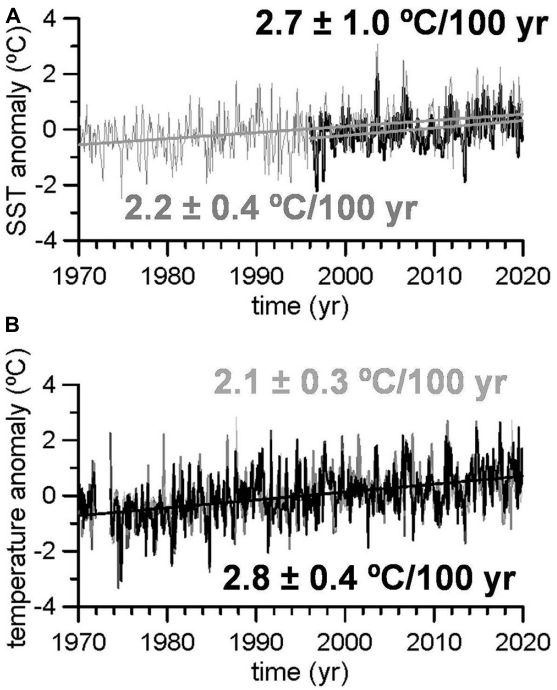

FIGURE 7 | (A) Temperature residuals or anomalies obtained from NCEP SST data at the Balearic Channels (black line, 39°–41° N, 1.9°–3.8° E) and at the Northern Sector (gray line, 41°–42.9° N, 1.9°–3.8° E). The Balearic Channels SST extends from 1996 to 2019, for comparison with the CTD time series. The Northern Sector time series extends from 1970 to 2019 for comparison with l'Estartit temperature time series. **(B)** Temperature residuals or anomalies at 0, 20, 50, and 80 m depth at the L'Estartit coastal station. The four time series are presented with different colors from black (0 m) to light gray (80 m), although they are not distinguished in this plot because they have very similar behavior.

TABLE 2 | NCEP/SST: Linear trends (b) and 95% confidence intervals (CI in °C/100yr) for the reanalysis SST obtained from NCEP.

NCEP/SST			
	Period	***b***	**CI**
Balearic Channels	1996–2019	**2.7**	1.0
Northern Sector	1970–2019	**2.2**	0.4
l'Estartit sea temperatura			
Depth	**Period**	***b***	**CI**
0 m	1970–2019	**2.8**	0.4
20 m	1970–2019	**2.6**	0.4
50 m	1970–2019	**2.7**	0.4
80 m	1970–2019	**2.1**	0.3
Sea level			
	Period	***b***	**CI**
Palma tide gauge	1997–2019	**2.4**	1.2
l'Estartit tide gauge	1990–2019	**3.2**	0.7
NCEP/Pressure			
	Period	***b***	**CI**
Balearic Channels	1997–2019	–0.003	0.050
Northern sector	1990–2019	**–0.041**	0.038

L'Estartit sea temperature: Linear trends and 95% confidence intervals (in °C/100yr) for the sea temperature time series at L'Estartit oceanographic station at four discrete depth levels. Sea level: Linear trends and 95% confidence intervals (in mm/yr) for the sea level time series at the Palma and the L'Estartit tide gauges. NCEP/Pressure: Linear trends and 95% confidence intervals (in mbar/yr) for the reanalysis atmospheric pressure time series at the Balearic Channels and the northern sector. In all cases, those values significant at the 95 % confidence level are presented in bold.

mass. On the contrary, the constancy of the LIW density suggests that its upward displacement could be linked to changes in the formation rate of deep waters.

Concerning the deep waters, different results were obtained when considering the water masses with $\sigma_\theta > 29.11$ kg/m^3 (method 1) or those with $\sigma_\theta > 29.1$ kg/m^3 (method 2). In the first case, the changes in potential temperature and salinity were not statistically significant, whereas the potential density decreased and the depth level occupied by these water masses became deeper with a linear trend of 20 dbar/yr (positive trends indicate higher pressure and therefore deeper levels, see **Table 1**). In the second case (see **Table 1** and **Figure 6**), this water mass became warmer, saltier, denser, and progressively occupied a shallower depth range. These, apparently contradictory results, simply reflect the impact of inter-annual and decadal variability on the estimation of long-term changes. Except for spring 2001, density values higher than 29.11 kg/m^3 started to be observed after winter 2004/2005. Inspecting carefully **Figure 6C** (see black dots corresponding to method 1), it becomes clear that the changes observed cannot be considered as progressive ones that could be represented by means of a linear trend. There is a sharp density increase during 2005 and 2006 clearly linked to the WMT (López-Jurado et al., 2005; Font et al., 2007; Smith et al., 2008; Schroeder et al., 2010), and then the density of these deep waters decreased and kept constant with values between 29.111 and 29.113 kg/m^3, being these values higher than those found in the deep waters of the Balearic Channels prior to 2005. These results simply evidence that changes estimated over short periods of time have to be considered very carefully and not considered as representative of the rate of change for long periods. **Figures 6A,B** shows that both, potential temperature and salinity, estimated by means of the method 2, experienced warming periods from the beginning of the series to 2003, from 2005 to 2010 and from 2012 to the end of the series, with cooling periods between them. Consequently, both time series exhibit three relative maxima. Very similar oscillations can be observed for the potential temperature and salinity of the WIW and LIW (**Figures 4**, **5**), although the maximum and minimum values would not correspond to exactly the same years. This oscillatory behavior is very likely the response of water masses to the internal variability of the ocean-atmosphere system, and it implies that selecting shorter periods of time would yield negative trends in some cases and much higher positive trends in others. A similar result was evidenced by Schroeder et al. (2019) when analyzing the waters flowing into the WMED through the Sicily Channel at

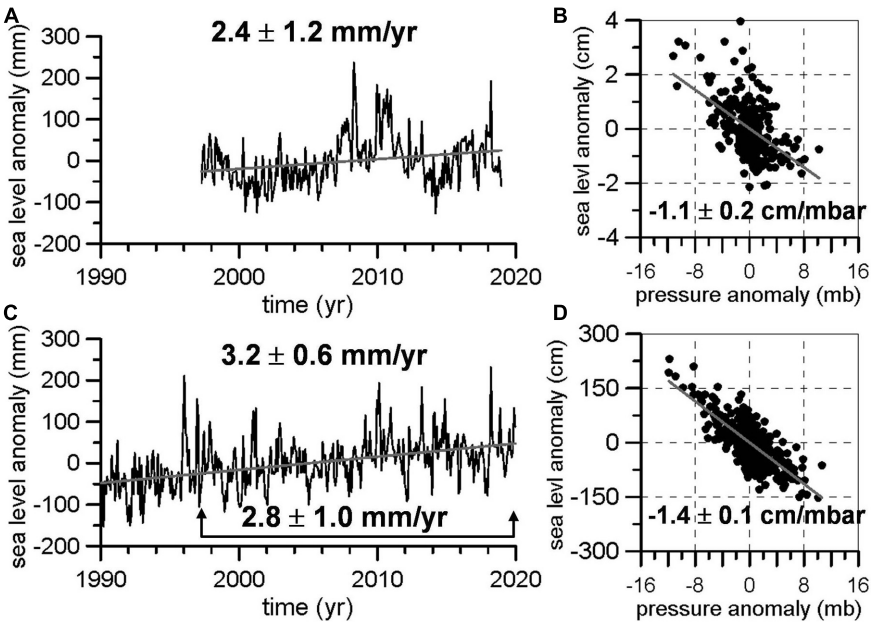

FIGURE 8 | (A) Time series of residuals or anomalies of sea level at the Palma de Mallorca tide gauge. **(B)** Linear regression of sea level residuals on atmospheric pressure at the Balearic Channels. The linear trend for the sea level time series and the slope for the regression are included. **(C)** Time series of sea level residuals at the L'Estartit tide gauge. Linear trends for the complete period, and the 1996–2019 period, are included. **(D)** Linear regression of sea level on atmospheric pressure at the Northern Sector.

400 m depth. The period analyzed, 1993–2018, was comparable to the one used at the present work and these authors found that the waters flowing from the EMED had increased their temperature and salinity at rates of 0.028°C/yr (2.8°C/100yr) and 0.008 yr^{-1} (0.8/100yr) which are even larger than the rates presented for intermediate and deep waters in the Balearic Sea in the present work. However, these authors also found sub-periods with different behavior, with negative trends from 2004 to 2010 and positive and intense trends from 2010 to 2018. In summary, intense changes observed over periods of 5 or even 10 years do not seem to reflect long-term changes in the heat and salt balance of the WMED, associated with long-term changes in the heat and fresh water fluxes with the atmosphere. Changes over short periods of time may simply be the consequence of heat and salt redistributions within the basin caused by changes in the circulation of water masses or alterations in the formation rates or sites of such water masses. On the contrary, the three consecutive temperature and salinity maxima observed in the WIW, LIW and WMDW time series (**Figures 4–6**) show increasing values that account for the linear trends reported for the complete period. Nevertheless, we have to admit that 24 years could also be considered as a short period of time for establishing the long-term behavior of water masses.

The lack of significance for the temperature trends of the AW and the lower degree of confidence for the salinity trends (90%, **Table 1**) could cast some doubts about the changes of the Mediterranean upper layer. WIW is formed by the winter cooling of AW in the continental shelf of the Gulf of Lions, the Ligurian Sea and the Catalan shelf (López-Jurado et al., 1995; Juza et al., 2013, 2019), without the influence of LIW. Therefore, the observed warming of this water mass should be associated with the warming or lower cooling of the AW. Concerning the deep waters in the WMED, previous works had suggested that their warming and salting was caused by the salinity increase of the water masses contributing to the formation of WMDW as saltier waters would reach the deep water density at a higher temperature. On the contrary, it could be argued that saltier waters, if affected by the same heat fluxes at the sea surface, would produce deep waters saltier but with the same temperature as in previous decades. A similar argument was proposed by Schroeder et al. (2010) to explain that the warming and salting of the new WMDW formed after winter 2004/2005 could not be only the result of extreme weather conditions during winter. The results already presented in this work show that the LIW, contributing to the WMDW formation, warmed during the period 1996–2019. Analyzing the L'Estartit temperature time series allowed establishing that the AW also experienced intense warming. Therefore, the warming of the WMDW is probably caused by the contribution of warmer AW and LIW, which in turn, should be linked to changes in the sea-atmosphere heat fluxes. Furthermore, the L'Estartit time series extend from 1970 to 2019. These 50-year time series make us conclude that the warming of the AW in the WMED is not the result of decadal variability, as the trends at L'Estartit can be representative of long-term changes. These results are confirmed by the analysis of the reanalysis SST time series in the Northern Sector and the Balearic Channels (**Table 2**). A similar argument could be used for the long-term salinity increase of deep waters. The salinity

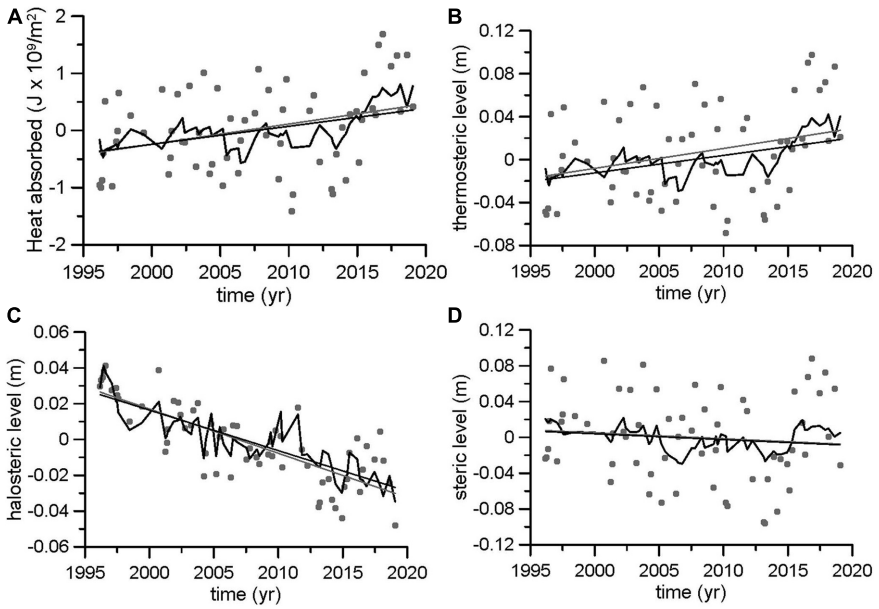

FIGURE 9 | Heat absorbed (in Joules × $10^9/m^2$, **A**), thermosteric **(B)**, halosteric **(C),** and steric **(D)** sea level (in m) in the Balearic Channels. For each campaign, the heat absorbed and the steric, thermosteric, and halosteric sea level are estimated as variations from the mean temperature and salinity profile averaged for the complete period. Gray dots correspond to the calculations from the sea surface to 1200 dbar, whereas the black lines correspond to the calculations excluding the upper 100 dbar.

TABLE 3 | Linear trends for the steric sea level, thermosteric sea level, halosteric sea level (b, mm/yr), and heat absorbed by a water column of one square meter (W/m^2).

Steric, thermosteric, and halosteric sea level from the sea surface

Depth	Steric		Thermos.		Halos.		*Q*	
	b	**CI**	***B***	**CI**	***b***	**CI**	**B**	**CI**
0–500	–0.44	1.62	1.21	1.35	**–1.61**	0.51	0.72	0.74
0–1000	–0.52	1.70	**1.66**	1.43	**–2.14**	0.47	**1.01**	0.79
0–1200	–0.66	1.80	**1.86**	1.50	**–2.47**	0.50	**1.12**	0.84
0–1300	–0.46	2.33	**2.04**	1.91	**–2.44**	0.68	**1.22**	1.05

Steric, thermosteric and halosteric sea level excluding the upper 100 dbar

Depth	Steric		Thermos.		Halos.		*Q*	
	b	**CI**	**B**	**CI**	**B**	**CI**	**B**	**CI**
100–500	–0.28	0.38	**0.98**	0.33	**–1.24**	0.29	**0.60**	0.20
100–1000	**–0.47**	0.47	**1.46**	0.48	**–1.91**	0.30	**0.89**	0.30
100–1200	**–0.65**	0.51	**1.63**	0.52	**–2.26**	0.33	**1.00**	0.32
100–1300	–0.45	0.68	**1.82**	0.68	**–2.25**	0.39	**1.11**	0.41

CI represents the confidence intervals for the same time series. The trends for the different components of the steric sea level are estimated for different pressure ranges indicated in the first column. Calculations are repeated including (rows 4–7) and excluding (rows 11–14) the upper 100 dbar. Those values significant at the 95% confidence level are typed in bold, and those significant at the 90% confidence level are typed in gray bold letters.

of the AW and LIW has increased from 1996 to 2019 (**Table 1** and **Figures 3**, **5**) and these positive trends have been transmitted to the deep waters by means of their contribution to the deep water formation.

According to the results dealing with changes affecting to the complete period of time (1996–2019), it can be concluded that the whole water column has warmed and increased its salinity in the Balearic Channels. These changes have affected all the water masses present at different depth ranges. As a consequence, the heat content of the water column (0–1200 dbar) has increased at a rate equivalent to a continuous heat uptake of 1.12 W/m^2. This rate is reduced to 1 W/m^2 when the upper 100 dbar are excluded (**Table 3** and **Figure 9A**). It should be noted that the global ocean energy gain was equivalent to 0.55 W/m^2 for the period

1971–2010. This value increased to 0.71 W/m^2 for the period 1993–2010 (Stocker et al., 2013). The trends shown in the present work are higher than those reported for the global ocean. This could indicate higher sensitivity of the Mediterranean Sea to the radiative imbalance of the Earth Climate System, maybe because of its reduced dimensions and semi-enclosed characteristics. However, the values reported for the global ocean relay within the uncertainty range estimated for the Mediterranean trends (see confidence intervals in **Table 3**). Another important result is the acceleration of the heat gain of both the global ocean (Stocker et al., 2013) and the WMED. The values estimated in the Balearic Channels from 1996 to 2019 range between 1 and 1.12 W/m^2 whereas those estimated by Vargas-Yáñez et al. (2017) for the period 1943–2015 in the WMED were between 0.2 and 0.6 W/m^2.

The heat absorbed by the water column has contributed to the sea level increase through the thermal expansion. The salinity increase seems to have had a larger influence since the steric sea level shows a decreasing trend around –0.6 mm/yr (**Table 3** and **Figure 9**). Jordá and Gomis (2013) showed that the steric component of sea level had decreased from 1960 to 2000 with a trend ranging between –0.3 and –0.9 mm/yr, depending on the hydrographic database used. This negative trend was due to an important contribution of the halosteric component, but also of the thermosteric one. Although the negative contribution of the halosteric component is in agreement with our results, the thermosteric negative contribution would not be supported by the present ones. The contribution of the halosteric component to the change of sea level along the 21st century is an open and interesting question as projections based on different emission scenarios differ in the salinity behavior of the Mediterranean Sea (Jordà et al., 2017). These discrepancies arise from the uncertainty in the salinity changes of the AW flowing into the Mediterranean Sea. According to some numerical simulations, the melting of polar ice would reduce the salinity of the AW flowing into the Mediterranean Sea and consequently of the MWs. On the contrary, other models show an increase of the MWs salinity as it would be dominated by the increase of evaporation and the decrease of precipitation projected for the 21st century in the Mediterranean region (Somot et al., 2006; Jordà et al., 2017). The time series analyzed in the present work show that, at least since the end of the 20th century and for the beginning of the 21st, the salinity of the different MWs is increasing and the rate of change is accelerating. An additional factor affecting the variations of sea level is the atmospheric pressure. Considering a negative trend of –0.003 mbar/yr and an inverse barometer effect of –1.1 cm/mbar in the Balearic Channels and at the Palma tide gauge, it can be estimated that the atmospheric pressure induced a positive trend of 0.033 mm/yr in sea level (the atmospheric pressure trend was very weak and not significant). The sea level trend at the Palma tide gauge was 2.4 mm/yr. Removing the steric component and the atmospheric pressure components, the linear trend for sea level caused by changes in the mass component is 3 mm/yr. The sea level at L'Estartit tide gauge has a linear trend of 3.2 mm/yr over 1970–2019. Considering the period 1997–2019 for comparison with the Palma tide gauge time series, the linear trend in sea level decreases to 2.8 mm/yr. Considering the negative trend of atmospheric pressure for the Northern Sector (–0.041 mbar/yr), and the inverse barometer effect for this region (–1.4 cm/mbar), it can be estimated an increase of 0.6 mm/yr in sea level associated with this effect. Taking into account the steric sea level estimated from the CTD time series in the Balearic Channels, the mass component of sea level at L'Estartit from 1997 to 2019 would be 2.9 mm/yr. Hence, when the atmospheric pressure and the steric component are considered, both the L'Estartit and Palma sea level time series show the same positive trends.

Besides these processes acting over long-term periods, or at least during the complete duration of the time series, there are abrupt changes that can produce alterations of the water mass properties on time scales of very few years. The WMT is probably the most marked event of such sudden and sharp changes in the WMED. **Figure 5A** shows that the potential temperature of LIW increased in a continuous way from 2000 to 2004 whereas the salinity of this water mass increased from 1996 to 2004. Both time series have a relative maximum during early 2004, before the onset of the WMT. The effect of salinity on density prevailed over that of temperature and the potential density increased from ∼29.065 kg/m^3 to ∼29.095 kg/m^3, which approximately correspond to the lower and upper limits of this water mass (**Figure 2**). To better interpret these results, the temperature and salinity profiles for each campaign were compared with the reference profiles obtained for the complete time series and the observed changes were decomposed into changes on isobaric levels, changes on isopycnal surfaces and changes caused by heaving, that is, vertical displacements of the isopycnals (**Figure 10**; Bindoff and McDougall, 1994; Zunino et al., 2012). **Figures 10C,D** shows changes in isobaric levels and shows that the temperature and the salinity at 600 dbar were lower than the reference values during the initial part of the time series (negative values), and continuously increased reaching a relative maximum in 2004. This result is the same already outlined in **Figure 5**. The isopycnal surfaces that occupied the 600 dbar level during this initial period corresponded to waters fresher and cooler than those corresponding to the reference profiles and these isopycnal surfaces progressively increased its temperature and salinity. The heaving contribution was positive, which means that this isobaric level was also occupied by lighter isopycnals, that is, isopycnal surfaces that occupied shallower levels in the reference profiles. This contribution slightly decreased from 1996 to 2004, indicating that the 600 dbar level was replaced by less shallow isopycnals. This would be the effect of an upward displacement of the isopycnals which is better observed in the reduction of the pressure levels of the isopycnals between 28.944 kg/m^3 and 29.091 kg/m^3 (**Figure 11**), which correspond to the density range of LIW (**Figure 2**). In spring 2004–2005, the potential temperature and salinity of the LIW core (**Figures 5A,B**) suffered a very abrupt decrease which was also observed in the temperature and salinity changes on isobaric surfaces in **Figures 10C,D**. This change was initially caused by a strong upward displacement of isopycnals and by the freshening and cooling of the isopycnals occupying this isobaric level. The effect of the vertical displacement was intensified during autumn 2005 and accounted for the cooling and freshening at the 600 dbar level. On the contrary, the

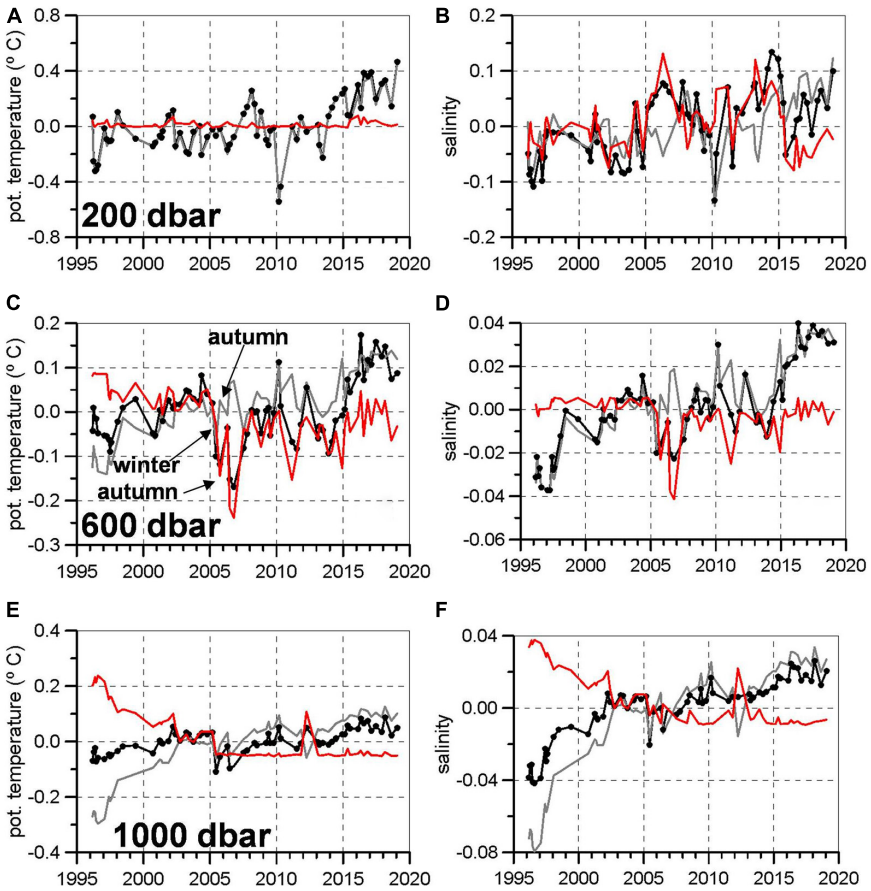

FIGURE 10 | Potential temperature **(A,C,E)** and salinity **(B,D,F)** variations from reference profiles (averaged for the complete time series) at three selected isobaric levels representative of different water masses: 200 dbar (WIW), 400 dbar (LIW), and 1000 dbar (DW). For each variable and isobaric level, the black line represents changes on isobaric levels, the gray line represents changes on isopycnals, the red line represents changes caused by isopycnal heaving, and black dots are the sum of isopycnal and heaving changes.

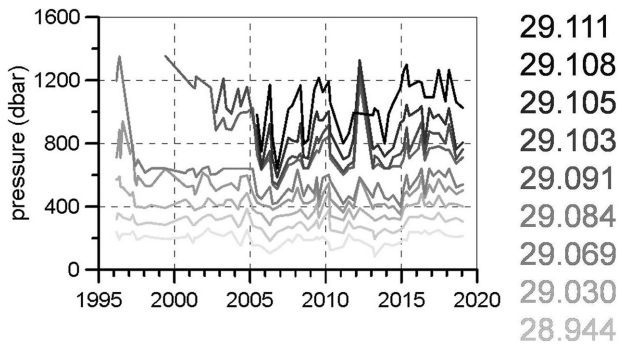

FIGURE 11 | Evolution of the depth (pressure level) of certain selected isopycnals representing different water masses from WIW to deep waters.

contribution of the changes on isopycnals during autumn 2005 was positive, as they became warmer and saltier. These vertical movements can also be seen in **Figure 11** where the above-mentioned isopycnals were displaced to lower pressure values. The upward displacement of isopycnals was accentuated during 2006 and caused a further decrease of the temperature and salinity at 600 dbar, although it was observed warming and salting on isopycnal surfaces. This process could also be observed at deeper levels. The 1000 dbar isobaric level is located in the mixing line between LIW and WMDW. This level experienced a temperature and salinity decrease caused by the upward displacement of isopycnals from 2004 to 2005. Such isopycnals also became fresher and cooler during 2004 and then warmer and saltier during 2006. The isopycnals in the range 29.103–29.108 kg/m^3 experienced a very large upward displacement that in some cases was from 1158 to 640 dbar (**Figure 11**). In addition, new density values appeared at the bottom layers of the Balearic Channels (e.g., the 29.111 kg/m^3 value in **Figure 11**).

The evolution of water mass properties described above is a clear effect of the WMT on the Balearic Channels. Previous works have hypothesized that the WMT was triggered by an accumulation of heat and salt in the intermediate layers of the WMED because of the arrival of warmer and saltier LIW/CIW (Cretan Intermediate Water) from the EMED after the Eastern Mediterranean Transient (Astraldi et al., 2002;

Gasparini et al., 2005; Schroeder et al., 2017). Other works consider that such accumulation was caused by the absence of deep water formation during the 1990s decade (Herrmann et al., 2010). The present dataset does not allow establishing which of these two hypotheses is right and we speculate that probably the WMT is the result of a combination of processes. The CTD time series collected at the Balearic Channels support this accumulation since 2000 in the case of heat, and since 1996 for salt (**Figures 5A,B**). The production of large volumes of very dense new WMDW (nWMDW) during the winters 2004/2005 and 2005/2006 displaced upwards the LIW and the deeper waters being the result of mixing between LIW and old WMDW. After this episode, the deep waters of the Balearic Channels were occupied by new waters with density values higher than those found before the WMT. The new value was around 29.112 kg/m^3 and kept constant until the end of the series (**Figure 6C**). However, both the densest waters ($\sigma_\theta >$ 29.11 kg/m^3) and the lighter deep waters considered in the present work ($\sigma_\theta >$ 29.1 kg/m^3) continued warming and salting until 2019 (**Figures 6A,B**). In this case, these changes were not caused by vertical displacements of water masses, but by changes over isopycnal surfaces (**Figures 10E,F**). A similar situation is found in the intermediate layer. The temperature and salinity at 600 dbar decreased abruptly in spring 2005. The first cause was the upward displacement of isopycnals (vertical contribution in **Figures 10C,D**) and a freshening and cooling of isopycnals (**Figures 10C,D**). This latter contribution could be linked to the transference of heat and salt from LIW to the nWMDW formed during that winter. After this episode, the temperature and salinity of LIW continued increasing, as was the case for the deep layers (**Figures 5**, **10C,D**) and as in that case, the contribution of vertical displacements was weak and remained constant along the time. These warming and salting processes were caused by changes in the water masses on isopycnals. The temperature and salinity trends were stronger after 2013 until the end of the series. Schroeder et al. (2019) reported an abrupt increase of the potential temperature and salinity of waters flowing into the WMED through the Sicily Channel. It is very likely that the acceleration of these trends in the Balearic Channels for the final part of the time series is the result of this heat and salt advection from the EMED.

CONCLUSION

In summary, the upper, intermediate, and deep layers of the Balearic Channels have become warmer and saltier from 1996 to 2019. The temperature and salinity variations have compensated each other and no long-term changes have been observed in the density of the AW, WIW, and LIW. The deep waters have also increased their density and the deepest layers of the channels are now occupied by waters denser than those found in this region prior to 2004/2005. The shift in the properties of the deep layers is caused by the WMT. The intermediate layer of the WMED is occupied by water masses formed in the EMED and therefore, the changes detected are imported from that basin. The temperature and salinity at intermediate layers increased during the years before the onset of the WMT, very likely because of the inflow of warmer and saltier waters through the Sicily Channel. An abrupt increase of temperature and salinity in the channel after 2010 is also observed with 2–3 years delay in the Balearic Channels. Consequently, the formation of saltier and warmer deep waters is highly influenced by the heat and salt advection from the EMED. Nevertheless, a local contribution from the WMED cannot be ignored as the AW in the Balearic Channels and at L'Estartit oceanographic station have become warmer and saltier during the analyzed period. The deep water formation processes or their absence produce the transfer of heat and salt from the upper and intermediate layers to the deep ocean. These processes and others that cannot be resolved with the present dataset impose a strong inter-annual and decadal variability in time series. Besides this variability, the long-term behavior of temperature and salinity along the whole water column seems to be progressive warming and salting, very likely as the result of a heat and salt imbalance in the Mediterranean Sea, associated with climate change. The heat gain estimated in other works for the global ocean is within the uncertainty ranges calculated from the CTD time series in the Balearic Sea. This warming would cause the rise of sea level, but its influence on the steric component of sea level is compensated by the salinity increase. However, when the sea level time series are corrected for the steric and atmospheric pressure effects, they show an increasing trend of 2.9–3 mm/yr, associated with changes in the mass component. Results from the tide gauges at L'Estartit and Palma de Mallorca are consistent.

DATA AVAILABILITY STATEMENT

The datasets presented in this study can be found in online repositories. The names of the repository/repositories and accession number(s) can be found below: http://www.ba.ieo.es/es/ibamar.

AUTHOR CONTRIBUTIONS

MJ developed and applied the geometry-based method for WIW detection and contributed to the manuscript redaction. MG-M and RB were responsible of the management of the project and experimental design. FM, MM, and EB were responsible of the CTD data processing. ET was responsible of the sea level and NCEP data processing and acquisition. JP and JS were responsible for the data acquisition and processing of the L'Esatrtit data. MV-Y and PV-B were responsible of the statistical analysis and manuscript redaction. All the authors contributed to the review of the manuscript and its final redaction.

FUNDING

This study has been supported by the research program RADMED ("Series Temporales de Datos Oceanográficos del

Mediterráneo") funded by Instituto Español de Oceanografía (IEO). Partial support has been also received from the Spanish "Programa Estatal De I+D+I Orientada a Los Retos De La Sociedad (RTI2018-100844-B-C32)" through project SAGA: Flujos zonales en el Océano Atlántico sur interior.

SUPPLEMENTARY MATERIAL

The Supplementary Material for this article can be found online at: https://www.frontiersin.org/articles/10.3389/fmars.2021.640535/full#supplementary-material

REFERENCES

Adloff, F., Somot, S., Sevault, F., Jordà, G., Aznar, R., Déqué, M., et al. (2015). Mediterranean Sea response to climate change in an ensemble of twenty first century scenarios. *Clim. Dyn.* 45, 2775–2802. doi: 10.1007/s00382-015-2507-3

Astraldi, M., Gasparini, G. P., Vetrano, A., and Vignudelli, S. (2002). Hydrographiccharacteristics and interannualvariability of water masses in the central Mediterranean: a sensitivity test for long-term changes in the Mediterranean Sea. *Deep Sea Res. I* 49, 661–680. doi: 10.1016/S0967-0637(01)00059-0

Barceló-Llull, B., Pascual, A., Ruiz, S., Escudier, R., Torner, M., and Tintoré, J. (2019). Temporal and spatial hydrodynamic variability in the Mallorca Channel (Western Mediterranean Sea) from eight years of underwater glider data. *J. Geophys. Res. Oceans* 124, 2769–2786. doi: 10.1029/2018JC014636

Bethoux, J. P. (1979). Budgets of the Mediterranean Sea. Their dependence on the local climate and on the characteristics of the Atlantic Waters. *Oceanol. Acta* 2, 157–163.

Bethoux, J. P., Gentili, B., Raunet, J., and Taillez, D. (1990). Warming trend in the Wetern Mediterranean deep water. *Nature* 347, 660–662. doi: 10.1038/347660a0

Bindoff, N. L., and McDougall, T. J. (1994). Diagnosing climate change and ocean ventilation using hydrographic data. *J. Phys. Oceanogr.* 24, 1137–1152. doi: 10.1175/1520-04851994024<1137:DCCAOV>2.0.CO;2

Borghini, M., Bryden, H., Schroeder, K., Sparnocchia, S., and Vetrano, A. (2014). TheMediterraneanisbecomingsaltier. *Ocean Sci.* 10, 693–700. doi: 10.5194/os-10-693-2014

Dubois, C., Somot, S., Calmanti, S., Carillo, A., Déqué, M., Dell'Aquilla, A., et al. (2012). Future projections of the surface heat and water budgets of the Mediterranean Sea in an ensemble of coupled atmosphere–ocean regional climate models. *Clim. Dyn.* 39, 1859–1884. doi: 10.1007/s00382-011-1261-4

Font, J., Puig, P., Salat, J., Palanques, A., and Emelianov, M. (2007). Sequence of hydrographic changes in NW Mediterranean deep water due to exceptional winter of 2005. *Sci. Mar.* 71, 339–346. doi: 10.3989/scimar.2007.71n2339

Garcia Martinez, M. C., Vargas Yanez, M., Moya, F., Zunino, P., and Bautista, B. (2018). The effects of climate change and rivers damming in the Mediterranean Sea during the Twentieth Century. *Int. J. Nat. Sci. Environ. Resour.* 8, 1–22. doi: 10.19080/IJESNR.2018.08.555741

Gasparini, G. P., Ortona, A., Budillon, G., Astraldi, M., and Sansone, E. (2005). The effect of the Eastern Mediterranean Transient on the hydrographic characteristics in the Strait of Sicily and in the Tyrrhenian. *Deep See Res. I* 52, 915–935. doi: 10.1016/j.dsr.2005.01.001

Herrmann, M., Sevault, F., Beuvier, J., and Somot, S. (2010). What induced the exceptional 2005 convection event in the northwestern Mediterranean basin? Answers from a modeling study. *J. Geophys. Res.* 115:C12051. doi: 10.1029/2010JC006162

Heslop, E. E., Ruiz, S., Allen, J., Lopez-Jurado, J. L., Renault, L., and Tintoré, J. (2012). Autonomous underwater gliders monitoring variability at "choke points" in our ocean system: a case study in the Western Mediterranean Sea. *Geophys. Res. Lett.* 39:L20604. doi: 10.1029/2012GL053717

Jordá, G., and Gomis, D. (2013). Reliability of the steric and mass components of the Mediterranean Sea level es estimated from hydrographic gridded products. *Geophys. Res. Lett.* 40, 3655–3660. doi: 10.1002/grl.50718

Jordà, G., Von Schuckmann, K., Josey, S. A., Caniaux, G., García-Lafuente, J., Sammartino, S., et al. (2017). The Mediterranean sea heat and mass budgets : estimates, uncertainties and perspectives. *Prog. Oceanogr.* 156, 174–208. doi: 10.1016/j.pocean.2017.07.001

Juza, M., Escudier, R., Vargas-Yáñez, M., Mourre, B., Heslop, E., Allen, J., et al. (2019). Characterization of changes in Western Intermediate Water properties enabled by an innovative geometry-based detection approach. *J. Mar. Syst.* 191, 1–12. doi: 10.1016/j.jmarsys.2018.11.003

Juza, M., Renault, L., Ruiz, S., and Tintoré, J. (2013). Origin and pathways of intermediate water in the Northewestern Mediterranean Sea using observations and numerical modelling. *J. Geophys. Res. Oceans* 118, 6621–6633. doi: 10.1002/2013JC009231

Kalnay, E., Kanamitsu, M., Kistler, R., Collins, W., Deaven, D., Gandin, L., et al. (1996). The NCEP/NCAR 40-Year reanalysis project. *Bull. Am. Meteorol. Soc.* 77, 437–471. doi: 10.1175/1520-04771996077<0437:TNYRP<2.0.CO;2

Lascaratos, A., Roether, W., Nittis, K., and Klein, B. (1999). Recent changes in deep water formation and spreading in the Eastern Mediterranean Sea: a review. *Prog. Oceanogr.* 44, 5–36. doi: 10.1016/S0079-6611(99)00019-1

Llasses, J., Jordà, G., and Gomis, D. (2015). Skills of differenthydrographic networks in capturing changes in the Mediterranean Sea at climatescales. *Clim. Res.* 63, 1–18. doi: 10.3354/cr01270

López-Jurado, J. L., Balbín, R., Amengual, B., Aparicio-González, A., Fernández de Puelles, M. L., García-Martínez, M. C., et al. (2015). The RADMED monitoring program: towards an ecosystem approach. *Ocean. Sci.* 11, 645–671. doi: 10.5194/osd-12-645-2015

López-Jurado, J. L., García-Lafuente, J., and Lacaya, N. (1995). Hydrographic conditions of the Ibiza channel during November 1990, March 1991 and July 1992. *Oceanol. Acta* 18, 235–243.

López-Jurado, J. L., González-Pola, C., and Vélez-Belchí, P. (2005). Observation of an abrupt disruption of the long-term warming trend at the Balearic Sea, Western Mediterranean, in summer 2005. *Geophys. Res. Lett.* 32:L24606. doi: 10.1029/2005GL024430

Mariotti, A., Pan, Y., Zeng, N., and Alessandri, A. (2015). Long-term climate change in the Mediterranean region in the midst of decadal variability. *Clim. Dyn.* 44, 1437–1456. doi: 10.1007/s00382-015-2487-3

Nielsen, J. N. (1912). "Hydrography od the Mediterranean and adjacent waters," in *Report on the Danish Oceanographical Expeditions 1908-1910 to the Mediterranean and Adjacent Seas*, Vol. I, Copenhagen, 72–191.

Nykjaer, L. (2009). Mediterranean Sea surface warming 1985-2006. *Clim. Res.* 39, 11–17. doi: 10.3354/cr00794

Pinot, J. M., and Ganachaud, A. (1999). The role of winter intermediate waters in spring-summer circulation of the Balearic Sea: 1. Hydrography and inverse modeling. *J. Geophys. Res.* 104, 29843–29864. doi: 10.1029/1999JC900071

Pinot, J.-M., López-Jurado, J. L., and Riera, M. (2002). The CANALES experiment (1996-1998). Interannual, seasonal, and mesoscale variability of the circulation in the Balearic Channels. *Prog. Oceanogr.* 55, 335–370. doi: 10.1016/S0079-6611(02)00139-8

Poulain, P.-M., Barbanti, R., Font, J., Cruzado, A., Millot, C., Gertman, I., et al. (2007). MedArgo: a drifting profiler program in the Mediterranean Sea. *Ocean Sci.* 3, 379–395. doi: 10.5194/osd-3-1901-2006

Rhein, M., Rintoul, S. R., Aoki, S., Campos, E., Chambers, D., Feely, R. A., et al. (2013). "Observations: ocean," in *Climate Change 2013: The Physical Science Basis. Contribution of Working Group I to the Fifth Assessment Report of the Intergovernmental Panel on Climate Change*, eds T. F. Stocker, D. Qin, G.-K. Plattner, M. Tignor, S. K. Allen, and J. Boschung (Cambridge: Cambridge University Press).

Roether, W., Manca, B. B., Klein, B., Bregant, D., Georgopoulos, D., Beitzel, V., et al. (1996). Recent changes in the Eastern Mediterranean deep waters. *Science* 271, 333–335. doi: 10.1126/science.271.5247.333

Rohling, E. J., and Bryden, H. L. (1992). Man-induced salinity and temperature increase in Western Mediterranean deep water. *J. Geophys. Res.* 97, 11191–11198. doi: 10.1029/92JC00767

Salat, J., and Font, J. (1987). Water mass structure near and offshore the Catalan coast during the winters of 1982 and 1983. *Ann. Geophys.* 5B, 49–54.

Salat, J., Pascual, J., Flexas, M., Chin, T. M., and Vazquez-Cuervo, J. (2019). Forty-five years of oceanographic and meteorological observations at a coastal station in the NW Mediterranean: a ground truth for satellite observations. *Ocean Dyn.* 69, 1067–1084. doi: 10.1007/s10236-019-01285-z

Sanchez-Gomez, E., Somot, S., and Mariotti, A. (2009). Future changes in the Mediterranean water budget projected by an ensemble of regional climate models. *Geophys. Res. Lett.* 36:L21401. doi: 10.1029/2009GL040120

Schroeder, K., Chiggiato, J., Ben Ismail, S., Borghini, M., Patti, B., and Sparnocchia, S. (2019). Mediterranean deep and intermediate water mass properties. In: copernicus marine service report, Issue 3. *J. Operational Oceanogr.* 12, s26–s30. doi: 10.1080/1755876X.2019.1633075

Schroeder, K., Chiggiato, J., Josey, S. A., Borghini, M., Aracri, S., and Sparnocchia, S. (2017). Rapid response to climate change in a marginal sea. *Sci. Rep.* 7:4065. doi: 10.1038/s41598-017-04455-5

Schroeder, K., Josey, S. A., Hermann, M., Grignon, L., Gasparini, G. P., and Bryden, H. L. (2010). Abrupt warming and salting of the Western Mediterranean Deep Water after 2005: atmiospheric forcing and lateral advection. *J. Geophys. Res.* 115:C08029. doi: 10.1029/2009JC005749

Schroeder, K., Millot, C., Bengara, L., Ben Ismail, S., Bensi, M., Borghini, M., et al. (2013). Long-term monitoring programme of the hydrological variability in the Mediterranean Sea: a first overview of the HYDROCHANGES network. *Ocean Sci.* 9, 301–324. doi: 10.5194/os-9-301-2013

Skliris, N., Sofianos, S. S., Gkanasos, A., Mantziafou, A., Versatis, V., Axaopoulos, P., et al. (2012). Decadal scale variability of sea surface temperatura in the Mediterranean Sea in relation to atmospheric variability. *Ocean Dyn.* 62, 13–30. doi: 10.1007/s10236-011-0493-5

Smith, R. O., Bryden, H. L., and Stansfield, K. (2008). Observations of new western mediterranean deep water formation using Argo floats 2004-2006. *Ocean Sci.* 4, 133–149. doi: 10.5194/os-4-133-2008

Somot, S., Sevault, F., and Déqué, M. (2006). Transient climate change scenario simulation of the Mediterranean Sea for the twenty-first century using a high-resolution ocean circulation model. *Clim. Dyn.* 27, 851–879. doi: 10.1007/s00382-006-0167-z

Somot, S., Sevault, F., Déqué, M., and Crépon, M. (2008). 21st century climate change scenario for the Mediterranean using a coupled Atmosphere-Ocean Regional ClimateModel. *Glob. Planet. Change* 63, 112–126. doi: 10.1016/j.gloplacha.2007.10.003

Stocker, T. F., Qin, D., Plattner, G.-K., Alexander, L. V., Allen, S. K., Bindoff, N. L., et al. (2013). "Technical Sum-mary," in *Climate Change 2013: The Physical Science Basis. Contribution of Working Group I to the Fifth Assess-ment Report of the Intergovernmental Panel on Climate Change*, eds T. F. Stocker, D. Qin, G.-K. Plattner, M. Tignor, S. K. Allen, J. Boschung, et al. (Cambridge: Cambridge University Press).

Theocharis, A., Nittis, K., Kontoyiannis, H., Papageorgiou, E., and Balopoulos, E. (1999). Climatic changes in the Aegean Sea influence theEastern Mediterranean thermohaline circulation(1986-1997). *Geophys. Res. Lett.* 26, 1617–1620. doi: 10.1029/1999GL900320

Tsimplis, M. N., and Baker, T. F. (2000). Sea level drop in the Mediterranean Sea: an indicator of deep wáter salinity and temperatura changes? *Geophys. Res. Lett.* 27, 1731–1734. doi: 10.1029/1999gl007004

Tsimplis, M. N., and Josey, S. A. (2001). . Forcing of the Mediterranean Sea by atmospheric oscillations over the North Atlantic. *Geophys. Res. Lett.* 28, 803–806. doi: 10.1029/2000GL012098

Vargas-Yáñez, M., García-Martinez, M. C., Moya, F., ópez-Jurado, J. L. L., Serra, M., Santiago-Domenech, R., et al. (2019). in *The Present state of Marine Ecosystems in the Spanish Mediterranean in a Climate Change Context*, ed. Grupo Mediterráneo de Cambio Climático (Málaga: Tuimagina editorial). ISBN: 978-84-09-13597-4. doi: 10.1029/2000gl012098

Vargas-Yáñez, M., García-Martíneza, M. C., Moya, F., Balbín, R., ópez-Jurado, J. L. L., Serra, M., et al. (2017). Updating temperature and salinity mean values and trends in the Western Mediterranean: the RADMED project. *Progr. Oceanogr.* 157, 27–46. doi: 10.1016/j.pocean.2017.09.004

Vargas-Yáñez, M., Mallard, E., Rixen, M., Zunino, P., García-Martínez, M. C., and Moya, F. (2012). The effect of interpolation methods in temperatura and salinity trends in the Western Mediterranean. *Medit. Mar. Sci.* 13/1, 118–125. doi: 10.12681/mms.28

Vargas-Yáñez, M., Zunino, P., Benali, A., Delpy, M., Pastre, F., Moya, F., et al. (2010). How much is the Western Mediterranean really warming and salting? *J. Geophys. Res.* 115:C04001. doi: 10.1029/2009JC005816

Vargas-Yáñez, M. M., Juza, R., Balbin, P., Velez-Belchí, M. C., García-Martínez, F., and Moya, A. (2020). Climatological temperature and salinity properties and associated water mass transports in the Balearic Channels using repeated observations from 1996 to 2019. *Front. Mar. Sci.* 7:568602. doi: 10.3389/fmars.2020.568602

Zunino, P., Schroeder, K., Vargas-Yáñez, M., Gasparini, G. P., Coppola, L., García-Martínez, M. C., et al. (2012). Effects of the Western Mediterranean Transition on the resident water masses: pure warming, pure freshening and pure heaving. *J. Mar. Syst.* 96-97, 15–23. doi: 10.1016/j.jmarsys.2012.01.011

Conflict of Interest: The authors declare that the research was conducted in the absence of any commercial or financial relationships that could be construed as a potential conflict of interest.

frontiers in Marine Science

ORIGINAL RESEARCH
published: 18 May 2021
doi: 10.3389/fmars.2021.664509

Contribution of Thermohaline Staircases to Deep Water Mass Modifications in the Western Mediterranean Sea From Microstructure Observations

Bruno Ferron[1], Pascale Bouruet-Aubertot[2], Katrin Schroeder[3], Harry L. Bryden[4], Yannis Cuypers[2] and Mireno Borghini[5]*

[1] Laboratoire d'Océanographie Physique et Spatiale, Univ Brest-CNRS-IFREMER-IRD-IUEM, Brest, France, [2] Sorbonne Université (UPMC, Univ Paris 06)-CNRS-IRD-MNHN, LOCEAN, Paris, France, [3] Consiglio Nazionale delle Ricerche – Istituto di Scienze Marine (CNR-ISMAR), Venice, Italy, [4] Ocean and Earth Science, University of Southampton, Southampton, United Kingdom, [5] Consiglio Nazionale delle Ricerche – Istituto di Scienze Marine (CNR-ISMAR), Lerici, Italy

OPEN ACCESS

Edited by:
Zhiyu Liu,
Xiamen University, China

Reviewed by:
Lei Zhou,
Shanghai Jiao Tong University, China
Shengqi Zhou,
South China Sea Institute of Oceanology (CAS), China

***Correspondence:**
Bruno Ferron
Bruno.Ferron@ifremer.fr

Specialty section:
This article was submitted to Physical Oceanography, a section of the journal Frontiers in Marine Science

Received: *05 February 2021*
Accepted: *20 April 2021*
Published: *18 May 2021*

Citation:
Ferron B, Bouruet-Aubertot P, Schroeder K, Bryden HL, Cuypers Y and Borghini M (2021) Contribution of Thermohaline Staircases to Deep Water Mass Modifications in the Western Mediterranean Sea From Microstructure Observations. Front. Mar. Sci. 8:664509. doi: 10.3389/fmars.2021.664509

Recent observations from profiles of temperature and salinity in the Algerian Sea showed that salt finger mixing can significantly warm and salinify the deep waters within a period of 2 years, thereby contributing to the erosion of deep water properties formed during winter convection episodes. In this study, heat, salt, and buoyancy fluxes associated with thermohaline staircases are estimated using microstructure observations from four locations of the Western Mediterranean Sea: The Tyrrhenian Sea, the Algerian Sea, the Sardino-Balearic Sea, and the Ligurian Sea. Those fluxes are compared to the rare estimates found in the Mediterranean Sea. Microstructure data show that the temperature variance dissipation rate is one to three orders of magnitude larger in the strong steps that separate weakly stratified layers than in the layers, while the turbulent kinetic energy dissipation rate remains usually weak both in steps and layers. In the steps, the turbulent eddy diffusivity of salt is on average twice as large as that of temperature. The buoyancy flux ratio decreases with the density ratio. It is found that staircases induce a downward heat transfer rate of 46 to 103 $\times$ 10^9 W over the whole western basin, and a downward salt transfer rate of 4.5 to 10.3 $\times$ 10^3 kg s^{-1} between 1000 and 2000 m. This heat convergence is 2–5 times as large as the western Mediterranean geothermal heat flux in this depth range. Over the whole western basin, heat and salt convergences from salt-fingering staircases are 50% to 100% of those generated by mechanical mixing. Finally, it is found that heat and salt convergences from geothermal heating, salt-fingering and mechanical mixing can balance a deep water upwelling of 0.4 $\times$ 10^6 m^3 s^{-1}.

Keywords: microstructure, double-diffusion, staircases, Mediterranean basin, turbulence, salt-fingering, upwelling, mixing

INTRODUCTION

Staircases form a remarkable characteristic of hydrological profiles of some regions of the western Mediterranean Sea. They sign up as a continuous succession of well mixed regions with weak vertical property gradients (layers) interlaced with strong interfaces (steps) with large property gradients. Interfaces have typical thicknesses of few meters up to few tens of meters, while layer thicknesses can reach several hundreds of meters. Such profiles were observed in the Tyrrhenian Sea (Johannessen and Lee, 1974; Molcard and Tait, 1977; Zodiatis and Gasparini, 1996) as well as in the Algerian Sea (Krahmann, 1997; Bryden et al., 2014, B14 hereinafter; Taillandier et al., 2020). Those studies showed that staircases often exhibit persistence over time from months to years, and strong lateral coherence that can reach several tens of kilometers to hundreds of kilometers. Such a spatial coherence was nicely illustrated from seismic images in the Tyrrhenian Sea where some interfaces were tracked up to 200 km (Buffett et al., 2017). The time coherence in the staircases of the central Tyrrhenian Sea was recently remarkably evidenced from a hydrographic station repeated from 2003 to 2016 (Durante et al., 2019).

Staircases formed between the warm and salty Levantine Intermediate Water (LIW) and the relatively colder and fresher deep waters. The large-scale vertical contrasts in temperature and salinity between those water masses lead to a density ratio $R_\rho = \alpha\theta_z/\beta S_z$ close to 1.25, where α is the thermal expansion coefficient, β is the haline contraction coefficient, θ_z and S_z are the large-scale vertical gradients of potential temperature and salinity, respectively. Such a low density ratio makes the water column prone to salt fingering, an instability process that builds upon the difference in molecular diffusivities of heat and salt (Turner, 1967; see Radko, 2013, for a recent extensive review of implied processes). This instability releases the potential energy stored in the salinity field and efficiently transfers heat and salt downward.

Recently, B14 used the time evolution of heat and salt contents between two hydrographic cruises in the Algerian Sea to derive averaged integral estimates of temperature, salt and buoyancy fluxes induced by salt fingering processes between 2008 and 2010. They estimated that the mean eddy diffusivity for heat and for salt in the staircase steps of the Algerian Sea were $K_T = 2.0 \times 10^{-5}$ m^2 s^{-1} and $K_S = 3.7 \times 10^{-5}$ m^2 s^{-1}, respectively.

In this study, we reverse the approach and use microstructure data from staircases of the western Mediterranean to derived eddy diffusivities, salt, heat and buoyancy fluxes with the assumption that salt fingering is the dominant process responsible for the staircases. The hydrology of staircases by region of the western Mediterranean and the characteristics of staircases derived from the microstructure are presented. Heat and salt fluxes from salt fingering, mechanical mixing and geothermal heating are estimated and their impact on the fate of deep water masses are discussed.

MATERIALS AND METHODS

Microstructure Data Set

The study of staircases relies on the microstructure dataset gathered on board the Urania R/V during five cruises with our deep microstructure profiles VMP-6000 (Rockland Scientific Int.): VENUS and ICHNUSSA in 2013, MEDOCC, EMSO, and ICHNUSSA in 2014 (Ferron et al., 2017). Additional microstructure profiles located along the French coast were not considered since they mostly sampled the upper 600 m of the water column; none of them showed any sign of staircases. The three profiles from the Ionian sea did not show any staircase structure. Some characteristics of the cruises are summarized in **Table 1**. A total of 134 profiles distributed over 66 distinct station locations were considered in this study (**Figure 1**).

Identification of Staircases

Profiles showing a staircase structure were selected after examining their temperature, salinity, and density profiles. Staircases are marked by a succession of mixed layers separated by stratified steps. Mixed layers are characterized by a quasi-homogeneous temperature, salinity and thus density, and are therefore different from homogeneous density layers issued from density-compensated temperature and salinity gradients (not considered here). The depth range at which a staircase starts and ends were selected by hand to avoid any inclusion of isolated mixed layers.

The hydrology used to identify layers and steps came from the seabird SBE 3F temperature and the SBE 4C conductivity sensors that equipped the microstructure profiler VMP-6000. Since the conductivity cell was not pumped, spiking was frequent when the cell crossed a staircase step. Consequently, the automatic identification of layer and step depths was done solely upon the temperature profile. Using both temperature and density to identify the boundaries of steps and layers gave less accurate results. The nearby CTD 911 profiles from the ship carousel exhibit somewhat less intense spiking. However, they were not used because steps and layers may be shifted in pressure in a complicated way and do not have necessarily the same shape as those from the VMP CTD, since both platforms were not exactly collocated in space and time. Averaging microstructure properties from the VMP on steps and layers identified from the CTD 911 would not produce accurate statistics.

Once manually given the depth range of a staircase, layer and step depths were automatically calculated. Layers were first identified as regions having a temperature gradient smaller than a critical depth dependent profile. This critical profile, θ_z^c, was defined the following way: (1) the potential temperature profile was first differentiated over a vertical distance of 0.5 m and the resulting raw temperature gradient was low-pass filtered using a moving-mean of 1 m length; (2) this filtered temperature gradient, θ_z^{lp}, was bin-averaged at 10 depth-points equally spaced and the resulting 10 points were linearly extrapolated at all depths to form a very large-scale temperature gradient profile, θ_z^{ls}; (3) this very large-scale temperature gradient was bounded by two values, $\theta_{z1} = 2 \times 10^{-4}$°C/m and $\theta_{z2} = 5 \times 10^{-4}$°C/m, to form

TABLE 1 | Oceanographic cruises that contributed to the microstructure data set used in this study (R/V URANIA).

Cruise name	Date	Research vessel	Number of full-depth VMP profiles	Number of profiles with staircases
VENUS	04/06/2013-25/06/2013	Urania	25	4
ICHNUSSA 2013	14/10/2013-30/10/2013	Urania	26	12
MEDOCC 2014	24/03/2014-10/04/2014	Urania	30	3
EMSO	26/06/2014-04/07/2014	Urania	13	2
ICHNUSSA 2014	13/11/2014-01/12/2014	Urania	40	18

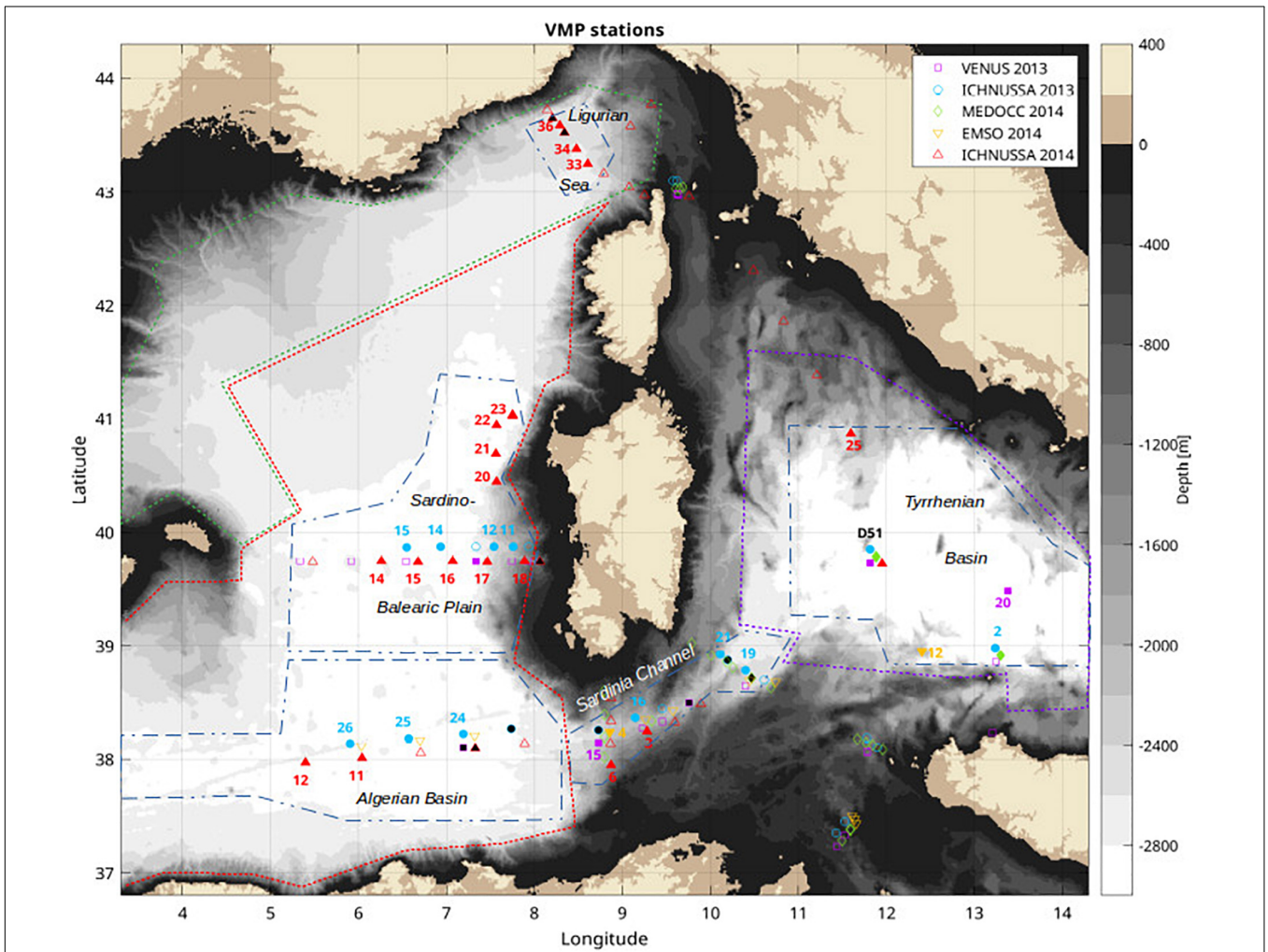

FIGURE 1 | Location of VMP stations gathered along five cruises done in 2013 and 2014. Each cruise has specific color and marker. For clarity, markers are offset around the VMP cast location to distinguish between cruises for a same station. When staircases with clear alternating steps and layers are observed on a profile, the marker is filled with the corresponding cruise color. Markers filled with black correspond with stations showing some smooth or fuzzy staircases that are not taken into account in this study. Unfilled markers are stations without any obvious staircases. Note that the numbering of a same station usually differs from a cruise to the other. Blue dashed-dotted lines delineate the maximum area attributed to the four regions showing staircases. The area of the Algerian Sea extends up to the Alboran Sea and that of the Tyrrhenian Sea extends slightly further eastward (cut for clarity). Colored dotted lines are used to delineate regions for mechanical mixing estimates: red for the Algerian Sea to the Northern boundary layer, green for the boundary layer, purple for the Tyrrhenian Sea, Sardinia Channel remains delimited by the blue dashed-dotted line.

the critical profile such that: $\theta_{z1} < \theta_z{}^c = \theta_z{}^{ls} < \theta_{z2}$; (4) finally, a layer was detected whenever $\theta_z{}^{lp} < \theta_z{}^c$. The step 3 ensures to detect layers in the upper part of the water column (i.e., 600–1000 m) where layers tend to have slightly larger temperature gradient than deeper layers. The two thresholds θ_{z1} and θ_{z2} apply to the western Mediterranean stratification and would need to be adjusted if the same method had to be applied to another oceanic region. The sensitivity of diagnosed layer thicknesses to θ_{z2} is larger than to θ_{z1} but remains small: changing θ_{z2} by a factor of 2 changes nearly 15% of layer thicknesses by 2–5 dbar, and

half as much by 5–10 dbar. As staircases are characterized by a continuous succession of layers and steps, steps were diagnosed as regions separating two layers.

The presence of temperature gradient inhomogeneities of small vertical extent within a layer can split layers in several segments separated by very thin steps, which a human-eye processing would not do. To avoid this segmentation of layers, steps were required to have a vertical extent of at least 2 m. The value of 2 m, which represents more than 3 s of data, was chosen since it also ensures a correct denoising of microstructure shear data from spurious platform vibrations (Goodman et al., 2006). In the same spirit, layers were required to have a length of at least 4 m.

The density ratio R_ρ is an important parameter for the characterization of the environment in which layers and steps develop. For a given layer number k on the vertical, R_ρ was calculated using the median temperature and median salinity difference between layer k−1 and k + 1. For a step number k on the vertical, R_ρ was calculated using the difference between the median temperature and median salinity difference of layer k above the step k and layer k + 1 below the step. The median was chosen rather than the mean since the median over a layer is not influenced by the smoothing of the conductivity cell at the boundary of mixed layers; it better represents the typical property value of a mixed layer.

Processing of Microstructure Data on Steps and Layers

Dissipation rates of turbulent kinetic energy, ε, were estimated from the variance of the vertical shear of horizontal velocities measured at centimetric scale by two shear probes mounted on the VMP. Assuming isotropy, the mean ε per unit mass reads $\varepsilon = 7.5\ \nu < u_z^2 >$, where ν is the viscosity of seawater, and $< u_z^2 >$ is the variance of the vertical shear of the horizontal velocity. Individual ε estimates obtained every meter were averaged over a layer or a step thickness (the reader is referred to Ferron et al., 2014, section 2a for further details of microstructure shear processing).

Dissipation rates χ were estimated from the vertical temperature gradient measured at centimetric scale by two fast thermistors (FP07) mounted on the VMP. For an isotropic turbulence, the rate at which temperature variance is dissipated reads $\chi = 6\ k_T < \theta'^2_z >$, where k_T is the molecular diffusivity for temperature and $< \theta'^2_z >$ is the variance of the microscale vertical temperature gradient θ'_z averaged over a layer/step thickness. This variance was estimated from the integration over the viscous-convective wavenumber range of the mean layer/step-temperature gradient spectra, which was obtained from the average of individual spectra over 0.5 m-length segments with half-segment overlaps. All segments were detrended and windowed with a Hanning function before taking the FFT. A first estimate of the variance was calculated from an integration of the temperature gradient spectra up to a maximum wavenumber k_{max}. The wavenumber k_{max} was the smallest wavenumber among the Batchelor wavenumber, $k_B = [\varepsilon/(\nu\ k_T^2)]^{1/4}$, the wavenumber k_{noise} above which the FP07 temperature was contaminated by noise, and the wavenumber k_{tr} associated with the limited time response τ of FP07 sensors [a conservative value τ of 0.01 s was chosen, Sommer et al., 2013; $k_{tr} = 1/(2\pi\tau w)$, where w is the downcast velocity]. The theoretical Batchelor spectra was then fitted to the averaged temperature gradient spectra so that both have the same variance when integrated up to k_{max}. The final temperature gradient variance was calculated by adding the missing variance from k_{max} to k_B from the fitted Batchelor spectra.

The dissipation ratio reads $\Gamma = \chi\ N^2/(2\ \varepsilon\ \theta_z^2)$, where N is the buoyancy frequency. Γ was estimated for each step with the dissipation rates (χ, ε) calculated on the step thicknesses as explained previously, the buoyancy frequency and temperature gradient being estimated from density and temperature differences across the step. Since Γ is formed from four noisy variables, it presents a significant scatter.

In the case of salt fingering, the heat to salt buoyancy flux ratio reads: $r_f = R_\rho\ K_T/K_S = \Gamma/(\Gamma + 1 - R_\rho^{-1})$ (Hamilton et al., 1989). The eddy diffusivity of temperature is given by the Osborn-Cox relationship $K_T = \chi/(2\ \theta_z^2)$ (Osborn and Cox, 1972). Stern (1975) found that the flux ratio for growing fingers can be expressed as: $r_{f-stern} = R_\rho\ -[R_\rho\ (R_\rho\ -1)]^{1/2}$. Radko et al. (2014) derived an expression for the flux ratio based on a fit to DNS results that reads: $r_{f-Radko} = a\ \exp(-bR_\rho\ ) + c$, where (a, b, c) = (2.709, 2.513, 0.5128). Both formulations will be used for comparison with our dataset.

Summary of the Method

From microstructure data, dissipation rates (χ, ε) were calculated. They were used to compute K_T and Γ with the combination of the CTD finestructure data measured concomitantly with the microstructure data. Assuming salt fingering is responsible for the generation of observed staircases, the knowledge of Γ allowed for the calculation of r_f, from which k_S is deduced. Once eddy diffusivities were known, the turbulent fluxes of temperature, $F_T = K_T\ d\theta/dz$, and salt, $F_S = K_S\ dS/dz$, were estimated.

For comparison, eddy diffusivities due to mechanical mixing were derived from ε using the Osborn relationship that reads: $K^{turb} = 0.2\ \varepsilon\ N^{-2}$ (Osborn, 1980), with a constant mixing efficiency of 0.2 for moderate turbulent intensity ($8.5 < Re_b = \varepsilon\ \nu^{-1}\ N^{-2} < 400$, where Re_b is the turbulent intensity or buoyancy Reynolds number; Bouffard and Boegman, 2013). Turbulent tracer fluxes generated by mechanical mixing can then be inferred multiplying K^{turb} by the appropriate finescale tracer gradients dθ/dz and dS/dz.

RESULTS

Geographical Distribution and Anatomy of Staircases

Hydrological stations with staircases are found in several regions of the western Mediterranean Sea (**Figure 1**, face-colored markers). Few of those stations (face-colored in black) have less marked transitions between steps and layers and/or

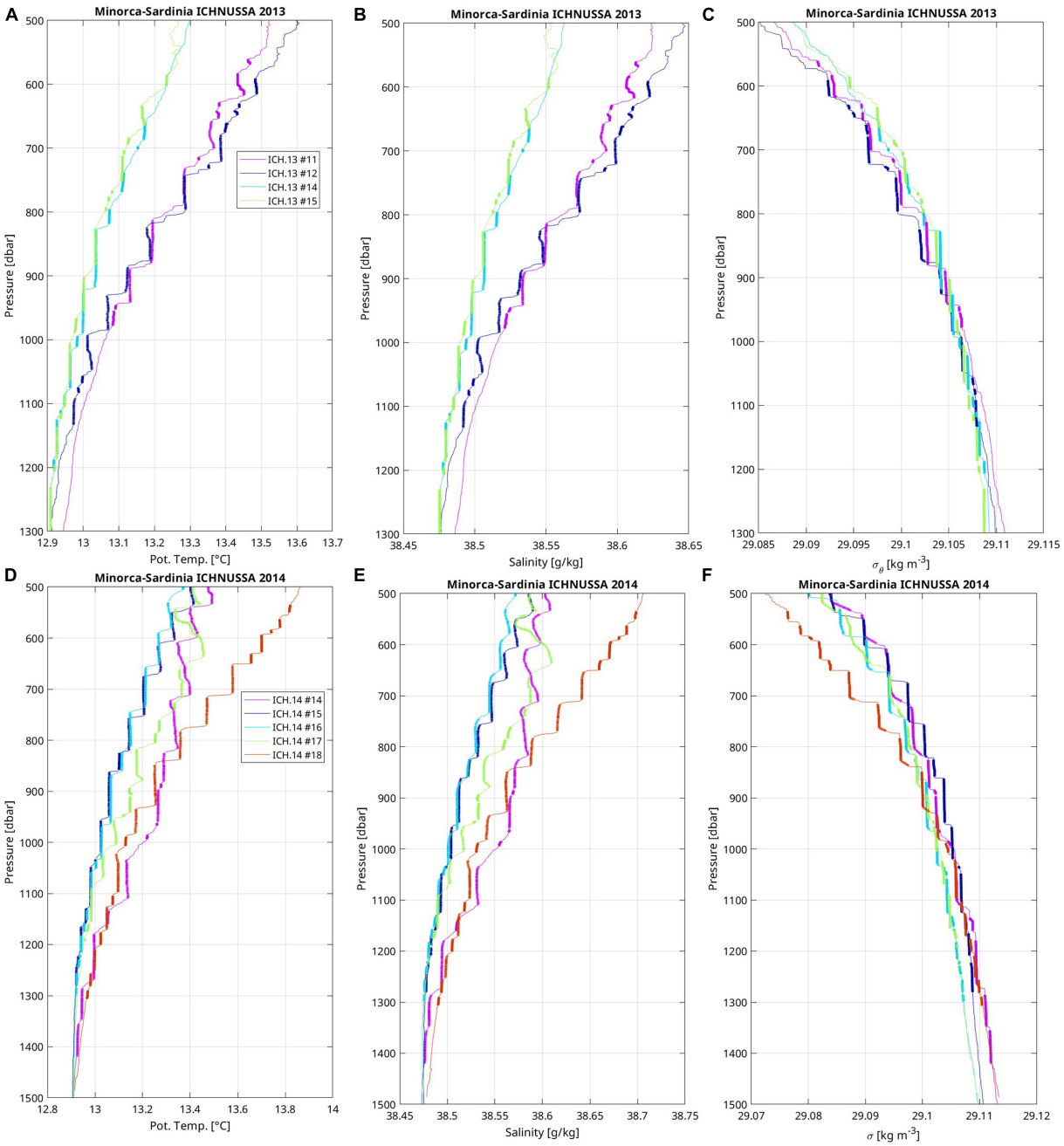

FIGURE 2 | Vertical profiles in staircases of **(A,D)** potential temperature, **(B,E)** salinity, and **(C,F)** potential density of stations located along the Minorca to Sardinia transect during **(A–C)** ICHNUSSA 2013, and **(D–F)** ICHNUSSA 2014 fall cruises. Station numbers are indicated in the figure legend **(A,D)** and located on the map (**Figure 1**). Layers are emphasized by thick lines with weak vertical gradient segments.

only few isolated layers and will not be considered in the following. Noticeable is also the property that staircases at a given station were not always present when the station was repeated along different cruises (**Figure 1**, color-filled versus empty markers). For instance, during the transect from Minorca to Sardinia, staircases are largely present during the ICHNUSSA fall cruises of 2013 and 2014, while only one station have staircases in the summer VENUS cruise of 2013. Advection patterns or staircase formation process may be responsible for such a variability. Oppositedly, the central station #51 from the Tyrrhenian sea always exhibited staircases as also reported by Durante et al. (2019).

Staircases are observed at several stations along the Minorca-Sardinia transect during ICHNUSSA 2013 (**Figures 2A–C**) and ICHNUSSA 2014 (**Figures 2D–F**). Those of 2013 lies in the range 600–1300 dbar, with an increase of the deeper limit of

the pressure range from Sardinia (sta. #11, 980 dbar) to the middle of the basin (sta. #15, 1300 dbar). The density of the deepest layer very slightly increases westward by 0.002 kg m^{-3} from station 11 to station 15 (the Mediterranean Sea is weakly stratified at depth; for instance, the averaged buoyancy frequency is 3×10^{-4} s^{-1} between 800 and 2400 dbar in this region). Most of the layers are remarkably mixed, but some also show slight decreases in temperature and salinity so as to produce layers with an homogeneous density. All profiles show layer thicknesses from few meters up to 60 m, one layer reaching 90 m (ICH. 13 #14). In that same region, layers observed in fall 2014 lie in the range 500–1400 dbar, similarly to 2013. Some profiles present remarkable sharp transitions between steps and well mixed layers both in temperature, salinity, and density (e.g., ICH. 14 #18, ICH. 14 #15 below 670 dbar). The sharpest transitions are better seen in temperature than in salinity or density because the unpumped conductivity cell has a longer response time than the temperature sensor due to its thermal mass effect. On this series of profiles, some layers are not fully mixed and instead exhibit weak temperature gradient compensated by salinity gradients (e.g., ICH. 14 #14). Along this transect, 59% (resp. 92%) of the steps have a thickness smaller than 10 dbars (resp. 20 dbars). Layers are on average thicker in 2014 than in 2013 on this transect: 33% (resp. 44%) of the layers have a thickness smaller than 20 dbars and 27% (resp. 7%) are thicker than 60 dbars.

During fall 2014, staircases are observed exceptionally as far north as to 41°N, off the western coast of Sardinia (**Figure 1**, sta. #20-23). They share many common characteristics with staircases located further south along the Minorca-Sardinia transect. For instance, many steps and layers of profiles ICH. 14 #20 and #22 (**Figures 3A–C**) show temperature-salinity properties close to those of ICH. 14 #15 and #16 (**Figures 2D–F**); layers and steps are often simply offset in pressure by few tens of dbars. Statistics on layer thicknesses are also similar to the fall 2014 Minorca-Sardinia transect with 23% of the layers having a vertical extent larger than 60 dbar. Those large-scale coherent observations are consistent with the large spatial coherence usually observed in staircases that can reach several hundreds of kilometers. Here, the distance between ICH. 14 #15 and #22 amounts to 153 km.

Consistently with observations made in 2006, 2008, and 2010 (B14), staircases were also found in the Algerian sea from 500 to 1300 dbars during the fall cruises of 2013 and 2014 (**Figures 3D–F**). In this region, 42% of layer thickness is smaller than 20 dbars and 11% is larger than 60 dbars.

In the Ligurian sea, three stations exhibited clear staircases between 500 and 1150 dbar during fall 2014 (**Figure 1**, #33, 34, 36). Steps tend to be thicker with weaker property gradients than in most previously presented profiles with staircases (**Figures 4A–C**). Along this transect, 40% (resp. 77%) of the steps have a thickness smaller than 10 dbars (resp. 20 dbars), which is lower than percentages along the Minorca-Sardinia transect of fall 2014 (resp. 59% and 92%). Most of the layers are well mixed in temperature and salinity. Their thickness follows statistics similar to other groups of staircase profiles: 47% of the layers are thinner than 20 dbars and 9% are thicker than 60 dbars.

In the central Tyrrhenian sea, the station #51 was sampled along four cruises (**Figure 1**). It was repeated twice, 7 days apart, during the spring cruise of 2014. This station shows the most impressive succession of layers and steps that extend from 600 to 2800 dbars (**Figures 5A–C**). Steps are rather thin and sharp with 73% (resp. 91%) of the steps thinner than 10 dbar (resp. 20 dbar), those percentages being close to steps observed on the Minorca-Sardinia transect. The D51 station has also the thickest layer of our dataset with a maximum value of about 400 dbars. For this station, 51% of the layers are thinner than 20 dbars, and 33% are thicker than 60 dbars. Among all regions of the western Mediterranean sampled with the VMP, the Tyrrhenian sea concentrates all the layers that have a thickness larger than 130 dbars (36 occurrences). The repetition of the D51 station shows that strong steps and thick layers are robust features that persist over time (i.e., around 1100 dbar, 1400 dbar, and 1800–1900 dbar), as shown by Durante et al. (2019). There also exists significant differences: in the upper part of the staircases (**Figure 5**, Inset 1), smooth profiles of temperature and salinity with no step are found for the VENUS sta. #3 between 600 and 820 dbar. Four months later, fourteen layers of thickness usually smaller than 15 dbar (one reaches 30 dbar) are present in that same pressure range (ICH. 13 #7). Five months later, only 3–4 layers are visible, the largest being 40 dbar-thick (MEDOCC #20 and 30). Seven months later, nine layers are present, three of them being thicker than 25 dbar (ICH. 14#24). Interestingly, this evolution in time is also found deeper at the step around 1100 dbar (**Figures 5A–C**, Inset 2), where rather smooth temperature and salinity profiles are found during VENUS, 3–4 small layers (<20 dbar thick) during ICHNUSSA 2013, and one thicker layer (40–55 dbar) for the following cruises. Properties and vertical position of layers are consistent over distances of at least 140 km, between D51 and stations located further to the southeast: temperature and salinity staircases are largely consistent from 700 to 2100 dbar between VENUS station #20 and the station #51 of MEDOCC, as well as for the layers between 1400 and 2100 dbar between station #51 and station #2 of ICHNUSSA 2013 (see station number on the map of **Figure 1**).

Density Ratio and Thickness of Steps and Layers

Radko et al. (2014) reported a significant connection between the density ratio and the shape of staircases: the step thickness sharply increases as the density ratio decreases (Radko, 2005, his **Figure 3**). He also noted that oceanic salt-finger staircases were only observed when $R_\rho < 2$. With these idea in mind, we now examine properties of density ratios, layer and step thicknesses.

The probability density function (PDF) of the density ratio of steps and layers follows the same distribution (**Figure 6A**). The PDF is maximum for R_ρ between 1.1 and 1.2 for both steps and layers and rapidly decays away from that maximum. The PDF shows that 68% (resp. 88%) of the layers have a R_ρ between 1.1 and 1.3 (resp. between 1.0 and 1.4). For the steps, 56% (resp. 80%) have a R_ρ between 1.1 and 1.3 (resp. 1.0 and 1.4). There was no noticeable difference between cruises. The mean density ratio of steps is 1.25.

The classification of R_ρ by geographical subregions shows that there are no striking regional differences (**Table 2**).

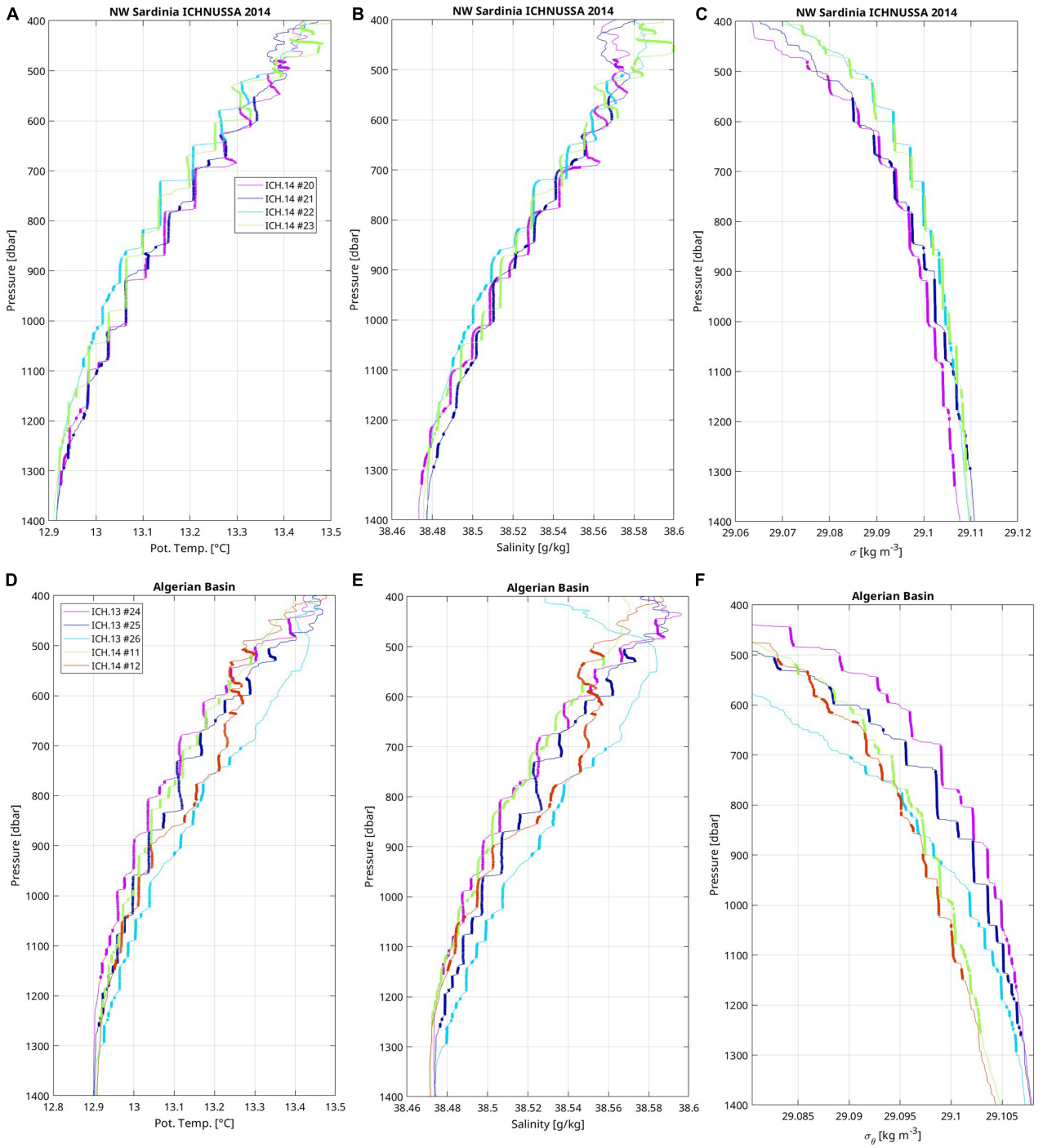

FIGURE 3 | Vertical profiles in staircases of **(A,D)** potential temperature, **(B,E)** salinity, and **(C,F)** potential density of stations located **(A–C)** to the north west of Sardinia during ICHNUSSA 2014, and **(D–F)** in the Algerian sea during ICHNUSSA 2013 and 2014 fall cruises. Station numbers are indicated in the figure legend **(A,D)** and located on the map (**Figure 1**). Layers are emphasized by thick lines with weak vertical gradient segments.

A group of layers with thicknesses larger than 30 dbar and a R_ρ exceeding 1.6 among those located west of Sardinia departs from the ensemble (**Figure 6B**, magenta points). A closer look at those points evidences layers that are less homogeneous than most other layers: their top to bottom potential temperature difference shows that 84% of them are marked by a temperature increase of at least 0.005°C, while this percentage drops to 16% for the layers with $R_\rho < 1.6$. Layers with slight temperature gradients compensated by salinity were noticed in the previous section (e.g., **Figures 2D–F**, sta.

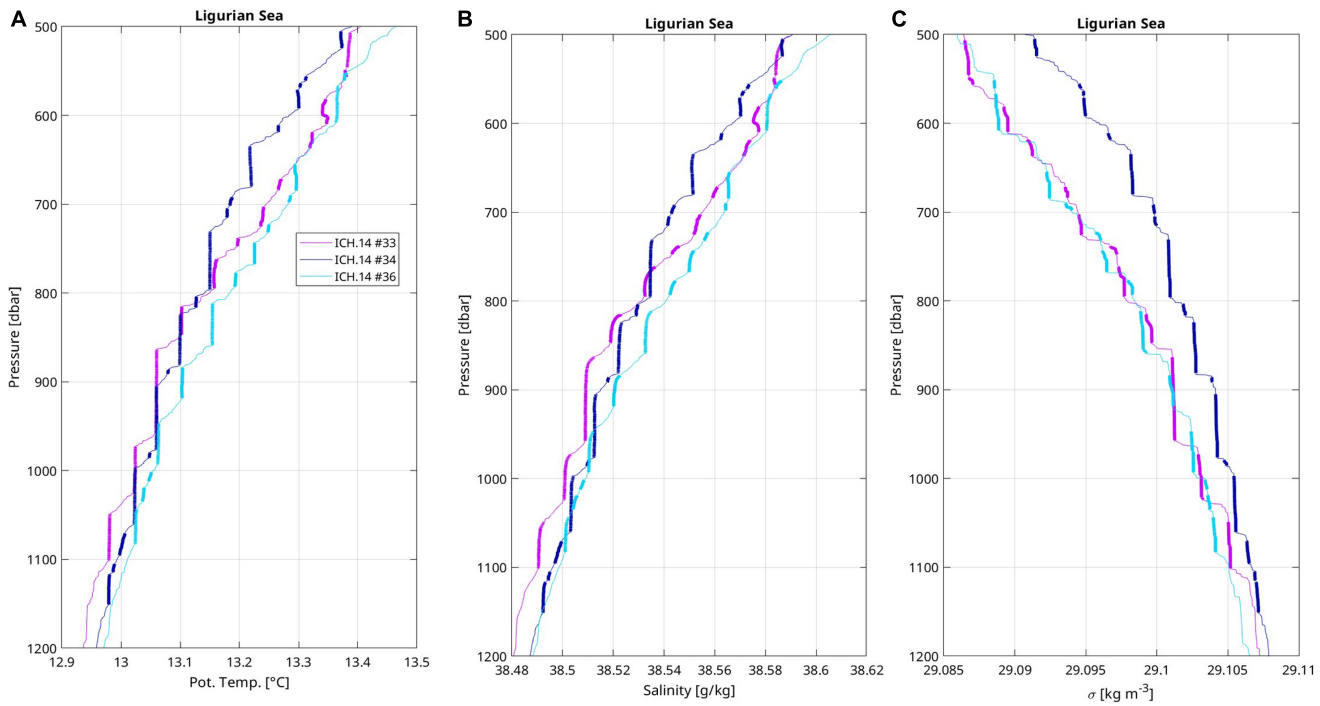

FIGURE 4 | Vertical profiles in staircases of **(A)** potential temperature, **(B)** salinity, and **(C)** potential density of stations located in the Ligurian sea during ICHNUSSA 2014. Station numbers are indicated in the figure legend **(A)** and located on the map (**Figure 1**). Layers are emphasized by thick lines with weak vertical gradient segments.

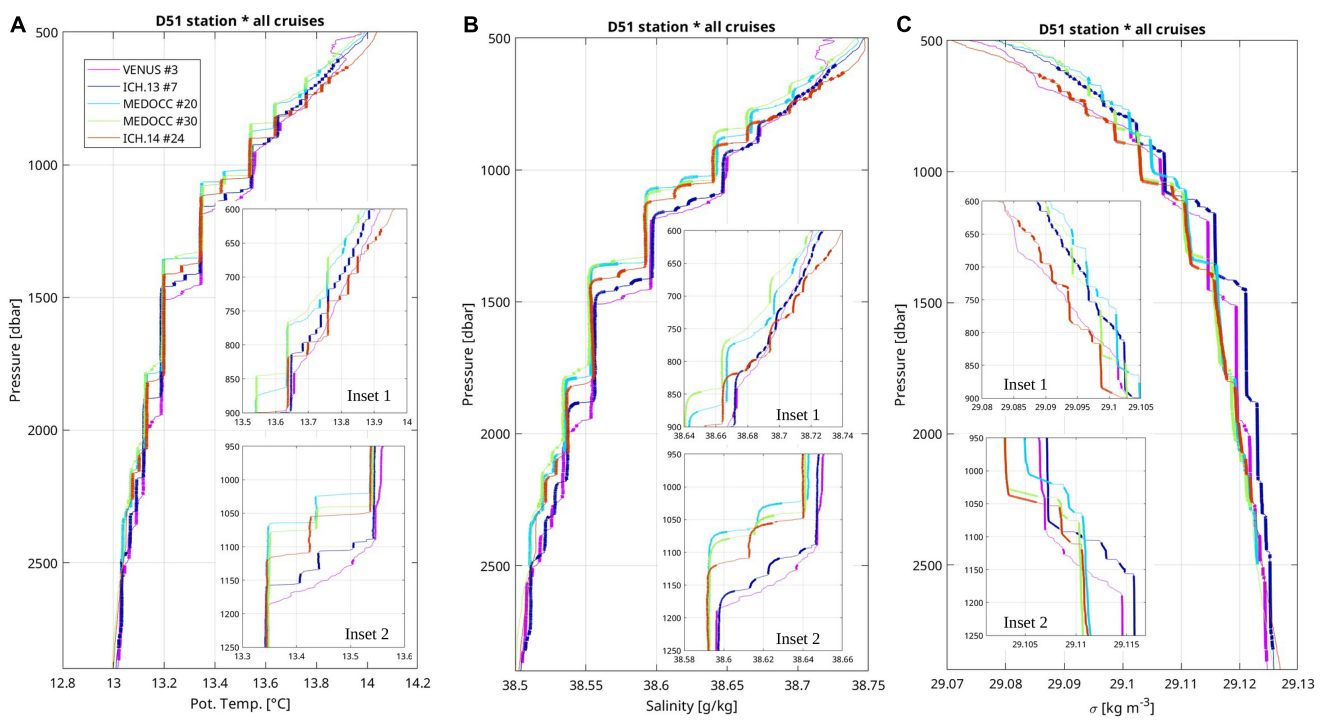

FIGURE 5 | Repeated vertical profiles of **(A)** potential temperature, **(B)** salinity, and **(C)** potential density at the D51 station located in the Tyrrhenian sea during four cruises in 2013–2014. Cruise names are indicated in the legend. Note that two realizations were done during the MEDOCC 2014 spring cruise. The D51 station is located on the map (**Figure 1**). Layers are emphasized by thick lines with weak vertical gradient segments. Insets 1 and 2 shows enlargements of the profile.

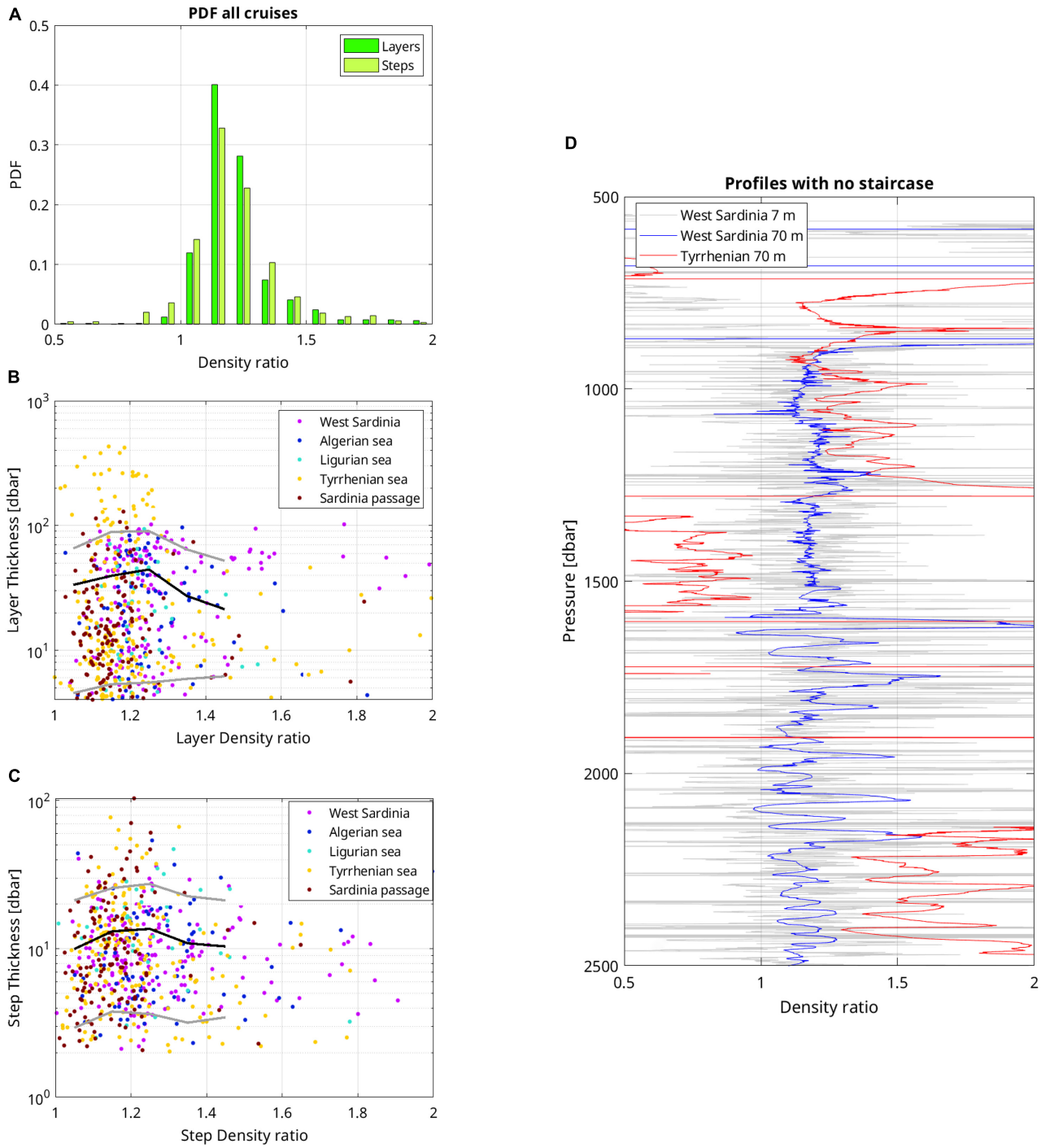

FIGURE 6 | Properties associated with density ratios R_ρ : **(A)** PDF of R_ρ for layers and steps, **(B)** relationship between layer thickness (log scale) and R_ρ by region (dots) with the overall mean (black line) and 10th- and 90th-percentile (gray lines) for bins having at least 30 members, **(C)** same as **(B)** for step thickness, **(D)** examples from VENUS 2013 cruise of density ratio profiles from two selected stations showing no staircase: sta. #12 (west Sardinia) along the Minorca-Sardinia transect, and sta. #21 in the southern Tyrrhenian (magenta numbers on **Figure 1**). The calculation of the R_ρ -profile is done with two depth intervals (7 m and 70 m).

ICH. 14 #14) and may be the sign of lateral intrusions as observed by Taillandier et al. (2020).

There is no indication of a clear relationship between step or layer thicknesses and density ratios (**Figures 6B,C**). The mean thickness per density ratio bin (black line) is rather flat, with small maxima around density ratios of 1.2–1.25. The 90th percentile of layer thickness (gray line) has a more pronounced maximum than that of step thickness due to the thick layers of

TABLE 2 | Regionally averaged characteristics of steps and layers with $1 < R_\rho < 1.5$.

	Sardino-Balearic Sea	Algerian Sea	Ligurian Sea	Tyrrhenian Sea	Sardinia Channel	Western Mediterranean
Averaged thickness [m] steps layers	1136	1130	1628	1357	1323	1238
Averaged ΔT [$\times 10^{-2}$°C] steps layers	3.56.5	2.44.6	3.25.9	3.77.0	2.95.6	3.36.2
Averaged ΔS [$\times 10^{-3}$ (psu)] steps layers	8.415	5.711	7.514	9.117	7.514	8.015
Averaged R_ρ steps layers	1.231.23	1.241.23	1.231.23	1.191.18	1.151.15	1.201.20
Averaged N [$\times 10^{-3}$ s^{-1}] step layer	0.251.7	0.231.3	0.231.2	0.251.9	0.221.1	0.241.6
Number of steps layers	153155	7074	3536	188199	125126	571590

the Tyrrhenian Sea. Nearly all (92%) of the largest thicknesses (layers > 100 m) have a R_ρ between 1 and 1.3. For a given density ratio, a large range of thicknesses are reached, and conversely a given thickness is found over a large range of density ratios. The absence of clear trend between thickness and density ratio may be attributed to several factors. First, the range of density ratio maybe too narrow to clearly exhibit a trend. This dataset has too few points to form any reliable mean in the range $1.5 < R_\rho < 2$. The large-scale background vertical profile of density ratio for profiles without staircase typically varies between 1.2 and 1.4 in the upper 2000 m, and up to 1.5 in the deep layers of the Tyrrhenian Sea (**Figure 6D**, blue and red lines). We cannot infer from this dataset what would be the step/layer thicknesses of staircases having a large-scale initial R_ρ larger than 1.5. However, we do observe some thicknesses with density ratios above 1.5. Second, the observed scatter may be explained by finestructure contamination: The calculation of the vertical profile of R_ρ using two different vertical intervals (7 m and 70 m) on profiles without staircase at the moment of the cruise illustrates that the shorter the interval, the larger the R_ρ range (**Figure 6D**). Thus, shorter steps and layers will exhibit more variability in their R_ρ. Third, another part of the scatter is related to the staircase formation itself. Recent direct numerical simulations (DNS) of oceanic salt fingering showed that, with a fixed background density ratio of 1.2, staircases develop with steps having a density ratio mostly contained in the range 1.5–1.8 (Yang et al., 2020). Despite DNS cannot reproduce large domains and the exact realism of oceanic conditions, it is interesting to note that the process of staircase formation changes the density ratio even when the large-scale density ratio is perfectly controlled. This DNS result is consistent with Radko (2005)'s equilibrium theory of staircases: starting from a background density ratio favourable to double-diffusive instability, staircases will develop steps and layers over few years; layers then progressively merge, increasing their thickness and the density ratio of steps, until an equilibrium is reached. For instance, for a starting background density ratio of 1.2, the density ratio of steps is expected reach 1.7 at the equilibrium, which can take decades (Radko, 2005; Radko et al., 2014). In the meantime, the density ratio of steps is expected to cover the range 1.2–1.7. Thus, the observed scatter may be a sign that staircases have not reached an equilibrium state.

Dissipation Rates of Steps and Layers

The distributions of kinetic energy dissipation rates ε of steps and layers are similar: 89% (resp. 82%) of the layers (resp. steps) have a low ε ranging between 3×10^{-11} and 3×10^{-10} W kg^{-1} (**Figure 7A**). The mean dissipation rate over all steps is equal to that of layers 1.2×10^{-10} W kg^{-1}. Low values of ε in staircase environments are a sign that layers are not produced by mechanical turbulence. It is in agreement with observations of staircases in other areas (Gregg and Sanford, 1987; St. Laurent and Schmitt, 1999; Radko et al., 2014). Since ε is usually weak in the stratified steps, the turbulence intensity Re_b is low: 57% of the steps have a Re_b less than 30 and 76% less than 100 (**Figure 7B**). Those low values found at interfaces are in agreement with previous findings when staircases are attributed to pure salt fingering processes ($Re_b < 30$) or salt fingering in presence of very weak mechanical turbulence (Gregg, 1988; Inoue et al., 2007). Only the Ligurian sea showed slightly enhanced ε, with averaged dissipation rates five times as large as in other regions (**Table 3** for steps, row 7; see also Ferron et al., 2017, **Figures 1B**, **3A**).

Contrastingly, the distribution of temperature variance dissipation rates χ of layers strongly differs from that of steps: 76% of the layers have a χ smaller than 5×10^{-11}°K^2 s^{-1} while 83% of the steps have a χ larger than this value (**Figure 7C**). Such a difference was also noticed by Schmitt et al. (2005) for staircases in the subtropical thermocline of the western Atlantic. The mean χ over all steps is 16 times larger than the mean over all layers (mean for steps is 1.7×10^{-9}°K^2 s^{-1}). Gregg and Sanford (1987) found a mean χ for both steps and layers larger by two orders of magnitude than for our dataset, but they observed nearly the same χ-ratio between steps and layers (factor of 19 for their dataset, vs. 16 here). Thermal variance dissipation rates χ observed in the steps of staircases is above typical values for Mediterranean regions deeper than 500 m, with weak ε, for which χ is usually smaller than 1×10^{-10}°K^2 s^{-1}. However, those large χ values occur in unusually large temperature gradients. Large-scale vertical temperature gradients below 500 m are typically smaller than 1×10^{-3}°K m^{-1}, while 80% of the staircase steps have a mean gradient larger than this value. In regions outside of staircases (but deeper than 150 m), χ increases with the vertical temperature gradient (**Figure 7D**, gray dots and black linear fit). It is thus not surprising to observe large values in the steps since

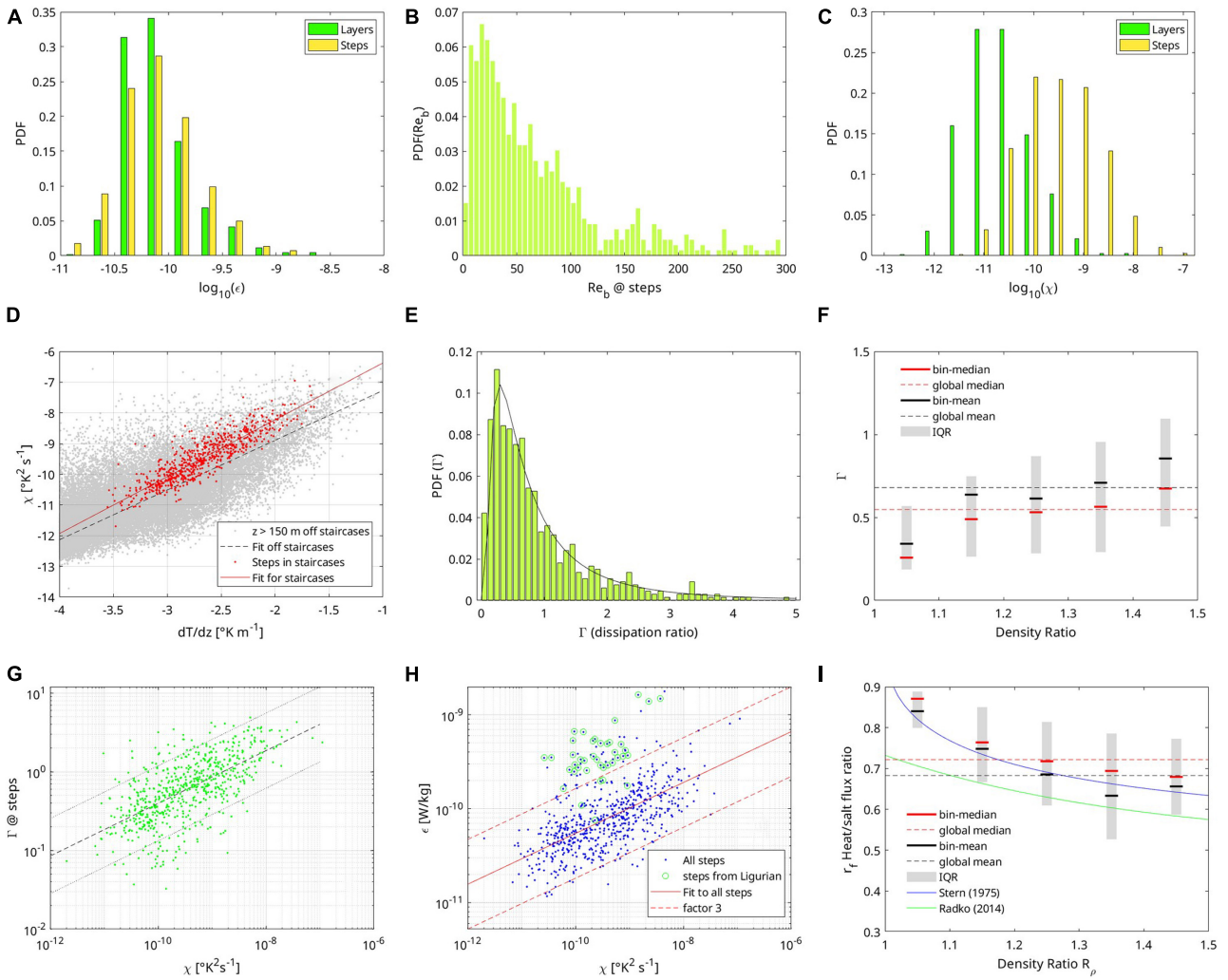

FIGURE 7 | (A) PDF of kinetic energy dissipation rates ε (units W kg^{-1}) for steps (yellow) and layers (green), **(B)** PDF of turbulence intensity Re_b for steps, **(C)** PDF of temperature variance dissipation rates χ ($°K^2\ s^{-1}$) for steps (yellow) and layers (green), **(D)** distribution of χ as a function of the vertical temperature gradient θ_z for regions without any staircase deeper than 150 m (gray dots with dashed black linear fit) and for the steps of staircases (red dots with dark red linear fit), **(E)** PDF of observed dissipation ratio Γ (bars) for steps with its lognormal fit (black line), **(F)** Γ per density ratio (R_ρ) bin with the median (red line) and mean (black line) for each bin and the global median (red dashed) and mean (black dashed) for bins having at least 30 steps, the interquartile range (IQR, 50% of the data, gray bars) shows the scatter of the data per bin, **(G)** Γ vs. χ for steps (green dots) with a fit in the loglog phase space (black dashed) and a factor of 3 range from the fit (dotted lines), **(H)** ε vs. χ for steps (all steps: blue dots; Ligurian: green circles) with a fit in the loglog phase space (red solid line) and a factor of 3 range (red dotted lines), **(I)** same as **(F)** for the heat to salt buoyancy-flux ratio r_f vs. R_ρ, with the Stern (1975) relationship (blue line).

they contain large temperature gradient. In the steps, χ follows a similar increase with temperature gradients (**Figure 7D**, red dots and red linear fit). But for a given temperature gradient in the typical observed range 1–10 × 10^{-3}°K m^{-1}, χ tends to be larger by a factor 3–4 when located in a staircase step than when there is no step.

Dissipation ratios Γ follow a lognormal distribution in agreement with previous findings (Oakey, 1985; Hamilton et al., 1993; **Figure 7E**). The goodness-of-fit as estimated from the Kolmogorov–Smirnov test (Massey, 1951; Press et al., 1992), shows that, with a probability-value of 0.90, the null hypothesis that the observed Γ-distribution follows a lognormal distribution cannot be rejected, as the probability-value is above the significance level of 0.05. The mean (resp. median) of Γ is 0.68 (resp. 0.55) for density ratios R_ρ in the range 1–1.5, with a lowest quartile at 0.19 and highest quartile at 1.1 (**Figure 7F**, only bins having at least 30 steps are plotted). Mean and median values of Γ increase with R_ρ as noticed in other studies (Hamilton et al., 1989, their Figure 3). For staircases below a Meddy (Mediterranean eddy in the Atlantic) with a similar R_ρ of 1.2-1.3 as found here on average, Hamilton et al. (1993) reported a median of 0.58, a lower quartile of 0.3, and upper quartile of 0.8. Our distribution shows a somewhat larger variance which may be attributed to the absence of data smoothing here (Hamilton et al., 1993, used 15 m-smoothed version of Γ calculated from 15 m-smoothed variables whereas our Γ is simply calculated

from variables estimated on step thicknesses, 77% of the step thicknesses being lower than 15 m). The distribution of Γ vs. R_ρ of this dataset is consistent with observations done in the North Atlantic Tracer Release Experiment (NATRE) in regions favorable to salt-fingering and for Richardson numbers larger than 1 (St. Laurent and Schmitt, 1999).

An increase of Γ is observed as a function of both increasing χ (**Figure 7G**) and dθ/dz, as χ and dθ/dz were shown to be related (**Figure 7D**). Linear fit in the loglog phase space shows that the Γ-estimates based on the fitted relationship $\Gamma = 10^a\ \chi^b$, where $a = 2.75$ and $b = 0.32$, predicts 90% (resp. 79%) of the observed Γ within a factor of 3 (resp. 2) for R_ρ in the range 1–1.5. In the same approach, ε tend to increase with χ (**Figure 7H**). The fitted relationship $\varepsilon = 10^a\ \chi^b$, where $a = -7.55$ and $b = 0.27$, predicts 91% (resp. 79%) of the observed ε within a factor of 3 (resp. 2) for R_ρ in the range 1-1.5. Most of (80%) ε stepping away from the fitted line by a factor larger than 3 belong to the Ligurian Sea (**Figure 7H**, green circles). Removing steps from the Ligurian Sea does not change the fit significantly ($a = 0.28$, $b = -7.48$; 92% of the observed ε within a factor 3, 84% within a factor of 2) since they only represent 4.5% of the steps.

The mean heat to salt buoyancy flux ratio r_f over all steps is estimated to 0.68 (median 0.72) for the density ratio range 1-1.5 (**Figure 7I**). Steps with abnormally large Γ were excluded in the next calculations (2% of the steps with $\Gamma > 5$). This flux ratio decreases from a mean of 0.84 (median of 0.87) to 0.66 (median of 0.68) as the density ratio increases from 1 to 1.5 (only bins with at least 30 steps are considered). The dependence of the flux ratio to R_ρ is consistent with experiments from McDougall and Taylor (1984) at those low R_ρ . The median flux ratio per density ratio bin is also consistent with the Stern (1975) estimates of the flux ratio of growing fingers (**Figure 7I**, black mean and blue line). The mean-binned flux ratio is 0.1 larger than the recently derived expression from a fit to DNS results (**Figure 7I**, green line from Radko and Smith, 2012). Observations from NATRE also exhibited the same decrease range (see St. Laurent and Schmitt, 1999, their Figure 10). The mean-binned heat to salt diffusivity ratio K_T/K_S decreases from 0.79 at R_ρ = 1.05 to 0.45 at R_ρ = 1.45. This decreasing trend is consistent with that observed at NATRE (St. Laurent and Schmitt, 1999) and from simulations (Stern et al., 2001). The averaged diffusivity ratio over all steps is 0.54. The mean diffusivity over all steps is 6.7×10^{-5} m^2 s^{-1} for temperature and 12.0×10^{-5} m^2 s^{-1} for salt. More interestingly, the regional-mean diffusivity varies from 3.6×10^{-5} m^2 s^{-1} (Ligurian Sea) to 9.8×10^{-5} m^2 s^{-1} (Tyrrhenian Sea) for temperature, and from 9.4×10^{-5} m^2 s^{-1} (Algerian Sea) to 20×10^{-5} m^2 s^{-1} (Ligurian Sea) for salt (**Table 3**, row K_T and K_S). Diffusivities from the Algerian Sea are consistent with those of the nearby Sardino-Balearic Sea. Diffusivities from the Sardinia Channel, which connects the Algerian Sea to the Tyrrhenian Sea, are midway between those of the two connected seas. Finally, we can note that those eddy diffusivities induced by salt-fingering are 2.5–5 times larger than what mechanical turbulence would produce given the weak turbulent kinetic energy dissipation rates, except for the Ligurian Sea where the opposite is found due to the larger levels of mechanical turbulence (**Table 3**, row K^{turb}).

DISCUSSION

Heat, Salt and Buoyancy Fluxes

From repeated zonal CTD transects in the Algerian Sea in 2006, 2008, and 2010, B14 noticed consistent staircase structures from about 600 to 1400 m. Below the staircases, in a transition region, they observed a coherent increase in temperature and salinity among the years and at all stations from the base of the staircases

TABLE 3 | Salt fingering properties with regional averaged estimates of temperature (K_T) and salt (K_S) eddy diffusivities, temperature flux (F_T), salt flux (F_S), buoyancy flux (J_b), kinetic energy dissipation rate (ε), flux ratio (r), heat and salt transfers.

	Sardino-Balearic Sea	Algerian Sea	Ligurian Sea	Tyrrhenian Sea	Sardinia Channel	Western Mediterranean
K_T [× 10^{-5} m s^{-2}]	5.0	5.1	3.6	9.8	7.8	6.3
K_S [× 10^{-5} m s^{-2}]	9.5	9.4	20	16	12	12
F_T [× 10^{-8}°C m s^{-1}]	−15.2 ± 11%	−9.4 ± 16%	−6.3 ± 19%	−14.0 ± 10%	−16.1 ± 11%	−11.9/−12 ± 8%
F_S [× 10^{-8} (psu) m s^{-1}]	−5.9 ± 10%	−3.8 ± 14%	−7.0 ± 13%	−6.0 ± 9%	−5.9 ± 10%	−5.0/−4.9 ± 7%
J_b [× 10^{-11} W kg^{-1}]	−10 ± 4%	−7.5 ± 5%	−38 ± 6%	−12 ± 4%	−8.1 ± 5%	−10.8/−9.5 ± 2%
ε [× 10^{-11} W kg^{-1}]	10 ± 3%	7.5 ± 5%	38 ± 6%	13 ± 3%	8.2 ± 6%	−11/−9.6 ± 2%
Γ	0.64	0.56	0.11	0.57	0.64	
Area max/min [× 10^6 m^2]	40,000/20,000	90,000/45,000	10,000/0	50,000/25,000	10,000/0	200,00090,000
Heat transfer [GW = × 10^9 W]	−26/−13 ± 11%	−36/−18 ± 16%	−2.7/0 ± 19%	−30/−15 ± 10%	−7.0/0 ± 11%	−103/−46 ± 8%
Salt transfer [× 10^3 kg s^{-1}]	−2.4/−1.2 ± 10%	−3.5/−1.7 ± 14%	−0.7/0 ± 13%	−3.1/−1.5 ± 9%	−0.6/0 ± 10%	−10.3/−4.5 ± 7%
Staircase depth range [m]	500–1300	400–1300	500–1200	600–2800	700–1200	
Number of steps	153	70	35	188	125	571

Quantities were calculated from steps in staircases. Negative signs indicate downward fluxes. Each region extends over an estimated maximum and minimum area (row 9) of salt-fingering activity used to infer the global averaged fluxes (weighted by max/min area) at the scale of the northwestern Mediterranean sea (last column). Maximum areas are delineated by the dashed-dotted blue lines on ***Figure 1****. Depth range of staircases and number of steps are given for each sub-region. Note that only steps with density ratio between 1 and 1.5 were considered (82% of the total amount of staircase steps). Uncertainties appearing in this table were computed from the only contribution of lognormally distributed errors in χ and ε, additional errors exist (see text).*

to 2300 m, below which new deep waters formed in 2006 spread. Since the transition region was isolated and not ventilated by significant convection events between 2008 and 2010, B14 assumed that the heat and salt convergence in the transition region was only due to the activity of salt finger processes. With those reasonable assumptions, they computed the heat and salt fluxes necessary to warm and salinify the transition region within 2 years. They found a downward flux $F_S^{08-10} = -5.35 \times 10^{-8}$ (psu) m s^{-1} for salt and $F_T^{08-10Alg} = -12.4 \times 10^{-8}$°C m s^{-1} for heat (a negative sign indicate a downward flux). Consequently, their buoyancy flux ratio is $r_f^{08-10Alg} = 0.74$. The superscript 08–10Alg means that the numbers stands as an average over 2008–2010 for the Algerian Sea. Those downward fluxes imply, for the steps, an eddy diffusivity $K_S^{08-10} = 3.7 \times 10^{-5}$ m^2 s^{-1} for salt and $K_T^{08-10Alg} = 2 \times 10^{-5}$ m^2 s^{-1} for temperature.

For comparison, we extracted from our dataset the profiles with steps and layers located in the Algerian Sea. They were used to compute the fluxes of heat and salt following the section "Summary of the Method". Note that our method is fully independent from that of B14. B14 observed a bulk increase of heat and salt content to calculate the needed heat and salt fluxes and the eddy diffusivities. In our study, we measure the eddy diffusivities with the microstructure and finestructure to calculate the implied downward fluxes.

We found fluxes of $F_S^{13-14Alg} = <-K_S \times dS/dz>_{steps} = -3.8\times10^{-8}$ (psu) m s^{-1} for salt and $F_T^{13-14Alg} = <-K_T \times dT/dz>_{steps} = -9.4 \times 10^{-8}$°C m s^{-1} for heat. The superscript 13–14Alg remind the reader that the numbers stand as an estimate from profiles measured over 2013–2014 for the Algerian Sea. Our fluxes are lower than B14 fluxes by 24% for heat and 29% for salt. Consequently, our buoyancy flux ratio is almost the same, $r_f^{13-14Alg} = 0.73$. Our estimates remain relatively consistent with B14 despite the period covered is not the same and the area covered by B14 is larger as it extends to the western part of the Algerian Sea. B14 produced fluxes averaged over 2 years while our estimates come from snapshots of staircases. However, consistency between B14 and our estimates is somewhat expected despite those differences. Indeed, B14 reported that staircases had a significant coherence between profiles distributed zonally as we observed for the staircases of the Tyrrhenian sea in this dataset. Thus, the location of our profiles confined to the eastern Algerian Sea may be less than an issue. Lateral coherence of staircases is commonly reported (Schmitt et al., 1987; Buffett et al., 2017). The period covered is not the same and certainly adds some variability, but here too, the existence of staircases over long period of time (several years, sometimes decades) is a usual observation that tend to introduce some time consistency between estimates. The larger source of differences may rather come from the limited number of profiles (five profiles with a total of 70 steps) in the Algerian Sea to make robust statistics (convergence of the mean). Noting that southern and northern regions of the Algerian Sea are connected by barotropic cyclonic gyres (Testor et al., 2005), we included the staircase profiles west of Sardinia, which adds 14 profiles with 153 steps to the former 70 steps (**Table 3**, last row). The downward heat flux associated with the Sardino-Algerian Sea increases to $F_T^{13-14Sard-Alg} = -13.2 \times 10^{-8}$°C m s^{-1} and the salt flux to $F_S^{13-14SardAlg} = -5.1 \times 10^{-8}$ (psu) m s^{-1}. The observed increase is due to the larger downward fluxes of the Sardinia-Balearic Plain (**Table 3**, column 2 and 3). Those latter estimates are within 6% of B14 estimates and give an idea of the sensitivity of the estimates and averaging. In this regard, estimates from the Ligurian Sea, which counts too few profiles with staircases, have probably the largest uncertainties from all regions.

The same calculation of fluxes were done for each region (**Table 3**). The Tyrrhenian Sea and the Sardinia Channel have slightly larger fluxes than other regions, all fluxes holding within a factor of two. A mean flux for the western Mediterranean sea can be formed weighting each regional flux with a corresponding area based on present and past observations. To take time variability into account, a minimum and maximum area of staircase activity was ascribed to each region (**Table 3**, row 9; maximum areas are delineated by the dashed-dotted blue lines on **Figure 1**), the Tyrrhenian and the Algerian seas showing the longest space-time staircase coherence. Bounding the area of staircases in the Ligurian Sea is the most uncertain due to a lack of staircase observations in space and time.

The derived fluxes rely on correct estimates of the dissipation rates χ and ε. A worse case scenario is to assume that individual estimates of χ and ε are blended with lognormally distributed errors, so that individual estimates are, on average, distant from the true value by a factor of 6 for χ and 3 for ε. The scatter is larger on χ since it requires the knowledge of both ε and the temperature spectra in the dissipation range, which does not necessarily resolve the spectral roll off. A first average of individual values of χ and ε is made on each step, which reduces the scatter to an average factor of 3.7 to 2 for χ, and 1.7 to 1.3 for ε, for typical step thicknesses increasing from 3 to 15 m (3/4 of the steps). Regional estimates of F_T and F_S are derived from averages of fluxes calculated at each step included in the region. The larger the cumulated thicknesses of steps in the region (which also depends on the number of available profiles), the smaller the error. The distribution of step thicknesses per region (**Figure 6C**) was used to propagate the errors in χ and ε to get the uncertainties in F_T and F_S per region (**Table 3**). Despite individual errors on χ and ε may be large in this worse case scenario, the final error on F_T and F_S are limited to 10-20% due to the "heavy" averaging.

Additional uncertainties can arise from processing issues and from the contribution of unobserved regions (representativity error). Processing issues cover the method used to locate the boundaries between layers and steps, which can somewhat influence the estimates of step and layer thicknesses and the determination of property gradients for instance. Another 10% of uncertainty could be ascribe to this sensitivity. The representativity of the data is another issue. For instance, we have no microstructure profile in the western part of the Algerian Sea although we know that staircases exist there (B14). The impact of missing microstructure observations due to unobserved regions or unobserved periods should not strongly change the results of **Table 3**. As already argued, staircases are often coherent over long time and long distances. The best example of the robustness of our estimates is evidenced in **Table 3**: from one

region to the other, regional fluxes remain within a factor of two despite regions are geographically distant with a variety of dynamical processes present in each basin (eddies, internal waves, surface forcings). However, for the Ligurian Sea, which has too few observations of staircases available and the largest epsilon as a result of intense dynamical processes (waves, eddies, and current), the uncertainty is larger but the area of staircase activity is smaller than in other regions.

Regional heat and salt transfer rates from intermediate depths of the saline and warm LIW to deep water masses are derived from the combination of regional fluxes and area over which staircases extend (heat transfer rate = $\rho_0\ C_p\ F_T\ A$, salt transfer rate = $\rho_0\ F_S\ A$, where A is the horizontal area of staircases, $\rho_0 = 1027$ kg m^{-3}, $C_p = 4200$ J°K^{-1} kg^{-1} is the heat capacity of seawater). The lower and upper area estimates of staircase activity give a range for the transfer rates (**Table 3**, row 10 and 11). On short timescale, such regional heat and salt transfers can increase the local temperature of a 1000 m-thick water column by 0.002–0.005°C over a year, and the local salinity by 0.001–0.002. These downward heat and salt inputs are then advected in the various sub-basins. Summing the minimum and maximum transfer rates associated with each region leads to an upper and a lower estimate of the staircase heat and salt transfers over the whole western Mediterranean Sea. The transfer rates amounts to 46–103 GW (1GW = 1×10^9 W) for heat, and 4.5–10.3 $\times$ 10^3 kg s^{-1} for salt over the whole western Mediterranean Sea (**Table 3**). The largest contributors are the Algerian and Sardino-Balearic seas and the Tyrrhenian sea for which staircases extend over large areas. On long timescales and at the scale of the whole western Mediterranean, such transfer rates are able to warm all waters from 1000 to 2000 m by 0.0007-0.0016°C per year and to increase their salinity by 0.0003-0.0007 per year (volume from 1000 to 2000 m: 4.8×10^{14} m^3).

As a consistency check, it is interesting to compare the averaged kinetic energy dissipation rate with the rate of potential energy release associated with double diffusion fluxes. In pure salt fingering, the release of potential energy by salt fingering is balanced by the dissipation rate of turbulent kinetic energy. The potential energy release rate or buoyancy flux, reads: $J_b = -g(\alpha F_T - \beta F_S)$. Note that the relative errors on J_b induced by errors in dissipation rates are smaller than those on F_T and F_S since errors on F_T and F_S are correlated. In all regions, the dissipation rate ε is almost equal to the buoyancy flux, which is expected since the salt fingering model is based on this equality.

More instructive is the regional estimate of the dissipation ratio. In all regions, except the Ligurian Sea, we observe an averaged Γ of 0.56–0.64. In the Ligurian Sea, Γ strongly decreases toward 0.11, a value typical of mechanical turbulence. The Ligurian Sea has also the largest regionally averaged turbulent intensity Re_b of 340 while other regions are between 75 and 150. Those observations confirm that Ligurian staircases occur in an environment marked by mechanical turbulence, though not sufficiently energetic enough to suppress staircase formation. Other regions are closer to pure salt-fingering environments.

Finally, this study provide us with one more piece of the puzzle for the fate of western Mediterranean sea deep waters. Following B14, we assume that most heat and salt convergences from salt-fingering fluxes occur between 1000 and 2000 m. In this depth range, the mean geothermal flux of 110 mW m^{-2} over the western Mediterranean (Ferron et al., 2017) brings about 20 GW. Thus, salt fingering brings 3-6 times as much heat to bottom waters as the geothermal heat flux. The fluxes associated with mechanical turbulence need also to be considered. Ferron et al. (2017) found that the geothermal heat flux was three times as efficient to raise the buoyancy as the mechanical turbulence. Indeed, mechanical turbulence increases the buoyancy with its turbulent heat fluxes on the one hand, but decreases the buoyancy with the turbulent salt fluxes on the other hand. A compensation that does not hold for geothermal heating. Thus, the separate contributions of heat and salt content generated by mechanical turbulence over the whole western Mediterranean need to be quantified. For that purpose, the divergence of mechanical turbulent fluxes were computed over the whole western Mediterranean Sea between 1000 and 2000 m. Since mechanical turbulence occurs everywhere, four areas were delimited covering larger areas than those attributed to the staircase activity: the boundary layer that conveys waters from the Ligurian Sea to the Balearic Sea with the Liguro-Provençal current (**Figure 1**, green dashed line), the region from the Algerian Sea to the boundary layer (**Figure 1**, red dashed line), the Tyrrhenian Sea (**Figure 1**, purple dashed line), and the Sardinia Channel (blue dashed-dotted line). Areas are given in **Table 4**. All dissipation profiles with and without staircase were considered for mechanical mixing. When staircases occurred at 1000 m or 2000 m, an arbitrary $p_{ds} = 10\%$ of the dissipation rate was accounted for participating to mechanical turbulence, the remaining $1 - p_{ds} = 90\%$ being ascribed to salt fingering process. This was motivated by the observation that most staircases occur in environments close to pure-salt fingering, as noted previously. Over the whole western Mediterranean Sea, we find that mechanical turbulence produces a heat convergence of 106 GW and a salt convergence of 9.2×10^3 kg s^{-1} between 1000 and 2000 m (**Table 4**). This result is not highly sensitive to the choice of p_{ds}. Increasing p_{ds} to 30% instead of 10% would increase the heat and salt convergence by 14% and 10%, respectively. The largest uncertainty comes from the area attributed to the boundary layer which was set, for consistency, to have the same enhanced turbulent mixing as the Ligurian Sea. The boundary layer accounts for 56% of the heat convergence and 71% of the salt convergence due to mechanical mixing, while it represents only 16% of the total western Mediterranean area. Increasing (resp. decreasing) the boundary layer area of enhanced mechanical mixing by 50% increases (resp. decreases) the heat convergence by 25% (range 80–133 GW) and salt convergence by 34% (range 6.2–12.3 $\times$ 10^3 kg s^{-1}) over the whole western Mediterranean Sea. This gives a reasonable idea of the uncertainty in heat and salt convergences due to an over- or under-estimation of the area of enhanced mechanical mixing in the whole western basin.

To summarize, taking the estimated ranges, geothermal heating, salt-fingering and mechanical mixing generates a heat convergence between 146 and 256 GW and a salt convergence between 11 and 23 $\times$ 10^3 kg s^{-1}. If, for a long period, there was no net injection of new deep waters, such convergences between 1000 and 2000 m would lead to an increase in temperature

TABLE 4 | Mechanical turbulence estimates of the difference in temperature flux ΔF_T, and in the salt flux ΔF_S, between 1000 and 2000 m.

	From Algerian Sea to northern boundary layer	Boundary layer (Ligurian to Balearic Sea)	Tyrrhenian Sea	Sardinia Channel	Western Mediterranean
ΔF_T [$\times 10^{-8}$°C m s^{-1}]	1.9	18.3	4	20.9	
ΔF_S [$\times 10^{-8}$ (psu) m s^{-1}]	0.5	8.5	0.9	5.4	
HT^{turb} [GW = $\times 10^9$ W]	23	59	16	9	106
HS^{turb} [$\times 10^3$ kg s^{-1}]	1.3	6.5	0.8	0.6	9.2
Area [$\times 10^6$ m^2]	280000	75000	90000	10000	455000

*Convergences of heat (HT^{turb}) and salt (HS^{turb}) between 1000 and 2000 m. The area ascribed to each region is given in this table and appears as a dotted-colored lines on **Figure 1**.*

of 0.002–0.004°C per year, and an increase in salt of 0.0007–0.0016 per year over the whole western basin. For comparison, Marty and Chiavérini (2010) found that temperature increased by 0.005°C per year and salinity by 0.0022 psu per year at 2000 m from repeated CTD in the Ligurian Sea from 1995 to 2005. For the same dataset, Borghini et al. (2014) noted that, for the 1995–2005 decade where there is little evidence for deep water formation in the western Mediterranean, the 1800–2000 m-deep water salinity and temperature increased at a rate of 0.0013–0.0041 per year and 0.0043–0.0057°C per year, respectively. Those numbers are relatively consistent with the heat and salt convergences we derived in this study in the absence of deep water formation, given the variability in the parameters (depth range of the estimates, period and representativity of estimates at the scale of the western basin).

In the last two decades, many episodes of deep convection were reported in the western basin, from which a yearly mean deep water formation rate of 0.3–0.9 Sv (1 Sv = 1 $\times$ 10^6 m^3 s^{-1}) was estimated (see Ferron et al., 2017, supporting information). This injection of deep water at depth forces an upwelling at the same mean rate over the basin. Noting that there is a mean 0.15 to 0.2°C (resp. 0.03–0.05) temperature (resp. salinity) difference between 1000 and 2000 m, a mean upwelling rate of 0.3–0.9 Sv induces a heat loss rate of 190–780 GW and a salt loss of 10 to 50 $\times$ 10^3 kg s^{-1} in this depth range. Thus, the addition of mechanical turbulence, salt-fingering, and geothermal inputs can balance the heat and salt loss produced by a 0.3–0.4 Sv mean upwelling rate. In case the upwelling is closer to 0.9 Sv, only 33% of the 780 GW heat loss and nearly 50% of the salt loss could be balance if we take the maximum convergence rates produced by mechanical turbulence and salt-fingering. The remaining heat and salt losses would produce, over a year, a 0.008°C temperature decrease and a 0.002 salinity decrease. Some interannual decrease may be temporarily seen in observations between 1000 and 2000 m, but the major long trend is an increase in heat and salt content due to the increasingly saltier and warmer new deep waters (Schroeder et al., 2016). Another complexity comes from the amount of deep water (say from 1000 to 2000 m in the deep basins) that is able to flow out of the Mediterranean through the Strait of Gibraltar. The larger this amount, the lower the heat and salt loss due to the upwelling of deep waters, since less amount of water has to upwell in the western basin through the 1000 m depth.

CONCLUSION

The numbers we derived for the western Mediterranean are of course indicative. Given the intensity of salt fingering fluxes relative to fluxes induced by mechanical turbulence, this study is one more work that points toward the necessity of taking salt fingering fluxes into account in numerical modeling of the ocean. Numerical models rarely take double diffusion processes into account despite they can induce heat, salt (and other properties) fluxes larger than those induced by mechanical turbulence over the large areas of staircase activity. The western Mediterranean Sea is a typical place where those fluxes are of importance due to the presence of the warm and salty LIW. There, double-diffusion produces heat and salt convergence as important as those induced by the mechanical mixing. Many other places in the world ocean are also subject to salt fingering or double-diffusive convection. Radko et al. (2014) recently proposed a parameterization that allows for the development of staircases in low resolution models, an effort that clearly needs to be pursued.

This study supports the need to strengthen observational efforts in the Mediterranean Sea in the future in order to reduce the uncertainties and to better document and understand the rapid evolution of heat and salt contents in relation with the climatic change. Oceanographers need to have good estimates of deep water formation rates, but we also need to improve our understanding of how much of these rates really represent a net mass transfer (Waldman et al., 2018). Finally, it is also clear that diapycnal fluxes need to be better constrained with microstructure and finestructure observations, in particular along boundaries.

DATA AVAILABILITY STATEMENT

The raw data supporting the conclusions of this article will be made available by the authors, without undue reservation. Data requests may be sent to the corresponding author.

AUTHOR CONTRIBUTIONS

BF, PB-A, KS, HB, and MB contributed to the data acquisition during cruises. BF processed the microstructure and finestructure data, performed the analysis, drafted the manuscript, and designed the figures. KS and MB involved in planning and

supervised the funding of the cruises. BF, PB-A, and YC supervised the funding of microstructure equipment. All authors provided critical feedback and helped shape the research, analysis and contributed to the final manuscript.

FUNDING

The microstructure profilers were funded by the French Agence Nationale de la Recherche (ANR) through grant ANR-JC05_50690 and by the French Institute for Marine Science (IFREMER). This project was funded by CNR-ISMAR, LOCEAN, LOPS, and the INSU-MISTRALS (Mediterranean Integrated STudies at Regional and Local Scales) program. BF was supported by the French National Centre for Scientific Research (CNRS). This study contributes to the HyMeX program (Hydrological cycle in the Mediterranean Experiment). Support was received from the European Commission – H2020 Framework Programme, JERICO NEXT through grant #654410. HB thanks the Royal Society and the Leverhulme Trust for supporting his involvement in this Mediterranean research.

ACKNOWLEDGMENTS

We thank all crew members of R/V Urania, Alberto Ribotti (CNR Oristano), and Stefania Sparnocchia (CNR ISMAR, Trieste) for their contribution to the organization of the ICHNUSSA and EMSO cruises, respectively. We also thank Stéphane Leizour for his useful technical assistance with VMPs all along the year and his implications in the cruise operations.

REFERENCES

Borghini, M., Bryden, H., Schroeder, K., Sparnocchia, S., and Vetrano, A. (2014). The Mediterranean is becoming saltier. *Ocean Sci.* 10, 693–700. doi: 10.5194/os-10-693-2014

Bouffard, D., and Boegman, L. (2013). A diapycnal diffusivity model for stratified environmental flows. *Dynam. Atmos. Oceans* 61–62, 14–34.

Bryden, H., Schroeder, K., Sparnocchia, S., Borghini, M., and Vetrano, A. (2014). Thermohaline staircases in the western Mediterranean Sea. *J. Mar. Res.* 72, 1–18.

Buffett, G. G., Krahmann, G., Klaeschen, D., Schroeder, K., Sallarès, V., Papenberg, C., et al. (2017). Seismic oceanography in the Tyrrhenian Sea: thermohaline staircases, eddies, and internal waves. *J. Geophys. Res.* 122, 8503–8523. doi: 10.1002/2017JC012726

Durante, S., Schroeder, K., Mazzei, L., Pierini, S., Borghini, M., and Sparnocchia, S. (2019). Permanent thermohaline staircases in the Tyrrhenian Sea. *Geophys. Res. Lett.* 46, 1562–1570. doi: 10.1029/2018GL081747

Ferron, B., Bouruet Aubertot, P., Cuypers, Y., Schroeder, K., and Borghini, M. (2017). How important are diapycnal mixing and geothermal heating for the deep circulation of the Western Mediterranean? *Geophys. Res. Lett.* 44, 7845–7854. doi: 10.1002/2017GL074169

Ferron, B., Kokoszka, F., Mercier, H., and Lherminier, P. (2014). Dissipation rate estimates from microstructure and finescale internal wave observations along the A25 Greenland–Portugal OVIDE line. *J. Atmos. Ocean. Technol.* 31, 2530–2543. doi: 10.1175/JTECH-D-14-00036.1

Goodman, L., Levine, E. R., and Lueck, R. G. (2006). On measuring the terms of the turbulent kinetic energy budget from an AUV. *J. Atmos. Oceanic Technol.* 23, 977–990. doi: 10.1175/JTECH1889.1

Gregg, M. C. (1988). "Mixing in the thermohaline staircase east of Barbados," in *Small Scale Turbulence and Mixing in the Ocean*, eds J. C. J. Nihoul and B. M. Jamart (Amsterdam: Elsevier), 453–470.

Gregg, M. C., and Sanford, T. B. (1987). Shear and turbulence in thermohaline staircase. *Deep Sea Res.* 34, 1689–1696.

Hamilton, J., Oakey, N. S., and Kelley, D. E. (1993). Salt-finger signatures in microstructure measurements. *J. Geophys. Res.* 98, 2453–2460.

Hamilton, J. M., Lewis, M. R., and Ruddick, B. R. (1989). Vertical fluxes of nitrate associated with salt fingers in the world's oceans. *J. Geophys. Res.* 94, 2137–2145.

Inoue, R., Yamazaki, H., Wolk, F., Kono, T., and Yoshida, J. (2007). An estimation of buoyancy flux for a mixture of turbulence and double diffusion. *J. Phys. Oceanogr.* 37, 611–625.

Johannessen, O. M., and Lee, O. S. (1974). A deep stepped thermo-haline structure in the Mediterranean. *Deep Sea Res. A* 21, 629–639. doi: 10.1016/0011-7471(74)90047-3

Krahmann, G. (1997). "Horizontal variability of thermohaline staircases in the western mediterranean, double-diffusive processes, 1996 summer study program," in *Geophysical Fluid Dynamics*, eds S. Meacham and D. Tucholke (Falmouth, MA: Woods Hole Oceanographic Institution), 331–347.

Marty, J. C., and Chiavérini, J. (2010). Hydrological changes in the Ligurian Sea (NW Mediterranean, DYFAMED site) during 1995–2007 and biogeochemical consequences. *Biogeosci. Discuss.* 7, 1377–1406.

Massey, F. J. (1951). The kolmogorov-smirnov test for goodness of fit. *J. Am. Stat. Assoc.* 46, 68–78. doi: 10.2307/2280095

McDougall, T. J., and Taylor, J. R. (1984). Flux measurements across a finger interface at low values of the stability ratio. *J. Mar. Res.* 42, 1–14.

Molcard, R., and Tait, R. I. (1977). "The steady state of the step structure in the Tyrrhenian Sea," in *A Voyage of Discovery*, ed. M. V. Angel (Amsterdam: Pergamon Press), 221–233.

Oakey, N. S. (1985). Statistics of mixing parameters in the upper ocean during JASIN phase 2. *J. Phys. Oceanogr.* 15, 1662–1675.

Osborn, T. R. (1980). Estimates of the local rate of vertical diffusion from dissipation measurements. *J. Phys. Oceanogr.* 10, 83–89. doi: 10.1175/1520-0485(1980)010<0083:EOTLRO>2.0.CO;2

Osborn, T. R., and Cox, C. S. (1972). Oceanic fine structure. *Geophys. Fluid Dyn.* 3, 321–345.

Press, W. H., Teukolshy, S. A., Vetterling, W. T., and Flannery, B. P. (1992). *Numerical Recipes in FORTRAN: The Art of Scientific Computing*. Cambridge, MA: Cambridge University Press, 963.

Radko, T. (2013). *Double-Diffusive Convection*. Cambridge, MA: Cambridge University Press, 344.

Radko, T. (2005). What determines the thickness of layers in a thermohaline staircase? *J. Fluid Mech.* 523, 79–98. doi: 10.1017/S0022112004002290

Radko, T., Bulters, A., Flanagan, J., and Campin, J. (2014). Double-diffusive recipes. Part 1: large-scale dynamics of thermohaline staircases. *J. Phys. Oceanogr.* 44, 1269–1284. doi: 10.1175/JPO-D-13-0155.1

Radko, T., and Smith, D. P. (2012). Equilibrium transport in double-diffusive convection. *J. Fluid Mech.* 692, 5–27. doi: 10.1017/jfm.2011.343

Schmitt, R. W., Ledwell, J. R., Montgomery, E. T., Polzin, K. L., and Toole, J. M. (2005). Enhanced diapycnal mixing by salt fingers in the thermocline of the tropical Atlantic. *Science* 308, 685–688. doi: 10.1126/science.1108678

Schmitt, R. W., Perkins, H., Boyd, J. D., and Stalcup, C. (1987). An investigation of the thermohaline staircase in the western tropical North Atlantic. *Deep Sea Res.* 34, 1655–1665.

Schroeder, K., Chiggiato, J., Bryden, H. L., Borghini, M., and Ismail, S. B. (2016). Abrupt climate shift in the Western Mediterranean Sea. *Nat. Sci. Rep.* 6:23009. doi: 10.1038/srep23009

Sommer, T., Carpenter, J. R., Schmid, M., Lueck, R. G., and Wüest, A. (2013). Revisiting microstructure sensor responses with implications for double-diffusive fluxes. *J. Atmos. Ocean. Technol.* 30, 1907–1923. doi: 10.1175/JTECH-D-12-00272.1

St. Laurent, L., and Schmitt, R. W. (1999). The contribution of salt fingers to vertical mixing in the North Atlantic tracer release experiment. *J. Phys. Oceanogr.* 29, 1404–1424. doi: 10.1175/1520-04851999029

Stern, M. E. (1975). *Ocean Circulation Physics*. Cambridge, MA: Academic Press.

Stern, M. E., Radko, T., and Simeonov, J. (2001). 3D salt fingers in an unbounded thermocline with application to the Central Ocean. *J. Mar. Res.* 59, 355–390.

Taillandier, V., Prieur, L., D'Ortenzio, F., Ribera d'Alcalà, M., and Pulido-Villena, E. (2020). Profiling float observation of thermohaline staircases in the western Mediterranean Sea and impact on nutrient fluxes. *Biogeosciences* 17, 3343–3366. doi: 10.5194/bg-17-3343-2020

Testor, P., Send, U., Gascard, J.-C., Millot, C., Taupier-Letage, I., and Béranger, K. (2005). The mean circulation of the southwestern Mediterranean Sea: algerian gyres. *J. Geophys. Res.* 110:C11017. doi: 10.1029/2004JC002861

Turner, J. S. (1967). Salt fingers across a density interface. *Deep-Sea Res. Oceanogr. Abstr.* 14, 599–611. doi: 10.1016/0011-7471(67)90066-6

Waldman, R., Brüggemann, N., Bosse, A., Spall, M., Somot, S., and Sevault, F. (2018). Overturning the Mediterranean thermohaline circulation. *Geophys. Res. Lett.* 45, 8407–8415. doi: 10.1029/2018GL078502

Yang, Y., Chen, W., Verzicco, R., and Lohse, D. (2020). Multiple states and transport properties of double-diffusive convection turbulence. *PNAS* 117, 14676–14681. doi: 10.1073/pnas.2005669117

Zodiatis, G., and Gasparini, G. P. (1996). Thermohaline staircase in the Tyrrhenian Sea. *Deep Sea Res.* 43, 655–678. doi: 10.1016/0967-0637(96)00032-5

Conflict of Interest: The authors declare that the research was conducted in the absence of any commercial or financial relationships that could be construed as a potential conflict of interest.

frontiers in Marine Science

ORIGINAL RESEARCH
published: 17 June 2021
doi: 10.3389/fmars.2021.672199

Pathways, Volume Transport, and Seasonal Variability of the Lower Deep Limb of the Pacific Meridional Overturning Circulation at the Yap-Mariana Junction

Jianing Wang[1,2,3], Fan Wang[1,2,3], Youyu Lu[4], Qiang Ma[1,2], Larry J. Pratt[5] and Zhixiang Zhang[1,2]*

[1] Key Laboratory of Ocean Circulation and Waves, Institute of Oceanology, Center for Ocean Mega-Science, Chinese Academy of Sciences, Qingdao, China, [2] Laboratory for Ocean and Climate Dynamics, Pilot National Laboratory for Marine Science and Technology, Qingdao, China, [3] College of Marine Science, University of Chinese Academy of Sciences, Beijing, China, [4] Bedford Institute of Oceanography, Fisheries and Oceans Canada, Dartmouth, NS, Canada, [5] Woods Hole Oceanographic Institution, Woods Hole, MA, United States

OPEN ACCESS

Edited by:
Vincenzo Artale,
Italian National Agency for New Technologies, Energy and Sustainable Economic Development (ENEA), Italy

Reviewed by:
Daigo Yanagimoto,
University of Tokyo, Japan
Adam Thomas Devlin,
The Chinese University of Hong Kong, China
Yeqiang Shu,
South China Sea Institute of Oceanology (CAS), China

***Correspondence:**
Fan Wang
fwang@qdio.ac.cn

Specialty section:
This article was submitted to Physical Oceanography, a section of the journal Frontiers in Marine Science

Received: 25 February 2021
Accepted: 27 April 2021
Published: 17 June 2021

Citation:
Wang J, Wang F, Lu Y, Ma Q, Pratt LJ and Zhang Z (2021) Pathways, Volume Transport, and Seasonal Variability of the Lower Deep Limb of the Pacific Meridional Overturning Circulation at the Yap-Mariana Junction. Front. Mar. Sci. 8:672199. doi: 10.3389/fmars.2021.672199

The lower deep branch of the Pacific Meridional Overturning Circulation (L-PMOC) is responsible for the deep-water transport from Antarctic to the North Pacific and is a key ingredient in the regulation of global climate through its influence on the storage and residence time of heat and carbon. At the Pacific Yap-Mariana Junction (YMJ), a major gateway for deep-water flowing into the Western Pacific Ocean, we deployed five moorings from 2018 to 2019 in the Eastern, Southern, and Northern Channels in order to explore the pathways and variability of L-PMOC. We have identified three main patterns for L-PMOC pathways. In Pattern 1, the L-PMOC intrudes into the YMJ from the East Mariana Basin (EMB) through the Eastern Channel and then flows northward into the West Mariana Basin (WMB) through the Northern Channel and southward into the West Caroline Basin (WCB) through the Southern Channel. In Pattern 2, the L-PMOC intrudes into the YMJ from both the WCB and the EMB and then flows into the WMB. In Pattern 3, the L-PMOC comes from the WCB and then flows into the EMB and WMB. The volume transports of L-PMOC through the Eastern, Southern, and Northern Channels all exhibit seasonality. During November–April (May–October), the flow pathway conforms to Pattern 1 (Patterns 2 and 3), and the mean and standard deviation of L-PMOC transports are -4.44 ± 1.26 (-0.30 ± 1.47), -0.96 ± 1.13 (1.75 ± 1.49), and 1.49 ± 1.31 (1.07 ± 1.10) Sv in the Eastern, Southern, and Northern Channels, respectively. Further analysis of numerical ocean modeling results demonstrates that L-PMOC transport at the YMJ is forced by a deep pressure gradient between two adjacent basins, which is mainly determined by the sea surface height (SSH) and water masses in the upper 2,000-m layer. The seasonal variability of L-PMOC transport is attributed to local Ekman pumping and westward-propagating Rossby waves. The L-PMOC transport greater than 3,500 m is closely linked to the wind forcing and the upper ocean processes.

Keywords: PMOC, mooring observations, seasonal variability, pathways, transport, Yap-Mariana Junction, Ekman pumping, Rossby waves

INTRODUCTION

The deep and bottom waters of the North Pacific Ocean have their origins in Antarctic and are carried by the northward lower deep branch of the Pacific Meridional Overturning Circulation (L-PMOC), also referred to as the Pacific Deep Western Boundary Current. Therefore, the L-PMOC impacts the transport and residence time of heat and carbon and plays an essential role in the global climate change (Johnson et al., 2007). However, observations in the deep layers are still limited, and large gaps remain in our knowledge of the L-PMOC pathways, mixing, and variability.

The general route of the L-PMOC has been inferred based on previous mooring and hydrography measurements (**Figure 1**). North of the mid-latitudes in the South Pacific, the L-PMOC layer corresponds to potential temperatures $\theta < 1.2°C$ and depths greater than ∼3,500 m (Kawabe et al., 2006, 2009). The L-PMOC separates from the Antarctic Circumpolar Current (ACC) and flows northward to the east of New Zealand and the Tonga-Kermadec Ridge (Whitworth et al., 1999) and then through the Samoan Passage (Rudnick, 1997; Voet et al., 2015) or around the Manihiki Plateau (Pratt et al., 2019). The L-PMOC continues northward and enters the Central Pacific Basin and bifurcates into the eastern and western branches (Johnson and Toole, 1993; Kawabe et al., 2003, 2006). The western branch passes through the Melanesian and East Mariana Basins (EMBs) and finally arrives at the Yap-Mariana Junction (YMJ) deep channels. However, its pathway after passing the YMJ is largely unknown. The L-PMOC carries the Lower Circumpolar Water (LCPW), which originates from the Southern Ocean (Callahan, 1972; Mantyla and Reid, 1983) and is characterized by a salinity maximum and a silica minimum (Johnson and Toole, 1993). Above the L-PMOC lies the upper deep branch of the PMOC (U-PMOC), which extends over a depth of ∼2,000–3,500 m. This layer also originates from the Southern Ocean but can arrive at the YMJ through a different route from the L-PMOC (Kawabe et al., 2003; Kawabe and Fujio, 2010; Wang et al., 2020). The U-PMOC carries the Upper Circumpolar Water (UCPW), which is relatively warm, fresh, oxygen-poor, and silica-rich compared to the LCPW (Kawabe et al., 2006; Kawabe and Fujio, 2010).

The YMJ is a major gateway for the L-PMOC flowing into the Western Pacific Ocean (WPO). We refer to the Philippine Sea and the West and East Caroline Basins, which are separated from the North Pacific by tall ridges, as WPO. The natural geographic constraint of the YMJ deep channel makes it a more convenient site for monitoring the variability of the L-PMOC. The site marks the junction of three deep channels: the Eastern Channel connecting to the Mariana Trench and the EMB, the Southern Channel connecting to the Yap Trench and the West Caroline Basin (WCB), and the Northern Channel connecting to the West Mariana Basin (WMB) (**Figure 1**). At the YMJ, Siedler et al. (2004) first presented the characteristics of the L-PMOC based on moored current meters deployed on the western side of the Northern Channel from October 1996 to March 1998. The L-PMOC was directed northward with a mean speed of 10.4 cm s^{-1} at 4,220 m. By combining data from Siedler et al. (2004) with new mooring observations on the western and eastern sides of the Northern Channel during 2014–2017, Wang et al. (2020) first revealed the seasonal variability of the L-PMOC and U-PMOC. During December–May, the L-PMOC flows northward at depths below ∼3,800 m with a speed exceeding 20 cm s^{-1} on the western side and is accompanied by a weaker southward return flow on the eastern side. During June–November, the L-PMOC becomes very weak, and the U-PMOC intensifies and flows southward at depths over ∼3,000–3,800 m on the eastern side of the channel. Analysis of the hydrography features suggested that before arriving at the Northern Channel, the U-PMOC intrudes into the WMB mainly through a shallower deep channel northeast of the Northern Channel after arriving at the Mariana Trench. The seasonal variations of the L-PMOC and U-PMOC are accompanied by geostrophically balanced seasonal intrusions of the LCPW and UCPW.

The lack of simultaneous observations in the three channels that meet at the YMJ has hindered our understanding of the distribution and variability of LCPW transport in the channels, key features in the climatologically important deep and bottom circulation in the WPO. To make progress on this topic, we deployed five moorings from 2018 to 2019 in the three channels mentioned above. The analysis of the observational result is first presented, and the underlying dynamics are explored through the analysis of the solution of a high-resolution numerical ocean model.

DATA

Mooring Data

As a part of the Scientific Observing Network of the Chinese Academy of Sciences (CASSON), one mooring was deployed in the Eastern Channel close to the Mariana Trench (hereafter referred to as MarM), one mooring deployed in the Southern Channel close to the Yap Trench (YapM), and three subsurface moorings deployed on the western, central, and eastern sides of the Northern Channel (WM, CM, and EM), respectively (black stars in the middle panel of **Figure 1**). The longitudes/latitudes and durations of MarM, YapM, WM, CM, and EM are 140.43°E/10.84°N from December 12, 2018 to December 24, 2019, 138.87°E/10.90°N from December 11, 2018 to December 25, 2019, 138.69°E/11.40°N from January 26 to December 26, 2019, 138.84°E/11.37°N from January 24 to December 25, 2019, and 139.05°E/11.60°N from January 23 to December 26, 2019, respectively. Each mooring was equipped with five to seven discrete Nortek Aquadopp deep current meters, and seven to 11 discrete SBE37-SM conductivity–temperature–depth (CTD) or RBR solo temperature (T) sensors between 3,000 m and the bottom. The detailed configurations of the mooring measurement are given in **Table 1**. Current meters measured point velocity in the deep layers hourly. The CTDs returned records of temperature, salinity, and pressure every 10 min. The Ts sampled temperature every 10 min. The measurement depths of Ts are obtained using the recorded depths of CTDs and the nominal separation depths between Ts and adjacent CTDs. The potential temperature corresponding to a measured T is derived using the salinity value from the CTD cast carried out

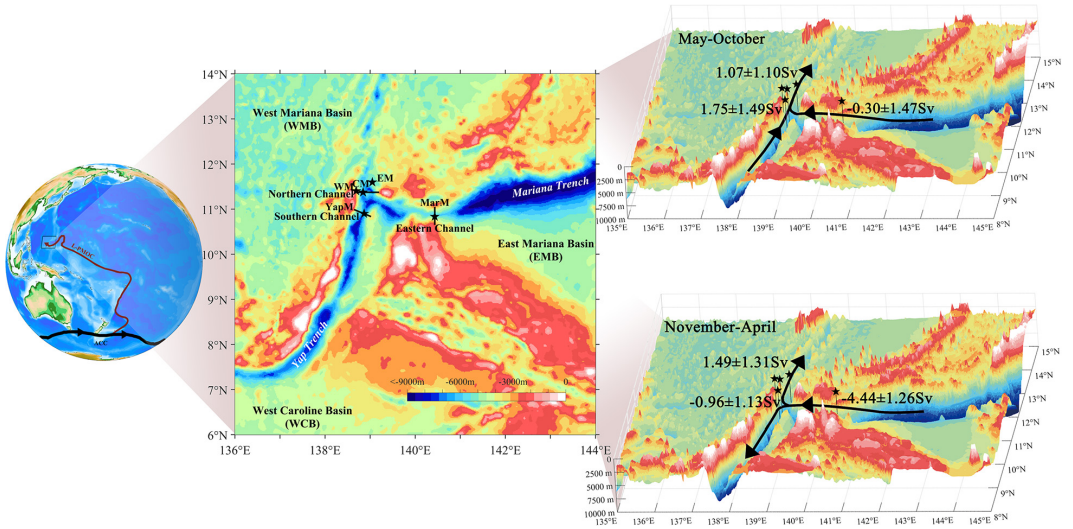

FIGURE 1 | (Left) Schematic flow pattern of lower deep branch of the Pacific Meridional Overturning Circulation (L-PMOC) from the Antarctic Circumpolar Current (ACC) to the western Pacific (after Siedler et al., 2004; Kawabe and Fujio, 2010). **(Middle)** Map of topography near the Yap-Mariana Junction showing locations of five moorings MarM, YapM, WM, CM, and EM (stars) and the cross sections of Eastern, Southern, and Northern Channels (lines). **(Right)** The seasonal pathways (arrows) and volume transports (numbers: mean ± standard deviation) of the L-PMOC during (right upper) May–October and (right lower) November–April are given based on the present study. Stars denote the mooring locations. The bathymetry is from ETOPO1.

during the mooring deployment. All data are low-pass filtered with a 72-h Lanczos filter to remove the effects of inertial fluctuations and tides and then averaged to derive the daily means. Velocity vectors were rotated to the along- and cross-channel directions (x and y axes) with positive x toward 90° (clockwise from north orientation, the same hereinafter) in the Eastern Channel, 23.25° in the Southern Channel, and 0° in the Northern Channel, respectively. The cross-channel section along the y-axis in each channel is denoted by a black line in the middle panel of **Figure 1**. In the Northern Channel, we assume that the observed along-channel velocities from the three moorings represent the flow across the section of 11.37°N, although their latitudes are slightly different. Velocity and temperature data were then interpolated vertically to 1-m intervals.

The MO Ocean Model Products

In order to gain insights into the variability of the L-PMOC at large spatiotemporal scales and to explore the underlying dynamics of the variations at the YMJ channels, we analyze two data assimilative global ocean modeling products created by Mercator Ocean (hereinafter MO), a contribution to the European Union Copernicus Marine Service[1]. The two products are the analysis product PSY4V3R1 and the reanalysis product GLORYS12V1. From PSY4V3R1, we take daily fields of sea surface height (SSH), temperature, salinity, and velocity during our observation period. From GLORYS12V1, we take the monthly fields of the same variables over 1993–2018. Both products are created using the NEMO ocean model. The model has a horizontal resolution of 1/12° in longitude/latitude and 50 vertical levels with a resolution of 1 m at the surface and of 450 m near the bottom. The model uses the ETOPO1 bathymetry dataset in regions deeper than 300 m depth. The atmospheric fields from the ECMWF (European Centre for Medium-Range Weather Forecasts) Integrated Forecast System are used to force the ocean model. The altimeter measured SSH, in situ temperature, and salinity vertical profiles, and the satellite remote-sensing sea surface temperatures are jointly assimilated. For more details on the two products, readers are referred to Lellouche et al. (2013, 2018). The monthly wind stress datasets over 1993–2018 from the ECMWF ERA Interim are also analyzed to understand the variations of the SSH and water density from the MO models. The Ekman pumping velocity (EPV) is calculated as EPV = curl(τ/f)/ρ, where curl(τ) is the curl of wind stress, f is the Coriolis parameter, and ρ = 1,021 kg m^{-3} is the mean water density within the Ekman layer.

[1]https://resources.marine.copernicus.eu/

OBSERVED VARIATIONS OF THE L-PMOC

Observed Deep Flow and Potential Temperature

The observed along-channel velocities (U_{along}) at five mooring sites all exhibit seasonal cycles, and this variability suggests interconnections. **Figure 2** presents the observed time-depth variations of potential temperature (θ) and U_{along} over depths greater than 3,000 m. Following previous studies (e.g., Johnson and Toole, 1993; Siedler et al., 2004; Wang et al., 2020), we take θ = 1.2°C as the boundary between the LCPW and UCPW,

TABLE 1 | The mooring locations and water depths, measurement periods, and instruments' names and mean depths.

Mooring name	Locations/water depth (m)	Measurement period (year/month/day)	Instruments: mean depth
MarM	140.43°E, 10.84°N/5,672 m	2018/12/12–2019/12/24	AQUA: 3,098, 3,597, 4,092, 4,600, 5,111, and 5,619 m RBR solo: 3,329, 3,588, 3,864, 4,334, 4,567, 4,801, and 5,292 m SBE37: 3,084 and 4,094 m
YapM	138.87°E, 10.90°N/6,806 m	2018/12/11–2019/12/25	AQUA: 2,975, 3,488, 3,993, 4,538, 5,002, and 5,567 m RBR solo: 3,208, 3,453, 3,698, 4,186, 4,446, 4,706, and 5,206 m SBE37: 2,963, 3,942, 4,949, and 5,462 m
WM	138.69°E, 11.40°N/4,774 m	2019/1/26–2019/12/26	AQUA: 3,054, 3,466, 3,858, 4,201, and 4,595 m RBR solo: 3,277, 3,892, and 4,429 m SBE37: 3,026, 3,424, 4,137, and 4,559 m
CM	138.84°E, 11.37°N/6,382 m	2019/1/24–2019/12/25	AQUA: 3,115, 3,577, 3,983, 4,386, 4,602, 5,093, and 5,658 m RBR solo: 3,092, 3,288, 3,777, 4,539, 4,805, and 5,314 m SBE37: 3,532, 4,295, 5,000, and 5,557 m
EM	139.05°E, 11.60°N/5,592 m	2019/1/23–2019/12/26	AQUA: 3,070, 3,565, 4,025, 4,354, 4,598, and 5,173 m RBR solo: 3,045, 3,290, 3,789, 4,303, and 4,803 m SBE37: 3,535, 3,936, 4,547, and 5,047 m

Instruments: AQUA is deep current meter manufactured by Nortek, RBR solo is temperature sensors manufactured by RBR, and SBE37 is conductivity–temperature–depth (CTD) sensor manufactured by Sea-Bird. The SBE37 temperature sensor has accuracy less than 0.002°C and a resolution of less than 0.0001°C. The RBR solo temperature sensor has an accuracy of ±0.002°C and a resolution of less than 0.00005°C.

corresponding to the lower and upper deep layers, respectively. In the Eastern Channel, both the lower and upper deep layers show westward inflow into the YMJ with core speed reaching 30 cm s^{-1} from the start of the measurement to the beginning of May 2019 and from November 2019 to the end of the measurement, and eastward outflow into the EMB or weak westward inflow from May to October 2019. In the Southern Channel, the core speed of the deep flow is reduced to 10 cm s^{-1}, and the flow southward into (northward out of) the WCB roughly corresponds to the deep inflow into (outflow out of) the YMJ in the Eastern Channel. We further calculate the lead–lag correlation of U_{along} at the MarM and YapM sites after applying a 31-day running mean to the observed time series (**Figure 3A**, same hereinafter). The correlation reaches peak values of 0.8–0.9 at the 95% confidence level with MarM leading YapM by 10–20 days at depths of 3,200–4,500 m, and with a nearly zero lag at depths greater than 4,500 m.

In the Northern Channel, the deep water at the WM site on average flows southward and northward in the upper and lower deep layers, respectively. In the lower deep layer, the relatively strong northward flow with a core speed of 10 cm s^{-1} prevails from the start of the measurement to June 2019 and from mid-November 2019 to the end of the measurement, roughly corresponding to the westward inflow to the YMJ from the Eastern Channel. This is consistent with the fact that the WM U_{along} is inversely correlated with the MarM U_{along} with $r = -0.6$ to –0.65 at a zero lag (**Figure 3B**). A negative relationship with $r = -0.6$ at a zero lag also occurs between the WM and YapM U_{along} at depths greater than 4,000 m (**Figure 3C**). The seasonal cycle of U_{along} at the WM site is relatively weak in the upper deep layer and strong in the lower deep layer. The core speed of L-PMOC is 10 cm s^{-1} in 2019, lower than the previously observed value of 20 cm s^{-1} in 1997 and 15 cm s^{-1} in 2017 at the WM site (Siedler et al., 2004; Wang et al., 2020). At the CM site, the northward flow is strong in both upper and lower deep layers with a core speed of 10 cm s^{-1} during most of the measurement time and becomes weak or reverses during July–August 2019. The correlation between CM and WM U_{along} reaches 0.75 with CM leading WM by 2–10 days at 3,000–4,000 m and becomes weak at 4,000–4,500 m (**Figure 3D**). At the EM site, U_{along} is dominated by a weak southward flow in both layers. The correlation of deep flow at the EM site with that at the WM or CM site is positive in the upper deep layer with EM leading WM or CM by ∼10 days and is negative in the lower deep layer with WM or CM leading EM by 10–20 days (**Figures 3E–F**).

At the five mooring sites, variations of the deep flows are accompanied by changes in water mass properties (**Figure 2**). At the MarM site, the relatively low (high) θ roughly corresponds to the intensified inflow (outflow) to the YMJ in the lower deep layer, suggesting the influence of the L-PMOC intrusions. At the YapM site, the change of θ has no significant correlation with that of U_{along} and exhibits a weak seasonal variation. This may be due to the strong influence of the intraseasonal variability induced by energetic surface eddies and/or topographic Rossby waves (Ma et al., 2019; Wang et al., 2020). At the three mooring sites in the Northern Channel, the increase in the southward flow speed corresponds to a decrease in θ in the upper deep layer, implying the influx of the southward U-PMOC. In the lower deep layer with θ larger than 1.1°C, the decrease in θ corresponds to the increase in the northward flow speed at the WM and CM sites and in the southward flow speed at the EM site, suggesting the presence of the northward L-PMOC at the WM and CM sites and the presence of the southward return flow of the L-PMOC at the EM site (Wang et al., 2020). It should be noted that in the layer with θ lower than 1.1°C at the CM site, a positive relationship between θ and the northward L-PMOC intrusion flow speed suggests that there could be the remnants of previously intruded LCPW with older age. The intrusion and absence of the new LCPW causes the height of the remnant

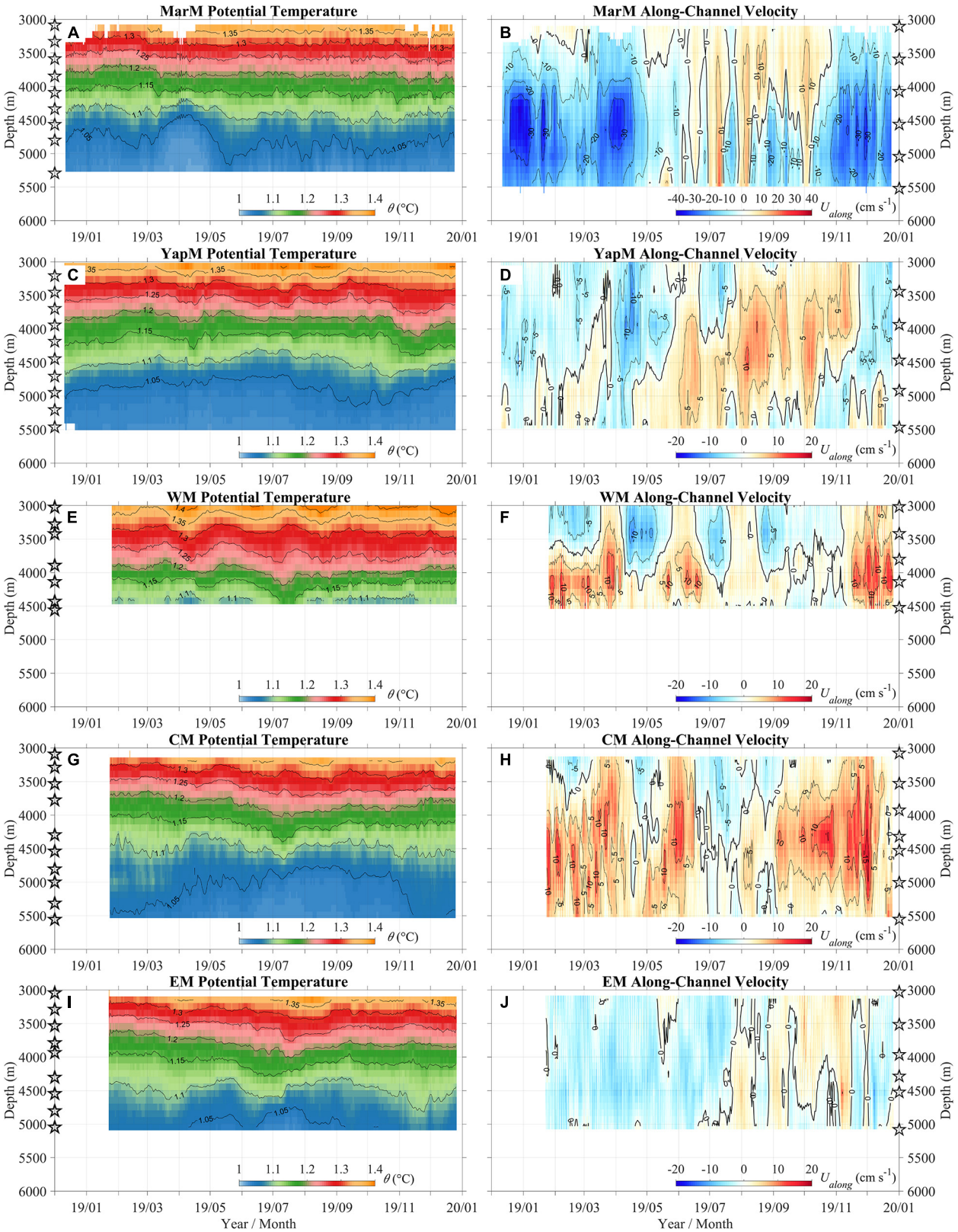

FIGURE 2 | Time-depth variations of (left) potential temperature θ and (right) along-channel velocity U_{along} observed by moorings MarM **(A,B)**, YapM **(C,D)**, WM **(E,F)**, CM **(G,H)**, and EM **(I,J)**. Open pentagrams indicate the depths of temperature sensors (left) and current meters (right).

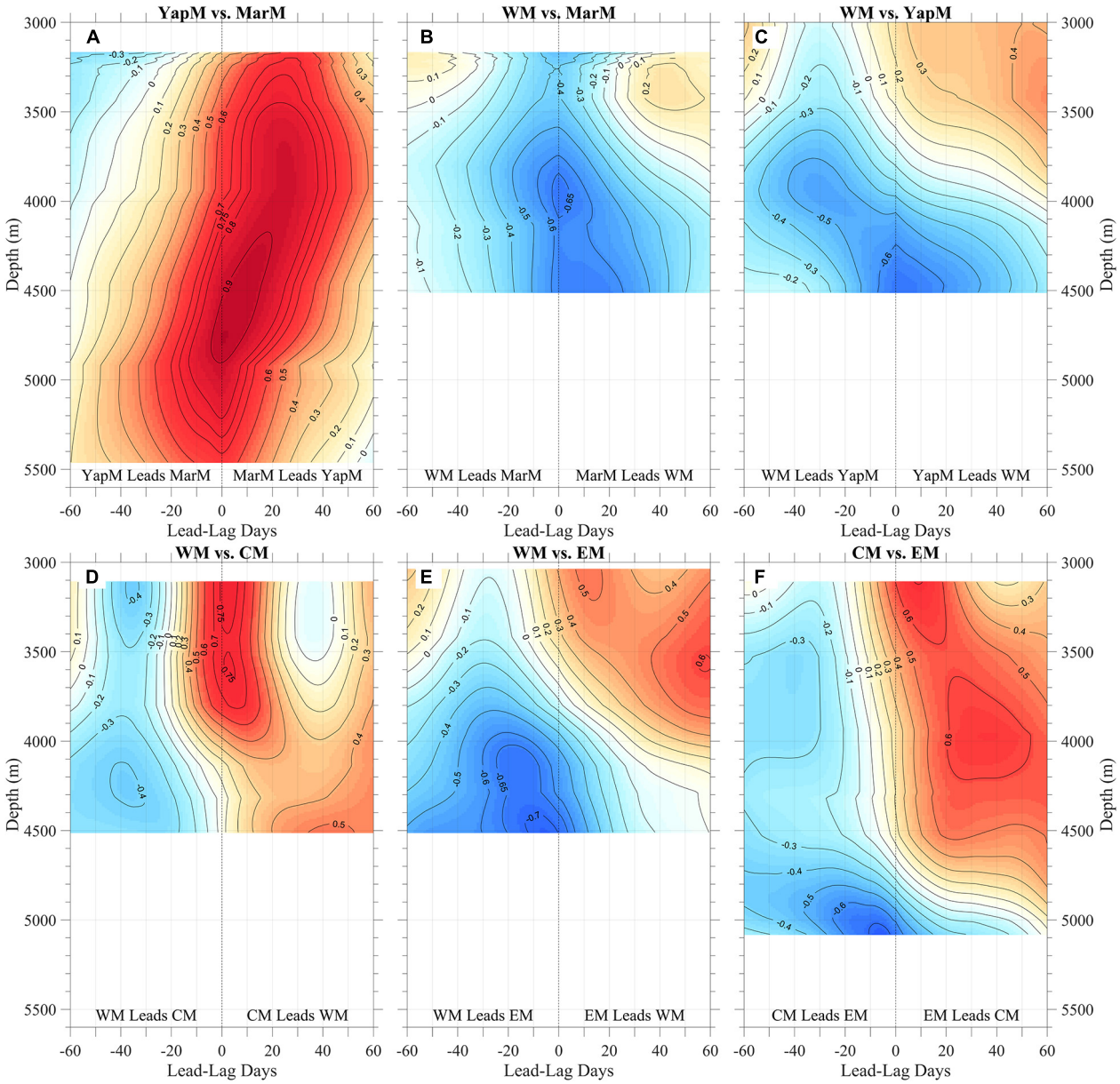

FIGURE 3 | Lead–lag correlations of observed deep along-channel velocities between **(A)** YapM and MarM, **(B)** WM and MarM, **(C)** WM and YapM, **(D)** WM and CM, **(E)** WM and EM, and **(F)** CM and EM.

LCPW to fall and rise, respectively. The presence of the remnant LCPW only at the CM site is likely due to the greater depth at this site.

Estimated Volume Transports Based on Observations

We next estimate the volume transports in different potential temperature classes through each channel. For each channel, we grid the section with a resolution of 10 m in the horizontal and vertical directions. The data from the mooring measurements are extrapolated and interpolated into these grids. For each mooring, the observed U_{along} and θ are first interpolated vertically, and then the deepest measured value is extrapolated uniformly downward to the bottom. However, U_{along} in the last grid nearest the bottom is set to zero. The next step is horizontal extrapolation/interpretation. In the Eastern and Southern Channels, the observed U_{along} and θ are extrapolated uniformly to the bilateral grids at each depth, except for setting U_{along} to zero in the grids nearest the channel sidewalls. In the Northern Channel, the values of U_{along} and θ on mooring WM (EM) are extrapolated uniformly westward (eastward) to the western (eastern) sidewall, except for setting U_{along} to zero in the grids nearest the channel sidewalls. For the grids between WM

and EM, the values of U_{along} and θ from moorings WM, CM, and EM at the same depth are linearly interpolated. The transect distributions of the MO modeled U_{along} and θ in the Eastern, Southern, Northern Channels (figure not shown) resemble those obtained from the above interpolation/extrapolation scheme. We then calculate the volume transports by integrating U_{along} from the isotherm depths of 1.15, 1.2, 1.25, and 1.3°C to the deepest layer and across the channel. We define the L-PMOC transport as all transport with θ less than 1.2°C.

The L-PMOC volume transports represented as mean ± standard deviation, are −2.43 ± 2.56 Sv (1 Sv = 10^6 m^3 s^{-1}) in the Eastern Channel and 0.42 ± 1.88 Sv in the Southern Channel during the 1-year cycle from December 15, 2018 to December 15, 2019, and 1.27 ± 1.23 Sv in the Northern Channel from January 26 to December 15, 2019 (**Figures 4A–C**). The L-PMOC transports in the three channels exhibit a prominent seasonal variation. An annual harmonic fit is applied to the time series of the estimated volume transports. Prior to the harmonic fit, each time series is smoothed with a 91-day running mean to focus on the variations longer than the intraseasonal time scales. We calculate R^2, defined as a ratio of the variance of the fitted time series to the variance of the smoothed observations. In the Eastern, Southern, and Northern Channels, the values of R^2 for the L-PMOC volume transports are 96, 91, and 85%, and the largest negative values of the fitted transport occur on January 26, February 8, and June 6, 2019, respectively. The variability of deep transports with θ less than 1.15, 1.25, and 1.3°C generally follow that with θ less than 1.2°C. The seasonal cycle of the L-PMOC transports in the three channels can be divided into two phases over November–April and May–October.

In order to explore the L-PMOC pathways at the YMJ, we plot the scatter diagram of the observed volume transports, with the *x*-axis, *y*-axis, and color shading denoting the transports in the Eastern, Southern, and Northern Channels, respectively (**Figure 4D**). The L-PMOC pathways can be mainly cataloged into three patterns based on the scatter diagram. In Pattern 1, the L-PMOC flows westward into the YMJ through the Eastern Channel and then bifurcates into the southern and northern branches. The southern branch passes through the Yap Trench and finally flows into the WCB, while the northern branch flows mainly through the Northern Channel into the WMB. In Pattern 2, the lower deep water flow comes partly from the WCB, directed northward through the Southern Channel, and partly from the EMB, directed westward through the Eastern Channel. Then the combined transport passes through the Northern Channel into the WMB. In Pattern 3, the lower deep water flow originates in the WCB and moves northward through the Southern Channel. A portion of this northward flow turns eastward and flows out of the YMJ region through the Eastern Channel. The deep flow through the Northern Channel is mainly northward and occasionally southward. In Patterns 2 and 3, the northward flow in the Southern Channel coming from the WCB can be regarded as the return flow of the L-PMOC. The flow pattern with eastward transport through the Eastern Channel and southward transport through the Southern Channel does not occur, suggesting that the lower deep transport cannot solely originate from the WMB. Pattern 1 mainly occurs during the seasonal phase from November to April, and Patterns 2 and 3 mainly occur during the seasonal phase from May to October. During November–April (May–October), the mean and standard deviation of the L-PMOC transports are −4.44 ± 1.26 (−0.30 ± 1.47), −0.96 ± 1.13 (1.75 ± 1.49), and 1.49 ± 1.31 (1.07 ± 1.10) Sv in the Eastern, Southern, and Northern Channels (right panels of **Figure 1**). The transports through three channels are imbalanced, especially during November–April. The possible reasons include uncertainty in the transport estimate, and the unknown transport through the deep channel east of the Southern Channel. During November–April, a part of deep water may flow southward into WCB through this channel.

SIMULATED VARIATIONS OF THE L-PMOC

From the pointwise mooring measurements of deep velocity and temperature, it is difficult to depict the deep flow across the large spatial scale at the YMJ. The observations covered only 1 year; hence, the robustness on the seasonal signal needs to be assessed with long time series of reliable ocean model simulations. Here, we resort to the high-resolution data-assimilated MO results. **Figure 5** shows the time-depth variations of the MO modeled U_{along} and θ at five locations, each in the horizontal model grid that is nearest to the site of one of the five moorings. The comparison of the model results with observations is assessed with the correlation coefficients and the normalized root-mean-square deviation ($\mathrm{NRMSE} = \sqrt{\frac{1}{n}\sum_1^n (\mathrm{Obs}-\mathrm{MO})^2}/(\max(\mathrm{Obs})-\min(\mathrm{MO}))$, where *n* is the number of data values), calculated for the daily time series of U_{along} and θ from observations (Obs) and the MO outputs (MO), after applying a 5-day running mean. At the YapM, MarM, and WM sites, the correlations are larger than 0.55 and NRMSEs are less than 35%. The agreements are poor at the CM and EM sites, mainly due to the failure of MO in reproducing the U-PMOC and the return flow of the L-PMOC, consistent with the previous evaluation in Wang et al. (2020).

We further calculate the modeled volume transport in the three channels (**Figures 6A–C**). There are four, five, and six simulated profiles in the transects of Eastern, Southern, and Northern Channels, respectively. We filled the missing data using the same interpolation/extrapolation scheme as used for the observations in the Northern Channel. During November–April (May–October) over the mooring measurement period, the mean and standard deviation of the modeled L-PMOC transports are −2.18 ± 1.69 (2.49 ± 1.44), −0.33 ± 1.47 (3.43 ± 1.33), and 1.20 ± 1.00 (0.37 ± 1.02) Sv in the Eastern, Southern, and Northern Channels. In the same order of the three channels calculated for the 5-day running mean L-PMOC transports from observation and model outputs, the correlations are 0.93, 0.77, and 0.37, and the *NRMSEs* are 29, 22, and 23%, respectively. During the same period as observations, the modeled L-PMOC transport also exhibits an evident seasonal cycle with R^2 reaching 93, 79, and 70%.

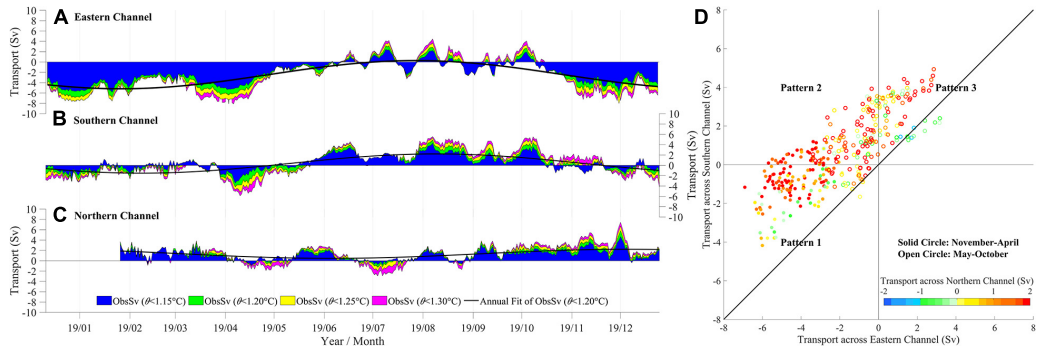

FIGURE 4 | Stacked histograms of observed volume transport in potential temperature classes with θ less than 1.15°C (blue), 1.2°C (green), 1.25°C (yellow), and 1.30°C (pink) through the **(A)** Eastern, **(B)** Southern, and **(C)** Northern Channels. The annual harmonic fit of observed volume transports with θ less than 1.2°C is superimposed by black line in panels **(A–C)**. **(D)** Scatter diagram of volume transports with θ less than 1.2°C through the Eastern Channel versus through the Southern Channel, with a thick line depicting the 1:1 ratio. The color shading denotes the volume transports with θ less than 1.2°C through the Northern Channel. Solid and open circles represent the values obtained during November–April and May–October, respectively.

In the Eastern Channel, the MO model reproduces well the seasonal variability but has biases in the magnitude, with smaller westward transport during November–April and larger eastward transport during May–October. In the Southern Channel, the MO model performs well in both the seasonal cycle and magnitude. In the Northern Channel, the MO model performs well during most of the measurement period but fails in reproducing the northward transport from mid-September to mid-November, leading to a low correlation. Despite these discrepancies, the similarity between the MO model and the observations in terms of the seasonal variation of the L-PMOC encourages further examination of the MO results to identify the seasonal variation of the L-PMOC over the whole YMJ region and over a longer time scale, and to explore the underlying mechanism.

Based on the MO daily transports during the mooring measurement period, we also plot a scatter diagram of the volume transports in three channels (**Figure 6D**). The results show three patterns similar to those obtained from the observations. However, the principal occurrence time of Pattern 2 is shifted to November–April. The flow patterns of the L-PMOC at the YMJ are depicted by the horizontal distributions of the depth-integrated MO velocity with θ less than 1.2°C during the three patterns (**Figure 7**). The flow pathways are generally in accordance with that inferred from observations.

The seasonal variability of the L-PMOC volume transports in the three channels is evident in the longer time series of the MO outputs over 1993–2018 (**Figure 8**). The "climatological" seasonal signals are obtained by applying the annual harmonic fit to each volume transport time series, and the fitted annual cycle explains 93, 94, and 80% of the total variance in the Eastern, Southern, and Northern Channels, respectively. This provides further evidence of the seasonal variability of the L-PMOC at the YMJ. The volume transports in the three channels over 1993–2018 also show variations at the interannual and longer time scales. During November–April, a decreasing trend appears in the L-PMOC transports from the EMB to the YMJ through the Eastern Channel and then from the YMJ to the WMB and WCB through the Northern and Southern Channels. In contrast, during May–October, an increasing trend appears in the L-PMOC transports from the WCB and WMB to the YMJ through the Southern and Northern Channels and then from the YMJ to the EMB through the Eastern Channel. However, such interannual variability cannot be verified with the limited observation and is not discussed further here.

FORCING MECHANISMS OF THE L-PMOC

The forcing mechanisms for the pathways and seasonal variability of the L-PMOC are explored through analysis of the MO model solutions. Deep-water exchange between two interconnected basins can be forced by the gradient of deep pressure along the channels (Sprintall et al., 2013). We select two representative sites on the northeastern and southwestern sides of the YMJ region (hereafter referred to as NE and SW, NE site: 140.83°E/10.83°N, SW site: 136.9°E/6.83°N, **Figure 9A**) and examine their pressure difference. At each point, the pressure P at the depth z is calculated using the hydrostatic equation $P = \int^{z} \rho g dz$ (where ρ is water density, g is gravitational acceleration, and η is SSH) based on the MO monthly data over 1993–2018. The correlations of monthly time series of the pressure difference between NE and SW ($P_{Diff} = P_{NE} - P_{SW}$) at 4,405 m with those of the modeled L-PMOC transports across the Eastern and Southern Channels reach −0.95 and −0.86, respectively. At depths greater than 2,000 m, the climatological monthly P_{Diff} is positive from November to April, corresponding well to the modeled L-PMOC transport from the EMB to the WCB, and is negative from May to October, corresponding well to the modeled return flow of L-PMOC from the WCB to the EMB (**Figures 8** and **9B**). Additional trials suggest that these results are not sensitive to the specific locations of two points in two adjacent basins.

At each depth, P_{Diff} is determined by SSH difference ($SSH_{diff} = SSH_{NE} - SSH_{SW}$) and the vertically integrated water density difference ($D_{Diff} = D_{NE} - D_{SW}$) from the surface to that

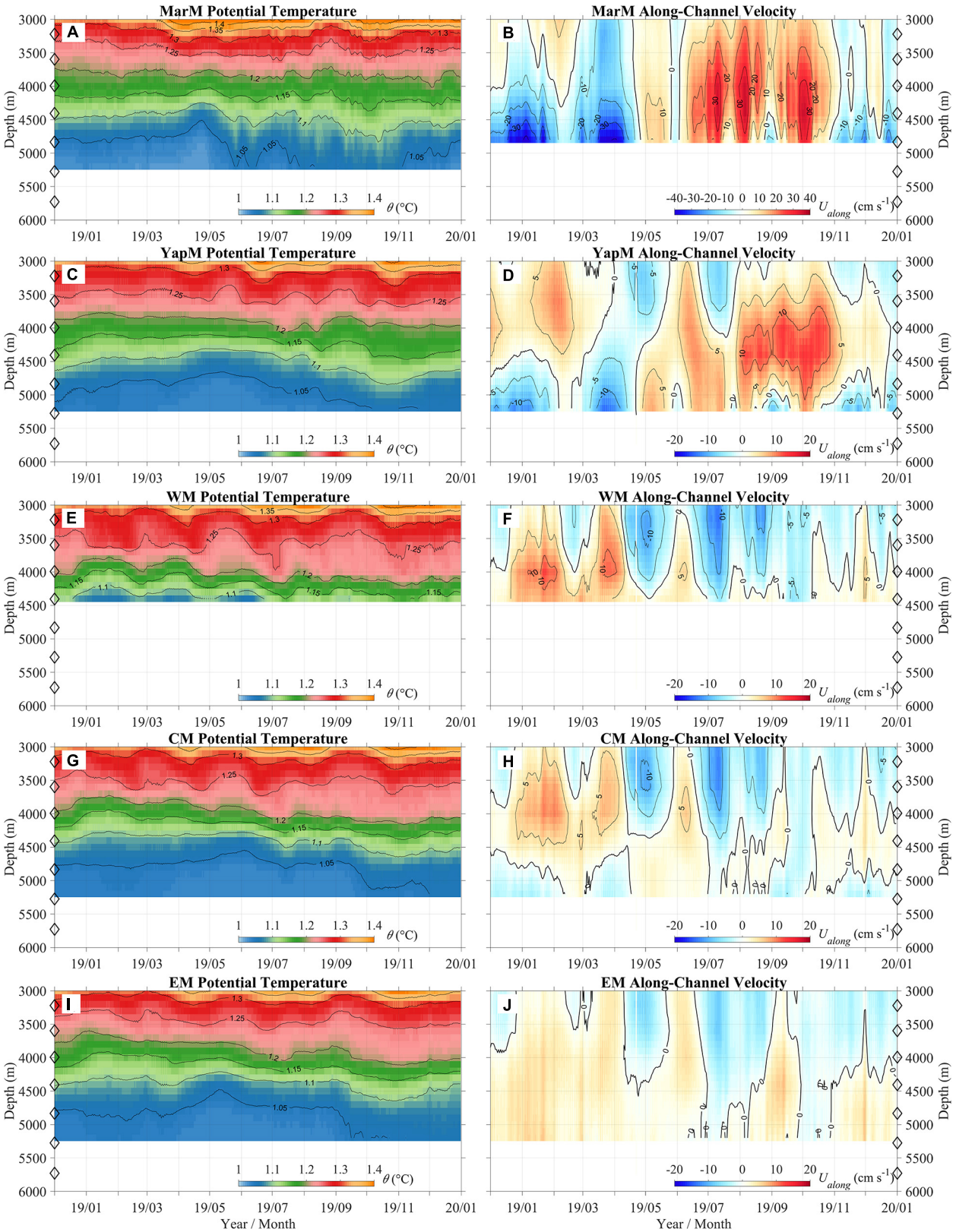

FIGURE 5 | Time-depth variations of MO modeled (left) potential temperature θ and (right) along-channel velocity U_{along} at the mooring sites of MarM **(A,B)**, YapM **(C,D)**, WM **(E,F)**, CM **(G,H)**, and EM **(I,J)**. Open diamonds indicate the depths of model vertical levels.

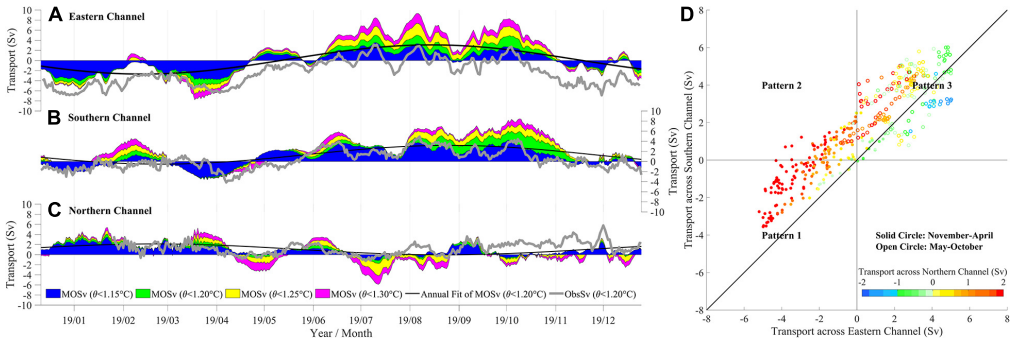

FIGURE 6 | Stacked histograms of MO modeled volume transport in potential temperature classes with θ less than 1.15°C (blue), 1.2°C (green), 1.25°C (yellow), and 1.30°C (pink) through the **(A)** Eastern, **(B)** Southern, and **(C)** Northern Channels. The annual harmonic of modeled volume transports with θ less than 1.2°C is superimposed by black line in panels **A–C**. The thick grey lines in panels **A–C** denote the observed volume transports with θ less than 1.2°C in three corresponding channels. **(D)** Scatter diagram of modeled volume transports with θ less than 1.2°C through the Eastern Channel versus through the Southern Channel, with a thick line depicting the 1:1 ratio. The color shading denotes the modeled volume transports with θ less than 1.2°C through the Northern Channel. Solid and open circles represent the values obtained during November–April and May–October, respectively.

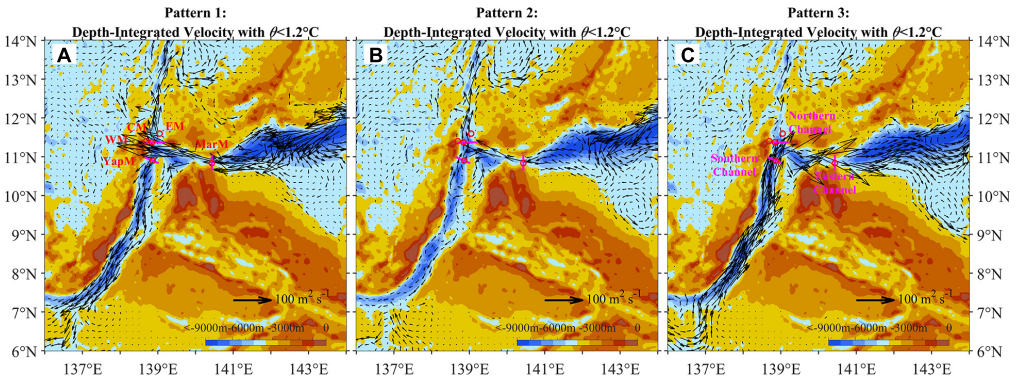

FIGURE 7 | Horizontal distributions of depth-integrated MO velocity with potential temperature θ < 1.2°C (arrows) averaged over Patterns **(A)** 1, **(B)** 2, and **(C)** 3 at the Yap-Mariana Junction. Patterns 1, 2, and 3 are defined in **Figure 6**. Locations of five subsurface moorings are denoted by red open circles. The cross sections of Eastern, Southern, and Northern Channels are indicated by pink lines. The bathymetry is from ETOPO1.

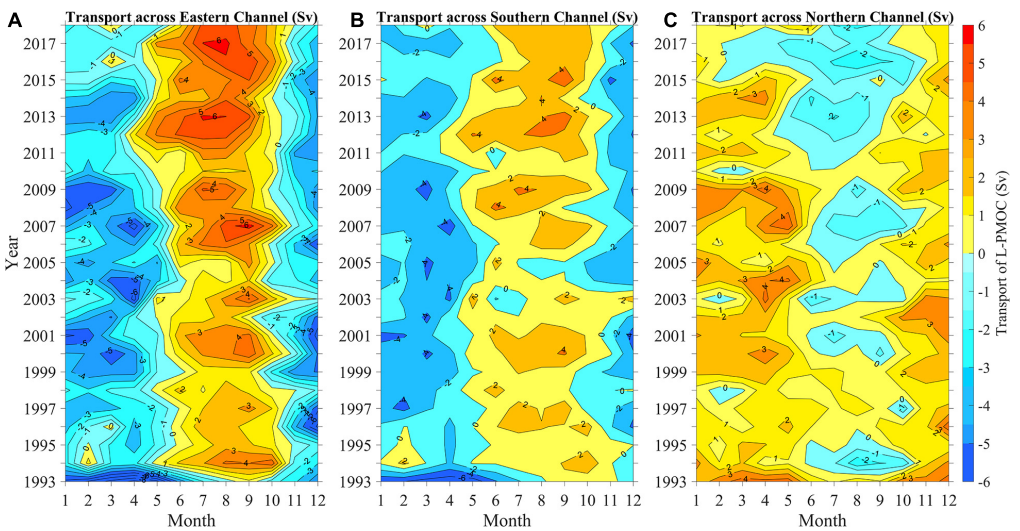

FIGURE 8 | MO monthly volume transports of the L-PMOC through the **(A)** Eastern, **(B)** Southern, and **(C)** Northern Channels from 1993 to 2018.

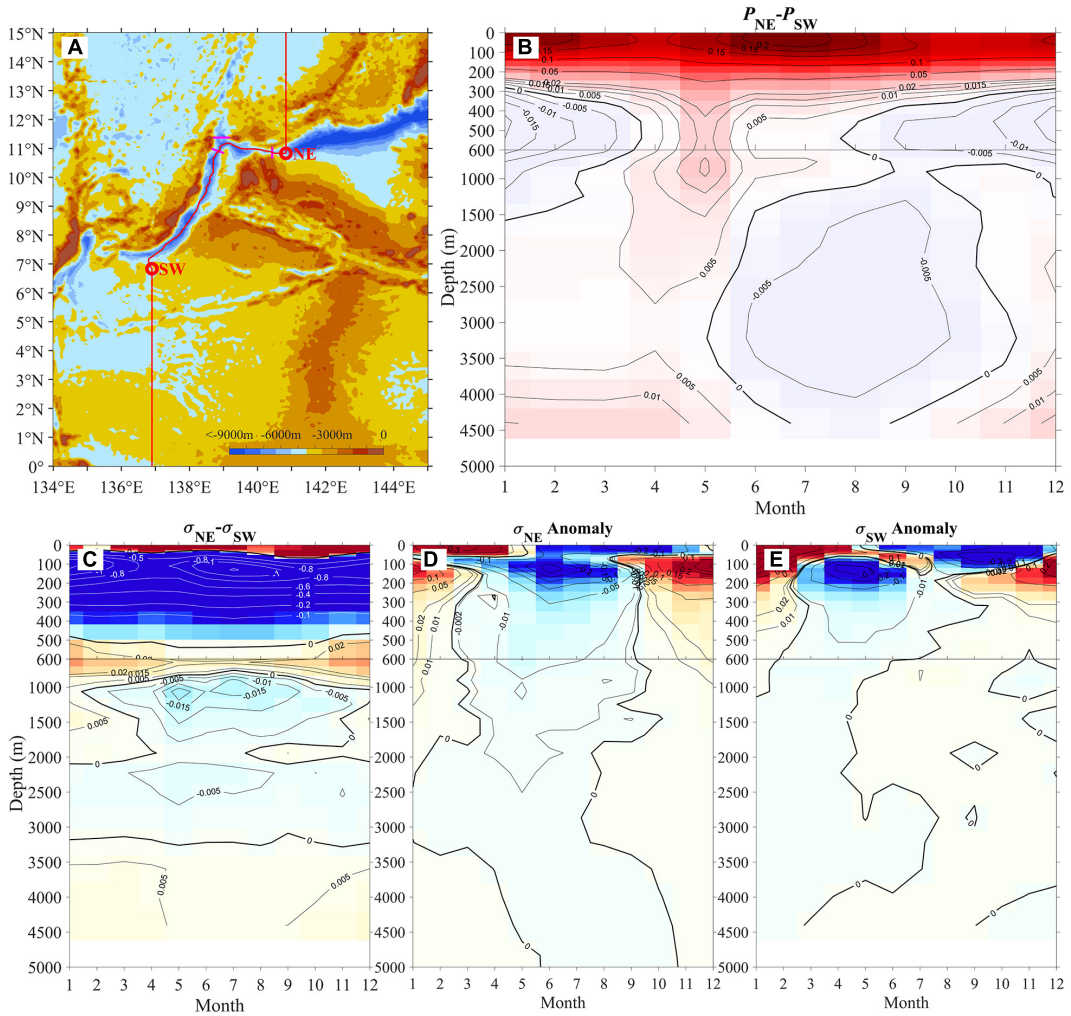

FIGURE 9 | (A) Map of topography near the Yap-Mariana Junction (YMJ) showing two representative sites (red circles) in the northeastern (NE) and southwestern (SW) sides of the YMJ channels and meridional section (red curve). Vertical distributions of climatological monthly **(B)** pressure and **(C)** potential density difference between the NE and SW sites, and potential density anomalies at the **(D)** NE and **(E)** SW sites.

depth. From the vertical distributions of climatological monthly P_{Diff} and D_{Diff} (**Figures 9B,C**), we can distinguish four key layers that play a decisive role in determining the mean value and variability of P_{Diff} in the lower deep layer. The four layers roughly correspond to the depth ranges over the upper 50 m with mean positive D_{Diff}, 50–500 m with mean negative D_{Diff}, 500–850 m with mean positive D_{Diff}, and 850–2,000 m with seasonal positive and negative D_{Diff}. At depths greater than 2,000 m, the value of D_{Diff} is very small, corresponding to the negligible change of P_{Diff} with depth.

The mean values of D_{Diff} in the above four layers are mainly related to the differences in water mass properties (**Figure 10**). In the surface mixed layer roughly over 0–50 m depth, the positive D_{Diff} can be related to the larger salinity at the NE than at the SW sites, which is caused by the difference in the air–sea water exchange (precipitation minus evaporation) between the two sites. The mean negative D_{Diff} at 50–500 m is mainly controlled by the potential temperature difference over the 22.5–25.5-σ_θ sublayer and by the salinity difference over the 25.5–27.0-σ_θ sublayer, respectively. In the upper sublayer, the potential temperature of the North Pacific Tropical Water (NPTW) at the NE site is higher than that of the North Pacific tropical subsurface water (TSSW, Wang et al., 2013) at the SW site. In the lower sublayer, the water mass at the SW site is the mixture of TSSW and Antarctic Intermediate Water (AAIW, Qu and Lindstrom, 2004), the salinity of which is higher than that of the North Pacific Intermediate Water (NPIW) at the NE site. The mean positive SSH_{diff} can be primarily related to the "steric" effects of D_{Diff} at 50–500 m.

In the two following layers, both sites are occupied by the AAIW at 500–850 m, and the mixture of the AAIW and the UCPW or the North Pacific Deep Water (NPDW) at 850–2,000 m. The UCPW occupies almost the same depth range as the NPDW. Compared to the NPDW, the UCPW is characterized

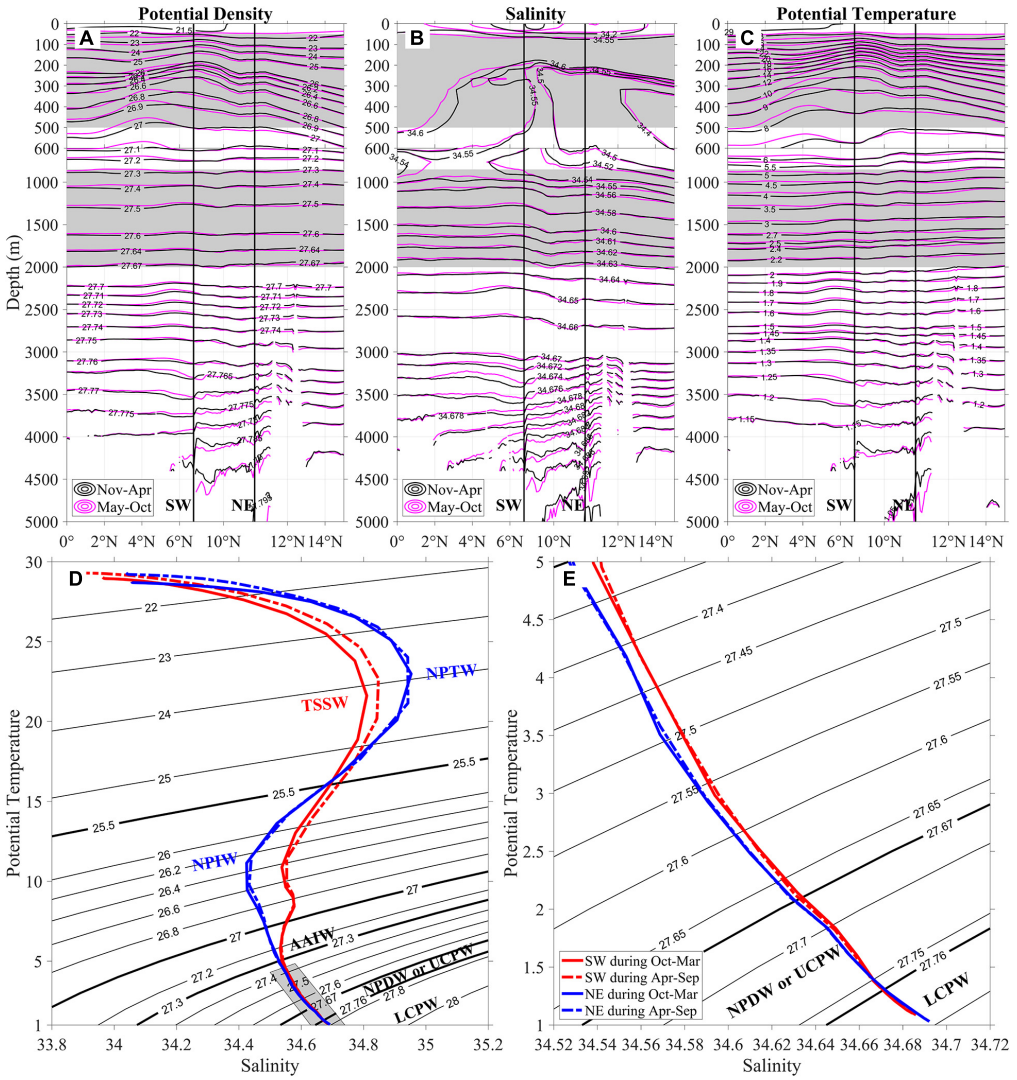

FIGURE 10 | Vertical distributions of mean **(A)** potential density, **(B)** salinity, and **(C)** potential temperature along the section denoted by red curve in **Figure 9A** during November–April (black contours) and May–October (pink contours). Gray shadings are superimposed to help separate four key layers for determining the pressure difference between NE and SW (see text). **(D)** Relationships between potential temperature and salinity at the SW and NE sites with **(E)** a zoomed-in view on the isopycnals below 27.35 kg m^{-3}.

by slightly higher salinity; however, the two water masses are difficult to identify locally (Kawabe and Fujio, 2010). The mean salinity and potential temperature in the two layers decrease northward (**Figure 10**). At 500–850 m, the mean positive D_{Diff} is related to the lower potential temperature at the NE than at the SW sites. At 850–2,000 m, the potential density is controlled by the potential temperature (salinity) over November–April (May–October), leading to the positive (negative) D_{Diff}.

Next, we explore the causes of seasonal variations of SSHs (**Figures 11C,D**) and water densities (**Figures 9D–E**) at the NE and SW sites. The seasonality of SSH_{diff} and D_{Diff} can be caused by both local Ekman pumping and the westward-propagating Rossby waves that are remotely forced (e.g., Vivier et al., 1999; Zhao et al., 2012). At the NE site, the SSHs during October–March and April–September are related to the westward propagation of negative and positive signals, respectively (**Figure 11C**). Their phase speeds approximately equal to 1.48 m s^{-1}, much higher than the typical phase speed of the 1st baroclinic mode Rossby wave along the NE's latitude (0.4 m s^{-1}, Kessler, 1990). This suggests that the signals are influenced by both the westward-propagating Rossby wave generated by EPVs in the eastern Pacific and the local Ekman pumping (**Figures 11A,C**). For the water density at the NE site, the forcing mechanism for its seasonal variability at depths shallower than 380 m is similar to that for the SSH (**Figures 11E,G**). At depths greater than 380 m, the local Ekman pumping effect vanishes, and the seasonal variability is mainly related to the Rossby waves generated by EPVs near 160°E (**Figure 11I**). The phase speed is estimated to be 0.2 m s^{-1}, very

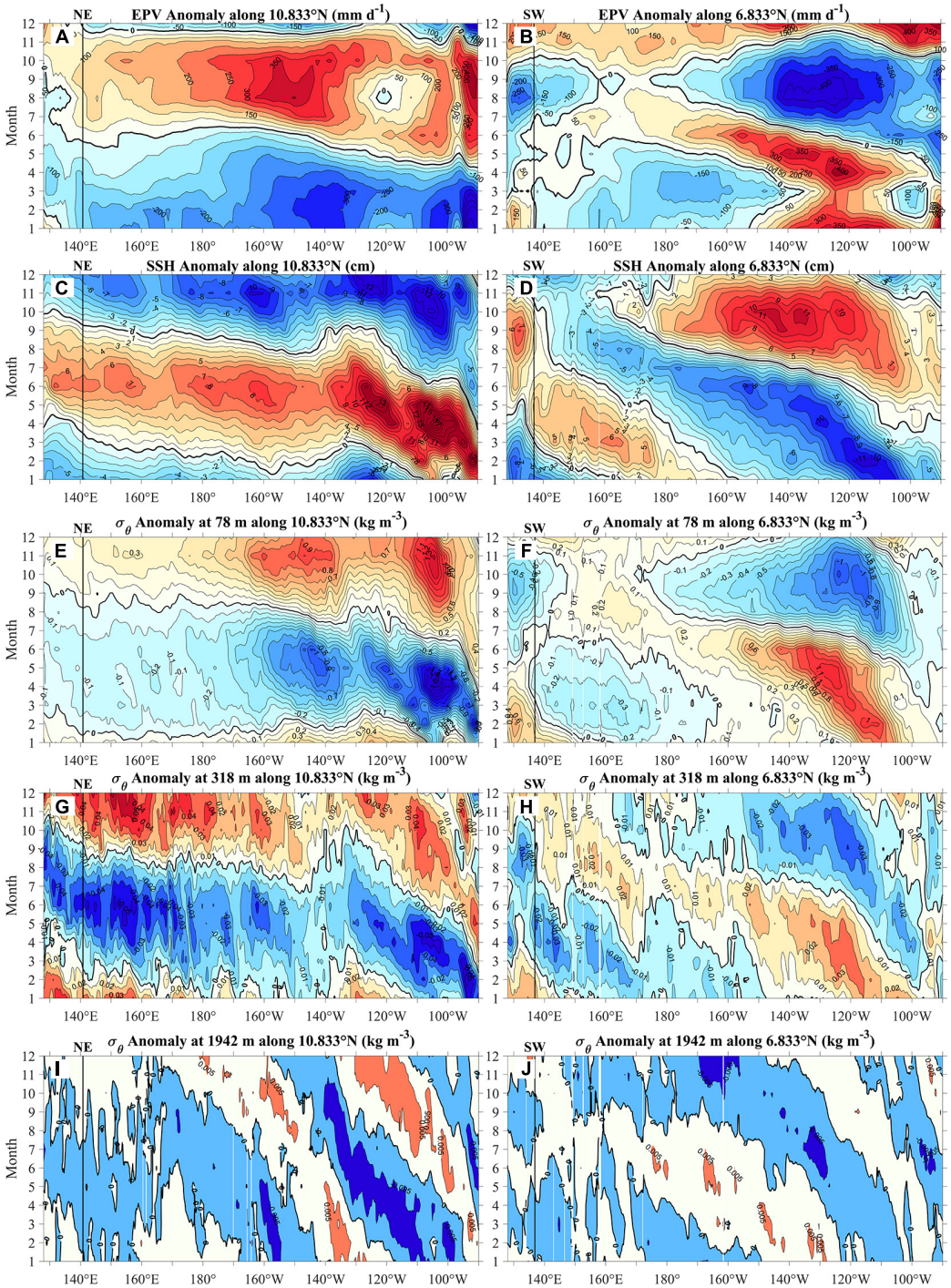

FIGURE 11 | Longitude-time variations of anomalies of **(A,B)** Ekman pumping velocity – EPV, **(C,D)** sea surface height – SSH, and potential density σ_θ at **(E,F)** 78 m, **(G,H)** 318 m, **(I,J)** 1942 m along the latitudes (10.833°N and 6.833°N) of (left) NE and (right) SW sites. Black lines denote the locations of NE and SW sites.

close to the typical speed of the 2nd baroclinic mode Rossby wave along the NE's latitude (0.16 m s^{-1}). At depths greater than 2,225 m, the 2nd baroclinic mode Rossby wave can also be seen in the central and eastern Pacific but is not visible in the western part due to the blocking of topography (figure not shown).

At the SW site, the negative and positive SSHs during November–February and July–October are produced by local negative and positive EPVs, respectively, while SSHs during March–June are related to the westward propagation of downwelling Rossby waves triggered by negative EPV near the

dateline (**Figures 11B,D**). The phase speed of the waves is 0.5 m s^{-1}, very close to the typical speed of the 2nd baroclinic mode Rossby waves along the SW's latitude (0.52 m s^{-1}). For the water density at the SW site, seasonal variability at depths less than 318 m is influenced primarily by the local EPVs and secondarily by the Rossby waves, resembling the behavior of SSHs (**Figure 11F**). At depths of 318–644 m, the influence from the local Ekman pumping is still present, but the Rossby waves are generated by the EPV near 150°E (**Figure 11H**). The westward-propagating wave speed is 0.10 m s^{-1}, very close to the typical phase speed of the 3rd baroclinic mode Rossby waves along the SW's latitude (0.13 m s^{-1}). At depths greater than 644 m, the contribution from the local Ekman pumping vanishes, and the 3rd baroclinic mode Rossby waves play a dominant role in the seasonal variability (**Figure 11J**). At depths greater than 3,221 m, the 3rd baroclinic mode Rossby waves can also be seen in the central and eastern Pacific but are not visible in the western part due to the topographic blocking (figure not shown).

In summary, the L-PMOC transport at the YMJ corresponds to the local pressure gradient between two interconnected basins in the lower deep layer. The differences in SSH and water density at depths less than 2,000 m between the NE and SW sites play a decisive role in forming the lower deep pressure gradient. In contrast, the water density difference at depths greater than 2,000 m plays a minor role. The local Ekman pumping and westward-propagating Rossby waves are combined to determine the seasonal variability of SSH and water density in the upper 2,000-m layer, and consequently the L-PMOC volume transport. That is to say, the L-PMOC transport greater than 3,500 m is closely linked to the wind forcing and the upper ocean processes at depths less than 2,000 m.

CONCLUSION

At the Pacific YMJ, a major gateway for L-PMOC flowing into the WPO, five subsurface moorings were deployed in three deep channels to reveal the pathways, volume transport, and seasonal variability of L-PMOC. The pathways of L-PMOC at the YMJ can be cataloged into three patterns. In the first pattern, the L-PMOC flows westward into the YMJ through the Eastern Channel, and then bifurcates into a southern branch, directed towards the WCB, and a northern branch, directed towards the WMB. In the second pattern, the lower deep water flows into the YMJ through the Eastern and Southern Channels, and then flows northward into the WMB. In the third pattern, a northward return flow of L-PMOC through the Southern Channel bifurcates into an eastward branch towards the EMB and a northward branch towards the WMB. The volume transport of L-PMOC through the Eastern, Southern, and Northern Channels exhibits seasonality. The L-PMOC pathway during November–April is consistent with Pattern 1, and that during May–October conforms to Patterns 2 and 3. The L-PMOC volume transports with θ less than 1.2°C, represented as mean ± standard deviations, are -4.44 ± 1.26 (-0.30 ± 1.47), -0.96 ± 1.13 (1.75 ± 1.49), and 1.49 ± 1.31 (1.07 ± 1.10) Sv in Eastern, Southern, and Northern Channels during November–April (May–October).

Large spatiotemporal fields of the MO model outputs were analyzed to explore the driving mechanism for the L-PMOC pathways and seasonality at the YMJ. The MO outputs generally perform well in simulating the seasonal variation of L-PMOC transports at the YMJ. The modeled flow pathways resemble that inferred from the observation. Long time series of MO monthly L-PMOC transports in three channels during 1993–2018 also exhibit evident seasonal variability. The L-PMOC transports at the YMJ are driven by local pressure gradients between two adjacent basins in the lower deep layer, mainly set up by differences in the SSH and water mass density in the upper 2,000-m layer. The local Ekman pumping and westward-propagating Rossby wave triggered by remote Ekman pumping are largely responsible for the seasonal variability of L-PMOC.

Most importantly, the relationship of the L-PMOC transport greater than 3,500 m at the YMJ with wind forcing and water mass properties over the upper 2,000 depths are established. This relationship can partially explain why the MO model has a good performance in simulating the L-PMOC. The reanalysis dataset usually has a good capability in reproducing the upper ocean processes due to the assimilation of observed wind, SSH, and in situ temperature and salinity vertical profiles in the upper 2,000-m layer. Additional analysis of the HYCOM GOFS 3.0 outputs suggests that the HYCOM model can also reproduce the volume transport and seasonal variability of L-PMOC quite well (figure not shown). Whether such a relationship can be applied to the L-PMOC transports in the upstream and downstream regions deserves further investigation. Filling in our descriptive picture and theoretical understanding of the L-PMOC system, and its variability on scales from seasonal to decades, remains a daunting challenge. It is hoped that our study will stimulate more in situ measurements in other locations along the L-PMOC route and more analyses and further improvements of the ocean models to quantify and understand the L-PMOC variability and forcing mechanisms.

DATA AVAILABILITY STATEMENT

The raw data supporting the conclusions of this article will be made available by the authors, without undue reservation.

AUTHOR CONTRIBUTIONS

JW and FW initiated the idea and designed the observation. JW analyzed the data and wrote the manuscript. FW, YL, QM, LP, and ZZ contributed to the refinements of the data analysis and manuscript writing. All authors contributed to the article and approved the submitted version.

FUNDING

This study was supported by the Strategic Priority Research Program of the Chinese Academy of Sciences (grant XDA22000000), the National Natural Science Foundation of China (grants 91958204 and 41776022), the Key Research

Program of Frontier Sciences, CAS (grant QYZDB-SSW-SYS034), and the International Partnership Program of CAS (grant 133137KYSB20180056). FW thanks the support from the National Natural Science Foundation of China (grants 41730534 and 41421005). QM thanks the support by the National Natural Science Foundation of China (grant 42006003).

REFERENCES

Callahan, J. E. (1972). The structure and circulation of deep water in the Antarctic. *Deep Sea Res. Oceanogr. Abstr.* 19, 563–575. doi: 10.1016/0011-7471(72)90040-x

Johnson, G. C., Mecking, S., Sloyan, B. M., and Wijffels, S. E. (2007). Recent bottom water warming in the Pacific Ocean. *J. Climate* 20, 537165–5375. doi: 10.1175/2007JCLI1879.1

Johnson, G. C., and Toole, J. M. (1993). Flow of deep and bottom waters in the Pacific at 10°N. *Deep Sea Res. I* 40, 371–394. doi: 10.1016/0967-0637(93)90009-R

Kawabe, M., and Fujio, S. (2010). Pacific Ocean circulation based on observation. *J. Oceanogr.* 66, 389–403. doi: 10.1007/s10872-010-0034-8

Kawabe, M., Fujio, S., and Yanagimoto, D. (2003). Deep-water circulation at low latitudes in the western North Pacific. *Deep Sea Res.* 50, 631–656. doi: 10.1016/S0967-0637(03)00040-2

Kawabe, M., Fujio, S., Yanagimoto, D., and Tanaka, K. (2009). Water masses and currents of deep circulation southwest of the Shatsky Rise in the western North Pacific. *Deep Sea Res. I* 56, 1675–1687. doi: 10.1016/j.dsr.2009.06.003

Kawabe, M., Yanagimoto, D., and Kitagawa, S. (2006). Variations of deep western boundary currents in the Melanesian Basin in the western North Pacific. *Deep Sea Res. I* 53, 942–959. doi: 10.1016/j.dsr.2006.03.003

Kessler, W. S. (1990). Observations of long rossby waves in the northern tropical pacific. *J. Geophys. Res. Oceans* 95, 5183–5217. doi: 10.1029/jc095ic04p05183

Lellouche, J. M., Greiner, E., Galloudec, O. L., Garric, G., Regnier, C., Drevillon, M., et al. (2018). Recent updates to the copernicus marine service global ocean monitoring and forecasting real-time 1/12° high-resolution system. *Ocean Sci.* 14, 1093–1126. doi: 10.5194/os-14-1093-2018

Lellouche, J. M., Le Galloudec, O., Drévillon, M., Régnier, C., Greiner, E., Garric, G., et al. (2013). Evaluation of global monitoring and forecasting systems at Mercator Ocean. *Ocean Sci.* 9:57. doi: 10.5194/os-9-57-2013

Ma, Q., Wang, F., Wang, J., and Lyu, Y. (2019). Intensified deep ocean variability induced by topographic rossby waves at the pacific yap−mariana junction. *J. Geophys. Res. Oceans* 124, 8360–8374. doi: 10.1029/2019JC015490

Mantyla, A. W., and Reid, J. L. (1983). Abyssal characteristics of the World Ocean waters. *Deep Sea Res. Part A Oceanogr. Res. Pap.* 30, 805–833. doi: 10.1016/0198-0149(83)90002-x

Pratt, L. J., Voet, G., Pacini, A., Tan, S., Alford, M. H., Carter, G. S., et al. (2019). Pacific abyssal transport and mixing: through the Samoan Passage versus around the Manihiki Plateau. *J. Phys. Oceanogr.* 49, 1577–1592. doi: 10.1175/JPO-D-18-0124.1

Qu, T., and Lindstrom, E. J. (2004). Northward intrusion of antarctic intermediate water in the western Pacific. *J. Phys. Oceanogr.* 34, 2104–2118. doi: 10.1175/1520-0485(2004)034<2104:nioaiw>2.0.co;2

Rudnick, D. (1997). Direct velocity measurements in the Samoan Passage. *J. Geophys. Res. Oceans* 102, 3293–3302. doi: 10.1029/96JC03286

Siedler, G., Holfort, J., Zenk, W., Müller, T. J., and Csernok, T. (2004). Deepwater flow in the Mariana and Caroline Basins. *J. Phys. Oceanogr.* 34, 566–581. doi: 10.1175/2511.1

Sprintall, J., Siedler, G., and Mercier, H. (2013). "Inter-ocean and interbasin exchanges," in *Ocean Circulation and Climate: A 21st Century Perspective*, eds G. Siedler, S. M. Griffies, J. Gould, and J. A. Church (Cambridge, MA: Elsevier Press), 493–552. doi: 10.1016/b978-0-12-391851-2.00019-2

Vivier, F., Kelly, K. A., and Thompson, L. (1999). Contributions of wind forcing, waves, and surface heating to sea surface height observations in the Pacific Ocean. *J. Geophys. Res. Oceans* 104, 20767–20788. doi: 10.1029/1999JC900096

Voet, G., Girton, J. B., Alford, M. H., Carter, G. S., Klymak, J. M., and Mickett, J. B. (2015). Pathways, volume transport, and mixing of abyssal water in the Samoan Passage. *J. Phys. Oceanogr.* 45, 562–588. doi: 10.1175/JPO-D-14-0096.1

Wang, F., Li, Y., Zhang, Y., and Hu, D. (2013). The subsurface water in the North Pacific tropical gyre. *Deep Sea Res. I* 75, 78–92. doi: 10.1016/j.dsr.2013.01.002

Wang, J., Ma, Q., Wang, F., Lu, Y., and Pratt, L. J. (2020). Seasonal variation of the deep limb of the Pacific meridional overturning circulation at Yap-Mariana junction. *J. Geophys. Res. Oceans* 125:e2019JC016017. doi: 10.1029/2019JC016017

Whitworth, T. III, Warren, B. A., Nowlin, W. D. Jr., Rutz, S. B., Pillsbury, R. D., and Moore, M. I. (1999). On the deep western-boundary current in the Southwest Pacific Basin. *Prog. Oceanogr.* 43, 1–54. doi: 10.1016/S0079-6611(99)00005-1

Zhao, J., Li, Y., Wang, F., Zhai, F., and Yu, X. (2012). Spatial-temporal patterns and driving mechanisms of semiannual variations in the Philippine Sea. *Deep Sea Res. Part A Oceanogr. Res. Pap.* 68, 105–115. doi: 10.1016/j.dsr.2012.07.001

Conflict of Interest: The authors declare that the research was conducted in the absence of any commercial or financial relationships that could be construed as a potential conflict of interest.

The reviewer YS declared a past co-authorship with one of the authors, FW, to the handling editor.

frontiers in Marine Science

ORIGINAL RESEARCH
published: 06 July 2021
doi: 10.3389/fmars.2021.672210

Observation, Preconditioning and Recurrence of Exceptionally High Salinities in the Adriatic Sea

Hrvoje Mihanović[1], Ivica Vilibić[1,2], Jadranka Šepić[3], Frano Matić[1], Zrinka Ljubešić[4], Elena Mauri[5], Riccardo Gerin[5], Giulio Notarstefano[5] and Pierre-Marie Poulain[5]*

[1] Institute of Oceanography and Fisheries, Split, Croatia, [2] Division for Marine and Environmental Research, Ruđer Bošković Institute, Zagreb, Croatia, [3] Faculty of Science, University of Split, Split, Croatia, [4] Faculty of Science, Department of Biology, University of Zagreb, Zagreb, Croatia, [5] National Institute of Oceanography and Applied Geophysics - OGS, Sgonico, Italy

The paper aims to describe the preconditioning and observations of exceptionally high salinity values that were observed in summer and autumn of 2017 in the Adriatic. The observations encompassed CTD measurements carried out along the well-surveyed climatological transect in the Middle Adriatic (the Palagruža Sill, 1961–2020), Argo profiling floats and several glider missions, accompanied with satellite altimetry and operational ocean numerical model (Mediterranean Forecasting System) products. Typically, subsurface salinity maximum, with values lower than 39.0, is observed in the Southern Adriatic (usually between 200 and 400 m), related to ingressions of saltier and warmer waters originating in the eastern Mediterranean (Levantine Intermediate Water—LIW). However, seasonally strong inflow of warm and high salinity waters ($S > 38.8$) has been observed much closer to the surface since spring 2015. The main LIW core deepened at the same time (to 400–700 m). Such double-maxima vertical pattern was eventually disturbed by winter convection at the beginning of 2017, increasing salinities throughout the water column. A new episode of very strong inflow of high salinity waters from the Northern Ionian was observed in late winter and spring of 2017, this time restricted almost to the surface. As most of 2017 was characterized by extremely dry conditions, low riverine inputs and warmer than usual summer over the Adriatic and Northern Ionian, salinity values above the sharp and shallow (15–40 m) thermocline significantly increased. The maximum recorded salinity was 39.26, as measured by the Argo float in the Southern Adriatic. Surface salinity maximum events, but with much lower intensity, have been documented in the past. Both past events and the 2017 event were characterized by (i) concurrence with overall high salinity conditions and cyclonic or transitional phase of the Adriatic-Ionian Bimodal Oscillating System, (ii) very low river discharges preconditioning the events for a year or more, (iii) higher-than-average heat fluxes during most of the summer and early autumn periods, forming a stable warm layer above the thermocline, and (iv) higher-than-average E-P (evaporation minus precipitation) acting on this warm surface layer. Importantly, the 2017 event was also preceded by strong near-surface inflow of very saline waters from the Northern Ionian in early 2017.

Keywords: surface salinity maximum, heat fluxes, river discharges, decadal salinity oscillations, Adriatic Sea

OPEN ACCESS

Edited by:
Katrin Schroeder, Institute of Marine Science (CNR), Italy

Reviewed by:
Francesco Marcello Falcieri, Institute of Marine Science (CNR), Italy
Dimitris Velaoras, Hellenic Centre for Marine Research (HCMR), Greece

****Correspondence:***
Hrvoje Mihanović
hrvoje.mihanovic@izor.hr

Specialty section:
This article was submitted to Physical Oceanography, a section of the journal Frontiers in Marine Science

Received: *25 February 2021*
Accepted: *09 June 2021*
Published: *06 July 2021*

Citation:
Mihanović H, Vilibić I, Šepić J, Matić F, Ljubešić Z, Mauri E, Gerin R, Notarstefano G and Poulain P-M (2021) Observation, Preconditioning and Recurrence of Exceptionally High Salinities in the Adriatic Sea. Front. Mar. Sci. 8:672210. doi: 10.3389/fmars.2021.672210

INTRODUCTION

For almost 70 years it has been known that the thermohaline and biogeochemical conditions oscillate substantially in the Adriatic Sea—the northernmost embayment of the Mediterranean Sea (**Figure 1**)—over a decadal timescale (Buljan, 1953; Buljan and Zore-Armanda, 1976; Civitarese et al., 2010; Batistić et al., 2014; Dautović et al., 2017). These oscillations reflect changes in the Adriatic-Ionian thermohaline circulation and are partly controlled by (i) the fresher waters originating from Northern Adriatic rivers, advected south-eastwards along the western Adriatic shore (Western Adriatic Coastal Current, WACC, Orlić et al., 1992; Artegiani et al., 1997), and (ii) deep outflow driven by the dense water formation (DWF) events in the South Adriatic Pit (SAP) through wintertime open ocean convection (Gačić et al., 2002) and on the Northern Adriatic shelf through extensive cooling (Bergamasco et al., 1999; Mihanović et al., 2013). The DWF processes generate both the North Adriatic Dense Water (NAdDW) and the Adriatic Deep Water (AdDW) that flow along the western slope of the Adriatic (Artegiani and Salusti, 1987; Vilibić and Mihanović, 2013) and out of the Adriatic (Gačić et al., 1996), supplying oxygen and other tracers to the deepest Eastern Mediterranean layers (Roether and Schlitzer, 1991; Malanotte-Rizzoli et al., 1997). In turn, warmer and high salinity ultraoligotrophic waters from the Levantine basin (Krom et al., 1991, 2004), the so-called Levantine Intermediate Water (LIW, Zore-Armanda, 1963; Artegiani et al., 1997), are advected toward the Northern Adriatic, along the eastern coastline within the Eastern Adriatic Current (EAC, Orlić et al., 1992).

This complex thermohaline circulation is subject to significant decadal variability which is related to the basin-wide circulation reversals that occur in the Northern Ionian Sea. Many studies show that these reversals are driven by the dense waters generated in the Adriatic that change the internal vorticity in the Northern Ionian Sea (Gačić et al., 2010, 2014; Rubino et al., 2020) and may alternate at quasi-regular time intervals with the Aegean DWF site, affecting the upper eastern Mediterranean Sea thermohaline cell and influencing the circulation in the Northern Ionian Sea (Theocharis et al., 2014; Reale et al., 2017). This mechanism is called the Adriatic-Ionian Bimodal Oscillating System (BiOS, Gačić et al., 2010). Another hypothesis states that the local wind curl changes are responsible for the observed decadal circulation changes (Pinardi et al., 2015; Nagy et al., 2019). In any case, periodical reversals of the North Ionian Gyre (NIG) bring either ultraoligotrophic highly saline waters from the Eastern Mediterranean or less oligotrophic waters of lower salinity from the Western Mediterranean to the Adriatic, flushing the Adriatic within a few years at maximum (Mosetti, 1983; Vilibić and Orlić, 2002; Franić, 2005; Vilibić et al., 2020). Such a self-sustainable reversals of circulation regimes may be impacted and modified by: (i) extraordinary Mediterranean-wide events like the Eastern Mediterranean Transient (EMT, Klein et al., 1999; Incarbona et al., 2016), which occurred from the late-1980s to the mid-1990s and additionally strengthened anticyclonic BiOS, resulting in an unprecedented change in biogeochemical properties in the Adriatic (Grbec et al., 2009; Vilibić et al., 2012), (ii) local wind-driven vortices (like Messina Rise Vortex and Pelops Gyre—see **Figure 1**), that may redirect the path of the Mid-Ionian Jet and therefore re-shape the circulation in the Northern Ionian Sea (Menna et al., 2019), (iii) climate change, as weakening of the Adriatic-Ionian thermohaline circulation has been observed (Vilibić et al., 2013), or other.

Substantial changes in thermohaline properties were observed in both Adriatic and Eastern Mediterranean basins during the recent decades, which might be a reflection of ongoing climate change in the Mediterranean (Giorgi, 2006; Gualdi et al., 2013). This includes the increase of sea surface temperatures throughout the basin (Pastor et al., 2018), largely related to both climate warming and multidecadal oscillations originating from the North Atlantic (Marullo et al., 2011; Skliris et al., 2012; Macias et al., 2013). Further, the substantial increase in surface salinity, especially after 2006, has been observed, conjoined with the reduction in advection of less saline Atlantic waters toward the Eastern Mediterranean (Kassis and Korres, 2020). The salinity increase has peaked in recent years (0.14 over a year between 2015 and 2018, Grodsky et al., 2019). Such an increase might be relevant for the change of the LIW source characteristics (Kubin et al., 2019), which in turn may change characteristics of the Western Mediterranean intermediate waters and alter the thermohaline characteristics of the whole basin (Ben Ismail et al., 2014; Vargas-Yáñez et al., 2017). This can also impact salinity distribution in the Adriatic Sea, where a substantial increase in salinity and change in its structure have been recently recorded (Kokkini et al., 2020).

Recent Adriatic observations, mostly by Argo profilers in the SAP between 2013 and 2016 and by CTD probes, reveal: (i) deepening of the saline LIW core from near-surface layers (50–100 m) in 2013 to 200–400 m in 2014 and further to 400–700 m in 2015–2016, while (ii) new surface and subsurface high salinity waters started to enter the SAP in spring 2015, with surface salinity as high as 38.9 in 2016, creating two salinity maxima in vertical profile (Babić et al., 2017; Hure et al., 2018; Kokkini et al., 2020). The wintertime conditions during 2013 were in favor of DWF, while 2014–2016 period was characterized by relatively mild winters. Additionally, a large freshwater load through rivers and precipitation, that created haline-driven stratification, was documented during 2014 (Mihanović et al., 2018; Kokkini et al., 2020). The surface inflow of high salinity waters from the Eastern Mediterranean continued in early 2017, preconditioning the record-breaking salinities observed in summer and autumn at the coastal Stončica station (CJ009 – see **Figure 1** for the location of the station) off the eastern Middle Adriatic coast, characterized by unusual "inverse" salinity vertical structure (with the highest salinities observed in the surface and near-surface layers, Beg Paklar et al., 2020). Such a vertical structure is uncommon in the Adriatic, but it regularly appears in the Levantine basin, preconditioning (among other) the LIW formation (Kubin et al., 2019). A sharp negative halocline is collocated with a sharp seasonal thermocline there, to the depths of 20 to a 100 m (Kubin et al., 2019; Kassis and Korres, 2020). The thermocline is developed and maintained by extensive heat gain and low wind conditions, while evaporation mostly affects surface waters, in particular during summer and autumn, increasing the surface salinity. Both thermocline and halocline deteriorate during the

LIW formation in winter. Surface salinity maxima are also known to occur in subtropical regions where they are related to extensive heating and evaporation (Bingham et al., 2014; Chen et al., 2018; Wang et al., 2019) during stable (low wind) weather conditions.

An interesting consequence of the unusual salinity conditions, hypothesized to be governed by local (heat and water fluxes) and remote (BiOS) drivers, documented in the eastern Middle Adriatic in 2017, was their effect on the microbial food web (Beg Paklar et al., 2020), in particular to the substantially lower bacterial production and abundance. In this manuscript we intend to provide a wider basin-scale picture of the air-sea interactions and circulation in the Adriatic-Ionian basin during the appearance of surface and near-surface high salinity maxima. Moreover, the availability of historic thermohaline data enabled us to investigate similar events, which occurred previously in the Adriatic Sea, and to determine more precisely the preconditioning and processes responsible for the occurrence of high salinities. Section "Data and methods" overviews measurements and other tools used to quantify thermohaline changes during 2017 and the respective preconditioning period, and during occurrences of historical high surface salinity events (1961–2016). Section "Thermohaline properties in 2017" displays basin-wide thermohaline observations and outputs of the Mediterranean Forecasting System operational numerical model for 2017. The processes contributing to anomalous thermohaline properties in 2017, occurring from decadal to daily scales, are documented in Section "Processes contributing to anomalous thermohaline properties in 2017". Section "Past high surface and near-surface salinity events in the Adriatic" focuses on the analysis of historical data in order to detect past events of surface salinity maximum and inverse subsurface halocline, and on investigation of the respective background processes. The results are discussed and the study is concluded in Section "Discussion and Conclusion," which also briefly documents the most recent (2018–2020) thermohaline observations in the Adriatic.

DATA AND METHODS

Thermohaline Data

Temperature and salinity data collected at the Palagruža Sill transect were acquired during five cruises in 2017, at 10–12 stations (**Figure 1** and **Table 1**). The sampling at the transect was done with Seabird 25 probe[1], which has accuracy of ± 0.002°C for temperature and ± 0.002 for salinity.

Long-term temperature and salinity data at the Palagruža Sill transect collected between 1961 and 2017 were analyzed and episodes of vertical salinity distributions that resemble the 2017 salinity distributions were extracted. These data were collected with monthly to seasonal resolution, using different sampling techniques (reversing thermometers and various CTD probes for temperature; titration with $AgNO_3$, portable induction salinometers and various CTD probes for salinity). The series were homogenized and used in different studies (e.g., Vilibić et al., 2013; Beg Paklar et al., 2020), in which more details on the measurements procedures can be found. We focused on episodes with surface salinity values higher than 38.8 observed on at least one station along the transect, between 0 and 20 m (considering them as high surface salinity events). This threshold was based on long-term monthly measurements at the Stončica station (CJ009), as it is at least one standard deviation above long-term average for any month of the year (Beg Paklar et al., 2020).

Three winter (November/December) and two spring (April/May) glider missions were carried out across the SAP between 2015 and 2017, roughly from Bari to Dubrovnik (**Figure 1** and **Table 1**). Teledyne Slocum gliders[2] were used, sampling temperature and salinity down to 1,000 m, using a Sea-Bird pumped payload CTD (GPCTD) with accuracies of ± 0.002°C and ± 0.002, respectively (Stommel, 1989; Merckelbach et al., 2008; Rudnick et al., 2012). The sensors were calibrated prior to each deployment. More details on glider campaigns may be found in Kokkini et al. (2020).

Thermohaline data from seven Argo floats that were profiling in the Adriatic and Northern Ionian between 2010 and 2017 were used in our study (Argo, 2021). The WMO numbers of the floats are: 1900848, 6901040, 6901822, 6901827, 3901978, 6901829, and 6901862. These measurements were conducted within the framework of the MedArgo programme (Poulain et al., 2007) and the European MOCCA project. Sea-Bird CTD sensors (model 41/41 CP) with initial accuracies of ± 0.002°C and ± 0.003 were used for temperature and salinity measurements, respectively, while all floats had cycle duration between 1 and 5 days and a parking pressure of 350 dbar. Initial accuracies indicate accuracies of Argo float sensors after their initial deployment, usually assessed by comparing the temperature and salinity values measured in the first few cycles to CTD data obtained shortly after the Argo float deployments (Nezlin et al., 2020). The parking depth for float 1900848 was changed to 150 dbar when it drifted to the Middle Adriatic area in the second part of 2010 (Vilibić and Mihanović, 2013). Moreover, recent data from Argo floats 3901978 (Southern Adriatic and Ionian), 6903250 (Southern Adriatic) and 6903263 (Jabuka Pit) were also analyzed, to document salinity properties in recent years (2018—2020). The parking depth of the float 6903250 was set to 1,000 dbar, as this is a Bio-Argo float and larger parking depth is usually set in order to limit the drift of the float in other zones with different biogeochemical characteristics. Therefore, it mostly remained within the inner perimeter of the South Adriatic Pit. On the other hand, the Jabuka Pit float 6903263 profiled the entire water column in a relatively small area during most cycles, as it was configured with a parking depth close to the bottom.

Ancillary Data

Daily heat and water (evaporation minus precipitation, E-P) fluxes were computed from the European Centre for Medium-Range Weather Forecasts (ECMWF) ERA-Interim dataset ([3]Dee et al., 2011) and averaged over the central part of the Southern Adriatic, representing open sea conditions in the area (**Figure 1**). Daily averaged data of Po River collected at the Pontelagoscuro sampling station were used to present variability in river discharges (**Figure 1**). Finally,

[1]www.seabird.com

[2]http://www.teledynemarine.com

[3]www.ecmwf.int

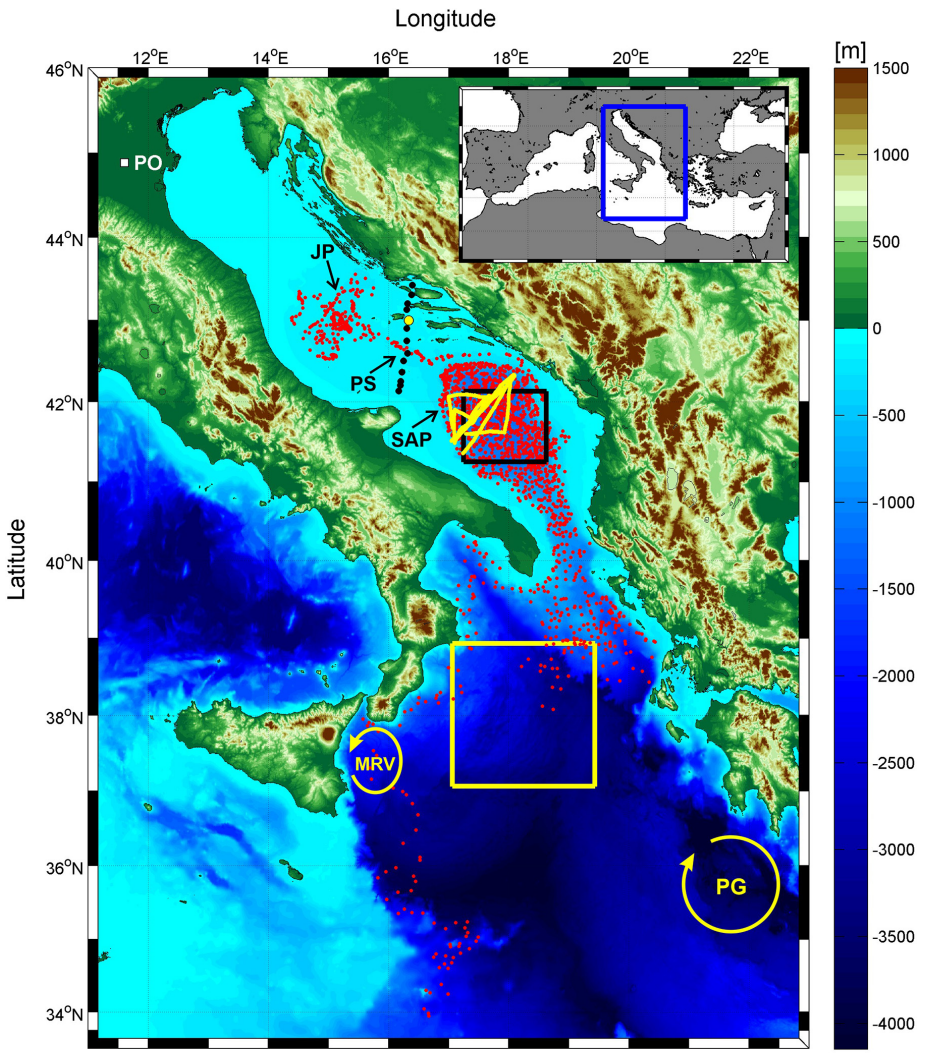

FIGURE 1 | The bathymetry of the Adriatic-Ionian basin. The positions of Argo profiles used in the study are denoted by small red dots. CTD stations at the Palagruža Sill transect are indicated by black dots, with Stončica station (CJ009) denoted by larger yellow dot. Glider trajectories in the Southern Adriatic are marked by yellow lines. JP, PS and SAP stand for the Jabuka Pit, the Palagruža Sill and the South Adriatic Pit, respectively. The black rectangle in the Southern Adriatic indicates the area over which heat and water fluxes were estimated. The yellow rectangle in the Northern Ionian represents the area used for computation of vorticity. The positions and the sense of rotation of the Messina Rise Vortex (MRV) and the Pelops Gyre (PG) are also indicated. Pontelagoscuro station, at which Po River discharge are measured, is indicated by the white square in the upper left part of the figure.

to detect anomalous conditions, the averages and standard deviations were computed for the period between 1979 and 2017 and compared versus actual values, all averaged on monthly time scale.

Mean absolute dynamic topography (ADT) data were used to quantify both seasonal variability in the surface circulation and the BiOS. ADT is AVISO+ (Gridded Sea Level Heights and derived variables – Mediterranean Sea) product with a 1/8° resolution that has been available since 1993 and can be accessed at http://marine.copernicus.eu. In order to quantify BiOS-driven variability, vorticity was estimated from the surface currents and averaged over the central part of the Northern Ionian Sea (**Figure 1**), following the procedure described by Shabrang et al. (2016).

The Mediterranean Forecasting System (MFS) results available at http://marine.copernicus.eu were used to assess the surface thermohaline properties and the circulation during 2017 (Clementi et al., 2019). The MFS numerical analysis and short-term forecasts are available since 2000 (Pinardi et al., 2003; Pinardi and Coppini, 2010). The MFS hydrodynamic system is implemented over the entire Mediterranean basin including tides and is composed of two elements: the Nucleus for European Modeling of the Ocean (NEMO v3.6) and third generation Wave Model (Wave Watch-III). Numerical solutions are corrected by a variational data assimilation scheme based on 3DVAR. The horizontal resolution of the model is 1/24° (around 4 km) and the model has 141 unevenly spaced vertical levels. It is forced by momentum, water and heat fluxes interactively computed using

TABLE 1 | The list of CTD cruises (Palagruža Sill), glider missions (Southern Adriatic), and Argo profilers (Northern and Central Ionian Sea, Middle and Southern Adriatic) presented in the study, including their deployment periods.

CTD cruises (Palagruža Sill)	Glider missions (Southern Adriatic)	Argo floats	
Dates	**Dates**	**Float number/Region**	**Dates**
19–20 Aug 2003	20 Nov–1 Dec 2015	1900848/Middle and Southern Adriatic	1 Mar 2010–15 Nov 2014
12–14 Aug 2005	22 Apr–1 May 2016	6901040/Southern Adriatic and Northern Ionian	31 Mar 2012–12 Oct 2014
22–24 Aug 2012	3–11 Dec 2016	6901822/Southern Adriatic	24 Mar 2013–27 Feb 2018
1–4 Oct 2016	6–8 May 2017	6901827/Southern Adriatic and Northern Ionian	13 May 2013–26 Jun 2018
23–24 Mar 2017	2–13 Dec 2017	6901829/Southern Adriatic and Northern Ionian	14 Feb 2014–21 Nov 2018
19–20 Jun 2017		6901862/Southern Adriatic, Northern and Central Ionian	27 Mar 2015–27 Jun 2019
22–25 Jul 2017		3901978/Southern Adriatic, Northern and Central Ionian	7 July 2017–present
13–14 Oct 2017		6903250/Southern Adriatic	10 Oct 2018–16 Jan 2021
6–7 Dec 2017		6903263/Middle Adriatic	24 Mar 2019–present
10–12 Aug 2020			

operational analysis and forecast fields from the ECMWF and the model predicted surface temperatures (Pettenuzzo et al., 2010).

THERMOHALINE PROPERTIES IN 2017

CTD Observations at the Palagruža Sill

The temperature and salinity observations taken at the Palagruža Sill transect (**Figure 2**) indicate high salinity conditions throughout 2017, in respect to values/data presented in previous Adriatic climatologies and literature (Buljan and Zore-Armanda, 1976; Artegiani et al., 1997; Lipizer et al., 2014; Beg Paklar et al., 2020). The bilinear interpolation (e.g., Kirkland, 2010) was used to plot these transects from available CTD casts, still likely resulting in some artifacts due to small number of CTD profiles along the transect, such as somewhat peculiar salinity vertical structures between the first three CTD casts on the right, which are likely generated by not accounting for the seamount in our interpolation. On 23–24 March 2017 (**Figure 2A**), the very surface waters started to warm up, while the NAdDW outflow, characterized by temperatures lower than 13°C and salinities lower than 38.8, was detected near the bottom. The outflow followed the DWF on the Northern Adriatic shelf which likely occurred in January 2017, when extreme cold periods, with severe bora events, were recorded in the Adriatic (DHMZ, 2018). Salinity in the Middle Adriatic in March 2017 was high, between 38.8 and 38.93 at the transect stations, except close to the eastern (entire water column) and western (near the surface) Adriatic coast. Salinity values near the bottom, at the core of the NAdDW flow, were around 38.8, which is much higher than the average of ∼38.6 in the period 1952–2010 (Vilibić et al., 2013). On 19–20 June 2017 (**Figure 2B**), the thermocline was well developed and relatively shallow (15–25 m), while salinity reached the maximum in the intermediate layers (∼38.94) where the LIW normally crosses the Palagruža Sill (Buljan and Zore-Armanda, 1976; Martin et al., 2009). Surface salinity in the central part of the transect (38.8–38.9) was slightly lower than in the intermediate layer (38.85–38.93), as was salinity in the deepest parts (∼38.8), where the NAdDW outflow can still be seen.

A month later, on 22–25 July 2017 (**Figure 2C**), the salinity and temperature measurements were still reflecting the LIW inflow at depths between 50 and 100 m and weakened NAdDW outflow in the intermediate and deep layers of the transect, respectively. However, the upper-layer temperature increased significantly, reaching almost 26°C. This very strong thermocline did not deepen compared to June measurements and was still at depths of around 15–25 m. Interestingly, the salinity maximum started to develop at the very surface of the transect, surpassing 39.0 at some stations. Such conditions continued to develop, peaking on 13–14 October 2017, when a clear surface pool of highly saline and warm waters was observed along most of the transect (**Figure 2D**). The depth of thermocline and halocline ranged from 20 m at the southern section of the transect to about 40 m off the coastal region of the northern part of the transect. The intensity of the thermocline and halocline was -2°C m^{-1} and -0.18 m^{-1}, respectively. The highest values of salinity in the central part of the transect exceeded 39.1.

The last 2017 cruise along the Palagruža Sill transect, carried out on 6–7 December (**Figure 2E**), indicated vertical homogenization of the waters along the whole transect, except in its deepest parts. The salinity decreased substantially in the surface layer (38.7–38.85), while high values of salinity (up to 38.94) were still observed near the bottom. The surface salinity recorded on monthly basis at the Stončica station (CJ009) was higher than 38.8 throughout 2017, and it was 2–2.5 standard deviations above the long-term average between June and November 2017, revealing exceptional conditions not previously documented for the Middle Adriatic (Beg Paklar et al., 2020).

Argo Profiling Floats and Glider Observations

Trajectories and Hovmöller diagrams of salinity in the upper 600 m of five Argo profiling floats active during 2017 in the Southern Adriatic, the Strait of Otranto and the Northern Ionian Sea are displayed in **Figure 3**. Interestingly, all floats recorded an exceptional maximum in the surface and near-surface salinity during summer and autumn seasons, peaking in values higher than 39.2 at the very surface. In particular, very high salinity values (above 38.9) can be detected in the upper 100 m in the Southern Adriatic (**Figures 3A,B**) since early March 2017 and

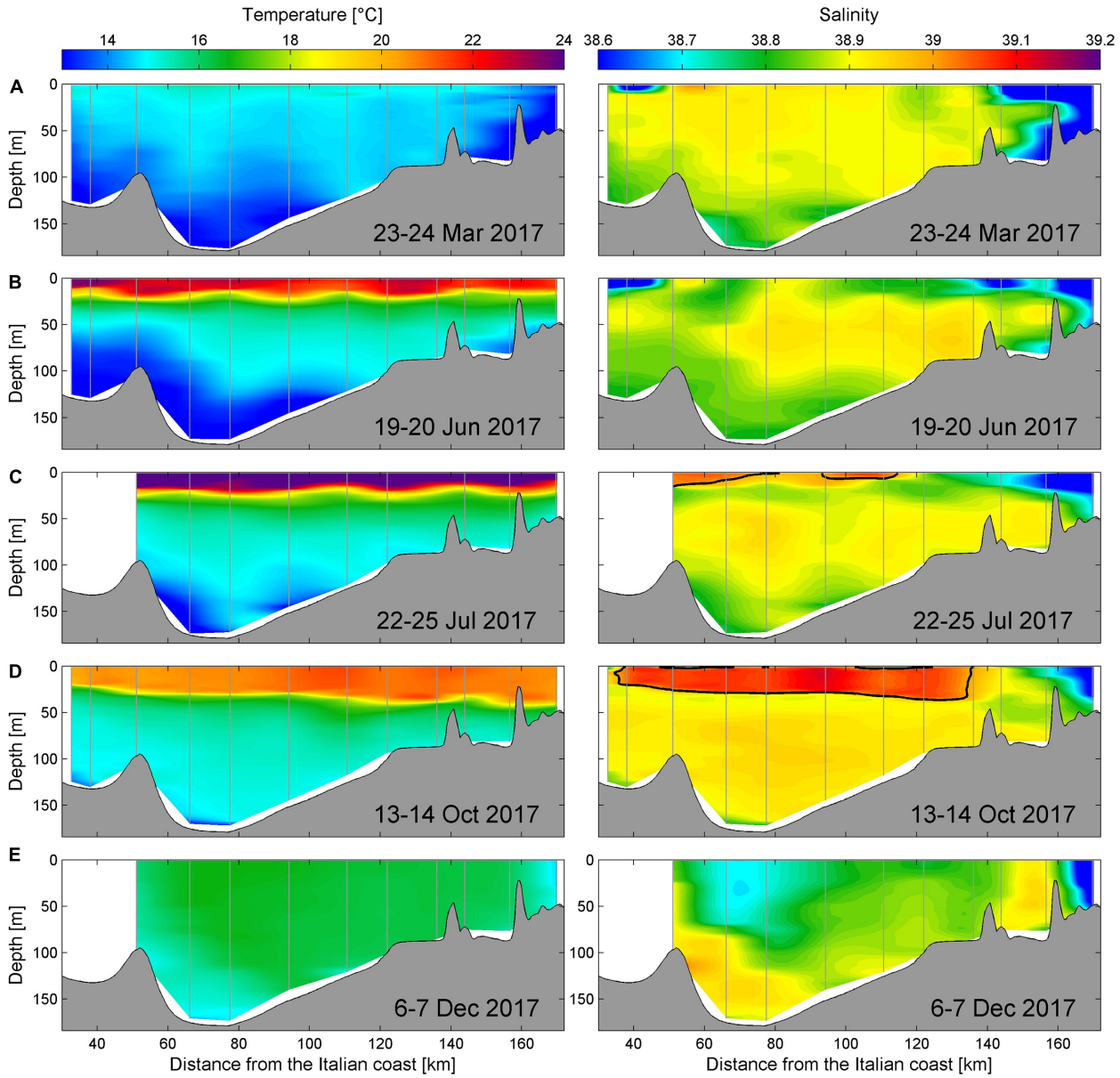

FIGURE 2 | Temperature and salinity measured at the Palagruža Sill transect: **(A)** 23–24 March 2017, **(B)** 19–20 June 2017, **(C)** 22–25 July 2017, **(D)** 13–14 October 2017 and **(E)** 6–7 December 2017. Salinity values higher than 39.0 are encircled with black line in salinity plots. Vertical gray lines denote CTD casts.

down to 200–300 m in the Strait of Otranto (**Figure 3E**) and the Northern Ionian Sea (**Figure 3D**) during most of 2017.

The surface pools of exceptionally high salinity waters (thick black line in left panels in **Figure 3** denotes 39.0 salinity contour) were first observed in the Argo profiling float data from the northeastern Ionian Sea, just southeast of the Strait of Otranto (Argo float 6901829; **Figure 3D**), at the end of May 2017. Then, during June these pools were observed by the Southern Adriatic floats (6901822 and 6901827; **Figures 3A,B**) and by another Northern Ionian float (6901862; **Figure 3E**). Surface salinity values were slightly lower than 39.0 at locations of most of the analyzed floats during most of July 2017 (except 6901827; **Figure 3B**). However, from late July all floats observed exceptionally high surface salinity values. Some of them were sampled till mid-October in the Northern Ionian (**Figures 3D,E**). Surface salinity in the Southern Adriatic peaked between August and October, and gradually decreased through November, as seen in the data of three Southern Adriatic floats (**Figures 3A–C**), likely pointing to enhanced vertical mixing.

Glider campaigns carried out in the Southern Adriatic during 2017 indicated the surface salinity maximum as early as May (**Figure 4A**), with values slightly lower than 39.0 in the layer between the surface and 50 m depth. This relatively short glider campaign (2 days) documented the surface salinity increase in

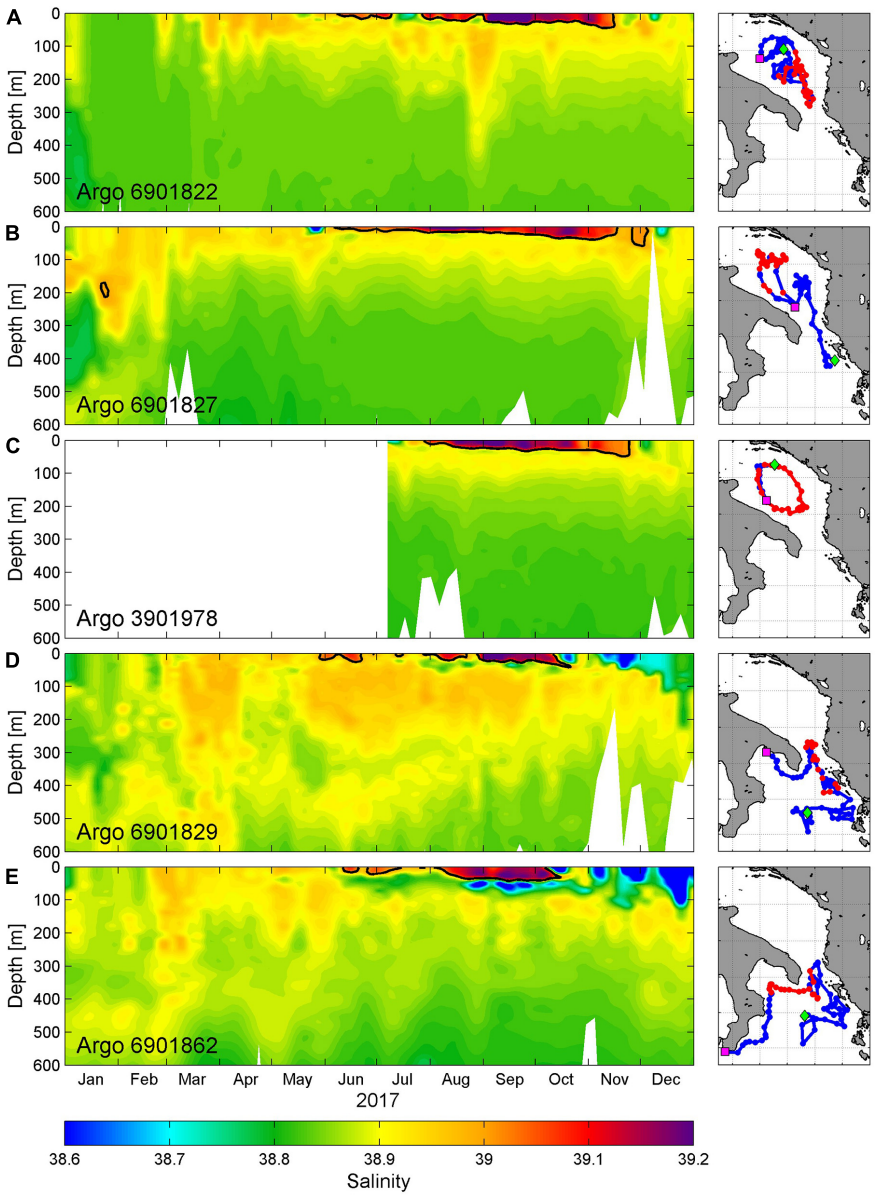

FIGURE 3 | (A) Hovmöller diagram of salinity data for Argo float 6901822 in the first 600 m in 2017 (left panel) with corresponding float trajectory (right panel). Thick black line in the left panel denotes 39.0 salinity contour, while the corresponding part of the trajectory is colored in red in the right panel. The location of the first vertical profile in 2017 is denoted by green diamond in right panel, while the last vertical profile in 2017 is marked with magenta square. **(B–E)** As in panel **(A)** except for Argo floats 6901827, 3901978, 6901829, and 6901862, respectively.

the central part of the SAP, as saline waters from the Northern Ionian were entering in the Southern Adriatic already in March 2017 (**Figures 3A,B**). The surface/subsurface salinity maximum was still present in the first 70–80 m along the central part of the Southern Adriatic transect (**Figure 4B**) between 2 and 6 December 2017, with values close to 39.0. Interestingly, the upper layer of warmer and highly saline waters deepened to 120 m toward the end of the glider mission, between 8 and 13 December 2017, elucidating the ongoing mixing, cooling and deepening of the surface salinity pool, most probably due to the atmospheric forcing (the crossing point between the "A-B" and "C-D" segments of the glider mission is indicated by letter "X," as this was the location that was sampled twice during this glider mission, on 4 December and on 12 December 2017).

Ocean Model Results

The model outputs from the Mediterranean Forecasting System show monthly evolution of surface salinity and current fields during 2017 (**Figure 5**). The model indicated that surface inflow of very saline surface waters (salinities above 38.9) was present from January to April 2017 between the Northern Ionian and Southern Adriatic, and that spread across the Southern Adriatic.

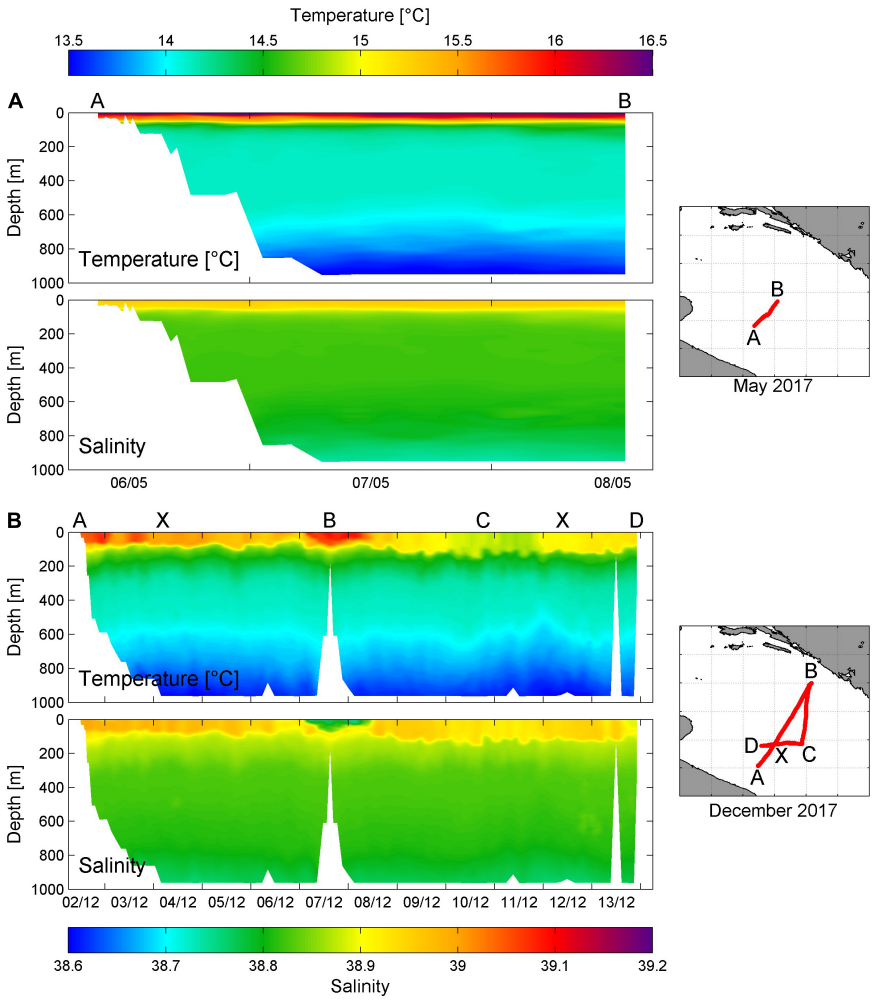

FIGURE 4 | (A) Glider temperature and salinity transects in the in the Southern Adriatic between 6 and 8 May 2017 (left panels) and the corresponding trajectory of the glider (right panel). **(B)** As in panel **(A)** except for glider transect from 2 to 13 December 2017. The crossing point between the "A–B" and "C–D" segments of the December 2017 glider mission is indicated by letter "X."

This process is also reflected in two Argo floats measurements (**Figures 3A,B**) and in the May 2017 glider data (**Figure 4**). Surface waters with such a high salinity values were then exposed to intense heating and evaporation during May and June (as it will be shown later) and a pool of exceptionally highly saline surface and near-surface waters (salinities surpassing 39.0) in the southwestern part of the SAP was already present in June 2017 (**Figure 5**). According to the model results, the transport between Adriatic and Ionian Seas was blocked by several gyres within the Strait of Otranto in June 2017. The high-salinity waters in the SAP were accompanied with weak currents, indicating their relative stationarity. Exceptionally high surface salinity (>39.0) could also be seen in the Northern Ionian Sea in June 2017, particularly in the cyclonic gyre just south of the Strait of Otranto.

The pool of high surface salinity waters in the SAP further developed and widened in July (**Figure 5**), while the modeled currents in the western part of the SAP were mostly southward oriented and the majority of these waters was leaving the Adriatic Sea. However, CTD measurements at the Palagruža Sill transect in July 2017 indicated exceptionally high surface salinity in the central and southern part of the transect (**Figure 2C**), possibly related to the inflow from the Southern Adriatic and local salinification above the thermocline. The surface salinity reached 39.2 in the central and southwestern parts of the SAP in August. The core of the exceptionally highly saline salinity waters remained in the SAP throughout September, and the enhanced EAC started to bring some of these waters northwestward over the Palagruža Sill. Simultaneously, the exchange between the Adriatic and the Northern Ionian significantly increased, enabling additional salt advection to the Southern Adriatic. The advection of highly saline surface waters toward the Palagruža Sill reached the maximum in October (**Figures 2D**, **5**) during which the overall along-basin surface transport was the highest. Signs of the surface salinity decrease began in November (**Figure 5**), but still keeping the maximum value in the central SAP.

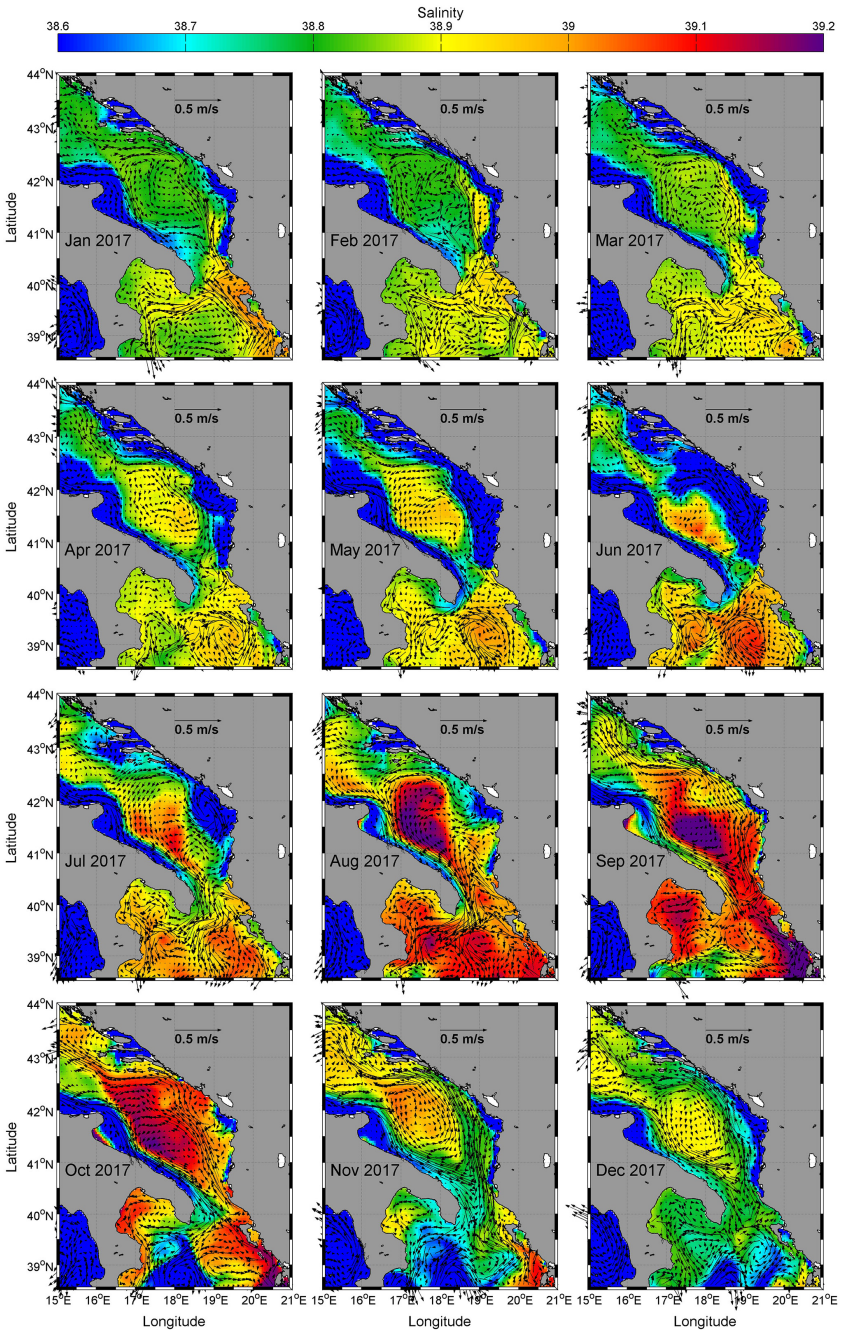

FIGURE 5 | Modeled surface currents (Mediterranean Forecasting System) and salinities, monthly averaged between January and December 2017.

PROCESSES CONTRIBUTING TO ANOMALOUS THERMOHALINE PROPERTIES IN 2017

Inflow of the Salty Surface Waters From the Ionian Sea Before 2017

The thermohaline variability in the Adriatic Sea is driven by a number of processes acting on daily to decadal timescales. Among these are quasi-decadal oscillations driven by the Adriatic-Ionian Oscillating Bimodal System (BiOS). Following Shabrang et al. (2016), who quantified the BiOS oscillations by computing vorticity in the Northern Ionian Sea, we computed surface vorticity in the Northern Ionian rectangle depicted in **Figure 1** for the 1993–2020 period using satellite altimetry geostrophic currents. It was found that it oscillated between positive and negative values, where positive values indicate cyclonic and negative values anticyclonic BiOS regimes in the

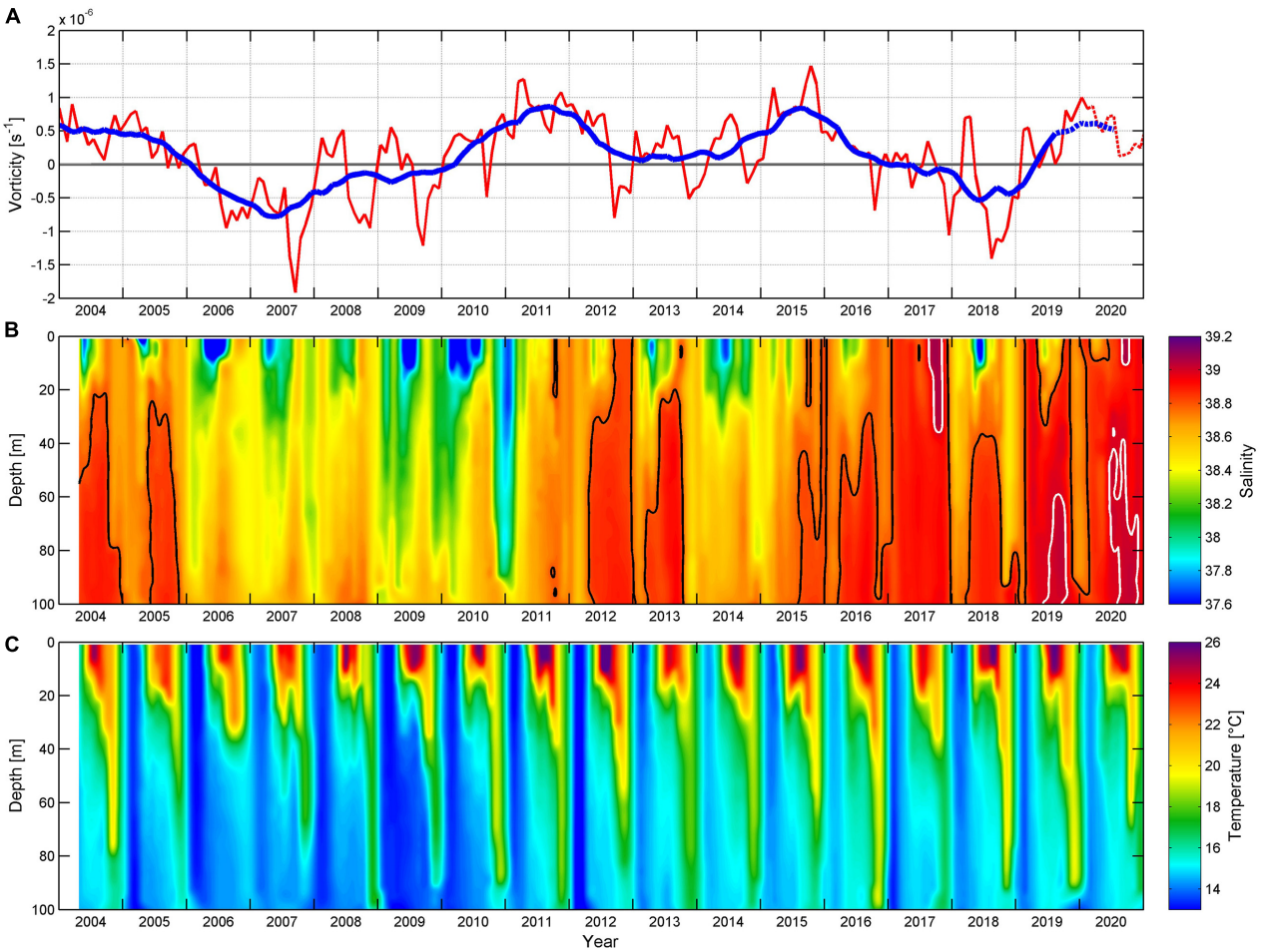

FIGURE 6 | (A) Monthly time series of the spatially averaged current vorticity (red line) and low-pass filtered (13 months) current vorticity (thick blue line) computed in the Northern Ionian Sea (37–39°N; 17–19.5°E) between January 2004 and December 2020. Dashed parts in panel **(A)** denote vorticity data based on near real time AVISO+ product. **(B)** Hovmöller diagram of salinity measurements at station CJ009 between April 2004 and December 2020. Thick black line in panel **(B)** indicates 38.8 salinity contour (high salinity conditions), while thick white line denotes 39.0 contour (exceptionally high salinities). **(C)** Hovmöller diagram of temperature measurements at station CJ009 between April 2004 and December 2020.

Northern Ionian Sea. When analyzing the vorticity between 2004 and 2020 (**Figure 6A**) i.e., during the period with a frequent (quasi-monthly) high quality CTD measurements available at the Palagruža Sill transect station CJ009 (**Figure 6B**), it appears that the cyclonic BiOS regime was present until 2005, switching to anticyclonic BiOS regime until the beginning of 2010, then again returning to cyclonic regime between the second half of 2010 and 2016 (with a weakening in 2012–2013, due to extraordinary DWF in winter of 2012, Gačić et al., 2014). Predominantly transient and anticyclonic regime was then observed during 2017 and 2018, shifting again to cyclonic circulation in 2019. Simultaneously, salinity at the station CJ009 (**Figure 6B**) exhibited a period with high values in 2004 and 2005 (reaching almost 38.9 in the intermediate and bottom layers), then it decreased to 38.2–38.6 between 2006 and 2010. New increase in salinity occurred during 2011, reaching maximum values close to 38.9 in 2012 in the intermediate and bottom layers (also exceeding 38.8 at the surface by the end of the year). Salinity values higher than 38.9 were also observed in 2013. The salinity then decreased in 2014 (36.7–38.7 in the intermediate and bottom layers), as it was a year characterized by abundant precipitation and higher than usual river discharges in the Adriatic Sea area (Kokkini et al., 2020; see also Section "Physical setting in 2017" for higher than usual Po River discharges during 2014). The salinity in the following 2 years rose again, surpassing 38.9 in the second part of 2016. During all these phases salinity mostly followed the BiOS-driven vorticity with a lag of 1–2 years, relating high salinity values with positive vorticity and *vice versa*. However, such an interaction was not clearly present in the 2017–2018 period, as exceptionally high salinities (above 39.0 in 2017) observed at the Palagruža Sill transect were associated with a weakening cyclonic BiOS phase switching to negative vorticity values and predominantly transient and anticyclonic BiOS regime.

As for temperature measurements at CJ009 (**Figure 6C**), seasonal signal is dominant, particularly close to the surface, indicating well developed seasonal thermocline. Moreover,

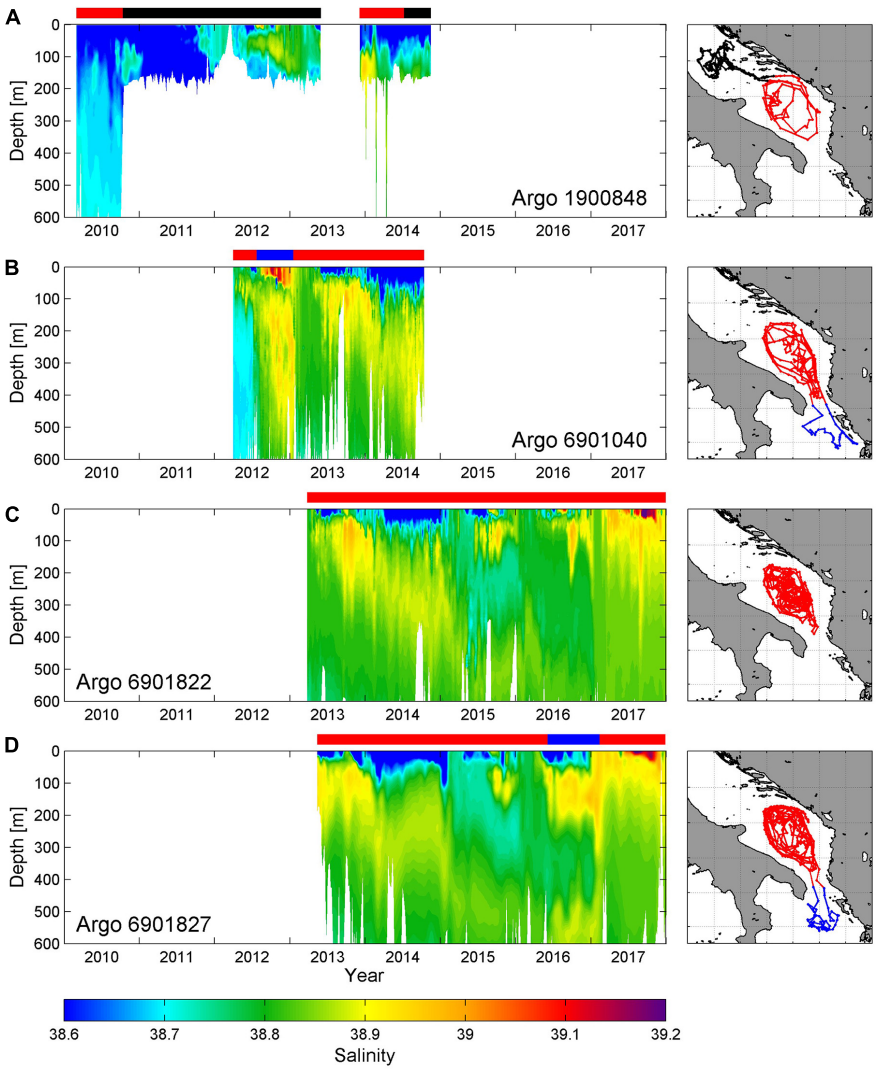

FIGURE 7 | (A) Hovmöller diagram of salinity data for Argo float 1900848 in the first 600 m in the period 2010–2014 (left panel) with corresponding float trajectory (right panel). **(B–D)** As in panel **(A)** except for Argo floats 6901040 (2012–2014), 6901822 (2013–2017) and 6901827 (2013–2017), respectively. Argo trajectories are colored depending on the location of the float (black–Middle Adriatic, red–Southern Adriatic, blue–Northern Ionian). The same color notation is used in horizontal bars above left panels, indicating periods during which Argos were profiling in respective areas.

intermediate and bottom temperatures followed salinity variations during BiOS regimes, as the Western Mediterranean intermediate waters that enter the Adriatic are characterized by lower temperature and salinity than waters originating in the Eastern Mediterranean (Vilibić et al., 2012).

The corresponding changes in salinity, as measured by Argo profiling floats between 2010 and 2017 in the Adriatic (the Adriatic Argo measurements are available since 2010), indicate the period of relatively lower salinity (below 38.6 in the upper 100 meters) observed in the Southern and Middle Adriatic in 2010 (**Figure 7A**). The salinity started to increase at the end of 2011 and during 2012 in both Middle (Argo float 1900848; **Figure 7A**) and Southern Adriatic (Argo float 6901040; **Figure 7B**), following the change to the cyclonic phase of the BiOS. Surface salinity maximum and a surface pool of saline waters were observed in the Strait of Otranto and the Northern Ionian Sea in summer and autumn 2012 (**Figure 7B**), and shortly during the summer in the Middle Adriatic (by the Argo float 1900848, **Figure 7A**). The vertical salinity profile (and vertical temperature profile, not shown) exhibited homogenization of the water column in the winter of 2013, apparently due to open-ocean convection (Mihanović et al., 2018). This mechanism and subsequent dense water outflow presumably triggered the Adriatic-Ionian thermohaline circulation (Orlić et al., 2006), inducing the subsurface LIW inflow in autumn 2013, at depths of 100–200 m. The LIW inflow gradually deepened in 2014 and 2015 to depths of about 200–400 m (**Figures 7A–C**), presumably driven by a weak open convection that pushed the LIW to even greater depths in 2015 and 2016 (400–700 m, Lučić et al., 2017; Hure et al., 2018; Kokkini et al., 2020). Simultaneously,

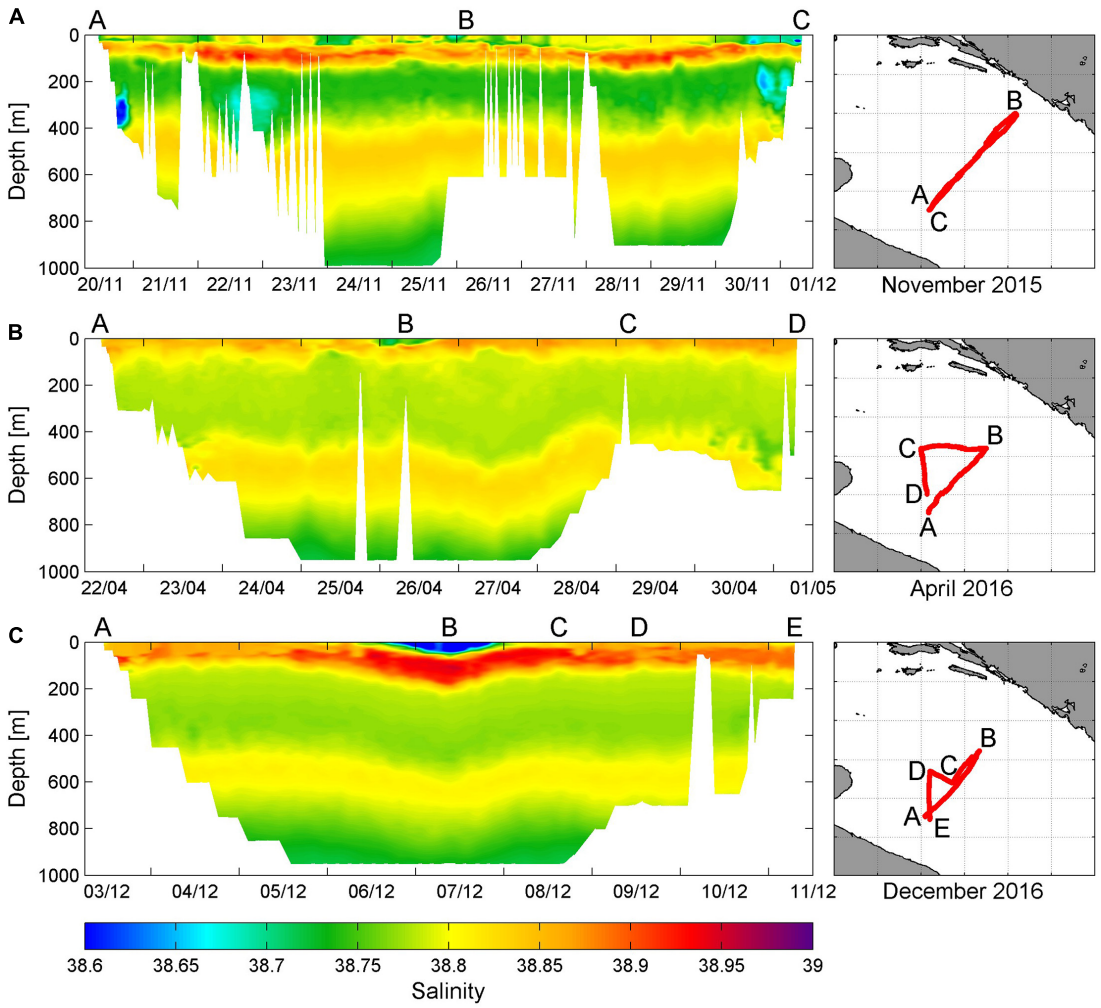

FIGURE 8 | (A) Glider salinity transect in the in the Southern Adriatic between 20 November and 1 December 2015 (left panel) and the corresponding trajectory of the glider (right panel). **(B)** As in panel **(A)** except for glider transect from 22 April to 1 May 2016. **(C)** As in panel **(A)** except for glider transect from 3 to 11 December 2016. Please note that the salinity scale for these glider transects is different than in **Figure 4**.

a subsurface high salinity core started to be observed in the Adriatic at depths between 50 and 200 m, with a patch firstly visible in the second part of 2015 and even stronger inflow in 2016 (**Figure 7C**).

The double salinity maxima that preceded high salinity conditions in 2017 were also observed during the BIOTA project (Bio-tracing Adriatic Water Masses) campaigns, that encompassed the eastern section of the SAP (Babić et al., 2017; Lučić et al., 2017; Hure et al., 2018), and in glider missions in the central SAP in 2015 and 2016 (**Figure 8**). The BIOTA measurements in late February/early March 2015 were the first indication of the double maxima pattern in the Southern Adriatic (e.g., Babić et al., 2017), with near-surface maximum values present in a narrow band along the northeastern shelf break (therefore not detected so early by Argo floats, which usually remained further offshore). These near-surface salinities were slightly lower than contemporaneous deep-water salinity maximum values. The salinity distribution in November 2015 (**Figure 8A**), prior to the winter period in which open convection may take place in the SAP, reproduces the double salinity maxima pattern across the whole SAP, i.e., subsurface salinity maximum (50–100 m) occasionally exceeding 38.9 and the deep salinity maximum at 400 to 600 m (with values up to 38.85). Interestingly, the subsurface salinity maximum value in the second part of 2015 dominated over the deep salinity maximum, although restricted to a narrower layer. The subsurface salinity maximum indicated a subsurface advection of saline waters from the Levantine basin, while the deep salinity maximum did not show large changes in the salt content. After a weak winter convection period in early 2016, the deep salinity maximum was still present, but it deepened to 550 to 700 m in the open Adriatic (**Figure 8B**). The near-surface salinity maximum moved toward the surface, with high salinity waters encompassing the first 100 m of the water column in the open sea. The maximum was deeper at the perimeter of the SAP (points A and D in **Figure 8B**). Very similar salinity distribution remained till the end of 2016 (**Figure 8C**),

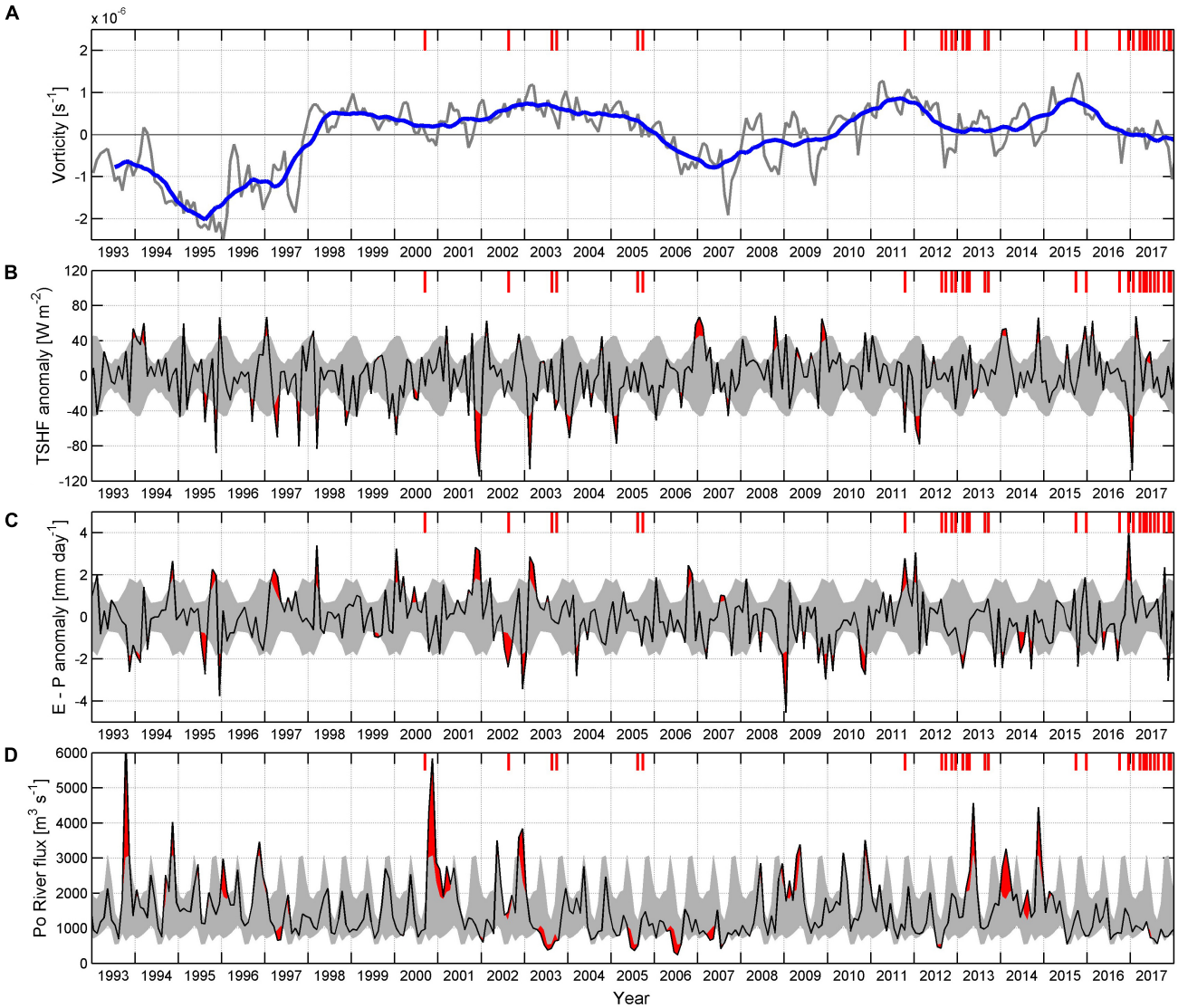

FIGURE 9 | (A) Monthly time series of the spatially averaged current vorticity (gray line) and low-pass filtered (13 months) current vorticity (blue line) computed in the Northern Ionian Sea (37–39°N; 17–19.5°E) between January 1993 and December 2017. **(B)** Monthly ERA-Interim total surface heat flux anomalies and **(C)** evaporation minus precipitation (E-P) anomalies averaged over the Southern Adriatic, together with **(D)** monthly Po River discharge between 1993 and 2017. Standard deviations (shaded in gray) were estimated for the period 1979–2017. Red shadings indicate values above or below one standard deviation. Red ticks in the upper part of each panel denote occurrence of surface or near-surface (0–20 m) salinity values higher than 38.8 observed on at least one station along the Palagruža Sill transect.

with a large salt content in the layer that is normally mixed by the open sea convection during severe wintertime forcing (the mixing can extend to 900 m, Gačić et al., 2002; Dunić et al., 2019).

In summary, the BiOS cyclonic regime in the Northern Ionian was increasing the salt content in the Adriatic for several years prior to 2017 by advecting more saline waters, presumably originating in the Levantine basin or/and the Aegean Sea, through the Strait of Otranto. This was particularly true for 2015–2016, following the cyclonic regime maximum in 2015 (**Figure 6A**), thus preconditioning the 2017 high salinity event. Moderate open ocean convection events between 2014 and 2016 deepened the salinity maximum to greater depths (below 500 m). At the same time, a new inflow of high salinity waters to the Adriatic took place near the surface in 2015 and 2016, i.e., at much shallower depths than was previously documented during Adriatic salt ingressions (e.g., Gačić et al., 1996; Vilibić and Orlić, 2001).

Physical Setting in 2017

A very strong open ocean convection episode occurred in January 2017, characterized by severe bora wind and extremely cold weather along the Adriatic Sea (DHMZ, 2018). The severity of the event can be observed from the surface heat anomalies averaged from ERA-Interim reanalysis over the open Southern

Adriatic (**Figure 9B**), which were the second most negative (after December 2001) during the entire satellite altimetry era (1993–2017). Heat losses in the Southern Adriatic were even stronger than the losses during the severe winter of 2012, which peaked in the Northern Adriatic but was of moderate intensity in the Southern Adriatic, causing a vertical mixing in the SAP that reached only 500 m depth (Mihanović et al., 2013). In 2017 the open ocean convection in the SAP was indeed much stronger and the water column was mixed to 700–800 m (**Figure 3A**; see also Kokkini et al., 2020). The mixing effectively destroyed the double salinity maxima vertical pattern that was present in 2015–2016 period, and high salinities were measured throughout the water column (above 38.8 between the surface and 700 m). The convection was preceded by high and positive E-P anomalies (**Figure 9C**) that additionally increased the salinity in the surface layer, while freshwater inflow by rivers was lower than average during most of 2016 (**Figure 9D**). This event enhanced the Adriatic-Ionian thermohaline circulation during late winter and spring 2017, but the inflow of warmer and highly saline waters from the Northern Ionian remained close to the surface, in the upper 100 m (see also **Figures 3A,B**, **5** and Section "Thermohaline properties in 2017").

Very low river discharges were also present during the whole 2017 (**Figure 9D**), while heat fluxes were higher than average in late spring and summer (**Figure 9B**), having the capacity to substantially heat the surface layer during the seasonal maximum in thermocline intensity in the summer (Buljan and Zore-Armanda, 1976). Precisely, heat fluxes in May and June 2017 were both above one standard deviation estimated over the period 1979–2017 and the largest in the period 1993–2017 for that part of the year (**Figure 9B**).

To summarize, one of the most intense cooling during the winter and heating in the following summer were present over most of the Southern Adriatic in 2017. They were related to an inflow of highly saline waters from the Northern Ionian in the surface layer during late winter and early spring 2017, together with a very low precipitation rate and extremely low river discharges between mid-2015 and the end of 2017.

Variations of Surface Geostrophic Currents

It is well known that the DWF and the respective outflow of the NAdDW and AdDW within and from the Adriatic strengthen the thermohaline circulation and cause seasonal oscillations of the inflow from the Ionian Sea, with maximum salinity values in summer and autumn in the Adriatic (Buljan and Zore-Armanda, 1976; Vilibić and Orlić, 2001; Orlić et al., 2006; see also **Figure 6B**). The strength of this seasonal cycle is evidenced by seasonal variations of monthly surface geostrophic currents, as estimated from the AVISO+ dataset (**Figure 10A**). The seasonal cycle was extracted from the data by least-squares fitting of the annual (12 months) and semi-annual (6 months) cosine functions separately for each grid point, following the general harmonic regression model (Wilks, 2020). The percentage of the seasonal circulation explaining total variance may surpass 40% in the Strait of Otranto (**Figure 10A**), reflecting seasonal variability in the exchange of water masses between the Adriatic and Ionian Seas. The seasonal oscillations in northward flow dominate there and may range from 10 to 20 cm/s (**Figure 10B**), reaching peak values during autumn and winter when they rapidly advect waters from the Northern Ionian to the Southern Adriatic. Interestingly, seasonal signal in surface geostrophic currents is also quite high in the area west of Cephalonia Island (Greece), and seasonal currents there are mostly in phase with currents in the Strait of Otranto (**Figures 10B,C**). The percentage of total geostrophic velocity variance explained by the seasonal signal in northward surface geostrophic currents may reach 30% in that area. Seasonal oscillations in surface currents have a range of about 10–20 cm/s (the same range as in the Strait of Otranto), peaking in autumn and winter.

These seasonal oscillations west of Cephalonia Island (i.e., in the eastern part of the Northern Ionian) are embedded on the decadal signal that strongly resembles the BiOS-driven changes in vorticity in the central part of the Northern Ionian Sea. The positive vorticity implies cyclonic BiOS regime (**Figure 9A**) and stronger northward currents in the eastern part of the Northern Ionian (**Figure 10C**) and the negative vorticity implies anticyclonic BiOS regime, and southward currents in the eastern part of the Northern Ionian (**Figure 10C**). However, the characteristics of the NIG reversals are also affected by the interaction between basin-wide and mesoscale circulation (Menna et al., 2019). Namely, the first two anticyclonic phases of the BiOS regime observed from satellite altimetry data (1993–1996 and 2006–2010) had some differences in basin-wide circulation, depending on the mesoscale characteristics of the Messina Rise Vortex and the Pelops Gyre. The effects of these differences were visible in changes of the northward flow west of Cephalonia, with much stronger southward currents present during the 1993–1996 anticyclonic mode, which was more negative (in terms of vorticity) than during the 2006–2010 anticyclonic mode (**Figure 10C**). During the 2005–2010 anticyclonic phase, the Messina Vortex Rise was zonally elongated (Menna et al., 2019), and the size and intensity of the NIG was reduced, therefore having lower impact on the currents in the eastern part of the Northern Ionian.

The matching between NIG reversals (**Figure 6A**) and northward flow along the eastern Ionian Sea (**Figure 10C**) was not preserved in the 2017–2018 period, when a relatively short reversal of the NIG (from cyclonic to anticyclonic) occurred in the Northern Ionian (**Figure 6A**). However, the northward currents west of Cephalonia Island remained steady (**Figure 10C**), implying that waters of higher salinities were still advected to the northernmost part of the Ionian Sea, and from there further to the Adriatic Sea (**Figures 3**, **5**). It appears that during this period variations of the Adriatic thermohaline properties, in particular of salinity, were more related to the persistence of the northward coastal flow along the western coast of Greece than to the BiOS regime occurring in the central Northern Ionian Sea. The latter may not always affect the eastern coastal regions of the Northern Ionian (Menna et al., 2019), where the flow of warm and highly saline waters originating from the Levantine region can continue to bring

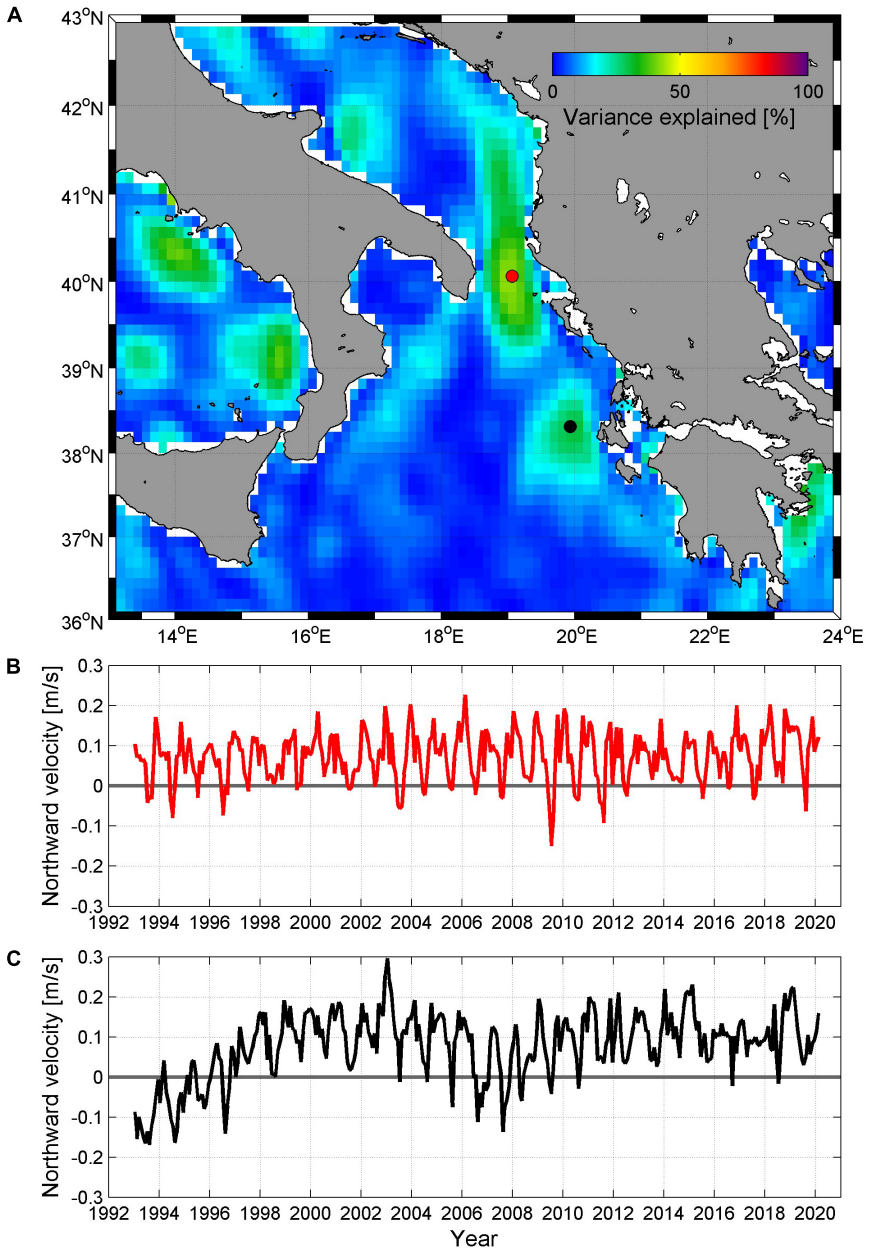

FIGURE 10 | (A) Percentage of total geostrophic velocity variance explained by the seasonal signal, with two grid points denoted by red (Otranto Strait) and black (west of Cephalonia Island, Greece). **(B)** AVISO+ northward monthly geostrophic currents at the Otranto Strait grid point. **(C)** AVISO+ northward monthly geostrophic currents at the grid point west of Cephalonia.

high salinity waters to the Adriatic even during transient or anticyclonic BiOS phase.

PAST HIGH SURFACE AND NEAR-SURFACE SALINITY EVENTS IN THE ADRIATIC

Here, we present the analysis of surface and near-surface salinity maxima observed over the Palagruža Sill transect between 1961 and 2016. The analysis was based on long-term measurements at the historical Stončica station (CJ009, **Figure 1**), which is the most regularly surveyed station at the Palaguža Sill transect. We looked at the transect observations characterized by surface or near-surface (0–20 m) salinities which were at least one standard deviation above the 1961–2016 mean summer values (Beg Paklar et al., 2020). This threshold was very close to 38.8. For an assessment of the processes eventually contributing to the maxima, we analyzed heat fluxes and E-P over the Southern Adriatic—using the ERA Interim dataset (available

from 1979), discharges of the major Adriatic river, Po River (available from 1961, Raicich, 1996; Vilibić et al., 2016), and the decadal oscillations driven by the BiOS regime (based on satellite altimetry data available since 1993). In general, from 1961 to 2016 several periods with high salinities along the Palagruža Sill transect were observed: 1968–1971, 1975–1976, 1978–1982, 1987–1990, and 1999–2005 (Mihanović et al., 2015; Matić et al., 2017) and in the 2011–2016 period (**Figure 7**). These periods (at least after 1993, when altimetry data became available) were mostly related to cyclonic circulation regime in the Northern Ionian Sea (with 1–2 years phase shift).

However, surface and near-surface high salinity events as defined above (with values higher than 38.8 observed between 0 and 20 m) were relatively rarely observed along the Palagruža Sill transect before 2000. More precisely, they occurred in December 1978, December 1981, October 1986, March 1987 and September 1989. Salinity conditions during the 1990s in the Middle Adriatic were mostly influenced by the very strong anticyclonic circulation regime in the Northern Ionian Sea, that probably started in late 1980s (Demirov and Pinardi, 2002), and lasted until 1997 (Gačić et al., 2010), additionally strengthened by the Eastern Mediterranean Transient. As satellite altimetry measurements are available since 1993, we focused on high salinity events corresponding to this period. The BiOS regime phase shifted to cyclonic by the end of 1997 and warm and saline waters from the Eastern Mediterranean started entering the Adriatic. However, it took several years before this continuous increase of the salinity in the Adriatic enabled values higher than 38.8 to be observed in the upper 20 m of the water column (high surface and near-surface salinity events that occurred at the Palagruža Sill transect are indicated by red ticks in the upper part of each panel in **Figure 9**). Therefore, high salinity events were not observed during 1990s along the Palagruža Sill transect. They occurred again during several summer-autumn periods between 2000 and 2005 (September 2000, August 2002, August and October 2003, August and September 2005), coinciding with the cyclonic phase of the BiOS and prolonged dry periods in the region, usually with warm summers. Several drought events were documented during this period, among them the infamous European heat wave of 2003 (Grbec et al., 2007; Spinoni et al., 2015, 2019). Preceding this summer, heat losses were quite high in February 2003, pointing to a possibility of the open ocean convection in the SAP, while the Northern Adriatic DWF also occurred, strongly affecting Adriatic-Ionian thermohaline circulation (Dorman et al., 2006; Orlić et al., 2006). Salinity distribution over the Palagruža Sill transect in August 2003 is shown in **Figure 11A**. Surface salinities over southern part of the transect surpassed 38.9, with the vertical extension to depths of about 10 m. Another salinity maximum was observed between 40 and 70 m, with values reaching almost 38.85. Such conditions continued at least till October 2003, with the deepening of the second maximum (not shown). Another dry year was 2005, when surface salinities higher than 38.8 were again observed at the transect in August (**Figure 11B**) and September.

During the successive anticyclonic BiOS phase (2006–early 2010) the near-surface salinities along the Palagruža Sill transect remained below 38.8. Additionally, Stončica station (CJ009) salinity values were lower than 38.8 at all sampled depths

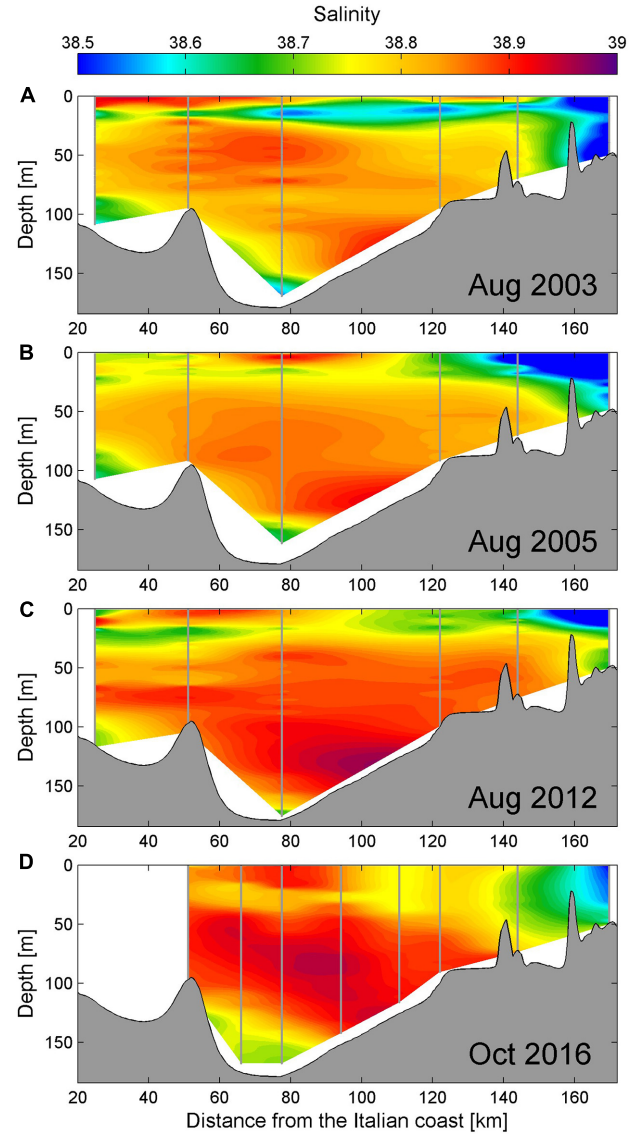

FIGURE 11 | (A) Salinity profile at the Palagruža Sill transect in the second half of August 2003. **(B–D)** As in panel **(A)** except for mid-August 2005, the second part of August 2012 and the beginning of October 2016, respectively. Vertical gray lines denote CTD casts.

throughout this period (**Figure 6B**). The next change in the Northern Ionian circulation (from anticyclonic to cyclonic) started in 2010 (Bessiéres et al., 2013), which resulted in renewed increase of salinity in the Southern and Middle Adriatic (**Figures 6B**, **7**). Near-surface salinities higher than 38.8 at the transect were first documented in October 2011. Severe winter conditions and resulting DWF in the Northern and Middle Adriatic during the winter of 2012 enhanced the Adriatic-Ionian thermohaline circulation, and a significant increase in salinities in the Adriatic was observed in the following months, resulting in several-months long period with salinity values higher than 38.8 at the Stončica station in the second half of

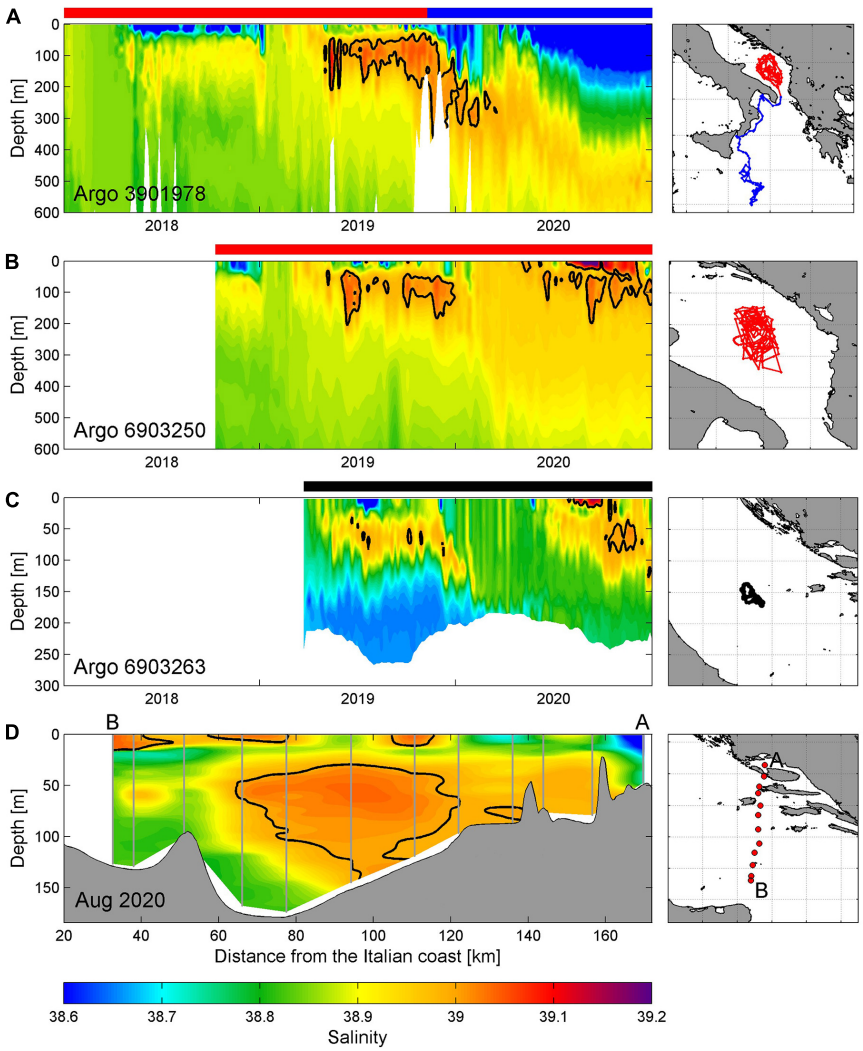

FIGURE 12 | (A) Hovmöller diagram of salinity data for Argo float 3901978 in the first 600 m in the period 2018–2020 (left panel) with corresponding float trajectory (right panel). **(B,C)** As in panel **(A)** except for Argo floats 6903250 in the first 600 m (2018–2020) and 6903263 between the surface and the bottom (2019–2020), respectively. Note that the vertical scale in panel **(C)** is between 0 and 300 m. **(D)** Salinity profile at the Palagruža Sill transect in mid-August 2020, with the map of CTD stations. Argo trajectories are colored depending on the location of the float (black–Middle Adriatic, red–Southern Adriatic, and blue–Northern Ionian). The same color notation is used in horizontal bars above left panels, indicating periods during which Argos were profiling in respective areas. Thick black line in left panels denotes 39.0 salinity contour. Vertical gray lines in panel **(D)** denote CTD casts.

2012 (**Figure 6B**). Moreover, the summer of 2012 was very dry and hot (**Figures 9B–D**), which again resulted in specific salinity distribution, with two salinity maxima present, one at the surface with values of about 38.9 in the southern section of the transect, and the other with values surpassing 38.92 between 100 and 140 m depth (**Figure 11C**). The discharges of the Po River were below average during most of 2011 and through the entire 2012 (**Figure 9D**) with extremely low values during the summer of 2012. In addition, a severe drought was present in the southeastern Europe (Spinoni et al., 2019). Summer heat fluxes in 2012 were much higher than average, and extremely high air temperatures were observed (DHMZ, 2014). The surface salinity maximum was also clearly seen in Argo profiling float measurements in the Northern Ionian Sea (Argo float 6901040; **Figure 7B**) and briefly in the Middle Adriatic, between mid-July and the end of August 2012 (Argo float 1900848; **Figure 7A**).

The intense outflow of very dense Adriatic waters during 2012 resulted in the change of the bottom pressure gradient and significant weakening of the cyclonic circulation in the Northern Ionian between the second half of 2012 and the beginning of 2014 (Gačić et al., 2014). However, salinity values in the Adriatic continued to increase throughout 2013 (**Figures 6B**, **7**) with high near-surface salinities observed in the central and southern part of the transect till April 2013 and another brief interval with salinities reaching 38.8 slightly above 20 m between August and September 2013. The following winter of 2014 was very mild and characterized by large freshwater load through rivers and precipitation that created haline-driven stratification (Mihanović

et al., 2018; Kokkini et al., 2020). Therefore, salinities decreased in the upper 100 m of the water column, but remained high in the intermediate and bottom layer (**Figure 7**). Although cyclonic circulation decreased in the Northern Ionian, northward flow along its most eastern part remained relatively strong and coherent (**Figure 10C**).

As cyclonic regime regained strength in late 2014 and peaked in 2015, continuous increase in Adriatic salinities was observed, with double maxima structure observed in 2015–2016 period in the Southern Adriatic, as already discussed in Section "Processes contributing to anomalous thermohaline properties in 2017." Surface salinity maximum (salinity values around 38.9) was present again in the central part of Palagruža Sill transect in early autumn 2016 (**Figure 11D**), with a subsurface layer of lower salinity (around 38.82) separating surface saline waters from the LIW inflow with even more saline waters in intermediate layers (values surpassing 39.94 around 80 m). Argo profiling float 6901822 also briefly captured a maximum in surface salinity in the central part of the SAP, with values of about 39.0 in the second half of August 2016 (**Figure 7C**). Similarly, as in previously presented cases, heating of surface layers (DHMZ, 2017) was higher than average during the summer season, but it was restricted mostly to June and July 2016 (**Figure 9B**). Thereafter, the surface heat fluxes were in the range of average values. Po River discharges were lower than average during most of the preconditioning period (**Figure 9D**), more precisely from the spring of 2015. This prolonged dry period between 2015 and 2017 was also essential preconditioning for the exceptionally high surface and near-surface salinity values in 2017. Finally, this surface salinity maximum in 2016, with values reaching 38.9, also corresponded to the cyclonic BiOS phase, as in several other examples shown above.

DISCUSSION AND CONCLUSION

Record-breaking surface and near-surface salinities were measured in the Middle and Southern Adriatic Sea in summer and autumn of 2017 bringing to our attention processes that may contribute to such observations. The first glimpse coming from investigations at local scale (coastal eastern part of the Middle Adriatic, Beg Paklar et al., 2020) documented that dry conditions, strong evaporation and extensive heating sustain specific vertical conditions, during which a near-surface highly saline layer is observed, in most cases separated from the second, deeper haline layer (as in July 2017—**Figure 2C** and in events shown in **Figure 11**). The 2017 autumn salinity conditions were even more specific, as the highest salinity values were observed in a layer between the surface and 25 to 40 m (**Figure 2D**), supported by high temperatures and strong thermocline and an increased inflow of highly saline waters from the Southern Adriatic. We extended the analysis to the Southern Adriatic and Northern Ionian for the 2017 event in present study. In addition, we also documented previous situations characterized by surface and near-surface salinity maxima (from time series measured at Palagruža Sill between 1961 and 2016), and assessed processes responsible for their appearance. Several important conclusions can be derived from our analysis:

- All documented events occurred during overall high salinity conditions in the Adriatic, i.e., during cyclonic regime of the Adriatic-Ionian Bimodal Oscillating System (BiOS). The 2017 event was somewhat specific as it occurred during the transient phase of the BiOS, but it was still supported by the persistent northward flow (toward the Adriatic) along the eastern coast of the Northern Ionian Sea,
- Dry conditions in the region and very low river discharges, in particular of the Po River, were found to precede the high surface and near-surface salinity events for a year or more, and
- Near-surface salinity maxima mostly occur during prolonged and extensive heating periods in summer and early autumn, which normally results in an increase in stratification and effective separation of surface waters. Further, they can occur even during moderate summers if the Adriatic salinities are generally high and summer is preceded by very dry conditions (e.g., summers of 2000 and 2005, see **Figure 11B**), with relatively high evaporation minus precipitation rates (i.e., low precipitation conditions).

The observed intensity of the surface and near-surface salinity maximum in 2017, i.e., exceptionally high salinity values and the intensity of the inverse subsurface halocline, were not documented in the Adriatic Sea until recently (Beg Paklar et al., 2020). High salinity conditions continued to be observed there even after 2017, despite apparent, although relatively short, reversal of the North Ionian Gyre in 2017 and 2018 (**Figure 6**). Salinities at the Palagruža Sill transect station CJ009 exceeded 38.8 near the surface again in 2019, with values higher than 39.0 observed at depths below 60 m during summer and early autumn (**Figure 6B**). Moreover, the most recent CTD and Argo data from 2020 indicate that exceptionally high surface salinities occurred again both in the Southern and Middle Adriatic during summer and autumn 2020 (in excess of 39.2 in the Southern Adriatic and 39.1 in the Middle Adriatic, between the surface and 15–20 m, **Figures 6B**, **12**).

In contrast, surface and near-surface salinity maxima regularly occur in the Levantine basin, in particular in the LIW formation region (Kubin et al., 2019). As the LIW region has gone through an extensive salinity increase in the recent decade (Grodsky et al., 2019; Kassis and Korres, 2020), one may wonder if these long-term changes in the Eastern Mediterranean have a significant effect on the BiOS regimes and their impact on the thermohaline changes in the Adriatic Sea or similar local manifestation are related to the observed salinity maxima in the Adriatic Sea. Quantification of remote vs. local/regional effects needs to be further investigated in the future.

We can confirm that the BiOS-driven changes in the Northern Ionian Sea vorticity and alterations between cyclonic and anticyclonic BiOS regime were generally strongly aligned with Adriatic salinity changes since the start of the satellite

altimetry measurements in 1993. However, the Adriatic salinities remained high even during the weak cyclonic BiOS regime (as in 2013–2014 period) or its relatively short reversal (2017–2018). What seems to be important during these periods as well is the coastal flow of saline Levantine waters along the eastern Ionian Sea, which mostly followed the BiOS regime till around 2010, but remained relatively stable (with seasonal fluctuations) during the past decade. Altimetry measurements in the Northern Ionian since 2010 indicate that these eastern flank flows might be less related to the general BiOS circulation pattern. Namely, this pattern was relatively weak in 2013–2014 period, and predominantly anticyclonic between 2017 and 2018 (**Figure 6A**), while northward flow persisted up until at least late 2019 (**Figure 10**). It is an open question whether such detachment between open sea and coastal processes in the Northern Ionian Sea will last for some time, or characteristic BiOS circulation patterns will restore at some time, once the inflow of Atlantic Water into the Eastern Mediterranean—restricted from mid-2000s (Kassis and Korres, 2020)—would eventually be re-established.

There might be several important consequences of salinity changes. The impact of exceptionally high salinities in the Middle Adriatic on the microbial food was already documented in 2017 (Beg Paklar et al., 2020). The documented anomalous physical conditions were conjoined with significantly lower bacterial production and lower abundance of the most studied picoplankton groups in comparison to values observed during the decade preceding 2017.

Another consequence is an extensive salinification of the Adriatic Sea, like the one observed during recent years, which might be less dependent on the BiOS regimes in the Northern Ionian Sea. The most recent Argo measurements—as of January 2021—indicate that salinities in the SAP are higher than 38.8 as deep as at least 1,000 m depth. Such conditions may substantially lower the advection of Western Mediterranean water to the Adriatic [as has been documented for the Eastern Mediterranean—Kassis and Korres (2020)]. These conditions may also precondition more frequent occurrences of exceptional surface and near-surface salinity maxima (with values higher than 39.0 close to the surface), as observed in 2017 and 2020, particularly since salinity increase has peaked in the Eastern Mediterranean in recent years (Grodsky et al., 2019). If such conditions become more frequent in the future, they might strongly change the microbial food web and beyond, as salinity is an important environmental factor for some picoplankton groups like *Prochlorococcus* (Mella-Flores et al., 2011).

Such salinity maxima and the overall increase in salinity in the Adriatic may affect the DWF in both Northern and Southern Adriatic (Mihanović et al., 2013), therefore impacting the thermohaline circulation and ventilation of deep Adriatic and Eastern Mediterranean layers. It is still not known how the recently observed salinization in subsurface and intermediate Adriatic layers, if it were to become more frequent in the future, would interplay with the bora-driven wintertime surface heat losses and the wind stress associated with the DWF, which are expected to remain the same or decrease in the future climate (Belušić Vozila et al., 2019; Denamiel et al., 2020). Namely, such high salinity conditions would lower the stability of the water column and therefore increase vertical mixing and the DWF. Both thermohaline data collected at the Palagruža Sill between 1952 and 2010 (Vilibić et al., 2013) and climate simulations (Somot et al., 2006) indicate a shallowing and/or weakening of the Adriatic thermohaline circulation, yet climate models are still far from providing reliable reproduction of thermohaline variability in the Adriatic Sea (Dunić et al., 2019). If the DWF decreases in the future climate, this might have a substantial impact on the deep Adriatic organisms, in particular on those residing along the perimeter of the Jabuka Pit depressions, which are known as nursery and spawning areas for a large number of Adriatic species (Zorica et al., 2020).

DATA AVAILABILITY STATEMENT

The original contributions presented in the study are included in the article/supplementary material, further inquiries can be directed to the corresponding author/s.

AUTHOR CONTRIBUTIONS

HM and IV developed the idea and the concept of the manuscript. HM, IV, and JS wrote the initial version of the manuscript. HM, FM, ZLJ, EM, RG, GN, and P-MP collected the data and performed the analyses. HM prepared the figures. All authors actively contributed to revisions of the manuscript, and read and approved the submitted version.

FUNDING

The Argo profiling float data were collected through the MedArgo programme and the European Maritime and Fisheries Fund MOCCA project (Project No: SI2.709624 | Call reference No: EASME/EMFF/2015/1.2.1.1) and made freely available under the International Argo Program in which the national programs contributed (https://www.ocean-ops.org/board?t=argo). The glider research was carried out by the National Institute of Oceanography and Applied Geophysics—OGS in the framework of ArgoItaly, funded by the Italian Ministry of University and Research. This work has been supported by the Croatian Science Foundation under projects ADIOS (IP-2016-06-1955), MAUD (IP-2018-01-9849), BivACME (IP-2019-04-8542), and ISLAND (IP-2020-02-9524). The research was also supported through the projects CAAT and HIDROLAB, funded by the European Union through European Structural and Investment Funds 2014–2020, with the respective contract numbers KK.01.1.1.04.0064 and KK.01.1.1.04.0053.

ACKNOWLEDGMENTS

To all researchers, engineers, technicians, and research vessel crews that were engaged in field collection of the thermohaline data. Absolute dynamic topography and surface geostrophic current data are provided through AVISO+ programme and

are available at Copernicus Marine Service pages (https://marine.copernicus.eu). The Mediterranean Forecasting System (MFS) results were also downloaded from Copernicus Marine Service pages (http://marine.copernicus.eu). Po River discharges at Pontelagoscuro station were kindly provided by the Regional Agency for Prevention, Environment and Energy of Emilia-Romagna, Italy (Arpae Emilia-Romagna). The comments raised by the two reviewers are greatly appreciated.

REFERENCES

Argo (2021). Argo float data and metadata from Global Data Assembly Centre (Argo GDAC). *SEANOE*. doi: 10.17882/42182

Artegiani, A., and Salusti, E. (1987). Field observation of the flow of dense water on the bottom of the Adriatic Sea during the winter of 1981. *Oceanol. Acta* 10, 387–391.

Artegiani, A., Bregant, D., Paschini, E., Pinardi, N., Raicich, F., and Russo, A. (1997). The Adriatic Sea general circulation, part I: air– sea interactions and water mass structure. *J. Phys. Oceanogr.* 27, 1492–1514. doi: 10.1175/1520-0485(1997)027<1492:tasgcp>2.0.co;2

Babić, I., Petrić, I., Bosak, S., Mihanović, H., Dupčić Radić, I., and Ljubešić, Z. (2017). Distribution and diversity of marine picocyanobacteria community: targeting of Prochlorococcus ecotypes in winter conditions (southern Adriatic Sea). *Mar. Genom.* 36, 3–11. doi: 10.1016/j.margen.2017.05.014

Batistić, M., Garić, R., and Molinero, J. C. (2014). Interannual variations in Adriatic Sea zooplankton mirror shifts in circulation regimes in the Ionian Sea. *Clim. Res.* 61, 231–240. doi: 10.3354/cr01248

Beg Paklar, G., Vilibić, I., Grbec, B., Matić, F., Mihanović, H., Džoić, T., et al. (2020). Record-breaking salinities in the middle Adriatic during summer 2017 and concurrent changes in the microbial food web. *Prog. Oceanogr.* 185:102345. doi: 10.1016/j.pocean.2020.102345

Belušić Vozila, A., Güttler, I., Ahrens, B., Obermann-Hellhund, A., and Telišman Prtenjak, M. (2019). Wind over the Adriatic region in CORDEX climate change scenarios. *J. Geophys. Res. Atmos.* 124, 110–130. doi: 10.1029/2018jd028552

Ben Ismail, S., Schroeder, K., Sammari, C., Gasparini, G. P., Borghini, M., and Aleya, L. (2014). Interannual variability of water mass properties in the Tunisia–Sicily channel. *J. Mar. Syst.* 135, 14–28. doi: 10.1016/j.jmarsys.2013.06.010

Bergamasco, A., Oguz, T., and Malanotte-Rizzoli, P. (1999). Modelling dense water mass formation and winter circulation in the northern and central Adriatic Sea. *J. Mar. Syst.* 20, 279–300. doi: 10.1016/s0924-7963(98)00087-6

Bessiéres, L., Rio, M. H., Dufau, C., Boone, C., and Pujol, M. I. (2013). Ocean state indicators from MyOcean altimeter products. *Ocean Sci.* 9, 545–560. doi: 10.5194/os-9-545-2013

Bingham, F. M., Busecke, J., Gordon, A. L., Giulivi, C. F., and Li, Z. (2014). The North Atlantic subtropical surface salinity maximum as observed by Aquarius. *J. Geophys. Res. Oceans* 119, 7741–7755. doi: 10.1002/2014jc009825

Buljan, M. (1953). Fluctuations of salinity in the Adriatic, Izvještaj Republičke ribarstveno-biološke ekspedicije "Hvar" 1948–1949. *Acta Adriat.* 2, 1–64.

Buljan, M., and Zore-Armanda, M. (1976). Oceanographic properties of the Adriatic Sea. *Oceanogr. Mar. Biol. Ann. Rev.* 14, 11–98.

Chen, G., Peng, L., and Ma, C. (2018). Climatology and seasonality of upper ocean salinity: a three-dimensional view from argo floats. *Clim. Dyn.* 50, 2169–2182. doi: 10.1007/s00382-017-3742-6

Civitarese, G., Gačić, M., Lipizer, M., and Borzelli, G. L. E. (2010). On the impact of the Bimodal Oscillating System (BiOS) on the biogeochemistry and biology of the Adriatic and Ionian Seas (Eastern Mediterranean). *Biogeosciences* 7, 3987–3997. doi: 10.5194/bg-7-3987-2010

Clementi, E., Pistoia, J., Escudier, R., Delrosso, D., Drudi, M., Grandi, A., et al. (2019). *Mediterranean Sea Physics Analysis and Forecast (CMEMS MED-Currents, EAS5 system) [Data set]. Copernicus Monitoring Environment Marine Service (CMEMS)*. Available Online at: https://doi.org/10.25423/CMCC/MEDSEA_ANALYSIS_FORECAST_PHY_006_013_EAS5 (accessed March 11, 2019).

Dautović, J., Vojvodić, V., Tepić, N., Ćosović, B., and Ciglenečki, I. (2017). Dissolved organic carbon as potential indicator of global change: a long-term investigation in the northern Adriatic. *Sci. Total Environ.* 587-588, 185–195. doi: 10.1016/j.scitotenv.2017.02.111

Dee, D. P., Uppala, S. M., Simmons, A. J., Berrisford, P., Poli, P., Kobayashi, S., et al. (2011). The ERA-Interim reanalysis: configuration and performance of the data assimilation system. *Q. J. R. Meteorol. Soc.* 137, 553–597.

Demirov, E., and Pinardi, N. (2002). Simulation of the Mediterranean Sea circulation from 1979 to 1993: part I. The interannual variability. *J. Mar. Syst.* 33-34, 23–50. doi: 10.1016/s0924-7963(02)00051-9

Denamiel, C., Tojčić, I., and Vilibić, I. (2020). Far future climate (2060–2100) of the northern Adriatic air–sea heat transfers associated with extreme bora events. *Clim. Dyn.* 55, 3043–3066. doi: 10.1007/s00382-020-05435-8

DHMZ (2014). *Reviews No. 24. Climate Monitoring and assessment for 2012 (in Croatian)*. Croatian: Croatian Meteorological and Hydrological Service.

DHMZ (2017). *Reviews No. 28. Climate Monitoring and assessment for 2016 (in Croatian)*. Croatian: Croatian Meteorological and Hydrological Service.

DHMZ (2018). *Reviews No. 29. Climate Monitoring and assessment for 2017 (in Croatian)*. Croatian: Croatian Meteorological and Hydrological Service.

Dorman, C. E., Carniel, S., Cavaleri, L., Sclavo, M., Chiggiato, J., Doyle, J., et al. (2006). February 2003 marine atmospheric conditions and the bora over the northern Adriatic. *J. Geophys. Res.* 111:C03S03.

Dunić, N., Vilibić, I., Šepić, J., Mihanović, H., Sevault, F., Somot, S., et al. (2019). Performance of multi-decadal ocean simulations in the Adriatic Sea. *Ocean Model.* 134, 84–109. doi: 10.1016/j.ocemod.2019.01.006

Franić, Z. (2005). Estimation of the Adriatic sea water turnover time using fallout ^{90}Sr as a radioactive tracer. *J. Mar. Syst.* 57, 1–12. doi: 10.1016/j.jmarsys.2004.11.005

Gačić, M., Borzelli, G. L. E., Civitarese, G., Cardin, V., and Yari, S. (2010). Can internal processes sustain reversals of the ocean upper circulation? the Ionian Sea example. *Geophys. Res. Lett.* 37:L09608.

Gačić, M., Civitarese, G., Kovačević, V., Ursella, L., Bensi, M., Menna, M., et al. (2014). Extreme winter 2012 in the Adriatic: an example of climatic effect on the BiOS rhythm. *Ocean Sci.* 10, 513–522. doi: 10.5194/os-10-513-2014

Gačić, M., Civitarese, G., Miserocchi, S., Cardin, V., Crise, A., and Mauri, E. (2002). The open-ocean convection in the Southern Adriatic: a controlling mechanism of the spring phytoplankton bloom. *Cont. Shelf. Res.* 22, 1897–1908. doi: 10.1016/s0278-4343(02)00050-x

Gačić, M., Kovačević, V., Manca, B., Papageorgiou, E., Poulain, P.-M., Scarazzato, P., et al. (1996). Thermohaline properties and circulation in the Otranto Strait. *Bull. Institut Oceanographie Monaco* 17, 117–145.

Giorgi, F. (2006). Climate change hot-spots. *Geophys. Res. Lett.* 33:L08707.

Grbec, B., Morović, M., Beg Paklar, G., Kušpilić, G., Matijević, S., Matić, F., et al. (2009). The relationship between the atmospheric variability and productivity in the Adriatic Sea area. *J. Mar. Biol. Assoc. U. K.* 89, 1549–1558. doi: 10.1017/s0025315409000708

Grbec, B., Vilibić, I., Bajić, A., Morović, M., Beg Paklar, G., Matić, F., et al. (2007). Response of the Adriatic Sea to the atmospheric anomaly in 2003. *Ann. Geophys.* 25, 835–846. doi: 10.5194/angeo-25-835-2007

Grodsky, S. A., Reul, N., Bentamy, A., Vandemark, D., and Guimbar, S. (2019). Eastern Mediterranean salinification observed in satellite salinity from SMAP mission. *J. Mar. Syst.* 198:103190. doi: 10.1016/j.jmarsys.2019.103190

Gualdi, S., Somot, S., May, W., Castellari, S., Déqué, M., Adani, M., et al. (2013). "Future climate projections," in *Regional Assessment of Climate Change in the Mediterranean, Advances in Global Change Research 50*, eds A. Navarra and L. Tubiana (Dordrecht: Springer), 53–118.

Hure, M., Mihanović, H., Lučić, D., Ljubešić, Z., and Kružić, P. (2018). Mesozooplankton spatial distribution and community structure in the South Adriatic Sea during two winters (2015, 2016). *Mar. Ecol.* 39:e12488. doi: 10.1111/maec.12488

Incarbona, A., Martrat, B., Mortyn, P. G., Sprovieri, M., Ziveri, P., Gogou, A., et al. (2016). Mediterranean circulation perturbations over the last five centuries: Relevance to past Eastern Mediterranean Transient-type events. *Sci. Rep.* 6:29623.

Kassis, D., and Korres, G. (2020). Hydrography of the Eastern Mediterranean basin derived from argo floats profile data. *Deep Sea Res. II* 171:104712. doi: 10.1016/j.dsr2.2019.104712

Kirkland, E. J. (2010). *Advanced Computing in Electron Microscopy, 2nd Edn.* Boston, MA: Springer.

Klein, B., Roether, W., Manca, B. B., Bregant, D., Beitzel, V., Kovačević, V., et al. (1999). The large deep water transient in the Eastern Mediterranean. *Deep Sea Res. I* 46, 37–414.

Kokkini, Z., Mauri, E., Gerin, R., Poulain, P.-M., Simoncelli, S., and Notarstefano, G. (2020). On the salinity structure in the South Adriatic as derived from float and glider observations in 2013–2016. *Deep Sea Res. II* 171:104625. doi: 10.1016/j.dsr2.2019.07.013

Krom, M. D., Herut, B., and Mantoura, R. F. C. (2004). Nutrient budget for the Eastern Mediterranean: implications for phosphorus limitation. *Limnol. Oceanogr.* 49, 1582–1592. doi: 10.4319/lo.2004.49.5.1582

Krom, M. D., Kress, N., Brenner, S., and Gordon, L. I. (1991). Phosphorus limitation of primary productivity in the eastern Mediterranean Sea. *Limnol. Oceanogr.* 36, 424–432. doi: 10.4319/lo.1991.36.3.0424

Kubin, E., Poulain, P.-M., Mauri, E., Menna, M., and Notarstefano, G. (2019). Levantine intermediate and Levantine deep water formation: an Argo float study from 2001 to 2017. *Water* 11:1781. doi: 10.3390/w11091781

Lipizer, M., Partescano, E., Rabitti, A., Giorgetti, A., and Crise, A. (2014). Qualified temperature, salinity and dissolved oxygen climatologies in a changing Adriatic Sea. *Ocean Sci.* 10, 771–797. doi: 10.5194/os-10-771-2014

Lučić, D., Ljubešić, Z., Babić, I., Bosak, S., Cetinić, I., Vilibić, I., et al. (2017). Unusual winter zooplankton bloom in the open southern Adriatic Sea. *Turk. J. Zool.* 41, 1024–1035. doi: 10.3906/zoo-1702-17

Macias, D., Garcia-Gorriz, E., and Stips, A. (2013). Understanding the causes of recent warming of Mediterranean waters. How much could be attributed to climate change? *PLoS One* 8:e81591. doi: 10.1371/journal.pone.0081591

Malanotte-Rizzoli, P., Manca, B. B., D'Alcala, M. R., Theocharis, A., Bergamasco, A., Bregant, D., et al. (1997). A synthesis of the Ionian Sea hydrography, circulation and water mass pathways during POEM-Phase I. *Prog. Oceanogr.* 39, 153–204. doi: 10.1016/s0079-6611(97)00013-x

Martin, P. J., Book, J. W., Burrage, D. M., Rowley, C. D., and Tudor, M. (2009). Comparison of model-simulated and observed currents in the central Adriatic during DART. *J. Geophys. Res. Oceans* 114:C01S05.

Marullo, S., Artale, V., and Santoleri, R. (2011). The SST multidecadal variability in the Atlantic-Mediterranean region and its relation to AMO. *J. Clim.* 24, 4385–4401. doi: 10.1175/2011jcli3884.1

Matić, F., Kovač, Ž, Vilibić, I., Mihanović, H., Morović, M., Grbec, B., et al. (2017). Oscillating Adriatic temperature and salinity regimes mapped using the Self-Organizing Maps method. *Cont. Shelf Res.* 132, 11–18. doi: 10.1016/j.csr.2016.11.006

Mella-Flores, D., Mazard, S., Humily, F., Partensky, F., Mahe, F., Bariat, L., et al. (2011). Is the distribution of Prochlorococcus and Synechococcus ecotypes in the Mediterranean Sea affected by global warming? *Biogeosciences* 8, 2785–2804. doi: 10.5194/bg-8-2785-2011

Menna, M., Reyes Suareza, N. C., Civitarese, G., Gačić, M., Rubino, A., and Poulain, P.-M. (2019). Decadal variations of circulation in the Central Mediterranean and its interactions with mesoscale gyres. *Deep Sea Res. II* 164, 14–24. doi: 10.1016/j.dsr2.2019.02.004

Merckelbach, L. M., Briggs, R. D., Smeed, D. A., and Griffiths, G. (2008). "Current measurements from autonomous underwater gliders," in *Proceedings of the 2008 IEEE/OES 9th Working Conference on Current Measurement Technology*, (Piscataway, NJ: IEEE).

Mihanović, H., Janeković, I., Vilibić, I., Kovačević, V., and Bensi, M. (2018). Modelling interannual changes in dense water formation on the northern Adriatic shelf. *Pure Appl. Geophys.* 175, 4065–4081. doi: 10.1007/s00024-018-1935-5

Mihanović, H., Vilibić, I., Carniel, S., Tudor, M., Russo, A., Bergamasco, A., et al. (2013). Exceptional dense water formation on the Adriatic shelf in the winter of 2012. *Ocean Sci.* 9, 561–572. doi: 10.5194/os-9-561-2013

Mihanović, H., Vilibić, I., Dunić, N., and Šepić, J. (2015). Mapping of decadal middle Adriatic oceanographic variability and its relation to the BiOS regime. *J. Geophys. Res. Oceans* 120, 5615–5630. doi: 10.1002/2015jc010725

Mosetti, F. (1983). A tentative attempt at determining the water flow through the Otranto Strait: the mouth of the Adriatic Sea. Criterion for applying the computation of dynamic height anomalies on the water budget problems. *Boll. Oceanol. Teor. Appl. I* 1, 143–163.

Nagy, H., Di Lorenzo, E., and El-Gindy, A. (2019). The impact of climate change on circulation patterns in the Eastern Mediterranean Sea upper layer using Med-ROMS model. *Prog. Oceanogr.* 175, 226–244. doi: 10.1016/j.pocean.2019.04.012

Nezlin, N., Dever, M., Halverson, M., Leconte, J.-M., Maze, G., Richards, C., et al. (2020). Accuracy and long-term stability assessment of inductive conductivity cell measurements on Argo floats. *J. Atmos. Ocean. Technol.* 37, 2209–2223. doi: 10.1175/jtech-d-20-0058.1

Orlić, M., Dadić, V., Grbec, B., Leder, N., Marki, A., Matić, F., et al. (2006). Wintertime buoyancy forcing, changing seawater properties, and two different circulation systems produced in the Adriatic. *J. Geophys. Res. Oceans* 112:C03S07.

Orlić, M., Gačić, M., and La Violette, P. E. (1992). The currents and circulation of the Adriatic Sea. *Oceanol. Acta* 15, 109–124.

Pastor, F., Valiente, J. A., and Palau, J. L. (2018). Sea surface temperature in the Mediterranean: trends and spatial patterns (1982–2016). *Pure Appl. Geophys.* 175, 4017–4029. doi: 10.1007/s00024-017-1739-z

Pettenuzzo, D., Large, W. G., and Pinardi, N. (2010). On the corrections of ERA-40 surface flux products consistent with the Mediterranean heat and water budgets and the connection between basin surface total heat flux and NAO. *J. Geophys. Res. Oceans* 115:C06022.

Pinardi, N., Allen, I., Demirov, E., De Mey, P., Korres, G., Lascaratos, A., et al. (2003). The Mediterranean ocean forecasting system: first phase of implementation (1998-2001). *Ann. Geophys.* 21, 3–20. doi: 10.5194/angeo-21-3-2003

Pinardi, N., and Coppini, G. (2010). Operational oceanography in the Mediterranean Sea: the second stage of development. *Ocean Sci.* 6, 263–267. doi: 10.5194/os-6-263-2010

Pinardi, N., Zavatarelli, M., Adani, M., Coppini, G., Fratianni, C., Oddo, P., et al. (2015). Mediterranean Sea large-scale low-frequency ocean variability and water mass formation rates from 1987 to 2007: a retrospective analysis. *Prog. Oceanogr.* 132, 318–332. doi: 10.1016/j.pocean.2013.11.003

Poulain, P.-M., Barbanti, R., Font, J., Cruzado, A., Millot, C., Gertman, I., et al. (2007). MedArgo: a drifting profiler program in the Mediterranean Sea. *Ocean Sci.* 3, 379–395. doi: 10.5194/os-3-379-2007

Raicich, F. (1996). On the fresh water balance of the Adriatic sea. *J. Mar. Syst.* 9, 305–319. doi: 10.1016/s0924-7963(96)00042-5

Reale, M., Salon, S., Crise, A., Farneti, R., Mosetti, R., and Sannino, G. (2017). Unexpected covariant behavior of the Aegean and Ionian Seas in the period 1987–2008 by means of a nondimensional sea surface height index. *J. Geophys. Res. Oceans* 122, 8020–8033. doi: 10.1002/2017jc012983

Roether, W., and Schlitzer, R. (1991). Eastern Mediterranean deep water renewal on the basis of chlorofluoromethane and tritium data. *Dyn. Atmos. Oceans* 15, 333–354. doi: 10.1016/0377-0265(91)90025-b

Rubino, A., Gačić, M., Bensi, M., Kovačević, V., Malačič, V., Menna, M., et al. (2020). Experimental evidence of long-term oceanic circulation reversals without wind influence in the North Ionian Sea. *Sci. Rep.* 10:1905.

Rudnick, D. L., Baltes, R., Crowley, M., Schofield, O., Lee, C. M., and Lembke, C. (2012). "A national glider network for sustained observation of the coastal ocean," in *Proceedings of the Ocean. 2012 MTS/IEEE Harnessing Power Ocean*, (Piscataway, NJ: IEEE).

Shabrang, L., Menna, M., Pizzi, C., Lavigne, H., Civitarese, G., and Gačić, M. (2016). Long-term variability of the southern Adriatic circulation in relation to North Atlantic Oscillation. *Ocean Sci.* 12, 233–241. doi: 10.5194/os-12-233-2016

Skliris, N., Sofianos, S., Gkanasos, A., Mantziafou, A., Vervatis, V., Axaopoulos, P., et al. (2012). Decadal scale variability of sea surface temperature in the Mediterranean Sea in relation to atmospheric variability. *Ocean Dyn.* 62, 13–30. doi: 10.1007/s10236-011-0493-5

Somot, S., Sevault, F., and Déqué, M. (2006). Transient climate change scenario simulation of the Mediterranean Sea for the twenty-first century using a high-resolution ocean circulation model. *Clim. Dyn.* 27, 851–879. doi: 10.1007/s00382-006-0167-z

Spinoni, J., Barbosa, P., De Jager, A., McCormick, N., Naumann, G., Vogt, J. V., et al. (2019). A new global database of meteorological drought events from 1951 to 2016. *J. Hydrol. Reg. Stud.* 22:100593. doi: 10.1016/j.ejrh.2019.100593

Spinoni, J., Naumann, G., Vogt, J. V., and Barbosa, P. (2015). The biggest drought events in Europe from 1950 to 2012. *J. Hydrol. Reg. Stud.* 3, 509–524. doi: 10.1016/j.ejrh.2015.01.001

Stommel, H. (1989). The slocum mission. *Oceanography* 2, 22–25. doi: 10.5670/oceanog.1989.26

Theocharis, A., Krokos, G., Velaoras, D., and Korres, G. (2014). "An internal mechanism driving the alternation of the Eastern Mediterranean dense/deep water sources," in *The Mediterranean Sea: Temporal Variability and Spatial Patterns, Geophysical Monograph Series*, eds G. L. Eusebi Borzelli, M. Gačić, P. Lionello, and P. Malanotte-Rizzoli (Washington, DC: AGU).

Vargas-Yáñez, M., García-Martínez, M. C., Moya, F., Balbín, R., López-Jurado, J. L., Serra, M., et al. (2017). Updating temperature and salinity mean values and trends in the Western Mediterranean: the RADMED project. *Prog. Oceanogr.* 157, 27–46. doi: 10.1016/j.pocean.2017.09.004

Vilibić, I., Matijević, S., Šepić, J., and Kušpilić, G. (2012). Changes in the Adriatic oceanographic properties induced by the Eastern Mediterranean Transient. *Biogeosciences* 9, 2085–2097. doi: 10.5194/bg-9-2085-2012

Vilibić, I., and Mihanović, H. (2013). Observing the bottom density current over a shelf using an Argo profiling float. *Geophys. Res. Lett.* 40, 910–915. doi: 10.1002/grl.50215

Vilibić, I., Mihanović, H., Janeković, I., and Šepić, J. (2016). Modelling the formation of dense water in the northern Adriatic: sensitivity studies. *Ocean Model.* 101, 17–29. doi: 10.1016/j.ocemod.2016.03.001

Vilibić, I., and Orlić, M. (2001). Least-squares tracer analysis of water masses in the South Adriatic (1967-1990). *Deep Sea Res. I* 48, 2297–2330. doi: 10.1016/s0967-0637(01)00014-0

Vilibić, I., and Orlić, M. (2002). Adriatic water masses, their rates of formation and transport through the Otranto Strait. *Deep Sea Res. I* 49, 1321–1340. doi: 10.1016/s0967-0637(02)00028-6

Vilibić, I., Šepić, J., and Proust, N. (2013). Weakening of the thermohaline circulation in the Adriatic sea. *Clim. Res.* 55, 217–225. doi: 10.3354/cr01128

Vilibić, I., Zemunik, P., Dunić, N., and Mihanović, H. (2020). Local and remote drivers of the observed thermohaline variability on the northern Adriatic shelf (Mediterranean Sea). *Cont. Shelf Res.* 199:104110. doi: 10.1016/j.csr.2020.104110

Wang, Y., Li, Y., and Wei, C. (2019). Subtropical sea surface salinity maxima in the South Indian Ocean. *J. Oceanol. Limnol.* 38, 16–29. doi: 10.1007/s00343-019-8251-5

Wilks, D. S. (2020). *Statistical Methods in the Atmospheric Sciences*, 4th Edn. Amsterdam: Elsevier.

Zore-Armanda, M. (1963). Les masses d'eau de la mer Adriatique. *Acta Adriat.* 10, 5–88.

Zorica, B., Čikeš Keč, V., Vrgoč, N., Isajlović, I., Piccinetti, C., Mandić, M., et al. (2020). A review of reproduction biology and spawning/nursery grounds of the most important Adriatic commercial fish species in the last two decades. *Acta Adriat.* 61, 89–100. doi: 10.32582/aa.61.1.7

Conflict of Interest: The authors declare that the research was conducted in the absence of any commercial or financial relationships that could be construed as a potential conflict of interest.

frontiers in Marine Science

ORIGINAL RESEARCH
published: 14 July 2021
doi: 10.3389/fmars.2021.671469

On the Circulation and Thermohaline Properties of the Eastern Mediterranean Sea

Milena Menna, Riccardo Gerin, Giulio Notarstefano, Elena Mauri, Antonio Bussani, Massimo Pacciaroni and Pierre-Marie Poulain*

Oceanography Section, National Institute of Oceanography and Applied Geophysics (OGS), Borgo Grotta Gegante, Italy

The circulation of the Eastern Mediterranean Sea is characterized by numerous recurrent or permanent anticyclonic structures, which modulate the pathway of the main currents and the exchange of the water masses in the basin. This work aims to describe the main circulation structures and thermohaline properties of the Eastern Mediterranean with particular focus on two anticyclones, the Pelops and the Cyprus gyres, using in-situ (drifters and Argo floats) and satellite (altimetry) data. The Pelops gyre is involved in the circulation and exchange of Levantine origin surface and intermediate waters and in their flow toward the Ionian and the Adriatic Sea. The Cyprus Gyre presents a marked interannual variability related to the presence/absence of waters of Atlantic origin in its interior. These anticyclones are characterized by double diffusive instability and winter mixing phenomena driven by salty surface waters of Levantine origin. Conditions for the salt finger regime occur steadily and dominantly within the Eastern Mediterranean anticyclones. The winter mixing is usually observed in December–January, characterized by instability conditions in the water column, a gradual deepening of the mixed layer depth and the consequent downward doming of the isohalines. The mixing generally involves the first 200 m of the water column (but occasionally can affect also the intermediate layer) forming a water mass with well-defined thermohaline characteristics. Conditions for salt fingers also occur during mixing events in the layer below the mixed layer.

Keywords: sub-basin anticyclones, surface dynamics, hydrological properties, vertical mixing, Eastern Mediterranean

OPEN ACCESS

Edited by:
Vincenzo Artale, Italian National Agency for New Technologies, Energy and Sustainable Economic Development (ENEA), Italy

Reviewed by:
George Zodiatis, University of Cyprus, Cyprus
Daniel Hayes, University of Cyprus, Cyprus

****Correspondence:***
Milena Menna
mmenna@inogs.it

Specialty section:
This article was submitted to Physical Oceanography, a section of the journal Frontiers in Marine Science

Received: *23 February 2021*
Accepted: *21 June 2021*
Published: *14 July 2021*

Citation:
Menna M, Gerin R, Notarstefano G, Mauri E, Bussani A, Pacciaroni M and Poulain P-M (2021) On the Circulation and Thermohaline Properties of the Eastern Mediterranean Sea. Front. Mar. Sci. 8:671469. doi: 10.3389/fmars.2021.671469

INTRODUCTION

The surface circulation of the Eastern Mediterranean Sea (EMS) is characterized by a cyclonic coastal circuit and by numerous multi-scale structures that interact in the interior of the basin (**Figure 1**). The main pathways of the Mid-Ionian Jet (MIJ) and the Mid-Mediterranean Jet (MMJ) divide the EMS in two regions (**Figure 1B**): the southern part marked by anticyclonic features and the northern part mainly characterized by cyclones (Menna et al., 2020) and quasi-decadal reversals of the surface circulation in the northern Ionian (from anticyclonic to cyclonic and vice versa), interpreted in terms of internal processes (Gačić et al., 2010, 2011, 2014; the Adriatic-Ionian Bimodal Oscillation System thoroughly described in Civitarese et al., 2010; Menna et al., 2019b; Rubino et al., 2020). Some of these circulation features are random or intermittent, others

are recurrent or permanent (Robinson et al., 1991; Malanotte-Rizzoli et al., 1997; Zodiatis et al., 2005; Menna et al., 2012; Ioannou et al., 2017). The surface currents of the EMS transport water of Atlantic origin (defined hereafter as Atlantic Water – AW) from west to east (Robinson et al., 2001; Millot and Taupier-Letage, 2005; Schroeder et al., 2012). The AW flows into the Ionian Sea through the Sicily Channel and bifurcates in two branches: the first branch transports the AW toward the north of the Ionian and southern Adriatic seas; the second branch transports the AW toward the Levantine Basin following the cyclonic circuit of coastal currents (LEC, CC, and AMC; acronyms are defined in the caption of **Figure 1B**) and the MIJ –MMJ path in the interior of the basin (Robinson et al., 2001; Hamad et al., 2005, 2006; Millot and Taupier-Letage, 2005; Schroeder et al., 2012). It can eventually interact with the sub-basin scale and mesoscale structures located along its path (Millot and Taupier-Letage, 2005).

The maps derived from drifter and altimetric data (**Figures 1B,C**) help to summarize the mean pathways of the surface current field and to identify the main permanent sub-basin scale features. Among these, four anticyclonic gyres dominate the circulation of the EMS: the Pelops Gyre (PG), the Ierapetra Gyre (IG), the Mersa-Matruh Gyre (MMG), and the Cyprus Gyre (CG). Note that, in this work the Mediterranean coherent structures driven by wind and/or topography and located in a fixed geographical area are called gyres, whereas the structures driven by the instability of strong coastal currents that frequently changes their location and lifetime are named eddies, following the indications of Schroeder et al. (2012). The main anticyclones of the EMS are classified as gyres because they are permanent structures forced by wind or generated by interaction between currents and bathymetry. They can somewhat change their position and size at interannual scales (they are not stationary), but are still confined in the same geographical area (i.e., the PG is located southwest of the Peloponnese; the IG southeast of Crete; the CG south of Cyprus; the MMG is squeezed among the Egyptian coast, the IG and the RG) and do not considerably change their position.

The main anticyclonic gyres of the EMS incorporate the Levantine Intermediate Water (LIW), making it sink and affecting its flow into all the Mediterranean basins at intermediate depths (Würtz, 2010). These structures are also characterized by the larger Mixed Layer Depth (MLD) during winter months compared to the whole EMS (with the exception of the cyclonic Rhodes Gyre – RG – where, convection phenomena deepen the MLD by up to 1000 m; Gertman et al., 1994), impacting the primary productivity and the consequent biological activities (see **Figure 1** of D'Ortenzio et al., 2005). The deepening of the mixed layer in the wintertime is usually associated with a strong decrease in surface chlorophyll-a (Lavigne et al., 2018) but, on the other hand, this deep mixing can also refill the near-surface nutrient stocks, as recently suggested by Dufois et al. (2016). Condie and Condie (2016) show that both cyclonic and anticyclonic ocean features have the potential to retain and support planktonic communities over many generations. Conditions inside anticyclones are likely to favor upwardly motile plankton.

The anticyclonic structures can play an important role in the transport and retention of marine litter. As recently discussed by Brach et al. (2018) in a comparative analysis between cyclonic and anticyclonic eddies, the latter shows a much stronger capability to entrap litter particles, due to the water convergence in their interior. More specifically, Ramirez-Llodra et al. (2013) show an accumulation of plastic debris on the sea floor in the area of the IG compatible with the gyre-induced process. The measurements of plastic concentration describe a patchy plastic distribution in the Mediterranean Sea related to the variability of the surface circulation (Cózar et al., 2015); major concentrations in the Levantine Basin (Zambianchi et al., 2017; Menna et al., 2020) coincide with the areas marked by the main anticyclonic gyres (see **Figure 2** of Cózar et al., 2015).

This article focuses on two out of four main anticyclones of the EMS, the PG and the CG. The PG is located on the eastern side of the northern Ionian Sea, southwest of the Peloponnese coast (**Figure 1B**). It is a sub-basin scale feature (diameter of $\sim$ 120 km; Pinardi et al., 2015) forced by the Etesian winds (Ayoub et al., 1998; Mkhinini et al., 2014; Menna et al., 2019b), which extends from the surface down to 800–1000 m depth (Malanotte-Rizzoli et al., 1997; Kovačević et al., 2015). In the late summer/fall the Etesian winds amplify their acceleration and the wind shear in the region of the western Cretan straits (Mkhinini et al., 2014), therefore larger anticyclonic vorticities are observed during these months in the surface layer of the PG region (see **Figure 4** of Menna et al., 2019b). At interannual scales, the internal forcing of the Ionian Basin and the outflow of dense waters from the Aegean Sea can influence the variability of the PG (Menna et al., 2019b). Downwelling processes in the core of this gyre are observed and described by Malanotte-Rizzoli et al. (1997); these phenomena affect the thermohaline properties of the Levantine Surface Water (LSW) and of the LIW layers. The PG contribute to the transport of the LIW toward the Adriatic Sea along the eastern Greek coastline (Malanotte-Rizzoli et al., 1997, 1999).

The CG is a dynamical feature located southwest of the Cyprus coast, characterized by seasonal and interannual variability in shape and dimension (Zodiatis et al., 2005; Menna et al., 2012; Mauri et al., 2019). This sub-basin gyre alternates periods of high eddy kinetic energy (larger than 200 cm^2s^{-2}) and diameter of $\sim$ 100 km with periods in which it extends eastward, merging with the Northern Shikmona Eddy (NSE) (Menna et al., 2012; Mauri et al., 2019) and forming a large anticyclonic structure with a diameter of 250–300 km (Menna et al., 2012). The CG is probably generated by the interaction between the currents and the topography in the region of the Eratosthenes seamount (Gerin et al., 2009) and extends from the surface down to 400 m depth (Zodiatis et al., 2005). During winter, the inner part of the CG is characterized by homogeneous salty water (39.2) down to 400 m depth and by downward doming of the LIW (Mauri et al., 2019). In fall the water column inside the CG shows a strong vertical stratification, with the presence of warm and salty LSW near the surface down to 40 m, the AW just below the LSW (50–100 m depth) and the LIW between 100 and 400 m. The isopycnals are characterized by an upward bending over the high salinity lens and a downward bending below it, typical of an anticyclonic eddy (Mauri et al., 2019). Below 400 m, and therefore

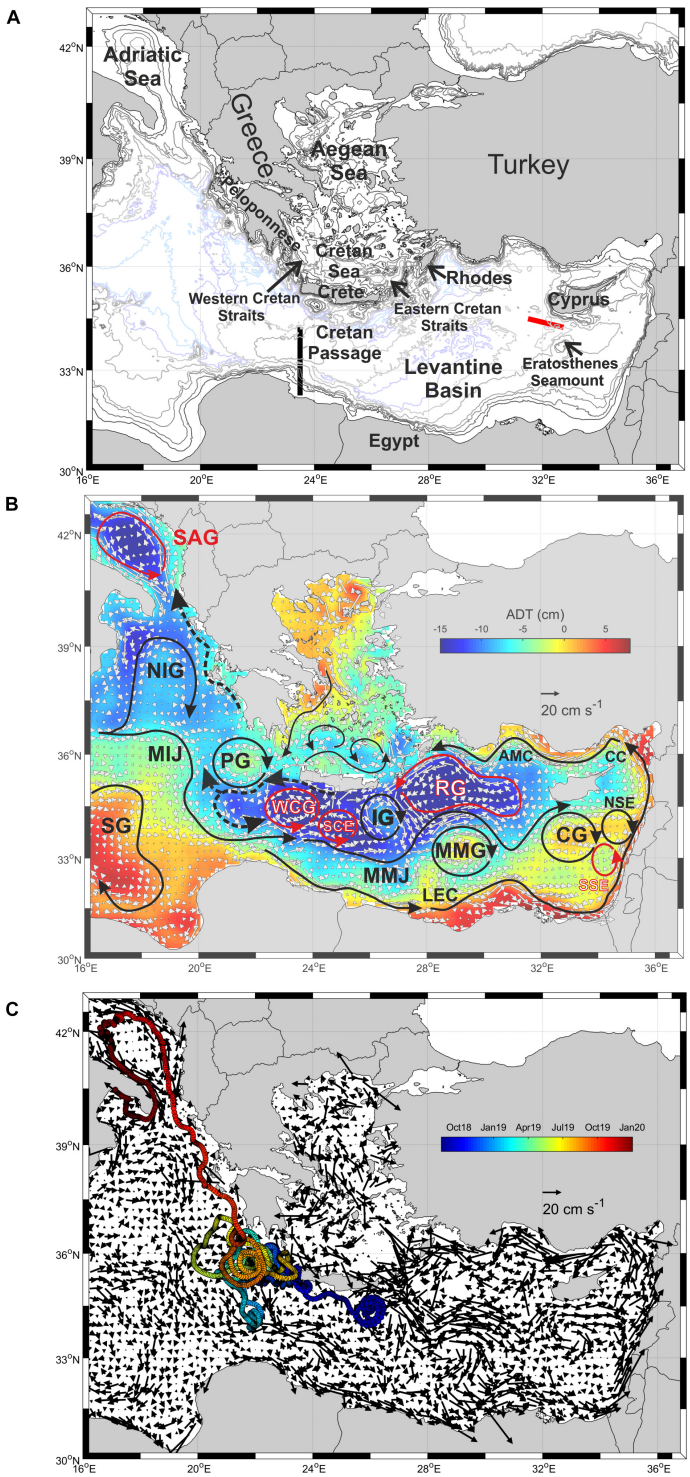

FIGURE 1 | (A) Geography and bathymetry of the EMS (the 200, 600, 1000, 1200, 2000, 2600, 3000, and 3600 m isobaths are showed with thin lines); black and red segments denote the location of transects used in **Figure 9**. **(B)** Mean geostrophic currents (white arrows) superimposed on the mean ADT (colors) derived from altimetry in 1993–2019; a schematic representation of the main currents and circulation structures, adapted from Menna et al. (2012; 2019b; 2020) and Mauri et al. (2019), are depicted with black and red arrows. **(C)** Mean drifter currents in spatial bins of 0.25° × 0.25° in the period 1990–2019 and trajectory of the drifter IMEI 300234065616590 color-coded in time. SAG, Southern Adriatic Gyre; NIG, Northern Ionian Gyre; SG, Sidra Gyre; MIJ, Mid-Ionia-Jet; PG, Pelops Gyre; WCG, Western Cretan Gyre; SCE, Southern Cretan Eddy; IG, Ierapetra Gyre; MMJ, Mid-Mediterranean Jet; LEC, Libyo-Egyptian Current; MMG, Mersa-Matruh Gyre; RG, Rhodes Gyre; CG, Cyprus Gyre; SSE, South Shikmona Eddy; NSE, North Shikmona Eddy; CC, Cilician Current; AMC, Asia Minor Current.

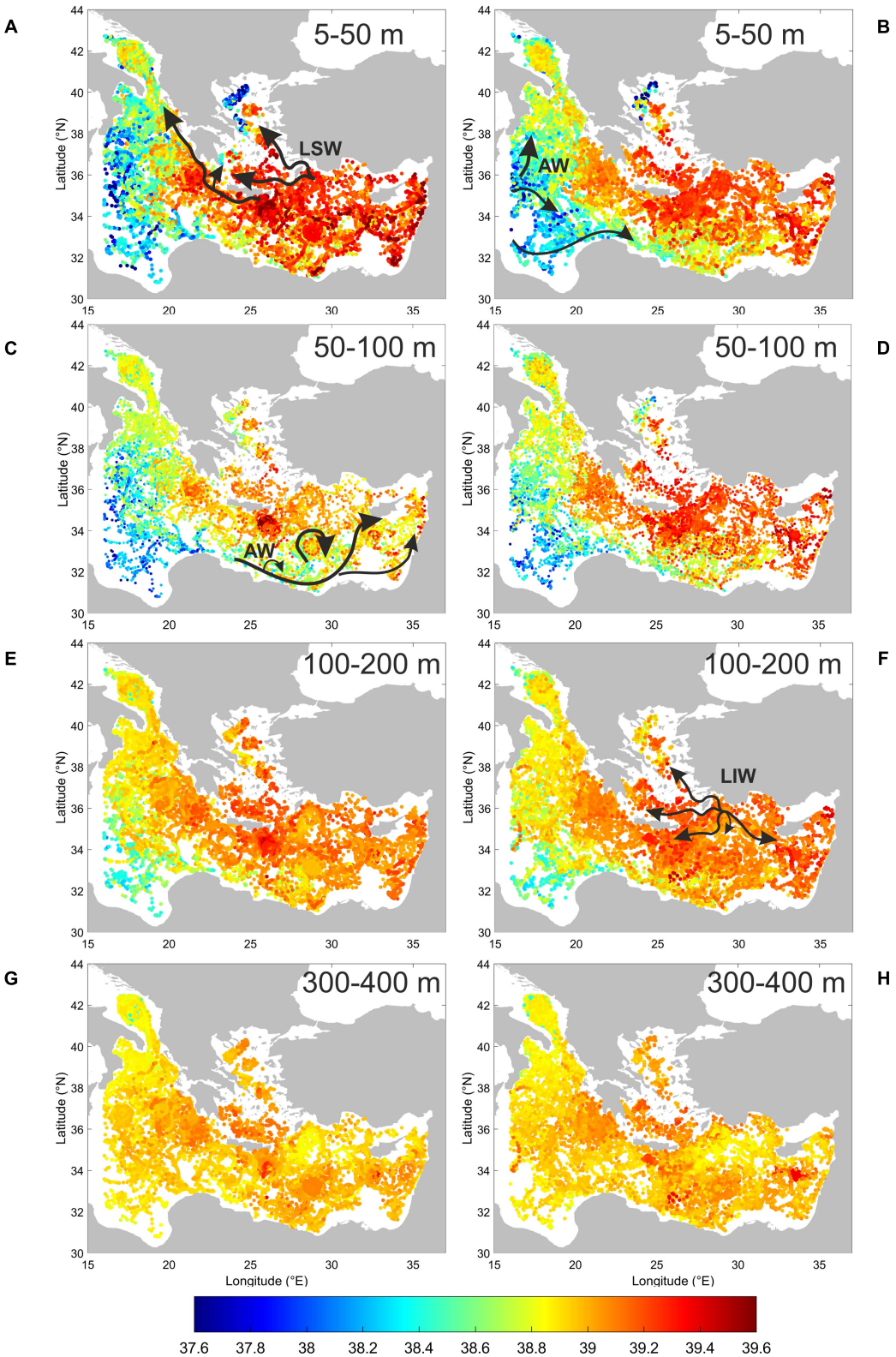

FIGURE 2 | Horizontal scatter plots of mean salinity derived by float in the 5–50 m **(A,B)**, 50–100 m **(C,D)**, 100–200 m **(E,F)**, 300–400 m **(G,H)** layers during summer/fall (left panels), and winter/spring (right panels) over the period 2003–2019. Black arrows in panel **(A,B,C)** show the pathway of the AW and LSW adapted from Malanotte-Rizzoli et al. (1997), Hamad et al. (2005); Millot and Taupier-Letage (2005); black arrows in panel **(F)** show the pathway of the LIW adapted from Hayes et al. (2019).

below the signature of the CG, there is the Levantine Deep Water (LDW) (Mauri et al., 2019).

In this article, in-situ data collected by autonomous instruments (drifters and Argo floats) are used, in conjunction with altimetry, wind and MLD products, to provide a comprehensive view of the surface and sub-surface features of the EMS, with particular focus on the PG and CG anticyclones. The vertical structures, hydrological characteristics, seasonal and interannual variability, water mass sinking and vertical mixing inside the anticyclones are delineated using the profiles of the Argo floats entrapped for long periods (months or years) inside the selected structures. New insights on the role of the anticyclones of the EMS in modulating the main currents and the exchange of the water masses in the whole basin are suggested and discussed. To our knowledge, this is the first time that the vertical structure of the aforementioned anticyclones is studied in such detail and with such a temporal extension, describing their surface dynamics, the water masses involved and the mixing processes that take place within them.

DATA AND ANALYSIS

Drifter Data

The drifter tracks used in this work were selected from the OGS Mediterranean drifter dataset (Menna et al., 2017) which cover the period 1990–2019. Drifter data were retrieved from the OGS own projects, but also from databases collected by other research institutions and by international data centers (Global Drifter Program, SOCIB, CORIOLIS, and MIO, etc.). The drifter sampling interval ranges from 6 h to 5 min, depending on the drifter design, the year of manufacture and the instrument positioning system. Drifter data were processed with standard procedures (editing and interpolation; Menna et al., 2017, 2018). In particular, we used a 36-h low-pass filter to remove tidal and inertial frequencies; then, we interpolated the drifter tracks every 6 h.

The interpolated sub-sampled data were grouped into 0.25° × 0.25° bins and pseudo-Eulerian statistics were computed following the method detailed in Poulain (2001) and Thomson and Emery (2001). The pseudo-Eulerian statistics correspond to the near-surface currents between 0 and 15 m depth.

Altimetry Data

The daily (1/8° Mercator projection grid) Absolute Dynamic Topography (ADT) and correspondent Absolute Geostrophic Velocities (AGV) derived from altimeter and distributed by CMEMS (product user manual CMEMS-SL-QUID_008-032-051) were considered. The ADT was obtained by adding the sea level anomaly to the 20-years synthetic mean estimated by Rio et al. (2014) over the 1993–2012 period.

The mean map of ADT and AGV were computed over the period 1993–2019 in bins of 0.25° × 0.25°, in order to be comparable with the drifter-inferred velocity map. Mean maps of ADT and AGV were also computed over the periods (months or years) in which selected floats were entrapped inside the PG and CG (**Table 1**). These maps help to confirm the presence of the floats inside the studied structures (by comparing the floats trajectory and the concurrent altimetry data; see for example **Figure 3A**) and to define the surface extension and the strength of the gyres.

The AGV fields were also used to estimate the relative vorticity (ζ), defined as the vertical component of the velocity field curl, as follows:

$$\zeta = \frac{\partial V}{\partial x} - \frac{\partial U}{\partial y}; \quad (1)$$

where, U and V are the velocity components. The resulting current vorticity fields were used to define the coordinates of the gyres center and to select the float profiles collected inside the structures (more details can be found in section "Float Data and Analysis").

Wind Data and Ekman Pumping Estimation

Wind velocity gridded data (W, with a spatial resolution of 31 km and a temporal resolution of 12 h) were downloaded from the ECMWF ERA5 global atmospheric reanalysis. Eddy induced Ekman pumping, associated with the spatial variation of wind-stress, was calculated from the curl of the wind stress (τ) as: $w_{EK} = \mathrm{curl}(\tau/\rho \cdot f)$, where, w is an estimate of the vertical velocity, ρ is the density of the water, here considered $\rho = 1028$ kg·m^3, and f is the Coriolis parameter that is variable with latitude and in the region of study is $\sim 10^{-4}$ rad·s^{-1}. The mean annual cycle of the Ekman pumping was extracted in the region of the PG (35°−36−5°N, 20.5°−22.5°E) and CG (33.5°−34.5°N, 32−34.5°E). Positive values of w_{EK} are associated with upward vertical velocities (upwelling), whereas negative values of w_{EK} indicate downward flow (downwelling).

Mixed Layer Depth

The MLD climatology used in this article[1] is described in Holte et al., 2017. It was computed using Argo profiles and a hybrid method (Holte and Talley, 2009). The climatology incorporates over 2,250,000 Argo profiles (through December 2019) producing a representative annual cycle of monthly mixed layer properties. The climatological values of MLD were extracted and averaged in the areas, where, the anticyclones are located (see section "Wind Data and Ekman Pumping Estimation" for the geographical limits of the anticyclones).

Moreover, the MLD was estimated from the individual float profiles selected in the region of the PG and CG, using the method of de Boyer Montégut et al. (2004) and the Gibbs-SeaWater (GSW) Oceanographic Toolbox (McDougall and Barker, 2011). This threshold method uses a temperature difference criterion, for which the MLD is the depth at which temperature changes by a given value with respect to the near-surface reference depth. The temperature difference used in this work is $\Delta t = 0.2$°C, as suggested by D'Ortenzio et al. (2005) for the Mediterranean Sea.

Float Data and Analysis

An overview of the salinity distribution in the whole EMS is obtained from the horizontal scatter plot of mean salinity derived

[1] http://mixedlayer.ucsd.edu

TABLE 1 | List of selected Argo float profiles with dates and positions of the first and the last profile considered in this work, parking and profiling depths, and the cycle period of each instrument. Surface gyres centers, diameters, and maximum speeds are derived from altimetry data.

Gyre	Float WMO	Cycles in the gyre	First profile	Last profile	Parking depth (m)	Profile depth (m)	Cycle period (days)	Diameter (km)	Max speed (cm/s)	Center position
Pelops	6901818	33–70	May 14, 2013	October 31, 2013	350	2000	5	Gyre 110 Core 60	15	35.69°N 22.06°E
	1900954	1–110	April 14, 2014	June 24, 2015	1000	1500	4	Gyre 80 Core 40	10	35.56°N 21.31°E
	6901885	36–85	April 27, 2015	January 27, 2016	350	1000	5	Gyre 120 Core 60	10	35.81°N 22.06°E
	6901887	1–89	November 13, 2014	February 26, 2016	350	1000	5	Gyre 100 Core 50	8-10	35.69°N 22.19°E
	6900423	1–349	April 25, 2016	May 15, 2017	1000	1500	1	Gyre 120 Core 60	10	35.69°N 21.32°E
	6901765 (Bio)	132–191	May 22, 2017	June 11, 2018	1000	1000	1/5/7	Gyre 110 Core 45	15	36.06°N 21.69°E
	3901976	1–23	November 6, 2018	February 24, 2019	350	2000	5	Gyre 120 Core 40	22	35.94°N 21.56°E
Cyprus	6900091	126–308	March 19, 2003	August 30, 2005	1000	1500	4.9	Gyre 160 Core 70	15	33.56°N 33.19°E
	6900665	1–39	July 8, 2008	January 14, 2009	350	700	5	Gyre 80 Core 40	15	33.81°N 32.44°E
	6900679	1–56	June 27, 2008	March 17, 2019	400	1000	1/5	Gyre 80 Core 40	15	33.81°N 33.43°E
	6900794	All	December 4, 2009	August 16, 2010	350	600/ 2000	1	Gyre 120 Core 60	20	33.69°N 33.56°E
	6901825	1–134	November 6, 2013	September 1, 2015	350	700	5	Gyre 120 Core 60	22	33.81°N 32.32°E
	6901897 (Bio)	130–163	August 30, 2015	February 11, 2016	200	800	5	Gyre 80 Core 40	18	33.81°N 32.56°E

from the float data in four vertical layers (5–50, 50–100, 100–200, and 300–400 m) over the period 2003–2019 (**Figure 2**). Such layers are representative of the typical depths of the main surface and intermediate water masses' distribution analyzed in this work and they were selected according to the knowledge available in literature. The seasonal maps are produced over two extended seasons, selected following Menna et al. (2012, 2020): summer/fall (July–December) and winter/spring (January–June).

The vertical extension and the thermohaline properties of the anticyclonic gyres are analyzed using Argo float vertical profiles of temperature and salinity from the upper 2000 m of the water column (Argo, 2020). In the Mediterranean Sea, the Argo floats are generally programmed to execute 5-day cycles alternating the profiling depth between 700 and 2000 m [see the MedArgo program in Poulain et al. (2007)]. Details about the missions of the floats selected for this work are listed in **Table 1**.

Among all the available data in the Mediterranean Sea, we selected the segment of the trajectories that correspond to floats entrapped in the PG and CG for a long period (months or years; see **Table 1**), using the concurrent altimetry data. The floats selected move inside the structures, more or less close to the center, describing an anticyclonic trajectory (**Figures 3A,C**). The profiles selection was then refined by using the mean vorticity fields concurrent with the periods in which the float transits and/or is trapped in the structure. The gyre center is defined as the point, where, the local minimum of vorticity field is observed (black square in **Figures 3A,C**); the distance of each float profile from the center is computed and the vorticity field is interpolated at the profile location (**Figures 3B,D**). The vorticity of an anticyclone is negative near its core, close to zero (slightly positive or negative) along the boundary between its core and its edge, and positive along the edge. Considering this behavior, we selected the distance D from the center at which numerous vorticity values become close to zero, and used this distance to define the core and the extension of the gyre (**Figures 3B,D**). All profiles with distances less than D from the center are considered in the core of the structure (red dots in **Figures 3A,C**; dots in the red shaded area in **Figures 3B,D**); all profiles with distances larger than D and lower than 2D are considered in the edge of the structure (cyan dots in **Figures 3A,C**; dots in the cyan shaded area in **Figure 3B**); all other profiles are discarded (blue dots in **Figure 3A**; dots in the blue shaded area in **Figure 3B**).

Most of the float profiles used in this work were validated using Delayed Mode Quality Control (DMQC) technique. The strategy adopted for DMQC is widely described in Wong et al. (2003); Böhme and Send (2005), Owens and Wong (2009); Notarstefano and Poulain (2013), and Cabanes et al. (2016). The accuracy of salinity measurements requested by Argo after the DMQC is 0.01. When DMQC data are not available, real-time data are used. The float salinity measurements selected in this article have a high level of accuracy: in each structure we performed a qualitative inter-comparison between the θ-S diagrams of the

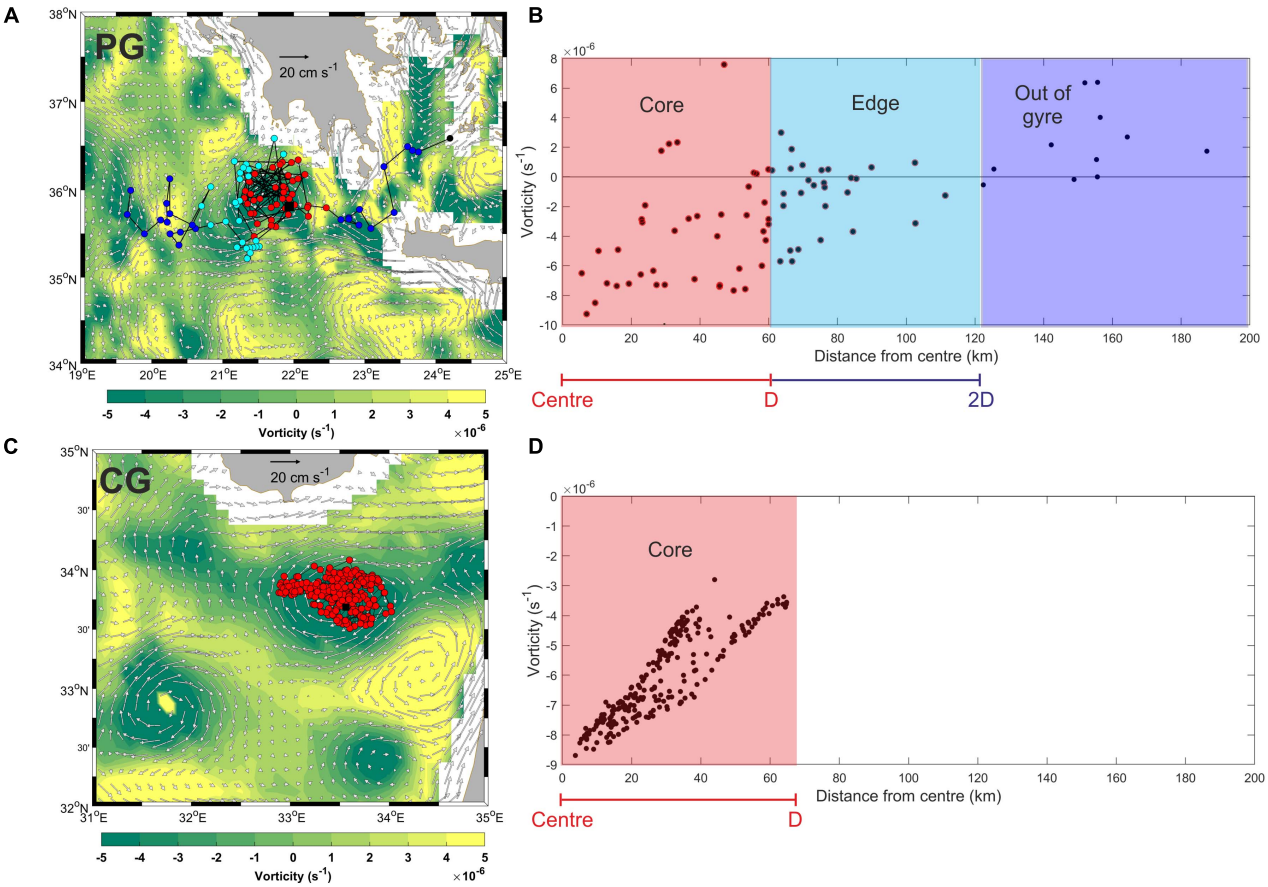

FIGURE 3 | Map of the trajectory (black line) and profile positions (colored dots) of the floats WMO 6901885, entrapped in the PG **(A)**, and WMO 6900794, entrapped in the CG **(C)**, superimposed on the concurrent mean maps of relative vorticity (background color) and AGV (white arrows). The centers of the gyres are represented by black squares. Vorticity values related to each profile versus the distance from gyre center obtained for the float WMO 6901885 in the PG **(B)** and for the float WMO 6900794 in the CG **(D)**.

floats entrapped in the anticyclones (**Figures 4A,B**). A zoom on the deepest and most uniform part of the water column (>800 m and < 1200 m; not shown) shows that the spread of salinity is within 0.02 at 13.7 θ level over a period of 6 years in the PG (from 2013 to 2019) and 13 years in CG (2003–2016). Moreover, the analysis of the θ-S curve of single floats does not reveal any systematic shift in time of the profiles, suggesting a good behavior of the conductivity sensor. Hence, the above mentioned small variations over such long periods are more likely imputable to a natural environmental variability and confirm the high reliability of the data used.

Vertical mixing events occurring inside the anticyclones are analyzed using an indicator of the water column stability known as Turner Angle (*Tu;* Ruddick, 1983). *Tu* gives information on the role of salinity and temperature gradients on the density gradients (Kubin et al., 2019). The types of instability are determined by the signs of the potential density θ and salinity gradients rather than by their absolute values (Meccia et al., 2016). In particular, when $|Tu| < 45$ the water column is stable; when $|Tu| > 90$ the water column is unstable with respect to both the temperature and salinity profile. The intermediate range shows two options: $-90 < Tu > -45$ indicates the conditions for diffusive convection (DC); whereas salt fingering can be expected if $45 < Tu > 90$. Double diffusion in the ocean occurs when temperature and salinity effects on density oppose each other, while the stratification is statically stable, and occurs because the molecular diffusivity of heat is nearly two orders of magnitude larger than that of salt (Stern, 1960). If both temperature and salinity increase with depth, the potential energy required to maintain the double diffusive instability is derived from the destabilizing temperature component of density (Bebieva and Timmermans, 2016). This type of double DC is referred to as DC and is associated with a DC staircase (a series of homogeneous layers in temperature and salinity separated by sharp gradients in temperature and salinity). The other type of double diffusion arises when temperature and salinity both decrease with depth (i.e., the salinity component of density is destabilizing) and is associated with salt fingers (SF), or a SF staircase.

An estimation of the flux of the AW perpendicular to the transects depicted in **Figure 1A** was obtained using the mean climatological density (ρ) values along the transects (derived by float data) and the monthly geostrophic velocity components

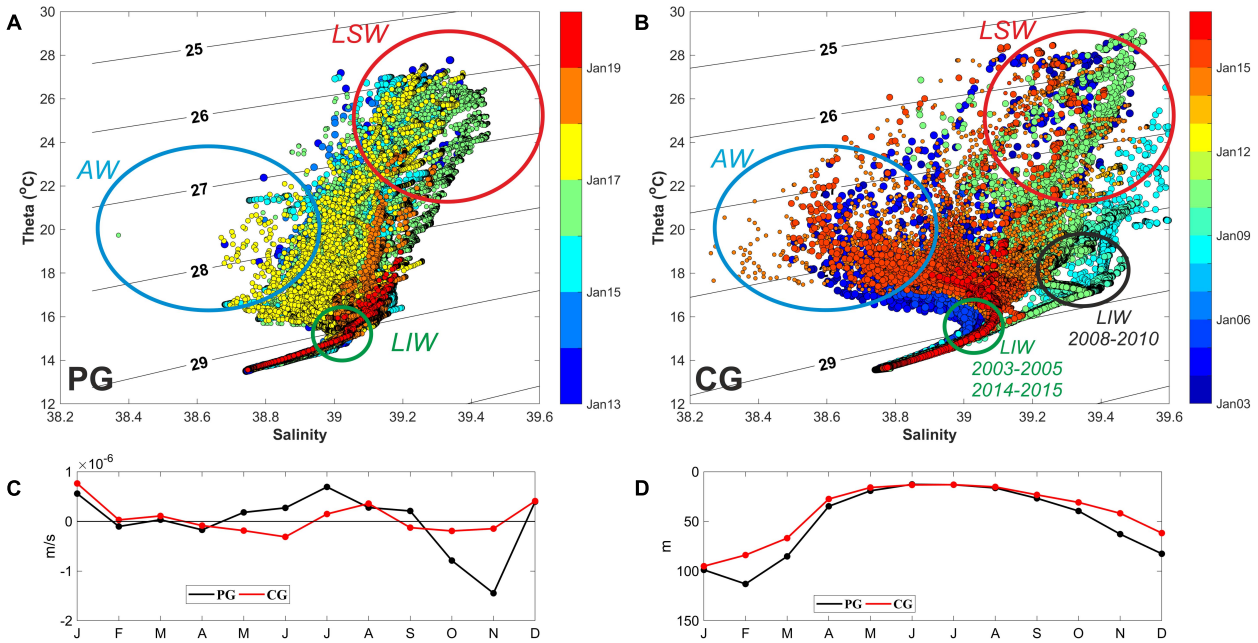

FIGURE 4 | θ/S diagrams of the profiles sampled in the **(A)** PG and **(B)** CG colored by the time. The location of the main water masses in the diagrams are highlighted with colored ellipses. Annual evolution of the Ekman pumping **(C)** and MLD **(D)** estimated in the period 2007–2019.

perpendicular to the transects (v, derived from altimetry). Mass transport is estimated as:

$$F = \iint \rho v dx dz \quad (2)$$

The horizontal dimension of the transects (dx) is of 55 km. In order to closely monitor he AW transport, the vertical dimension (dz) and the density along the Cretan transect (depicted in black in **Figure 1A**) were defined over the layer 0–100 m depth, whereas those of the Cyprus Passage transect (depicted in red in **Figure 1A**) were defined over the layer 50–100 m depth. For this estimate, we used the AGV considering their direction and strength as representative of the surface layer between 0 and 100 m depth. Transects locations and orientations were designed to intercept the main pathways of the AW in the Levantine Basin.

RESULTS

Surface Statistics

The mean maps of ADT, AGV and pseudo-Eulerian drifter velocities in bins of 0.25°× 0.25° are used to depict the surface circulation in the EMS (**Figures 1B,C**). Qualitatively, the two datasets fit rather well and describe the same morphology (shapes, locations and horizontal extension of the main permanent and quasi-permanent circulation features). A quantitative comparison between the two datasets is out of the scope of this work, but it is interesting to note that quantitative discrepancies are imputable to (i) the wind driven and ageostrophic currents included in the drifter velocity measurement (Poulain et al., 2012), (ii) the spatial and temporal gaps due to the non-uniform drifter density (Poulain et al., 2012), and (iii) the spatial smoothing applied to the satellite altimetry data (Pujol and Larnicol, 2005). More details on the circulation structures (Schroeder et al., 2012) and more extensive comparisons between drifter and altimetry derived currents in the EMS can be found in the literature (Gerin et al., 2009; Menna et al., 2012, 2019a,b, 2020; Poulain et al., 2012).

New interesting features, not yet described in the literature, are depicted with dashed black arrows in **Figure 1B**. They consist of a northward current that connects the Ionian and the Adriatic Sea moving along the eastern Greek coast and a westward current that connects the Levantine and the Ionian Basin moving from the southern Crete coast, feeding the northern branch of the Western Cretan Gyre (WCG). These features are confirmed by the pseudo-Eulerian statistics derived by drifters in **Figure 1C**. The trajectory of the drifter IMEI 300234065616590 (colored dots in **Figure 1C**), deployed southeast of Crete (in the IG) in October 2018, links the above described currents and outlines the potential pathway of the LSW between the Levantine and Ionian – Adriatic seas. Along this path, the PG plays an important role in the recirculation and distribution of the LSW in the western part of the EMS. A direct connection between the Ionian and the Adriatic Sea along the eastern Greek coast was already suggested by Malanotte-Rizzoli et al. (1997) in the intermediate layer (200–600 m depth).

Analysis of Thermohaline Properties

Figure 2 gives an overview of the salinity distribution in the EMS as detected by floats in the period 2003–2019. The AW coming from the west fills the surface layer of the Ionian Sea

west of 20°E and enters the Levantine Basin moving along the southern coast (**Figure 2B**). In the Levantine, the mean depth of the AW increases and its pathway can be followed in the 50–100 m layer (**Figures 2C,D**). The AW moves with the coastal currents and the MMJ, recirculating within the sub-basin scale and mesoscale structures located along its path (**Figures 2C,D**). The salty LSW (S > 39.05) is formed in the Levantine Basin during summer/fall and fills the first 50 m of the water column (**Figure 2A**), in agreement with the observations of Malanotte-Rizzoli and Robinson (2012). The pathway of the LSW described in the literature [marked with black arrows in **Figure 2A**, adapted from Malanotte-Rizzoli et al. (1997) and Velaoras et al. (2014) shows its intrusion in the Cretan Passage, in the Ionian and Aegean seas Malanotte-Rizzoli et al. (1997); Theocharis et al. (1999), Alhammoud et al. (2005); Velaoras and Lascaratos (2010), and Vervatis et al., 2011)]. The LSW enters the Aegean Sea through the eastern Cretan straits, mainly carried by the Asia Minor Current (AMC in **Figure 1B**; Kontoyiannis et al., 1999) and bifurcates in a branch that feeds the Cretan Sea moving westward, and a second one that moves towards the north (Zodiatis, 1991, 1993; Theocharis et al., 1993). The largest mean salinity values (up to 39.7) are observed along the eastern Levantine coast and in the IG (**Figure 2A**). The distribution of the surface salinity during winter/spring gives an indication of the spreading of the LSW in the EMS (**Figure 2B**). Salty waters are observed in the eastern and northern Levantine, in the southern Aegean and in the southeastern Ionian. Relative high salinity values (*S* = 38.8–39) are also detected in the north-eastern Ionian and in the south Adriatic seas (Southern Adriatic Gyre –SAG; **Figure 2B**; see the geographical location of the SAG in **Figure 1B**), suggesting a northward coastal transport of the LSW carried out by the surface currents along the eastern Ionian coast (**Figure 1B**). The LSW is one of the preconditioning factors of the LIW formation during winter; the winter cooling increases the density of the surface waters and the LSW starts to mix with the underlying waters down to depths of 200–400 m forming the LIW (Malanotte-Rizzoli and Robinson, 2012). The signal of the LIW with a subsurface salinity maximum, is clearly identifiable between 100 and 400 m in the Levantine Basin (**Figures 2E–H**); an indication of the LIW pathway is given by the black arrows in **Figure 2F**, adapted from Hayes et al. (2019). Larger salinity values are observed in the southern Aegean Sea, along the eastern Levantine coast, in the IG and CG regions in the layer of 100–200 m (**Figures 2E,F**). In the intermediate layer, between 300 and 400 m depth, the salinity maximum is identified in the core of the IG and CG structures (**Figures 2G,H**).

We selected 7 floats for the PG (664 profiles) and 6 floats for the CG (667 profiles) that spent part of their life inside the structures (**Table 1**), to cover the widest possible time period and highlight the seasonal and interannual variabilities. The water masses, sampled in the first 2000 m of the water column in the regions of the PG and CG, are shown in the θ/S diagrams of **Figure 4** and their thermohaline characteristics summarized in **Table 2**. The results of **Table 2**, rather than being an exhaustive classification of the thermohaline characteristics of the individual water masses, are intended to provide their range of thermohaline variability within the different structures. The ranges reported in this article are in agreement with recent results available in the literature for the EMS (see **Table 2**).

The θ/S diagrams show the presence of three main water masses (**Figure 4**). The LSW is characterized by the salinity maximum (S > 39.05), potential temperature larger than 20°C and potential densities smaller than 28 kg m^{-3} (**Figure 4** and **Table 2**). The AW, characterized by the lowest salinity and potential temperature of 16–21°C, is detected only sporadically in the PG (a few profiles in the area of the θ/S occupied by the AW; **Figure 4A**). The LIW layer is characterized by potential density larger than 28.7 kg m^{-3} and salinity of 38.85–39.2. The LIW sampled in the CG in 2008–2010 is warmer and saltier than that sampled before and after this period, allowing to identify two different LIW "cores" in the CG (**Figure 4B**). These outcomes are addressed in more detail in sub-section "Pelops Gyre" and sub-section "Cyprus Gyre," along with an accurate description of the thermohaline properties and mixing.

Figures 4C,D provide an overview of the annual climatology of the atmospheric forcing and MLD in the PG and CG. In the wind-forced PG, the Ekman pumping shows the largest negative values (downward flow) in fall, in concomitance with the strengthening of the Etesian winds, and weak positive ones (upward flow) in spring and summer. The Ekman pumping effect is reduced in the region of CG; this structure is not driven by the wind, indeed the input of the wind stress curl is positive (cyclonic) in this area (see **Figure 2** of Amitai et al., 2019). The annual evolution of the MLD is similar for both the gyres, with values smaller than 30 m in the period March-October and increasing values between November and February (**Figure 3D**). High mean MLD values, larger than 100 m, are observed in the region of the PG in February.

For each gyre, the θ/S diagram and the contour diagram of salinity and turner angle are shown in **Figures 5–8**. The float profiles selected for each structure are sorted in the figures chronologically according to the periods covered by the data.

Pelops Gyre

The PG is sampled almost continuously by 7 floats in the period 2013–2019 (**Figure 5**). The main gaps in the data occur in October 2013–April 2014, February–April 2016, and June–November 2018. The PG center is generally located between 35.5—36.1°N and 21.3°—22.1°E (**Table 1**) and its vertical extension reaches ∼ 800–900 m depth (**Figure 5A**; the vertical extension of the PG is indicatively represented by the isohaline of 38.85). The surface dynamics of the gyre, described averaging the ADT and AGV fields concurrent with the float trajectory, define a mean diameter of 80 – 120 km and maximum speeds of 15 cm/s in 2013, smaller than 10 cm/s in 2014–2018 and larger than 20 cm/s in 2019 (**Table 1**).

In summer/fall (July–October), the upper layer of the PG (50–80 m depth; **Figure 5A**) is filled by the LSW, characterized by high salinity maximum (S > 39.1), the largest potential temperature and potential densities smaller than 27.5 kg m^{-3} (see water mass details in **Table 2** and **Figure 4A**). The AW, characterized by lowest salinity and potential temperature of 16–21°C, enter the PG only sporadically (a few profiles in the

TABLE 2 | Water masses of the EMS and their thermohaline properties inside.

Water mass	Geographical region	References	Density (kg m^{-3})	Salinity (psu)	Temperature (°C)	Depth range (m)
LSW	Eastern Mediterranean	Cardin et al., 2015		>39.15	>18	0–50 m
	Eastern Levantine	Ozer et al., 2017		39–39.7	22–29	
	CG	Mauri et al., 2019		>39.15	>18.6	0–80 m
	Levantine Sea	Kassis and Korres, 2020		>39.1		
	PG – Ionian Sea	This article	25.5–27.5	39.1–39.4	20–27	0–80
	CG– Eastern Levantine	This article	25.2–28	39.15–39.6	20–29	0–80
LIW	Southern Levantine	Techtmann et al., 2015		39.1–39.2	15.5–16	
	Eastern Mediterranean	Cardin et al., 2015		38.85–39.24	14–15.5	
	Eastern Levantine	Ozer et al., 2017		38.95–39.35	15.2–17.5	
	CG	Mauri et al., 2019		39–39.15	16.5–18	
	PG – Ionian Sea	This article	28.75–29.1	38.9–39.05	14.5–16	250–700
	CG 2003–2004; 2014–2016 – Eastern Levantine	This article	28.7–29	38.85–39.2	14–17	120–400
	CG 2008–2010 – Eastern Levantine	This article	28.5–28.85	>39.2	16–19	200–400
AW	Southern Levantine	Techtmann et al., 2015		38.6–39.5	17.5–26.3	
	Eastern Levantine	Ozer et al., 2017		38.6–39.1	16–23	
	Ionian Sea	Kassis and Korres, 2020		38.66–38.93		
	PG – Ionian Sea	This article	26.7–28.4	38.62–38.82	16–22	80–100
	CG 2003–2004; 2014–2016 – Eastern Levantine	This article	27–28.2	38.1–38.85	17–21	50–120
Mixing water (winter/spring)	PG – Ionian Sea	This article	28–28.9	39.05–39.15	16–18	0–200
	CG 2003–2004; 2014–2016 – Eastern Levantine	This article	28.4–28.8	39–39.1	15–18	0–400
	CG 2008–2010– Eastern Levantine	This article	28–29	39.2–39.4	16–18	0–200

area of the θ/S diagram meet the thermohaline characteristics of the AW; **Figure 4A**). A thin vein of AW is recorded in the structure in summer/fall 2013 and 2017, located below the LSW at 80 m depth (**Figure 5A**). The LIW layer, characterized by densities larger than 28.75 kg m^{-3} and salinities of 38.9–39.05, is generally located between 250 and 450 m; it is deeper (400–700 m depth) for the profiles collected in 2018–2019. In late fall – early winter, the fast decrease of temperature in the saline surface layer of the PG leads to a rapid increase in density (gradual downward bending of the isopycnals and isohalines) with consequent water sink and mixing with waters of the underlying layer. The water mass formed by the winter mixing shows intermediate thermohaline characteristics between the LSW and the LIW (**Table 2**) and fills the layer between 0 and 200 m during winter–spring seasons in the PG. Under the LIW layer, between 800 and 1000 m, the floats detect the signature of the CIW in the PG (S = 38.85–38.9; σ = 29.1–29.15; **Figures 4A**, **5A**).

The analysis of the water column stability and stratification (Tu), superimposed on the time series of the MLD derived by float profiles, is shown in **Figure 5B**. The clearest and dominant feature in the water column within the PG is the proneness to double diffusion and in particular to the SF regime ($-90 < Tu > -45$; orange colored zones in **Figure 5B**). In July–October, the upper layer of the anticyclone (**Figure 5A**) is saltier and warmer than the underlying water and, at the interface between these water masses (located just below the signature of the MLD, **Figure 5B**, and/or the maximum salinity gradient, **Figure 5A**, at 50–80 m depth), the water column shows a thin layer prone to the SF regime (**Figure 5B**). Immediately below this layer, approximately between 50 and 150 m, we observe a layer with stable conditions (colored in green in **Figure 5B**), characterized by homogeneous thermohaline properties, that corresponds to the mixing – produced water. Another layer characterized by stable conditions is located between 250 and 600 m (depth changes over the years), and corresponds to the LIW. Areas located between the two stable layers, as well as those located below the LIW to the whole vertical extent of the PG, are affected by SF. The sensitivity of the Ionian 200–1000 m layer to the SF condition was previously highlighted by Zodiatis (1992) and Kioroglou et al. (2014), by analysing CTD profiles, and by Meccia et al. (2016) using model reanalysis products. In late fall, the MLD starts to increase typically reaching a depth between 150 and 300 m in the period January–March. In 2015, float data show the maximum MLD over the examined period (∼ 440 m depth); the occurrence of this "deep mixing"

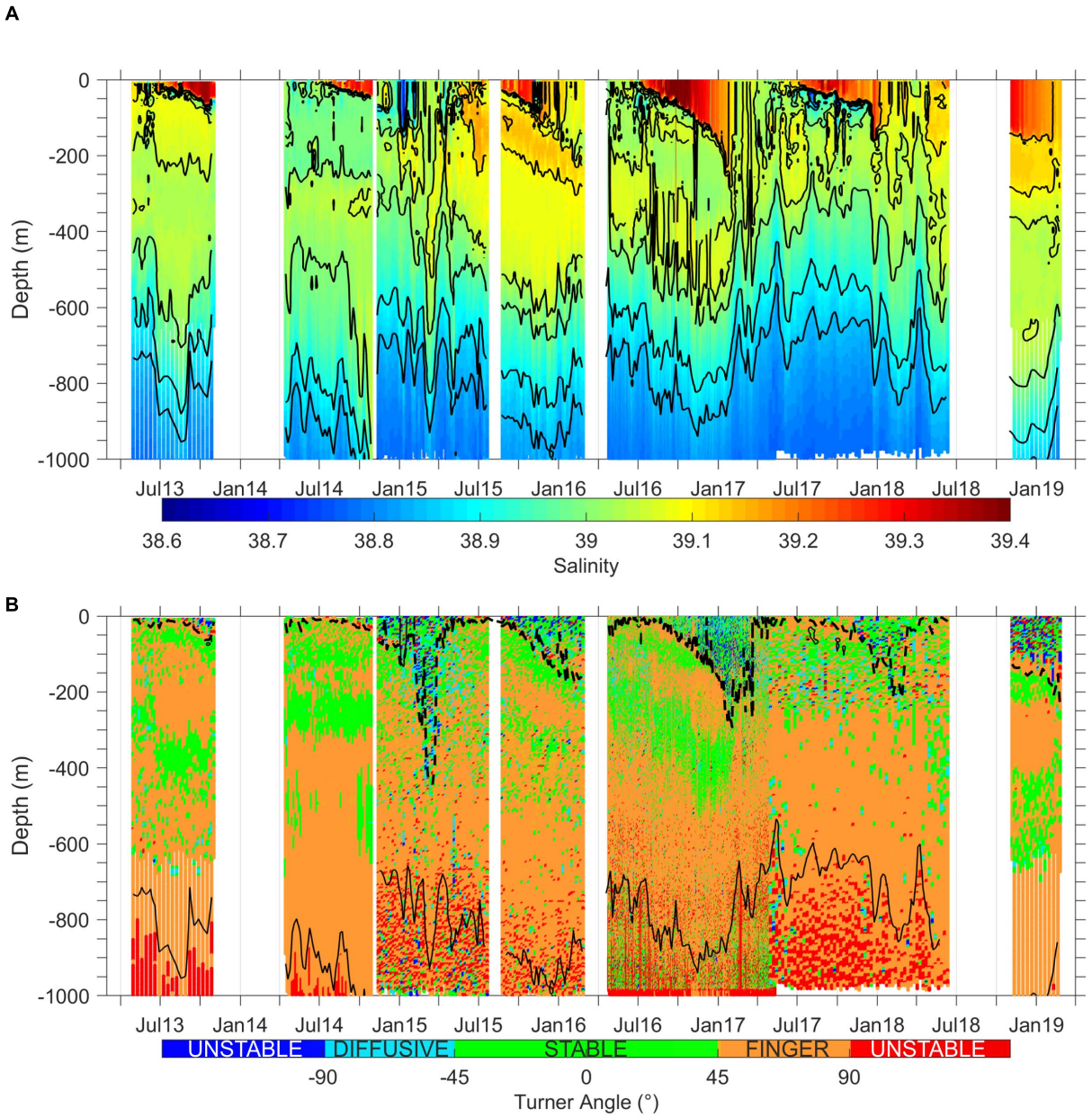

FIGURE 5 | Contour diagrams of the salinity **(A)** and turner angle **(B)** versus depth and time for the float entrapped in the PG. Black continuous lines in **(A)** are the isohalines 38.85, 39, 39.05, and 39.15; black dashed line in **(B)** is the MLD estimated by float profiles; black continuous line in **(B)** is the isohaline 38.85.

event is also clearly documented by the contour diagrams of salinity (**Figure 5A**), potential temperature and potential density (not shown). The part of the water column involved in the deepening of the MLD becomes instable ($|Tu| > 90$; blue dots in **Figure 5B**) and thus prone to mixing phenomena. Conditions for SF also occur during mixing events in the layer below the mixed layer. Layers located below the vertical extension of the PG show instable conditions (red and blue dots in the deep layer of **Figure 5B**), suggesting the occurrence of deep mixing phenomena.

Cyprus Gyre

The CG was sampled by Argo floats intermittently since January 2003. The periods in which data are available are: 2003–2005, 2008–2010, and 2014–2016 (**Table 1**). The CG center is located between 33.5°N and 33.85°N and 32.4–33.5°E and the gyre extends from the surface to about 400 – 600 m depth (**Figures 6–8**; the vertical extension of the CG is indicatively represented by the isohaline of 38.85). The surface signature of the gyre shows a mean diameter between 80 and 160 km (**Table 1**), in agreement with the results of Prigent and Poulain (2017). The maximum

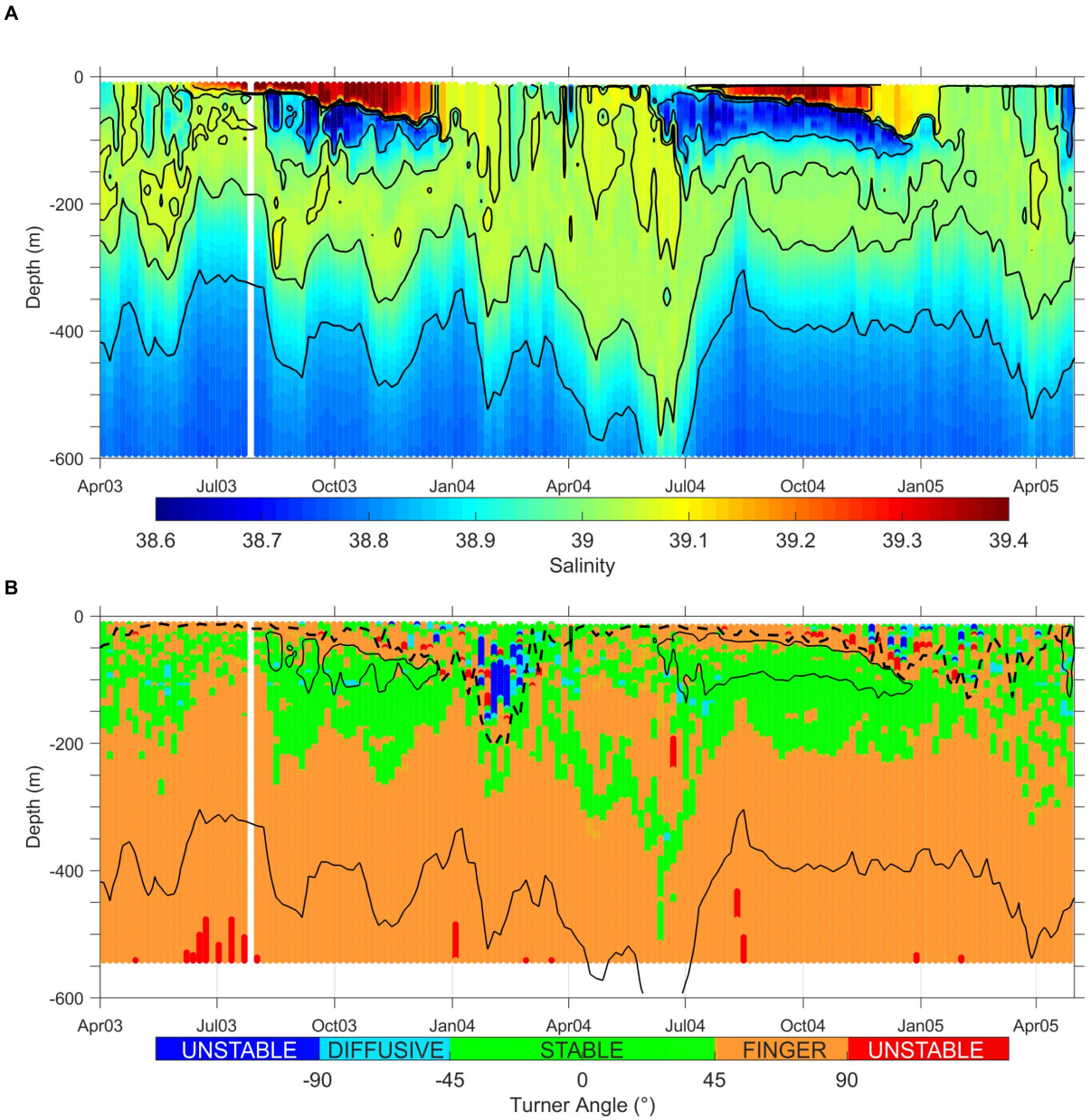

FIGURE 6 | Contour diagrams of the salinity **(A)** and turner angle **(B)** versus depth and time for the float entrapped in the CG in 2003–2005. Black continuous lines in **(A)** are the isohalines 38.85, 39, 39.05, and 39.15; black dashed line in **(B)** is the MLD estimated by float profiles; black continuous line in **(B)** is the isohaline 38.85.

surface speeds detected in the periods sampled by floats range between 15 and 22 cm/s, but it is interesting to remind that the CG area is characterized by high variability as a result of its interaction with the MMJ and the South Shikmona Eddy (SSE; located south east of the CG; see **Figure 1B**). For instance, an extensive analysis, carried out in the CG in February–May 2017 using drifter data, reveals a diameter of 80–100 km and a maximum speed of 50 cm/s (Prigent and Poulain, 2017; Mauri et al., 2019).

The CG presents a strong interannual variability with two main thermohaline patterns. The first pattern is observed in the periods 2003–2005 (**Figure 6A**) and 2014–2016 (**Figure 8A**), when the CG shows a seasonal alternation of a homogeneous water column during winter/spring (0–400 m depth) and a stratified condition during summer/fall. The summer/fall stratification is characterized by the following layers: the LSW in the first 50–80 m depth ($S > 39.15$); a vein of AW between 50 and 120 m depths ($S < 38.85$); the LIW between 120 and 350–400 m (salinities between 38.85 and 39.1). The second thermohaline pattern occurs in the period 2008–2010, when the CG is filled by a homogeneous layer of salty water ($S > 39.2$) distributed between 0 and 450 m depth (**Figure 7A**). In this

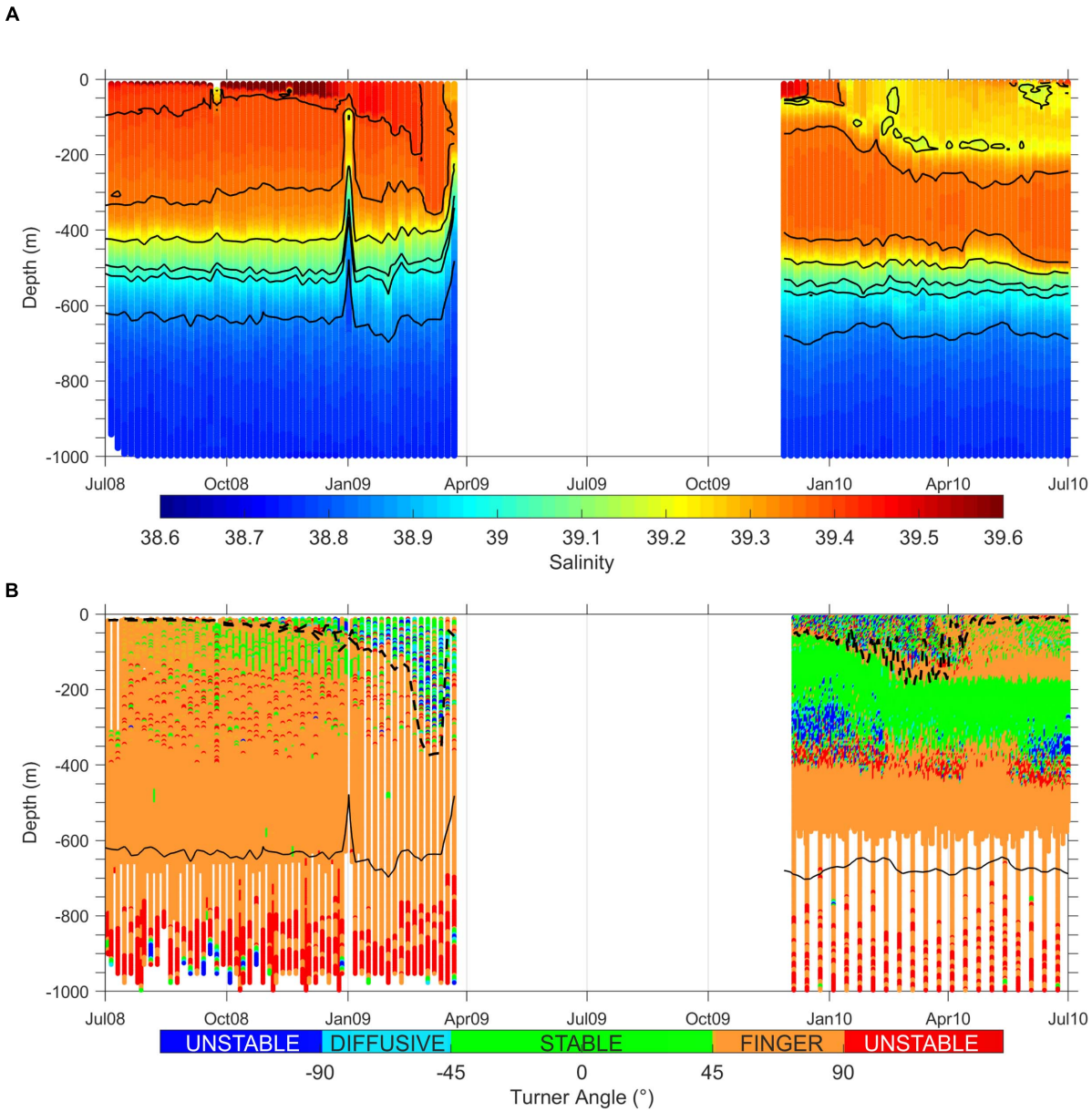

FIGURE 7 | Contour diagrams of the salinity **(A)** and turner angle **(B)** versus depth and time for the float entrapped in the CG in 2008–2010. Black continuous lines in **(A)** are the isohalines 38.85, 39, 39.05, 39.2, 39.35, and 39.4; black dashed line in **(B)** is the MLD estimated by float profiles; black continuous line in **(B)** is the isohaline 38.85.

layer, the thermohaline characteristics remain approximately unchanged over all the seasons without any AW signal. Seasonal intrusion of the LSW with salinity values up to 39.4 are observed in the first 50 m of the water column during summer/fall (**Figures 4B**, **7A**). Winter cooling in 2009 and 2010 favors the sinking of LSW from the surface to 400 m and 200 m depths, respectively (**Figure 7A**), maintaining the high salinity of the upper homogeneous layer. The thermohaline characteristics of the LIW detected in the CG during 2008–2010 show larger salinities and lower densities compared to the other periods analyzed (**Figure 4B**).

During the first thermohaline mode (periods 2003–2005, and 2014–2016), in the layer 0–50 m of the water column, the CG shows unstable conditions in late fall/winter and SF conditions in summer/early fall. Stable conditions are observed in the layer between 50 and 200 m (**Figures 6B**, **8B**). Below 200 m, the water column is prone to the SF mode which extends to the whole depth of the gyre. When the winter mixing is sufficiently intense and deep, involving the 0 – 200 m layer (January–March 2004; **Figure 6A**), the stability condition inside the CG (January–March 2004; **Figure 6B**) are similar to those observed in the PG: two stable layers are detected at 70–100 m and 200–300 m depths

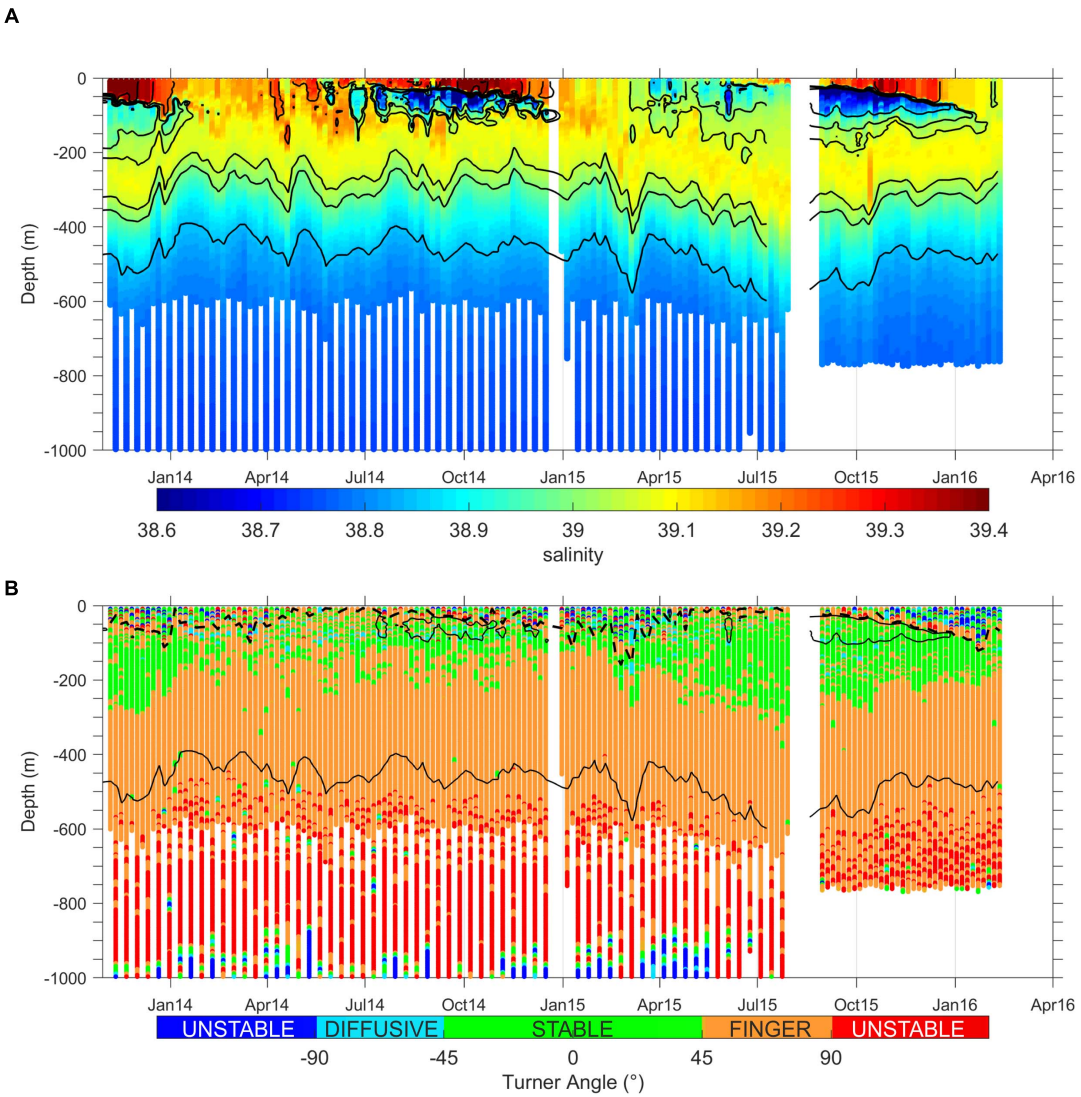

FIGURE 8 | Contour diagrams of the salinity **(A)** and turner angle **(B)** versus depth and time for the float entrapped in the CG in 2014–2016. Black continuous lines in **(A)** are the isohalines 38.85, 39, 39.05, 39.2, 39.35, and 39.4; black dashed line in **(B)** is the MLD estimated by float profiles; black continuous line in **(B)** is the isohaline 38.85.

interspersed by a SF layer. The water mass formed by the winter mixing shows intermediate thermohaline characteristics between the LSW and the LIW (**Table 2**) and fills the first 300–400 m of the water column during winter.

During the second thermohaline mode (period 2008–2010), the water mass produced by winter mixing shows salinities of 39.2 and fills the layer 0–200 m. Stable conditions are observed in the core of the LIW layer (200–400 m depth) and instability at its interface with the underlying layers.

Layers located below the signature of the CG (depths larger than 600 m) show mixing conditions (red and blue dots in the deeper layer of **Figures 7B**, **8B**), as already observed in the PG. These layers are filled by the LDW, formed in the core of the RG and recently described in Kubin et al. (2019) (θ = 13.7–14.5°C, S = 38.8–38.9).

DISCUSSION

The anticyclones of the EMS play a crucial role in the distribution of the surface and intermediate water masses of Levantine origin, both inside the Levantine Basin and in the whole EMS. In this article, float data available within two structures, the PG and CG, were analyzed in detail. The PG is involved in the transport of the LSW and of the LIW toward the northern Ionian and south Adriatic seas (**Figure 2**). The LSW turns anticyclonically in the upper layer of the PG before joining the weak, northward surface coastal current described by the mean maps of altimetry and drifter data (**Figures 1B,C**). This current is northward oriented, whatever the circulation mode of the NIG (cyclonic or anticyclonic; see **Figure 2** of Menna et al., 2019b and Notarstefano et al., 2019). The LSW transported by the

coastal northward current along the western Greek coast could be responsible for the near-surface salinity maximum observed by Kokkini et al. (2018, 2020) in the South Adriatic Pit (SAP) during 2015–2016, by Kassis and Korres (2020) in 2005–2010 and by Mihanovic et al. (2021) in 2017. These authors describe an anomalous salinity pattern in the SAP, where, the maximum is located in the near-surface layer (around 100 m depth) instead of in the intermediate layer occupied by the LIW. These salty water masses in the near-surface layer, with a salinity of 38.9 (Kokkini et al., 2020), can be ascribed to an intrusion of the LSW, of Aegean or Levantine origin, further modified during its journey toward the south Adriatic.

In summer, the effect of surface temperature warming combined with the evaporation rates produces the formation of the LSW in the Levantine Basin (Hecht et al., 1988). This water mass strongly influences the seasonal variability of the analyzed anticyclonic gyres, affecting the water column stratification in summer/fall and the mixing events in winter. The LSW, entrapped in the anticyclones in summer/fall, fills the first 50/80 m of the water column, with a wider range of salinity values in the CG (S = 39.15–39.6; **Figure 4B**) and lower salinities in the PG (S = 39.1–39.4; **Figure 4A**). In summer/fall the CG frequently shows, below the salinity maximum of the LSW, a salinity minimum ascribable to the AW, generally located between 50/80 and 150 m (**Figures 6**, **8**). This sub-surface layer of AW characterizes only sporadically the vertical structure of the PG (**Figures 4**, **5**). The layer between 50/80 and 200 m depth in the PG and CG is filled by a water mass with intermediate thermohaline characteristics between the LSW and the LIW (**Figures 4–8**). This water mass is the result of the mixing phenomena occurring in winter.

In terms of water column stability, the PG and the CG are strongly characterized by the SF regime alternated to winter mixing events (**Figures 5–8**). The sensitivity of the Ionia Sea to the SF is attributed to the hot and saline LIW waters filling the basin from 200 to 400 m at various places, overlying the less saline and colder resident waters (Zodiatis, 1992; Onken and Brambilla, 2003; Kioroglou et al., 2014). This condition also occurs in the PG not only in the layer below the LIW, but also in the subsurface layer (50–80 m depth) at the interface between the saltier and warmer LSW and the underlying water (**Figure 5**). In the layer below 1000 m, the water column of the Ionian Basin is considered stable with some sporadic shifts toward the SF or DC regimes caused by temporary intrusions of waters with different thermohaline properties (Kioroglou et al., 2014; Meccia et al., 2016). This condition does not occur in the PG, where, the layers located below its vertical extension (red and blue dots in the deep layer of **Figure 5B**) show instability down to 2000 m (not shown), suggesting the occurrence of deep mixing phenomena in this layer. In the Levantine Basin double diffusion processes are linked to the SF regime in the first 1000 m depth (Meccia et al., 2016; Kubin et al., 2019) and to the DC at larger depths (Meccia et al., 2016). In the interior of the CG, the SF condition is clearly predominant in the layer below the LIW (**Figures 6–8**), whereas the mixing conditions dominate the layer below the signature of the CG (depths larger than 600 m; red and blue dots in the deeper layer of **Figures 7B**, **8B**).

The gradual deepening of the MLD and the consequent downward doming of the isohalines, is usually observed in November–January in the PG and in January–March in the CG (**Figures 5–8**). The mixing generally involves the first 200 m of the water column, but occasionally can affect both the LSW and the LIW layers, as in winter 2015 in the PG (**Figure 5A**). The water mass formed by the winter mixing fills the surface layer of the gyres between 0 and 400 m during winter–spring seasons.

The CG presents two different behaviors in the periods analyzed. In 2003–2005 and 2014–2016, it is characterized by seasonal variability with the alternance of a homogeneous water column during winter/spring (0–400 m depth), and a stratified condition during summer/fall. The AW, observed inside the CG in the layer of 50–120 m depth (S < 38.85), during winter mixes with the overlying LSW and favors the dilution of the water formed during the mixing events (**Figures 6**, **8**). Otherwise, in the period 2008–2010 the CG shows a slight seasonal variability

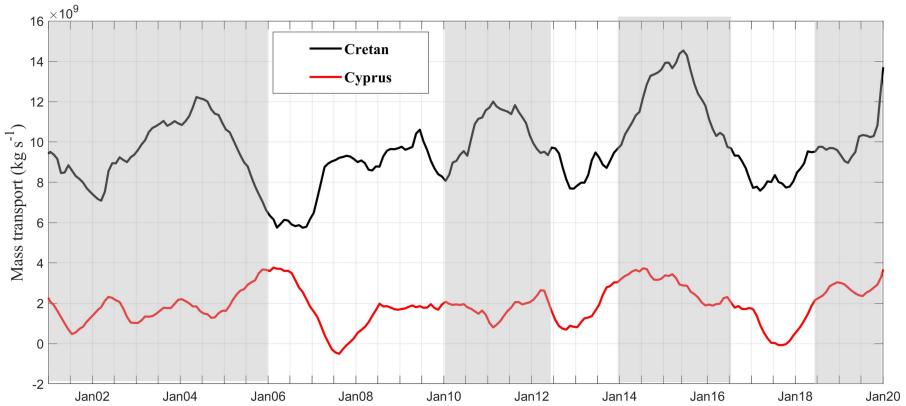

FIGURE 9 | Timeseries of the Mass transport across transects shown in **Figure 1A** in the period 2001–2019: the black transect located in the Cretan Passage and the red transect located southwest of Cyprus. Periods with cyclonic NIG are emphasized in light gray. Positive values of the mass transport indicate eastward/northeastward flows through the Cretan/Cyprus transects, respectively.

and it is filled by a homogeneous layer of salty water (S > 39.2), distributed between 0 and 400 m depth. Under this condition, winter cooling favors the sinking of LSW from the surface down to 400 m depth (**Figures 2G,H**, **7**), helping to maintain the high salinity of the upper homogeneous layer. The signal of AW is not detected in the CG in the period 2008–2010, therefore the winter mixing phenomena occur between two highly saline water masses (the LSW and LIW), supporting the production of a saltier mixing water and deepening the depth of the LIW layer (**Figure 7** and **Table 2**). The thermohaline differences observed between these periods can be related to the quasi-decadal reversal of the surface circulation in the NIG, from anticyclonic to cyclonic and vice versa. This connection is supported by the timeseries of the mass transport (**Figure 9**) estimated through two transects of the EMS: transect located at Cretan Passage (depicted in black in **Figure 1A**) intercepts the flow of AW from the Ionian toward the Levantine in the first 100 m of the water column (see the AW partway in **Figures 2B,C**; positive values of mass transport indicate an eastward flow); transect located southwest of Cyprus (depicted in red in **Figure 1A**) intercepts the inflow of AW transported by the MMJ in the CG region in the layer of 50–100 m depth (**Figures 1B**, **2C**; positive values of mass transport indicate a northeastward flow). The fluctuations of the time series of mass transport at Cretan Passage are in line with the quasi-decadal NIG reversals, with the strengthening of the AW transport toward the Levantine Basin during cyclonic circulation modes (emphasized in light gray in **Figure 9**) and its weakening during the anticyclonic circulation modes. In the periods 2003–2005 and 2014–2015, the NIG is cyclonic, favoring the flow of the AW toward the Levantine (larger mass transport at Cretan Passage; **Figure 9**) with a resulting decrease in salinity of the LSW and LIW layers (Civitarese et al., 2010; Ozer et al., 2017; Menna et al., 2019b). In the period 2008–2010 the NIG is instead anticyclonic, favoring the enhanced flow of the low saline AW toward the northern Ionian and South Adriatic seas and its reduction toward the Levantine Basin (reduced mass transport at Cretan Passage; **Figure 9**), with a consequent salinity increase in the Levantine (Civitarese et al., 2010; Ozer et al., 2017; Menna et al., 2019b). In transect located southwest of Cyprus, although the quasi-decadal variability is less evident, minima values of the AW transport are observed during anticyclonic periods; the absolute minimum of the time series is observed in 2007–2008, concurrently to the disappearance of the AW signal in the CG (**Figure 7**). This mechanism can explain the recent result of Hayes et al. (2019), which detect the deepest depth of the LIW layer in the Levantine Basin just in the region of the CG, using glider and float data in 2002–2014. LIW layer depths larger than 500 m estimated by Hayes et al. (2019) are in agreement with those estimated in this article over the period 2008–2010 (**Figure 7**). It is interesting to add that the floats of 2008–2010 are characterized by a prevalence of profiles in the center of the structure, while those from the periods 2003–2005 and 2014–2015 move over a larger area that includes both the center and the border of the gyre. The presence of a high salinity core in the CG is a characteristic already observed from glider data collected in fall 2016 (Mauri et al., 2019).

The results on the water column stability in the deeper layer, below the anticyclones signature, suggest the role of these structures in transporting energy, slat and heat from the surface layer to the bottom promoting deep mixing (**Figures 5–8** panels B). These observations are consistent with the model studies on the role of coherent anticyclones in the penetration of available potential energy toward the deeper ocean layers, with the consequent increasing of the mixing at depth (e.g., Koszalka et al., 2010). This deep mixing can also refill the near-surface nutrient stocks, as recently suggested by Dufois et al. (2016).

CONCLUSION

A detailed picture of the EMS, with particular focus on two anticyclonic gyres (PG and CG), is delineated using in-situ (surface drifters, Argo floats) and satellite (altimetry) data. The most important results derived from this study can be summarized as follows:

1. Two interesting features of the current field, not yet described in the literature, have been identified. The first one is a recurrent westward current, which moves from southwest coast of Crete, feeding the northern branch of the WCG toward the Ionian Sea (**Figures 2B,C**). This current interacts with the PG and could be responsible for the transport of the LSW toward the southern Ionian Sea, recently identified by Kassis and Korres (2020). The second feature is the northward current that connect the Ionian and the Adriatic seas, moving along the western Greek coast (**Figure 2B**). This current is northward oriented, whatever the circulation mode of the NIG.
2. The geographical location of PG (**Figures 1B,C**) allows it to remain quite isolated from the thermohaline circulation of AW (**Figure 1A**), therefore this water mass is detected only sporadically in its interior (**Figures 4A**, **5A**), while it is widely intercepted in the regions west of the gyre (**Figures 2A,B**). On the other hand, this structure is more involved in the circulation and exchange of surface and intermediate waters of Levantine origin (LSW and LIW) and in their flow toward the west and the north (**Figure 2**).
3. The CG, located along the path of the MMJ (**Figures 1B,C**), is involved in the thermohaline circulation of the AW in the years characterized by cyclonic NIG. The mass transport of AW toward the CG is of $\sim 2{\cdot}10^9$ – $3.5{\cdot}10^9$ kg·s^{-1} during cyclonic NIG (**Figure 9**). Seasonal intrusions of saltier LSW are observed in summer/fall in the first 50 m of the water column, and the AW is located under the layer of LSW (50–120 m; **Figures 6**, **8**). In the years characterized by anticyclonic NIG, the transport of AW toward the CG is strongly reduced (values close to zero or slightly negative; **Figure 9**) and the salinity inside the CG increases, forming a homogeneous high saline layer (0–400 m), whereas the AW is not detected in its interior (**Figure 7**).

4. The LSW and the LIW recirculate in the PG and, from there, they are redirected toward the northern Ionian and Adriatic seas (**Figures 2A–D**), following the northward current located along the eastern Greek coast (**Figures 1B,C**).
5. Mixing events observed in the anticyclones of the EMS are the results of winter mixing and double diffusive instability. Mixing events occur in winter inside the anticyclones of the EMS producing a water mass with intermediate thermohaline properties between the LSW and the LIW (**Table 2**). In spring/summer at the interfaces between the LSW and the underlying water and between the LIW and the underlying water, the water column shows a structure prone to the fingers regime (**Figures 5B**, **6B**, **7B**, **8B**). SF transport heat and salt downward making the underlying waters warmer, saltier and denser. Borghini et al. (2014), discussing SF observed in the deep layers of the Tyrrhenian Basin, state that this process is steady because the stratification with warmer saltier LIW above colder fresher deep waters enables double diffusion processes to proceed year-round. Given these remarks and considering the water column structure of the EMS (**Figure 2**), we expect a stable salt finger condition also in the eastern Mediterranean not only within the anticyclones but also in other regions, i.e., in the Levantine Basin. In the EMS, the salt finger process not only affects the deep layer below the LIW but, due to the presence of the warm and salty LSW, also the sub-surface layer from the base of the halocline to the top of the LIW layer.

The ending consideration of this article is on the role of the LSW in the main oceanographic processes of the EMS. This mass of water is still relatively poorly studied compared to the more noted and widely investigated LIW. Nevertheless, it probably deserves a more relevant role, because: (i) it influences the production of the LIW itself, triggering the mechanisms of dense water formation in the Levantine; (ii) it activates the mixing processes within the EMS anticyclones; (iii) in some years it also influences the preconditioning mechanisms of dense water formation in the southern Adriatic by providing a high contribution of salinity close to the surface.

DATA AVAILABILITY STATEMENT

Publicly available datasets were analyzed in this study. This data can be found here: https://nodc.inogs.it/metadata/doidetails?doi=10.6092/7a8499bc-c5ee-472c-b8b5-03523d1e73e9 (the DOI associated to the dataset is: 10.6092/7A8499BC-C5EE-472C-B8B5-03523D1E73E9), https://resources.marine.copernicus.eu/?option=com_csw&view=details&product_id=INSITU_MED_NRT_OBSERVATIONS_013_035, and https://doi.org/10.17882/42182.

AUTHOR CONTRIBUTIONS

MM conceived the subject, performed the data analysis, and wrote the manuscript. RG performed part of data analysis. RG and GN curated the data, wrote, reviewed, and edited the manuscript. EM helped to investigate the subject. AB and MP collected and processed the data and contributed to the analysis tools. EM and P-MP reviewed the manuscript and acquired the funding. All authors contributed to the article and approved the submitted version.

FUNDING

This research was founded by the Italian Ministry of University and Research, as part of the Argo-Italy program, and by the European Commissions, as part of the Copernicus CMEMS-TAC program (82-CMEMS-TAC-INSITU).

ACKNOWLEDGMENTS

The authors would like to thanks all the people who have deployed drifters and floats and made their data available in the Mediterranean Sea. This study has been conducted using E.U. Copernicus Marine Service Information. Argo float data were collected and made freely available by the International Argo Program and the national programs that contribute to it (https://argo.ucsd.edu, https://www.ocean-ops.org). The Argo Program is part of the Global Ocean Observing System.

REFERENCES

Alhammoud, B., Béranger, K., Mortier, L., Crépona, M., and Dekeyserc, I. (2005). Surface circulation of the Levantine Basin: comparison of model results with observations. *Prog. Oceanogr.* 66, 299–320. doi: 10.1016/j.pocean.2004.07.015

Amitai, Y., Ashkenazy, Y., and Gildor, H. (2019). The effect of the wind-stress over the Eastern Mediterranean on deep-water formation in the Adriatic Sea. *Deep Sea Res. II* 164, 5–13. doi: 10.1016/j.dsr2.2018.11.015

Argo. (2020). Argo Float Data and Metadata From Global Data Assembly Centre (Argo GDAC). SEANOE. doi: 10.17882/42182

Ayoub, N., Le Traon, P.-Y., and De Mey, P. (1998). A description of the Mediterranean surface variable circulation from combined ERS-1 and TOPEX/POSEIDON altimetric data. *J. Mar. Syst.* 18, 3–40. doi: 10.1016/S0924-7963(98)80004-3

Bebieva, Y., and Timmermans, M.-L. (2016). An examination of double-diffusive processes in a mesoscale eddy in the Arctic Ocean. *J. Geophys. Res. Oceans* 121, 457–475. doi: 10.1002/2015JC011105

Böhme, L., and Send, U. (2005). Objective analyses of hydrographic data for referencing profiling float salinities in highly variable environments. *Deep Sea Res. II* 52, 651–664. doi: 10.1016/j.dsr2.2004.12.014

Borghini, M., Bryden, H., Schroeder, K., Sparnocchia, S., and Vetrano, A. (2014). The Mediterranean Sea is becoming saltier. *Ocean Sci.* 10, 693–700. doi: 10.5194/os-10-693-2014

Brach, L., Deixonne, P., Bernard, M. F., Durand, E., Desjean, M. C., Perez, E., et al. (2018). Anticyclonic eddies increase accumulation of microplastic in the North Atlantic subtropical gyre. *Mar. Pollut. Bull.* 126, 191–196.

Cabanes, C., Thierry, V., and Lagadec, C. (2016). Improvement of bias detection in Argo float conductivity sensors and its application in the North Atlantic. *Deep Sea Res. I* 114, 128–136.

Cardin, V., Civitarese, G., Hainbucher, D., Bensi, M., and Rubino, A. (2015). Thermohaline properties in the Eastern Mediterranean in the last three decades: is the basin returning to pre-EMT situation? *Ocean Sci.* 11, 53–66. doi: 10.5194/os-11-53-2015

Civitarese, G., Gačić, M., Eusebi Borzelli, G. L., and Lipizer, M. (2010). On the impact of the bimodal oscillating system (BiOS) on the biogeochemistry and biology of the Adriatic and Ionian Seas (eastern Mediterranean). *Biogeosciences* 7, 3987–3997. doi: 10.5194/bg-7-3987-2010

Condie, S., and Condie, R. (2016). Retention of plankton within ocean eddies. *Glob. Ecol. Biogeogr.* 25, 1264–1277. doi: 10.1111/geb.12485

Cózar, A., Sanz-Martín, M., Martí, E., González-Gordillo, J. I., Ubeda, B., Gálvez, J. Á, et al. (2015). Plastic accumulation in the Mediterranean Sea. *PLoS One* 10:e0121762. doi: 10.1371/journal.pone.0121762

de Boyer Montégut, C., Madec, G., Fischer, A. S., Lazar, L., and Iudicone, D. (2004). Mixed, layer depth over the global ocean: an examination of profile data and a profile-based climatology. *J. Geophys. Res.* 109:C12003. doi: 10.1029/2004JC002378

D'Ortenzio, F., Iudicone, D., de Boyer Montegut, C., Testor, P., Antoine, D., Marullo, S., et al. (2005). Seasonal variability of the mixed layer depth in the Mediterranean Sea as derived from in situ profiles. *Geophys. Res. Lett.* 32:L12605. doi: 10.1029/2005GL022463

Dufois, F., Hardman-Mountford, N. J., Greenwood, J., Richardson, A. J., Feng, M., Herbette, S., et al. (2016). Impact of eddies on surface chlorophyll in the South Indian Ocean. *J. Geophys. Res. Oceans* 119, 8061–8077. doi: 10.1002/2014JC010164

Gačić, M., Borzelli, G. L. E., Civitarese, G., Cardin, V., and Yari, S. (2010). Can internal processes sustain reversals of the ocean upper circulation? The Ionian Sea example. *Geophys. Res. Lett.* 37:L09608. doi: 10.1029/2010GL043216

Gačić, M., Civitarese, G., Borzelli, G. L. E., Kovacevic, V., Poulain, P.-M., Theocharis, A., et al. (2011). On the relationship between the decadal oscillations of the Northern Ionian Sea and the salinity distributions in the Eastern Mediterranean. *J. Geophys. Res.* 116:C12002. doi: 10.1029/2011JC007280

Gačić, M., Civitarese, G., Kovacevic, V., Ursella, L., Bensi, M., Menna, M., et al. (2014). Extreme winter 2012 in the Adriatic: an example of climatic effect on the BiOS rhythm. *Ocean Sci.* 10, 513–522. doi: 10.5194/os-10-513-2014

Gerin, R., Poulain, P.-M., Taupier-Letage, I., Millot, C., Ben Ismail, S., and Sammari, C. (2009). Surface circulation in the Eastern Mediterranean using Lagrangian drifters (2005-2007). *Ocean Sci.* 5, 559–574.

Gertman, I. F., Ovchinnikov, I. M., and Popov, Y. I. (1994). Deep convection in the eastern basin of the Mediterranean Sea. *Oceanology* 34, 20–25.

Hamad, N., Millot, C., and Taupier-Letage, I. (2005). A new hypothesis about the surface circulation in the eastern basin of the Mediterranean Sea. *Prog. Oceanogr.* 66, 287–298.

Hamad, N., Millot, C., and Taupier-Letage, I. (2006). The surface circulation in the eastern basin of Mediterranean Sea. *Sci. Mar.* 70, 457–503.

Hayes, D., Poulain, P.-M., Testor, P., Mortier, L., Bosse, A., and Du Madron, X. (2019). Review of the circulation and characteristics of intermediate water masses of the Mediterranean–implications for cold-water coral habitats. *Coral Reefs Mediterr. (CORM)* 9, 1–26.

Hecht, A., Pinardi, N., and Robinson, A. R. (1988). Currents, water masses, eddies and jets in the Mediterranean Levantine Basin. *J. Phys. Oceanogr.* 18, 1320–1353.

Holte, J., and Talley, L.-D. (2009). A new algorithm for finding mixed layer depths with applications to Argo data and Subanctarctic Mode Water formation. *J. Atmos. Ocean. Technol.* 26, 1920–1939. doi: 10.1175/2009JTECHO543.1

Holte, J., Talley, L.-D., Gilson, J., and Roemmich, D. (2017). An Argo mixed layer climatology and database. *Geophys. Res. Lett.* 44, 5618–5626. doi: 10.1002/2017GL073426

Ioannou, A., Stegner, A., Le Vu, B., Taupier-Letage, I., and Speich, S. (2017). Dynamical evolution of intense Ierapetra eddies on a 22 year long period. *J. Geophys. Res. Oceans* 122, 9276–9298. doi: 10.1002/2017JC013158

Kassis, D., and Korres, G. (2020). Hydrography of the Eastern Mediterranean basin derived from argo float profile data. *Deep Sea Res. II* 171:104712. doi: 10.1016/j.dsr2.2019.104712

Kioroglou, S., Tragou, E., Zervakis, V., Georgopulos, D., Herut, B., Gertman, I., et al. (2014). Vertical diffusion processes in the Eastern Mediterranean–Black Sea system. *J. Mar. Syst.* 135, 53–63. doi: 10.1016/j.jmarsys.2013.08.007

Kokkini, Z., Mauri, E., Gerin, R., Poulain, P.-M., Simoncelli, S., and Notarstefano, G. (2020). On the salinity structure in the South Adriatic as derived from float and glider observations in 2013-2016. *Deep Sea Res. II* 171:104625. doi: 10.1016/j.dsr2.2019.07.013

Kokkini, Z., Notarstefano, G., Poulain, P.-M., Mauri, E., Gerin, R., and Simoncelli, S. (2018). Unusual salinity pattern in the South Adriatic Sea. in von Schuckmann et al., 2018. *J. Oper. Oceanogr.* 11(supl. 1), S1–S142.

Kontoyiannis, H., Theocharis, A., Balopoulos, E., Kioroglou, S., Papadopoulos, V., Collins, M., et al. (1999). Water fluxes through the Cretan Arc Straits, Eastern Mediterranean Sea: March 1994 to June 1995. *Progr. Oceanogr.* 44, 511–529.

Koszalka, I., Ceballos, L., and Bracco, A. (2010). Vertical mixing and coherent anticyclones in the ocean: the role of stratification. *Nonlin. Proces. Geophys.* 17, 37–47. doi: 10.5194/npg-17-37-2010

Kovačević, V., Ursella, L., Gacic, M., Notarstefano, G., Menna, M., Bensi, M., et al. (2015). On the Ionian thermohaline properties and circulation in 2010-2013 as measured by Argo floats. *Acta Adriat.* 56, 97–114.

Kubin, E., Poulain, P.-M., Mauri, E., Menna, M., and Notarstefano, G. (2019). Levantine intermediate and levantine deep water formation: an Argo float study from 2001 to 2017. *Water* 11:1781. doi: 10.3390/w11091781

Lavigne, H., Civitarese, G., Gacic, M., and D'Ortenzio, F. (2018). Impact of decadal reversals of the north Ionian circulation on phytoplankton phenology. *Biogrosciences* 15, 4431–4445. doi: 10.5194/bg-15-4431-2018

Malanotte-Rizzoli, P., Manca, B. B., Ribera D'Alcalà, M., Theocharis, A., Bergamasco, A., Bregant, D., et al. (1997). A synthesis of the Ionian Sea hydrography, circulation and water masses pathways during POEM-Phase I. *Progr. Oceanogr.* 39, 153–204.

Malanotte-Rizzoli, P., Manca, B. B., Ribera D'Alcalà, M., Theocharis, A., Brenner, S., Budillon, G., et al. (1999). The Eastern Mediterranean in the 80s and in the 90s: the big transition in the intermediate and deep circulations. *Dyn. Atmos. Oceans* 29, 365–395.

Malanotte-Rizzoli, P., and Robinson, A. (2012). *Ocean Processes in Climate Dynamics: Global and Mediterranean Examples*. Berlin: Springer Science & Business Media, 419.

Mauri, E., Sitz, L., Gerin, R., Poulain, P.-M., Hayes, D., and Gildor, H. (2019). On the variability of the circulation and water mass properties in the Eastern Levantine Sea between September 2016–August 2017. *Water* 11:1741. doi: 10.3390/w11091741

McDougall, T. J., and Barker, P. M. (2011). *Getting Started with TEOS-10 and the Gibbs Seawater (GSW) Oceanographic Toolbox, SCOR/IAPSO WG127*. 28 .

Meccia, V. L., Simoncelli, S., and Sparnocchia, S. (2016). Decadal variability of the turner angle in the Mediterranean Sea and its implications for double diffusion. *Deep Sea Res. I* 114, 64–77. doi: 10.1016/j.dsr.2016.04.001

Menna, M., Gerin, R., Bussani, A., and Poulain, P.-M. (2017). *The OGS Mediterranean Drifter Database: 1986-2016. Technical Report 2017/92 Sez. OCE 28 MAOS*. Trieste: OGS.

Menna, M., Notarstefano, G., Poulain, P.-M., Mauri, E., Falco, P., and Zambianchi, E. (2020). Surface picture of the Levantine Basin as derived by drifter and satellite data, Section 3.5 in von Schuckmann et al., 2020, Copernicus Marine Service Ocean State Report, 4. *J. Oper. Oceanogr.* S1–S172. doi: 10.1080/1755876X.2020.1785097

Menna, M., Poulain, P.-M., Bussani, A., and Gerin, R. (2018). Detecting the drogue presence of SVP drifters from wind slippage in the Mediterranean Sea. *Measurement* 125, 447–453. doi: 10.1016/j.measurement.2018.05.022

Menna, M., Poulain, P.-M., Ciani, D., Doglioli, D., Notarstefano, G., Gerin, R., et al. (2019a). New insight of the Sicily Channel and southern Tyrrhenian Sea variability. *Water* 11:1355. doi: 10.3390/w11071355

Menna, M., Poulain, P.-M., Zodiatis, G., and Gertman, I. (2012). On the surface circulation of the Levantine sub-basin derived from Lagrangian drifter and satellite altimetry data. *Deep Sea Res. I* 65, 46–58. doi: 10.1016/j.dsr.2012.02.008

Menna, M., Reyes Suarez, N. C., Civitarese, G., Gacic, M., Poulain, P.-M., and Rubino, A. (2019b). Decadal variations of circulation in the Central Mediterranean and its interactions with the mesoscale gyres. *Deep Sea Res. Oceans II* 164, 12–24. doi: 10.1016/j.dsr2.2019.02.004

Mihanovic, H., Vilibich, I., Sepic, J., Matic, F., Ljubesic, Z., Mauri, E., et al. (2021). Observation, preconditioning and recurrence of exceptionally high salinities in the Adriatic Sea. This issue. *Front. Mar. Sci.* doi: 10.3389/fmars.2021.672210

Millot, C., and Taupier-Letage, I. (2005). Circulation in the Mediterranean Sea. *Handb. Environ. Chem.* 5, 29–66.

Mkhinini, N., Coimbra, A. L. S., Stegner, A., Arsouze, T., Taupier-Letage, I., and Beranger, K. (2014). Long-lived mesoscale eddies in the Eastern Mediterranean Sea: analysis of 20 years of AVISO geostrophic velocities. *J. Geophys. Res. Oceans* 119, 8603–8626. doi: 10.1002/2014JC010176

Notarstefano, G., Menna, M., and Legeais, J. F. (2019). Reversal of the Northern Ionian circulation in 2017. in von Schuckmann et al., 2019. *J. Oper. Oceanogr.* 12:S108. doi: 10.1080/1755876X.2019.1633075

Notarstefano, G., and Poulain, P.-M. (2013). Delayed Mode Quality Control of Argo Saliniy Data in the Mediterranean Sea: a Regional Approach. Technical Report 2013/103 Sez. OCE 40 MAOS. Sgonico. 19.

Onken, R., and Brambilla, E. (2003). Double diffusion in the Mediterranean Sea: observation and parametrization of salt finger convection. *J. Geophys. Res.* 108:8124. doi: 10.1029/2002JC001349

Owens, W. B., and Wong, A. P. S. (2009). An improved calibration method for the drift of the conductivity sensor on autonomous CTD profiling floats by θ-S climatology. *Deep Sea Res.* 56, 450–457. doi: 10.1016/j.dsr.2008.09.008

Ozer, T., Gertman, I., Kress, N., Silverman, J., and Herut, B. (2017). Interannual thermohaline (1979-2014) and nutrient (2002-2014) dynamics in the Levantine surface and intermediate water masses, SE Mediterranean Sea. *Glob. Planet. Change* 151, 60–67. doi: 10.1016/j.gloplacha.2016.04.001

Pinardi, N., Zavatarelli, M., Adani, M., Coppini, G., Fratianni, C., Oddo, P., et al. (2015). Mediterranean Sea large-scale low-frequency ocean variability and water mass formation rates from 1987 to 2007: a retrospective analysis. *Prog. Oceanogr.* 132, 318–332. doi: 10.1016/j.pocean.2013.11.003

Poulain, P.-M. (2001). Adriatic Sea surface circulation as derived from drifter data between 1990 and 1999. *J. Mar. Syst.* 29, 3–32.

Poulain, P.-M., Barbanti, R., Font, J., Cruzado, A., Millot, C., Gertman, I., et al. (2007). MedArgo: a drifting profiler program in the Mediterranean Sea. *Ocean Sci.* 3, 379–395. doi: 10.5194/osd-3-1901-2006

Poulain, P.-M., Menna, M., and Mauri, E. (2012). Surface geostrophic circulation of the Mediterranean Sea derived from drifter and satellite altimeter data. *J. Phys. Oceanogr.* 42, 973–990. doi: 10.1175/JPO-D-11-0159.1

Prigent, A., and Poulain, P.-M. (2017). *On the Cyprus Eddy Kinematics*. Technical Report, OGS 2017/77 Sez. OCE 19 MAOS. Sgonico: OGS.

Pujol, M.-I., and Larnicol, G. (2005). Mediterranean Sea eddy kinetic energy variability from 11 years of altimetric data. *J. Mar. Syst.* 58, 121–142. doi: 10.1016/j.jmarsys.2005.07.005

Ramirez-Llodra, E., De Mol, B., Company, J. B., Coll, M., and Sardà, F. (2013). Effects of natural and anthropogenic processes in the distribution of marine litter in the deep Mediterranean Sea. *Progr. Oceanogr.* 118, 273–287. doi: 10.1016/j.pocean.2013.07.027

Rio, M. H., Pascual, A., Poulain, P.-M., Menna, M., Barcelò, B., and Tintorč, J. (2014). Computation of a new mean dynamic topography for the Mediterranean Sea from model outputs, altimeter measurements and oceanographic in situ data. *Ocean Sci.* 10, 731–744. doi: 10.5194/os-10-731-2014

Robinson, A. R., Golnaraghi, M., Leslie, W. G., Artegiani, A., Hecht, A., Lazzoni, E., et al. (1991). The eastern Mediterranean general circulation: features, structure and variability. *Dyn. Atmos. Oceans* 15, 215–240.

Robinson, A. R., Leslie, W. G., Theocharis, A., and Lascaratos, A. (2001). *Mediterranean Sea Circulation, Encyclopedia of Ocean Science*. Cambridge, MA: Academic Press, 1689–1706. doi: 10.1006/rwos.2001.0376

Rubino, A., Gačić, M., Bensi, M., Kovačević, V., Malačič, V., Menna, M., et al. (2020). Experimental evidence of long-term oceanic circulation reversals without wind influence in the North Ionian Sea. *Sci. Rep.* 10:1905. doi: 10.1038/s41598-020-57862-6

Ruddick, B. R. (1983). A practical indicator of the stability of the water column to double-diffusivity activity. *Deep Sea Res. A* 30, 1105–1107.

Schroeder, K., Garcia-Lafuente, J., Josey, S. A., Artale, V., Buongiorno Nardelli, B., Carrillo, A., et al. (2012). "Circulation of the Mediterranean Sea and its variability," in *Climate of the Mediterranean Region: From the Past to the Future*, ed. P. Lionello (Oxford: Elsevier), 187–256. doi: 10.1016/B978-0-12-416042-2.00003-3

Stern, M. E. (1960). The Salt-Fountain and thermohaline convection. *Tellus* 12, 172–175.

Techtmann, S. M., Fortney, J. L., Ayers, K. A., Joyner, D. C., Linley, T. D., Pfiffner, S. M., et al. (2015). The Unique chemistry of Eastern Mediterranean water masses selects for distinct microbial communities by depth. *PLoS One* 10:e0120605. doi: 10.1371/journal.pone.0120605

Theocharis, A., Balopoulos, E., Kioroglou, S., Kontoyiannis, H., and Iona, A. (1999). A synthesis of the circulation and hydrography of the South Aegean Sea and the Straits of the Cretan Arc (March 1994–January 1995). *Prog. Oceanogr.* 44, 469–509.

Theocharis, A., Georgopoulos, D., Lascaratos, A., and Nittis, K. (1993). Water masses and circulation in the central region of the Eastern Mediterranean: Eastern Ionian, South Aegean, and Northwest Levantine, 1986–1987. *Deep Sea Res. II* 40, 1121–1142.

Thomson, R. E., and Emery, W. (2001). *Data Analysis Method in Physical Oceanography*. Amsterdam: Elsevier Science, 654.

Velaoras, D., Krokos, G., Nittis, K., and Theocharis, A. (2014). Dense intermediate water outflow from the Cretan Sea: a salinity driven, recurrent phenomenon, connected to thermohaline circulation changes. *J. Geophys. Res. Oceans* 119, 4797–4820. doi: 10.1002/2014JC009937

Velaoras, D., and Lascaratos, A. (2010). North-Central Aegean Sea surface and intermediate water masses and their role in triggering the Eastern Mediterranean Sea. *J. Mar. Syst.* 83, 58–66. doi: 10.1016/j.jmarsys.2010.07.001

Vervatis, V. D., Sofianos, S. S., and Theocharis, A. (2011). Distribution of the thermohaline characteristics in the Aegean Sea related to water mass formation processes (2005–2006 winter surveys). *J. Geophys. Res.* 116:C09034. doi: 10.1029/2010JC006868

Wong, A. L. S., Johnson, J. M., and Owens, W. B. (2003). Delayed-mode calibration of autonomous CTD profiling float salinity data θ-S climatology. *J. Atmos. Ocean. Tech.* 20, 308–318.

Würtz, M. (2010). *Mediterranean Pelagic Habitat: Oceanographic and Biological processes, an Overview*. Málaga: IUCN – Med.

Zambianchi, E., Trani, M., and Falco, P. (2017). Lagrangian transport of marine litter in the Mediterranean Sea. *Front. Environ. Sci.* 5:5. doi: 10.3389/fenvs.2017.00005

Zodiatis, G. (1991). Water masses and deep convection in the Cretan Sea during late winter 1987. *Ann. Geophys.* 9, 367–376.

Zodiatis, G. (1992). Lens formation in the SE Ionian Sea and double diffusion. *Ann. Geophys.* 10, 935–942.

Zodiatis, G. (1993). Circulation of the Cretan Sea water masses (Eastern Mediterranean Sea). *Oceanol. Acta* 16, 107–114.

Zodiatis, G., Drakopoulos, P., Brenner, S., and Groom, S. (2005). Variability of Cyprus warm core eddy during the CYCLOPS project. *Deep Sea Res.* 52, 2897–2910. doi: 10.1016/j.dsr2.2005.08.020

Conflict of Interest: The authors declare that the research was conducted in the absence of any commercial or financial relationships that could be construed as a potential conflict of interest.

frontiers in Marine Science

ORIGINAL RESEARCH
published: 11 August 2021
doi: 10.3389/fmars.2021.657119

Seasonal Evolution of Cape Darnley Bottom Water Revealed by Mooring Measurements

Genta Mizuta[1], Yasushi Fukamachi[2,3], Daisuke Simizu[4], Yoshimasa Matsumura[5], Yujiro Kitade[6], Daisuke Hirano[2,7†], Masakazu Fujii[4,8], Yoshifumi Nogi[4,8] and Kay I. Ohshima[2,7]*

[1] Graduate School of Environmental Earth Science, Hokkaido University, Sapporo, Japan, [2] Arctic Research Center, Hokkaido University, Sapporo, Japan, [3] Global Station for Arctic Research, Global Institution for Collaborative Research and Education, Hokkaido University, Sapporo, Japan, [4] National Institute of Polar Research, Tachikawa, Japan, [5] Atmosphere and Ocean Research Institute, The University of Tokyo, Kashiwa, Japan, [6] Department of Marine Resources and Environment, Graduate School of Marine Science and Technology, Tokyo University of Marine Science and Technology, Tokyo, Japan, [7] Institute of Low Temperature Science, Hokkaido University, Sapporo, Japan, [8] Department of Polar Science, School of Multidisciplinary Sciences, Graduate University for Advanced Studies, Tachikawa, Japan

OPEN ACCESS

Edited by:
Nadia Lo Bue, National Earthquake Observatory (INGV), Italy

Reviewed by:
Pasquale Castagno, University of Naples Parthenope, Italy
Paul Spence, The University of Sydney, Australia

***Correspondence:**
Genta Mizuta
mizuta@ees.hokudai.ac.jp

†Present address:
Daisuke Hirano, National Institute of Polar Research, Tachikawa, Japan; Department of Polar Science, School of Multidisciplinary Sciences, Graduate University for Advanced Studies, Tachikawa, Japan

Specialty section:
This article was submitted to Physical Oceanography, a section of the journal Frontiers in Marine Science

Received: *22 January 2021*
Accepted: *12 July 2021*
Published: *11 August 2021*

Citation:
Mizuta G, Fukamachi Y, Simizu D, Matsumura Y, Kitade Y, Hirano D, Fujii M, Nogi Y and Ohshima KI (2021) Seasonal Evolution of Cape Darnley Bottom Water Revealed by Mooring Measurements. Front. Mar. Sci. 8:657119. doi: 10.3389/fmars.2021.657119

This study examines the seasonal evolution of Cape Darnley Bottom Water (CDBW), using the results of mooring and hydrographic measurements in the slope region off Cape Darnley in 2008–2009 and 2013–2014. Newly formed CDBW began reaching the western and nearshore part of the slope region off Cape Darnley in April, spread to the offshore and eastern part in May, and reached the easternmost part in September. The potential temperature and salinity decreased and the neutral density increased when newly formed CDBW reached mooring sites. Potential temperature-salinity properties of CDBW changed over time and location. The salinity of the source water of CDBW estimated from potential temperature-salinity diagrams started to increase at a nearshore mooring in late April, which is about 2 months after the onset of sea-ice production, and continued to increase during the ice production season. It is most probable that the accumulation of brine in the Cape Darnley polynya produces the seasonal variation of potential temperature-salinity properties of CDBW. Two types of CDBW were identified. Cold and less saline CDBW and warm and saline CDBW were present in Wild and Daly Canyons, respectively. This indicates that the salinity of the source water of CDBW increased in the westward direction. CDBW exhibited short-term variability induced by baroclinic instability.

Keywords: sea ice, seasonal evolution, mooring measurement, Cape Darnley Bottom Water, Antarctic Bottom Water

1. INTRODUCTION

Antarctic Bottom Water (AABW) is the major source of the bottom water of the world ocean. AABW spreads directly into the Atlantic Ocean and, in a modified form as the denser part of the Lower Circumpolar Deep Water (LCDW), into the Pacific and Indian Oceans, forming the lower cell of the meridional overturning circulation (Mantyla and Reid, 1983; Orsi et al., 1999). The formation of AABW enhances the exchange of heat and fresh water between the surface layer, which is exposed to the atmosphere, and the deep layer, which has a large volume and heat content, contributing to the maintenance of the global climate. Compared with the North Atlantic Deep Water, which is formed by the cooling of saline Atlantic Water in the Greenland and Nordic Seas,

AABW is characterized by low temperature and low salinity (Mantyla and Reid, 1983) because its formation is accompanied by sea-ice production (Foster and Carmack, 1976).

Antarctic Bottom Water is formed from shelf water (SW), which is characterized by the near-freezing temperature and high salinity. High sea-ice production in polynyas on the shelf is the source of SW. SW is transformed into AABW as it descends the slope and mixes with ambient water. The Weddell and Ross Seas, which have large continental embayments with major continental ice shelves, are two distinct formation sites of AABW (Jacobs et al., 1970; Foster and Carmack, 1976). A third formation site of AABW was identified off the Adélie and George V Land coast (Rintoul, 1998), where enhanced sea-ice production in the coastal polynya directly causes the formation of SW and thus AABW (Williams et al., 2010). In addition, the fourth site for AABW formation has been speculated to exist in the eastern sector of the Weddell-Enderby Basin (Meredith et al., 2000; Meijers et al., 2010). A map the of sea-ice production estimated from satellite-derived heat flux (Tamura et al., 2008) suggested that the Cape Darnley polynya (light shaded area in **Figure 1**) is the site with the second–highest production of sea ice around Antarctica after the Ross Ice Shelf polynya. Ohshima et al. (2013) conducted mooring measurements off Cape Darnley and showed that newly formed AABW descends the slope and reaches the abyss. This newly formed AABW is referred to as Cape Darnley Bottom Water (CDBW).

In addition to the Cape Darnley polynya, several polynyas with relatively high ice production are distributed on the western (lee) side of the landfast ice or glacier tongue in East Antarctica (Nihashi and Ohshima, 2015). Among them, the Vincennes Bay polynya possibly contributes to the production of the upper layer of AABW in the East Antarctic (Kitade et al., 2014). However, based on nearly 3,000 temperature and salinity profiles from autonomous floats along the East Antarctic coast between 50 and 128°E, the region off Cape Darnley appears to be the main AABW source (Wong and Riser, 2013).

The results of a numerical experiment using a nonhydrostatic ocean model showed that SW spreads along the canyons of the slope (Nakayama et al., 2014). As it descends the slope, SW forms a westward bottom-intensified current and is transformed into CDBW mixed with the overlying modified Circumpolar Deep Water (mCDW; Hirano et al., 2015). Dense water affected by CDBW is transported westward by the Slope Current along the continental slope (Wong and Riser, 2013; Aoki et al., 2020). Couldrey et al. (2013) argued that the recent southward migration of the Antarctic Circumpolar Current enhanced the mixing of CDBW with warm mCDW in the Cape Darnley region, with the warming signal of CDBW reaching the eastern Weddell Gyre. Offshore transport of CDBW may also enhance the intrusion of mCDW into the shelf region, which may enhance the melting of ice shelves (Morrison et al., 2020).

The purpose of this study is to examine the seasonal evolution and horizontal distribution of CDBW. For this purpose, we

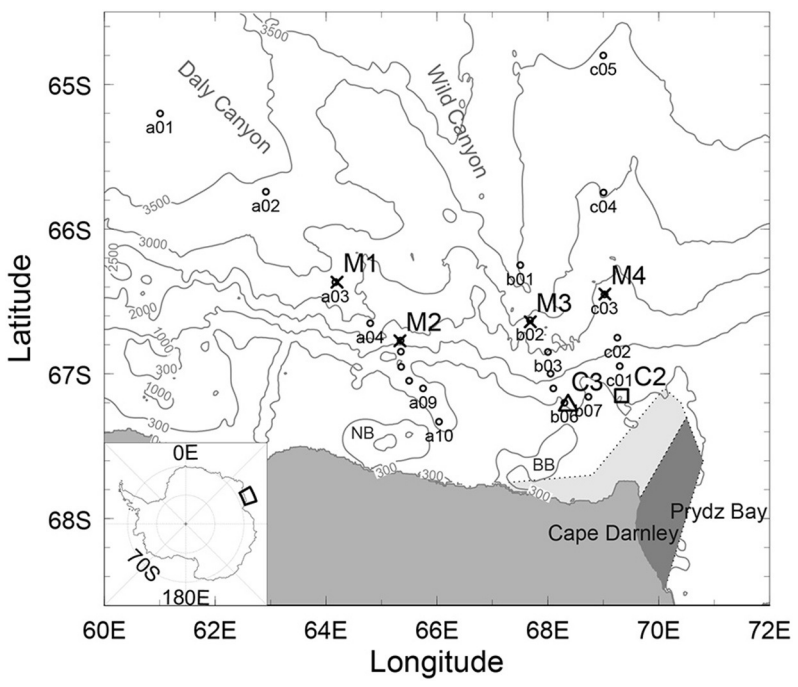

FIGURE 1 | A bathymetry map of the study area (International Bathymetric Chart of the Southern Ocean, IBCSO: Arndt et al., 2013). Locations of moorings M1–M4 and conductivity, temperature, and depth (CTD) stations are shown by crosses and circles, respectively. The Cape Darnley polynya and grounded ice are shaded by light and dark gray, respectively. Locations of moorings C2 and C3 are shown by a square and a triangle, respectively. Transects passing stations a01–a10, b01–b07, and c01–c05 are defined as transects A, B, and C, respectively. BB and NB indicate Burton and Nielsen Basins, respectively. The thick solid line in the inset map shows the location of the study area.

analyze temperature, salinity, and velocity data obtained from the mooring and hydrographic measurements off Cape Darnley. We use data obtained from four moorings deployed in the slope region in 2008–2009 and two moorings deployed in the shelf region in 2013–2014 and hydrographic data obtained in 2009. Ohshima et al. (2013) provided the first evidence of the formation of CDBW, using mooring data collected in 2008–2009. They mostly investigated newly formed CDBW descending Wild Canyon, which is located just off the Cape Darnley polynya. Although it was also suggested that part of CDBW descends down Daly Canyon, which is located to the west of the Wild Canyon, the characteristics of CDBW in Daly Canyon was not examined. They also did not investigate the seasonal variation of the characteristics of CDBW. In this study, we examine the spatial variation of the characteristics of CDBW, combining results of the mooring measurements with hydrographic data obtained in broad regions including both Wild and Daly Canyons. We also examine the seasonal variation of the characteristics of CDBW. It is shown that potential temperature-salinity properties of CDBW changed with the season, because the salinity of the source water of CDBW increased with time. Thus, we examine the mechanism of the seasonal variation of potential temperature-salinity properties of CDBW, using sea ice production rate in the Cape Darnley polynya and salinity data obtained by moorings on the shelf. When CDBW arrived at mooring sites, a clear periodic variability of velocity, temperature, and salinity with the period of 3–5 days has been observed (Ohshima et al., 2013). We also examine the physical mechanism of this variability. This study is organized as follows. In section 2, we describe the mooring and hydrographic measurements. Results of these measurements are presented in section 3. In this section, we examine the seasonal evolution, horizontal distribution, and the short-term variability of CDBW. Section 4 provides a study summary and conclusions.

2. DATA

Figure 1 shows the locations of the mooring sites and hydrographic stations. Four moorings, M1–M4, were deployed in February 2008–January 2009 off Cape Darnley in an extensive Japanese mooring program conducted as a part of the International Polar Year (Ohshima et al., 2013). The Cape Darnley polynya is located on the western side of the grounded iceberg tongue, which is located between 69 and 71°E. Four moorings were deployed in the north and northwest regions of the Cape Darnley polynya. Moorings M2 (bottom depth: 1,437 m) and M4 (depth: 1,824 m) were located in the upper part of the slope, whereas moorings M1 (depth: 2,923 m) and M3 (depth: 2,608 m) were located in the deeper part of Daly and Wild Canyons, respectively. To supplement results obtained from these moorings, we also analyzed temperature and salinity data obtained at two additional moorings, C2 (depth: 368 m) and C3 (depth: 355 m), which were deployed near the shelf break in 2013–2014 (**Figure 1**). The moorings were equipped with conductivity-temperature sensors (CT sensors; Sea-Bird SBE-37 MicroCAT), downward-looking acoustic Doppler current profilers (ADCP; Teledyne RD Instruments WorkHorse Sentinel 300), and current meters (Union Engineering RU-1, with the exception of Aanderaa RCM7 being used at mooring C3). These instruments were deployed within 300 m from the bottom (**Table 1**).

Sampling intervals of the moored instruments were 2 h for the current meters, 1 h for the ADCPs, and 5 or 10 min for the CT sensors. We applied a Godin filter to salinity and temperature data and subsampled the filtered data at 1 h intervals. Then, we removed the tidal component from all temperature, salinity, and velocity data using a Lanczos-cosine filter (Lancz7) with a cutoff period of 34.29 h (Emery and Thomson, 2001). In contrast to the Ross Sea, where strong tides are observed (Whitworth and Orsi, 2006), the tidal current was weaker than 5 cm s^{-1} at our mooring sites. Hence, we expect that the tidal energy included in the filtered data is negligible, even though a small amount of the energy of the O1 tidal constituent tends to be passed through a Lancz7 filter.

Hydrographic measurements were carried out along three transects when moorings M1–M4 were recovered in January 2009 (**Figure 1**). We defined transects A, B, and C as transects passing stations a01–a10, b01–b07, and c01–c05, respectively. The hydrographic data were obtained by TR/V Umitaka-Maru using a conductivity, temperature, and depth profiler (CTD; Sea-Bird SBE911 plus with SBE43). Conductivity (and dissolved oxygen) data were calibrated by bottle samples. We calculated neutral density, γ_n, using the method of Jackett and McDougall (1997) for both mooring and CTD measurements; however, we found that γ_n included a large uncertainty on the shelf and the upper part of the slope, as described by Williams et al. (2010). Hence, we used the potential density referenced to 2,500 dbar, σ_{25}, to compare the densities obtained at all mooring sites.

As a measure of the mass of brine rejected in the Cape Darnley polynya, we used sea-ice production estimated by the

TABLE 1 | Mooring location, bottom depth, period, and instrument.

Site	Longitude, Latitude	Depth (m)	Period	Instrument (distance)
M1	64–11.894E, 66–22.002S	2,923	Feb/16/2008–Jan/22/2009	CM (285 m) ADCP (102 m) CT (23, 51, 174, 284 m)
M2	65–19.909E, 66–46.328S	1,437	Feb/16/2008–Jan/22/2009	CM (259 m) ADCP (102 m) CT (25, 52, 255 m)
M3	67–41.016E, 66–38.444S	2,608	Feb/17/2008–Jan/23/2009	CM (20, 226 m) CT (26, 55, 105, 224 m)
M4	69–01.717E, 66–26.958S	1,824	Feb/17/2008–Jan/24/2009	CM (306 m) CT (26, 105, 304 m)
C2	69–19.79E, 67–09.06S	368	Feb/25/2013–Feb/25/2014	ADCP (293 m) CT (35, 300 m)
C3	68–21.94E, 67–13.04S	355	Feb/25/2013–Feb/23/2014	CM (31, 189 m) CT (45, 183 m)

Acronyms CM, ADCP, and CT represent current meter, acoustic Doppler current profiler, and conductivity-temperature sensors, respectively. Numbers in parentheses in the last column indicate the distance of the instrument from the bottom.

ice thickness, which was derived from the Advanced Microwave Scanning Radiometer-Earth Observing System (AMSR-E) data and a heat flux calculation (Nakata et al., 2019, 2021). We used a time series of sea-ice production in the Cape Darnley polynya, the domain of which is shown in Figure 1 of Tamura et al. (2008). In addition to the International Bathymetric Chart of the Southern Ocean (IBCSO: Arndt et al., 2013), we used bathymetry data obtained by a shipboard multi-narrow beam echo sounder (MBES; L-3 Communications ELAC Nautik SeaBeam3020) to examine the precise bathymetry around mooring M3. The bathymetry data were constructed from MBES data obtained by R/V Hakuho-Maru in 2008, 2016, and 2019 and Icebreaker Shirease in 2009–2013. The seawater sound velocity used in MBES was corrected by real-time data obtained by the surface water velocity meter and by temperature and salinity profiles obtained by CTD and expendable CTD.

3. RESULTS

Figure 2 shows potential temperature-salinity (θ-S) diagrams for all CTD stations. The black, blue, and red lines indicate data in the offshore, slope, and shelf regions, which are defined as the regions where the bottom depth is greater than 3,000 m, between 1,000 and 3,000 m, and smaller than 1,000 m, respectively. Using this diagram, we can identify major water masses distributed off Cape Darnley, following the definitions provided by Whitworth et al. (1998). Water characterized by a near-freezing temperature and salinity higher than 34.5 was present in the shelf region. This water corresponds to SW. SW was present at stations a08, a09, and a10, which were located in a small depression on the shelf. In the offshore and slope regions, water denser than $\gamma_n = 28.27$ kg m^{-3} was present near the bottom. This water corresponds to AABW. In some studies, water denser than $\gamma_n = 28.27$ kg m^{-3} and warmer than the freezing temperature is divided into modified Shelf Water (mSW) and AABW, which are present near the shelf and in the offshore region, respectively (Orsi and Wiederwohl, 2009; Wong and Riser, 2013); however, we do not divide AABW into mSW and AABW, because many mooring sites and CTD stations were located in the slope region, in which the boundary between mSW and AABW is not clear enough. Warm deep water existing above AABW is Circumpolar Deep Water (CDW; $28.03 < \gamma_n < 28.27$ kg m^{-3}), whereas cold surface water characterized by the temperature minium is Antarctic Surface Water (AASW; $\gamma_n < 28.03$ kg m^{-3}). As shown by blue and red lines, CDW was mixed with AASW and transformed into mCDW in the slope and shelf regions.

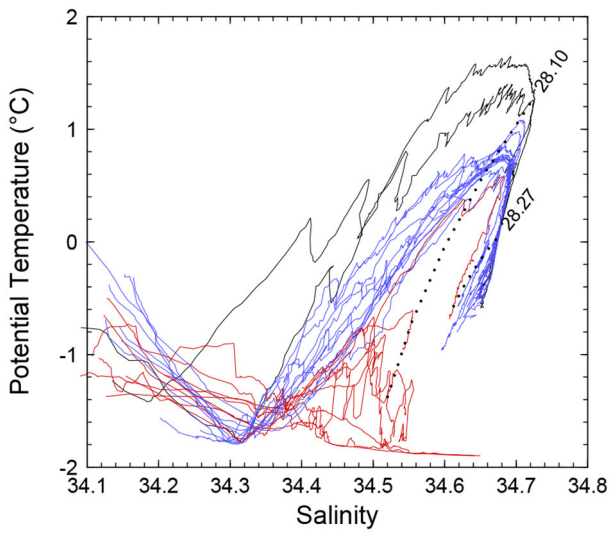

FIGURE 2 | θ-S diagrams for all CTD stations. Black, blue, and red lines indicate data in the offshore, slope, and shelf regions. The potential temperature and salinity at depths shallower than 40 m are not shown. The dotted lines indicate the contours of γ_n.

Figure 3 shows the vertical section of potential temperature and salinity on transect B. Cold and less saline water was present along the bottom of the slope. The gray dashed lines indicate the $\gamma_n = 28.10$ and 28.27 kg m^{-3} neutral surfaces. Because γ_n exceeded 28.27 kg m^{-3}, the cold and less saline water on the slope is CDBW. The $\gamma_n = 28.27$ kg m^{-3} neutral surface shoaled toward the coast, indicating that CDBW was accompanied by a westward current that intensified near the bottom (Hirano et al., 2015). The $\gamma_n = 28.10$ kg m^{-3} neutral surface was close to the maximum local temperature at offshore stations. Spreading along this neutral surface, CDW can mix with AASW near the shelf, and a front was formed between the two at the shelf break (**Figure 3A**). This front corresponds to the Slope Front (Whitworth et al., 1998).

3.1. General Properties of CDBW

In this section, we examine the general properties of temperature, salinity, and velocity of CDBW obtained by mooring measurements. **Figure 4** shows the mean flow and standard deviation ellipses at two depths at moorings M1–M4. Here, the direction of the isobath at each mooring site is indicated by the long blue bars. The mean flow was directed westward at mooring M2, which was consistent with the direction of the Antarctic Slope Current (Meijers et al., 2010). The Antarctic Slope Current was also present at mooring M4, although the mean flow was weaker than the standard deviation there. Standard deviation ellipses were polarized (anisotropic) at moorings M2 and M3. Both the mean flow and major axis of the standard deviation ellipse were directed along the isobath at mooring M2, suggesting that the direction of the flow was restricted by bottom topography (**Figure 4A**). Such features were also present at mooring M3 for the bathymetry based on MBES observation (**Figure 4B**). As suggested in **Figure 3**, CDBW was accompanied by a bottom intensified current. The mean speed at mooring M3 increased from 7 cm s^{-1} at 226 m from the bottom to 14 cm s^{-1} at 20 m from the bottom, which was consistent with a bottom intensified current driven by CDBW.

Figure 5 shows the time series of the along-isobath and across-isobath velocities for the deepest velocity data at moorings M1–M4. The along-isobath velocity increased during the period from May to November, especially at moorings M2 and M3. The temporal variability of velocity was also amplified in the same

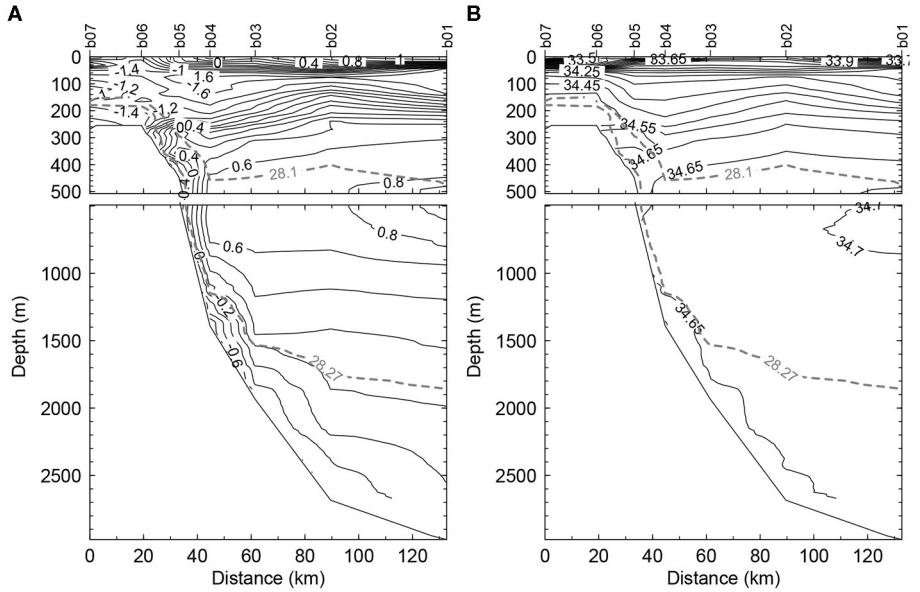

FIGURE 3 | Contours of **(A)** potential temperature and **(B)** salinity on transect B. The gray dashed lines indicate the contours of γ_n.

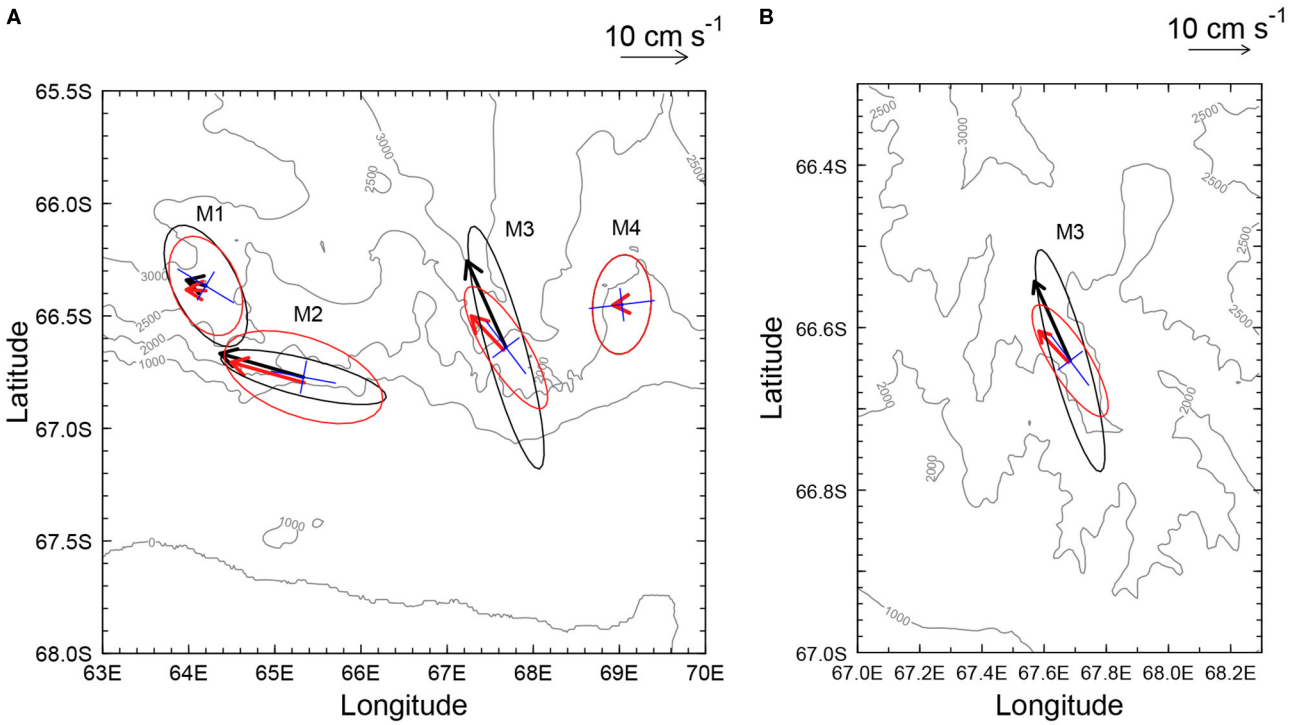

FIGURE 4 | Vectors of the mean velocity and standard deviation ellipses in **(A)** the entire mooring region and **(B)** the region around mooring M3. The black vectors and ellipses indicate the mean velocity and standard deviation ellipses for the deepest velocity data. The red vectors and ellipses indicate the mean velocity and standard deviation ellipses for the shallowest velocity data. Contours in **(A,B)** indicate the isobath based on IBCSO and a shipboard MBES observation, respectively. The bathymetry was not obtained by multi-narrow beam echo sounder (MBES) in part of the region in **(B)**. In that region, bathymetry was supplemented by the global relief model ETOPO1 (Amante and Eakins, 2009). The long and short blue bars indicate the direction parallel and normal to the isobath, respectively. The direction of the isobath at mooring M3 and other mooring sites was estimated from the bathymetry data based on shipboard MBES observation and IBCSO, respectively.

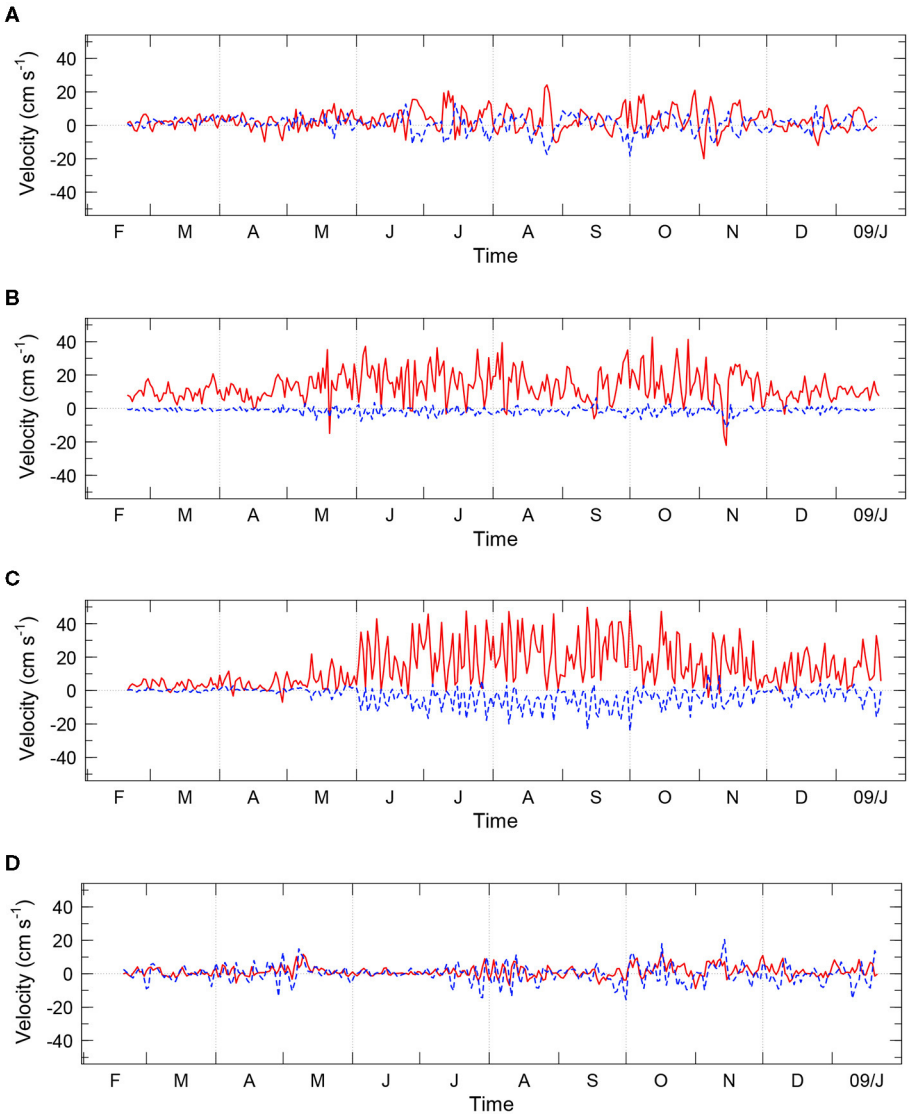

FIGURE 5 | Time series of the along-isobath velocity, u', (red line) and across-isobath velocity, v', (blue dashed line) for the deepest velocity data at mooring **(A)** M1, **(B)** M2, **(C)** M3, and **(D)** M4.

period. The along-isobath velocity at mooring M3 oscillated almost regularly at a period of 3–5 days. We will examine the mechanism of this variability in section 3.4.

Figure 6 shows the time series of potential temperature, salinity, and γ_n near the bottom at each mooring site. Potential temperature and salinity started to decrease in April at mooring M2, in May–June at moorings M1 and M3, and in September at mooring M4. With the decrease of potential temperature and salinity, γ_n increased. Since γ_n exceeded 28.27 kg m^{-3}, except for April–May at mooring M2 where the uncertainty of γ_n was large, water observed at mooring sites mostly corresponds to AABW or CDBW. Thus, cold and less saline water observed at moorings M1–M4 corresponds to the newly formed CDBW, whereas warmer water corresponds to other AABW. At moorings M2 and M3, the current speed increased along with the arrival of the newly formed CDBW (**Figure 5**). The decrease in potential temperature and salinity was large at moorings M2 and M4 in the upper part of the slope, compared with moorings M1 and M3 in the deeper part of the slope, indicating that CDBW is modified by the mixing with ambient water as it descends the slope.

Potential temperature decreased first in April at mooring M2, which was located in the upper part of the slope; it subsequently decreased in May-June at moorings M1 and M3, which were located in the deeper part of the slope, and in September at mooring M4, which was the easternmost mooring. Thus, the potential temperature decreased earlier at moorings, which were located in the western and shallower regions. According to the laboratory and numerical experiments, when dense water forms on the shelf, geostrophic adjustment finishes shortly

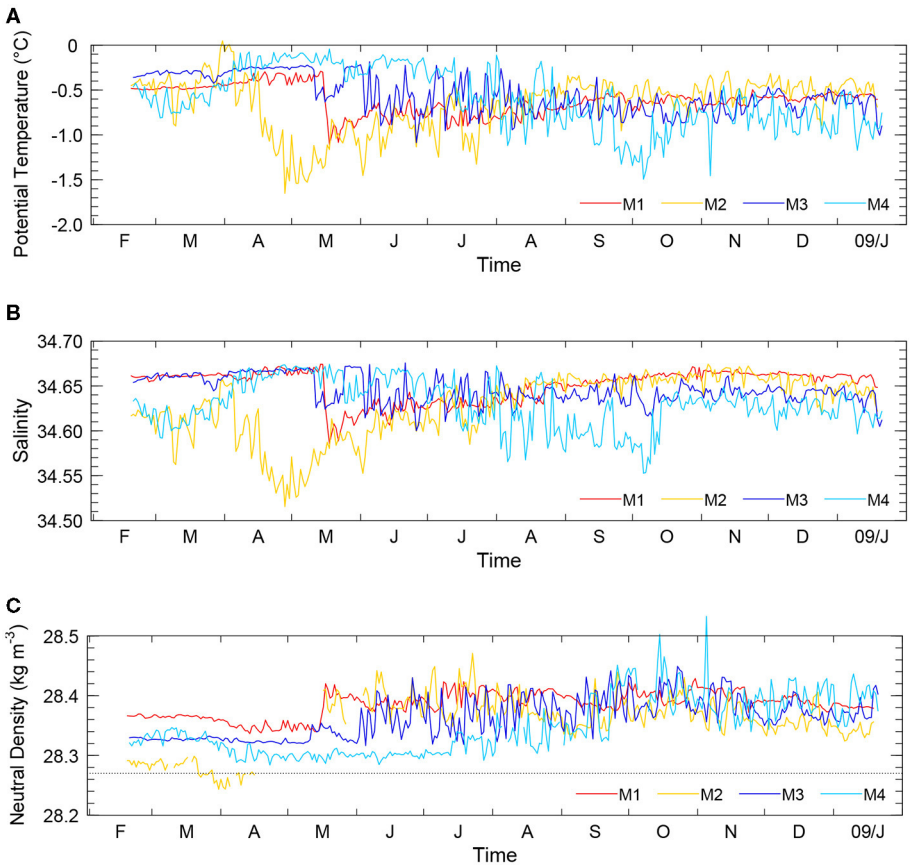

FIGURE 6 | Time series of **(A)** potential temperature, **(B)** salinity, **(C)** and γ_n obtained by the deepest conductivity-temperature (CT) sensors at moorings M1 (red), M2 (orange), M3 (blue), and M4 (light blue). In **(C)**, lines are not drawn in the period when the uncertainty of γ_n exceeds 0.03 kg m^{-3}. The horizontal dotted line in **(C)** indicates γ_n = 28.27 kg m^{-3}.

after the formation, and the dense water flows westward along the isobath in the southern hemisphere. Afterward, the dense water slowly spreads in the offshore direction in time and the downstream region in space (Chapman and Gawarkiewicz, 1995; Baines and Condie, 1998). The difference in the timing of the temperature decrease between moorings M1–M4 is consistent with experimental results by Chapman and Gawarkiewicz (1995) and Baines and Condie (1998). Because mooring M4 was located about 100 km north of the Cape Darnley polynya (**Figure 1**), dense water observed at this mooring may correspond to the newly formed AABW from Prydz Bay (Williams et al., 2016), which is located east of Cape Darnley. Williams et al. (2016) showed that newly formed AABW starts to be exported from Prydz Bay in September, which approximately coincides with the timing of temperature decrease at mooring M4. Hence, Prydz Bay may be the source of water observed at mooring M4. On the other hand, as we will show later, the characteristics of water observed at moorings M3 and M4 are similar to each other, except that the former is modified more strongly by the mixing with ambient water. Thus, both the Cape Darnley region and Prydz Bay are the possible source of newly formed AABW observed at mooring M4.

To examine the seasonal evolution of newly formed CDBW, we divided the mooring period evenly into four parts. We defined periods February 16–May 12, May 12–August 6, August 6–October 31, and October 31–January 25, 2009, as periods P1, P2, P3, and P4, respectively. The length of each period is 86 days. **Figure 7** shows the vertical distribution of mean σ_{25} in periods P1–P4 at each mooring. At moorings M1–M3, σ_{25} near the bottom increased between periods P1 and P2, whereas σ_{25} increased between periods P2 and P3 at mooring M4. This increase in σ_{25} indicates the arrival of newly formed CDBW, as it was shown in **Figure 6**. With the arrival of newly formed CDBW, σ_{25} increased by 0.02–0.04 kg m^{-3} at all depths except for the uppermost CT sensors at mooring M4. Newly formed CDBW was distributed within 100–300 m or more from the bottom. σ_{25} also increased near the bottom at CTD stations near moorings M3 and M4 (solid lines in **Figure 7**), indicating that newly formed CDBW was present at these CTD stations.

3.2. The Seasonal Evolution of CDBW and Its Source Water

In this section, we examine more precisely the seasonal evolution of the characteristics of CDBW. **Figure 8** shows θ-S

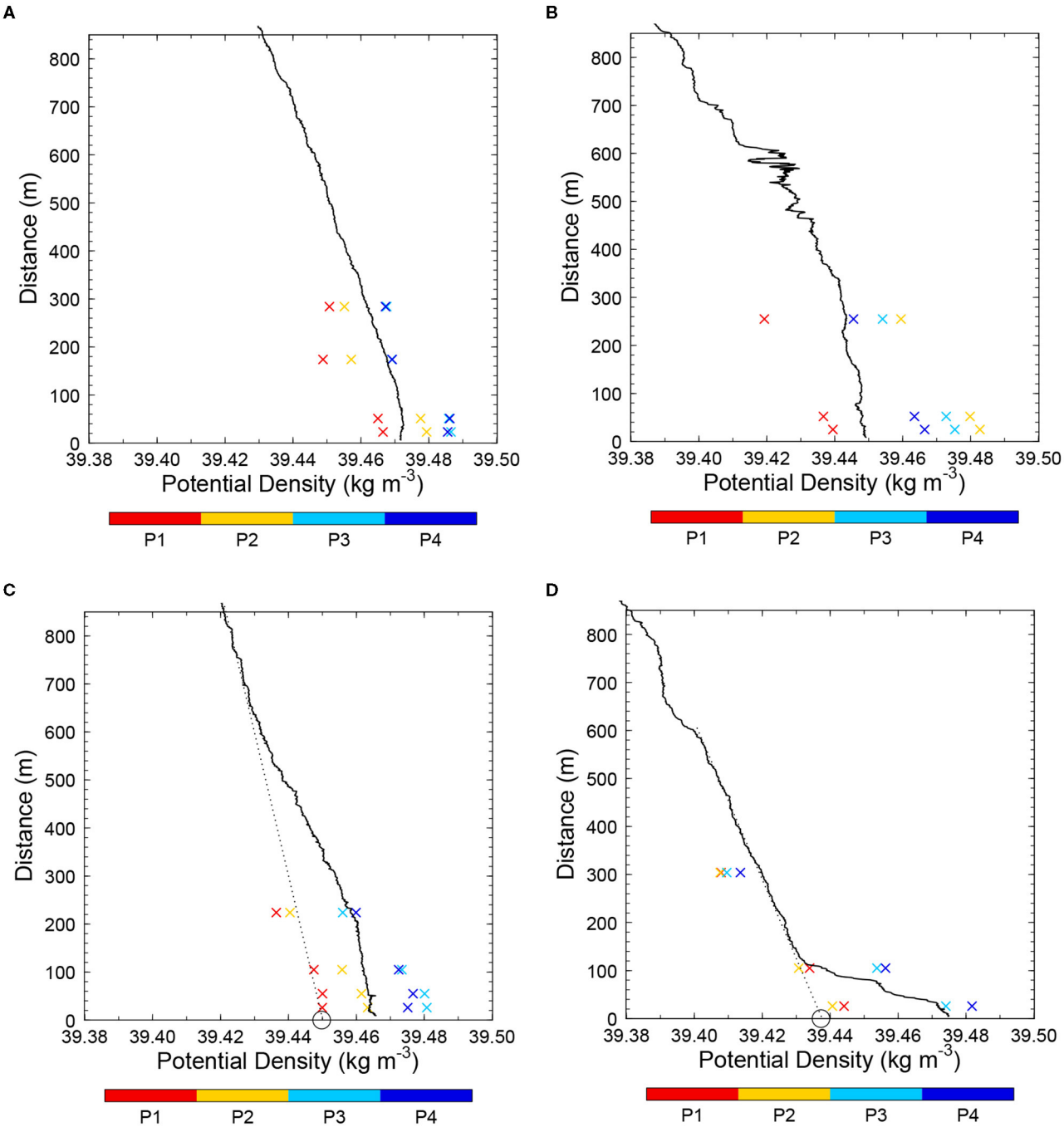

FIGURE 7 | Seasonal variability of the vertical distribution of σ_{25} at mooring **(A)** M1, **(B)** M2, **(C)** M3, and **(D)** M4. The vertical axis indicates the distance from the bottom. The red, orange, light blue, and blue crosses indicate mean σ_{25} in periods P1, P2, P3, and P4, respectively. The solid lines in **(A–D)** indicate the vertical distribution of σ_{25} at CTD stations, a03, a05, b02, and c03, respectively. The circles and dotted lines in **(C,D)** indicate values of σ_{Ab} and fitting lines used in section 3, respectively. The details are discussed in the text.

diagrams for the deepest CT sensors at each mooring. The plus signs are plotted in 1 day interval, and the color of the plus signs indicates periods P1–P4. In periods P1 and P2, data were scattered along a straight line for each mooring except for period P1 at mooring M1, indicating the mixing of two water masses. That is, it is suggested that CDBW observed at the mooring sites were formed by the mixing between cold and less saline water and warm and saline water. For the rest of this study, this line is referred to as the mixing line. At mooring M2, even though data were scattered along two different mixing lines in periods

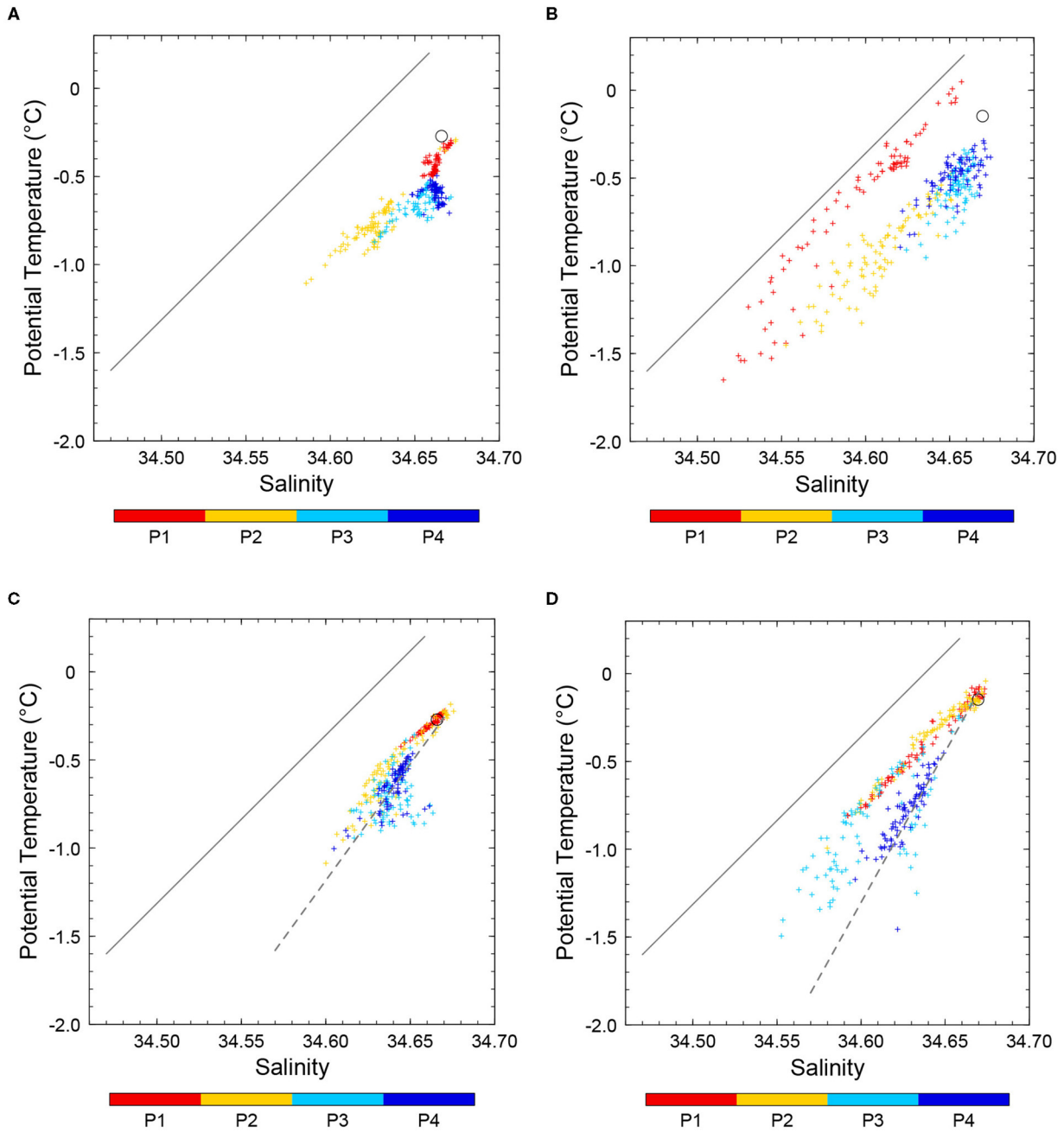

FIGURE 8 | θ-S diagrams for the deepest CT sensors at mooring **(A)** M1, **(B)** M2, **(C)** M3, and **(D)** M4. The red, orange, light blue, and blue pluses indicate salinity and potential temperature in periods P1, P2, P3, and P4, respectively. The gray lines indicate the mean slope of the mixing line in periods P1 and P2. The gray dashed lines in **(C,D)** indicate the mixing line in period P4 at moorings M3 and M4, respectively. The circles indicate the point, $(S, \theta) = (S_{Ab}, \theta_{Ab})$, which is used in the Results Section. The details are discussed in the text.

P1 and P2, the slopes of the mixing lines were similar to each other. The slopes of the mixing lines at the other three moorings were also similar to those at mooring M2. We determined the slope of the mixing line in each period for all moorings, fitting salinity and potential temperature by a linear function. The principal components regression was used for the fitting. Because the variance of salinity is much smaller than that of potential temperature, we normalized salinity and potential temperature with their standard deviation in the entire mooring period, when we calculated the regression. The slope of the mixing lines and the proportion of the variance explained by the first principal component are listed in **Supplementary Table 1**. The slopes of the mixing lines in periods P1 and P2 at moorings M2–M4 and in period P2 at mooring M1 were 8–11 and quite close to each

other. More than 95% of the variance was explained by the first principal component for these mixing lines, indicating that data fit well to these mixing lines. Gray lines in **Figures 8A–D** indicate the mean slope of these mixing lines. In periods P1 and P2, data at all moorings were scattered along a line that is nearly parallel to this gray line except for period P1 at mooring M1, indicating that mixing lines at all moorings were nearly parallel to each other in these periods. This was also the case for mixing lines at shallower CT sensors (not shown).

At moorings M3 and M4, which were located in and upstream of Wild Canyon, respectively, data were scattered along another mixing line in periods P3 and P4. For example, gray dashed lines in **Figures 8C,D** indicate the mixing line in period P4 at these moorings. Since the slope of the mixing line was larger than that in periods P1 and P2, it is suggested that CDBW in periods P3 and P4 consisted of cold water with a salinity that was higher than that in periods P1 and P2. In contrast, in periods P3 and P4, CDBW observed at mooring M1, which was located in Daly Canyon, was warmer and saltier than that at moorings M3 and M4. Since potential temperature and salinity data of this warm and saline CDBW were not located along the mixing line obtained at moorings M3 and M4, the source of CDBW at the mooring M1 was likely different from that at moorings M3 and M4. Relatively warm and saline CDBW was also observed at the mooring M2, which was located upstream of Daly Canyon. Thus, cold and less saline CDBW and warm and saline CDBW were present near Wild and Daly Canyons, respectively.

Using θ-S diagrams shown in **Figure 8**, we estimate the salinity of source water of CDBW and examine the mechanism of the temporal and spatial variation of the characteristics of CDBW shown in **Figure 8**. As suggested in **Figure 8**, CDBW is formed by the mixing of cold and less saline water and warm and saline water. We assume that the former and the latter correspond to SW, which is the source water of CDBW, and ambient water, respectively. Then, the salinity and potential temperature of CDBW obtained by CT sensors are expressed as

$$S_C = r_{SW} S_{SW} + (1 - r_{SW}) S_A \tag{1}$$

$$\theta_C = r_{SW} T_f + (1 - r_{SW}) \theta_A \tag{2}$$

where S_C, S_{SW}, and S_A are salinity of CDBW, SW, and ambient water, respectively, θ_C and θ_A are the potential temperature of CDBW and ambient water, respectively, T_f is the freezing tempetature, and r_{SW} is the mixing ratio of SW. In Equation (2), we assumed that potential temperature of SW is T_f. Equations 1 and 2 represent the mixing line. If we know S_A and θ_A, we can calculate S_{SW} and r_{SW} from S_C and θ_C using these equations.

To obtain S_A and θ_A, we examine the vertical distribution of the potential temperature and salinity observed at all CTD stations (**Supplementary Figure 1**). At station c05, which was the deepest and easternmost station, the newly formed CDBW was absent, except for the thin layer near the bottom (**Supplementary Figures 1E,F**). Thus, we assume that S_A and θ_A are salinity and potential temperature at station c05. Thick orange lines in **Figures 9A,B** indicate a θ-S curve for S_A and θ_A. We can express this curve in a functional form as follows:

$$\theta_A = f(S_A)\,. \tag{3}$$

The point $(S, \theta) = (S_A, \theta_A)$ is located on this curve.

We assume that ambient water spreads along isopycnals and that SW is mixed with ambient water as it is transported from the shelf to the mooring sites. Since CTD station c05 is located in the deep region, the deeper part of the water at CTD station c05 cannot reach to the mooring sites. We define S_{Ab}, θ_{Ab}, and σ_{Ab} as salinity, potential temperature, and σ_{25} of the most dense ambient water that can reach to each mooring site, respectively. The point P in **Figures 9A,B** indicate the position of $(S, \theta) = (S_{Ab}, \theta_{Ab})$ at moorings M2 and M4, respectively. SW cannot mix with ambient water below the point P. We will describe how S_{Ab}, θ_{Ab}, and σ_{Ab} were determined later in this section.

As shown in **Figure 8**, the slope of the mixing line was approximately constant in periods P1 and P2, whereas the slope of the mixing line in periods P3 and P4 was larger than that in periods P1 and P2 at moorings M3 and M4. Thus, we estimate S_{SW} and θ_{SW} by combining two different methods. The solid line in **Figures 9A,B** indicates a line passing through the point P. The slope of this line is the same as that of the gray line in **Figure 8**, that is, the mean slope of mixing lines at all moorings in periods P1 and P2. We estimate S_{SW} and r_{SW} of CDBW located in the regions above and below this line as follows. In both regions, ambient water that is mixed with SW corresponds to AABW or the deep part of CDW.

- When the point $(S, \theta) = (S_C, \theta_C)$, which indicates S and θ of CDBW, is located above the solid line (**Figure 9A**), we assume that the mixing line is parallel to this line for simplicity, based on results shown in **Figure 8**. That is,

$$s = \frac{\theta_C - \theta_A}{S_C - S_A} \tag{4}$$

  where s is the slope of the solid line. Then, we can determine S_{SW} and r_{SW}, using Equations (1–4). For example, when the point (S_C, θ_C) is located at point a (open triangle) in **Figure 9A**, the gray line, which is parallel to the (black) solid line and passes through point a, corresponds to the mixing line for this CDBW. Then, point b (solid triangle), which is the crossing of the mixing line and freezing line, $\theta = T_f$ (long dashed line), corresponds to $(S, \theta) = (S_{SW}, T_f)$. Similarly, point c (gray triangle), which is the crossing of the mixing line and the thick orange line, corresponds to $(S, \theta) = (S_A, \theta_A)$.

  If point a is located below the solid line, point c is located below point P, which corresponds to $(S, \theta) = (S_{Ab}, \theta_{Ab})$ (even if such point c exists). This means that σ_{25} of ambient water exceeds σ_{Ab} and contradicts the assumption. Thus, we can apply the method described here only when the point (S_C, θ_C) is located above the solid line.
- When the point (S_C, θ_C) is located below the solid line (**Figure 9B**), we simply assume the following:

$$S_A = S_{Ab} \quad \text{and} \quad \theta_A = \theta_{Ab}\,. \tag{5}$$

  Hence, the point P corresponds to the point $(S, \theta) = (S_A, \theta_A)$. Then, we can determine S_{SW} and r_{SW}, substituting Equation 5 to Equations 1 and 2. For example, when the point (S_C, θ_C) is located at point d (open square) in **Figure 9B**, the gray dashed line, which passes through points d and P, corresponds to the

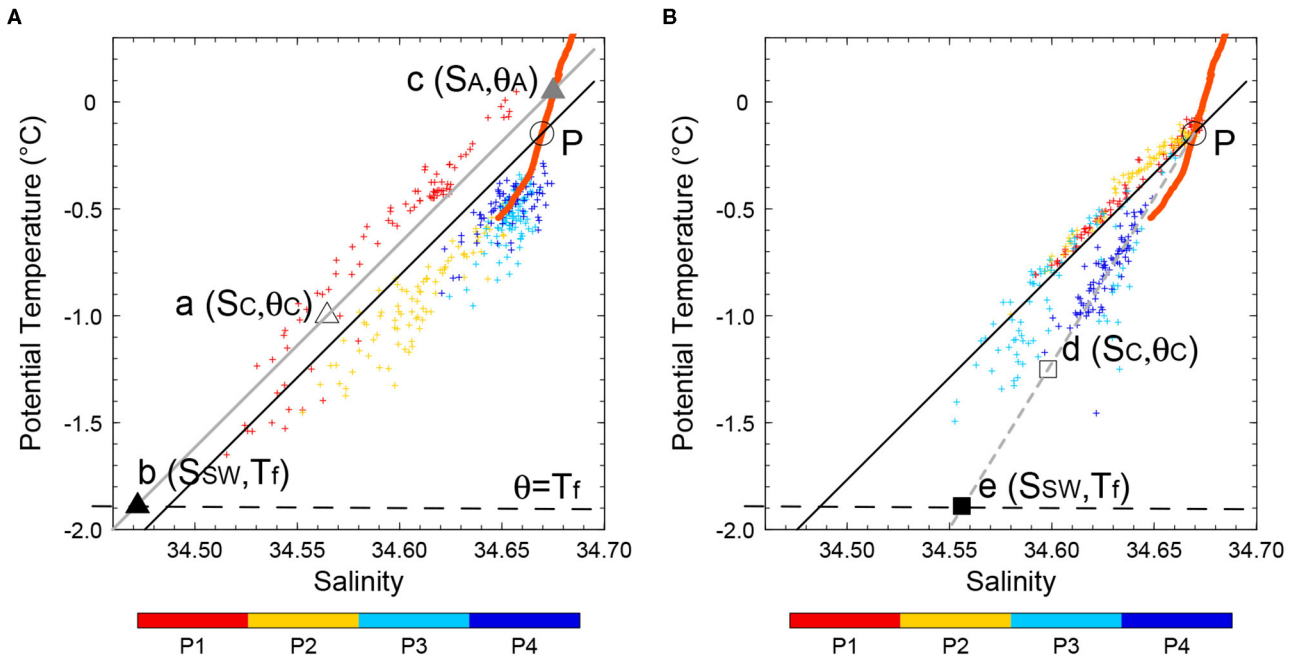

FIGURE 9 | Schematic showing how to determine mixing lines, S_{SW}, S_A, and θ_A. The solid line indicates a line passing through the point P (circle). The thick orange line indicates a θ-S curve for CTD station c05. The long dashed line indicates the freezing line, $\theta = T_f$. The gray line in **(A)** indicates the mixing line for CDBW located at point *a* (triangle). This CDBW is formed by the mixing of SW located at point *b* (black triangle) with ambient water located at point *c* (gray triangle). The dashed gray line in **(B)** indicates the mixing line for CDBW located at point *d* (square). This CDBW is formed by the mixing of SW located at point *e* (solid square) with ambient water located at point P. As in **Figure 8B**, the pluses with colors in **(A,B)** indicate (S, θ) data obtained by the deepest CT sensor at moorings M2 and M4, respectively. The details are discussed in the text.

mixing line for this CDBW. The slope of the mixing line is larger than the solid line, which is consistent with the results shown in **Figure 8**. Then, point *e* (solid square), which is the crossing of the mixing line and the freezing line, corresponds to $(S, \theta) = (S_{SW}, T_f)$.

When (S_C, θ_C) is very close to point P, the value of S_{SW} is sensitive to a small change in S_C and θ_C. Thus, we did not use results when $r_{SW} < 0.05$.

We determined σ_{Ab} from the vertical distribution of σ_{25} at CTD stations b02 and c03, which were located near moorings M3 and M4, respectively (**Figures 7C,D**). At these stations, σ_{25} increased due to the newly formed CDBW near the bottom. Dotted lines in **Figures 7C,D** indicate the line fitted to σ_{25} in the layer above the newly formed CDBW. We obtained these lines fitting σ_{25} within 600–1,000 m and 100–500 m from the bottom by the least square method for CTD stations b02 and c03, respectively. These lines approximately represent the vertical distribution of σ_{25} that is not affected by CDBW. Then, we extrapolated these lines and defined σ_{Ab} as the value of σ_{25} extrapolated to the bottom (circles in **Figures 7C,D**). Then, we define S_{Ab} and θ_{Ab} as values of S_A and θ_A on the isopycnal surface of $\sigma_{25} = \sigma_{Ab}$ at CTD station c05. The layers occupied by CDBW and other AABW were difficult to discriminate at moorings M1 and M2 (**Figures 7A,B**). Hence, we used S_{Ab} obtained at moorings M3 and M4 for moorings M1 and M2, respectively, because bottom depths at moorings M3 and M1 and those at moorings M4 and M2 were similar to each other. The position of (S_{Ab}, θ_{Ab}) at each mooring site is indicated by circles in **Figure 8**. We can verify that at moorings M3 and M4, the circles and (θ, S) data in periods P3 and P4 were approximately aligned on the same line. To examine how strongly the results of S_{SW} and r_{SW} depend on the value of S_{Ab} (and θ_{Ab}), we changed the value of S_{Ab}. Isopycnal surfaces $\sigma_{25} = \sigma_{Ab}$ for moorings M3 and M4 were located at depths of 2,860 and 2,424 m at CTD station c05, respectively. We substituted values of S and θ at depths 500 m shallower than these depths to S_{Ab} and θ_{Ab}, respectively. We also substituted values of S and θ just above the thin layer of CDBW near the bottom to S_{Ab} and θ_{Ab}, respectively. However, the change in S_{SW} and r_{SW} was <0.02 and 0.1, respectively. Thus, results of S_{SW} and r_{SW} do not strongly depend on the value of S_{Ab} (and θ_{Ab}).

Figures 10A,B show the time series of S_{SW} and r_{SW}, respectively. In some period in April–June, S_{SW} and r_{SW} are not shown because r_{SW} was <0.05. The salinity of source water of CDBW, S_{SW}, at mooring M1 was similar to that at mooring M2 in May–November, indicating that CDBW at moorings M1 and M2 originated from the same source. The source of CDBW at moorings M3 and M4 was less saline compared with that of CDBW at moorings M1 and M2, corresponding to lower salinity at these moorings (**Figure 6B**). The mixing ratio, r_{SW}, was higher at moorings M2 and M4, which were located in the upper part of the slope, compared with that at moorings M1

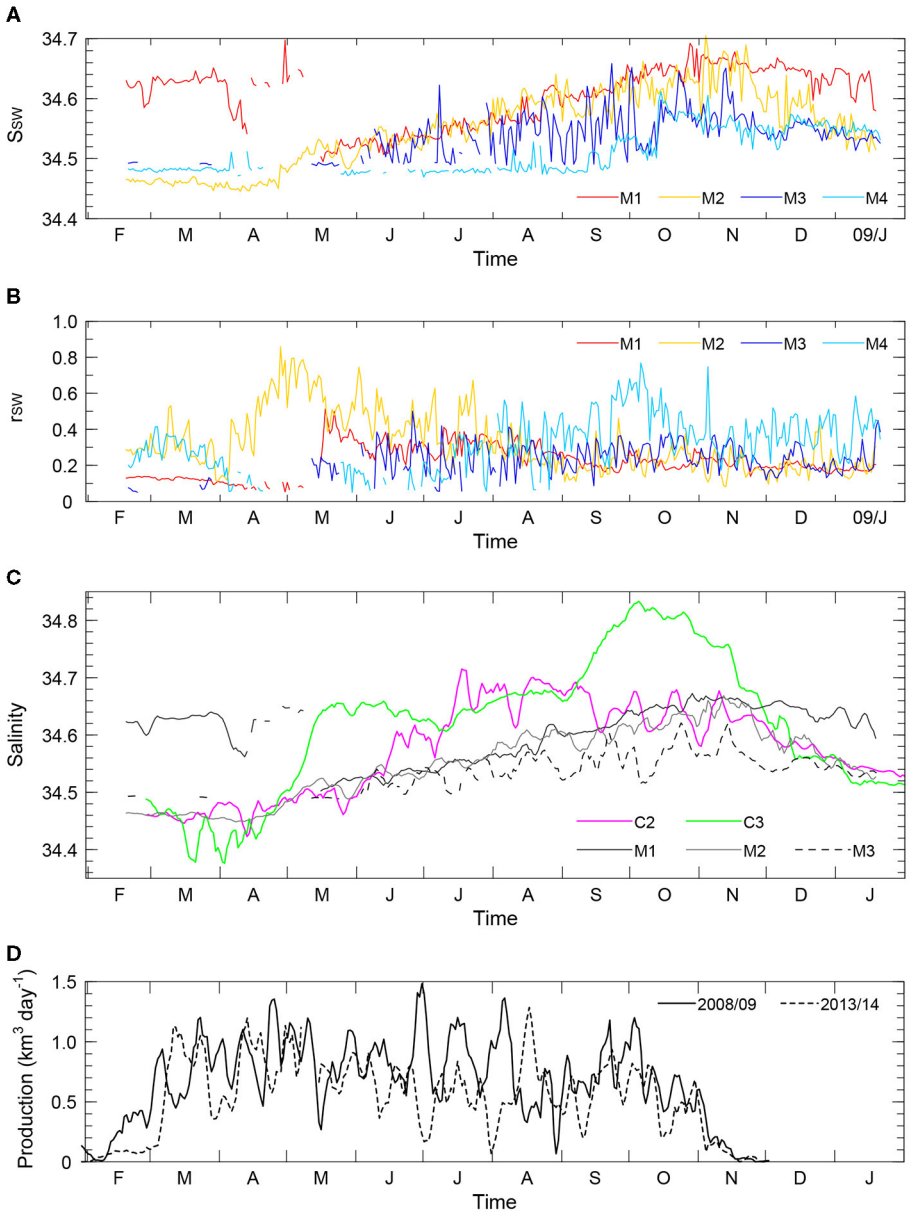

FIGURE 10 | (A,B) Time series of **(A)** S_{SW} and **(B)** r_{SW} for the deepest CT sensors at moorings M1 (red), M2 (orange), M3 (blue), and M4 (light blue). **(C)** Time series of salinity at moorings C2 (magenta) and C3 (green). The solid, gray, and dashed lines in **(C)** indicate S_{SW} at moorings M1, M2, and M3, respectively. **(D)** Time series of sea-ice production in the Cape Darnley polynya in 2008–2009 (solid line) and 2013–2014 (dashed line). A 5 day running mean is taken for data in **(C,D)**. The lines are not drawn for S_{SW} and r_{SW} in the period of $r_{SW} < 0.05$ in **(A–C)**.

and M3, which were located in the deeper region. Thus, CDBW mixes with ambient water as it descends the slope. The mixing ratio increased in April and decreased in May at mooring M2 and increased in September and decreased in October at mooring M4, corresponding to the change in potential temperature (**Figure 6A**). At mooring M2, S_{SW} started to increase in late April. At mooring M1, S_{SW} started to increase about 1 month later, when S_{SW} at mooring M2 reached about 34.5. Because moorings M1 and M2 were located in the shallower and deeper part of the slope, respectively, it is suggested that CDBW cannot reach the deep region until salinity and density get high enough. At moorings M3 and M4, S_{SW} started to increase 2 and 5 months later than at mooring M2, respectively. At all moorings, S_{SW} continued to increase until October–November.

Figure 10C compares S_{SW} with salinity obtained by the deepest CT sensors at moorings C2 and C3, which were deployed at the shelf break in 2013–2014. Potential tempetature at these moorings was close to the freezing point from February to November (not shown). Thus, SW or AASW was present at these mooring sites. The value of S_{SW} at moorings M1–M3 approximately compares with the salinity at mooring C2 except for July–August. Sea-ice production in the Cape Darnley polynya

in 2013–2014 was similar to that in 2008–2009, except that the sea-ice production in the former was smaller than in the latter in June–July (**Figure 10D**). Thus, we expect that salinity in 2008–2009 at moorings C2 and C3 was similar to that shown in **Figure 10**. The salinity at mooring C3 was higher than that at mooring C2. There are two possible explanations for this feature. First, because mooring C3 was located west of mooring C2, brine rejected in the Cape Darnley polynya likely accumulated in SW as it is advected westward. Second, the salinity of SW tends to be increased in a depression (Williams et al., 2008). Thus, salty SW at mooring C3 may originate from Burton Basin, which is a small depression located south of mooring C3 (**Figure 1**). When we estimated S_{SW}, we assumed that SW only mixes with ambient AABW or CDW; however, SW is also mixed with less saline mCDW in shallow regions near the shelf break (Foster and Carmack, 1976), as suggested by a θ-S diagram shown in **Figure 2**. Thus, S_{SW} obtained in this analysis may be the lower bound of the real value.

The salinity at moorings C2 and C3 started to increase in April, which is about 2 months after the onset of sea-ice production. Within 1 month after that, S_{SW} at mooring M2 started to increase in late April. Thus, SW at the shelf break quickly reached mooring M2. As long as sea ice was produced, both salinity at mooring C3 and S_{SW} continued to increase. Salinity at mooring C3 attained the maximum in October, whereas S_{SW} at moorings M1–M4 continued to increase for about 1 month after that, possibly because saline SW was still descending the slope. These results indicate that S_{SW} increased because brine rejected from sea ice was accumulated in the Cape Darnley polynya. Then, θ-S properties of CDBW varied with S_{SW}, as shown in **Figure 8**.

3.3. Horizontal Distribution of CDBW

Because the locations of moorings M1–M4 were limited in space, it is not clear how CDBW spreads horizontally. Thus, we examine the horizontal distribution of CDBW, using the results of CTD measurements. **Figure 11C** shows θ-S diagrams for CTD stations on the easternmost transect C. In this figure, symbols are plotted at 200 m intervals, starting from the bottom. Hence, the number of symbols is proportional to the thickness of water. At all stations on this transect, potential temperature was higher than -0.3°C, except for the thin layer near the bottom. As shown in **Supplementary Figures 1E,F**, this cold and less saline layer was limited to about 100 m from the bottom. Mooring M4 was located on transect C. The newly formed CDBW was not observed until September at this mooring. Thus, newly formed CDBW was almost absent on transect C.

Figures 11A,B show θ-S diagrams for CTD stations on transects A and B, respectively. Moorings M1 (and M2) and M3 were located on transects A and B, respectively. At stations on these transects, potential temperature was lower than -0.3°C near the bottom, corresponding to newly formed CDBW. Because the number of symbols in the region below $\theta = -0.3^{\circ}$C was large in **Figures 11A,B** compared with that in **Figure 11C**, the thickness of CDBW on transects A and B was larger than that on transect C. As shown in **Supplementary Figures 1A–D**, cold and less saline water, which is colder than -0.3°C, was present within 200–500 m from the bottom on transects A and B, except for CTD station b07. Thus, supplied from the Cape Darnley polynya, the thickness of the newly formed CDBW significantly increased between transects B and C. A small amount of CDBW was also present at CTD station c05 on transect C. Because SW with salinity higher than 34.6 is distributed in Prydz Bay, which is east of Cape Darnley (**Figure 1**), cold AABW distributed at CTD station c05 may not be CDBW but newly formed AABW from Prydz Bay (Williams et al., 2016).

Cape Darnley Bottom Water on transect A was warm and saline compared with that on transect B. The gray crosses in **Figures 11A,B** indicate potential temperature and salinity in periods P3–P4 obtained by the deepest CT sensors at moorings M1 and M3, respectively. Potential temperature and salinity near the bottom obtained at CTD stations roughly coincide with those observed by moorings. Thus, CDBW on transects A and B were the remnant of warm and saline CDBW and cold and less saline CDBW observed at moorings M1 and M3, respectively. As shown in **Figures 6**, **10**, CDBW was present at mooring sites when CTD observation was performed in January 2009. CDBW was present even at CTD stations a01 and b01, which were the offshore most stations on transects A and B, respectively. Thus, CDBW extended offshore, at least beyond these stations. The gray crosses in **Figure 11C** indicate potential and salinity in period P4 obtained by the deepest CT sensors at moorings M4. Again, potential temperature and salinity obtained at CTD stations on transect C roughly coincide with those observed by mooring M4. Although CDBW observed at mooring M4 was colder than that at mooring M3, potential temperature and salinity at moorings M3 and M4 were approximately aligned on the same line. Thus, the source waters of CDBW observed at these moorings have characteristics similar to each other. Although newly formed AABW at mooring M4 may originate from Prydz Bay, CDBW may also reach mooring M4.

3.4. Short-Term Variability of CDBW

As shown in **Figure 5**, the temporal variability of velocity was amplified when newly formed CDBW reached mooring sites, suggesting that the variability was induced by the outflow of CDBW. **Figure 12** shows the variance-preserving spectra of the kinetic energy calculated from the deepest current meter data at moorings M1–M4. For comparison, power spectra calculated from filtered and unfiltered velocities are shown by the solid and dashed lines, respectively. The power spectra had maximum peaks at frequencies of 0.11, 0.27, and 0.23 cpd, which correspond to periods of 9.1, 3.8, and 4.3 days, at moorings M1, M3, and M4, respectively. A second peak was also found at the frequency of 0.20 cpd at mooring M3. No clear peak was found at mooring M2, although the power spectrum was large between the frequencies of 0.02 and 0.03 cpd. The power spectrum also had small peaks associated with O1, K1, M2, and S2 tidal constituents (the dashed line in **Figure 12**); however, the energy of tidal currents was small.

The power spectra at other depths also had peaks at the same frequencies as those shown in **Figure 12** (not shown). To examine the vertical structure of the variability represented by these peaks, we calculated cross-spectra between the velocity and potential temperature at all depths for each mooring. We used the

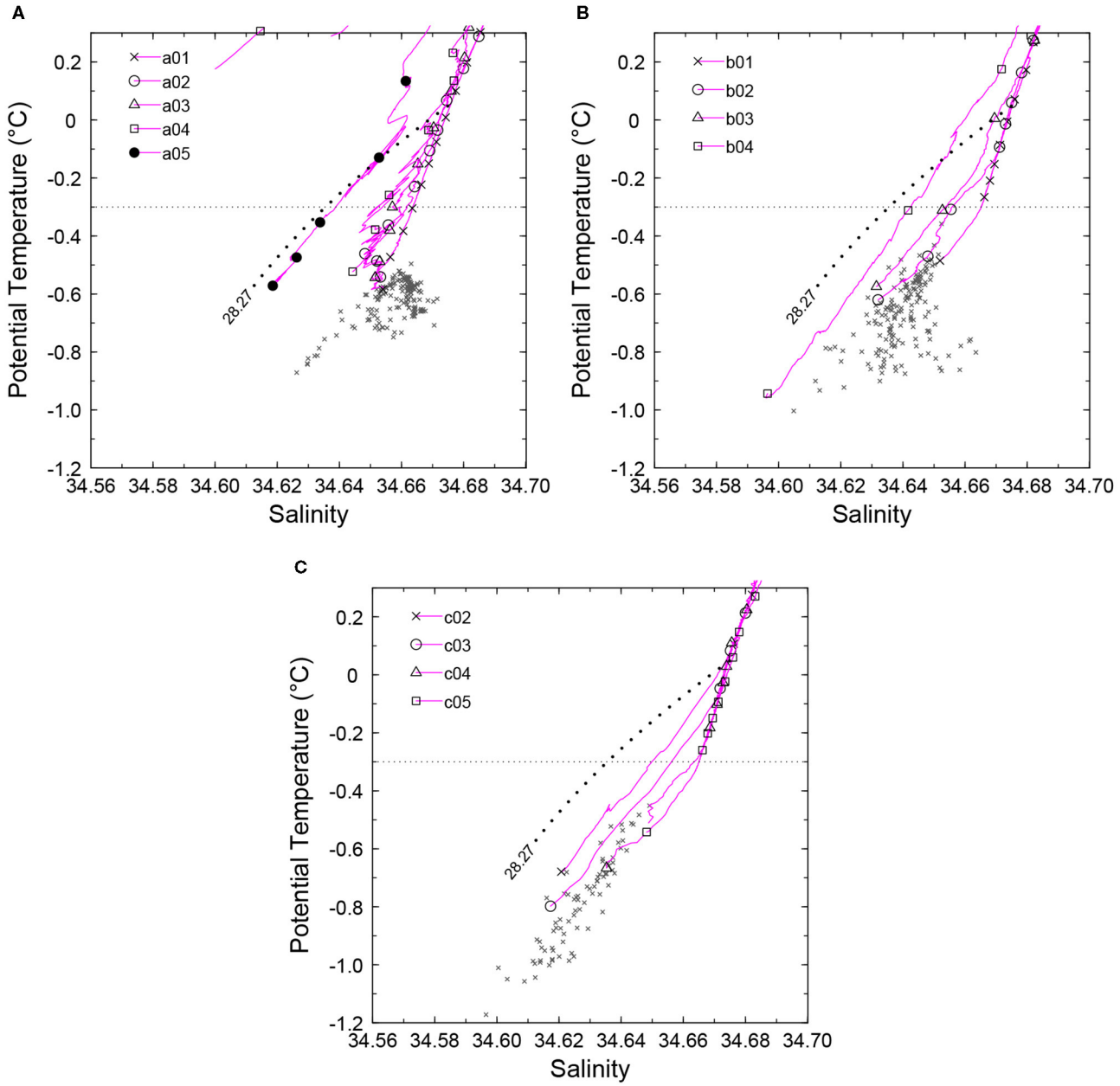

FIGURE 11 | Comparison of θ-S diagrams for moorings and CTD measurement. The gray crosses in **(A,B)** indicate data for the deepest CT sensors at moorings M1 and M3 in periods P3 and P4, respectively. The gray crosses in **(C)** indicate data for the deepest CT sensors at moorings M4 in period P4. Magenta lines with symbols indicate θ-S curves for CTD stations **(A)** a01–a05, **(B)** b01–b04, and **(C)** c02–c05. Symbols are plotted at 200 m intervals, starting from the bottom for CTD measurement. The dotted horizontal line indicates $\theta = -0.3$°C.

velocity parallel to the major axes of standard deviation ellipses, u_{maj}, because it represents the most significant component of the velocity variability. We used u_{maj} obtained at the deepest depth at each mooring as a reference, and calculated cross-spectra between the velocity and potential temperature at all depths with this reference. Because the velocity data near the bottom were not available at mooring M4, we used potential temperature measured at the deepest depth as a reference for this mooring.

Figure 13 shows the vertical distribution of the phase of the u_{maj} and potential temperature at the frequency band around the peaks of the power spectra. The phases of u_{maj} and potential temperature were tilted in the vertical direction, except for u_{maj} at moorings M3 and M4. The tilt of the phase of u_{maj} was opposite to that of the potential temperature. The directions of the tilts are consistent with those obtained in a baroclinic instability problem (Pedlosky, 1987). The phase of the potential temperature relative to u_{maj} at mooring M2 differed from that at moorings M1 and

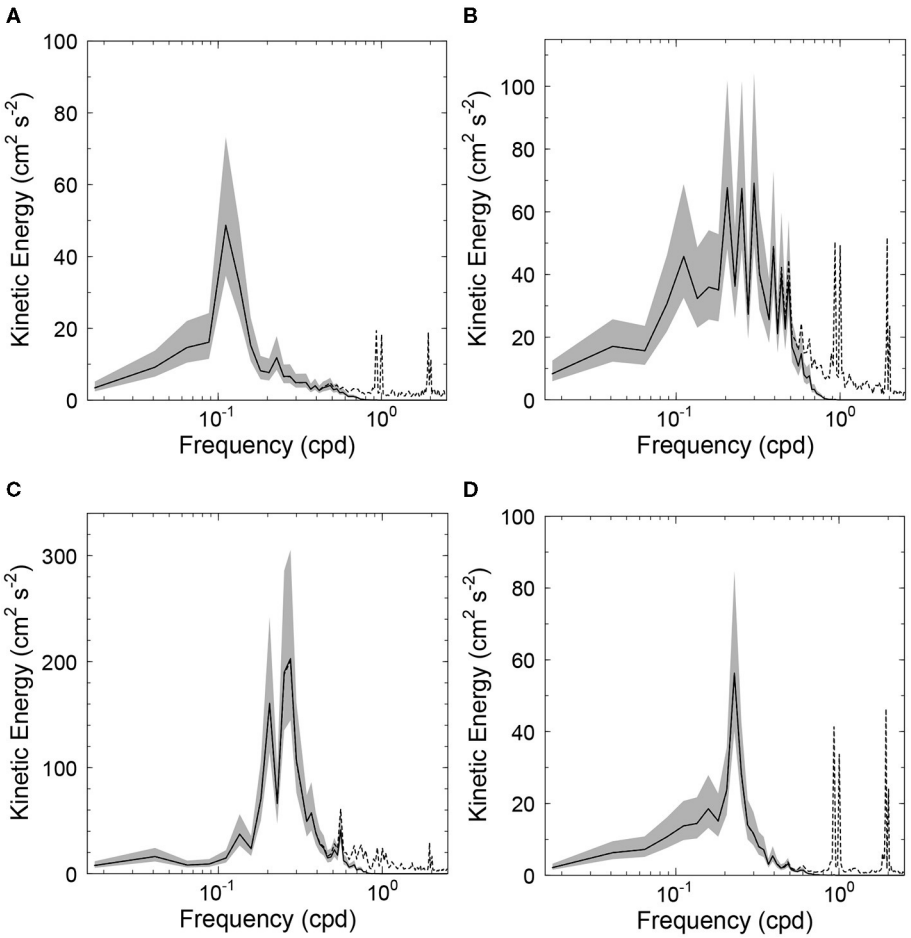

FIGURE 12 | The variance-preserving spectrum of the kinetic energy obtained by the deepest current meter (CM) at moorings **(A)** M1, **(B)** M2, **(C)** M3, and **(D)** M4. The solid and dashed lines indicate the power spectrum calculated from the filtered and unfiltered velocities, respectively. The 95% confidence limit of the former is shaded. Note that the vertical scale is different in each panel.

M3 by nearly 180°. This feature is not surprising, because the along-isobath velocity, which is approximately the same as u_{maj}, has the opposite sign on the onshore and offshore sides of eddies produced by baroclinic instability. The phase difference between potential temperature and u_{maj} indicates that moorings M1 and M3 were located on the offshore side of eddies, whereas mooring M2 was located on the onshore side of eddies (Pedlosky, 1987).

We compare the frequency of the variability obtained at moorings with that of a baroclinically unstable wave theoretically predicted by a three-layer quasi-geostrophic model (refer to **Appendix** for details). For simplicity, we adopted a quasi-geostrophic model, although the quasi-geostrophic approximation may not be exactly valid at mooring sites. The interface between the first and second layers represents the main pycnocline, and the third layer represents the newly formed CDBW. Using this model, we calculated the complex phase velocity, c, of the unstable wave. The angular frequency and growth rate of the unstable wave are expressed as kc_r and kc_i, respectively, where k is the wavenumber and c_r and c_i are the real and imaginary parts of c, respectively.

Since the peak of the power spectrum was clear and the phase of potential temperature was significantly tilted at mooring M3, we focus on this mooring. Based on the results of the mooring measurements, we set the thickness of the third layer, $H_3 = 200$ m, the basic flow in the third layer, $U_3 = -0.2$ ms^{-1}, and the density difference between the second and third layers, $\Delta\rho_2 = 0.03$ kg m^{-3}. We determined the thickness of the first layer, H_1, and the density difference between the first and second layers, $\Delta\rho_1$, based on the depth of the node and the internal deformation radius of the first baroclinic mode, respectively, calculated from the results of the CTD measurement. For simplicity, we assumed that the basic flow in the first and second layers vanishes and that the perturbation is uniform in the direction normal to the basic flow. To determine the bottom slope, α, we fitted the bottom depth around mooring M3 with a linear function, using a Gaussian weight. The bottom slope was 0.05 and 0.04, when the e-folding scale of the Gaussian weight was 1 and 2 km, respectively. We neglected the meridional change of the planetary vorticity because it is small compared with the change in the potential vorticity due to the bottom slope.

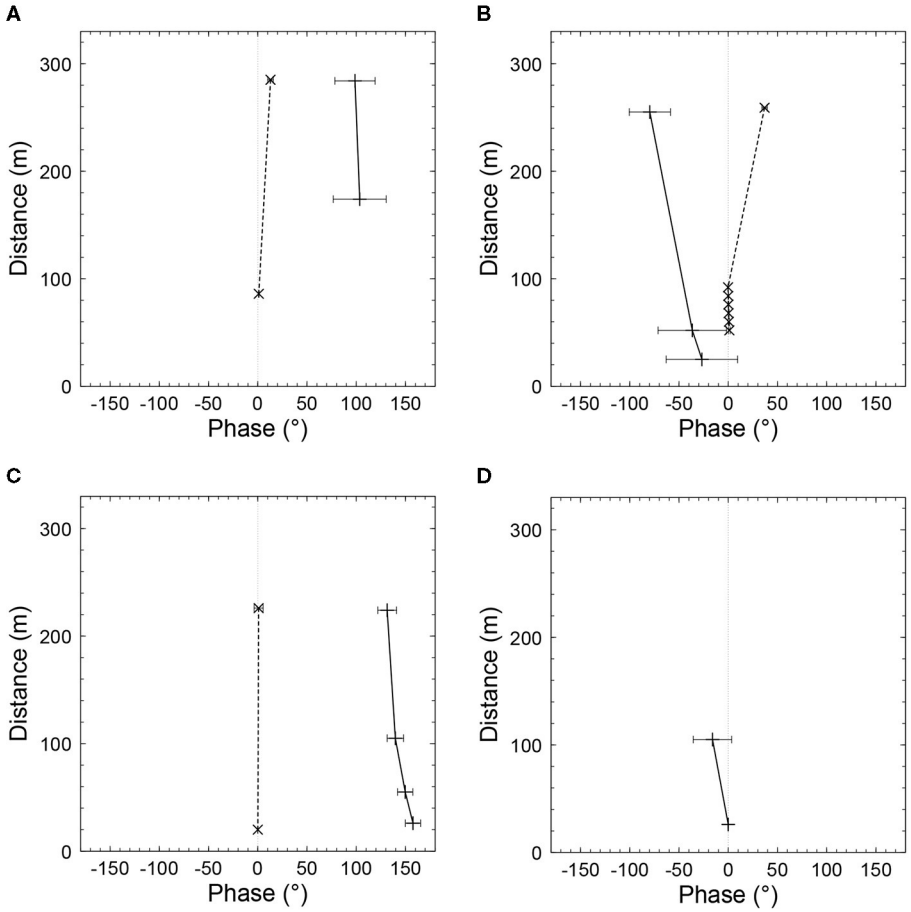

FIGURE 13 | Vertical distribution of the phase of potential temperature (solid line and pluses) and u_{maj} (dashed line and crosses) at moorings **(A)** M1, **(B)** M2, **(C)** M3, and **(D)** M4. The phase in the frequency band of 0.094–0.156, 0.25–0.313, 0.25–0.313, and 0.156–0.234 cpd is shown for moorings M1, M2, M3, and M4, respectively. The vertical axis indicates the height from the bottom. The horizontal bars indicate the 95% confidence limit of the phase. The symbols are not drawn at depths where the 95% confidence limit exceeds 60°.

Figure 14 shows the growth rate, kc_i, and the angular frequency, kc_r, of the most unstable wave as a function of the bottom slope, α. The basic flow was unstable when α was <0.09. The dotted horizontal line indicates the angular frequency of the peak of the power spectrum at mooring M3. Because the bottom slope at mooring M3 was 0.04–0.05, the frequency of the variability at mooring M3 agrees with that of the most unstable wave. To examine the sensitivity of kc_r on the speed of basic flow, U_3, we changed U_3 by $\pm 30\%$ (gray lines in **Figure 14**). We find that kc_r does not significantly depend on the value of U_3. We also verified that kc_r does not significantly depend on H_3, $\Delta\rho_2$, and other parameters. Thus, the variability observed at mooring M3 is most likely induced by the instability of CDBW flowing along the bottom.

4. SUMMARY

We examined the seasonal evolution of CDBW, using results of moorings and CTD measurement in the slope region off the Cape Darnley polynya. Starting in April, the potential temperature and salinity decreased and γ_n increased, indicating that newly formed CDBW arrived at the mooring sites. CDBW first arrived at mooring M2, which was located in the western and shallow region. Then, CDBW subsequently spread to the mooring sites in the more offshore and eastern regions by September. Along with the arrival of CDBW, the current speed near the bottom increased at moorings M2 and M3, suggesting the flow was induced by CDBW. The newly formed CDBW was distributed within 100–300 m or more from the bottom.

θ-S properties of CDBW varied seasonally. From a θ-S diagram for moored CT sensors, it is suggested that CDBW is formed by the mixing between two water masses: one is cold and less saline water corresponding to the source water of CDBW and the other is warm and saline ambient water. The seasonal variation of θ-S properties of CDBW indicated that the salinity of the source water of CDBW increased with time. Based on the distribution of water properties on a θ-S diagram, we estimated the salinity, S_{SW}, of the source water of CDBW. The value of S_{SW} roughly agrees with the salinity of SW observed near the shelf break. S_{SW} at mooring M2, which was located in the upper

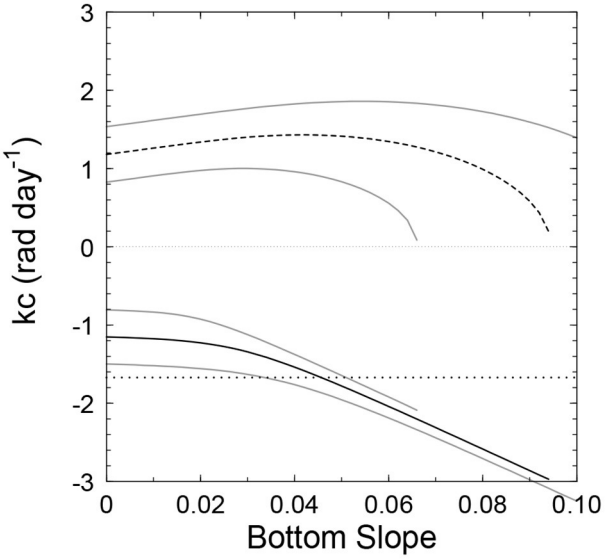

FIGURE 14 | The angular frequency, kc_r, (solid line) and the growth rate, kc_i, (dashed line) of the most unstable wave as a function of the bottom slope, α. The dotted horizontal line indicates the angular frequency of the peak of the power spectrum at mooring M3. The gray lines indicate kc_r and kc_i obtained when U_3 was changed by ±30%. The gray line for kc_r is not drawn when the unstable wave is absent.

part of the slope, started to increase in late April, which is about 2 months after the onset of sea-ice production. Then, S_{SW} at other mooring sites started to increase from May to September. As long as sea ice was produced, both S_{SW} and salinity at the shelf break continued to increase. These results indicate that S_{SW} increased with time because brine rejected in the Cape Darnley polynya accumulated on the shelf. Thus, S_{SW} and θ-S properties of CDBW vary due to the accumulation of brine in the Cape Darnley polynya.

Two types of CDBW were identified. Cold and less saline CDBW was present at mooring M3, which was located in Wild Canyon, and warm and saline CDBW was present at moorings M1 and M2, which were located in and upstream of Daly Canyon, respectively. Hence, CDBW in Daly Canyon was warmer and saltier than that in Wild Canyon. S_{SW} of the source water of CDBW in Daly Canyon was also higher than that in Wild Canyon. Because Daly Canyon is located to the west of Wild Canyon, these results suggest that brine rejected in the Cape Darnley polynya accumulated in SW as it is advected westward. Thus, the sea-ice production in the Cape Darnley polynya is an important factor that affects the variation of θ-S properties of CDBW in both space and time. According to CTD measurement, the thickness of newly formed AABW significantly increased between the transects located on the eastern and western sides of the Cape Darnley polynya, corresponding to the supply of CDBW from the polynya. Both the cold and less saline CDBW and warm and saline CDBW spread offshore along Wild and Daly Canyons, respectively.

When CDBW arrived at the mooring sites, the short-term variability of the velocity was apparent, especially at mooring M3. The power spectrum of the kinetic energy had peaks at periods between 3.8 and 9.1 days. The vertical distribution of the phase of u_{maj} and the potential temperature was mostly tilted in the opposite direction, being consistent with that obtained in a baroclinic instability problem. The frequency of the variability at mooring M3 agrees with that of the most unstable wave obtained by a three-layer quasi-geostrophic model. Thus, the variability was most likely induced by the baroclinic instability of CDBW.

In this study, we focused on the mixing process of CDBW in the slope region. While S_{SW} roughly agreed with the salinity of SW near the shelf break, more saline SW with a salinity exceeding S_{SW} was also observed. SW probably mixes with less saline mCDW near the shelf break, as suggested by Foster and Carmack (1976). To understand the entire formation process of CDBW, we need winter hydrographic data covering broader regions. Hydrographic observations from floats and instrumented seals may be able to contribute to the increase of such data (Wong and Riser, 2013; Williams et al., 2016). These analyses are left for future research.

DATA AVAILABILITY STATEMENT

The datasets presented in this article are not readily available because analysis by authors have not fully finished for some data. Requests to access the datasets should be directed to Kay I. Ohshima, ohshima@lowtem.hokudai.ac.jp.

AUTHOR CONTRIBUTIONS

GM analyzed all the data and wrote the manuscript with comments by all other authors. YF conducted the mooring observations with KO, YM, and DS. YK and DH conducted hydrographic observations. MF processed the bathymetric data. YN contributed to bathymetry data acquisition. The project was led by KO. All authors contributed to the article and approved the submitted version.

FUNDING

The present study was supported by Grants-in-Aid for Scientific Research (20221001, 20540419, 25241001, 17H01157, 17H06317, 20H05707, and 23340135) of the Ministry of Education, Culture, Sports, Science and Technology in Japan, and the Science Program of Japanese Antarctic Research Expedition.

ACKNOWLEDGMENTS

We are deeply indebted to the officers, crew, and scientists on board TR/V Umitaka-maru, R/V Hakuho-maru, and icebreaker Shirase for their help with field observations. The sea ice production data were provided by Kazuki Nakata.

SUPPLEMENTARY MATERIAL

The Supplementary Material for this article can be found online at: https://www.frontiersin.org/articles/10.3389/fmars.2021.657119/full#supplementary-material

REFERENCES

Amante, C., and Eakins, B. W. (2009). *ETOPO1 Global Relief Model converted to PanMap layer format.* NOAA-National Geophysical Data Center. *PANGAEA*. doi: 10.1594/PANGAEA.769615

Aoki, S., Katsumata, K., Hamaguchi, M., Noda, A., Kitade, Y., Shimada, K., et al. (2020). Freshening of antarctic bottom wate off cape darnley, East Antarctica. *J. Geophys. Res.* 125:e2020JC016374. doi: 10.1029/2020JC016374

Arndt, J. E., Schenke, H. W., Jakobsson, M., Nitsche, F. O., Buys, G., Goleby, B., et al. (2013). The International Bathymetric Chart of the Southern Ocean (IBCSO) version 1.0—a new bathymetric compilation covering circum-Antarctic waters. *Geophys. Res. Lett*. 40, 3111–3117. doi: 10.1002/grl.50413

Baines, P. G., and Condie, S. (1998). "Observations and modelling of Antarctic downslope flows: a review," in *Ocean, Ice, and Atmosphere: Interactions at the Antarctic Continental Margin, Vol. 75 of Antarctic Research Series*, eds S. Jacobs and R. Weiss (Washington, DC: AGU), 29–49.

Chapman, D. C., and Gawarkiewicz, G. (1995). A numerical study of dense water formation and transport on a shallow, sloping continental-shelf. *J. Geophys. Res.* 100, 4489–4507. doi: 10.1029/94JC01742

Couldrey, M. P., Jullion, L., Naveira Garabato, A. C., Rye, C., Herraiz-Borreguero, L., Brown, P. J., et al. (2013). Remotely induced warming of Antarctic bottom water in the eastern Weddell gyre. *Geophys. Res. Lett*. 40, 2755–2760. doi: 10.1002/grl.50526

Emery, W., and Thomson, R. (2001). *Data Analysis Methods in Physical Oceanography*. Boston, MA: Elsevier Science.

Foster, T. D., and Carmack, E. C. (1976). Frontal zone mixing and Antarctic bottom water formation in southern Weddell Sea. *Deep Sea Res*. 23, 301–317. doi: 10.1016/0011-7471(76)90872-X

Hirano, D., Kitade, Y., Ohshima, K. I., and Fukamachi, Y. (2015). The role of turbulent mixing in the modified shelf water overflows that produce cape darnley bottom water. *J. Geophys. Res*. 120, 910–922. doi: 10.1002/2014JC010059

Jackett, D. R., and McDougall, T. J. (1997). A neutral density variable for the world's oceans. *J. Phys. Oceanogr*. 27, 237–263. doi: 10.1175/1520-0485(1997)027andlt;0237:ANDVFTandgt;2.0.CO;2

Jacobs, S. S., Amos, A. F., and Bruchhau, P. M. (1970). Ross-Sea oceanography and Antarctic bottom water formation. *Deep Sea Res*. 17, 935. doi: 10.1016/0011-7471(70)90046-X

Kitade, Y., Shimada, K., Tamura, T., Williams, G. D., Aoki, S., Fukamachi, Y., et al. (2014). Antarctic bottom water production from the vincennes bay polynya, East Antarctica. *Geophys. Res. Lett*. 41, 3528–3534. doi: 10.1002/2014GL059971

Mantyla, A. W., and Reid, J. L. (1983). Abyssal characteristics of the world ocean waters. *Deep Sea Res. A Oceanogr. Res. Pap*. 30, 805–833. doi: 10.1016/0198-0149(83)90002-X

Meijers, A. J. S., Klocker, A., Bindoff, N. L., Williams, G. D., and Marsland, S. J. (2010). The circulation and water masses of the Antarctic shelf and continental slope between 30 and 80°E. *Deep Sea Res. II Top. Stud. Oceanogr*. 57, 723–737. doi: 10.1016/j.dsr2.2009.04.019

Meredith, M., Locarnini, R., Van Scoy, K., Watson, A., Heywood, K., and King, B. (2000). On the sources of weddell gyre antarctic bottom water. *J. Geophys. Res*. 105, 1093–1104. doi: 10.1029/1999JC900263

Morrison, A. K., Hogg, A. M., England, M. H., and Spence, P. (2020). Warm Circumpolar Deep Water transport toward Antarctica driven by local dense water export in canyons. *Sci. Adv*. 6:eaav2516. doi: 10.1126/sciadv.aav2516

Nakata, K., Ohshima, K. I., and Nihashi, S. (2019). Estimation of thin-ice thickness and discrimination of ice type from AMSR-E passive microwave data. *IEEE Trans. Geosci. Remote Sens*. 57, 263–276. doi: 10.1109/TGRS.2018.2853590

Nakata, K., Ohshima, K. I., and Nihashi, S. (2021). Mapping of active frazil for Antarctic coastal polynyas, with an estimation of sea-ice production. *Geophys. Res. Lett*. 48:e2020GL091353. doi: 10.1029/2020GL091353

Nakayama, Y., Ohshima, K. I., Matsumura, Y., Fukamachi, Y., and Hasumi, H. (2014). A numerical investigation of formation and variability of Antarctic bottom water off cape darnley, East Antarctica. *J. Phys. Oceanogr*. 44, 2921–2937. doi: 10.1175/JPO-D-14-0069.1

Nihashi, S., and Ohshima, K. I. (2015). Circumpolar mapping of Antarctic coastal polynyas and landfast sea ice: relationship and variability. *J. Climate* 28, 3650–3670. doi: 10.1175/JCLI-D-14-00369.1

Ohshima, K. I., Fukamachi, Y., Williams, G. D., Nihashi, S., Roquet, F., Kitade, Y., et al. (2013). Antarctic Bottom Water production by intense sea-ice formation in the Cape Darnley polynya. *Nat. Geosci*. 6, 235–240. doi: 10.1038/ngeo1738

Orsi, A. H., Johnson, G. C., and Bullister, J. L. (1999). Circulation, mixing, and production of Antarctic Bottom Water. *Progr. Oceanogr*. 43, 55–109. doi: 10.1016/S0079-6611(99)00004-X

Orsi, A. H., and Wiederwohl, C. L. (2009). A recount of Ross Sea waters. *Deep Sea Res. II Top. Stud. Oceanogr*. 56, 778–795. doi: 10.1016/j.dsr2.2008.10.033

Pedlosky, J. (1987). *Geophysical Fluid Dynamics*. New York, NY: Springer-Verlag.

Rintoul, S. R. (1998). "On the origin and influence of Adélie Land Bottom Water," in *Ocean, Ice, and Atmosphere: Interactions at the Antarctic Continental Margin, Vol. 75 of Antarctic Research Series*, eds S. Jacobs and R. Weiss (Washington, DC: AGU), 151–171.

Tamura, T., Ohshima, K. I., and Nihashi, S. (2008). Mapping of sea ice production for Antarctic coastal polynyas. *Geophys. Res. Lett*. 35:L07606. doi: 10.1029/2007GL032903

Whitworth, T. III., and Orsi, A. H. (2006). Antarctic Bottom Water production and export by tides in the Ross Sea. *Geophys. Res. Lett*. 33:L12609. doi: 10.1029/2006GL026357

Whitworth, T. III., Orsi, A. H., Kim, S. J., Nowlin, W. D., and Locarnini, R. (1998). "Water masses and mixing near the Antarctic slope front," in *Ocean, Ice, and Atmosphere: Interactions at the Antarctic Continental Margin, Vol. 75 of Antarctic Research Series*, eds S. Jacobs and R. Weiss (, Washington, DC: AGU), 1–27.

Williams, G. D., Aoki, S., Jacobs, S. S., Rintoul, S. R., Tamura, T., and Bindoff, N. L. (2010). Antarctic Bottom Water from the Adélie and George V Land coast, East Antarctica (140-149°E). *J. Geophys. Res*. 115:C04027. doi: 10.1029/2009JC005812

Williams, G. D., Bindoff, N. L., Marsland, S. J., and Rintoul, S. R. (2008). Formation and export of dense shelf water from the Adélie Depression, East Antarctica. *J. Geophys*. Res. 113:C04039. doi: 10.1029/2007JC004346

Williams, G. D., Herraiz-Borreguero, L., Roquet, F., Tamura, T., Ohshima, K. I., Fukamachi, Y., et al. (2016). The suppression of Antarctic Bottom Water formation by melting ice shelves in Prydz Bay. *Nat. Commun*. 7:12577. doi: 10.1038/ncomms12577

Wong, A. P. S., and Riser, S. C. (2013). Modified shelf water on the continental slope north of Mac Robertson Land, East Antarctica. *Geophys. Res. Lett*. 40, 6186–6190. doi: 10.1002/2013GL058125

Conflict of Interest: The authors declare that the research was conducted in the absence of any commercial or financial relationships that could be construed as a potential conflict of interest.

frontiers in Marine Science

ORIGINAL RESEARCH
published: 24 August 2021
doi: 10.3389/fmars.2021.656737

Investigation of the Inherent Variability of the Mediterranean Sea Under Contrasting Extreme Climatic Conditions

Angeliki Sampatakaki[1,2], Vassilis Zervakis[1], Ioannis Mamoutos[1,2], Elina Tragou[1], Alexandra Gogou[2], Maria Triantaphyllou[3] and Nikolaos Skliris[4]*

[1] Department of Marine Sciences, University of the Aegean, Mytilene, Greece, [2] Hellenic Centre for Marine Research, Institute of Oceanography, Anavyssos, Greece, [3] Faculty of Geology and Geoenvironment, National and Kapodistrian University of Athens, Athens, Greece, [4] Ocean and Earth Science, University of Southampton, Southampton, United Kingdom

The internal variability of the thermohaline circulation of the Mediterranean Sea is examined under contrasting extreme thermal and mass atmospheric forcing conditions. Three millennium-long numerical simulation experiments were performed under: (a) the current climatology, (b) a strong buoyancy forcing (SBF) scenario due to cold and dry conditions resembling the Younger Dryas event, and (c) a weak buoyancy forcing (WBF) scenario due to S1a sapropel deposition-like conditions (warm and wet). To isolate the inherent variability of the system, independent of interannual atmospheric forcing variability, the latter was defined as a perpetual year pertinent to each experiment. Self-diagnosed heat and salt fluxes, consistent to sea-surface characteristics of the above periods, forced three millenium-long, relaxation-free numerical experiments. These simulations were preceded by initial spin-up periods. The inherent spatiotemporal variability of the Mediterranean Sea was analyzed using the empirical orthogonal function (EOF) and spectral analysis on the simulated density fields. Our results revealed that the Mediterranean Sea exhibits high sensitivity to climatic conditions, allowing its circulation to change from anti-estuarine (for the SBF scenario, leading to a buoyancy loss to the atmosphere) to estuarine (for the WBF scenario, corresponding to a buoyancy gain from the atmosphere). In all three experiments, the interannual and decennial variabilities dominate in upper layers, and the decennial variability dominates in the Gibraltar and Sicily Straits. Under current climatic conditions the first two EOF modes express only 60% of the density variability in the deep layers. This contribution exceeds 90% under more extreme conditions. Moreover, the first EOF modes correspond to a basin-wide in-phase variability of the deep layers under the reference and WBF conditions. During SBF conditions the first modes reveal a vertical buoyancy exchange between upper and deeper layers. The second EOF mode of deep waters under both extreme scenarios showed that the western and eastern basins exchange buoyancy in decennial (for the cold/dry) and interdecennial (for the warm/humid) timescales. The residence time of the Eastern Mediterranean deep water was diagnosed to be centennial, semicentennial, and intercentennial for the cases of current period, SBF, and WBF, respectively.

Keywords: Mediterranean Sea, variability, extreme climatic conditions, inherent variability, BiOS mechanism

OPEN ACCESS

Edited by:
Ming Li,
University of Maryland Center for Environmental Science (UMCES), United States

Reviewed by:
Paul Myers,
University of Alberta, Canada
Jian Zhao,
University of Maryland Center for Environmental Science (UMCES), United States

****Correspondence:***
Angeliki Sampatakaki
sampatakaki@aegean.gr

Specialty section:
This article was submitted to Physical Oceanography, a section of the journal Frontiers in Marine Science

Received: *21 January 2021*
Accepted: *05 July 2021*
Published: *24 August 2021*

Citation:
Sampatakaki A, Zervakis V, Mamoutos I, Tragou E, Gogou A, Triantaphyllou M and Skliris N (2021) Investigation of the Inherent Variability of the Mediterranean Sea Under Contrasting Extreme Climatic Conditions. Front. Mar. Sci. 8:656737. doi: 10.3389/fmars.2021.656737

INTRODUCTION

The Mediterranean Sea is characterized as a concentration basin (Nielsen, 1912; Sverdrup et al., 1942). Atlantic water enters as a surface current through the Gibraltar Strait and travels eastward along the southern shores of the Mediterranean Sea, undergoing the transformation of its characteristics, whereas the discharge of the Mediterranean water to the Atlantic occurs *via* the intermediate and deepest layers. The overturning circulation pattern of the Mediterranean Sea is powered by the formation of deep waters in the Gulf of Lions (Stommel, 1972) for the western subbasin and in the Adriatic (Malanotte-Rizzoli et al., 1997) and Aegean Seas (Zervakis et al., 2000; Nittis et al., 2003) for the eastern one, while the Levantine intermediate water (LIW) has a key role to these formations (Lascaratos et al., 1993; Theocharis, 2009). Numerous three-dimensional (3D) numerical models have been developed to simulate the circulation characteristics of the Mediterranean Sea and their evolution throughout the instrumental period (e.g., Wu and Haines, 1996; Skliris et al., 2007; Somot et al., 2008; Oddo et al., 2009; Beuvier et al., 2010; Pinardi et al., 2015).

Nevertheless, the overturning circulation of the Mediterranean Sea was not always the same as is recorded today. In the past the Mediterranean basin occasionally exhibited periods of dramatic reduction of deep-water ventilation, which can be identified in the sedimentary record by the presence of sapropels. These dark organic-rich layers are found throughout the Eastern Mediterranean, the Tyrrhenian Sea, and some parts of the Western Mediterranean and demonstrate wet and warm climatic conditions dominating the basin. The sedimentary record shows their reoccurrence in the past 7 million years while, in the last 450,000 years (ka), a minimum of 11 sapropel layers were formed (e.g., Rohling, 1994; Rohling et al., 2015; Andersen et al., 2018). The warm periods of sapropel deposition have been linked to Milankovitch cycles and precession minima (e.g., Rossignol-Strick, 1985; Lourens et al., 1996). The last sapropel deposition S1 was recorded during the Holocene Climatic Optimum (∼10–6 ka BP). Both S1 sapropel sublayers (S1a and S1b) correspond to the warmest and most humid Holocene intervals for the Mediterranean, respectively (Gogou et al., 2007; Triantaphyllou et al., 2009a,b, 2016; Geraga et al., 2010; Triantaphyllou, 2014).

In contrast, the cool event of Younger Dryas was recorded just before the onset of the Holocene. Younger Dryas (12.9–11.7 ka BP) was the driest interval of the past 20,000 years (Alley, 2000; Carlson, 2013), and its impact has been recorded all over the Mediterranean Sea (e.g., Kotthoff et al., 2008).

The abovementioned changes recorded in the Mediterranean Sea sediments are linked with atmospheric forcing variability. Climatic teleconnections have been proposed to be linked with the Younger Dryas event (Cacho et al., 2001; Gogou et al., 2007; Marino et al., 2009). For the sapropel deposition intervals, data from the different sites indicate that, during these warm periods, the Eastern Mediterranean Sea was influenced by increased river discharges due to an enhanced monsoon activity over North Africa (Rossignol-Strick, 1985; Almogi-Labin et al., 2009; Athanasiou et al., 2015, 2017; Rohling et al., 2015) and a higher amount of rainfall around the Northern borderlands (Gogou et al., 2007; Kotthoff et al., 2008; Triantaphyllou et al., 2016).

In the last postglacial period, sediment records indicate that climatic alterations over the Mediterranean Sea between the warm and cold intervals may have modified the sea circulation in the subbasins and the Mediterranean outflow as well (Llave et al., 2006; Toucanne et al., 2012; El Frihmat et al., 2014; Jiménez-Espejo et al., 2015; Rohling et al., 2015; Tachikawa et al., 2015; Dubois-Dauphin et al., 2017). In the postglacial period, most 3D numerical paleo-modeling simulations referred to the S1 sapropel deposition period (Myers et al., 1998; Myers and Rohling, 2000; Myers, 2002; Meijer and Tuenter, 2007; Adloff et al., 2011; Grimm et al., 2015). Several simulations of the Mediterranean circulation during sapropel formation period converge to the finding that the basin continued to function as an overall concentration basin, at least regarding the Gibraltar exchange (Myers et al., 1998; Myers, 2002; Meijer and Tuenter, 2007; Adloff et al., 2011), a conclusion that is not necessarily supported by the sediment record (e.g., Thunell and Williams, 1989). We are not aware of efforts to numerically simulate the 3D Mediterranean circulation during the Younger Dryas period. In any case, all paleoceanographic simulations of the Mediterranean aim to reconstruct the long-term mean circulation and hydrographic characteristics of the basin. Of course, the lack of instrumental climatological information during the paleo periods, combined with the low sedimentation rate in the basin, constitutes a limiting factor to the simulations, especially in regard to the interannual to interdecennial variability.

However, both the observational record and the simulations of the basin-wide circulation converge to the conclusion that, in the last 50 years, the Mediterranean has exhibited a very energetic decennial variability, even in its deep and bottom layers (e.g., Robinson et al., 2001; Roether et al., 2007; Schroeder et al., 2016). In the 1980s, the interannual variability of the Mediterranean deep waters was first evidenced as a long-term linear trend in the western basin (Lacombe et al., 1985). The lack of frequent measurements in the Eastern Mediterranean until the mid-1980s delayed the revelation of any variability until the discovery of a major shift of dense water formation from the Adriatic to the Aegean Sea that took place between 1987 and 1993 and is known since then as the Eastern Mediterranean Transient (EMT) (Roether et al., 2007). Recent numerical hindcasts of the Mediterranean circulation spanning several decades have successfully reproduced a significant interdecennial variability of the deeper layers and dense-water formation processes (Pinardi et al., 2015; Waldman et al., 2018).

The interdecennial variability observed during the instrumental period has been attributed mainly to atmospheric forcing (e.g., Béranger et al., 2010; Incarbona et al., 2016; Somot et al., 2018); however, a significant part of the variability has been attributed to the internal dynamics of the basin. Waldman et al. (2018), analyzing a 31-year-long hindcast, showed that about 28% of the deep convection events can be attributed to the chaotic behavior of the system. Several mechanisms have been

identified as a contributor to this chaotic behavior, of which the most prominent one—for the eastern Mediterranean—may be the Adriatic-Ionian Bimodal Oscillating System (BiOS; Gačić et al., 2010; Theocharis et al., 2014). Several theoretical and experimental studies have shown that internal dynamics may be responsible for the observed variability of the system, attributing the interannual–interdecennial variability of the overturning circulation and observed alteration of deep-water formation sites to internal exchange processes, causing a stochastic resonance-type behavior (Ashkenazy et al., 2012; Crisciani and Mosetti, 2016; Rubino et al., 2020).

Thus, several Mediterranean circulation analyses converge to the conclusion that interior dynamics are responsible for the interannual–interdecennial variability of its deeper layers in the instrumental period. However, as the mean overturning circulation and the corresponding density stratification of the Mediterranean Sea can vary over geological timescales, how would this affect the inherent variability of the basin in the decennial to centennial periods?

This study aimed to investigate the internal/inherent variability of the Mediterranean Sea under extreme cases of thermohaline functioning. To achieve this aim, three long-term numerical experiments were designed and performed to simulate the circulation of the basin under the climatic conditions typical of (a) the current (instrumental) period, hereafter called as the "reference" period, (b) the Younger Dryas-like cold and dry period, hereafter called as the "strong buoyancy forcing" (SBF) period, and (c) the warm and humid period of the S1a sapropel deposition-like interval, hereafter called as the "weak buoyancy forcing" (WBF). As shown in the following sections, SBF corresponds to a strong buoyancy *loss* from the sea to the atmosphere, whereas WBF corresponds to a buoyancy gain. Long-term simulations, forced by a perpetual year, are performed until "equilibria" states are reached. The heat and freshwater fluxes are diagnosed and then applied to the model experiments for a period of 1,000 more years. The internal/inherent variability of the basin under the three climatic scenarios was examined using the empirical orthogonal function (EOF) and spectral analyses.

MATERIALS AND METHODS

Experimental Setup of the Model

Baseline Model (Reference Period)

The Princeton Ocean Model (POM, Blumberg and Mellor, 1987) was used with a configuration for the Mediterranean Sea similar to that carried out in the study by Skliris et al. (2007). The model uses 25 sigma layers and its horizontal resolution is $1/4^\circ \times 1/4^\circ$. The western boundary of the model is located in the Atlantic Ocean, and the inflow through the boundary, temperature, and salinity are prescribed from the Mediterranean Oceanic Database (MODB) seasonal climatology (see details in Skliris and Lascaratos, 2004; Skliris et al., 2007). The model uses artificial surface fluxes based on the bulk formulae as mentioned in Skliris et al. (2007), i.e., Rosati and Miyakoda (1988), exploiting the empirical formula of Reed (1977) for cloud attenuation and of Bignami et al. (1995) for long-wave radiation, while the calculation of sensible and latent heat fluxes follows the neutral Budyko (1963) scheme. The surface boundary conditions of the heat and salt fluxes are initially relaxed to the MODB (Brasseur et al., 1996) seasonal climatology (Equations 1 and 2). Precipitation is taken from the monthly data set as proposed by Jaeger (1976). The model is driven by a perpetual year atmospheric forcing of the monthly averages obtained, from 1973 to 1993, using 6-h European Center for Medium Range Weather Forecasts (ECMWF) reanalysis data and is initialized from the MODB spring temperature and salinity fields (for more details about the model, see Skliris et al., 2007).

The surface boundary conditions of the heat flux F_H and the salt flux F_S at the air–sea interface for the spin-up are given by

$$F_H = Q_N + C_T\left(T^c - T_1\right) \quad (1)$$

$$F_s = (E - P)\,S_1 + C_S\left(S^c - S_1\right) \quad (2)$$

where Q_N is the net heat flux at the air–sea interface, P is the precipitation and E is the evaporation, T^c and S^c are the seasonally averaged climatological sea surface temperature (SST) and salinity from the MODB (Brasseur et al., 1996), and T_1 and S_1 are the temperature and salinity of the top-level of the model, respectively.

As we would like to investigate long-term internal dynamics without damping terms, the model was set up to run with no internal relaxation, and only the following modifications were applied to the model configuration mentioned in the study of Skliris et al. (2007): the outflow of River Po into the Adriatic was added to the original model as a source point (according to Skliris et al., 2007 river runoff setup), with the average discharges of river being equal to 2,000 m^3s^{-1}, corresponding to the average discharges of rivers into the Adriatic (Ludwig et al., 2009) and a sinusoidal variation with a range of 500 m^3s^{-1} and two peaks a year in spring and autumn. For the Dardanelles exchange, the salinity of the inflow water and the outflow water was set to 29.6 and 38.9 throughout the year, respectively (Ünlüata et al., 1990). For the Nile River, discharges prior to the Aswan Dam construction are considered as described by Skliris et al. (2007), in all the experiments.

Then, the correction coefficients of the surface heat and salinity fluxes are estimated and redesignated as follows: the root-mean-square error (RMS) index was used to compare the surface seasonal values of temperature and salinity fields of the Mediterranean Sea, as produced by the model runs with the modified correction coefficients after a 40 year spin-up, with the respective climatological values. The RMS index was applied again on the average seasonal values produced by the model to an average depth of 300 m with the corresponding climatology values. The average of the results of the indicator on temperature and salinity in the surface and at an average depth of 300 m gave the final choice of correction coefficients (C_T, C_S).

The baseline model was spun-up for 320 years and reached its steady state from the first 160 years run.

Baseline Model (Reference Period): Application of Diagnosed Fluxes

According to previous studies (Myers and Haines, 2000; Pisacane et al., 2006), the diagnosed fluxes are applied to the model and the internal variability of the basin is examined.

The diagnosed monthly heat and freshwater fluxes were estimated after the spin-up period, and the model ran for another 1,000 years with these fixed fluxes.

The monthly diagnosed freshwater fluxes F_F were calculated by

$$F_F = E - P + \frac{C_S\,(S^c - S_m)}{S_m} D \tag{3}$$

where S_m is the monthly averaged surface salinity as calculated from the last year of the spin-up of the model and D is the thickness of the first σ-layer of the model.

The monthly diagnosed surface heat fluxes $F_H^{'}$ were calculated by

$$F_H^{'} = Q_N + C_T\left(T^c - T_m\right) \tag{4}$$

where T_m is the monthly average temperature of the top-level of the model as calculated from the final year of the spin-up period.

The application of the diagnosed heat and salt fluxes as boundary conditions allowed the model to run free of any relaxation terms, leading to realistic SST and salinity fields. The relaxation terms of the model were removed to ensure that any observed internal variability of the basin would not be a product of artificial nudging (Weaver and Hughes, 1992).

Baseline (Reference Period): Model Validation

The reference experiment is evaluated based on the comparison of hydrographic characteristics in the interior of the basin between a recent climatology [from the available temperature and salinity profiles from 1900 to 2015 (Iona et al., 2018)] and the last 500 years of the simulation.

The evaluation of the simulations has been conducted *via* a comparison of the mean vertical profiles and the combined θ/S diagrams (**Figure 1**). Overall, the simulation exhibits a faithful reproduction of the vertical structure of the water column and an impressive agreement in the θ/S diagrams despite the presence of significant biases in the deeper layers. The simulation possibly underestimates the temperature by about 1°C and the salinity by about 0.3 psu. Such biases are not acceptable for operational simulations employing data assimilation or process studies using relaxation within the water column; however, we consider them acceptable in the framework of the present simulation, especially considering the agreement in the water masses as displayed in the θ/S diagram.

An indirect way to evaluate the overall performance of the simulation regarding deep water formation processes is *via* the overturning stream function, which is presented in the Results section of this study, in comparison to the results of the extreme forcing simulations.

Setting Up the Model for Extreme Climatic Conditions

To determine the extreme conditions required for the two experiments, we selected to simulate two contrasting cases in regard to the Mediterranean hydrographic conditions, at least as witnessed immediately before or within the Holocene period in the geological record. The period selected as a representative of the least stratified conditions was the Younger Dryas period (12,900–11,600 years BP, Cheng et al., 2020) during which the basin suffered a great buoyancy loss due to predominant cold and dry conditions. The period chosen as a representative of the highest stratification in the Mediterranean was the S1a sapropel deposition period (10,200–8,000 years BP, Triantaphyllou et al., 2016). To approach such conditions in the simulations, the forcing fields of the baseline model were modified as described below, based on the reconstructed sea surface data of marine cores and the insolation of each simulating period.

Determination of the Paleo-Modeling Adjustments

First of all, spatially averaged temperature (*at*) and salinity (*as*) ratios were used to assess the heat and freshwater fluxes from the SST and salinity fields. The coefficients *at* and *as* were calculated for each extreme period (**Table 1**) to provide the necessary sea surface conditions that will lead to the related forcing fluxes:

$$at_s = \frac{T_{12}}{T_0} \quad at_w = \frac{T_{9.1}}{T_0}$$

where T_{12} and $T_{9.1}$ are the averages of the alkenone-reconstructed SST data from marine cores 434G, 293G (Rodrigo-Gámiz et al., 2014), 161-977A (Martrat et al., 2007), GeoB7702-3 (Castañeda et al., 2010), 9501 (Almogi-Labin et al., 2009), MNB-3 (Gogou et al., 2007), and SL-152 (Emeis unpublished data; Gogou et al., 2016) from the Mediterranean basin (**Figure 2**) for the periods 12,300–11,700 cal BP for the Younger Dryas and 9,400–8,800 cal BP for the S1a sapropel deposition intervals, respectively. These intervals were selected because they represent "time steps," where the conditions of Younger Dryas and S1a sapropel formation are fully developed in all core sites of the Mediterranean basin. The abovementioned cores were selected as the sources of reconstructed SST information because they were available for both the past periods of interest and represent the temperature in both the eastern and western subregions. T_0 is the average spring value of the Mediterranean SST from the modern climatology (MODB) because the alkenone-reconstructed core data express the spring or winter SST (Emeis et al., 2000).

Similar to at_s and at_w, as_s and as_w were defined as the ratios of average near-surface salinities recorded in 12 and 9.1 ky BP, respectively (based on the reconstructions by Emeis et al., 2000 with a ratio of 0.25‰) to the mean of modern climatology (MODB). Here, it must be noted that the abovementioned coefficients are numerical indices not carrying any spatial information. These coefficients are applied as a spatially homogeneous correction to the current-era fields (Equations 7 and 8), and the spatial variability of the paleoclimatic simulations is generated by the model dynamics. Thus, the spatial patterns of the SST and salinity are not imposed by the corresponding core reproductions, which have been used to determine a horizontally homogeneous temporal change of the boundary conditions.

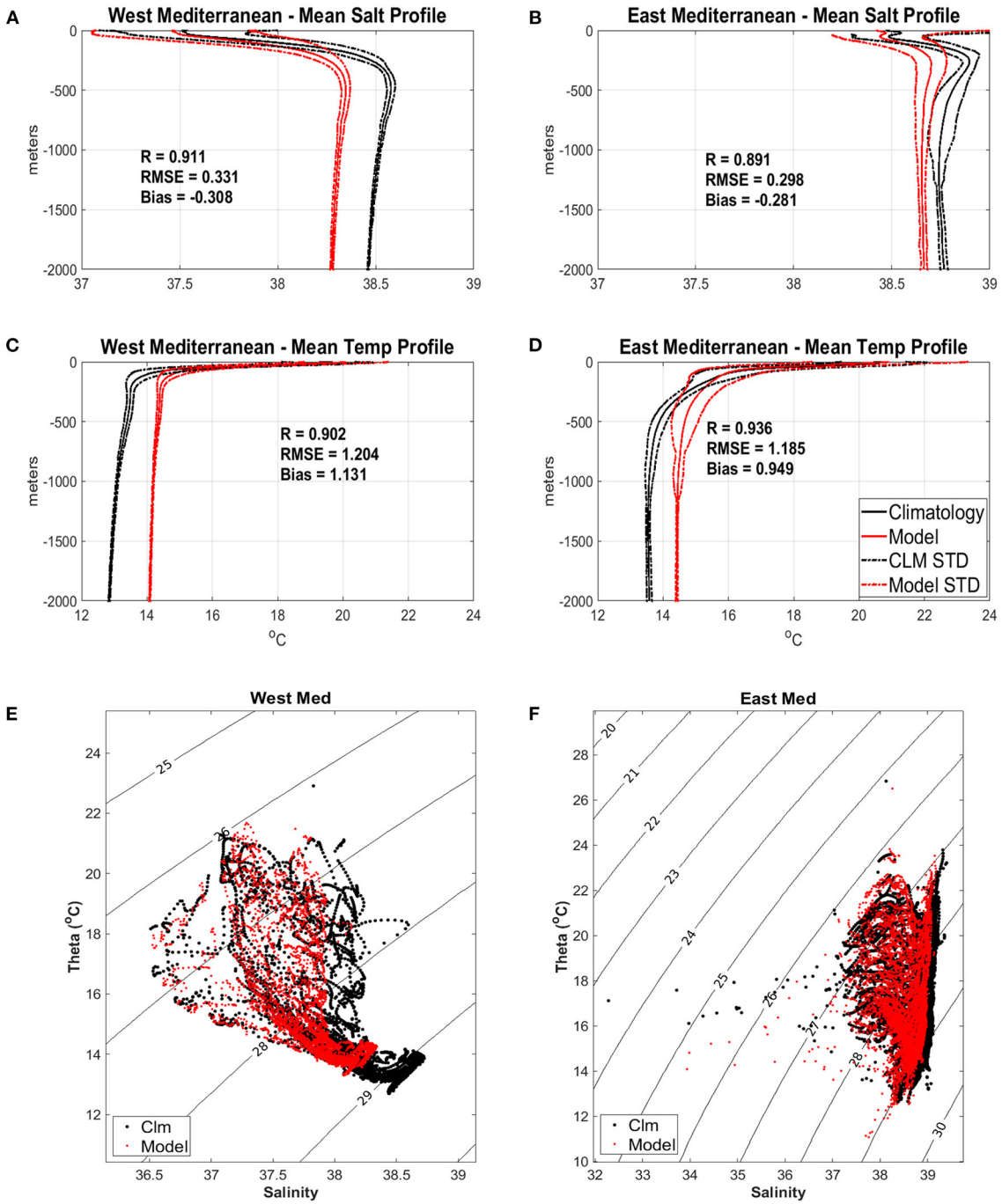

FIGURE 1 | Comparison of simulated (red) and observed (black) salinity (top) and temperature (middle) profiles for the Western **(A,C)** and Eastern **(B,D)** basins. Both mean profiles (solid lines) and mean ± one standard deviation (STD) (dashed lines) over the complete data sets are presented. The comparison of the mean values is extended to the corresponding θ/S diagrams in the bottom panels **(E,F)**.

To reproduce the seasonality of 12 and 9.1 ky BP periods, the monthly values of the heat fluxes were transformed using the factors $r_s = \frac{Q_{S_s}}{Q_{S_0}}$, $r_w = \frac{Q_{S_w}}{Q_{S_0}}$, where the terms r_s and r_w (**Figure 3A**) are given by the ratio of monthly average insolation at 38° latitude in 12 and 9.1 ky BP (Q_{S_s} and Q_{S_w}, respectively) to the corresponding insolation during the instrumental period (Q_{S_0}), based on the solar radiation calculations of Berger (1978) and Berger and Loutre (1991), exploiting the algorithm of Huybers and Eisenman (2006). Note that hereafter the subscript "s" denotes the experiment held under SBF (strong buoyancy

TABLE 1 | Values of the correction coefficients applied to the reference model to reach extreme case sea surface conditions similar to paleoceanographic conditions.

Period	Coefficients	
	at **(temperature)**	***as*** **(salinity)**
Younger Dryas	0.95	1.06
S1a sapropel deposition	1.16	0.95

loss and enhanced mixing conditions), whereas the subscript "w" signifies WBF (buoyancy gain and highly stratified conditions).

It should be noted here that, for the extreme climatic simulations, the exchanges through the Dardanelles Straits were not taken into consideration. This may not be consistent with the current conditions but is more compatible with the past periods that have been used to obtain the heat and freshwater forcing fields, as the water exchange between the Mediterranean Sea and the Black Sea was fully established only after the S1a sapropel deposition (∼8.7 ka BP, Sperling et al., 2003; 7.5 ka BP, Triantaphyllou et al., 2016) and the Black Sea was not a major freshwater contributor for the S1 deposition (e.g., Rohling et al., 2015). The momentum forcing and bathymetry remain unchanged in the context of hereby described experiments.

SBF: Model Set Up and Run

To implement the experiment held under SBF, simulating conditions similar to those of the Younger Dryas period, the monthly fields of heat flux (Q_N) and net evaporation (E_N) of the current period were transformed as:

$$Q_{N_s} = r_s \left(Q_S - \frac{Q_U}{a} \right) \quad (5)$$

$$E_{N_s} = k r_s E_N \quad (6)$$

where Q_{N_s} and E_{N_s} are the estimated monthly values of net heat flux and evaporation for the SBF period, respectively, r_s is the carrier of the seasonality difference between modern and Younger Dryas periods, Q_S is the solar radiation flux, and Q_U is the net heat flux from the other three heat flux components. The parameter k (Equation 6) is defined as the ratio of the net evaporation during the paleoceanographic period under investigation, over the current values. For the case of the Younger Dryas simulation, k has been empirically estimated to 1.8 after several numerical experiments. As the sea surface salinities of this period are comparable with the current values of the Red Sea, we used the net evaporation rate of the latter as a reference point to empirically estimate the parameter k. After spinning up the model, the mean sea surface salinity was compared to the mean core data reconstructions of the Younger Dryas, and the most suitable parameter value was selected. The increase in net evaporation E_N is equivalent to a lesser increase of evaporation E combined with a concurrent decrease of precipitation P or a change of $E-P$. The parameter α (Equation 5) was set equal to at_s and expresses the extra heat loss during Younger Dryas climatic conditions. For the extreme climatic simulations, it was assumed that the ratio of the heat fluxes is proportionate with the ratio of the SSTs and that is expressed by the parameter a.

Thus, the formulae for the surface boundary conditions (Equations 1 and 2) were used to determine the heat flux F_{H_s} and the salt flux F_{S_s} for the SBF experiment event at the air–sea interface and were modified as:

$$F_{H_s} = Q_{N_s} + C_T \left(at_s T^c - T_1 \right) \quad (7)$$

$$F_{S_s} = as_s E_{N_s} S_1 + C_S \left(as_s S^c - S_1 \right) \quad (8)$$

The modern-climatology values T^c and S^c were multiplied by the ratios at_s and as_s, respectively, to simulate mixed-period surface values, similar to those found in the Younger Dryas period. The model was initialized from the current climatology and then spun up for a total of 400 years while reaching a steady state after 160 years.

Similar to the baseline model runs, after the completion of the initial spin-up, the salt and heat monthly diagnosed fluxes (**Figure 3B**) were estimated, and the model was turned toward the diagnosed atmospheric fluxes and run for another 1,000 years.

WBF: Model Set Up and Run

According to the SBF simulation experiment, the circulation of the Mediterranean Sea was simulated under WBF (actually, weak buoyancy gain experiment). The final state of the Mediterranean, after the SBF experiment, was defined as the initial conditions of the WBF simulation. Given that the basin obtained the characteristics of a well-mixed basin after a 400-year-long period of spin-up run, the new forcing conditions were applied after gradually reducing the net evaporation and increasing the net heat flux over the basin until they reached the WBF experiment forcing values.

Similar to the calculations for the SBF experiment, the monthly fields of Q_{N_w} and E_{N_w} for the stratified conditions were estimated by replacing the term r_s with r_w in Equations (5) and (6).

For the surface fluxes (Equations 7 and 8), the coefficients at_s and as_s were replaced with at_w and as_w, respectively. In Equation (5) the parameter α was set equal to 1. Furthermore, in regard to the application of Equation (6), numerical experiments showed that the abrupt replacement of the parameter $k = 1.8$ (as used in the SBF experiment) to $k = 0.8$ (a realistic estimate of the reduced evaporation over the Mediterranean during the S1a deposition period (Myers, 2002; Meijer and Tuenter, 2007) caused numerical instability and blow up of the simulation. To reach the S1a period-like conditions, it was necessary to vary the evaporation ratio k as follows: For the first 80 years, the value $k = 1$ was used. For the next 200 running years, the coefficient k was set to 0.5, indicating half of the current evaporation rate. Finally, the model ran for 520 more years with $k = 0.8$. The model spin-up lasted 800 years totally. A steady state was reached after 120 years of the last k modification (the 440th year of spin-up).

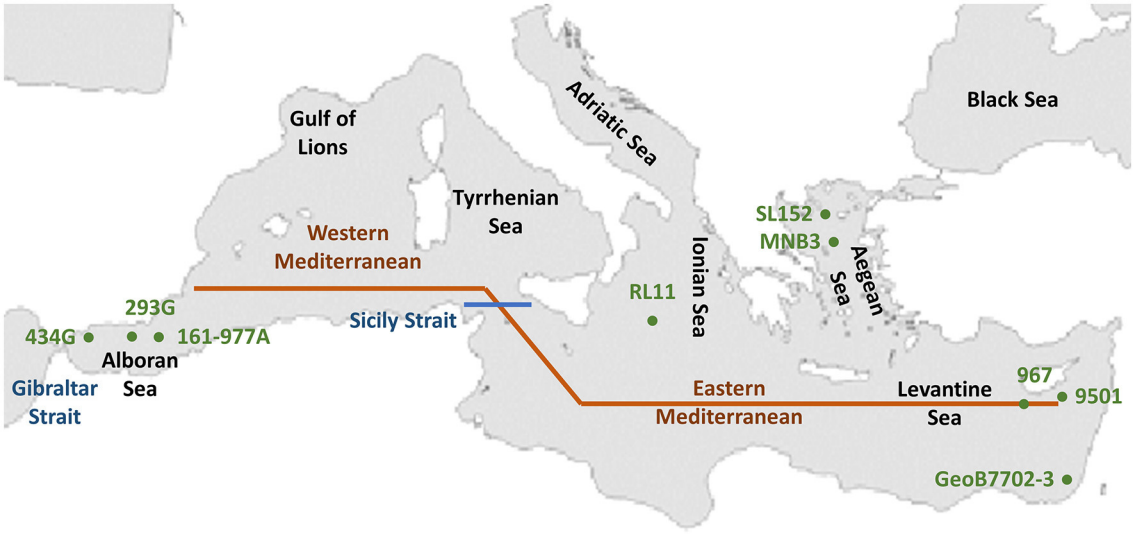

FIGURE 2 | Marine core sites and transects used in the present study.

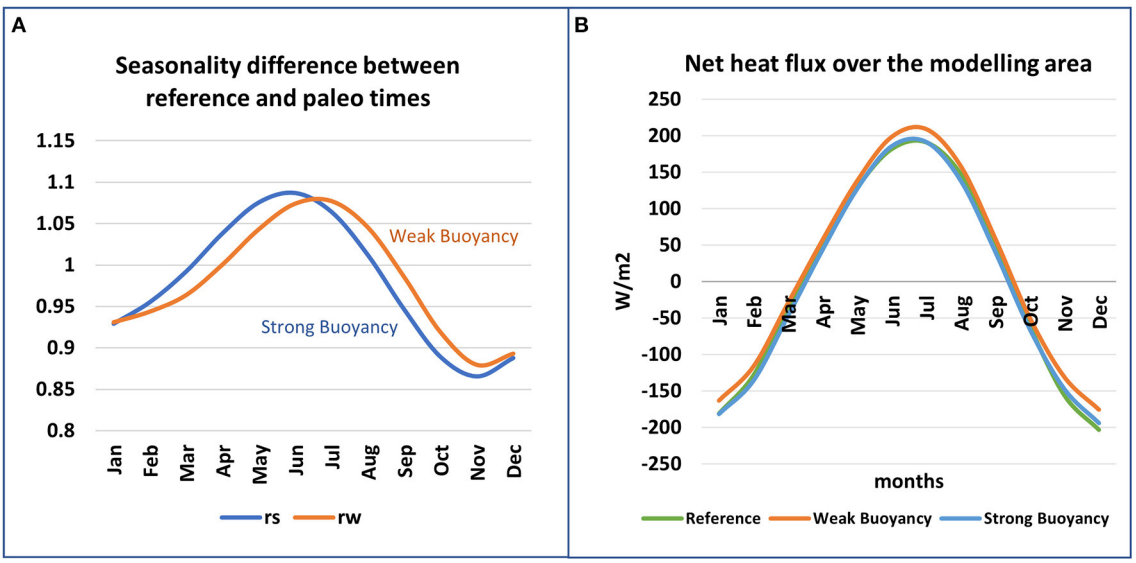

FIGURE 3 | (A) The term *r* gives the ratio of monthly average insolation at 38° latitude in 12 and 9.1 ky BP to the corresponding insolation during the instrumental period, **(B)** the net heat flux with the applied diagnosed fluxes for each experiment. The green line corresponds to the reference period, the blue to strong buoyancy forcing (SBF; Younger Dryas-like conditions), and the red one to the weak buoyancy forcing (WBF; S1a sapropel deposition-like conditions).

Then, in accordance with previous experiments and to enable the study of inherent centennial variability, the model was switched to the diagnosed boundary conditions and ran for another 1,000 years.

The seasonal cycle of the diagnosed surface heat fluxes for each experiment is shown in **Figure 3B**. The mean annual net heat flux in the Gibraltar Strait for each period was calculated to be +1.0 Wm^{-2} for the current period (a positive sign denoting eastward net heat flux, which corresponds to a surface heat loss), +5.5 Wm^{-2} for the strong buoyancy, and −6.8 Wm^{2} for the WBF.

Moreover, regarding the net freshwater fluxes applied for the experiments, the ratios of the diagnosed net E–P fluxes to the current value were calculated to be 2.8 and 0.63 for the SBF and WBF experiments respectively (computed on a mean annual basis).

Analysis of the Results

The basic characteristics of the mean circulation reproduced by each experiment and the interdecennial/intercentennial variability of the basin are described as follows.

Deep-Water Residence Time

The residence time of Eastern Mediterranean deep water was defined as the mean annual ratio V_M/R of the last 100 years of the model running with the diagnosed fluxes, where V_M is the volume of the Eastern Mediterranean Sea waters below 300 m (the depth below which the Aegean Sea is considered to influence the whole eastern basin) and R is the inflow of dense waters into the Eastern Mediterranean through the corresponding straits connecting them to the deep water sources of the basin, as represented by a double integral:

$$R = \int_{l_1}^{l_2} \int_{-h(x)}^{0} U dz dx$$

where

- For the reference climate simulation and the SBF experiment, U is the velocity of the incoming to the eastern basin dense waters through the Otranto Strait (for Adriatic-originated dense waters) and the Cretan Arc Straits (for Aegean-originated waters).
- For the WBF runs, U is the velocity of the incoming dense water to the eastern basin *via* the Sicily Strait since (as it is shown below) our simulation revealed that, during that period, the Western Mediterranean imports the buoyancy from the Eastern basin, in complete contrast to its current function.

Buoyancy Calculations

To investigate the thermohaline functioning of the Mediterranean Sea (concentration or dilution basin characteristics) under different extreme climatic conditions, the integrated lateral advective buoyancy fluxes through the Gibraltar and Sicily Straits were calculated for the last 500 years of simulations with the diagnosed fluxes by

$$F = \int_{l_1}^{l_2} \int_{-h(x)}^{0} -g\,(\rho - \rho_o)\, u dz dx$$

where l_2 *and* l_1 are the lateral limits of the transect, $h\,(x)$ is the bottom depth along the transect, ρ is the density at each point of the transect, ρ_o is the mean density of the corresponding basin, and u is the velocity component normal to the transect at each point.

Variability Analysis

To investigate the inherent spatial and temporal variability of the Mediterranean Sea, the EOF analysis was applied to the mean annual density fields of the last 500 years running with the diagnosed fluxes for each experiment, at different depths (30, 100, 200, 400, 800, 1,200, and 2,000 m), breaking each field data into "modes of variability." Following the terminology of Björnsson and Venegas (2001), the spatial patterns that are found are referred to in the text as EOFs and the time series as expansion coefficients. The importance of each EOF pattern is referred to as a contribution.

In all experiments, eight modes were found to represent 99.5% or more of the variability for all depths. For each mode, the power spectrum of the expansion coefficient was calculated to provide a description of the temporal variability of the mode. The spectra presented here calculated with seven sequential segments at a 50% overlay. When spectral shapes suggested that most of the energy lies in centennial variability, spectra were also computed using only three segments at a 50% overlay to provide the information of the lowest possible frequencies. However, for the purpose of clarity and consistency, the spectral results hereby presented are calculated using seven segments with a length of 125 years per segment.

To identify the most dominant frequencies of variability, the spectra of the simulated variability are compared with the theoretical continuous red-noise spectra of the same variance. To calculate the latter, first, the decorrelation time scale of each EOF expansion coefficient is computed, and then, the red-noise spectrum of a process exhibiting this decorrelation timescale is estimated (Hasselmann, 1976).

Finally, a cross-correlation between the expansion coefficients of modes at different depths was used to identify and cluster the layers with similar variability.

RESULTS

Overturning Functioning of the Mediterranean Sea Under Different Climatic Conditions

The simulation experiments produced three different thermohaline circulation patterns (**Figures 4**, **5**).

The mean millennial overturning circulation of the Mediterranean Sea for each numerical experiment reveals that both the basins behave as concentration basins in the reference and SBF experiments, whereas the eastern Mediterranean clearly becomes a dilution basin under the WBF conditions. A comparison of the zonal—vertical transport (computed as streamfunction fields) of the reference period (**Figure 4A**) to the corresponding calculations from the instrumental period (Adloff et al., 2011, 2015) suggests that the western basin shows significant differences while the eastern Mediterranean exhibits a very similar overturning circulation: the present simulation produces more waters that reach deeper layers in comparison to the results of (Adloff et al., 2011, 2015). Given the necessary compromises (primarily in terms of model resolution and the temporal average of atmospheric forcing) accepted to sustain a millennial simulation and independence from external variability and the good results from the comparison with climatology (see the section "Baseline (Reference Period): Model Validation"), we consider the results acceptable for our purpose.

As expected, the SBF simulation (**Figure 4B**) produces more dense water in the eastern basin compared to the reference experiment (**Figure 4A**), whereas the results in the western basin are rather surprising, due to the production of dense water extending over a larger area of the basin; however, most of the produced water does not reach the maximum depths of the basin, possibly due to a higher stratification in the deeper layers.

In the WBF experiment, the eastern Mediterranean switches to a dilution basin, exporting surface waters to the west (**Figure 4C**). The western basin exhibits some weak dense-water

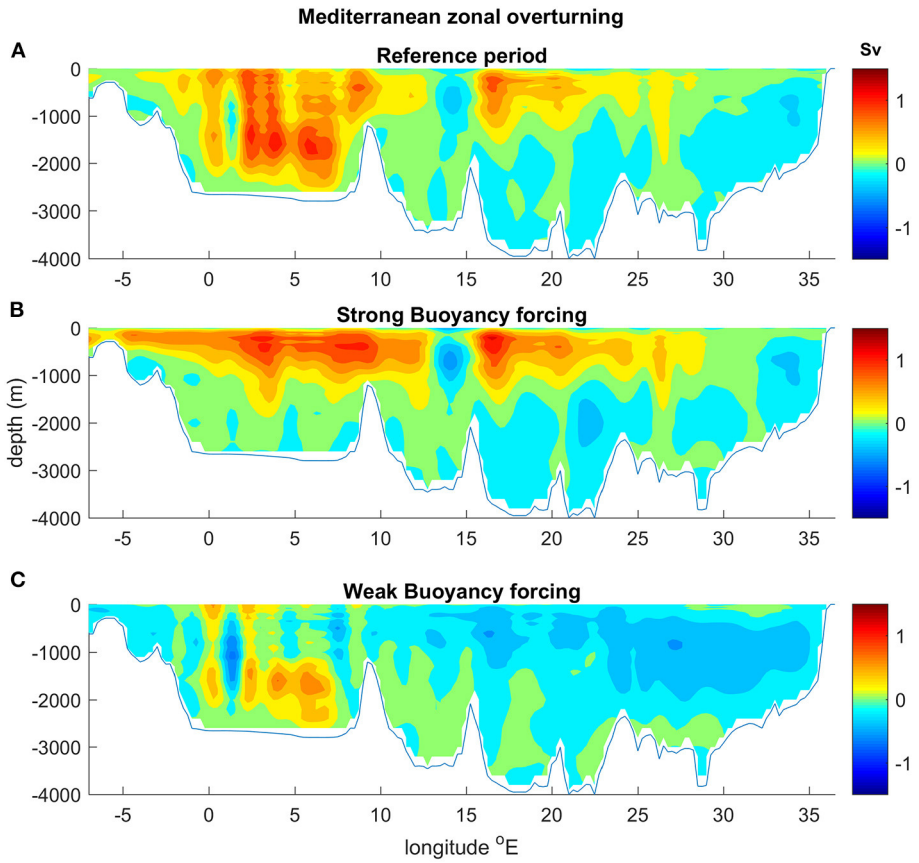

FIGURE 4 | The Mediterranean zonal overturning transport (estimated *via* streamfunction computation) for **(A)** the reference period, **(B)** the SBF, and **(C)** the WBF, as produced by the model experiments under the diagnosed fluxes. The transport is given in Sverdrups.

formation cells at the longitude of the Gulf of Lions; however, at both connecting Straits (Gibraltar and Sicily) the streamfunction sign suggests an exchange typical of dilution basins.

The thermohaline functioning of the Mediterranean basin as a whole can be assessed by examining the exchange in the Strait of Gibraltar (**Figure 5**). The reference simulation produces (as expected) a two-layer exchange, with the surface inflow of Atlantic waters and the outflow of Mediterranean waters below the depth of 100 m. This corresponds to a striking but consistent three-layer buoyancy exchange, with buoyancy import at the top and bottom layers and a thin layer of weak buoyancy export from 80 to 120 m, at the region of mixing between the two water masses (**Figure 5A**). Under SBF, the exchange is intensified and the interface between the two layers deepens to 130 m depth (as the net import from the Atlantic has to balance the enhanced net evaporation). Atlantic water flows into the basin through a layer extending from the surface to a depth of about 130m, whereas below that depth dense Mediterranean water is exported to the Atlantic Ocean. Under these conditions, the buoyancy-exporting layer is diminished at the interface depth. A comparison of the corresponding density transects along a zonal section of the Mediterranean reveals overall denser waters in both the basins during both experiments, and a zonal density gradient with denser waters in the eastern basin. In contrast, for the WBF (during a warm and humid climate), light waters and strong stratification dominate in the Eastern Mediterranean, and dense water is exported from the western basin to the eastern one (**Figure 5F**). During this period, the thermohaline functioning of the whole basin is reversed and the Mediterranean Sea acts as an estuarine basin, exporting upper and intermediate waters to the Atlantic (**Figures 5E,F**). Sluggish intermediate Mediterranean water from 30 to 180 m depths moves toward the Atlantic, which feeds the Mediterranean basin through deeper layers. The buoyancy export takes place through the surface and near-bottom layers, whereas the sluggish, thick intermediate layer is a net but an insignificant buoyancy importer.

Moreover, according to the calculation described in section Deep-Water Residence Time, the residence time of the Eastern Mediterranean deep waters was calculated to be centennial (∼100 years), semicentennial (∼55 years), and intercentennial (semi-millennium, ∼540 years), for reference climate conditions, the SBF experiment, and the WBF simulation, respectively.

Having described the millennial-scale climate of the basin for the three experiments, we can proceed to examine the

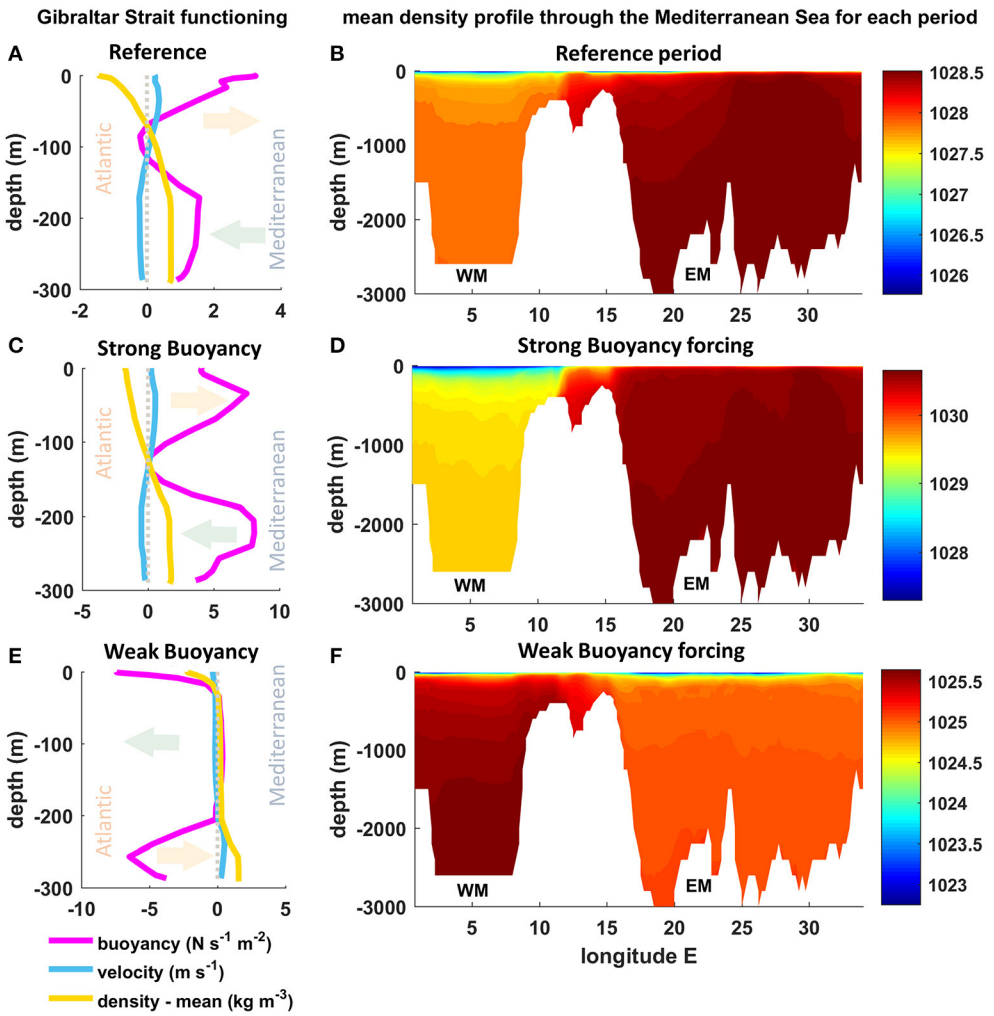

FIGURE 5 | Functioning of the Mediterranean Sea under the climate conditions of the three experiments: reference (top), SBF (middle), and WBF (lower panels). **(A,C,E)** reveal the overall functioning of the Mediterranean Sea as witnessed by the exchange at Gibraltar Strait. The pink arrow denotes the inflow of Atlantic water, whereas the light blue arrow corresponds to the outflow from the Mediterranean. The density distribution along the transect of **Figure 2** along the Mediterranean is shown in **(B,D,F)**. In all figures, the values are annual means, averaged over the last 100 years run with the diagnosed fluxes for each experiment.

inherent variability of the circulation at the interannual and intercentennial periods. Firstly, we will examine the variability of the thermohaline functioning of the whole basin, as evidenced by the Gibraltar exchanges (section Buoyancy and Its Variability in the Gibraltar and Sicily Straits). After that, the analysis is extended to the spatiotemporal variability of the interior of the basin, as revealed by the EOF analysis of the density fields (section EOF Analysis).

Buoyancy and Its Variability in the Gibraltar and Sicily Straits

Integrated buoyancy fluxes through the Gibraltar and Sicily Straits for the last 500 years of simulations using the diagnosed fluxes are presented in **Figures 6**, **7**. To reveal the inherent variability of the exchange (and thus the corresponding variability of the functioning of the basin), variance-preserving spectra of the buoyancy fluxes were calculated for each period.

According to the traditional oceanographic notation, northward and eastward directions are defined as positive to comprehend the direction of buoyancy flux through the Straits.

For the Gibraltar Strait (flow along the east–west axis), the buoyancy exchange corresponds to an inflow for the reference simulation (mean of 0.88×10^7 N/s, **Figure 6A**) and also an even stronger inflow for the SBF experiment (mean 3.74×10^7 N/s, **Figure 6C**); for the WBF simulation, the negative values indicate the net buoyancy export from the Mediterranean Sea (mean -1.04×10^7 N/s, **Figure 6E**), i.e., the import of dense waters from the Atlantic. These calculations suggest that the Mediterranean Sea shows two "opposite" phases between the experiments. It behaves as a concentration basin under the reference and SBF conditions and as a dilution basin during the WBF experiment.

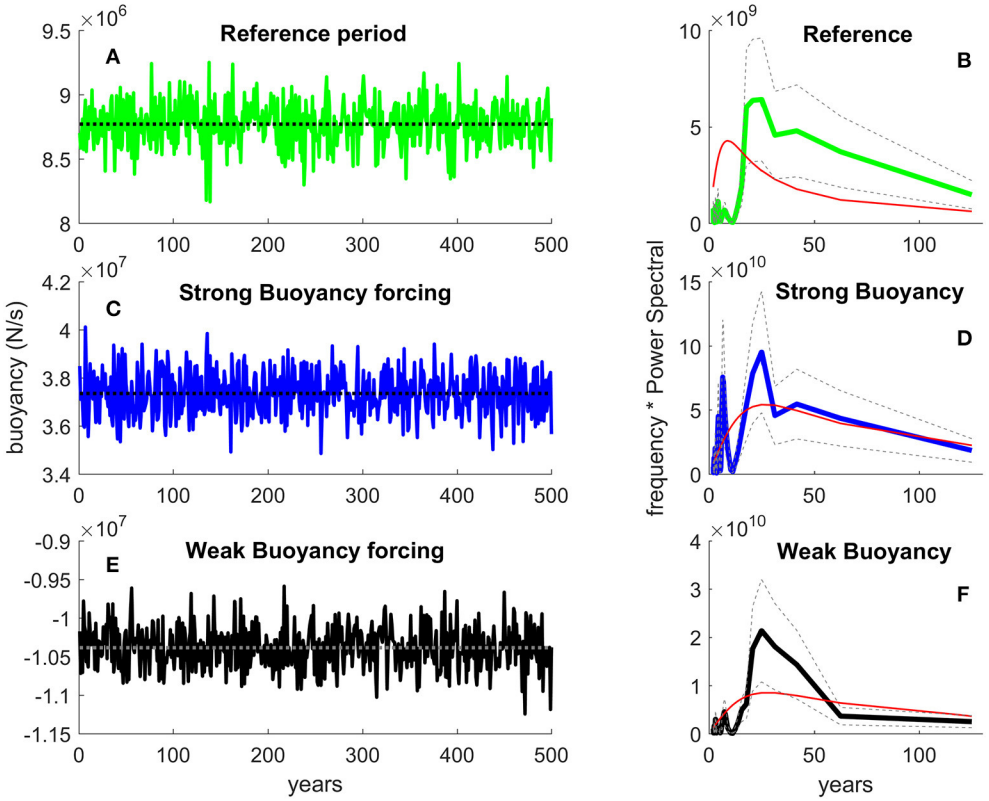

FIGURE 6 | Transect-integrated buoyancy fluxes **(A,C,E)** and variance-preserving spectra **(B,D,F)** through the Gibraltar Strait of the last 500 years of simulations with the diagnosed fluxes for the reference **(A,B)**, SBF **(C,D)** and WBF **(E,F)** experiments. The dashed gray lines surrounding the mean spectral estimate correspond to the 90% confidence intervals. For comparison, the corresponding normalized red noise of the same variance is overlaid (red lines). Positive values correspond to eastward buoyancy flux.

For the Sicily Strait, where the flow is mainly meridional, the negative buoyancy flux values observed during the reference period (mean -0.67×10^7 N/s, **Figure 7A**) and SBF (mean -2.59×10^7 N/s, **Figure 7C**) simulations indicate that dense water from the eastern basin is exported to the western. The positive flux during the WBF period (mean 4.84×10^6 N/s, **Figure 7E**) shows an opposite functioning. The Eastern Mediterranean under these climatic conditions functions also as a dilution basin in agreement with the analysis mentioned in section Overturning Functioning of the Mediterranean Sea Under Different Climatic Conditions.

The long-term simulations revealed that the integrated buoyancy fluxes at the Straits oscillate on different timescales, but in all the experiments, a decennial variability dominates in both the Gibraltar and Sicily Straits (**Figures 6B,D,F**, **7B,D,F**).

The variance-preserving spectra of the buoyancy flux through the Gibraltar Strait (**Figures 6B,D,F**) reveals that the variability is mainly intercentennial (peaking at a period of about 20–25 years), whereas interannual periods are responsible for a significantly smaller part of the variance. We note a relatively higher contribution of interannual variability (at periods of around 5 years) in the SBF experiment compared to the reference period and the diminishing contribution of interdecennial variability during the WBF experiment.

In the Sicily Strait, the interannual and interdecennial variabilities dominate the variance of the buoyancy exchange (**Figures 7B,D,F**). For all experiments, the spectral peaks are concentrated in the periods between 10 and 25 years, whereas a secondary peak appears at a period of about 40 years for the reference period. As in the case of Gibraltar, the interdecennial periods do not contribute much to the variance of the buoyancy exchange.

EOF Analysis

There is probably no better way to describe the mean spatiotemporal variability of a basin than EOF analysis. The eight lowest modes of spatiotemporal variability obtained from the EOF analysis in seven depths characterizing the shallow (30 and 100 m), intermediate (200 and 400 m), and deeper layers (800, 1,200, and 2,000 m) of the Mediterranean, account for >99.5% of the density variability. In the reference period, the variability of density is observed to be a synthesis of several modes with important contribution of each mode even at deeper layers—the first two EOF modes at 1,200-m depth express only 60% of

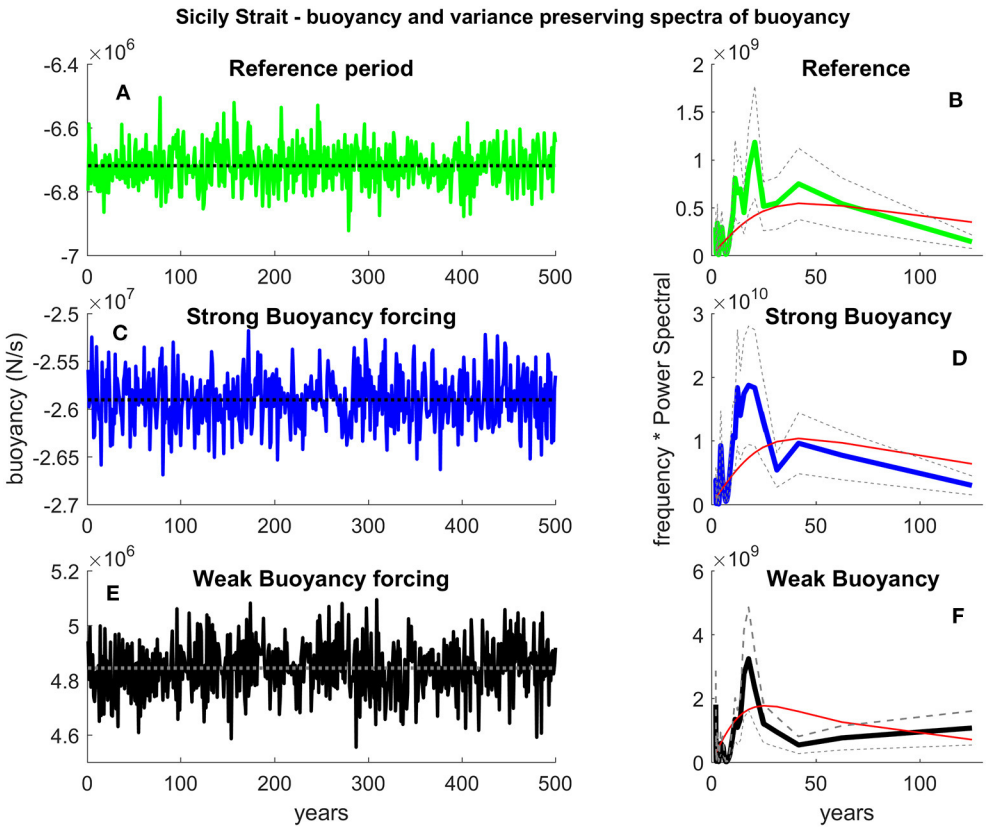

FIGURE 7 | (A–F) Transect-integrated buoyancy flux through the Sicily Strait (as in **Figure 6**). Positive values correspond to a northward buoyancy flux.

the variability. In contrast, the density variability of the deeper layers at extreme climatic simulations can be described by only the first two EOF modes as they represent more than the 90% of the variability (**Figure 8A**).

Qualitative characterization of the more pronounced oscillation scales, as produced by the variance-preserving spectra of the expansion coefficients, for all depths and for the three experiments is shown in **Figure 8B**. Interannual variability refers to the main spectral peaks in the period between 2 and 9 years, the decennial between 10 and 20 years, the interdecennial between 21 and 80 years, the centennial between 80 and 120, and the intercentennial over 120 years. In all the experiments, the interannual and decennial variabilities dominate in upper layers. The deeper layers of the current period show also interdecennial and centennial variability. Considering that the variability at all depths is a contribution of several EOF modes during the current period, it is shown that the variability in upper layers is a synthesis of interannual and decennial modes and in the deeper layers the variability is more a synthesis of centennial and decennial/interdecennial oscillations (**Figures 8A,B**). In case of SBF conditions, the upper layers are dominated by the decennial and interannual variabilities, whereas in deeper layers the first two EOF modes exhibit intercentennial and interdecennial oscillations, respectively. Higher EOF modes with a low contribution to deeper layers show a decennial variability. For the WBF simulation, the modes of the upper layers show mostly an interannual variability. In deeper layers, the first two modes express intercentennial and centennial oscillations, respectively. Higher modes with a very low contribution to the variability have an interannual and a decennial variance.

Spatial and Temporal EOF Variability and Clustering

In each experiment, expansion coefficients of the modes from the different depths were subjected to a cross-correlation analysis to identify modes representing vertically coherent motions. Finding the depths that exhibit a similar temporal variability (correlation $> 95\%$) leads to the identification of respective horizontal EOF modes representing vertically coherent motions.

In the following sections, the most dominant EOF modes exhibiting vertically coherent variability are presented.

Reference Period

In the deeper layers of the reference period, the variability is dominated by interdecennial periods of density variability with a maximum of ∼63 years. This variability is recorded in the second and first mode at the layers of 800 m depth and the deeper layers, respectively (**Figure 9**) and corresponds to an oscillation of almost the entire Mediterranean Sea in phase agreement between the depths of 800 and 2,000 m. The contribution of this variability ranges from 24.8 to 51.8% in the upper and

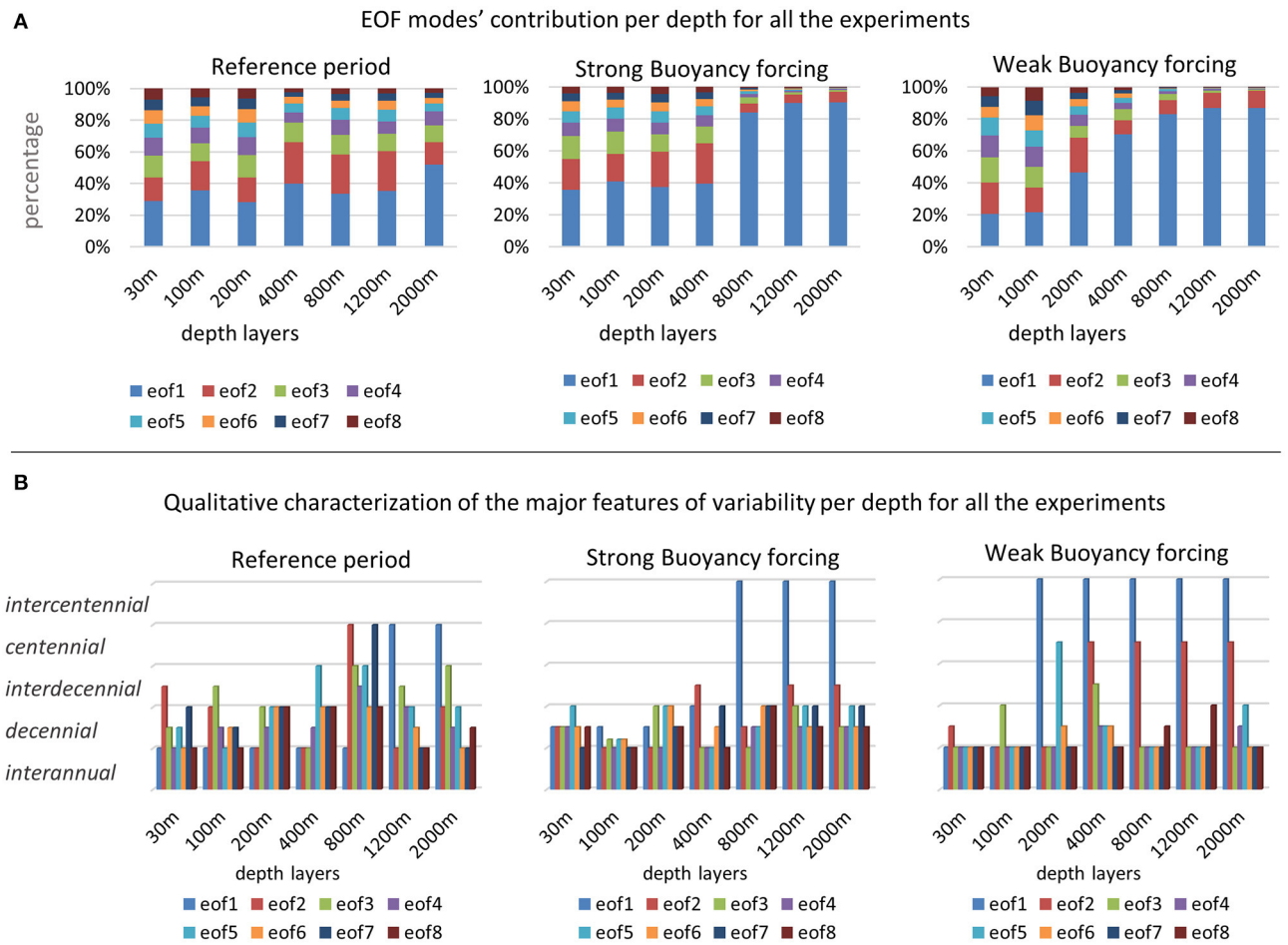

FIGURE 8 | (A) Empirical orthogonal function (EOF) mode contribution and **(B)** qualitative characterization of the dominant temporal variability of the first eight EOF modes of density variability at all depths for the three experiments (reference buoyancy forcing, SBF, and WBF).

deeper layers, respectively. This mode of oscillation exhibits its peak variability in the Western Mediterranean, with reduced amplitudes in the Eastern basin, and probably reflects the dense-water formation processes, which are more energetic and exhibit great variability in the western basin. This variability can also be associated with the renewal time of the deep water of the Mediterranean Sea.

The EOF analysis of the reference period also reveals an interannual variability, with a moderate coherence from the upper to deeper layers, showing strong opposite phases in a part of the Eastern Mediterranean, southwest of Crete. **Figure 10** presents the two clusters of intermediate (200 and 400 m depth) and deeper depths (800 and 1,200 m). Upper depths (200 and 400 m) are in phase with the mode of 1,200 m depth and out of phase with the first EOF of 800 m. This variability is related to the dense water export from the Aegean Sea, which appears to be related to a gyre-like circulation in the Ionian basin (based on the EOF amplitude distribution around the basin, observed at all depths, but more clearly in the deeper layers), a mechanism reminiscent of the BIOS mechanism.

SBF Experiment

As revealed through the EOF analysis of the results of the SBF experiment, the major variability caused by extremely cold and dry atmospheric conditions over the Mediterranean is found in the first mode and is related to a vertical exchange of buoyancy between the deep intermediate (800 m) and the very deep layers of the basin (>1,200 m). Thus, this variability is related to a variation of the deep stratification of the Mediterranean and is characterized by very long temporal scales (**Figure 11**). In the correlated depths of 800, 1,200, and 2,000 m, this variability is expressed by the first EOF modes and represents over 83% of the variability of the basin in deep waters (83.9, 89.6, and 89.9% at 800, 1,200, and 2,000 m, respectively).

The second mode of variability in the deep layers describes the buoyancy exchange between eastern and western basins (**Figure 12**). The variance-preserving spectra of the expansion coefficient indicate a strong decennial (∼14 years) and interdecennial variability of density. The interdecennial variability may correspond to the water residence time of the Eastern Mediterranean, as calculated earlier. The 14-year peak is

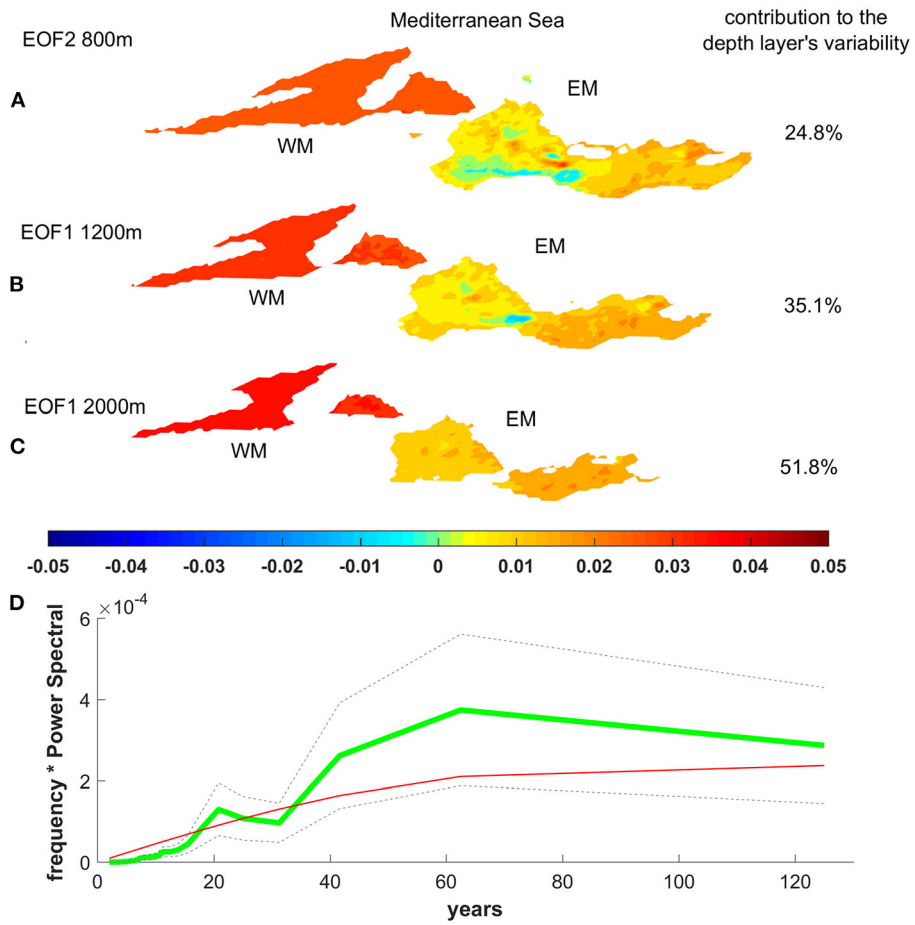

FIGURE 9 | The second EOF mode of 800 m depth **(A)** and the first EOF modes of 1,200 and 2,000 m of the current experiment **(B,C)**, whose expansion coefficients are well-correlated. Here the variance-preserving spectrum of the 2,000 m first EOF is presented (green line), along with its 95% confidence intervals (dashed gray lines) and the normalized red noise (red line) **(D)**.

near to a 13-year cycle that is present at the buoyancy variability of Sicily Strait and may represent the pulses of feeding the western basin with the dense water of the Eastern Mediterranean Sea. Note that this mode exhibits a strong amplitude at 1,200 m in the Tyrrhenian Sea and minimal signature in the Algero-Provencal basin, but its signal is strong throughout the western basin at the deeper layers, a fact signifying the role of the lateral advection of Levantine waters and the subsequent formation in the Gulf of Lions and dispersion in the bottom layers.

Stratified Period Experiment

In the period of extreme stratification (caused by excessive warm and humid conditions), the first EOF modes from 200 to 2,000 m depth show that the whole Mediterranean Sea is in phase and oscillates in intercentennial timescales (**Figure 13**). The variance contribution of the first mode ranges from 46.4% at 200 m to 86.5% at 2,000 m depth. The increased values of the Eastern basin suggest that this variability is driven by this basin, and the intercentennial variability is in accordance with the residence time of the Eastern basin waters that has been estimated to be ∼540 years.

The second EOF modes of deeper layers (800, 1,200, and 2,000 m depth) of the stratified period experiment exhibits an interdecennial variability (∼63 years) (**Figure 14**). All three depths are in phase with the negative values in the Western Mediterranean and close to zero, which gradually are becoming positive with depth in the Eastern. The two subbasins exhibit a phase difference, suggesting that this mode represents a lateral buoyancy exchange; furthermore, this process appears to be driven by the Western Mediterranean (in accordance with a reversal of the buoyancy exchange between the eastern and western basins during highly stratified conditions similar to the S1a sapropel formation period, as described in section Overturning Functioning of the Mediterranean Sea Under Different Climatic Conditions). Furthermore, a signal of opposite phase to that of the Western Mediterranean is concentrated south

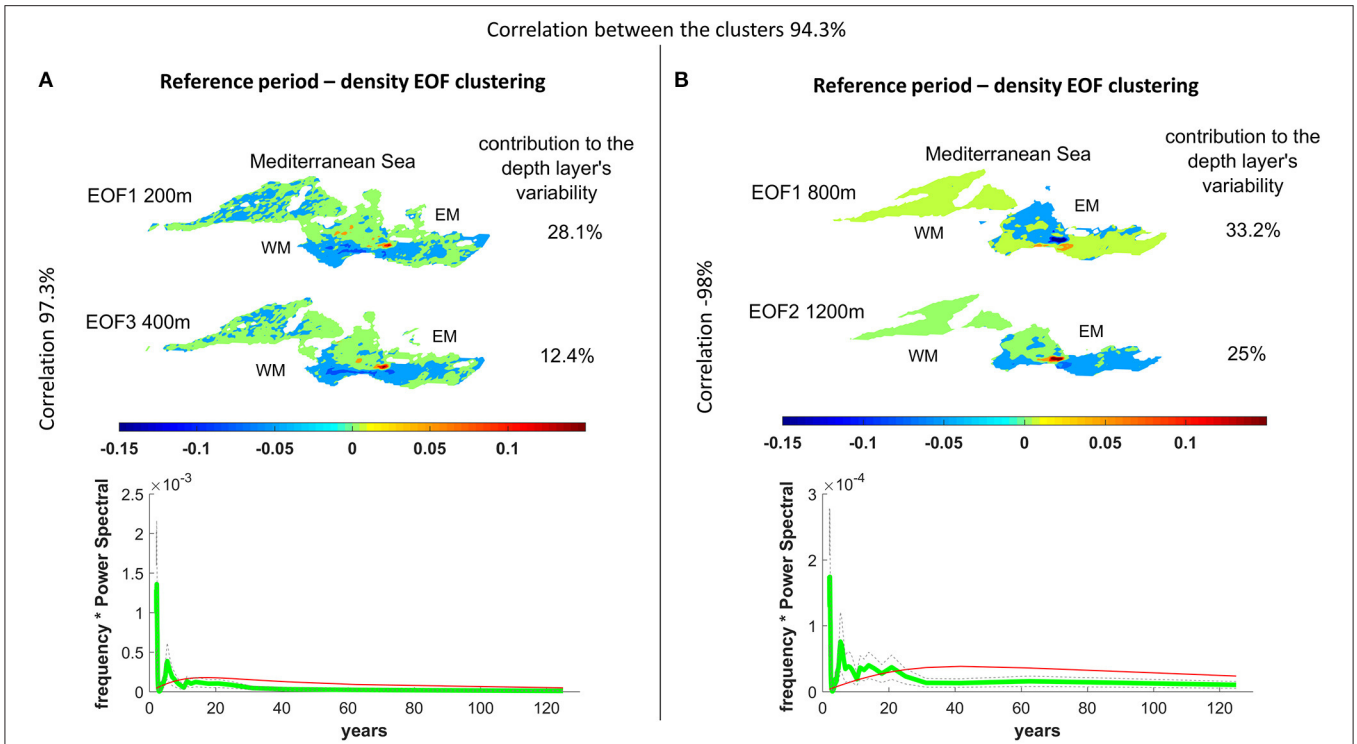

FIGURE 10 | As in **Figure 9**, for the two clusters of **(A)** intermediate (first EOF of 200 m and third EOF of 400 m depth) and **(B)** deeper layers (first EOF of 800 m and second EOF of 1,200 m) with a 2-year cycle of variability as shown from the variance-preserving spectrum of the EOF modes of 400 **(A)** and 1,200 m **(B)**, respectively.

of Crete at 800 m, but gradually fills the deeper layers of the eastern basin.

DISCUSSION

Although the extreme climate simulations are not designed to reproduce the paleocirculations of S1a sapropel deposition and Younger Dryas event (our adjustment does not involve any modification of the wind-stress fields and sea level of these periods). Topper and Meijer (2015) have used numerical simulations to show that the size of the Gibraltar restriction may affect the salinity and temperature of the whole basin but that the size does not have much impact on the inter-basin exchanges and circulation, especially of the Eastern basin. Thus, it is possible to assess the validity of our results based on paleoceanographic analyses of the Younger Dryas and S1a periods, keeping in mind that our simulations cannot be treated as reproductions of the paleocirculation.

Comparison of SBF Results to the Sedimentary Records From Younger Dryas

The overturning circulation of the SBF period in the Mediterranean Sea is presented as more energetic than the current one and as more intense in the eastern basin. The buoyancy exchange in the Gibraltar Strait under these conditions is much more intense than today. In agreement, grain size records from the northern and the southern parts of the Gulf of Cadiz reveal enhanced Mediterranean outflow water velocity (Toucanne et al., 2007) and a strong advection of the Mediterranean outflow water to the Atlantic during the Younger Dryas period (El Frihmat et al., 2014), respectively. Paleoceanographic analysis also suggests an even stronger export of LIW into the western basin during the Younger Dryas event (Dubois-Dauphin et al., 2017).

The residence time of the Eastern Mediterranean deep waters during the strong buoyancy conditions calculated on a semicentennial timescale. This calculation is also reflected in the interdecennial cycles of the inherent oscillations of deep waters, from first and second EOF modes of variability of deeper layers.

Comparison of WBF Results to S1a Sapropel Deposition Period

This study suggests that the Mediterranean Sea exhibited an estuarine behavior during the WBF experiment. Circulation pattern reversal during the sapropel deposition has already been proposed by Thunell and Williams (1989). Although other model studies for the S1 sapropel deposition proposed that the Mediterranean Sea circulation remained anti-estuarine (Myers et al., 1998; Myers, 2002; Meijer and Tuenter, 2007; Adloff et al., 2011), benthic foraminiferal carbon isotope variations indicate a significant presence of North Atlantic Central Water mass in the southern part of the Gulf of Cadiz (El Frihmat et al., 2014) in agreement with our results. Moreover, based on the contourite grain size from the Gulf of Cadiz (core MD99-2341, 582 m

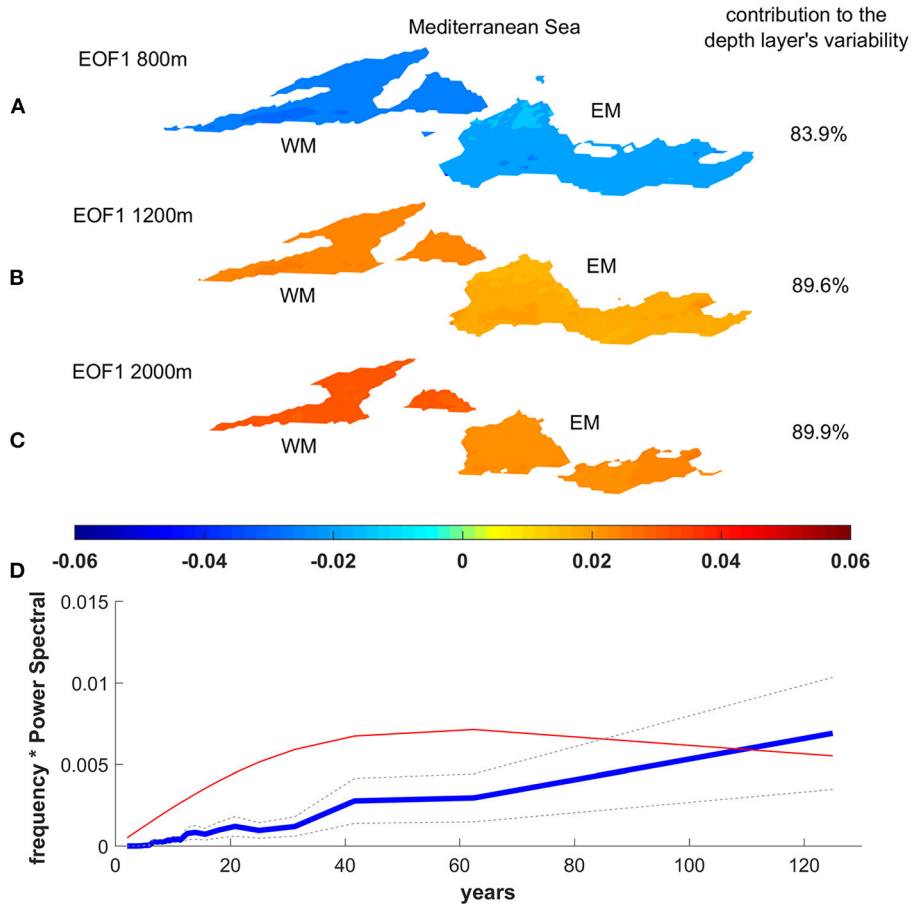

FIGURE 11 | The first EOF modes of 800 **(A)**, 1,200 **(B)**, and 2,000 m **(C)** depth of the SBF experiment, whose expansion coefficients are well-correlated. Here, the variance-preserving spectrum of the 2,000 m first EOF is presented as **(D)**.

depth), a sluggish Mediterranean water outflow is inferred during the Early Holocene, synchronous with sapropel S1 (Toucanne et al., 2007), and records from the Alboran Sea indicate relative low oxygenation (Jiménez-Espejo et al., 2015). Recent findings from neodymium isotopic composition in foraminifera and corals of the Western Mediterranean Sea (Dubois-Dauphin et al., 2017) imply that, during S1a-like conditions, the Western Mediterranean is not very sensitive to hydrological contributions from the eastern basin and that the intermediate water of the western basin is mainly locally formed.

The results of the WBF period simulation suggest also that, in the Sicily Strait, the western basin feeds the eastern with denser waters (**Figure 5**). This functioning could be an explanation for the total lack of sand grains and layer barren of foraminifera in Malta Graben (Ferraro et al., 2018), which indicates different processes on the seafloor.

The residence time of the Eastern Mediterranean deep waters under WBF was calculated to be semimillennial. This calculation is reflected in the inherent oscillation of deep waters, from the first EOF modes of the variability of the intermediate and deeper layers. The estimate of intercentannial variability (**Figure 13**) relates well with the dominant variability, 300–600 years, of the enrichment of the redox-sensitive trace metals during the early S1 in the Eastern Mediterranean (Jilbert et al., 2010).

Records from the Adriatic Sea (Tesi et al., 2017) indicated that a weakening of North Adriatic Deep Water production controlled the sapropel development in the Adriatic and Ionian Seas and that the Adriatic S1 onset was synchronous with the other sites of the Eastern Mediterranean, suggesting a wide-basin, physical-driven mechanism, which hampered the dense water formation over the entire Eastern Mediterranean Sea. Notably, during S1 sapropel deposition, the sediment core findings of the Aegean Sea reveal that sapropel was deposited in dysoxic/oxic conditions (Abu-Zied et al., 2008; Triantaphyllou et al., 2009b, 2016; Triantaphyllou, 2014) and that local deep-water formation for the North Aegean Sea during S1 is documented by Schmiedl et al. (2010). This functioning of the Aegean Sea may relate with the interdecennial internal variability to the region and with limited dense water production during the stagnant periods of the Mediterranean Sea (**Figure 14**), suggesting EMT-like events

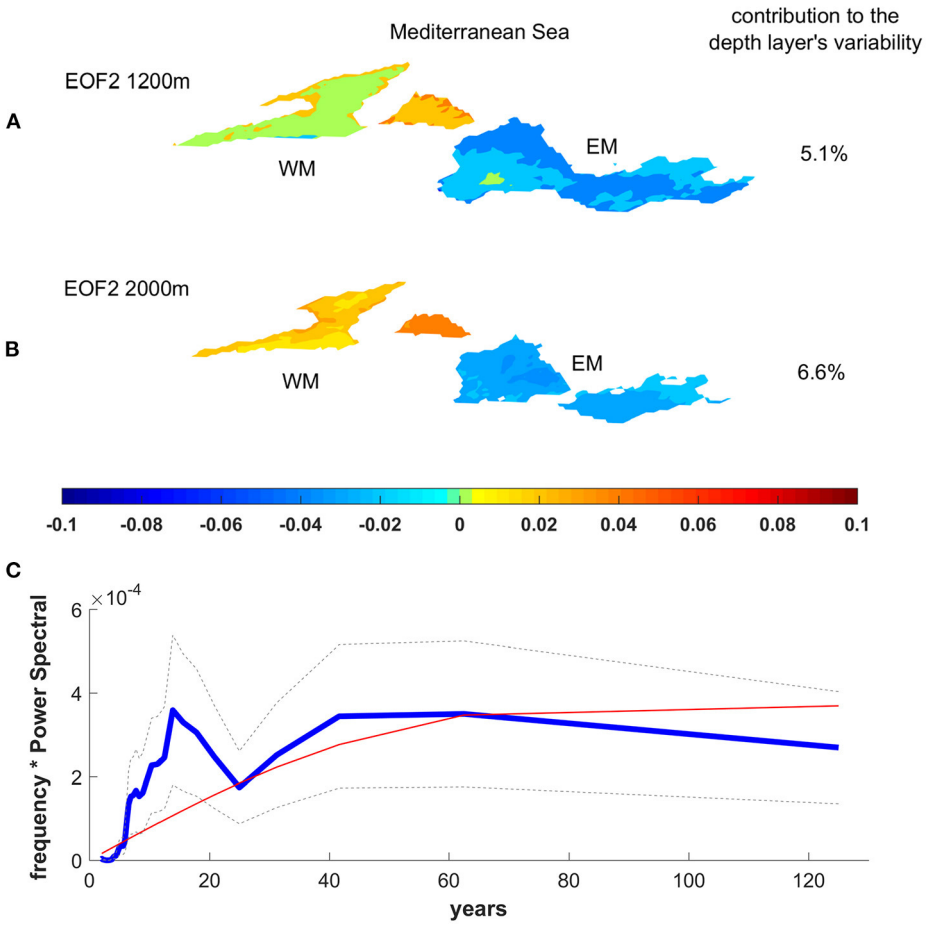

FIGURE 12 | The second EOF modes of 1,200 **(A)** and 2,000 m **(B)** depth layers of the SBF experiment, whose expansion coefficients are well-correlated. Here, the variance-preserving spectrum of the 2,000 m first EOF is presented as **(C)**.

during the stratified period. Relevant EMT-type events have been also recognized over the last five centuries (Incarbona et al., 2016).

Comparing the Three Experiments

The model results revealed that the Mediterranean Sea exhibits high sensitivity to climatic conditions, its functioning may alternate from concentration to estuarine and that the basin presents inherent interannual, interdecennial, and intercentennial variability. Maybe the most striking result regarding the mean overturning circulation is that, under the reference period, deep water formation in the western basin appears to be stronger and deeper than that during the SBF experiment. This result requires further investigation; however, this paradox has been also pointed out by Cisneros et al. (2019), who, combining oceanographic mooring measurements and sediment cores from the western Mediterranean, argue that the strongest dense-water formation events do not coincide with the coldest winters over the region. Investigation of this result is beyond the scope of this study; however, it is a very intriguing finding.

In all experiments, the upper layers of the basin are dominated by the interannual/decennial variability. The long-term simulations revealed that the integrated buoyancy fluxes in the Straits oscillate on different timescales, but in all the experiments, a decennial variability dominates in the Gibraltar and Sicily Straits.

The second EOF modes of deep waters under both the paleoclimate scenarios showed that the western and eastern basin functions on opposite phases in decennial (for the mixed case) and centennial (for the stratified case) timescales of variability. Especially in the case of the stratified conditions, the phase difference between the western Mediterranean and the region south of Crete suggests the possible existence of a mechanism similar to BIOS (Borzelli et al., 2009; Gačić et al., 2010), which refers to the buoyancy exchange, not between the Adriatic and the Aegean Sea but, between the Western and Eastern basins (where the deep water formation response in the Eastern basin

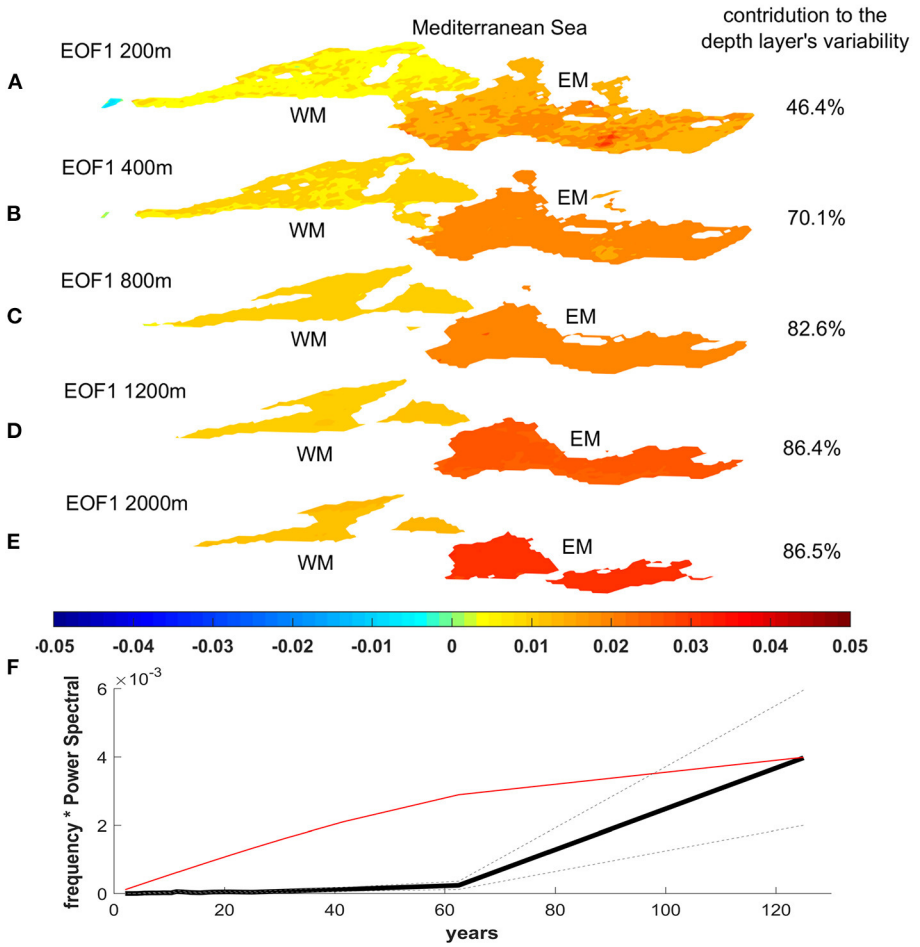

FIGURE 13 | The first EOF modes from 200 to 2,000 m depth **(A–E)** of the WBF experiment, whose expansion coefficients are well-correlated. Here, the variance-preserving spectrum of the 2,000 m first EOF is presented as **(F)**.

is centered in the Aegean Sea, most probably due to the lack of buoyancy input through the Dardanelles). This observation requires further investigation (especially the processes involved in this result), which however exceeds the context of this study.

More than 90% of the deep layer variability of the Mediterranean basin under extreme climatic conditions can be described by the first two EOF modes. The deeper Mediterranean basin under the current climate conditions is a synthesis of modes of variability, which is more than those during the other two experiments (the two first modes express only ∼60%). The above suggests that, during both extreme climatic conditions, the deeper layers tend to exhibit larger lateral scales of circulation features. Having excluded momentum forcing and vorticity exchange between atmosphere and ocean as a potential source of this result, the sources of this behavior could be different for the two extreme cases, ranging from different internal Rossby radii associated to the different stratification profiles to the isolation of the deeper layers during the highly stratified conditions.

A comparison of the spectra of the lateral buoyancy exchanges through the Straits and of the spectra of the density variability through the EOF analysis is rather revealing: the buoyancy flux variability at the Straits is dominated by interdecennial periods, throughout all experiments, whereas the deep-water density EOF temporal variability is dominated by centennial periods, especially for the WBF experiment. This difference could partly be attributed to the fact that the Strait exchanges are affected by the variability at the surface/intermediate layers, which is of a higher frequency than the deeper layers and is partly due to the impact of barotropic motions on the Strait exchanges, which, being faster in response, would tend to shift the spectrum to higher frequencies.

A dominant oscillation mode is identified both at the reference and the WBF experiments and exhibits depth coherent, in-phase inter-decadal oscillations in the deeper layer, which are more energetic in the western basin and diminish in the eastern Mediterranean. This motion is related to the overturning

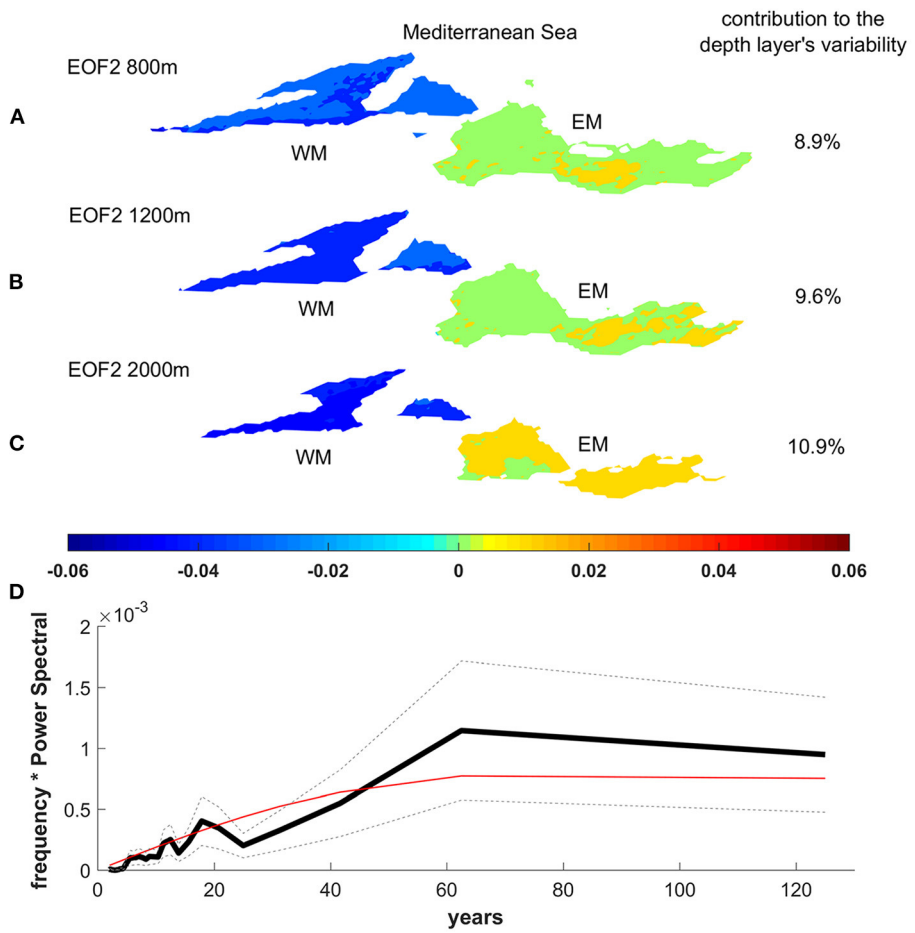

FIGURE 14 | The second EOF modes of 800, 1,200, and 2,000 m depth **(A–C)** of the WBF experiment, whose expansion coefficients are well-correlated. Here, the variance-preserving spectrum of the 2,000 m second EOF is presented as **(D)**.

mechanisms of the western Mediterranean, which still operate under the WBF conditions.

Another interesting mechanism of inherent variability is the exchange of buoyancy between the intermediate and deep layers observed at the SBF simulation. This mechanism reflects the alternation of deep water formation (which enhances deep stratification, carrying buoyancy upward) and subsequently a gradual homogenization through turbulent mixing, which gradually homogenizes the water preconditioning for the next formation event.

Finally, EOF modes exhibiting phase differences between the eastern and the western basins reveal another inherent mechanism of a lateral buoyancy exchange through the Sicily Channel. It is a mechanism known to the Mediterranean oceanographic community, which has witnessed at least a part of it through the recognition of the role of inter-basin water exchange on deep water formation processes in the western Mediterranean (e.g., Amitai et al., 2021).

This study has been only a preliminary effort to investigate the inherent dynamics of the Mediterranean Sea under extremely different stratification conditions. The heat and freshwater atmospheric forcing for the two experiments have been adjusted based on two extreme cases within the Holocene period. However, our simulation cannot be regarded as efforts to reproduce the exact circulation during the Younger Dryas and the S1a sapropel deposition periods, as the atmospheric heat and freshwater fluxes have been diagnosed from SST and salinity records, the momentum forcing has remained the same as in the current period (a dynamical inconsistency for the atmospheric circulation), the perpetual year assumption for the forcing violates the very important role of the interannual variability on the Mediterranean deep water formation processes, and the bathymetric changes due to sea-level variability (important especially at the connecting Straits) have not been considered. An effort to reproduce the circulation during these two periods of the Holocene requires all the above issues to be addressed. However, this study has shed light on the characteristic trends

of the inherent variability of the Mediterranean and furthermore revealed possible processes similar to the BIOS mechanism acting between the two major Mediterranean basins.

CONCLUSIONS

The aim of the present study was to investigate the spatiotemporal characteristics of the inherent variability of the Mediterranean Sea at two extremely different climate states from the Holocene period, as well as the present climate state. To achieve that aim, three long-term simulation experiments were designed: the instrumental period of 1973–1993 was selected based on the simulations by Skliris and Lascaratos (2004), Skliris et al. (2007) as a reference. The numerical experiment simulating the Mediterranean under a strong buoyancy loss to the atmosphere used sea surface conditions similar to the Younger Dryas period, a cold and dry period for the atmosphere. The experiment simulating the weak buoyancy gain from the atmosphere used the sea surface conditions from the period of S1a sapropel deposition, a period characterized by a maximum stratification and warm and humid atmospheric conditions.

The model used in these studies was modified accordingly by removing all climatological relaxation terms, adopting a perpetual year approach (to remove external forcing) and applying monthly diagnosed heat and freshwater fluxes at the surface, as estimated from the sea surface properties given by instrumental climatology for the reference period and sedimental record for the two extreme climate experiments. To simulate as closely as possible the Younger Dryas and S1a periods, solar irradiance was modified accordingly, and the Mediterranean was isolated from the Black Sea.

The mean hydrographic conditions arising from the two extreme case experiments show that, during the SBF experiment, overturning is accelerated, the export of dense Eastern Mediterranean waters to the western basin is intensified, and the residence times become significantly shorter than present-day values. On the other hand, the WBF experiment, through which the Mediterranean gains buoyancy from the atmosphere and switches to a dilution basin, results in an estuarine Eastern Mediterranean, a western basin exhibiting local cells of limited dense-water formation and multi-centennial residence times of the deep waters.

The results of the simulations showed that the inherent variability of the Mediterranean (as revealed through the water density fields) is dominated by inter-decennial oscillations at the present climate, a result supported by a multitude of observational and simulation studies. The Mediterranean imports the buoyancy from the Atlantic, and this lateral exchange exhibits an inherent to the basin interannual variability dominated by inter-decadal periods (with a peak at about 25 years). The inherent variability of the Gibraltar exchange peaks at the same frequencies during both extreme case experiments despite a higher buoyancy import during the SBF experiment and the change of sign during the WBF experiment. The buoyancy exchange in the Sicily and Gibraltar Straits exhibits similar behavior.

Regarding the internal variability of the Mediterranean throughout the SBF and WBF experiments, the major difference from the reference simulation (representing the present climate) is an increased contribution of intercentennial variability to the total variance, especially in the case of the Mediterranean exhibiting an estuarine flow (WBF experiment). In the SBF case, a significant contribution comes from the interannual and inter-decadal periods, which is probably related to the shortening of the residence times of deep waters.

The EOF analysis has revealed the mechanisms of either a lateral buoyancy exchange between the adjacent basins, vertical exchange between the intermediate and deeper layers as well as BIOS-like features for the present climate.

DATA AVAILABILITY STATEMENT

The raw data supporting the conclusions of this article will be made available by the authors, without undue reservation.

AUTHOR CONTRIBUTIONS

AS contributed to developing the concept of this work, designing the numerical experiments, performed all the model runs and the production of the figures, and produced a major part of the analysis and the manuscript. VZ and ET contributed to the design of the numerical experiments, the analysis of the results, and editing of the manuscript. AG and MT contributed to the design of the experiments, selecting the periods of the paleoceanographic record to be used for the diagnosis of the atmospheric forcing, and also for the manuscript. IM has contributed to the modifications of the POM model version to run under the diagnosed fluxes and its implementation. NS has provided the model code and forcing fields for the simulations of the current conditions and his expertise and guidance. All authors contributed to the article and approved the submitted version.

FUNDING

This work has been funded by the project MedEcos (Decadal-Scale Variability of the Mediterranean Ecosystem) and jointly funded by the EU F.P.6 ERA-network MarinERA and by the Greek General Secretariat of Research and Technology, Ministry of Development (project number 2010SE01380001).

ACKNOWLEDGMENTS

The authors are grateful to Vincenzo Artale for his valuable advice and suggestions. The comments of the two reviewers contributed greatly to improving the work. AS acknowledges support through a PhD fellowship (HCMR), by the Action National Network on Climate Change and its Impacts – CLIMPACT, funded by the Public Investment Program of Greece (GSRT, Ministry of Development and Investments).

REFERENCES

Abu-Zied, R. H., Rohling, E. J., Jorissen, F. J., Fontanier, Ch., Casford, J. S. L., and Cooke, S. (2008). Benthic foraminiferal response to changes in bottom-water oxygenation and organic carbon flux in the eastern Mediterranean during LGM to Recent times. *Mar. Micropaleontol.* 67, 46–68. doi: 10.1016/j.marmicro.2007.08.006

Adloff, F., Mikolajewicz, U., Kučera, M., Grimm, R., Maier-Reimer, E., Schmiedl, G., et al. (2011). Upper ocean climate of the Eastern Mediterranean sea during the Holocene insolation maximum – a model study. *Clim. Past* 7, 1103–1122. doi: 10.5194/cp-7-1103-2011

Adloff, F., Somot, S., Sevault, F., Jordà, G., Aznar, R., Déqué, M., et al. (2015). Mediterranean sea response to climate change in an ensemble of twenty first century scenarios. *Clim. Dyn.* 45, 2775–2802. doi: 10.1007/s00382-015-2507-3

Alley, R. B. (2000). The Younger Dryas cold interval as viewed from central Greenland. *Quat. Sci. Rev.* 19, 213–226. doi: 10.1016/S0277-3791(99)00062-1

Almogi-Labin, A., Bar-Matthews, M., Shriki, D., Kolosovsky, E., Paterne, M., Schilman, B., et al. (2009). Climatic variability during the last ∼ 90 ka of the southern and northern Levantine Basin as evident from marine records and speleothems. *Quat. Sci. Rev.* 28, 2882–2896. doi: 10.1016/j.quascirev.2009.07.017

Amitai, Y., Ashkenazy, Y., and Gildor, H. (2021). The effect of the source of deep water in the eastern mediterranean on western mediterranean intermediate and deep water. *Front. Marine Sci.* 7:1215. doi: 10.3389/fmars.2020.615975

Andersen, M. B., Matthews, A., Vance, D., Bar-Matthews, M., Archer, C., and de Souza, G. F. (2018). A 10-fold decline in the deep Eastern Mediterranean thermohaline overturning circulation during the last interglacial period. *Earth Planetary Sci. Lett.* 503, 58–67. doi: 10.1016/j.epsl.2018.09.013

Ashkenazy, Y., Stone, P. H., and Malanotte-Rizzoli, P. (2012). Box modeling of the Eastern Mediterranean sea. *Phys. A Stat. Mech. Appl.* 391, 1519–1531. doi: 10.1016/j.physa.2011.08.026

Athanasiou, M., Bouloubassi, I., Gogou, A., Klein, V., Dimiza, M. D., Parinos, C., et al. (2017). Sea surface temperatures and environmental conditions during the "warm Pliocene" interval (∼ 4.1–3.2 Ma) in the Eastern Mediterranean (Cyprus). *Glob. Planet. Change* 150, 46–57. doi: 10.1016/j.gloplacha.2017.01.008

Athanasiou, M., Triantaphyllou, M. V., Dimiza, M. D., Gogou, A., and Theodorou, G. (2015). Zanclean/Piacenzian transition on Cyprus (SE Mediterranean): calcareous nannofossil evidence of sapropel formation. *Geo Marine Lett.* 35, 367–385. doi: 10.1007/s00367-015-0414-6

Béranger, K., Drillet, Y., Houssais, M.-N., Testor, P., Bourdallé-Badie, R., Alhammoud, B., et al. (2010). Impact of the spatial distribution of the atmospheric forcing on water mass formation in the Mediterranean sea. *J. Geophys. Res.* 115:C12041. doi: 10.1029/2009JC005648

Berger, A. (1978). Long-term variations of daily insolation and Quaternary climatic changes. *J. Atm. Sci.* 35, 2362–2367. doi: 10.1175/1520-0469(1978)035<2362:LTVODI>2.0.CO;2

Berger, A., and Loutre, M. F. (1991). Insolation values for the climate of the last 10 million years. *Quat. Sci. Rev.* 10, 297–317. doi: 10.1016/0277-3791(91)90033-Q

Beuvier, J., Sevault, F., Herrmann, M., Kontoyiannis, H., Ludwig, W., Rixen, M., et al. (2010). Modeling the Mediterranean sea interannual variability during 1961–2000: focus on the Eastern Mediterranean transient. *J. Geophys. Res.* 115:C08017. doi: 10.1029/2009JC005950

Bignami, F., Marullo, S., Santoleri, R., and Schiano, M. E. (1995): Longwave radiation budget in the Mediterranean sea. *J. Geophys. Res.* 100, 2501–2514. doi: 10.1029/94JC02496

Björnsson, H., and Venegas, S. A. (2001). *A Manual for EOF and SVD Analyses of Climatic Data*. Montreal, QC: McGill University.

Blumberg, A. F., and Mellor, G. L. (1987). "A description of a three-dimensional coastal ocean circulation model," in *Three-Dimensional Coastal Ocean Models, Coastal Estuarine Science*, ed N. S. Heaps (Washington, DC: AGU), 1–16.

Borzelli, G. L. E., Gacic, M., Cardin, V., and Civitarese, G. (2009). Eastern Mediterranean transient and reversal of the Ionian sea circulation. *Geophys. Res. Lett.* 36:L15108. doi: 10.1029/2009GL039261

Brasseur, P., Beckers, J. M., Brankart, J. M., and Schoenauen, R. (1996). Seasonal temperature and salinity field in the Mediterranean sea: climatological analysis of a historical data set. *Deep Sea Res.* 43, 159–192. doi: 10.1016/0967-0637(96)00012-X

Budyko, M. I. (1963). *Atlas of the Heat Balance of the Earth*. Glabnaia Geofiz. Observ., Hydrometeorolocial Service, Moscow.

Cacho, I., Grimalt, J. O., Canals, M., Sbaffi, L., Shackleton, N. J., Schönfeld, J., et al. (2001). Variability of the Western mediterranean sea surface temperatures during the last 25000 years and its connection with the northern hemisphere climatic changes. *Paleoceanography* 16, 40–52. doi: 10.1029/2000PA000502

Carlson, A. E. (2013). The younger dryas climate event. *Encycl. Quaternary Sci.* 3, 126–134. doi: 10.1016/B978-0-444-53643-3.00029-7

Castañeda, I. S., Schefuß, E., Pätzold, J., SinninghеDamsté, J. S., Weldeab, S., and Schouten, S. (2010). Millennial-scale sea surface temperature changes in the eastern Mediterranean (Nile River Delta region) over the last 27,000 years. *Paleoceanography* 25:PA1208. doi: 10.1029/2009PA001740

Cheng, H., Zhang, H., Spötl, C., Baker, J., Sinha, A., Li, H., et al. (2020). Timing and structure of the Younger Dryas event and its underlying climate dynamics. *Proc. Nat. Acad. Sci. U.S.A.* 117, 23408–23417. doi: 10.1073/pnas.2007869117

Cisneros, M., Cacho, I., Frigola, J., Sanchez-Vidal, A., Calafat, A., Pedrosa-Pàmies, R., et al. (2019). Deep-water formation variability in the north-western Mediterranean sea during the last 2500 yr: a proxy validation with present-day data. *Glob. Planet. Change* 177, 56–68. doi: 10.1016/j.gloplacha.2019.03.012

Crisciani, F., and Mosetti, R. (2016). Is the bimodal oscillating Adriatic-Ionian circulation a stochastic resonance? *Bollettino Geofisica Teorica Appl.* 57, 275–285. doi: 10.4430/bgta0176

Dubois-Dauphin, Q., Montagna, P., Siani, G., Douville, E., Wienberg, C., Hebbeln, D., et al. (2017). Hydrological variations of the intermediate water masses of the western Mediterranean sea during the past 20 ka inferred from neodymium isotopic composition in foraminifera and cold-water corals. *Clim. Past* 13, 17–37. doi: 10.5194/cp-13-17-2017

El Frihmat, Y., Hebbeln, D., Jaaidi, E. B., and Mhammdi, N. (2014). Late Quaternary history of the Mediterranean outflow to the southern part of the Gulf of Cadiz, evidence from benthic foraminiferal carbon isotope Histoire de l'écoulement méditerranéen vers le Sud du Golfe de Cadix au Quaternaire terminal, argument à partir des isotopes du carbone des foraminifères benthiques. *Bull. l'Institut Sci. Rabat Sect. Sci. Terre* 36, 27–37. Available online at: http://www.israbat.ac.ma/?page_id=251

Emeis, K. C., Struck, U., Schulz, H. M., Rosenberg, R., Bernasconi, S., Erlenkeuser, H., et al. (2000). Temperature and salinity variations of Mediterranean sea surface waters over the last 16,000 years from records of planktonic stable oxygen isotopes and alkenone unsaturation ratios. *Palaeogeogr. Palaeoclimatol. Palaeoecol.* 158, 259–280. doi: 10.1016/S0031-0182(00)00053-5

Ferraro, S., Sulli, A., Di Stefano, E., Giaramita, L., Incarbona, A., Mortyn, P. G., et al. (2018). Late Quaternary palaeoenvironmental reconstruction of sediment drift accumulation in the Malta Graben (central Mediterranean sea). *Geo Marine Lett.* 38, 241–258. doi: 10.1007/s00367-018-0534-x

Gačić, M., Borzelli, G. L. E., Civitarese, G., Cardin, V., and Yari, S. (2010). Can internal processes sustain reversals of the ocean upper circulation? The Ionian sea example. *Geophys. Res. Lett.* 37:L09608. doi: 10.1029/2010GL043216

Geraga, M., Ioakim, C., Lykousis, V., Tsaila-Monopolis, S., and Mylona, G. (2010). The high resolution palaeoclimatic and palaeoceanographic history of the last 24,000 years in the central Aegean sea, Greece. *Palaeogeogr. Palaeoclimatol. Palaeoecol.* 287, 101–115. doi: 10.1016/j.palaeo.2010.01.023

Gogou, A., Bouloubassi, I., Lykousis, V., Arnaboldi, M., Gaitani, P., et al. (2007). Organic geochemical evidence of Late Glacial–Holocene climate instability in the North Aegean sea. *Palaeogeogr. Palaeoclimatol. Palaeoecol.* 256, 1–20. doi: 10.1016/j.palaeo.2007.08.002

Gogou, A., Triantaphyllou, M. V., Bouloubassi, I., Kouli, K., Rousakis, G., Emeis, K. C., et al. (2016). "Multi-proxy evidences for paleoceanographic changes in the eastern Mediterranean during the Holocene: connections to regional and global-scale climatic variability patterns," in *Medclivar 2016 Conference* (Athens: University of Athens).

Grimm, R., Maier-Reimer, E., Mikolajewicz, U., Schmiedl, G., Müller-Navarra, K., Adloff, F., et al. (2015). Late glacial initiation of Holocene eastern Mediterranean sapropel formation. *Nat. Commun.* 6:7099. doi: 10.1038/ncomms8099

Hasselmann, K. (1976). Stochastic climate models. Part I: theory. *Tellus* 28, 473–484. doi: 10.3402/tellusa.v28i6.11316

Huybers, P., and Eisenman, I. (2006). *Integrated Summer Insolation Calculations.* NOAA/NCDC Paleoclimatology Program Data Contribution #2006–079, Harvard University.

Incarbona, A., Martrat, B., Mortyn, P., Sprovieri, M., Ziveri, P., Gogou, A., et al. (2016). Mediterranean circulation perturbations over the last five centuries: relevance to past Eastern Mediterranean transient-type events. *Sci. Rep.* 6:29623. doi: 10.1038/srep29623

Iona, A., Theodorou, A., Watelet, S., Troupin, C., Beckers, J.-M., and Simoncelli, S. (2018). Mediterranean sea Hydrographic Atlas: towards optimal data analysis by including time-dependent statistical parameters. *Earth Syst. Sci. Data* 10, 1281–1300. doi: 10.5194/essd-10-1281-2018

Jaeger, L. (1976). Monatskarten des Niedersschlags Pδr die gange. *Erde. Ber. Dtsch. Wetterdienstes* 18, 1–38.

Jilbert, T., Reichart, G. J., Mason, P., and de Lange, G. J. (2010). Short-time-scale variability in ventilation and export productivity during the formation of Mediterranean sapropel S1. *Paleoceanography* 25:PA4232. doi: 10.1029/2010PA001955

Jiménez-Espejo, F. J., Pardos-Gené, M., Martínez-Ruiz, F., Garcia-Alix, A., van de Flierdt, T., Toyofuku, T., et al. (2015). Geochemical evidence for intermediate water circulation in the westernmost Mediterranean over the last 20kyrBP and its impact on the Mediterranean outflow. *Glob. Planet. Change* 135, 38–46. doi: 10.1016/j.gloplacha.2015.10.001

Kotthoff, U., Müller, U. C., Pross, J., Schmiedl, G., Lawson, I.T, Schootbrugge, B., and Schulz, H. (2008). Lateglacial and Holocene vegetation dynamics in the Aegean region: an integrated view based on pollen data from marine and terrestrial archives. *Holocene* 18, 1019–1032. doi: 10.1177/0959683608095573

Lacombe, H., Tchernia, P., and Gamberoni, L. (1985). Variable bottom water in the Western Mediterranean basin. *Progress Oceanogr.* 14, 319–338. doi: 10.1016/0079-6611(85)90015-1

Lascaratos, A., Williams, R. G., and Tragou, E. (1993). A mixed-layer study formation of Levantine Intermediate Water. *J. Geophys. Res.* 98, 14739–14749. doi: 10.1029/93JC00912

Llave, E., Schönfeld, J., Hernández-Molina, F. J., Mulder, T., Somoza, L., Díaz del Río, V., et al. (2006). High-resolution stratigraphy of the Mediterranean outflow contourite system in the Gulf of Cadiz during the late Pleistocene: the impact of Heinrich events. *Mar. Geol.* 227, 241–262. doi: 10.1016/j.margeo.2005.11.015

Lourens, L. J., Antonarakou, A., Hilgen, F. J., Van Hoof, A. A. M., Vergnaud-Grazzini, C., and Zachariasse, W. J. (1996). Evaluation of the Plio-Pleistocene astronomical timescale. *Paleoceanography* 11, 391–341. doi: 10.1029/96PA01125

Ludwig, W., Dumont, E., Meybeck, M., and Heussner, S. (2009). Review: river discharges of water and nutrients to the Mediterranean and Black sea: major drivers for ecosystem changes during past and future decades?. *Prog. Oceanogr.* 80, 199–217. doi: 10.1016/j.pocean.2009.02.001

Malanotte-Rizzoli, P., Manca, B. B., D'Alcalà, M. R., Theocharis, A., Bergamasco, A., Bregant, D., et al. (1997). A synthesis of the Ionian sea hydrography, circulation and water mass pathways during POEM-Phase I. *Prog. Oceanogr.* 39, 153–204. doi: 10.1016/S0079-6611(97)00013-X

Marino, G., Rohling, E. J., Sangiorgi, F., Hayes, A., Casford, J. L., Lotter, A. F., et al. (2009). Early and middle Holocene in the Aegean sea: interplay between high and low latitude climate variability. *Quat. Sci. Rev.* 28, 3246–3262. doi: 10.1016/j.quascirev.2009.08.011

Martrat, B., Grimalt, J. O., Shackleton, N. J., de Abreu, L., Hutterli, M. A., and Stocker, T. F. (2007). Four climate cycles of recurring deep and surface water destabilizations on the Iberian Margin. *Science* 317, 502–507. doi: 10.1126/science.1139994

Meijer, P. T., and Tuenter, E. (2007). The effect of precession-induced changes in the Mediterranean freshwater budget on circulation at shallow and intermediate depth. *J. Marine Syst.* 68, 349–365. doi: 10.1016/j.jmarsys.2007.01.006

Myers, P. G. (2002). Flux-forced simulations of the paleocirculation of the Mediterranean. *Paleoceanography* 17, 9-1–9-7. doi: 10.1029/2000PA000613

Myers, P. G., and Haines, K. (2000). Seasonal and interannual variability in a model of the mediterranean under derived flux forcing. *J. Phys. Oceanogr.* 30, 1069–1082. doi: 10.1175/1520-0485(2000)030<1069:SAIVIA>2.0.CO;2

Myers, P. G., Haines, K., and Rohling, E. J. (1998). Modeling the paleocirculation of the Mediterranean: the last glacial maximum and the Holocene with emphasis on the formation of sapropel S1. *Paleoceanography* 13, 586–606. doi: 10.1029/98PA02736

Myers, P. G., and Rohling, E. J. (2000). Modeling a 200-yr interruption of the holocene sapropel S1. *Quaternary Res.* 53, 98–104. doi: 10.1006/qres.1999.2100

Nielsen, J. N. (1912). *Hydrography of the Mediterranean and Adjacent Seas. Danish Oceanographic Expeditions 1908-10*. Copenhagen: Report I, 72–191.

Nittis, K., Lascaratos, A., and Theocharis, A. (2003). Dense water formation in the Aegean sea: numerical simulations during the Eastern Mediterranean transient. *J. Geophys. Res*. 108, 1–15. doi: 10.1029/2002JC001352

Oddo, P., Adani, M., Pinardi, N., Fratianni, C., Tonani, M., and Pettenuzzo, D. (2009). A nested Atlantic- Mediterranean sea general circulation model for operational forecasting. *Ocean Sci.* 5, 461–473. doi: 10.5194/os-5-461-2009

Pinardi, N., Zavatarelli, M., Adani, M., Coppini, G., Fratianni, C., Oddo, P., et al. (2015). Mediterranean sea large-scale low-frequency ocean variability and water mass formation rates from 1987 to 2007: a retrospective analysis. *Prog. Oceanogr.* 132, 318–332. doi: 10.1016/j.pocean.2013.11.003

Pisacane, G., Artale, V., Calmanti, S., and Rupolo, V. (2006). Decadal oscillations in the Mediterranean sea: a result of the overturning circulation variability in the eastern basin?. *Clim. Res.* 31, 257–271. doi: 10.3354/cr031257

Reed, R. K. (1977): On estimating insolation over the ocean. *J. Phys. Oceanogr*. 7, 482–485. doi: 10.1175/1520-0485(1977)007<0482:OEIOTO>2.0.CO;2

Robinson, A. R., Leslie, W. G., Theocharis, A., and Lascaratos, A. (2001). *Mediterranean Sea Circulation, Encyclopedia of Ocean Science*. Cambridge, MA: Academic Press, 1689–1706. doi: 10.1006/rwos.2001.0376

Rodrigo-Gámiz, M., Martínez-Ruiz, F., Rampen, S. W., Schouten, S., and SinninghеDamsté, J. S. (2014). Sea surface temperature variations in the western Mediterranean Sea over the last 20 kyr: a dual-organic proxy (UK'37 and LDI) approach. *Paleoceanography* 29, 87–98. doi: 10.1002/2013PA002466

Roether, W., Klein, B., Manca, B. B., Theocharis, A., and Kioroglou, S. (2007). Transient Eastern Mediterranean deep waters in response to the massive dense-water output of the Aegean sea in the 1990s. *Progress Oceanogr.* 74, 540–571. doi: 10.1016/j.pocean.2007.03.001

Rohling, E. J. (1994). Review and new aspects concerning the formation of eastern Mediterranean sapropels. *Mar. Geol.* 122, 1–28. doi: 10.1016/0025-3227(94)90202-X

Rohling, E. J., Marino, G., and Grant, K. M. (2015). Mediterranean climate and oceanography, and the periodic development of anoxic events (sapropels). *Earth Sci. Rev.* 143, 62–97. doi: 10.1016/j.earscirev.2015.01.008

Rosati, A., and Miyakoda, K. (1988): A general circulation model for upper ocean circulation. *J. Phys. Oceanogr*. 18, 1601–1626. doi: 10.1175/1520-0485(1988)018<1601:AGCMFU>2.0.CO;2

Rossignol-Strick, M. (1985). Mediterranean Quaternary Sapropels, an immediate response of the African monsoon to variation of insolation. *Palaeogeogr. Palaeoclimatol. Palaeoecol.* 49, 237—263. doi: 10.1016/0031-0182(85)90056-2

Rubino, A., Gačić, M., Bensi, M., Kovačević, V., Malačič, V., Menna, M., et al. (2020). Experimental evidence of long-term oceanic circulation reversals without wind influence in the North Ionian sea. *Sci. Rep.* 10:1905. doi: 10.1038/s41598-020-57862-6

Schmiedl, G., Kuhnt, T., Ehrmann, W., Emeis, K. C., Hamann, Y., Kotthoff, U., et al. (2010). Climatic forcing of eastern Mediterranean deep-water formation and benthic ecosystems during the past 22 000 years. *Quat. Sci. Rev.* 29, 3006–3020. doi: 10.1016/j.quascirev.2010.07.002

Schroeder, K., Chiggiato, J., Bryden, H., Borghini, M., and Ismail, S. B. (2016). Abrupt climate shift in the Western Mediterranean sea. *Sci. Rep.* 6:23009. doi: 10.1038/srep23009

Skliris, N., and Lascaratos, A. (2004). Impacts of the Nile river damming on the thermohaline circulation and water mass characteristics of the Mediterranean sea. *J. Marine Syst.* 52, 121–143. doi: 10.1016/j.jmarsys.2004.02.005

Skliris, N., Sofianos, S., and Lascaratos, A. (2007). Hydrological changes in the Mediterranean sea in relation to changes in the freshwater budget: a numerical modelling study. *J. Marine Syst*. 65, 400–416. doi: 10.1016/j.jmarsys.2006.01.015

Somot, S., Houpert, L., Sevault, F., Testor, P., Bosse, A., Taupier-Letage, I., et al. (2018). Characterizing, modelling and understanding the climate variability of the deep water formation in the North-Western Mediterranean sea. *Clim. Dyn*. 51, 1179–1210. doi: 10.1007/s00382-016-3295-0

Somot, S., Sevault, F., Déqué, M., and Crépon, M. (2008). 21st century climate change scenario for the Mediterranean using a coupled atmosphere–ocean regional climate model. *Glob. Planet. Change* 63, 112–126. doi: 10.1016/j.gloplacha.2007.10.003

Sperling, M., Schmiedl, G., Hemleben, Ch., Emeis, K. C., Erlenkeuser, H., and Grootes, P. M. (2003). Black sea impact on the formation of eastern Mediterranean sapropel S1? Evidence from the Marmara sea. *Palaeogeogr. Palaeoclimatol. Palaeoecol.* 190, 9–21. doi: 10.1016/S0031-0182(02)00596-5

Stommel, H. (1972). Deep winter-time convection in the western Mediterranean sea. *Studies in Phys. Oceanogr.* 2, 207–218.

Sverdrup, H., Johnson, M. W., and Fleming, R. H. (1942). *The Oceans Their Physics, Chemistry, and General Biology*. New York, NY: Prentice-Hall, Inc., 642–651.

Tachikawa, K., Vidal, L., Cornuault, M., Garcia, M., Pothin, A., Sonzogni, C., et al. (2015). Eastern Mediterranean sea circulation inferred from the conditions of S1 sapropel deposition. *Clim. Past* 11, 855–867. doi: 10.5194/cp-11-855-2015

Tesi, T., Asioli, A., Minisini, D., Maselli, V., Dalla Valle, G., Gamberi, F., et al. (2017). Large-scale response of the Eastern Mediterranean thermohaline circulation to African monsoon intensification during sapropel S1 formation'. *Quat. Sci. Rev.* 159, 139–154. doi: 10.1016/j.quascirev.2017.01.020

Theocharis, A., Krokos, G., Velaoras, D., and Korres, G. (2014). "An internal mechanism driving the alternation of the Eastern Mediterranean dense/deep water sources," in *The Mediterranean Sea*, eds G. L. Eusebi Borzelli, M. Gačić, P. Lionello, and P. Malanotte-Rizzoli (Washington, DC: American Geophysical Union; Hoboken, NJ: John Wiley & Sons, Inc), 113–137.

Theocharis, A. (2009). "Variability of the thermohaline properties in the Eastern Mediterranean during the post-EMT period (1995–2008) and SST changes in the Aegean (1985–2008)," in *CIESM, 2009, Dynamics of Mediterranean Deep Waters. CIESM Workshop Monographs, Vol. 38* (Malta), ed F. Briand, 35–40.

Thunell, R., and Williams, D. (1989). Glacial–Holocene salinity changes in the Mediterranean sea: hydrographic and depositional effects. *Nature* 338, 493–496. doi: 10.1038/338493a0

Topper, R. P. M., and Meijer, P. (2015). Changes in Mediterranean circulation and water characteristics due to restriction of the Atlantic connection: a high-resolution ocean model. *Clim. Past* 11, 233–251. doi: 10.5194/cp-11-233-2015

Toucanne, S., Jouet, G., Ducassou, E., Bassetti, M. A., Dennielou, B., Minto'o, C. M. A., et al. (2012). A 130,000-year record of Levantine Intermediate Water flow variability in the Corsica Trough, western Mediterranean sea. *Quat. Sci. Rev.* 33, 55–73. doi: 10.1016/j.quascirev.2011.11.020

Toucanne, S., Mulder, T., Schönfeld, J., Hanquiez, V., Gonthier, E., Duprat, J., et al. (2007). Contourites of the Gulf of Cadiz: a high-resolution record of the paleocirculation of the Mediterranean outflow water during the last 50,000 years. *Palaeogeogr. Palaeoclimatol. Palaeoecol.* 246, 354–366. doi: 10.1016/j.palaeo.2006.10.007

Triantaphyllou, M., Gogou, A., Dimiza, M.D., Kostopoulou, S., Parinos, C., Rousakis, G., et al. (2016). Holocene climatic optimum centennial-scale paleoceanography in the NE Aegean (Mediterranean sea). *Geo Marine Lett.* 36, 51–66. doi: 10.1007/s00367-015-0426-2

Triantaphyllou, M. V. (2014). Coccolithophore assemblages during the Holocene Climatic Optimum in the NE Mediterranean (Aegean and northern Levantine Seas, Greece): paleoceanographic and paleoclimatic implications. *Quat. Int.* 345, 56–67. doi: 10.1016/j.quaint.2014.01.033

Triantaphyllou, M. V., Antonarakou, A., Kouli, K., Dimiza, M., Kontakiotis, G., Papanikolaou, M., et al. (2009a). Late Glacial–Holocene ecostratigraphy of the south-eastern Aegean sea, based on plankton and pollen assemblages. *Geo Marine Lett.* 29, 249–267. doi: 10.1007/s00367-009-0139-5

Triantaphyllou, M. V., Ziveri, P., Gogou, A., Marino, G., Lykousis, V., Bouloubassi, I., et al. (2009b). Late Glacial–Holocene climate variability at the south-eastern margin of the Aegean sea. *Mar. Geol.* 266, 182–197. doi: 10.1016/j.margeo.2009.08.005

Ünlüata, U., Oguz, T., Latif, M., and Özsoy, E. (1990). "On the physical oceanography of the Turkish straits," in *The Physical Oceanography of Sea Straits. NATO ASI Series (Mathematical and Physical Sciences), Vol 318*, ed J. Pratt (Dordrecht: Springer). doi: 10.1007/978-94-009-0677-8_2

Waldman, R., Somot, S., Herrmann, M., Sevault, F., and Isachsen, P. E. (2018). On the chaotic variability of deep convection in the Mediterranean sea. *Geophys. Res. Lett.* 45, 2433–2443. doi: 10.1002/2017GL076319

Weaver, A. J., and Hughes, T. M. C. (1992). *Stability and Variability of the Thermohaline Circulation and Its link to Climate*. Centre for earth and Ocean Research, McGill University, Montreal, QC, 92–95, 56.

Wu, P., and Haines, K. (1996). Modeling the dispersal of Levantine Intermediate Water and its role in Mediterranean deep water formation. *J. Geophys. Res.* 101, 6591–6607. doi: 10.1029/95JC03555

Zervakis, V., Georgopoulos, D., and Drakopoulos, P. G. (2000). The role of the North Aegean in triggering the recent Eastern Mediterranean climatic changes. *J. Geophys. Res.* 105, 26103–26116. doi: 10.1029/2000JC900131

Conflict of Interest: The authors declare that the research was conducted in the absence of any commercial or financial relationships that could be construed as a potential conflict of interest.

frontiers in Marine Science

ORIGINAL RESEARCH
published: 21 September 2021
doi: 10.3389/fmars.2021.672437

Mixing in the Tyrrhenian Interior Due to Thermohaline Staircases

*Sara Durante[1], Paolo Oliveri[2], Rajesh Nair[3] and Stefania Sparnocchia[4]**

[1] Istituto di Scienze Marine, Consiglio Nazionale delle Ricerche, Naples, Italy, [2] Istituto Nazionale di Geofisica e Vulcanologia, Bologna, Italy, [3] Istituto Nazionale di Oceanografia e di Geofisica Sperimentale, Trieste, Italy, [4] Istituto di Scienze Marine, Consiglio Nazionale delle Ricerche, Trieste, Italy

Thermohaline staircases are a well-known peculiar feature of the Tyrrhenian Sea. Generated by extensive double diffusion processes fueled by lateral intrusions, they are considered to be the most stable of all the staircases that have been detected in the world ocean, seeing their persistence of more than 40 years in the literature. Double diffusion leads to efficient vertical mixing, potentially playing a significant role in guiding the diapycnal mixing. The present study investigates this process of mixing in the case of the Tyrrhenian staircases by calculating the heat and salt fluxes in their gradient zones (interfaces) and the resulting net fluxes in adjacent layers using hydrological profiles collected from 2003 to 2016 at a station in the heart of the basin interior. The staircases favor downward fluxes of heat and salt, and the results of the calculations show that these are greater where temperature and salinity gradients are also high. This condition is more frequently encountered at thin and sharp interfaces, which sometimes appear as substructures of the thicker interfaces of the staircases. These substructures are hot spots where vertical fluxes are further accentuated. Due to the increasing salt and heat content of the Levantine Intermediate Water (LIW) during the observation period, a rise in the values of the fluxes was noted in the portion of the water column below it down to about 1800 m. The data furthermore show that internal gravity waves can modulate the structure of the staircases and very likely contribute to the mixing, too, but the sampling frequency of the time series is too large to permit a proper assessment of these processes. It is shown that, at least during the period of observation, the fluxes due to salt fingers do not reach the bottom layer but remain within the staircases.

Keywords: Tyrrhenian Sea, thermohaline staircases, salt fingers, diapycnal mixing, heat and salt fluxes

OPEN ACCESS

Edited by:
Frédéric Cyr, Northwest Atlantic Fisheries Centre, Canada

Reviewed by:
Vincent Taillandier, Centre National de la Recherche Scientifique (CNRS), France
Jared Penney, University of Waterloo, Canada

****Correspondence:***
Stefania Sparnocchia
stefania.sparnocchia@ts.ismar.cnr.it

Specialty section:
This article was submitted to Physical Oceanography, a section of the journal Frontiers in Marine Science

Received: *25 February 2021*
Accepted: *27 August 2021*
Published: *21 September 2021*

Citation:
Durante S, Oliveri P, Nair R and Sparnocchia S (2021) Mixing in the Tyrrhenian Interior Due to Thermohaline Staircases. Front. Mar. Sci. 8:672437. doi: 10.3389/fmars.2021.672437

INTRODUCTION

Thermohaline staircases are a characteristic of the central part of the Tyrrhenian Sea, the deepest and most isolated basin of the Western Mediterranean (**Figure 1**). They are an alternation of homogeneous temperature and salinity layers, and high gradient interfaces, the thicknesses of which can reach several hundreds and tens of meters, respectively. Observed more frequently in the depth range of 600–2500 m (e.g., Zodiatis and Gasparini, 1996), such staircases extended up to 3000 m after the year 2010 (Durante et al., 2019). It is worth noting that among the Mediterranean sub-basins, the Tyrrhenian Sea is the most susceptible to salt fingering, and the one with the strongest likelihood of sustaining the processes leading to their formation (Meccia et al., 2016).

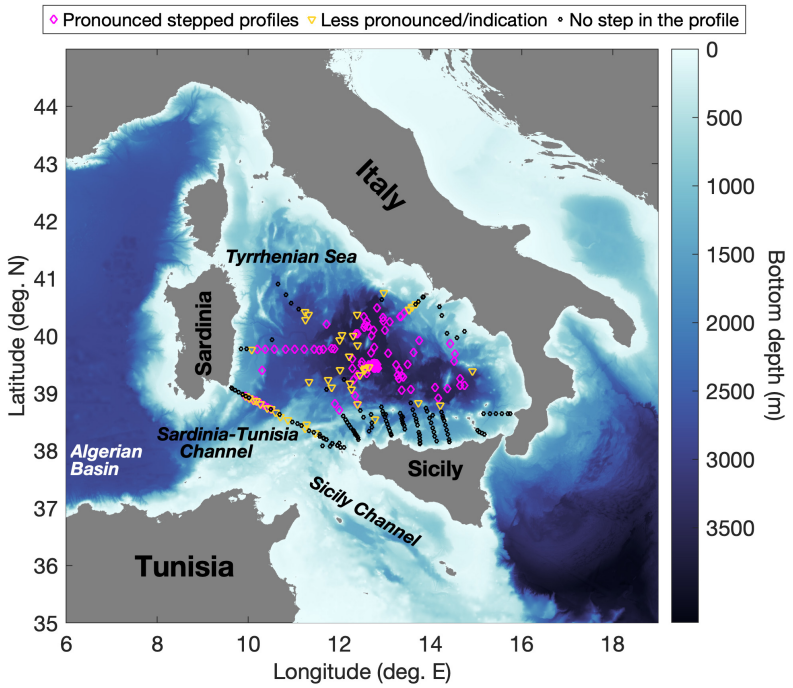

FIGURE 1 | The Tyrrhenian Sea (Western Mediterranean); symbols denote stations from Johannessen and Lee (1974), Molcard and Williams (1975), Zodiatis and Gasparini (1996), Sparnocchia et al. (1999), Falco et al. (2016), Durante et al. (2019), Sparnocchia and Borghini (2019), and Taillandier et al. (2020), indicating the locations where well-defined/less-defined stepped profiles or profiles with no indication of steps were reported. The bathymetry is that of the GEBCO Bathymetric Compilation Group (2019), and the colormap used is from Thyng et al. (2016).

Documented for the first time by Johannessen and Lee (1974), these peculiar structures have been the subject of various studies that have demonstrated their persistence over time (Falco et al., 2016; Durante et al., 2019; Taillandier et al., 2020) as well as their spatial coherence (Molcard and Williams, 1975; Zodiatis and Gasparini, 1996; Buffett et al., 2017). Zodiatis and Gasparini (1996) in particular, using their extensive dataset which covered a large part of the southern Tyrrhenian Sea, were able to demonstrate that the staircase phenomenon affects at least 22% of the basin with a lateral coherence of 150 km, and is more pronounced (thicker mixed layers, thinner interfaces with maximum gradients and a larger number of steps) in its deeper part. This is also evident from the distribution of profile types taken from the literature in **Figure 1**. Moving toward the basin's periphery, the structures become weaker, and finally disappear completely. This feature of the structures is consistent with the dynamics of the basin which increases from the center toward the borders where advection is prevalent and diffusive convection is prevented (Astraldi and Gasparini, 1994; Zodiatis and Gasparini, 1996).

The Tyrrhenian water column is mainly a three-layer system consisting of the surface Atlantic Water (AW), the Levantine Intermediate Water (LIW) and the Tyrrhenian Deep Water (TDW). The LIW is generated in the Eastern Mediterranean and is identified by an associated salinity maximum. It enters the Tyrrhenian Sea from the Sicily Channel. A major part turns right and flows directly eastward following the northern coast of Sicily, circulating cyclonically within the basin along the boundaries in the 200–700 m depth range roughly. Reaching the eastern coast of Sardinia, it flows southward to finally exit the Tyrrhenian toward the Western Mediterranean (Béranger et al., 2004). The TDW is the product of the mixing between the Western Mediterranean Deep Water (WMDW) entering the Tyrrhenian Sea via the Sardinia-Tunisia Channel and waters of eastern Mediterranean origin, i.e., LIW and Eastern Mediterranean Deep Waters (Sparnocchia et al., 1999; Millot and Taupier-Letage, 2005). Fuda et al. (2002) hypothesized that water denser than TDW found in the deep Tyrrhenian (2000–3500 m) might form locally occasionally, but this hypothesis was not supported by further observations. The circulation of the TDW is not well-characterized due to the lack of data (Vetrano et al., 2010) but is expected to be cyclonic along-slope due to the Coriolis effect, tracing a basin-wide gyre before leaving through a southwest passage close to Sardinia (sill at ∼2000 m) (Millot and Taupier-Letage, 2005).

Lateral exchange processes between the boundary currents and the interior of the basin have been reported by Zodiatis and Gasparini (1996). More recent studies (Budillon et al., 2009; Vetrano et al., 2010) have revealed a complex circulation in the south-eastern part of the basin, with meanders and some persistent and transient cyclonic and anticyclonic structures involving the surface and intermediate layers. These exchange processes are responsible for lateral intrusions which supply the central part of the basin with warmer and saltier water, thus supporting the staircases. Lateral intrusions which alter the stratification of otherwise homogeneous steps in the form of local

inversions of temperature and salinity with increasing depth are also sometimes observed (Zodiatis and Gasparini, 1996, their Figure 5; Merryfield, 2000). The continuous lateral input of warm, salty water and the weak dynamics of the basin in the deep layers (Hopkins, 1988; Astraldi and Gasparini, 1994; Zodiatis and Gasparini, 1996) contribute to maintaining the general pattern of the established structure of the relevant portion of the water column over time, though specific characteristics may change somewhat leading to slightly differing shapes of profiles between one observation and another (Durante et al., 2019).

In recent years, the LIW has undergone significant warming and an increase in salinity (Schroeder et al., 2017, 2020), which should therefore have increased its contribution to the salt fingering processes in the Tyrrhenian basin. Furthermore, following the Western Mediterranean Transition (WMT), a new warmer, saltier and denser Western Mediterranean Deep Water (nWMDW) has formed (Schroeder et al., 2008) that has progressively spread from its region of origin along routes to Gibraltar and the Tyrrhenian Sea (Schroeder et al., 2016). Entering the Tyrrhenian Sea, the nWMDW has a lower temperature and salinity than the resident deep waters but a higher density that causes it to cascade down to the bottom of the basin and settle under the deep water already present there (see Figure 2C in Schroeder et al., 2016). According to Durante et al. (2019), this new water at the bottom introduces an additional demand for downward fluxes of heat and salt, enhancing salt fingering processes.

Salt fingers reinforce heat and salt fluxes in the open ocean, strongly contributing to the diapycnal vertical mixing (St. Laurent and Schmitt, 1999; Schmitt et al., 2005). They are an effective mixing mechanism in the deep water of the Western Mediterranean (Bryden et al., 2014), and are believed to be the cause of the observed increases in deep water temperature and salinity over the past 50 years along with deep water formation events (Borghini et al., 2014). However, calculating their contribution to the vertical transport of heat and salt from hydrological observations is not easy as this is usually based on approximations of relative flux laws that have not been definitively verified yet as applicable for every situation observed in the ocean.

The laboratory-derived flux laws, also known as the 4/3 flux laws, relate the salt finger fluxes to the 4/3 power law of the difference in salinity across a fingering interface ($\Delta S^{4/3}$) and the density ratio (Turner, 1967; Linden, 1973; Schmitt, 1979; McDougall and Taylor, 1984). But they have been found to overestimate fluxes by more than an order of magnitude (Gregg and Sanford, 1987; Lueck, 1987; Schmitt, 1988) because the high-gradient interfaces observed at sea are thicker than laboratory predictions for them.

Kunze (1987) was the first to propose a model of heat and salt fluxes for finite-length salt fingers, such as those found in observations. His main challenge was properly understanding the length and lengthening in time of the fingers. Since the observed interfaces are thicker than the maximum finger length (tens of cm) predicted by the 4/3 flux laws, they must either consist of several layers of fingering zones separated by convective regions (as suggested by Linden, 1978) or be a statistical ensemble of growing fingers. Thus, the laboratory flux laws that apply to interfaces with only one layer of salt fingers give incorrect fluxes for many of the steps observed in the ocean. In his formulation, Kunze (1987) gave an alternative argument in support of the Stern number constraint for collective instability (Stern, 1969) and a solution for both thin (∼30 cm) and thicker interfaces. This model reproduces laboratory behavior if a single finger fills the entire interface and is more suitable for thick interfaces, typical of oceanic thermohaline staircases, reproducing fluxes over an order of magnitude lower than the those predicted by the 4/3 flux laws.

More recently, Radko and Smith (2012), questioning whether the Stern (1969) and Kunze (1987) hypothesis could be extended to include the case of the very low Stern numbers associated with many of the laboratory experiments, emphasized the role played by secondary instabilities of the salt fingers. These typically grow much faster than the collective instability modes and are independent of the specific values of the Stern number (Holyer, 1984). Their theory, which assumes that the fully developed equilibrium state is characterized by the comparable growth rates of primary and secondary instabilities, leads to a set of equations for the non-dimensional heat and salt fluxes and the flux ratio.

Direct numerical simulations (Radko, 2003, 2005; Radko et al., 2014b) show that the equilibrium structure of a staircase is achieved by a sequence of merging events initially involving relatively thin and unsteady layers generated by instabilities within a smooth stratification. These layers merge continuously, building up the average layer thickness to a maximum value whereupon the equilibrium structure of the staircase is reached. Most oceanic staircases are in the quasi-equilibrium state, and the initial phase of formation of layers from smooth stratification and their systematic thickening subsequently have not been recorded. Nonetheless, in the case of the Tyrrhenian staircases, the varying numbers of such layers observed at different times, the diversity encountered in their sizes and the shapes of their interfaces (which sometimes include small, homogeneous and relatively thick sub-layers) suggest that some process of merging actually occurs (Durante et al., 2019).

Ma and Peltier (2021) further extended the Radko theory by simulating the formation and evolution of staircases starting from an inhomogeneous background stratification to better explain what happens in the real ocean. We will show later that, although they use different functions to represent the flux ratio, the parameterizations of Radko and Smith (2012) and Ma and Peltier (2021) produce nearly coincident salt and heat fluxes when applied to our dataset.

In this study, the Tyrrhenian staircase system presented by Durante et al. (2019) is examined in greater detail, particularly from the perspective of its evolution over time. Relevant fluxes of salt and heat have been calculated employing the parameterization of the Kunze (1987) model for thick interfaces proposed by Hebert (1988), as well as the Radko and Smith (2012) and the Ma and Peltier (2021) models (hereafter referred to as H88, RS12, and MP21, respectively). The main objective is to better formulate this system and assess its contribution to vertical mixing in the Tyrrhenian basin, paying attention also to the role played by the substructures observed inside the thick, layered interfaces. Our results have been evaluated by comparing

them to those obtained from hydrological profiles in the same region by Zodiatis and Gasparini (1996) and Falco et al. (2016), the latter with the same parameterizations we use in this study. Another valuable source of comparison is the very recent study by Ferron et al. (2021), published in this issue. They estimate heat, salt and buoyancy fluxes using microstructure observations from four locations in the western Mediterranean, including our region in the Tyrrhenian Sea. Finally, we present a method for the semi-automatic detection of the boundaries of the interfaces in a stepped profile, specifically developed for our data, as an aid to extract information useful in the calculation of the associated heat and salt fluxes.

The paper is organized in the following way. In Section "Materials and Methods," we present the data, the detection algorithm, the methods used for calculating heat and salt fluxes, and the comparison of the performances of the respective models underpinning the different sets of computations that were performed. In Section "Results," we present an analysis of the long-term evolution of the Tyrrhenian staircase system and describe some of its salient features. We then present the results of the calculations of salt finger fluxes through interfaces, including an analysis of how they change when substructures are present. The two successive sections contain a discussion of the results and our overall conclusions, respectively.

MATERIALS AND METHODS

Data

The dataset consists of a time series of vertical temperature and salinity profiles collected by the Consiglio Nazionale delle Ricerche (CNR) at a station located at a depth of about 3500 m in the central Tyrrhenian Sea (39.78083 deg N, 11.88333 deg E) over the period 2003–2016. This dataset has been presented and intensively studied in Durante et al. (2019), and is available on the open marine science data publication portal, SEANOE (Borghini et al., 2019). It contains 21 hydrological profiles, roughly one every six months with gaps in 2008 and 2009. The dataset can be considered highly homogeneous in terms of technical characteristics and quality. There are two reasons why this is so. One is that the instrument used to collect most of the profiles was the same Sea-Bird SBE 911plus Conductivity-Temperature-Depth (CTD) probe. The other is that the applied data qualification procedures were identical for every profile. The vertical profiles were collected with a sampling frequency of 24 Hz and an average probe descent rate of 1 m s^{-1}. The SBE 911plus CTD system mounts a SBE 3plus and a SBE 4 sensor for measuring temperature and conductivity, respectively, with corresponding manufacturer-declared accuracies of 0.001°C and 0.0003 S m^{-1}. These accuracies for the temperature and conductivity measurements are commensurate with an accuracy of roughly 0.003 in salinity (PSS-78). The temperature and conductivity sensors of the CTD probe were regularly calibrated at the NATO-CMRE Center in La Spezia until 2014, and subsequently by the manufacturer or by the OGS Oceanographic Calibration Center in Trieste. To verify the probe's post-calibration performances for temperature and salinity measurements, it was often deployed with redundant temperature and conductivity sensors. In addition, in the specific case of salinity, probe readings were checked, and if necessary corrected, using values for the property obtained by analyzing water samples collected for this very purpose onboard with a Guildline Autosal or a Guildline Portasal bench salinometer. As a rule, the data acquired with the CTD probe were processed by means of the standard data processing package supplied by its manufacturer, Sea-Bird Scientific. In each profile, the measured temperature (ITS-90, °C) and salinity (PSS-78, practical salinity) data were averaged at every dbar in the vertical. The resulting values were used with the TEOS-10 software v3.06 (McDougall and Barker, 2011) to calculate the absolute salinity (SA) in g kg^{-1} and the conservative temperature (CT) in °C, these variables being the best estimates for ocean temperature and salinity (Jackett et al., 2006; Millero et al., 2008; IOC et al., 2010). In the present version of the TEOS-10 software, the SA is obtained by multiplying the practical salinity by 1.004715428571429 g kg^{-1}.

Detection of Interfaces

To extract the upper and lower limits of the interfaces in a stepped profile, we developed an algorithm in Matlab which we applied below the LIW that we identified by the maximum SA value (SA_{max}). The entire procedure is summarized by the diagram in **Figure 2** and explained below.

The portion of the vertical profile below the LIW can be likened to an expression of a noisy piecewise function composed of two kinds of alternating subsections. The first kind has been defined by us as a "layer." This subsection is characterized by a low variability in the property of interest (CT or SA) and a high variability in the pressure. The second one – which we have called an "interface" – is a subsection where the above situation is reversed, showing a high variability in properties and a low variability in the pressure. So, we based our algorithm on the following two criteria:

(i) the variability of CT (or SA) in the layers is smaller than a threshold value δ, and
(ii) the variability of CT (or SA) in the interfaces is larger than a threshold value ε.

The upper limit of an interface is a point j_u in the profile where it transforms from layer to interface. Similarly, the lower limit of an interface is a point j_l where the opposite occurs. Let N be the number of water column samples, $\theta = \{\theta_1, ..., \theta_N\}$, of the variable under examination (CT or SA). Then, if σ is its standard deviation in any given interval of pressure, j_u and j_l must satisfy the following conditions, namely:

$$\sigma\left\{\theta_{j_u-N_\delta}, \ldots, \theta_{j_u}\right\} < \delta \; and \; \sigma\left\{\theta_{j_u}, \ldots, \theta_{j_u+N_\varepsilon}\right\} > \varepsilon \quad (1)$$

$$\sigma\left\{\theta_{j_l-N_\varepsilon}, \ldots, \theta_{j_l}\right\} > \varepsilon \; and \; \sigma\left\{\theta_{j_l}, \ldots, \theta_{j_l+N_\delta}\right\} < \delta \quad (2)$$

where N_δ and $N\varepsilon$ are the number of points adjacent to the corner points under scrutiny and are used to verify whether the conditions with respect to the δ and ε thresholds are met.

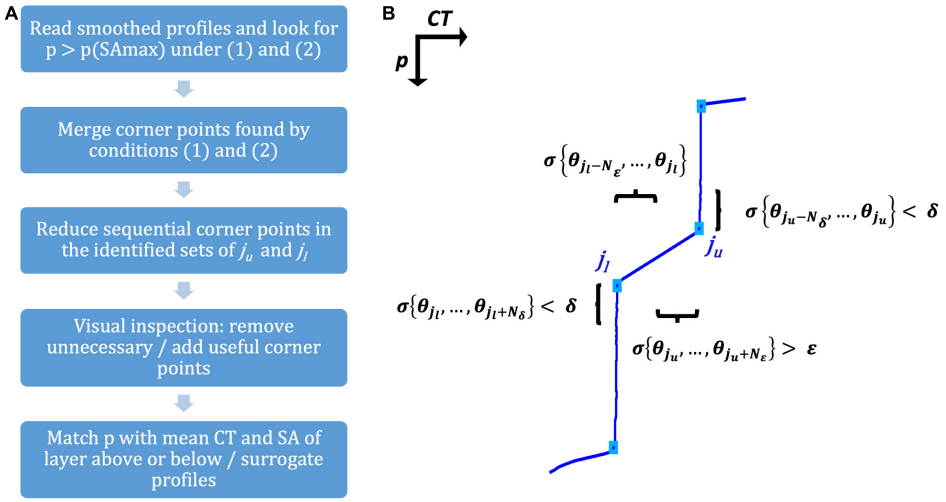

FIGURE 2 | (A) Outline of the interface detection procedure, indicating the main steps. **(B)** Detail of a CT profile with staircases illustrating the conditions (1) and (2) explained in Section "Detection of Interfaces" used to detect corner points j_u and j_l; N_δ and N_ε are the set of points adjacent to points j_u and j_l where the two conditions apply.

To simplify the entire proceeding, the search for j_u and j_l (the corner points) was performed on the CT profiles only and, when identified, their corresponding pressure, CT and SA values were noted. To eliminate unwanted variability and make it easier for the automatic procedure to detect transitions from layers to interfaces and vice versa, we smoothed the original profiles by applying a moving average low-pass filter with a 15 dbar window. Following Durante et al. (2019), satisfactory values for δ and ε were set as 10^{-4} °C and 10^{-3} °C, respectively. After some sensitivity tests, we found that considering the closest 5 points ($N_\delta = 5$) was sufficient to verify the desired low CT variability whereas the establishment of the opposite condition required addressing 10 points ($N\varepsilon = 10$). Furthermore, requisites (1) and (2) were both satisfied by multiple small groups of points spaced 1 dbar apart from each other. Subsequently, after the detection step, we tasked the algorithm with eliminating all the redundant points, keeping only the last of the sequential j_u and the first of the sequential j_l corner points because of their association with a greater ε variability. Finally, the ensuing derived profiles were superimposed on the corresponding recorded profiles, and the vertical alternation of interfaces and layers was verified by visual inspection. Any redundant corner points noticed again at this stage were eliminated by hand. Also, a few corner points that were missed by the algorithm were now added. To focus on the well-developed portion of a staircase conceived as a coherent succession of conspicuous homogeneous layers, we have selected those of thicknesses greater than 50 m. In doing so, we omit the small transient layers at the top of the staircases where the high variability suggests that there are no equilibrium conditions and therefore no justifiable way to apply the formulations (3), (4), and (5) described in the following subsection to calculate the relative heat and salt fluxes. We also ruled out the layers presenting inversions in the profiles of May 2010 (812–872 dbar and 895–1160 dbar), August 2010 (874–991 dbar), December 2010 (709–776 dbar), and May 2011 (699–752 dbar, 870–911 dbar, and 1075–1148 dbar). Finally, the small layers within the interfaces with substructures (see Section "Fluxes in Interfaces with a Stepped Substructure") were ignored, and this type of interface was identified merely by its uppermost and lowermost limits while calculating fluxes. The results of the procedure are shown in **Figure 3**.

The last step was to set the values of CT and SA for the corner points as the mean values of CT and SA in the adjoining layers (the layer above for the j_u corner points and the layer below for the j_l corner points), leading to the surrogate profiles of **Figure 4** which retain all the main properties of the thermohaline staircases and have been used to calculate the fluxes through the interfaces sandwiched between the main layers.

Calculation of Heat and Salt Fluxes

The local heat and salt fluxes, F_T and F_S – i.e., the heat and salt fluxes at the observed interfaces – were calculated using the H88 formulation of the Kunze (1987) model for thick interfaces, the RS12 model that accounts for secondary instabilities of salt fingers and the MP21 model which was developed for an inhomogeneous background stratification. In the formulations of the fluxes that follow, we consider the vertical (z) axis positive downward.

The H88 equations are:

$$\begin{cases} F_S = 2\nu\left\langle\frac{\partial S}{\partial z}\right\rangle\left(\sqrt{R_\rho}+\sqrt{R_\rho-1}\right)^2 \\ F_T = \gamma\frac{\beta}{\alpha}F_S \\ \gamma = \sqrt{R_\rho}\left(\sqrt{R_\rho}-\sqrt{R_\rho-1}\right) \end{cases} \quad (3)$$

where ν is the molecular viscosity of seawater, and $\langle\frac{\partial S}{\partial z}\rangle$ is the salinity gradient in the interface. $R_\rho = \frac{\alpha\left(\frac{\partial T}{\partial z}\right)}{\beta\left(\frac{\partial S}{\partial z}\right)}$ is the density ratio (Turner, 1973), $\gamma = \frac{\alpha F_T}{\beta F_S}$ is the flux ratio (Kunze, 1987),

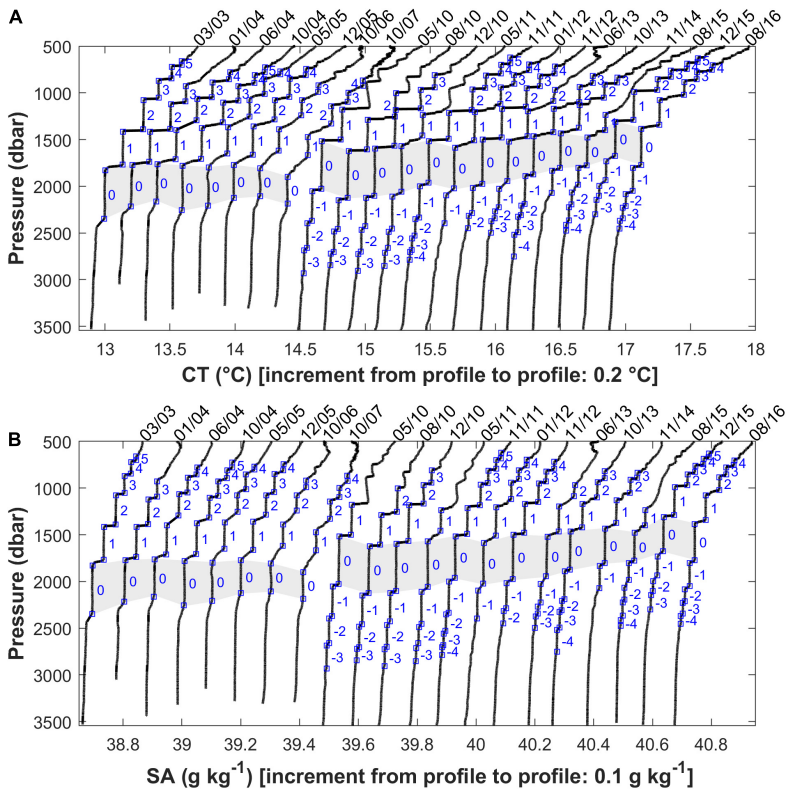

FIGURE 3 | Original (i.e., not smoothed) temperature **(A)** and salinity **(B)** profiles from each cruise with the relevant selected corner points (blue squares) overlaid on each one; the temperature profiles are offset by 0.2°C and the salinity profiles by 0.1 g kg^{-1} from cruise to cruise for better viewing. The gray band highlights the thickest layers found, numbered "0." The layers above and below it are labeled sequentially with positive and negative numbers, respectively, in their natural order of succession going up or going down.

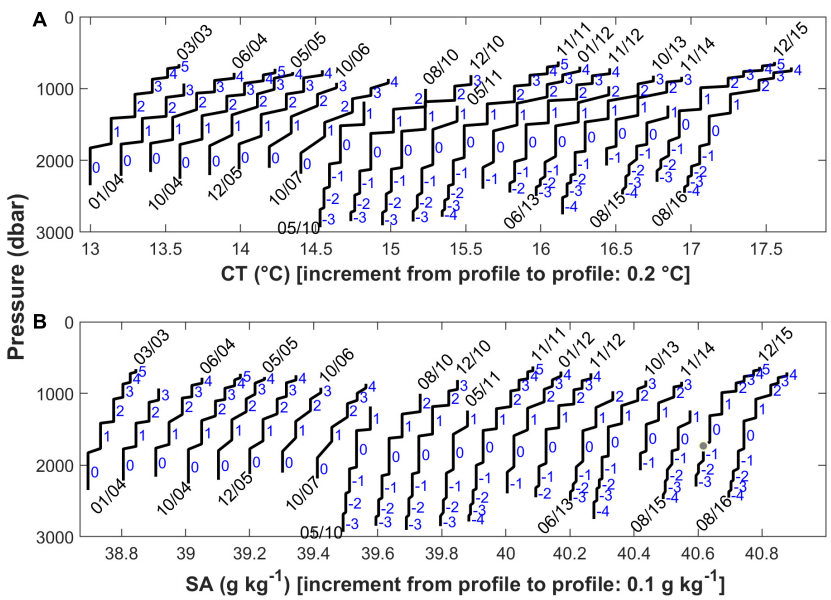

FIGURE 4 | (A) CT (°C) and **(B)** SA (g kg^{-1}) profiles for each cruise obtained by matching the depth level of every detected corner point with the average value of CT and SA in the layer above (for a j_u corner point) or below (for a j_l corner point) it. Profiles are offset by 0.2°C and 0.1 g kg^{-1} from cruise to cruise for better viewing. The layers are numbered as in **Figure 3**.

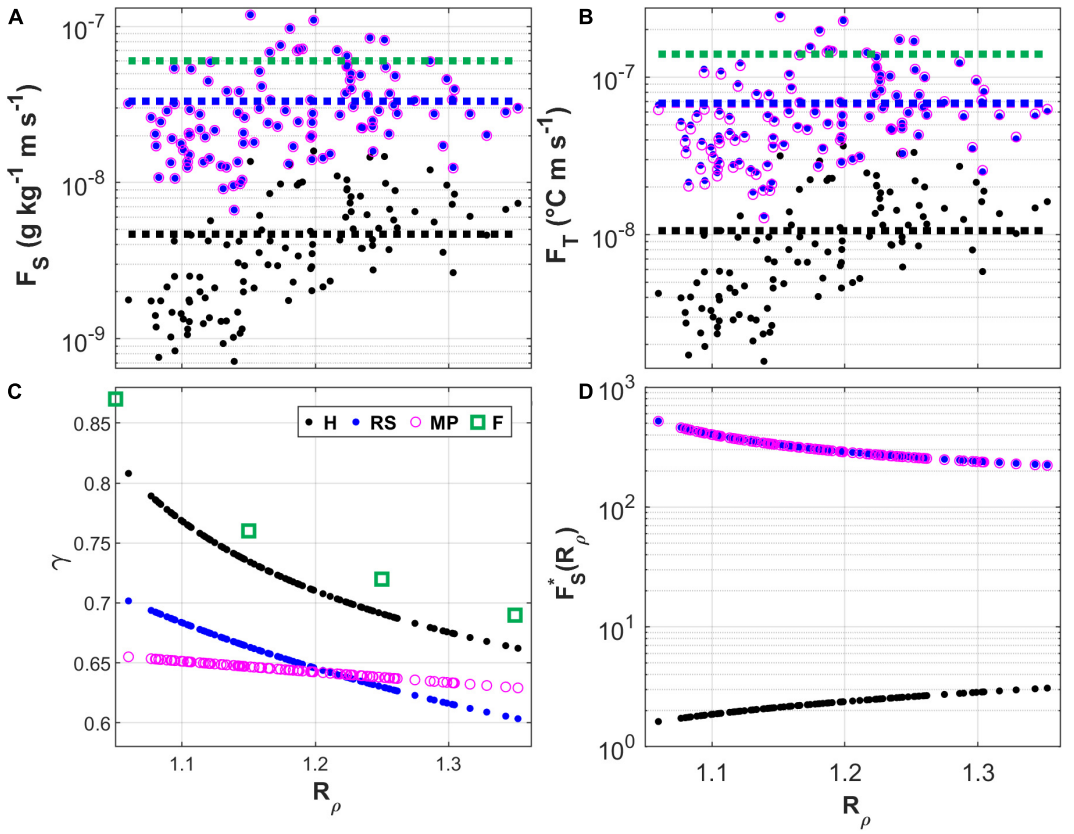

FIGURE 5 | (A–C) Comparison of the calculations of salt flux, heat flux, and flux ratio with different methods (H = H88; RS = RS12; MP = MP21; F = Ferron et al., 2021). **(D)** The relationship between salt fluxes and R_ρ ; $F_S^*(R_\rho)$ denotes the part dependent on R_ρ in equations (3)–(5). In **(A)** and **(B)**, the dashed lines represent mean values calculated for the period 2013–2014 in the 600–2800 m depth range, and the axes expressing the fluxes are set to the logarithmic scale.

and α and β are the thermal expansion and haline contraction coefficients for seawater.

These flux laws are valid for interfaces thicker than 30 cm and represent the maximum temperature and salinity fluxes due to salt fingers observed there. Therefore, they are also suitable for our staircase system where the interfaces are several tens of meters thick.

Equations (4.1) of Radko and Smith (2012), which provide non-dimensional fluxes, were transmuted into the dimensional domain by considering equations (2.3) of the same paper. The operation furnishes us with the dimensional eddy diffusivities of heat and salt as functions of the non-dimensional fluxes, $F_T{}^*$ and $F_S{}^*$, which we then multiply by the respective vertical gradients of CT and SA (Fick's diffusion model). So, the dimensional fluxes can be written as follows:

$$\begin{cases} F_S = K_S\left\langle\frac{\Delta S}{\Delta z}\right\rangle = k_T R_\rho\left(\frac{a}{\sqrt{R_\rho - 1}} + b\right)\left\langle\frac{\partial S}{\partial z}\right\rangle, \quad (a,\ b) = (135.7,\ -62.75) \\ F_T = K_T\left\langle\frac{\Delta T}{\Delta z}\right\rangle = k_T\gamma\left(\frac{a}{\sqrt{R_\rho - 1}} + b\right)\left\langle\frac{\partial T}{\partial z}\right\rangle \\ \gamma = a_\gamma exp\left(-b_\gamma R_\rho\right) + c_\gamma, \qquad (a_\gamma,\ b_\gamma,\ c_\gamma) = (2.709,\ 2.513,\ 0.5128) \end{cases} \tag{4}$$

where $k_T = 1.4 \times 10^{-7}$ m^2 s^{-1} is the molecular diffusivity of heat, and K_T and K_S are the dimensional eddy diffusivities of heat and salt, respectively.

Ma and Peltier (2021) gave functional forms for the flux ratio and the eddy diffusivities [their equation (1)]. The latter were used to derive the parameterizations of heat and salt fluxes as above, obtaining:

$$\begin{cases} F_S = K_S\left\langle\frac{\Delta S}{\Delta z}\right\rangle = \frac{k_T R_\rho}{\gamma}\frac{a}{(R_\rho - 1)^b R_\rho^c}\left\langle\frac{\partial S}{\partial z}\right\rangle, \ (a,\ b,\ c) = (78.09,\ 0.52,\ 0.87) \\ F_T = K_T\left\langle\frac{\Delta T}{\Delta z}\right\rangle = k_T\frac{a}{(R_\rho - 1)^b R_\rho^c}\left\langle\frac{\partial T}{\partial z}\right\rangle \\ \gamma = a_\gamma R_\rho^3 + b_\gamma R_\rho^2 + c_\gamma R_\rho + d_\gamma, \\ \qquad (a_\gamma, b_\gamma, c_\gamma, d_\gamma) = (-0.00068,\ 0.0163,\ -0.125,\ 0.77) \end{cases} \tag{5}$$

For the calculation, the differential terms $\left(\left\langle\frac{\partial S}{\partial z}\right\rangle, \left\langle\frac{\partial T}{\partial z}\right\rangle\right)$ in equations (3), (4), and (5) have been discretized and approximated with $\left(\frac{\Delta SA}{\Delta z}, \frac{\Delta CT}{\Delta z}\right)$ (henceforth termed as SA_z and CT_z), where ΔSA (ΔCT) is the difference between the mean value of SA (CT) in the layers above and below an interface (i.e., the mixed layers of the surrogate profiles of **Figure 4**) and Δz is the thickness of the interface itself in meters. α, β and R_ρ were calculated with the TEOS-10 software (McDougall and Barker, 2011) for the pressure level associated with the point demarcating the interface using the temperature (CT) and salinity (SA) values of the adjacent layer. The routine that calculated R_ρ also generated a value for the Turner angle (Tu) because of

the relation $R_\rho = -tan\left(Tu + 45\ deg\right)$ (Ruddick, 1983) linking the two parameters. The molecular viscosity, ν, was calculated for all the surrogate profiles using the Seawater Thermophysical Properties Library (Sharqawy et al., 2010; Nayar et al., 2016), and a representative average value of 1.24×10^{-6} m^2 s^{-1} was derived from the obtained values.

We have estimated the contributions of the heat and salt fluxes, F_T and F_S, to the local buoyancy as $g\alpha F_T$ and $g\beta F_S$, where g is gravitational acceleration (9.8 m^2 s^{-1}). Then, the net buoyancy flux was quantified as the difference between these two buoyancy constituents: $F_b = g\left(\beta F_s - \alpha F_t\right)$. The salt finger instability produces vertical fluxes diffusing heat and salt down along their mean gradients. However, the vertical transport of salt is more efficient than that of heat. Consequently, the haline component of the buoyancy flux exceeds its thermal equivalent, resulting in an up-gradient flux of density (Turner, 1967; St. Laurent and Schmitt, 1999).

The flux calculations with the three methods are compared in **Figure 5**, which also shows the mean salt and heat fluxes and the flux ratio estimated by Ferron et al. (2021) from microstructure observations in the same area in the period 2013–2015. Although they use different functional relationships, RS12 and MP21 produced values for the salt and heat fluxes that are quite similar, with only very small differences in the case of heat (**Figures 5A,B**). These values are higher than those obtained for the same fluxes with H88 by a factor of 5 and 6 for heat and salt, respectively. The discrepancies are due to the differences in the underlying assumptions and parameterizations. Those between H88 and R12 have already been reported by Bryden et al. (2014) and Falco et al. (2016), and arise from the distinctive parameterizations with respect to R_ρ and on the specific constants used. This is immediately evident from **Figure 5D**, where the dependency of the salt flux on the density ratio in the three models is presented. The parameterizations of RS12 and MP21 provide values which decrease with R_ρ while that of H88 does the opposite. Disparities are also found in the dependence of the salt flux on the salinity gradient (not shown), which are due exclusively to the use of different constants in the models: numerically, the molecular viscosity in equations (3) and the molecular diffusivity of heat in equations (4) and (5), diverge from each other by an order of magnitude.

The comparison of the mean salt and heat fluxes obtained by Ferron et al. (2021) (green dashed line in **Figures 5A,B**) with those calculated by us from our dataset for the same period and depth range (blue and black dashed lines) as them showed that their computational scheme is much closer to RS12 and MP21 than to H88. The flux ratio values we obtained with our data (**Figure 5C**) are arranged exactly along the theoretical curves imposed by the equations (3), (4), and (5), i.e., $\gamma^{RS} = f\left(e^{-R_\rho}\right)$, $\gamma^{MP} = f\left(R_\rho^3\right)$, and $\gamma^{H} = f\left(R_\rho\right)$. They are close to 0.7, as could be expected in a salt finger regime (Schmitt, 1979), but are slightly lower in the RS12 and MP21 parameterizations than in H88. The H88 results for the flux ratio are more consistent with the values derived for the parameter from the microstructure observations. The flux ratio parameterization of MP21 varies only slightly when compared to those of both RS12 and H88 in our density ratio range. Overall, however, they resemble the fluxes coming from RS12 rather closely.

RESULTS

Time Evolution of the Thermohaline Properties in the Measurement Period

Durante et al. (2019) have already shown that thermohaline properties change over time and along the water column, and relate these changes to the variations observed in the LIW. Here, we carry this study forward by analyzing how the salinity and temperature at the level of the LIW and in the underlying layers changed over the period covered by the observations, and examining the natures of the associated trends.

Figures 6A,B shows the maximum salinity value and corresponding temperature for each profile, which denote the LIW signal in our observational domain. Furthermore, it presents the average salinity and temperature in the layers labeled 0 and 1 in **Figure 3** and in the deep layer. Layer 0 is the thickest layer in each profile (located within the gray area in **Figure 3**) and layer 1 lies just above it. Both layers are well-developed in all the profiles, and correspond to the main-middle pair of layers in Figure 4 of Durante et al. (2019). We have identified the deep layer as the part of the water column comprising the last 500 dbar above the bottom which is not affected by the formation of steps. However, the average values of the two parameters and associated trends do not change significantly even if we reduce its thickness to just 100 dbar from the bottom. We have not shown the standard deviations associated with the mean values in the figure because they are very small in all the layers, and are not appreciable on the plot scale.

Trends of salinity and temperature are estimated as the slopes, accompanied by their standard errors, of a linear regression model. The LIW shows warming and salinification trends of 0.019 ± 0.005 °C yr^{-1} and 0.0036 ± 0.0006 g kg^{-1} yr^{-1}, in line with the values reported by Schroeder et al. (2017) for the same trends in the Strait of Sicily (0.024 °C yr^{-1} and 0.006 yr^{-1}; the latter value does not change if expressed in g kg^{-1} yr^{-1}). Our somewhat lower values can be attributed to the changes the LIW undergoes due to mixing with the waters it encounters during its journey from the Strait of Sicily to our measurement area (Millot and Taupier-Letage, 2005). Another possible reason for this slight diminution is the fact that the core of the LIW moves mainly along the boundaries of the Tyrrhenian Sea, so its signal in our area tends to be principally modulated by lateral advection (Astraldi and Gasparini, 1994; Zodiatis and Gasparini, 1996). The layers 0 and 1 also present warming and salinification trends, but they are slower compared to those of the LIW. The temperature varies at a rate of 0.011 ± 0.001 °C yr^{-1} in both layers, and the salinity by 0.0031 ± 0.0004 g kg^{-1} yr^{-1} in layer 1 and 0.0032 ± 0.0004 g kg^{-1} yr^{-1} in layer 0. In the case of the deep layer, the variations of the two properties are very small and their trends are contrary to those characterizing the water column above (-0.0023 ± 0.0004 °C yr^{-1} and -0.0005 ± 0.0004 g kg^{-1} yr^{-1}). The trends of the deep layer coincide with the intrusion of less salty (<38.68 g kg^{-1}) and colder (<12.93°C)

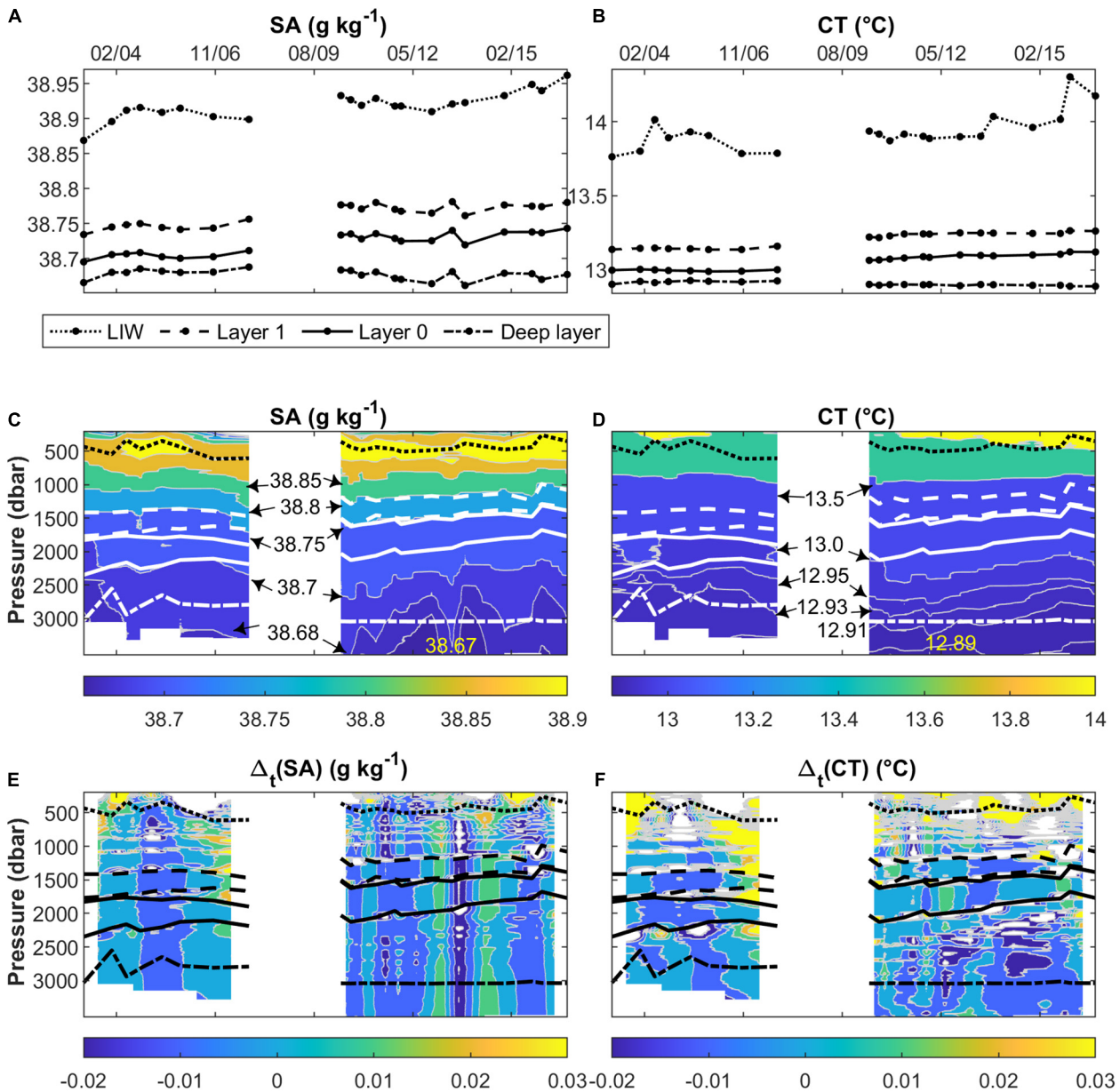

FIGURE 6 | Evolution over time of salinity (SA) and temperature (CT). **(A)** and **(B)** show the variation of the maximum salinity and its corresponding temperature value (LIW), together with the average values of SA and CT in the layers 0 and 1 of the staircases, and in the last 500 dbar above the bottom. **(C)** and **(D)** present the behaviors of salinity and temperature with respect to pressure and time. **(E)** and **(F)** the same, only this time for the calculated difference in salinity and temperature between two consecutive times instead. In **(C–F)**, the position of the LIW and the previously specified 0, 1 and deep layers are indicated using the types of lines ascribed to them in the legend of **(A)** and **(B)**.

water (**Figures 6C,D**) coming from the Western Mediterranean (Schroeder et al., 2016). This intrusion is present from December 2010 to December 2015. It is not persistent and is more visible in salinity than in temperature. It is not observed in May 2011, June 2013, November 2014, and August 2015, which correspond to periods when the 38.68 g kg^{-1} isoline sinks toward the bottom, as can be seen in **Figure 6C**. In January and November 2012, and in October 2013, the lowest salinity value of the whole dataset, equalling 38.66 g kg^{-1}, is observed below 3250 dbar. The detected intrusion seems to be causing the isolines of both salinity and temperature to rise. The layers 0 and 1 behave likewise, with an upward displacement. **Figure 3** shows that the entire staircase system is subjected to this uplifting. The deep layer appears isolated from those above it and does not seem to benefit at all from the possible heat and salt inputs driven downward by the salt fingering phenomenon.

The differences noted in salinity and temperature at the same pressure level at two consecutive times (**Figures 6E,F**)

suggest that our profiles are contaminated by internal waves (see Figure 1d in van Haren and Gostiaux, 2012, for a possible corroboration). Over time, such differences swing back and forth between positive and negative values in extended portions of the water column, suggesting that they are caused by low salinity, low temperature or high salinity, high temperature water types being pushed up and down by wave motion. This pattern is complicated by cases in which the layer is squeezed from above and below due to the probable passage of out-of-phase waves, which mainly occurs in the period 2003–2007. Internal gravity waves occupy a frequency range bounded by the local inertial frequency below and by the Brunt-Väisälä frequency above (Garrett and Munk, 1975). In the Tyrrhenian Sea, where our observations were made, the local inertial period is 18.7 h. This is an upper limit for the sampling time needed to resolve internal waves. Our coarse sampling interval does not allow us to resolve the frequencies of internal waves, and therefore to investigate how they interact with the staircases. In deep water and far from topography, as in our case, the contribution of such waves to the vertical mixing could be relevant (Munk and Wunsch, 1998).

Staircase Properties

The staircase system consists of a series of main layers (thicker than 90 dbar) with several thinner layers above and, from 2010, below, which are separated by interfaces showing a rich variety of structures. Durante et al. (2019, their Table 1) classified the interfaces into four classes: sharp, slope, steppy, and rough. Sharp interfaces present relatively large gradients of temperature and salinity in a short vertical interval (what we expect for a theoretical staircase in equilibrium), such as those observed above 1500 dbar in **Figure 3** in March 2003 and April 2004. Slope interfaces are like sharp interfaces, but thicker (the gradients are more extensive vertically). They are common at the base of a staircase (seen, for example, from May 2010 onward in the same figure), but are also found at intermediate depths (as noticeable between layers 1 and 2 in June and October 2004, again in **Figure 3**). Steppy interfaces, like those evident between layers 1 and 2 in October 2013 and November 2014, incorporate small layers which may or may not be homogeneous (i.e., they might have small gradients from top to bottom or in the middle) with additional interfaces between them. Rough is a further attribute which characterizes some of the slope and steppy interfaces that show certain kinds of irregularities. To simplify, we will consider only the three main types of interfaces, i.e., sharp, slope and steppy, regardless of their roughness, in this section.

The layers can vary in number from one profile to another, and their level of development may also differ. They are more abundant in the period 2010–2016 than in the period 2003–2007. The thickest layer in each profile (layer 0, in **Figure 3**) migrates upward from 2010 onward when more layers can be distinguished below it. The thickness of each layer varies over time. For example, the thickness of layer 0 is 510 m in March 2003, 280 m in October 2007, 502 m in May 2010, and 380 m in August 2016.

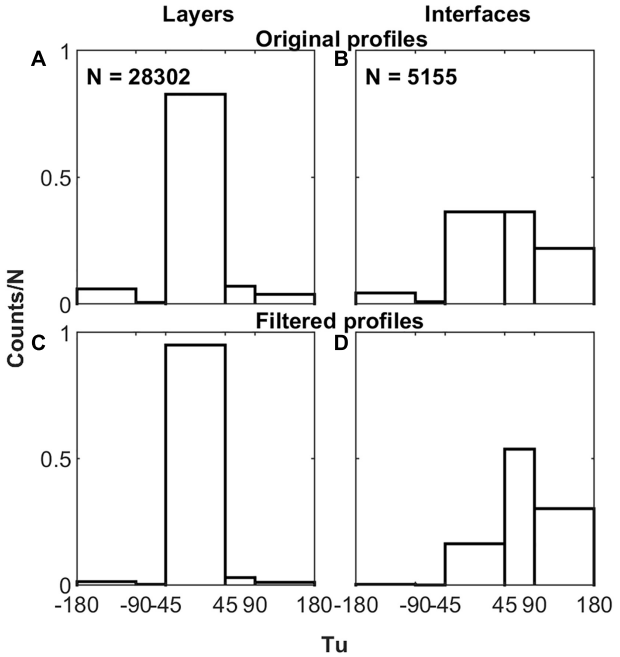

FIGURE 7 | (A,C) Histograms categorizing the density of observations in the layers extracted from the original and filtered profiles on the basis of the Turner angle. **(B,D)** The same, only this time for the interfaces instead of the layers.

The prevailing patterns of stratification are reflected in the distributions of the values of the Turner angle associated with the layers and the interfaces, as shown in **Figure 7**. The figure presents histograms depicting the density of observations relating to the layers and the interfaces obtained from the untreated and the low-pass filtered data with a vertical resolution of 1 dbar in different bins of the local Turner angle. The dominant stratification within the layers is of the stable type ($-45 < Tu < 45$ deg), embracing 83% and 95% of the observations in the original and filtered profiles, respectively. Other configurations are also present, including the gravitationally unstable type, but to a smaller extent, so they are largely removed by the filter. Similarly, within the interfaces, various configurations are observed, with stable and finger ($45 < Tu < 90$ deg) types prevailing. There are interfaces that include gravitationally unstable zones ($Tu > 90$ deg), too. In terms of the fraction of observations they represent, the three mentioned interface configurations are distributed thus in the untouched and filtered sets of profiles, respectively - stable: 36%, and 16%; finger: 36%, and 54%; gravitationally unstable: 26%, and 30%. Filtering the original profiles brings out the finger instability type as the prevalent configuration. It is worth noting that even in the filtered profiles there remain areas within the interfaces that are gravitationally unstable.

To identify the main features of the typical staircase, we used the surrogate profiles of **Figure 4**. Note that the perturbations within layers and interfaces are therefore not considered. The thickness of the layers, h_l, ranges from 60 to 510 m (**Figure 8A**), and shows a tendency to increase

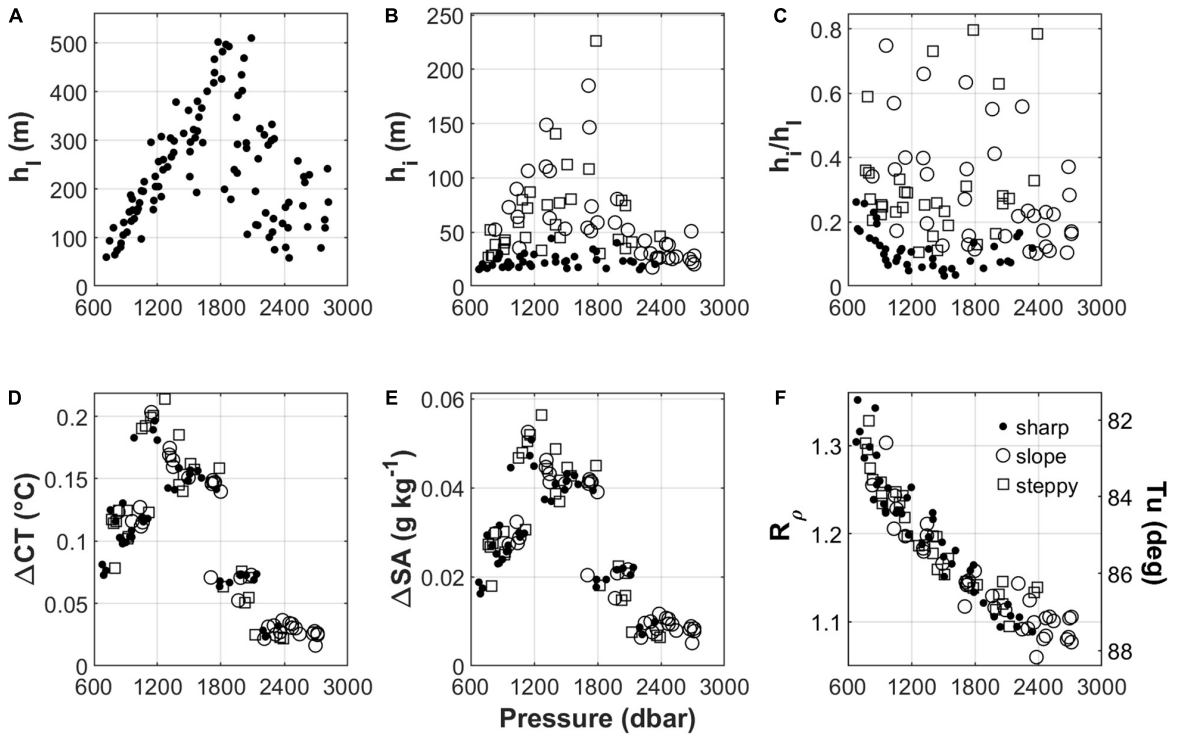

FIGURE 8 | Main features of the staircase system vs. pressure (dbar). **(A)** Layer thickness (m), referring to the midpoint of the layer. **(B)** Interface thickness (m), referring to the midpoint of the interface. **(C)** Ratio between the thickness of the interface and the underlying layer. **(D,E)** Differences of the temperature (°C) and the salinity (g kg^{-1}) across an interface. **(F)** Density ratio (left axis) and the correspondent values of the Turner angle (right axis). In **(B–F)**, the values corresponding to the different types of interfaces (sharp, slope, steppy) are denoted by the symbols ascribed to them in the legend of **(F)**.

linearly with depth down to about 1850 dbar. At greater depths, h_l decreases. As for the interfaces, their thickness, h_i, is very variable, ranging from 15 m to several hundreds of meters (**Figure 8B**). The thickest interfaces are those of the slope and steppy types. The sharp interfaces have, at most, thicknesses of 44 m. **Figure 8C** presents the ratios between the thicknesses of the interfaces and their underlying layers. We noticed that sharp interfaces are never more than quarter the size of their underlying layers. On the contrary, the other two types of interfaces can reach sizes of up to 40% of the extensions of the layers below them, and sometimes even more. According to Zhurbas and Ozmidov (1984), the ratio between the thicknesses of the interfaces and the underlying layers may vary depending on the process that generated the step they are part of. In particular, from theoretical reasoning and some considerations on the geometric properties of a profile containing steps, they derived qualitative reference limits for this ratio in the presence of different generation mechanisms. They suggested that the characteristic range for double diffusion should be $0.02 \leq \frac{h_i}{h_l} \leq 0.25$. Higher values would indicate the dominance of other processes such as the kinematic effect of internal waves (∼1) and the local effects of turbulent mixing (intermediate values, between 0.25 and 1). Unfortunately, we are unable to quantify the possible effects of similar processes on the Tyrrhenian staircases as this would require additional data which we do not have. However, in the case of slope interfaces, which often also show roughness, it is very likely that there are other processes in action besides double diffusion. In the case of steppy interfaces, a separate discussion should be made, going into the details of their substructure and evaluating the ratio between each sub-interface and sub-layer. The values we report for the ratio in **Figure 8C** are certainly overestimated for steppy interfaces, because we have established their thicknesses for the calculations by considering them in their entirety, i.e., from the top to the bottom.

The differences in temperature and salinity across the interfaces, ΔCT and ΔSA, corresponding to the disparities between the layer above and below the interface in the two properties, vary in the range 0.02–0.2 °C and 0.005–0.06 g kg^{-1}, respectively (**Figures 8D,E**). The greatest variations are observed in the pressure range 980–1800 dbar, regardless of the type of interface.

The values obtained for the density ratio R_ρ and the Turner angle Tu (**Figure 8F**), falling as they do in the limits $71.6 < Tu < 90\ deg$ and $1 < R_\rho < 2$ describing a fingering regime (Ruddick, 1983), confirm the ubiquitousness of the phenomenon in the area. R_ρ (Tu) decreases (increases) from the top to the bottom, where it tends to approach unity, and is always less than 1.7. This is usually associated with the appearance of step-like structures in vertical T-S profiles (Schmitt, 1981; Schmitt et al., 1987; Radko et al., 2014a). The lowest values of R_ρ are associated

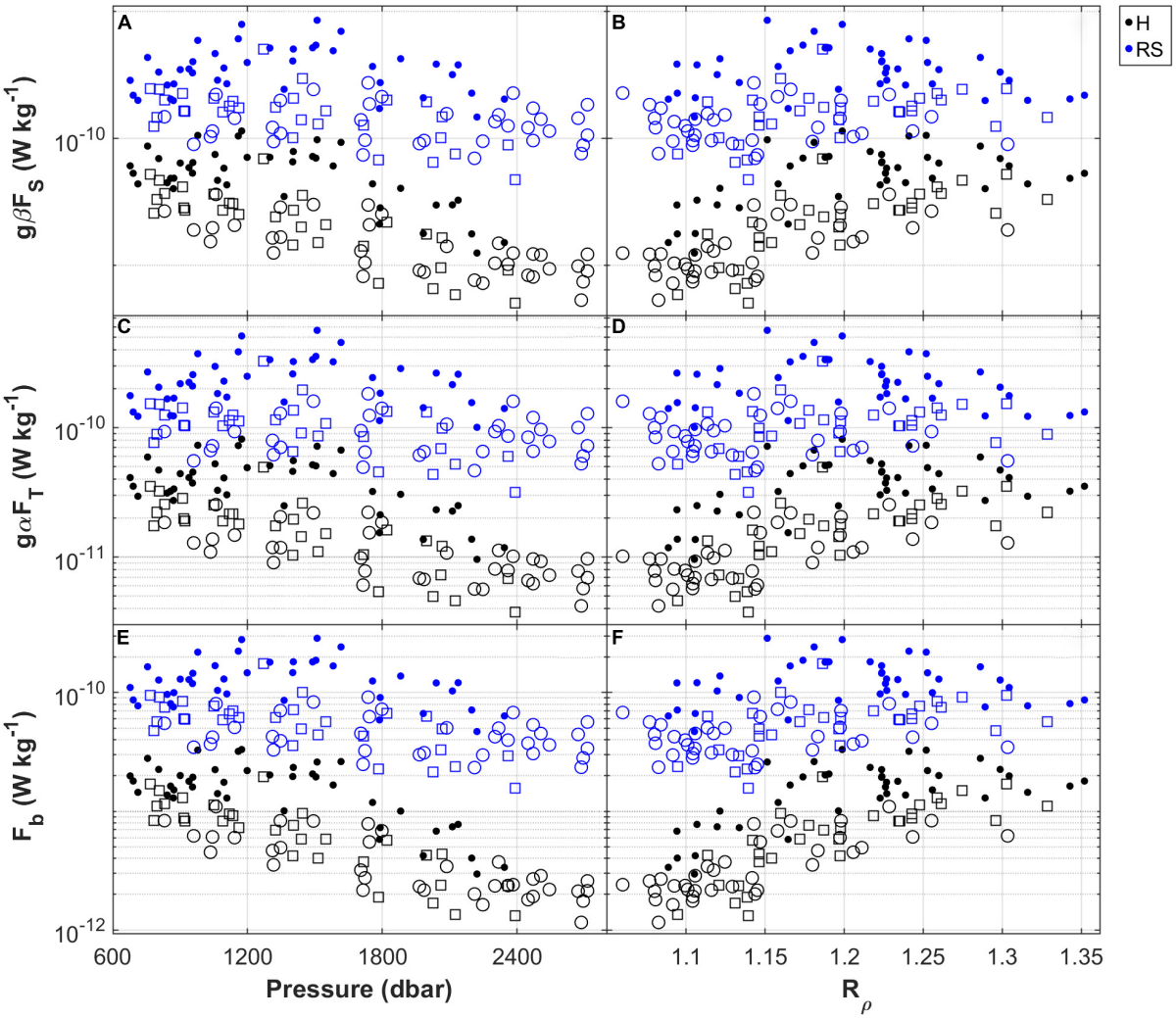

FIGURE 9 | (A,C,E) The salt and heat contributions ($g\beta F_S$ and $g\alpha F_T$) to the buoyancy flux and the net buoyancy flux (F_b) versus pressure. **(B,D,F)** The same, but this time versus the density ratio (R_ρ) instead of pressure. Sharp, slope and steppy interfaces are represented by a black circle, a white circle and a white square, respectively. In the legend, H and RS refer to H88 and RS12, respectively. The axes expressing the fluxes are set to the logarithmic scale.

with slope interfaces, which are frequently found at the bases of the staircases.

Heat and Salt Fluxes Through Interfaces

Local fluxes vary both with depth (pressure) and in time. We began by examining the variabilities of the salt and heat contributions to the buoyancy, namely $g\beta F_S$ and $g\alpha F_T$, and their difference, the net buoyancy flux F_b, with the pressure p and the density ratio, R_ρ. Plots of $g\beta F_S$, $g\alpha F_T$, and F_b with respect to p (**Figures 9A,C,E**) and R_ρ (**Figures 9B,D,F**) almost mirror each other, reflecting the R_ρ *(p)* relationship already evidenced in **Figure 8F**. As already noted, the fluxes obtained with RS12 are higher than those calculated with H88, but the trends of the estimates as a function of the pressure and of the density ratio are almost the same in both the cases. The values are generally larger in the portion of the water column between 600 and 1800 dbar where $R_\rho > 1.15$, mainly in correspondence with sharp interfaces. Below 1800 dbar, they start to decrease, reaching minima at the bottoms of the staircases, typically in the presence of slope interfaces. To provide a sort of reference "frame" for broadly characterizing the portion of the water column affected by the staircase phenomenon at the studied location in terms of the fluxes, we have used our results to estimate some basic statistics for them in different pressure ranges, as reported in **Table 1**. The decrease in the fluxes with depth is greater in the results obtained with H88. The average net buoyancy flux obtained from the RS12 parameterization is $(0.8 \pm 0.6) \times 10^{-10}$ W kg^{-1} – close to the value of $(1.2 \pm 4\%) \times 10^{-10}$ W kg^{-1} obtained by Ferron et al. (2021) for it in the same region, and by Bryden et al. (2014) for the staircase in the Algerian basin (1×10^{-10} W kg^{-1}) – while that from H88 is about an order of magnitude lower, approximately $(0.10 \pm 0.08) \times 10^{-10}$ W kg^{-1}.

The ratio between heat (salt) fluxes and the vertical gradients of temperature (salinity) provides an estimate of the eddy

TABLE 1 | Some basic statistics (mean, standard deviation, minimum, and maximum) summarizing the fluxes calculated in different pressure ranges with the two models, H88 and RS12.

Pressure range	$g\beta F_S$				$g\alpha F_T$				F_b				N
	mean	std	min	max	mean	std	min	max	mean	std	min	max	
(dbar)	(10^{-10} W kg^{-1})				(10^{-10} W kg^{-1})				(10^{-10} W kg^{-1})				
					Hebert (1988)								
600–1200	0.48	0.24	0.15	1.14	0.33	0.17	0.11	0.81	0.15	0.07	0.05	0.33	40
1200–1800	0.36	0.26	0.07	0.98	0.26	0.19	0.05	0.72	0.10	0.07	0.02	0.26	33
1800–2400	0.15	0.09	0.05	0.41	0.12	0.07	0.04	0.31	0.04	0.02	0.01	0.10	25
2400–3000	0.09	0.02	0.05	0.12	0.07	0.02	0.04	0.10	0.02	0.01	0.01	0.03	10
600–3000	**0.33**	**0.26**	**0.05**	**1.14**	**0.24**	**0.18**	**0.04**	**0.81**	**0.10**	**0.08**	**0.01**	**0.33**	**108**
					Radko and Smith (2012)								
600–1200	2.71	1.48	0.90	7.89	1.71	0.95	0.55	5.09	1.00	0.53	0.35	2.79	40
1200–1800	2.80	1.96	0.68	8.50	1.83	1.28	0.45	5.63	0.97	0.68	0.23	2.86	33
1800–2400	1.74	1.05	0.47	4.23	1.19	0.71	0.32	2.86	0.56	0.33	0.16	1.38	25
2400–3000	1.25	0.36	0.76	1.84	0.86	0.25	0.53	1.28	0.39	0.11	0.23	0.56	10
600–3000	**2.38**	**1.59**	**0.47**	**8.50**	**1.55**	**1.02**	**0.32**	**5.63**	**0.83**	**0.57**	**0.16**	**2.86**	**108**

N is the number of data points in each sample. The values in boldface are those obtained for the entire pressure range considered (600–3000 dbar).

diffusivities of heat (salt). **Figure 10** shows the relationships of the heat and salt fluxes, F_T and F_S, with their respective gradients, CT_z and SA_z. The two datasets are aligned along straight lines whose slopes can be considered representative of the eddy diffusivities in our salt finger region: $K_S = (6.2 \pm 0.1) \times 10^{-6}$ m^2 s^{-1} and $K_T = (3.56 \pm 0.02) \times 10^{-6}$ m^2 s^{-1} with H88, and $K_S = (3.80 \pm 0.09) \times 10^{-5}$ m^2 s^{-1} and $K_T = (1.92 \pm 0.07) \times 10^{-5}$ m^2 s^{-1} with RS12.

Time series of local heat and salt contributions to the buoyancy flux calculated with RS12 are shown in **Figure 11** (the equivalent resulting from the application of H88 is provided as **Supplementary Figure 1**). Comparing the two periods 2003–2007 and 2010–2016, it can be seen that the fluxes in the first period are weaker than those in the second, even in the presence of sharp interfaces. Furthermore, in both the periods, there are situations where the fluxes are low along the entire water column. This happened from May 2005 to October 2007, in May 2011 and in June 2013, and corresponded with occasions when interfaces were rough and predominantly of the slope or steppy type. In May 2005, October 2006, and October 2007, the entire profile was rough (Table 1 in Durante et al., 2019). These profiles are squeezed from above and below, probably due to the passage of out-of-phase internal waves (as previously mentioned in Section "Time Evolution of the Thermohaline Properties in the Measurement Period"), considerably reducing their thicknesses. The profiles of January 2012 and August 2015 also show particularly low fluxes, but with interfaces which are steppy. We will evaluate this kind of situation better in the following section.

Another point to underline is that the strongest fluxes seem to be occurring mainly between 700 and 1600 dbar, which confirms the process is much more intense below the lower limit of the LIW. The largest fluxes occur at the upper boundaries of layers 1 or 2 in the first period, and layers 0 or 1 in the second period. Furthermore, the portion of the water column affected by high fluxes moves upward, a consequence of the upward migration of the staircases. Vertical displacements of layers and interfaces have been ascribed to the action of internal waves (Johannessen and Lee, 1972; Schmitt et al., 1987). This would seem to explain the vertical displacements in the period 2003–2007, when the staircases showed both upward and downward movement. But since 2010, even though there is an up-and-down swing, a trend is also evident with all the major layers moving upward by several hundred meters. This coincides with the formation of additional layers below 2000 dbar. We think that the intrusion of nWMDW near the bottom plays a role here, both by pushing the old resident water upward and by causing new steps to be generated as a result of the enhancement of the necessary downward heat and salt fluxes. However, it should be emphasized that the fluxes through the interfaces that separate these supplementary layers are small: just 6–27% of the highest values ($g\alpha F_T = 5.63 \times 10^{-10}$ W kg^{-1} and $g\beta F_S = 8.50 \times 10^{-10}$ W kg^{-1}), obtained between layer 1 and layer 0 in May 2010.

Figure 12 shows the net fluxes of salinity and temperature in the layers situated between pairs of interfaces for which the fluxes were calculated (see **Figure 11**). The net flux in a layer is the upper interface flux minus the lower interface flux. A negative net flux means that the layer exports the property. A positive net flux means exactly the opposite. The last layer depicted in **Figure 12** is the penultimate layer of the staircase identified in **Figure 3**. We cannot calculate the net fluxes in the first and last layers of the staircase because we do not know their ingoing and outgoing fluxes, respectively. There is a tendency of the staircase to gain salt and heat (positive net fluxes) in the layers located at intermediate and deep depth levels, while those above are more inclined to lose

them. Net fluxes in layers 1 and 0 are predominantly positive and those in layer -1 (observed only from 2010 onward) are always positive. These are the thickest layers in the vertical sequence, layer 0 being the thickest of all, followed by the other two. At different times, at least one of these layers has net positive fluxes. The only exception is observed in June 2004, where we only have the net fluxes in layer 1, and they are negative; however, the layer 2 above has positive net fluxes of high magnitude, indicating it is the layer gaining salt.

Moving to the base of the staircase, we see that the penultimate layers have mainly positive net fluxes, with very few exceptions, so they also tend to gain salt and heat. This is in addition to the fact that from 2010 onward, the fluxes in the deeper interfaces are very small compared to those obtained for the central part of the staircases. This result might explain the trend reported in Section "Time Evolution of the Thermohaline Properties in the Measurement Period" for the deep layer, suggesting that it is generally isolated from what is happening above and does not benefit much from the heat and salt intake pushed downward by the salt fingering process.

Assessing the impact of net fluxes on the heat and salt content of a specific layer is challenging, and near to impossible, seeing that we do not know how long they are effective. However, just to give an idea, a positive net flux on the order of 10^{-7} would raise the salinity (temperature) of 100 m of the water column by an amount equal to the trend calculated in section "Time evolution of the thermohaline properties in the measurement period" for layers 0 and 1 in about 1 month (4 months). Since the thicknesses of the two layers are greater than 100 m, it follows that the actual times would be longer. The reality is still more complicated. As shown in **Figure 12**, the net fluxes can even be two orders of magnitude lower, and layers can retain or release the relevant properties depending on the existing conditions. What is certain is that staircases play a significant role in the transfer of temperature and salt downward in the Tyrrhenian Sea, and therefore contribute in a noteworthy way to the diapycnal mixing in the area where they are found.

Fluxes in Interfaces With a Stepped Substructure

In the calculations presented in the previous section, we simplified the steppy interfaces as delimited by their uppermost and lowermost limits, ignoring any internal substructure. The approximation, while reasonable for the period 2003–2007 during which it is difficult to discern finer detail within such interfaces, is not always readily applicable later. This is particularly evident in the profiles corresponding to the interval extending from January 2012 to August 2016, which we examine below.

First, for each of the steppy interfaces shown in **Figure 13A**, we selected all the points identifiable visually in the original profiles as the ends of its sub-layers and sub-interfaces by hand. The original profiles were used because many of these

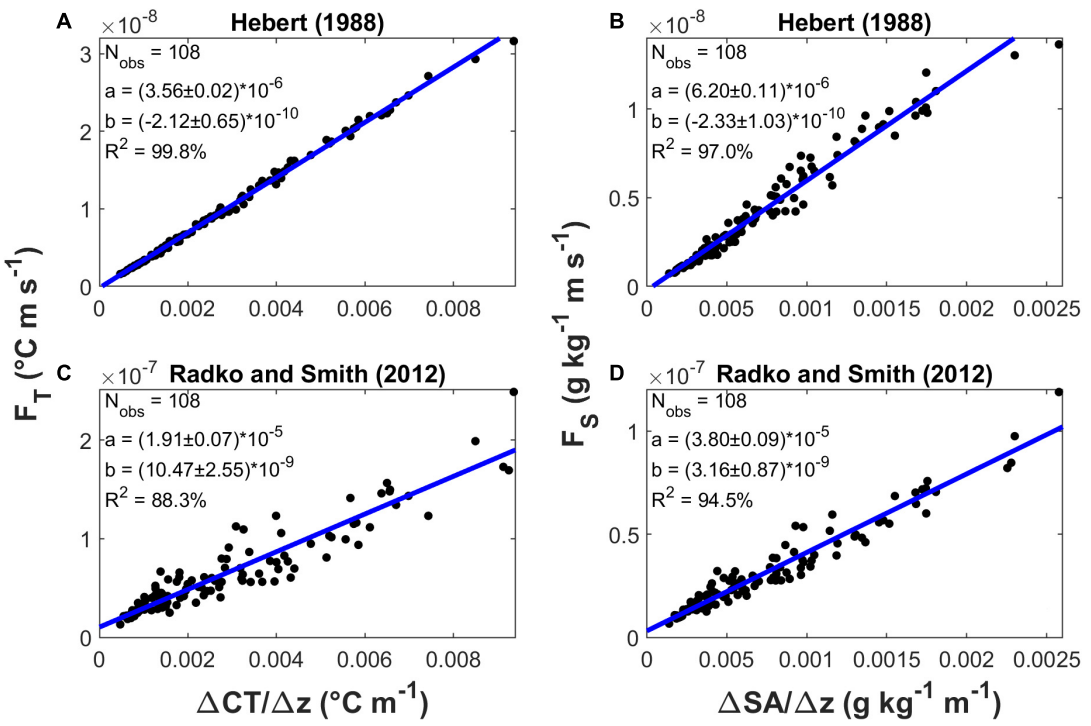

FIGURE 10 | Fluxes versus gradients. **(A)** Heat flux F_T (°C m s^{-1}) versus CT gradient (°C m^{-1}), with H88. **(B)** Salinity flux F_S (g kg^{-1} m s^{-1}) versus SA gradient (g kg^{-1} m s^{-1}), with H88. **(C)** Heat flux F_T (°C m s^{-1}) versus CT gradient (°C m^{-1}), with RS12. **(D)** Salinity flux F_S (g kg^{-1} m s^{-1}) versus SA gradient (g kg^{-1} m s^{-1}), with RS12. Each panel includes the slope (a) and the intercept (b) of a linear fit (Matlab function fitlm) to presented data, accompanied by their standard errors; a value for R^2 is also reported.

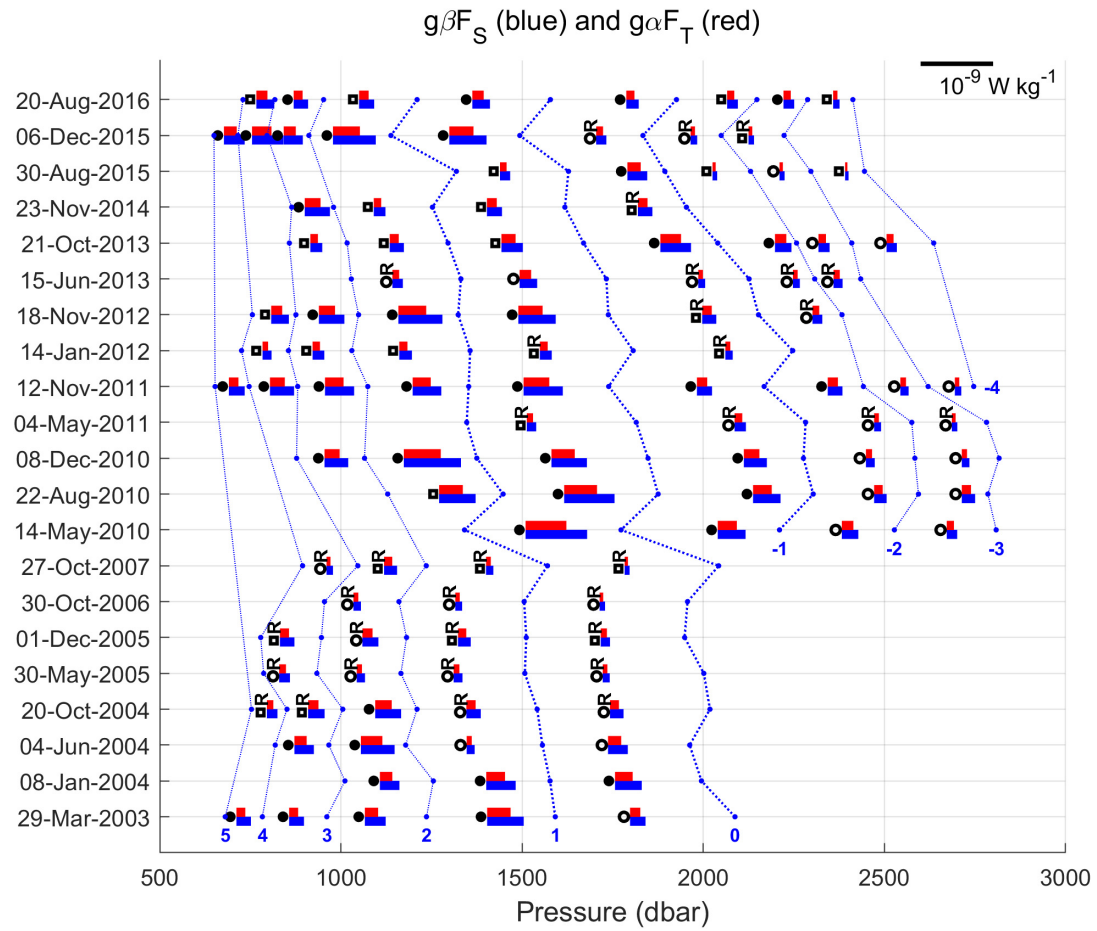

FIGURE 11 | The heat and salt contributions ($g\alpha F_T$ and $g\beta F_S$) to the buoyancy flux over time, calculated with RS12. Each value is represented by a colored bar: blue for the salinity and red for the temperature. The scale is 10^{-9} W kg^{-1}. Sharp, slope and steppy interfaces are represented by a black circle, a white circle and a white square, respectively. Rough interfaces are identified with the capital letter "R." A layer is delineated by a blue line running through its middle.

substructures had been filtered out in their surrogates. Then, we recalculated the fluxes through the now more resolved interfaces and compared the results to those obtained by us for them in our previous calculations (**Figures 13B,C**).

The number of homogeneous layers embedded in the steppy interfaces varies from one profile to another and with the depth, and so do their thicknesses which range from a few meters to some tens of meters. The largest sub-layers, 36, 54, and 35 m thick, are in the profiles of January 2012, November 2014 and December 2015. The shape of the interfaces changes from profile to profile too, taking on different forms, including sharp (in November 2012 and December 2015) and slope (in June 2013). Although there seems to be a continuity in the evolution of some substructures between consecutive profiles – for example, the large sub-layer of November 2014 which occupies the space previously occupied by the steppy interface of October 2013 that suggests a merging event of some kind – we cannot say with certainty if this is actually true. The long intervals of time between successive samplings strongly limit our ability to follow relevant step changes with the required degree of exactitude. In fact, what we see at a given moment is a realization of the staircase which could have occurred any number of times in the 4–12 months between one observation and the next. However, it is worth mentioning that the direct numerical simulations of Ma and Peltier (2021) took about 2 years on a physical timescale to reach equilibrium from the initial background gradient perturbation. During this time, their system evolved through merging events. The changes we observed between October 2013 and November 2014 seem to reasonably conform to the temporal frame they determine for the evolution and establishment of "stable" staircases.

From the comparison of fluxes in **Figures 13B,C**, it is immediately evident that they are larger in the presence of steppy interfaces, resulting 5–13 times greater than those calculated with their corresponding rectified analogs. The highest values are found in the vicinity of sub-layers with thicknesses greater than 20 m. In the case of the June 2013 profile, the interfaces are very elongated vertically, so the gradients are small, and the fluxes are much lower than those of the typical steppy interfaces.

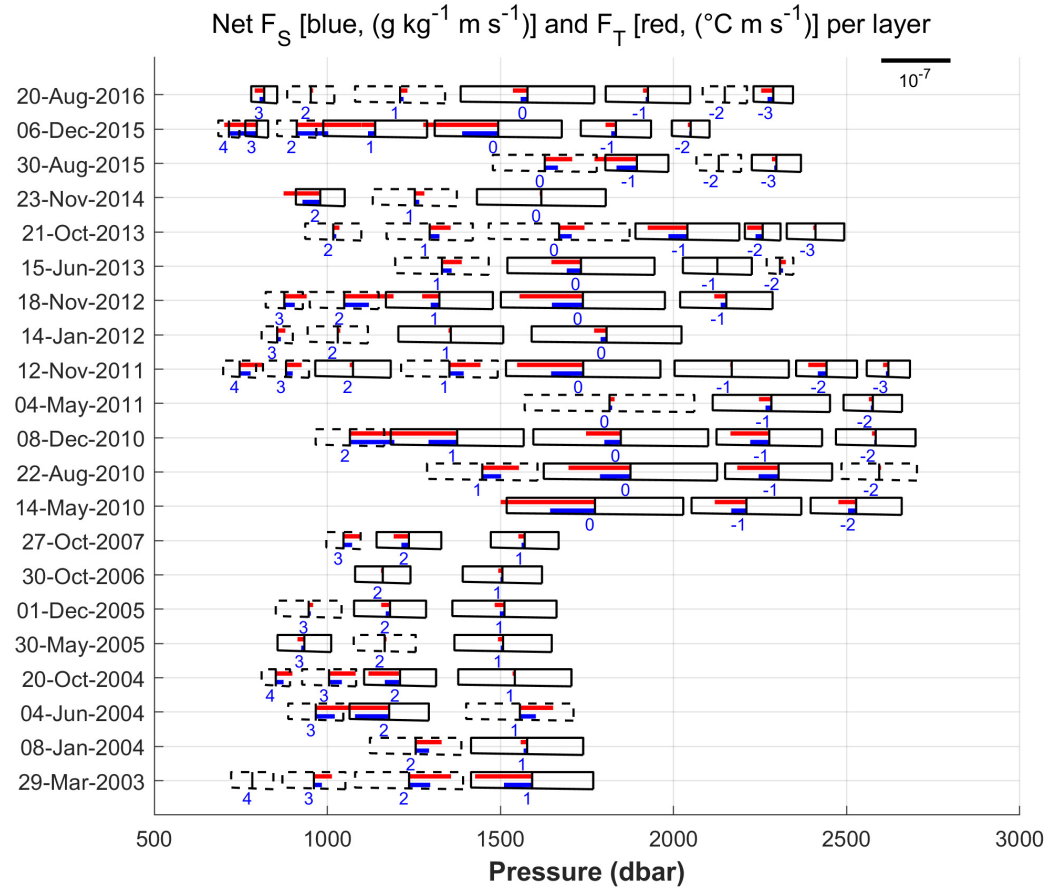

FIGURE 12 | The net fluxes of salinity and temperature (RS12) associated with the layers, i.e., the upper interface flux minus the lower interface flux for each layer. The rectangles represent the layers, numbered following the scheme laid down in **Figure 3**. A dashed line delimiting a layer means that it exports more salinity/temperature than it receives, and a similar solid line means exactly the opposite. The orientation of a flux bar to the left or to the right indicates a net flux into or out of a layer, respectively.

On the other hand, the November 2012 and December 2015 profiles, which have sharp interfaces, provide comparable values, though still slightly lower than the maximum ones obtained from the steppy interfaces. This suggests that steppy interfaces are hot spots for enhanced mixing.

Using the flux values obtained in this section, the sign of all the net fluxes in layers 0 and 1 in **Figure 12** would change from negative to positive except for the one from the October 2013 profile which has a particularly efficient sharp interface at its lower limit. The calculations in this section show how challenging it is to obtain salt finger fluxes from CTD profiles. Apart from the variability introduced by the specific parameterization adopted, the schematization used to represent the interfaces can also affect the nature and quality of the overall results. The different sets of values that we have calculated, however, give an idea of the magnitude of the possible effects of these factors. Of course, this knowledge can be improved upon with more data, especially from microstructure profilers and datasets with a temporal resolution adequate enough to resolve other pertinent processes such as those related to internal waves which are capable of accelerating the redistribution of the properties involved within the water column.

DISCUSSION

We have shown that staircases are very well-defined and persistent over time in the Tyrrhenian Sea, confirming the findings of Durante et al. (2019). Even if there are exceptions, the stratification is predominantly stable inside the layers and generally unstable in the finger sense within the interfaces (**Figure 7**). In the layers, small variations of temperature and salinity can be observed which make the existent stratification locally unstable and drive convective overturning (the gravitationally unstable zones in **Figure 7**). According to Radko (2005), the slight inhomogeneity of the convective strata has a stabilizing effect on a staircase because it tends to suppress possible spontaneous merging events between adjacent layers. As for the interfaces, conformations other than the finger type are present in the stratification there.

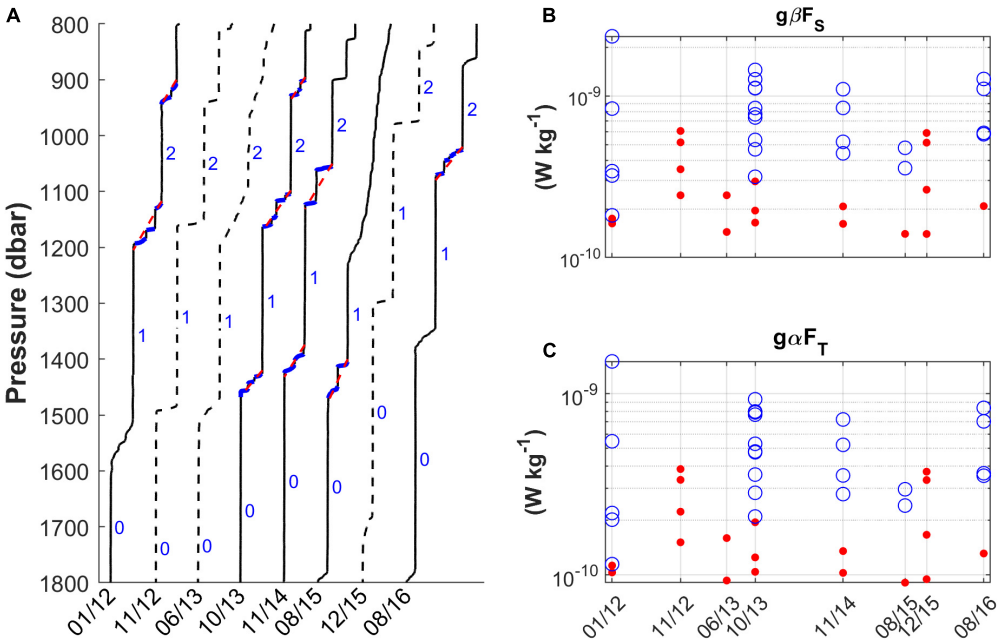

FIGURE 13 | (A) Evolution of the Tyrrhenian staircases between 800 and 1800 dbar from January 2012 to August 2016. Steppy interfaces are delineated in blue. The dashed red lines represent their approximations, with the upper and lower limits demarcated. **(B,C)** Comparison of the estimated contributions of salt and heat to the buoyancy flux (RS12) for the steppy (blue circles) and rectified (solid red circles) interfaces. The axes expressing the fluxes are set to the logarithmic scale.

Since their very first observations in the region (Molcard and Williams, 1975; Williams, 1975), it was evident that the interfaces were not always characterized by one single uniform temperature/salinity gradient. Instead, they could incorporate a varying number of smaller gradient zones for these properties. Linden (1978) explained this sub-structure by hypothesizing that it was due to salt fingers out of equilibrium, unlike those in the sharp interfaces which are always in equilibrium with the convective motions of the surrounding layers. He was able to reproduce this type of salt fingers in the laboratory verifying that thin subsidiary interfaces and layers can form in a thick interface through finger convection alone. Stepped interfaces thus indicate enhanced transfer of properties between adjacent layers (as in **Figure 13**), which occurs through the development and breakdown of the salt finger field. So, they can be considered as hot spots for mixing. In terms of the fluxes, such interfaces are the result of the adjustment of the system to the equilibrium state: when the gradients are higher, the fluxes are large, and the interface tends to become thinner to accommodate them; similarly, when the gradients are low, the fingers need to lengthen to provide the fluxes needed to maintain overall stability. The Tyrrhenian staircases, therefore, change over time, as our dataset shows. However, while the shapes and the number of layers and interfaces of the staircases can vary, their core part remains coherent in all the observations (**Figure 3**). Our profile in the period 2003–2007 revealed a persistent layer – the thickest of those present – centered around 2000 m. After 2010, this layer migrated slightly upward when additional homogenous layers developed below it. The displacement corresponds to an intrusion of nWMDW near the bottom, as highlighted in Durante et al. (2019), which introduced an additional demand for salt and heat fluxes to sustain overall stability. Also, from 2010 onward, we noticed an intensification of the vertical fluxes of heat and salt in terms of both size as well as distribution along the water column. This coincides with the increase in the salt and heat content of the LIW over the last decade (Durante et al., 2019; Schroeder et al., 2020). The analysis of the trends in the temperature and salinity of the thicker layers of the staircases showed that, on average, they follow the patterns of the trends of these properties reported for the LIW.

The transfers of salt and heat through a staircase modulate its structure. Interfaces and layers change continuously to accommodate them, thereby ensuring a general balance and a lingering stability. However, there are indications that other processes may interfere, such as the passage of internal gravity waves generated by the interaction of tidal currents and rough topography (Holloway and Merrifield, 1999; Nycander, 2005). These waves are able to travel great distances from the point of generation before breaking and transferring energy to small scales (Alford, 2003). The southern Tyrrhenian Sea is home to a large number of seamounts (Rovere et al., 2015), which could be the origin of the waves affecting the staircases under study. The analysis of the temporal evolution of the profiles has allowed the detection of signs of the presence of the related periodic motions. However, our sampling frequency is inadequate to resolve them, so we are unable to assess their role. Besides reshaping the staircase, internal waves can also contribute significantly to mixing. This topic needs further study and measurements. The observation of the internal wave signals

in our profiles is apparently in contrast with the result of Buffett et al. (2017) who, measuring the internal wave field by seismic oceanography, found that such waves were only weakly present at the depth levels generally corresponding to the centers of the staircases.

The Tyrrhenian staircases redistribute heat and salt downward, retaining most of what is transferred (**Figure 12**). This is consistent with our observation that the deep layer has seen no increasing trends in temperature and salinity, which, instead, are observed in the central layers of the staircases. The core of the staircases is made up of homogeneous layers, hundreds of meters high, that nevertheless present a distinct developmental pattern. Occasionally, smaller layers which remain for shorter times are added to the major ones. In our data, we found these small layers chiefly at the top and bottom of the main staircases, but it must be said that 30-50 m thick layers were also observed inside steppy interfaces. How long they persist is not deducible from our data due to the low sampling frequency, but they could be an indication of merging events (Radko et al., 2014b). The direct numerical simulations of Ma and Peltier (2021) show that merging is faster in the low gradient regions of a staircase than in the high gradient ones, and takes approximately 2 years to reach the equilibrium state. They have suggested that it would probably take longer in the real ocean.

Calculating salt and heat fluxes from hydrological data is challenging because the results can vary depending on the method adopted. In this study, we used three methods, H88, RS12 and MP21. RS12 and MP21 give very similar results, so we consider them to be comparable and utilize the RS12 estimates only in our deliberation here. The heat and salt fluxes obtained with RS12 differ from those estimated using H88 by a factor of 5 or 6. Furthermore, the values generally provided by RS12 were on the order of 10^{-10} W kg^{-1} whereas those of H88 were an order lower. This difference had already been noted by Falco et al. (2016) when they made similar calculations using profiles acquired north-west of our station, near the boundary of the area affected by the salt fingers shown in **Figure 1**. Their farthest offshore station is 146 km away from ours, and therefore subject to different dynamics and conditions of stratification. Furthermore, they report measurements made in the month of November in 2006 and 2010. Despite these differences, we tried comparing our results for the flux calculations obtained with observations from October 2006 and December 2010 against theirs for November 2006 and 2010. The estimates were in good agreement for 2010 but not for 2006, when our fluxes were around five times lower. It must be said that their station, unlike ours, is directly affected by the circulation path of the LIW, whose core seasonally spreads laterally also. So, it is very possible that their measurements are more influenced by the LIW.

We have also compared our results with those of Zodiatis and Gasparini (1996). They had directly applied Kunze's (1987) parameterization for calculating fluxes to hydrological measurements made in April 1992 at the same station as ours (i.e., eleven years before our first profile). Their fluxes are about double of what we get with H88 and one-third of those we obtain with RS12. Considering their method, we would have expected their results to match ours with H88 more closely. However, it should be specified that they don't use the H88 parameterizations and do not provide details on how they calculated some of the coefficients of the Kunze (1987) equations, which depend not only on temperature and salinity but also on the vertical velocity.

From these comparisons, we conclude that it is not possible to infer whether H88 or RS12 provides better results. Only direct measurements of the fluxes or the eddy diffusivities of heat and salt can resolve this question. The first microstructure observations in our area were recently published by Ferron et al. (2021), who present 5 profiles inherent to our stations collected in the period 2013–2014. The estimates they give for the heat and salt fluxes support the case for considering that RS12 is more reliable in performing these calculations than H88 (**Figures 5A,B**). Their mean values are $F_T = (14.0 \pm 10\%) \times 10^{-8}$ °C m s^{-1} and $F_S = (6.02 \pm 9\%) \times 10^{-8}$ g kg^{-1} m s^{-1}. Our corresponding mean values (with standard deviations) obtained with RS12 from 3 CTD profiles collected in the same period are $F_T = (7 \pm 5) \times 10^{-8}$ °C m s^{-1} and $F_S = (3 \pm 2) \times 10^{-8}$ g kg^{-1} m s^{-1}.

As concerns the eddy diffusivities, Ferron et al. (2021) obtained $K_S = 16 \times 10^{-5}$ m^2 s^{-1} and $K_T = 9.8 \times 10^{-5}$ m^2 s^{-1}. From a linear regression carried out using all our data, we obtained $K_S = (6.2 \pm 0.1) \times 10^{-6}$ m^2 s^{-1} and $K_T = (3.56 \pm 0.02) \times 10^{-6}$ m^2 s^{-1} with H88 and $K_S = (3.80 \pm 0.09) \times 10^{-5}$ m^2 s^{-1} and $K_T = (1.92 \pm 0.07) \times 10^{-5}$ m^2 s^{-1} with RS12. Falco et al. (2016), presenting the calculations for K_S only, obtained values for this parameter in the range (1.19–1.66) $\times 10^{-6}$ m^2 s^{-1} for the computation with Kunze (1987) and (3.11–6.31) $\times 10^{-5}$ m^2 s^{-1} with RS12. Onken and Brambilla (2003) evaluated the two eddy diffusivities from analytical expressions expressed as a function of depth obtained from the statistics of R_ρ derived using an extended dataset and a presumed mixing law. For the Tyrrhenian Sea, they found high eddy diffusivities from 400 to 1000 m (the depth to which they had data), and values of (2–5.3) $\times 10^{-5}$ m^2 s^{-1} and (1–1.5) $\times 10^{-5}$ m^2 s^{-1} for K_S and K_T, respectively, which correspond quite well with our RS12 values for the same parameters.

Thus, despite some uncertainty stemming from the comparison with the microstructure observations, we can conclude that the fluxes and eddy diffusivities provided by the RS12 (or MP21) model are probably more robust than those obtained with H88. In any case, regardless of the "exact" values of the fluxes and their related parameters, all the methods provide the same picture of staircase evolution, therefore supporting all our arguments.

CONCLUSION

In this study, we carry forward the analysis initiated by Durante et al. (2019) on the thermohaline staircase system of the Tyrrhenian Sea. We have analyzed the temporal evolution of the staircases, and found that other phenomena besides double diffusion could be important for this system. These include internal gravity waves generated inside the basin and perturbations coming from outside it (e.g., the intrusion of a

new deep water on the bottom which has changed the deep stratification).

We also determine the fluxes of salt and heat by the salt fingers associated with the staircases, establishing them as contributors to the overall vertical mixing. Estimates of the related eddy diffusivities are also presented, which could be used to parameterize the effects of this phenomenon on mixing in ocean circulation models applied to the Mediterranean Sea.

Staircases are usually considered as enhancers of heat and salt fluxes in the open ocean, strongly affecting diapycnal mixing (St. Laurent and Schmitt, 1999; Schmitt et al., 2005) and capable of influencing regional climate and dynamics by contributing significantly to the transformation of water masses (McDougall and Whitehead, 1984; Talley and Yun, 2001). The vertical transport of heat and salt by the Tyrrhenian staircases is recognized as the dominant mechanism for the exchange of properties between the LIW and the deep waters of the Western Mediterranean (Zodiatis and Gasparini, 1996). However, the contributions of other phenomena such as internal waves and the scales connected with them remain open issues that will need to be addressed in the future with the help of suitable measurements.

Another important aspect of the Tyrrhenian staircases that emerges from our study is the way they drive heat and salt downward while continuing to retain most of what is transferred in their cores. This "stored" heat and salt is of course eventually redistributed by horizontal advection – also to neighbouring basins, thereby contributing to the Mediterranean Sea overturning circulation (Pinardi et al., 2019), though we lack the data necessary to demonstrate this. What our data do show is that the staircases tend to block heat and salt fluxes to the deepest layers.

The processes governing the formation and evolution of thermohaline staircases must be taken into account in studies of the Tyrrhenian circulation, and the efficient vertical transport that similar structures permit should be adequately factored into oceanic and climate models where the parameterization of diapycnal mixing continues to be a major uncertainty in assessing the ocean's ability to sequester heat, pollutants, and carbon dioxide (Schmitt et al., 2005).

Merging phenomena occurring within staircases are still poorly understood, but our evidence of the intensification of fluxes in steppy interfaces embedding small layers several tens of meters thick suggests that they could have a greater importance and impact on the diapycnal mixing than previously thought.

It is hoped our analysis will provide fruitful directions for new research. Addressing the inherent uncertainties that continue to dog the determination of salt finger fluxes, also in relation to other possible mixing mechanisms, will require many additional kinds of measurements (such as those on very fine scales, often beyond the capabilities of a standard CTD package) and the reliable quantification of existing vertical shears.

DATA AVAILABILITY STATEMENT

The CTD data that were used in this study are available at https://www.seanoe.org/data/00475/58697/.

AUTHOR CONTRIBUTIONS

SD prepared the data, contributed to data analysis and calculation, and wrote the first version of the manuscript. PO developed the algorithm for interface detection. RN helped to improve the discussion of the results presented, assisted with the critical revisions of the manuscript, and participated in preparing its final version. SS supervised the work, contributed to the data analysis and calculation, and wrote the final version of the manuscript. All authors contributed to the article and approved the submitted version.

ACKNOWLEDGMENTS

We would like to thank all the people who contributed to the creation of the dataset used for this study, in particular Mireno Borghini. We also thank the reviewers for their valuable suggestions and constructive criticism which greatly helped to improve our original manuscript. This work is a follow-up of the Ph.D. dissertation of SD at University Parthenope of Naples.

SUPPLEMENTARY MATERIAL

The Supplementary Material for this article can be found online at: https://www.frontiersin.org/articles/10.3389/fmars.2021.672437/full#supplementary-material

REFERENCES

Alford, M. (2003). Redistribution of energy available for ocean mixing by long-range propagation of internal waves. *Nature* 423, 159–162. doi: 10.1038/nature01628

Astraldi, M., and Gasparini, G. P. (1994). "The seasonal characteristics of the circulation in the Tyrrhenian Sea," in *Seasonal and interannual variability of the Western Mediterranean Sea*, ed. E. La Viollette (Washington, DC: American Geophysical Union). doi: 10.1029/CE046p0115

Béranger, K., Mortier, L., Gasparini, G.-P., Gervasio, L., Astraldi, M., and Crépon, M. (2004). The dynamics of the Sicily Strait: a comprehensive study from observations and models. *Deep Sea Res. Part II Top. Stud. Oceanogr.* 51, 411–440. doi: 10.1016/j.dsr2.2003.08.004

Borghini, M., Bryden, H. L., Schroeder, K., Sparnocchia, S., and Vetrano, A. (2014). The Mediterranean is becoming saltier. *Ocean Sci.* 10, 693–700.

Borghini, M., Durante, S., Ribotti, A., Schroeder, K., and Sparnocchia, S. (2019). *Thermohaline Staircases in the Tyrrhenian Sea Experimental dataset (2003-2016)*. SEANOE. Available online at: https://www.seanoe.org/data/00475/58697/ (accessed September 2, 2021).

Bryden, H., Schroeder, K., Borghini, M., Vetrano, A., and Sparnocchia, S. (2014). "Mixing in the deep waters of the western Mediterranean," in *The Mediterranean Sea: Temporal Variability and Spatial Patterns: AGU Geophysical Monograph Series*, Vol. 202, eds G. L. E. Borzelli, M. Gacic, P. Lionello, and M. P.

Rizzoli (Oxford: John Wiley & Sons, Inc.), 51–58. doi: 10.1002/9781118847572.ch4

Budillon, G., Gasparini, G. P., and Schroeder, K. (2009). Persistence of an eddy signature in the Central Tyrrhenian Basin. *Deep Sea Res. Part II* 56, 713–724. doi: 10.1016/j.dsr2.2008.07.027

Buffett, G. G., Krahmann, G., Klaeschen, D., Schroeder, K., Sallarès, V., Papenberg, C., et al. (2017). Seismic oceanography in the Tyrrhenian Sea: thermohaline staircases, eddies, and internal waves. *J. Geophys. Res. Oceans* 122, 8503–8523. doi: 10.1002/2017JC012726

Durante, S., Schroeder, K., Mazzei, L., Pierini, S., Borghini, M., and Sparnocchia, S. (2019). Permanent thermohaline staircases in the Tyrrhenian Sea. *Geophys. Res. Lett.* 46, 1562–1570. doi: 10.1029/2018GL081747

Falco, P., Trani, M., and Zambianchi, E. (2016). Water mass structure and deep mixing processes in the Tyrrhenian Sea: results from the VECTOR project. *Deep Sea Res. I* 113, 7–21. doi: 10.1016/j.dsr.2016.04.002

Ferron, B., Bouruet-Aubertot, P., Schroeder, K., Bryden, H. L., Cuypers, Y., and Borghini, M. (2021). Contribution of thermohaline staircases to deep water mass modifications in the western Mediterranean sea from microstructure observations. *Front. Mar. Sci.* 8:664509. doi: 10.3389/fmars.2021.664509

Fuda, J.-L., Etiope, G., Millot, C., Favali, P., Calcara, M., Smriglio, G., et al. (2002). Warming, salting and origin of the Tyrrhenian Deep Water. *Geophys. Res. Lett.* 29:1898.

Garrett, C., and Munk, W. (1975). Space-time scales of internal waves: a progress report. *J. Phys. Oceanogr.* 1, 196–202. doi: 10.1029/JC080i003p00291

GEBCO Bathymetric Compilation Group (2019). *The GEBCO_2019 Grid - A Continuous Terrain Model of the Global Oceans and Land*. Southampton: British Oceanographic Data Centre, National Oceanography Centre, NERC.

Gregg, M. C., and Sanford, T. B. (1987). Shear and turbulence in thermohaline staircases. *Deep Sea Research* 34, 1689–1696. doi: 10.1016/0198-0149(87)90017-3

Hebert, D. (1988). Estimates of salt-finger fluxes. *Deep Sea Res. A* 35, 1887–1901. doi: 10.1016/0198-0149(88)90115-X

Holloway, P. E., and Merrifield, M. A. (1999). Internal tide generation by seamounts, ridges, and islands. *J. Geophys. Res.* 104, 25937–25951. doi: 10.1029/1999JC900207

Holyer, J. Y. (1984). The stability of long, steady, two-dimensional salt fingers. *J. Fluid Mech.* 147, 169–185. doi: 10.1017/S0022112084002044

Hopkins, T. S. (1988). Recent observations on the intermediate and deep water circulation in the Southern Tyrrhenian Sea. *Oceanologica Acta, Special Issue* 9, 41–50.

IOC, SCOR, and IAPSO (2010). *The International Thermodynamic Equation of Seawater – 2010: Calculation and Use of Thermodynamic Properties.* Intergovernmental Oceanographic Commission, Manuals and Guides No. 56. Paris: UNESCO, 196.

Jackett, D. R., McDougall, T. J., Feistel, R. D., Wright, G., and Griffies, S. M. (2006). Algorithms for density, potential temperature, Conservative Temperature and freezing temperature of seawater. *J. Atmos. Ocean. Technol.* 23, 1709–1728. doi: 10.1175/JTECH1946.1

Johannessen, O. M., and Lee, O. S. (1972). "A deep stepped thermohaline structure deep in the Mediterranean," in *Proceedings of the SACLANTCEN Conference Proceedings*, Vol. 7, 126–143. Available online at: http://hdl.handle.net/20.500.12489/582 (accessed September 2, 2021).

Johannessen, O. M., and Lee, O. S. (1974). A deep stepped thermo-haline structure in the Mediterranean. *Deep Sea Res. Oceanogr. Abstr.* 21, 629–639. doi: 10.1016/0011-7471(74)90047-3

Kunze, E. (1987). Limits on growing, finite-length salt fingers: a Richardson number constraint. *J. Mar. Res.* 45, 533–556. doi: 10.1357/002224087788326885

Linden, P. F. (1973). On the structure of salt fingers. *Deep Sea Res.* 20, 325–340. doi: 10.1016/0011-7471(73)90057-0

Linden, P. F. (1978). The formation of banded salt finger structure. *J. Geophys. Res.* 83, 2902–2912. doi: 10.1029/JC083iC06p02902

Lueck, R. G. (1987). Microstructure measurements in a thermohaline staircase. *Deep Sea Res.* 34, 1677–1688. doi: 10.1016/0198-0149(87)90016-1

Ma, Y., and Peltier, W. R. (2021). Gamma instability in an inhomogeneous environment and salt-fingering staircase trapping: determining the step size. *Phys. Rev. Fluids* 6:033903. doi: 10.1103/PhysRevFluids.6.033903

McDougall, T. J., and Barker, P. M. (2011). Getting Started with TEOS-10 and the Gibbs Seawater (GSW) Oceanographic Toolbox: SCOR/IAPSO WG127, ISBN 978-0-646-55621-5. 28. Available at: http://www.teos-10.org/pubs/Getting_Started.pdf (accessed September 2, 2021).

McDougall, T. J., and Taylor, J. R. (1984). Flux measurements across a finger interface at low values of the stability ratio. *J. Mar. Res.* 42, 1–14. doi: 10.1357/002224084788506095

McDougall, T. J., and Whitehead, J. A. (1984). Estimates of the relative roles of diapycnal, isopycnal and double-diffusive mixing in Antarctic Bottom Water in the North Atlantic. *J. Geophys. Res.* 89, 10479–10483. doi: 10.1029/JC089iC06p10479

Meccia, V. L., Simoncelli, S., and Sparnocchia, S. (2016). Decadal variability of the Turner angle in the Mediterranean Sea and its implications for double diffusion. *Deep Sea Res. I* 114, 64–77. doi: 10.1016/j.dsr.2016.04.001

Merryfield, W. J. (2000). Origin of thermohaline staircases. *J. Phys. Oceanogr.* 30, 1046–1068.

Millero, F. J., Feistel, R., Wright, D. G., and McDougall, T. J. (2008). The composition of Standard Seawater and the definition of the Reference-Composition Salinity Scale. *Deep Sea Res. Part I Oceanogr. Res. Pap.* 55, 50–72. doi: 10.1016/j.dsr.2007.10.001

Millot, C., and Taupier-Letage, I. (2005). "Circulation in the Mediterranean Sea," in *The Handbook of Environmental Chemistry: Water Pollution*, Vol. 5K, ed. A. Saliot (Berlin: Springer), 29–66. doi: 10.1007/b107143

Molcard, R., and Williams, A. J. III (1975). Deep stepped structure in the Tyrrhenian Sea. *Mém. Soc. R. Sci. Liège* 6, 191–210.

Munk, W. H., and Wunsch, C. I. (1998). Abyssal recipes. II: energetics of tidal and wind mixing. *Deep Sea Res. Part I* 45, 1977–2010.

Nayar, K. G., Sharqawy, M. H., Banchik, L. D., and Lienhard, J. H. V. (2016). Thermophysical properties of seawater: a review and new correlations that include pressure dependence. *Desalination* 390, 1–24. doi: 10.1016/j.desal.2016.02.024

Nycander, J. (2005). Generation of internal waves in the deep ocean by tides. *J. Geophys. Res* 110:C10028. doi: 10.1029/2004JC002487

Onken, R., and Brambilla, E. (2003). Double diffusion in the Mediterranean Sea: observation and parameterization of salt finger convection. *J. Geophys. Res.* 108:8124. doi: 10.1029/2002JC001349

Pinardi, N., Cessi, P., Borile, F., and Wolfe, W. C. (2019). The Mediterranean Sea overturning circulation. *J. Phys. Oceanogr.* 49, 1699–1721. doi: 10.1175/JPO-D-18-0254.1

Radko, T. (2003). A mechanism for layer formation in a double-diffusive fluid. *J. Fluid Mech.* 497, 365–380. doi: 10.1017/S0022112003006785

Radko, T. (2005). What determines the thickness of layers in a thermohaline staircases? *J. Fluid Mech.* 523, 79–98. doi: 10.1017/S0022112004002290

Radko, T., and Smith, D. P. (2012). Equilibrium transport in double-diffusive convection. *J. Fluid Mech.* 692, 5–27. doi: 10.1017/jfm.2011.343

Radko, T., Bulters, A., Flanagan, J. D., and Campin, J.-M. (2014a). Double-Diffusive recipes. Part I: large-scale dynamics of thermohaline staircases." *J. Phys. Oceanogr.* 44, 1269–1284. doi: 10.1175/JPO-D-13-0155.1

Radko, T., Flanagan, J. D., Stellmach, S., and Timmermans, M.-L. (2014b). Double-diffusive recipes. Part II: layer -merging events. *J. Phys. Oceanogr.* 44, 1285–1305.

Rovere, M., Bo, M., Alessi, J., Paoli, C., Fiori, C., and Roccatagliata, N. (2015). "Seamounts and Seamount-Like Structures of the Tyrrhenian," in *SeaAtlas of the Mediterranean Seamounts and Seamount-Like Structures*, eds M. Würtz and M. Rovere (Gland: IUCN).

Ruddick, B. (1983). A practical indicator of the stability of the water column to double-diffusive activity. *Deep Sea Res.* 30, 1105–1107. doi: 10.1016/0198-0149(83)90063-8

Schmitt, R. W. (1979). Flux measurements on salt fingers at an interface. *J. Mar. Res.* 37, 419–436.

Schmitt, R. W. (1981). Form of the temperature-salinity relationship in the Central Water: evidence for double-diffusive mixing. *J. Phys. Oceanogr.* 11, 1015–1026.

Schmitt, R. W. (1988). "Mixing in a thermohaline staircase," in *Small-Scale Turbulence and Mixing in the Ocean: Elsevier Oceanography Series*, Vol. 46, eds J. C. J. Nihoul and B. M. Jamart (Amsterdam: Elsevier Science Publishers), 435–452. doi: 10.1016/S0422-9894(08)70563-4

Schmitt, R. W., Ledwell, J. R., Montgomery, E. T., Polzin, K. L., and Toole, J. M. (2005). Enhanced diapycnal mixing by salt fingers in the thermocline of the tropical Atlantic. *Science* 308, 685–688. doi: 10.1126/science.1108678

Schmitt, R. W., Perkins, H., Boyd, J. D., and Stalcup, M. C. (1987). C-SALT: an investigation of the thermohaline staircase in the western tropical North Atlantic. *Deep Sea Res. Part A* 34:10. doi: 10.1016/0198-0149(87)90014-8

Schroeder, K., Chiggiato, J., Bryden, H. L., Borghini, M., and Ben Ismail, S. (2016). Abrupt climate shift in the Western Mediterranean Sea. *Sci. Rep.* 6:23009. doi: 10.1038/srep23009

Schroeder, K., Chiggiato, J., Josey, S. A., Borghini, M., Aracri, S., and Sparnocchia, S. (2017). Rapid response to climate change in a marginal sea. *Sci. Rep.* 7:4065. doi: 10.1038/s41598-017-04455-5

Schroeder, K., Cozzi, S., Belgacem, M., Borghini, M., Cantoni, C., Durante, S., et al. (2020). Along-Path evolution of biogeochemical and carbonate system properties in the intermediate water of the Western Mediterranean. *Front. Mar. Sci.* 7:375. doi: 10.3389/fmars.2020.00375

Schroeder, K., Ribotti, A., Borghini, M., Sorgente, R., Perilli, A., and Gasparini, G. P. (2008). An extensive western Mediterranean deep water renewal between 2004 and 2006. *Geophys. Res. Lett.* 35:L18605. doi: 10.1029/2008GL035146

Sharqawy, M. H., Lienhard, J. H. V., and Zubair, S. M. (2010). Thermophysical properties of seawater: a review of existing correlations and data. *Desalination Water Treat.* 16, 354–380. doi: 10.5004/dwt.2010.1079

Sparnocchia, S., and Borghini, M. (2019). Cruise PRIMO93 (CNR IT): Hydrographic Measurements in the Sicily Channel and in the Southern Tyrrhenian Sea, 1993. Sea scientific open data publication. Available online at: https://www.seanoe.org/data/00486/59802/ (accessed September 2, 2021).

Sparnocchia, S., Gasparini, G. P., Astraldi, M., Borghini, M., and Pistek, P. (1999). Dynamics and mixing of the Eastern Mediterranean outflow in the Tyrrhenian basin. *J. Mar. Syst.* 20, 301–317. doi: 10.1016/S0924-7963(98)00088-8

St. Laurent, L., and Schmitt, R. W. (1999). The contribution of salt fingers to vertical mixing in the North Atlantic tracer release experiment. *J. Phys. Oceanogr.* 29, 1404–1424.

Stern, M. E. (1969). Collective instability of salt fingers. *J. Fluid Mech.* 35, 209–218. doi: 10.1017/S0022112069001066

Taillandier, V., Prieur, L., D'Ortenzio, F., Ribera d'Alcalà, M., and Pulido-Villena, E. (2020). Profiling float observation of thermohaline staircases in the western Mediterranean Sea and impact on nutrient fluxes. *Biogeosciences* 17, 3343–3366. doi: 10.5194/bg-17-3343-2020

Talley, L. N., and Yun, J. Y. (2001). The role of cabbeling and double diffusion in setting the density of the North Pacific Intermediate Water salinity minimum. *J. Phys. Oceanogr.* 31, 1538–1549.

Thyng, K. M., Greene, C. A., Hetland, R. D., Zimmerle, H. M., and DiMarco, S. F. (2016). True colors of oceanography: guidelines for effective and accurate colormap selection. *Oceanography* 29, 9–13. doi: 10.5670/oceanog.2016.66

Turner, J. S. (1967). Salt fingers across a density interface. *Deep Sea Res.* 14, 599–608. doi: 10.1016/0011-7471(67)90066-6

Turner, J. S. (1973). *Buoyancy Effects in Fluids*. Cambridge: Cambridge University Press.

van Haren, H., and Gostiaux, L. (2012). Energy release through internal wave breaking. *Oceanography* 25, 124–131. doi: 10.5670/oceanog.2012.47

Vetrano, A., Napolitano, E., Iacono, R., Schroeder, K., and Gasparini, G. P. (2010). Tyrrhenian Sea circulation and water mass fluxes in spring 2004: observations and model results. *J. Geophys. Res.* 115:C06023. doi: 10.1029/2009JC005680

Williams, A. J. (1975). Images of ocean microstructure. *Deep Sea Res.* 22, 811–829. doi: 10.1016/0011-7471(75)90085-6

Zhurbas, V. M., and Ozmidov, R. V. (1984). Forms of step like structure of the oceanic thermocline and their generation mechanisms. *Oceanology* 24, 153–157.

Zodiatis, G., and Gasparini, G. P. (1996). Thermohaline staircase formations in the Tyrrhenian Sea. *Deep Sea Res. I* 43, 655–678.

Conflict of Interest: The authors declare that the research was conducted in the absence of any commercial or financial relationships that could be construed as a potential conflict of interest.

Publisher's Note: All claims expressed in this article are solely those of the authors and do not necessarily represent those of their affiliated organizations, or those of the publisher, the editors and the reviewers. Any product that may be evaluated in this article, or claim that may be made by its manufacturer, is not guaranteed or endorsed by the publisher.

Advantages of publishing in Frontiers

OPEN ACCESS
Articles are free to read for greatest visibility and readership

FAST PUBLICATION
Around 90 days from submission to decision

HIGH QUALITY PEER-REVIEW
Rigorous, collaborative, and constructive peer-review

TRANSPARENT PEER-REVIEW
Editors and reviewers acknowledged by name on published articles

Frontiers
Avenue du Tribunal-Fédéral 34
1005 Lausanne | Switzerland

Visit us: www.frontiersin.org
Contact us: frontiersin.org/about/contact

REPRODUCIBILITY OF RESEARCH
Support open data and methods to enhance research reproducibility

DIGITAL PUBLISHING
Articles designed for optimal readership across devices

FOLLOW US
@frontiersin

IMPACT METRICS
Advanced article metrics track visibility across digital media

EXTENSIVE PROMOTION
Marketing and promotion of impactful research

LOOP RESEARCH NETWORK
Our network increases your article's readership